POLITECHNIKA RZESZOWSKA

im. Ignacego Łukasiewicza

WYDZIAŁ CHEMICZNY

PRACA DOKTORSKA

OPRACOWANIE I OPTYMALIZACJA METOD OBRAZOWANIA SPEKTROMETRIĄ MAS DO ANALIZY ZWIĄZKÓW MAŁOCZĄSTECZKOWYCH

mgr inż. Sumi Krupa

Promotor pracy:
dr hab. Joanna Nizioł, prof. PRz

Rzeszów, 2026

Pragnę serdecznie podziękować mojej promotor

Pani dr hab. Joannie Nizioł, prof. PRz

za możliwość udziału w realizacji projektu,
przekazaną wiedzę i doświadczenie oraz ciągłą motywację do dalszej pracy,
jak również za cierpliwość okazaną mi podczas realizacji doktoratu.

Serdecznie dziękuję

Panu prof. dr hab. Tomaszowi Rumanowi, prof. PRz

za możliwość rozwoju naukowego i wsparcie w realizacji badań
oraz ogrom uzyskanej wiedzy i doświadczenia.

Dziękuję za współpracę i nieocenioną pomoc
pracownikom Katedry Chemii Nieorganicznej i Analitycznej, w szczególności
dr mgr inż. Anecie Płazie-Altamer oraz dr mgr inż. Arturowi Kołodziejowi
za ciągłe wsparcie i gotowość do pomocy.

.

NARODOWE CENTRUM NAUKI

Rozprawa doktorska została opracowana w wyniku realizacji projektu NCN SONATA BIS 12 „System do obrazowania spektrometrią mas w trzech wymiarach (3D MSI)” (nr 2022/46/E/ST4/00016).

Spis treści

Wykaz stosowanych skrótów

^{109}AgNPs	nanocząstki srebra-109 (ang. silver-109 nanoparticles)
^{109}AgNPs-LDI	laserowa desorpcja/jonizacja wspomagana nanocząstkami srebra-109 (z ang. silver-109 nanoparticles assisted laser desorption/ionization)
APCI	jonizacja chemiczna pod ciśnieniem atmosferycznym (z ang. atmospheric pressure chemical ionization)
APPI	fotojonizacja pod ciśnieniem atmosferycznym (z ang. atmospheric pressure photoionization)
AuNPs	nanocząstki złota (ang. gold nanoparticles)
AuNPs-LDI	laserowa desorpcja/jonizacja wspomagana nanocząstkami złota (z ang. gold nanoparticles assisted laser desorption/ionization)
bbCID	szerokopasmowa dysocjacja indukowana zderzeniami(z ang. broadband collision induced dissociation)
DA-APPI	fotojonizacja pod ciśnieniem atmosferycznym wspomagana dopantem (z ang. dopant-assisted-atmospheric pressure photoionization)
DDA	tryb akwizycji zależny od danych (z ang. data dependent acquisition)
DESI	desorpcja/jonizacja elektrorozpylaniem (z ang. desorption electrospray ionization)
DIA	tryb akwizycji niezależny od danych (z ang. data independent acquisition)
DOE	optyczny element dyfrakcyjny (z ang. diffractive optical element)
EI	jonizacja elektronowa (z ang. electron ionisation)
ESI	jonizacja elektrorozpylaniem (z ang. electrospray ionization)
FFPE	utrwalone w formalinie i zatopione w parafinie (z ang. formalin-fixed paraffin-embedded)

GC-MS	chromatografia gazowa sprzężona ze spektrometrią mas (z ang. gas chromatography-mass spectrometry)
IR	podczerwień (z ang. infrared)
ITO	tlenek indowo-cynowy (z ang. indium tin oxide)
LA	ablacja laserowa (z ang. laser ablation)
LAESI	laserowa ablacja z jonizacją elektrorozpylaniem (z ang. laser ablation electrospray ionization)
LARAPPI/CI	laserowa ablacja ze zdalną fotojonizacją/jonizacją chemiczną pod ciśnieniem atmosferycznym (z ang. laser ablation remote atmospheric pressure photoionization/chemical ionization)
LARESI	laserowa ablacja ze zdalną jonizacją elektrorozpylaniem (z ang. laser ablation-remote electrospray ionization)
LASiS	synteza poprzez ablację laserową w roztworze (z ang. laser ablation synthesis in solution)
LC-MS	chromatografia cieczowa sprzężona ze spektrometrią mas (z ang. liquid chromatography-mass spectrometry)
LIDT	próg uszkodzenia indukowanego promieniowaniem laserowym (z ang. laser-induced damage threshold)
LLOQ	dolna granica oznaczalności (z ang. lower limit of quantification)
LOD	granica wykrywalności (z ang. limit of detection)
LOQ	granica oznaczalności (z ang. limit of quantification)
MALDI	laserowa desorpcja/jonizacja wspomagana matrycą (z ang. matrix-assisted laser desorption/ionization)
MS	spektrometria mas (z ang. mass spectrometry)
MSI	obrazowanie spektrometrią mas (z ang. mass spectrometry imaging)
nanoPALDI	laserowa desorpcja/jonizacja wspomagana nanocząstkami (z ang. nanoparticle assisted laser desorption/ionization)

NMR	magnetyczny rezonans jądrowy (z ang. nuclear magnetic resonance)
OCT	optymalna temperatura cięcia (z ang. optimal cutting temperature)
QToF	kwadrupol sprzężony z analizatorem mas typu czasu przelotu (z ang. quadrupole-time of flight)
S/N	stosunek intensywności sygnału do szumu (z ang. signal-to-noise)
SALDI	laserowa desorpcja/jonizacja wspomagana powierzchnią (z ang. surface-assisted laser desorption/ionization)
SIMS	spektrometria mas jonów wtórnych (z ang. secondary ion mass spectrometry)
SRM	monitorowanie wybranych reakcji fragmentacji (z ang. selected reaction monitoring)
TLC	chromatografia cienkowarstwowa (z ang. thin-layer chromatography)
UHPLC	ultrasprawna chromatografia cieczowa (z ang. ultra-high performance liquid chromatography)
UHRMS	ultrawysokorozdzielcza spektrometria mas (z ang. ultra-high resolution mass spectrometry)
VIP-HESI	jonizacja elektrorozpylaniem z podgrzewaniem gazu desolwatacyjnego i sondą izolowaną próżniowo (z ang. vacuum insulated probe-heated electrospray ionization**)**
VUV	próżniowy nadfiolet (z ang. vacuum ultraviolet)

Wprowadzenie

Analityka związków małocząsteczkowych jest kluczowa dla zrozumienia procesów biologicznych, diagnostyki medycznej, rozwoju leków, ochrony środowiska, bezpieczeństwa żywności, a także innowacji oraz rozwoju nowoczesnych technologii, stanowiąc fundament wielu dziedzin nauki i przemysłu. Konwencjonalne metody analizy związków małocząsteczkowych oparte na homogenizacji lub ekstrakcji próbki nie dostarczają informacji o przestrzennym rozmieszczeniu związków chemicznych w badanym obiekcie. Tradycyjne metody obrazowania oparte na znakowaniu, w tym mikroskopia fluorescencyjna pozwalają na wizualizację wybranych struktur lub cząsteczek z wysoką specyficznością i rozdzielczością przestrzenną, są jednak ograniczone przez dostępność specyficznych przeciwciał lub znaczników. W związku z tym, możliwa jest detekcja ograniczonej liczby związków w jednej analizie. Metody obrazowania spektrometrią mas (MSI) pozwalają na uzyskanie informacji o rozmieszczeniu, w zależności od typu preparatu i parametrów analitycznych, setek związków w próbce bez potrzeby ich znakowania [1]. Informacje te mogą zostać wykorzystane jako narzędzie do analizy potencjalnych biomarkerów chorobowych, szczególnie nowotworowych, metabolizmu leków, oraz profilowania metabolomicznego i lipidomicznego [2]. Najczęściej wykorzystywane w analizie związków małocząsteczkowych techniki MSI to laserowa desorpcja/jonizacja wspomagana matrycą (MALDI) [3], desorpcja/jonizacja elektrorozpylaniem (DESI) [4] i spektrometria mas jonów wtórnych (SIMS) [5]. Niektóre techniki wykorzystują ablację laserową aby umożliwić rejestrację danych o rozmieszczeniu związków w analizach MSI, np. laserowa ablacja z jonizacją elektrorozpylaniem (LAESI) [6].

Metody MSI pozwalające na wizualizację przestrzennego rozmieszczenia związków chemicznych w trzech wymiarach (3D-MSI) zwykle przedstawiają rekonstrukcję wykonaną na podstawie wyników 2D-MSI serii kolejnych skrawków tego samego obiektu [7]. Analizy 3D-MSI związków małocząsteczkowych w serii kolejnych skrawków opisane w literaturze wykonane zostały m.in. przy użyciu techniki MALDI oraz DESI [8]. Alternatywnym podejściem w 3D-MSI jest usuwanie materiału w głąb wybranego obszaru próbki nazywane profilowaniem wgłębnym. Ta metoda jest szczególnie szeroko stosowana w obrazowaniu 3D z wykorzystaniem techniki SIMS [9,10]. Podejścia te są jednak obarczone istotnymi ograniczeniami wynikającymi z wieloetapowego przygotowania próbek, podatności na powstawanie artefaktów analitycznych oraz konieczności kompromisu pomiędzy rozdzielczością przestrzenną a zakresem analizowanego obszaru, co wskazuje na brak efektywnych metod bezpośredniego obrazowania 3D związków małocząsteczkowych.

Tematyka badań zrealizowanych w ramach niniejszej rozprawy doktorskiej skupia się na optymalizacji aparatury oraz jej walidacji w celu opracowania metody MSI w trzech wymiarach. Prace optymalizacyjne miały na celu opracowanie metody 3D-MSI pozwalającej na analizę obiektów biologicznych o wymiarach do kilkudziesięciu milimetrów i wizualizację rzeczywistego rozmieszczenia związków małocząsteczkowych w tkankach. Badania obejmowały również analizy różnorodnych obiektów biologicznych, takich jak tkanki zwierzęce, ludzkie oraz hodowle mikrobiologiczne. Prace badawcze miały na celu rozwój technik MSI, które umożliwiają dokładniejsze i bardziej kompleksowe analizy w kontekście metabolomiki. Wynikiem prowadzonych badań jest zbiór publikacji, stanowiący podstawę niniejszej rozprawy doktorskiej.

Przedstawiona tematyka badawcza jest jednocześnie wyraźnie związana z dyscypliną inżynieria chemiczna. Związek ten wynika nie tylko z analitycznego charakteru prowadzonych badań, lecz przede wszystkim z konieczności projektowania, rozwoju i walidacji złożonego układu analityczno-pomiarowego oraz z optymalizacji parametrów procesu ablacji, desorpcji i jonizacji. Istotnym elementem pracy była również analiza zależności pomiędzy parametrami pracy układu a jakością i powtarzalnością uzyskiwanych danych. Związek z inżynierią chemiczną wzmacniają także badania dotyczące technologii otrzymywania nanocząstek srebra-109 i złota jako materiałów wspomagających proces desorpcji i jonizacji w technikach LDI-MS/MSI, obejmujące dobór sposobu ich wytwarzania oraz ocenę wpływu ich właściwości fizykochemicznych na efektywność procesu analitycznego. Całość sytuuje rozprawę w obszarze nowoczesnych badań inżynieryjno-technicznych prowadzonych na styku chemii analitycznej, nanotechnologii i inżynierii chemicznej z elementami najnowszych technologii optycznych.

Wykaz publikacji wchodzących w skład cyklu publikacji stanowiącego rozprawę doktorską

[P1] J. Nizioł, **S. Krupa**, W. Szuberla, T. Ruman**,** Advances in metallic nanostructures-assisted laser desorption/ionization mass spectrometry imaging of biological samples: A review, *Analytica Chimica Acta,* **2025**, 1366, 344256 (IF = 6.0, MNiSW = 100)

[P2] A. Płaza-Altamer, A. Kołodziej, **S. Krupa**, J. Nizioł, T. Ruman, Infrared pulsed fiber laser-produced gold and silver-109 nanoparticles for laser desorption/ionization mass spectrometry of steroid hormones, *Rapid Communications in Mass Spectrometry,* **2023**, 37, e9621 (IF = 1.7, MNiSW = 70)

[P3] S. Krupa, J. Nizioł, Fiber Laser-Generated Silver-109 Nanoparticles for Laser Desorption/Ionization Mass Spectrometry of Illicit Drugs, *Journal of the American Society for Mass Spectrometry,* **2024**, 35, 1156-1167 (IF = 2.7, MNiSW = 70)

[P4] J. Nizioł, M. Misiorek, **S. Krupa**, T. Ruman, Infrared Laser-Based Selected Reaction Monitoring Mass Spectrometry Imaging of Banana (Musa spp.) Tissue—New Method for Detection and Spatial Localization of Metabolites in Food, Food Analytical Methods, **2023**, 17, 236-250 (IF = 3.0, MNiSW = 70)

[P5] T. Ruman, **S. Krupa**, J. Nizioł, Direct Three-Dimensional Mass Spectrometry Imaging with Laser Ablation Remote Atmospheric Pressure Photoionization/Chemical Ionization, *Analytical Chemistry,* **2024**, 96, 13326-13334 (IF = 6.7, MNiSW = 140)

[P6] S. Krupa, W. Szuberla, J. Nizioł, A. Ossolińska, K. Ossoliński, T. Ruman, Broadband collision-induced dissociation mass spectrometry imaging, *Journal of the American Society for Mass Spectrometry,* **2025**, 36, 1443-1455 (IF = 2.7, MNiSW = 70)

[P7] J. Szulc, T. Grzyb, J. Nizioł, **S. Krupa**, W. Szuberla, T. Ruman, Direct 3D Mass Spectrometry Imaging Analysis of Environmental Microorganisms, *Molecules*, **2025**, 30, 1317 (IF = 4.6, MNiSW = 140)

[P8] S. Krupa, T. Ruman, J. Nizioł, Metabolic Impact of Pesticides on Radish: 2D and 3D Mass Spectrometry Imaging of Metabolites in *Raphanus sativus, Journal of Agricultural and Food Chemistry,* **2025**, 73, 29229-29244 (IF = 6.2, MNiSW = 140)

[P9] S. Krupa, T. Ruman, W. Szuberla, J. Nizioł, Analysis of the spatial distribution of metabolites in *Aloe vera* leaves by mass spectrometry imaging and UHPLC-UHRMS, *Scientific Reports*, **2025**, 15, 3502 (IF = 3.9, MNiSW = 140)

Łącznie: IF = 37,5 MNiSW = 940

1. Wstęp teoretyczny

1.1. Analiza związków małocząsteczkowych

Za związki małocząsteczkowe przyjmowane są powszechnie związki o masie nie większej niż 1500 Da [11,12]. Są nimi m.in. aminokwasy, kwasy organiczne, monosacharydy, lipidy, wtórne metabolity roślinne, a także niektóre leki. Analiza tych związków jest podstawą badań z zakresu metabolomiki. Metody analityczne stosowane do identyfikacji i charakterystyki strukturalnej związków małocząsteczkowych w metabolomice i dyscyplinach pokrewnych (takich jak lipidomika czy toksykologia) obejmują przede wszystkim chromatografię cieczową sprzężoną ze spektrometrią mas (LC-MS), chromatografię gazową sprzężoną ze spektrometrią mas (GC-MS), oraz spektroskopię magnetycznego rezonansu jądrowego (NMR). Techniki te opierają się na odmiennych zjawiskach fizykochemicznych co determinuje różnice w ich czułości, selektywności oraz zakresie zastosowań w analizie różnych klas metabolitów.

GC-MS jest szeroko stosowana do analizy lotnych i średniolotnych związków małocząsteczkowych, w tym estrów, eterów, kwasów organicznych czy alkoholi. Zapewnia wysoką efektywność rozdzielania chromatograficznego i powtarzalne widma fragmentacji, które umożliwiają identyfikację związków za pomocą bibliotek widm [13]. GC-MS wymaga zazwyczaj chemicznej derywatyzacji związków nielotnych lub termicznie niestabilnych, co zmienia chemiczną postać analitów, wydłuża etap przygotowania próbki i może wpływać na powtarzalność i dokładność wyników oraz stanowi dodatkowe źródło zmienności analitycznej [14].

LC-MS stała się jedną z najpowszechniej stosowanych platform analitycznych w metabolomice, ponieważ umożliwia analizę szerszego zakresu związków, w tym polarnych, nielotnych i termicznie nietrwałych bez konieczności derywatyzacji. Łącząc rozdział chromatograficzny z detekcją spektrometrią mas o wysokiej czułości, LC-MS umożliwia profilowanie różnych klas metabolitów, w tym także lipidów, steroidów i ksenobiotyków. Metoda ta oferuje wysoką czułość i selektywność oraz może być stosowana w różnych trybach chromatograficznych (np. chromatografii w układzie faz odwróconych lub chromatografii oddziaływań hydrofilowych) w celu identyfikacji określonych grup metabolitów. Niemniej jednak, LC-MS może być podatna na zjawisko supresji jonowej wynikającej z efektów matrycowych, a interpretacja wyników niecelowanej analizy może być utrudniona bez odpowiednich bibliotek widm i danych MS/MS dotyczących fragmentacji związków [15].

Kolejną istotną techniką stosowaną w analizie związków małocząsteczkowych jest spektroskopia NMR, dzięki której możliwe jest wykrywanie związków na podstawie właściwości magnetycznych jąder atomowych. NMR jest wysoce powtarzalną metodą, która pozwala na analizę próbki bez jej niszczenia i wymaga minimalnego przygotowania próbki. Sprawia to, że jest szeroko stosowana do profilowania metabolomicznego płynów biologicznych, takich jak mocz, osocze i surowica. Jednak w porównaniu z technikami opartymi na spektrometrii mas, NMR charakteryzuje się znacznie niższą czułością, co ogranicza jego zdolność do wykrywania metabolitów o stosunkowo niskim stężeniu w próbce [16].

1.2. Obrazowanie związków małocząsteczkowych spektrometrią mas

Obrazowanie spektrometrią mas pozwala na wizualizację przestrzennego rozmieszczenia cząsteczek i atomów w badanej próbce [17]. MSI umożliwia zarówno celowaną, jak i niecelowaną analizę badanych obiektów o dużym zróżnicowaniu w składzie chemicznym, takich jak tkanki, w celu charakterystyki ich profilu metabolomicznego..

Obrazowanie spektrometrią mas wymaga przypisania danych MS do odpowiedniego piksela/woksela. Z tego względu nie wszystkie techniki jonizacji używane w klasycznym MS umożliwiają prowadzenie analiz MSI, ponieważ nie umożliwiają próbkowania materiału w określonej lokalizacji przestrzennej. Dotyczy to dotychczasowo opublikowanych konfiguracji m.in. jonizacji elektronami (EI), jonizacji elektrorozpylaniem (ESI), jonizacji chemicznej pod ciśnieniem atmosferycznym (APCI), fotojonizacji pod ciśnieniem atmosferycznym (APPI,). W konsekwencji powszechnie wykorzystywanymi w MSI technikami są MALDI, SALDI (laserowa desorpcja/jonizacja wspomagana powierzchnią), SIMS, DESI oraz techniki wykorzystujące próbkowanie metodą ablacji laserowej (LA). Z wyjątkiem obrazowania SIMS, które jest stosowane głównie do analizy rozmieszczenia pierwiastków i metabolitów w obiektach w skali mikro (rzędu kilku do kilkuset mikrometrów), wszystkie wymienione metody były stosowane do obrazowania metabolitów w tkankach biologicznych o wymiarach rzędu kilku do kilkudziesięciu milimetrów, co stanowi zakres analiz wykonanych w ramach niniejszej pracy doktorskiej.

W opracowywaniu technik MSI obejmujących próbkowanie i jonizację najważniejszymi parametrami, które należy uwzględnić, są: ciśnienie, pod którym znajdować się będzie próbka, sposób przygotowania próbki do analizy oraz rozdzielczość przestrzenna możliwa do uzyskania w analizie. Parametry te szczegółowo opisane zostały w rozdziałach 1.2.1 – 1.2.3.

1.2.1. Warunki próbkowania w analizach MSI

Jednym z parametrów różnicujących techniki MSI jest ciśnienie, pod którym prowadzony jest proces próbkowania, często połączony z procesem jonizacji. Ze względu na zmiany morfologiczne zachodzące w próbce pod wpływem warunków wysokiej próżni, szczególnie ważne jest uwzględnienie tego parametru w przypadku obrazowania materiału biologicznego. Materiał biologiczny, taki jak tkanki lub kolonie mikroorganizmów na żelu agarowym, ulega odwodnieniu w warunkach wysokiej próżni, co może prowadzić do kurczenia i/lub pękania próbki. Zmiany te uniemożliwiają wiarygodne odwzorowanie rozmieszczenia związków chemicznych w analizowanym materiale w porównaniu do rozmieszczenia *in vivo* [18]. Klasyczne techniki MSI, w których próbkowanie zachodzi w warunkach wysokiej próżni, to MALDI-MSI, SALDI-MSI i obrazowanie SIMS. Natomiast DESI-MSI oraz techniki wykorzystujące ablację laserową umożliwiają próbkowanie w warunkach ciśnienia atmosferycznego. Prowadzenie analiz w warunkach ciśnienia atmosferycznego stanowi kluczowy element metod MSI opracowanych w niniejszej pracy doktorskiej, umożliwiając ograniczenie artefaktów związanych z dehydratacją próbki oraz wiarygodne obrazowanie trójwymiarowe materiałów biologicznych o wysokim stopniu uwodnienia.

1.2.2. Przygotowanie próbek biologicznych do MSI

Proces przygotowania próbki do analizy MSI jest kluczowy, ze względu na konieczność zachowania przestrzennego rozmieszczenia związków chemicznych w badanym obiekcie odpowiadającego ich rzeczywistemu rozmieszczeniu *in vivo*. Ryzyko wystąpienia artefaktów oraz zmian metabolicznych w materiale biologicznym pojawia się już w momencie pobrania próbki. Metodą stosowaną do zahamowania procesów degradacji tkanek jest najczęściej mrożenie szokowe [1].

Etap preparatyki próbki jest wyjątkowo istotny w przypadku metod MALDI oraz SALDI. Przygotowanie próbki do analizy MALDI-MSI różni się ze względu na rodzaj analizowanego obiektu. Analizy MALDI-MSI mogą być wykonywane na skrawkach zamrożonych tkanek, w tym przekrojach całego organizmu, tkankach utrwalonych w formalinie i zatopionych w parafinie (FFPE, z ang. formalin-fixed paraffin-embedded) lub na hodowlach komórkowych i sferycznych agregatach komórkowych [19]. Najczęściej analizie MALDI-MSI poddawane są zamrożone tkanki, których przygotowanie rozpoczyna się od sekcjonowania w kriostacie w temperaturze -20°C [17]. Optymalna grubość skrawka określona została jako 1-6 μm [20,21].

Grubość skrawka wpływa na wartości intensywności sygnału oraz stosunek sygnału do szumu (S/N), między innymi ze względu na zmianę odległości między powierzchnią próbki a przewodzącym podłożem, na którym umieszczona jest próbka. Tkanka może być zatopiona w żelatynie, karboksymetylocelulozie, mieszaninie hydroksypropylometylocelulozy i poliwinylopirolidonu lub agarozie, jeżeli uzyskanie skrawków jest trudne technicznie. Stosowanie medium OCT może powodować utratę informacji o występujących w próbce związkach ze względu na sygnały o dużej intensywności łatwo jonizującego polimeru [17]. Skrawki tkanki przenoszone są na płytki szklane pokryte powłoką z tlenku indowo-cynowego (ITO) lub metalowe i odwadniane w eksykatorze. W analizie białek, przed pokryciem matrycą próbka jest przemywana (w zależności od celu analizy) odpowiednimi rozpuszczalnikami w celu usunięcia soli i lipidów, które mogą zaburzać proces kokrystalizacji białek z matrycą, lub z barwników, jeśli tkanka była poddana wcześniej barwieniu histologicznemu [19]. W roku 2007 opublikowane zostały badania opisujące możliwość analiz proteomicznych MALDI-MSI tkanek FFPE pozostałych po badaniach histologicznych [22]. Od tego czasu MALDI-MSI wykorzystano do analizy rozmieszczenia peptydów, białek, lipidów i innych metabolitów [19]. Tkanki FFPE oczyszczane są z parafiny z wykorzystaniem ksylenu i etanolu [17]. Hodowle komórkowe przygotowywane są do analizy MALDI-MSI przez trawienie trypsyną, odwirowywanie i przemywanie solą fizjologiczną buforowaną fosforem. Zawiesina komórek w buforze jest nakładana na płytki tego samego typu jak w przypadku tkanek i osuszana. Sferyczne agregaty komórkowe zawieszane są w roztworze żelatyny, poddawane kriosekcji i nakładane na płytki [19].

Procedura nanoszenia matrycy jest istotnym etapem procesu przygotowania próbki do MALDI-MSI. Aby uzyskać równomierne pokrycie próbki matrycą stosowane mogą być automatyczne rozpylacze. Dzięki wykorzystaniu automatycznego rozpylania osiągalne są mniejsze rozmiary nanoszonych na powierzchnię próbki kropel matrycy niż w przypadku rozpylania ręcznego. Kryształy powstające na powierzchni próbki w wyniku zautomatyzowanego rozpylania mogą osiągać rozmiary poniżej 5 μm [23]. Minimalna wielkość uzyskanych kryształów matrycy jest jednym z czynników, który ogranicza rozdzielczość przestrzenną MALDI-MSI. Inną metodą nanoszenia matrycy wykorzystywaną w analizach MALDI-MSI jest sublimacja. W porównaniu z rozpylaniem powoduje mniejsze przemieszczanie się związków chemicznych na powierzchni próbki ze względu na brak użycia rozpuszczalnika. Z tego powodu jednak czułość pomiaru może być mniejsza, jako że rozpuszczalnik pomaga w migracji związków do kryształów matrycy [17]. Dzięki zastosowaniu metody sublimacji możliwe było uzyskanie kryształów o rozmiarze 0,2 μm [24].

Ze względu na metody pozyskiwania tkanek analogiczne do analiz MALDI-MSI oraz wykorzystywanie instrumentów MS o tej samej konfiguracji, SALDI-MSI dzieli z MALDI-MSI wiele etapów preparatyki próbki. Różni je przede wszystkim rodzaj materiału wspomagającego proces desorpcji/jonizacji oraz sposób jego aplikacji. Nanomateriały wykorzystywane w SALDI-MSI to przede wszystkim nanocząstki złota, srebra, tlenku tytanu oraz nanomateriały oparte na węglu i krzemie [25]. Analizy wykazały powinowactwo niektórych nanomateriałów do tworzenia adduktów z cząsteczkami zawierającymi konkretne elementy strukturalne, takie jak atomy siarki w przypadku nanocząstek srebra i złota, a także wiązania podwójne i układy aromatyczne w przypadku nanocząstek srebra [26]. Dobór nanomateriałów do SALDI, podobnie jak dobór matryc w MALDI, może być uzależniony od trybu pomiarowego, natomiast nanocząstki złota i srebra wykazały skuteczność w analizach w trybie rejestracji jonów zarówno dodatnim jak i ujemnym [27]. Oprócz typu nanomateriału, jego parametry wpływające na efektywność desorpcji/jonizacji w SALDI-MS/MSI to przede wszystkim wielkość i porowatość nanostruktury [28,29]. Rozmiary wykorzystywanych w analizach SALDI-MSI nanomateriałów mieszczą się zazwyczaj w zakresie 2-100 nm dla nanocząstek sferycznych [30,31], 0,4-50 nm dla nanowarstw [32,33], 2-100 nm dla nanopowłok [34], 30-60 nm dla nanopłytek [35] i 4-700 nm dla nanorurek [36,37]. Mniejsze nanocząstki (<30 nm) wykazują głównie rezonanse dipolowe, co skutkuje intensywną absorpcją i rozpraszaniem światła w zakresie widzialnym. Natomiast większe nanocząstki (>60 nm) mogą wykazywać dodatkowe rezonanse kwadrupolowe, zwiększone efekty rozpraszania i przesunięcie maksimów absorpcji ku czerwieni (ang. redshift). Zjawisko to, zależne od rozmiaru nanostruktur, pozwala na optymalizację ich właściwości fizykochemicznych zgodnie z określonymi wymaganiami pomiarowymi [38]. Synteza nanomateriałów również jest istotnym elementem mającym wpływ na wydajność jonizacji, ze względu na różnice w możliwości kontroli wielkości, kształtu i stabilności powstających nanostruktur. Często wykorzystywana synteza chemiczna pozwala na wysoce kontrolowany proces pod względem jednorodności wielkości cząsteczek, skutkować może jednak zanieczyszczeniem nieprzereagowanych substratów, stabilizatorów i produktów reakcji w zawiesinie powstałych nanostruktur, co może utrudnić interpretację widm masowych [39]. Metodą zapewniającą wysoką czystość otrzymanej zawiesiny jest metoda ablacji laserowej, polegająca na skierowaniu wiązki lasera impulsowego na powierzchnię materiału umieszczonego w cieczy, z którego powstać mają nanostruktury. Synteza poprzez ablację laserową w roztworze (LASiS) wykorzystuje bezpieczne rozpuszczalniki organiczne i wodę, które stanowią mniejsze zagrożenie środowiskowe niż niektóre substancje wykorzystywane w syntezie chemicznej [40,41].

Metody aplikacji nanomateriałów zależą od wybranej techniki obrazowania. W analizach SALDI-MSI (gdzie próbkę nanosi się na zmodyfikowane podłoże) stosuje się m.in. metodę imprintu, osadzania, implantacji oraz rozpylanie magnetronowe [25]. Z kolei w technice nanoPALDI-MSI (gdzie nanomateriały aplikuje się bezpośrednio na badaną tkankę) najpowszechniejszą metodą jest rozpylanie zawiesin koloidalnych nanostruktur. Rozpylanie stosowane jest w przypadku zawiesin koloidalnych nanostruktur. Nanostruktury są zawieszone w rozpuszczalniku, który zapewnia ich stabilność ale odparowuje stosunkowo szybko. W przypadku nadmiaru rozpuszczalnika nanostruktury mogą ulegać delokalizacji na powierzchni próbki. Rozpylanie wielu warstw nanostruktur może skutkować powstawaniem agregatów lub niehomogenicznym rozmieszczeniem struktur na powierzchni próbki [25]. Metoda imprintu polega na przeniesieniu związków chemicznych z powierzchni próbki na powierzchnię nanomateriału poprzez bezpośredni kontakt. Wykonywanie imprintu może wiązać się z utratą rozdzielczości ze względu na podatność na przemieszczanie się związków chemicznych w obrębie imprintu. Morfologia powierzchni nanomateriału wpływa na efektywność analizy. Czułość analizy jest większa dla związków małocząsteczkowych, gdy powierzchnia wykazuje większą porowatość, natomiast dla związków wielkocząsteczkowych przy mniejszej porowatości [42]. Metoda osadzania polega na przeniesieniu próbki na powierzchnię nanosubstratu i pozostawienie jej na nim na czas analizy. Metoda osadzania wymaga wykorzystania skrawków o bardzo małej grubości (<5 µm), aby zapewnić odpowiednią wydajność jonizacji.

DESI-MSI opisywana jest często jako metoda niewymagająca rozbudowanego wstępnego przygotowania próbki. W analizie DESI-MSI nie jest wykorzystywana matryca, co ułatwia proces przygotowania próbki do analizy. Próbka natomiast, jak w pozostałych technikach MSI, musi być płaska, aby uniknąć zróżnicowania sygnału ze względu na zmianę odległości próbka-emiter DESI. W analizach DESI-MSI i nanoDESI-MSI zwykle wykorzystywane są skrawki o grubości około 10-12 µm uzyskane dzięki kriosekcji, natomiast badania Jiang i in. wykazały, że większa grubość analizowanej próbki może wpłynąć na zwiększenie intensywności sygnałów oznaczanych związków [43].

Techniki wykorzystujące LA jako metodę próbkowania również wymagają, aby powierzchnia była płaska. Jeżeli głębokość ablacji jest mniejsza niż grubość próbki, to wymiar ten nie jest parametrem wpływającym na intensywność otrzymywanych sygnałów. Efektywna ablacja laserowa uwodnionych próbek nie wymaga aplikacji dodatkowej matrycy.

Wykorzystywana jest najczęściej wiązka laserowa o długości fali z zakresu średniej podczerwieni (mid-IR) [44,45]. Promieniowanie mid-IR pozwala na efektywną ablację tkanek ze względu na zgodność długości fali lasera z pasmami absorpcyjnymi drgań rozciągających wiązań O–H cząsteczek wody [46]. W technikach, takich jak laserowa ablacja ze zdalną jonizacją elektrorozpylaniem (LARESI) system ablacji laserowej wykorzystany do etapu próbkowania połączony został zdalnie ze źródłem jonów spektrometru mas [47]. Takie rozwiązanie pozwala na wykorzystanie jednego systemu próbkowania do analiz z wykorzystaniem innych kompatybilnych metod jonizacji, np. APCI.

1.2.3. Rozdzielczość przestrzenna pomiarów

W oprogramowaniu do obrazowania MS analizowanemu obszarowi próbki przypisywana jest siatka rastrowa reprezentująca fragmenty wybranego obszaru w formie pikseli. W każdym pikselu rejestrowane są dane MS. Wymiary piksela warunkowane są przez wielkość obszaru próbkowania zależną np. od średnicy plamki lasera używanego do desorpcji i/lub ablacji oraz przez krok skanowania. Jeżeli krok skanowania, czyli odległość pomiędzy środkami sąsiadujących pikseli, jest równy rozmiarowi obszaru próbkowania, to próbkowanie zachodzi z rozdzielczością przestrzenną odpowiadającą temu rozmiarowi. Jest to klasyczny sposób próbkowania w MSI. Gdy krok skanowania jest większy, to pomiędzy punktami pomiarowymi pozostaje nienaruszony materiał. Taka konfiguracja określana jest jako undersampling i prowadzi do zmniejszenia rozdzielczości uzyskiwanych obrazów jonowych. Konfiguracja, w której krok skanowania jest mniejszy niż średnica obszaru próbkowania definiowana jest jako oversampling [48]. Stosowany jest głównie w przypadku, gdy klasyczna metoda próbkowania skutkowałaby występowaniem artefaktów analitycznych lub niecałkowitym usunięciem materiału, co wynika z profilu (kształtu) krateru poablacyjnego.

Maksymalna rozdzielczość technik MALDI i SALDI w dużym stopniu zależy od wielkości struktur materiału wspomagającego mechanizm desorpcji/jonizacji, które opisane zostały w rozdziale 1.2.2 niniejszej rozprawy doktorskiej. W licznych analizach rozdzielczość uzyskiwana przy zastosowaniu MALDI-MSI wynosiła 30-100 μm [49]. Rozdzielczość ta pozwala na rozróżnienie struktur będących miejscem akumulacji związków w tkankach ludzkich, zwierzęcych i roślinnych. W ciągu ostatnich 10 lat dostępne stały się komercyjnie instrumenty MALDI z możliwością osiągnięcia rozdzielczości przestrzennej <10 μm, a modyfikacje ich konfiguracji pozwoliły na osiągnięcie rozdzielczości nawet 1,4 μm [50].

Rozdzielczość przestrzenna uzyskiwana w DESI-MSI zwykle wynosi od 150 do 200 µm [51], jednakże rozdzielczość przestrzenna 35 µm mogła zostać osiągnięta dzięki optymalizacji warunków eksperymentalnych [52]. Aby zwiększyć rozdzielczość przestrzenną, opracowany został wariant DESI, określany jako nano-DESI. Analizy MSI wykonywane tą metodą osiągają rozdzielczość przestrzenną nawet 7–10 µm [53,54].

Rozdzielczość przestrzenna uzyskana techniką LAESI wynosi zwykle około 200 µm [55–57], czyli jest znacząco mniejsza niż m.in. w MALDI. Modyfikacje układu optycznego systemu, na przykład wykorzystanie pikosekundowego lasera, pozwalają na uzyskanie rozdzielczości przestrzennej ≤100 µm [58,59]. Obecnie najmniejsza uzyskana wartość rozdzielczości przestrzennej w analizie LAESI-MSI to 40 µm [60]. Technika LARESI zastosowana w MSI pozwoliła na analizę w zakresie rozdzielczości 175 do 300 µm [47].

1.2.4. Parametry ablacji laserowej wpływające na wyniki analiz MSI

Aby zastosować ablację laserową w spektrometrii mas rozważone muszą zostać kluczowe parametry samej wiązki laserowej (takie jak jej średnica, dywergencja oraz stabilność propagacji), jak również parametry układu optycznego (np. ogniskowa soczewki skupiającej). Na parametry ablacji laserowej wpływają zarówno właściwości wiązki, jak i konfiguracja układu optycznego, w szczególności ogniskowa elementów skupiających, transmisja i próg uszkodzenia optyki dla stosowanej długości fali oraz stabilność propagacji wiązki. Parametry te determinują rozmiar plamki w ognisku, gęstość energii na powierzchni próbki oraz powtarzalność procesu ablacji. Wykorzystywane mogą zostać również soczewki skupiające cylindryczne w celu korekcji wiązki eliptycznej na wiązkę kołową. W zależności od typu lasera i toru optycznego wykorzystane mogą zostać również soczewki korygujące aberracje sferyczne i filtry optyczne promieniowania lasera [61].

Rozmiar plamki ogniskowanej wiązki laserowej na powierzchni próbki może być regulowany przez zmianę długości fali, ogniskową soczewki, oraz średnicy wiązki padającej [62]. Stabilność kierunkowa wiązki (ang. beam pointing stability) jest kluczowa dla powtarzalności punktów pomiarowych w ablacji laserowej. Nawet niewielkie zmiany w dywergencji lub odchylenia osi optycznej wiązki mogą prowadzić do błędów w lokalizacji punktów pomiarowych oraz do niejednorodności ablacji [63]. Położenie talii wiązki oraz zasięg Rayleigha, czyli zakres wzdłuż osi optycznej (osi Z), w którym średnica plamki pozostaje zbliżona do minimalnej, są kolejnymi parametrami wpływającymi na jednorodne usuwanie materiału z próbki. Rozdzielczość przestrzenna jest ściśle związana z parametrami ogniskowania: mniejsza plamka pozwala uzyskać wyższą rozdzielczość, ale wymaga precyzyjnego pozycjowania układu optycznego. Ograniczenia rozdzielczości mogą wynikać z dywergencji wiązki i aberracji elementów optycznych, co należy uwzględnić również w profilowaniu wgłębnym.

Równie istotnymi parametrami wiązki są fluencja, energia impulsu oraz czas trwania impulsu. Aby ablacja mogła zajść przekroczony musi zostać próg ablacji (ang. ablation treshold) wyrażany czasem wartością fluencji. Jej wartość jest bezpośrednio uzależniona od energii impulsu, jako że fluencja definiowana jest jako gęstości energii na powierzchni próbki. W przypadku niskich fluencji gęstość elektronów energetycznych pozostaje niska. W konsekwencji energia lasera jest deponowana głównie w płytkim obszarze. Przy wyższych fluencjach istotny staje się udział przewodzenia nośników, a obszar wpływu ciepła jest definiowany przez głębokość penetracji ciepła napędzanego elektronami [64]. W przypadku laserów nanosekundowych mechanizm absorpcji energii przez materiał zależy zarówno od długości fali promieniowania, jak i od czasu trwania impulsu. O możliwości bezpośredniego wzbudzenia elektronowego lub fotojonizacji decyduje przede wszystkim energia fotonu, natomiast stosunkowo długi czas trwania impulsu sprzyja przekazywaniu energii do sieci krystalicznej i nasileniu procesów termicznych. Dłuższy czas trwania impulsu pozwala na stopniową absorpcję energii przez materiał, co sprawia, że zachodzą procesy termiczne, takie jak parowanie i topienie, które ostatecznie prowadzą do usunięcia materiału. Wykorzystując femtosekundowe lasery elektrony zostają wzbudzone w czasie 1-20 pikosekund. Energia cieplna przekazana do materiału napędza mechanizmy nietermiczne prowadzące do ablacji. Przy niskiej energii impulsu lasera wpływającej na naprężenie materiału absorbcja energii wywołuje powstawanie fal powodujących spalację, czyli termomechaniczną fragmentację i wyrzut cząstek materiału. Przy wysokiej fluencji, lasera bezpośrednie przejście materiału stałego w metastabilną ciecz następuje bez wrzenia ze względu na krótki czas nagrzewania. Następuje wybuch związany z szybkim przechodzeniem przegrzanej cieczy w postać mieszaniny pary i kropelek cieczy wyrzucanych z materiału [41].

Profil energetyczny wiązki laserowej ma bezpośredni wpływ na jednorodność ablacji i wiarygodność przypisania sygnałów do współrzędnych przestrzennych w MSI. Wiązki o rozkładzie Gaussa charakteryzują się maksymalnym natężeniem w centrum i spadkiem intensywności wraz z odległością od osi optycznej wiązki, co może prowadzić do nierównomiernego usuwania materiału. Nierównomierna ablacja wpływa negatywnie na powtarzalność pomiarów i może generować artefakty w trójwymiarowej rekonstrukcji obrazu [65]. Aby uzyskać równomierny rozkład energii w plamce, stosuje się metody kształtowania wiązki (ang. beam shaping), wykorzystujące m.in. homogenizatory optyczne.

Wpływ zastosowania homogenizatora optycznego zaprezentowany został na rysunku 1. Dostosowane do założeń 3D-MSI kształtowanie profilu umożliwia minimalizację lokalnych różnic w gęstości mocy, co jest niezbędne dla uzyskania powtarzalnych kraterów ablacyjnych o płaskim dnie w profilowaniu wgłębnym.

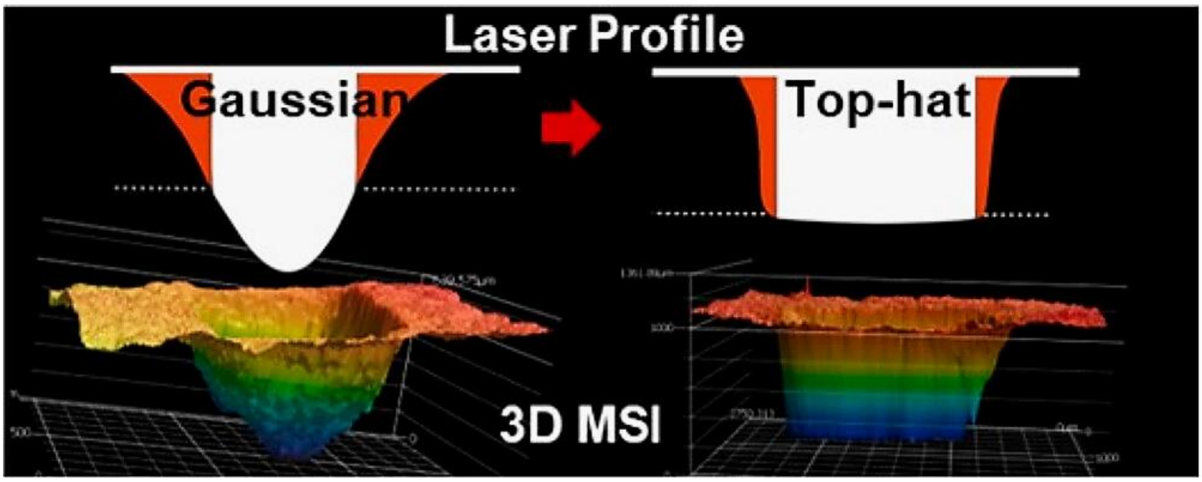

Rys.1. Profil wiązki o rozkładzie Gaussa oraz wiązkę o profilu typu top-hat i odpowiadające im wizualizacje kształtu obszaru poddanego ablacji [65].

Konsekwencje nierównomiernego profilu energetycznego obejmują błędy w przestrzennym przypisaniu sygnałów analitycznych w MSI oraz artefakty w rekonstrukcji trójwymiarowej, w tym deformacje warstw i zaburzenia mapowania dystrybucji analitów. Z powyższych względów kontrola parametrów układu optycznego w istotny sposób wpływa na wiarygodność danych półilościowych i ilościowych. Straty energii w układzie optycznym powinny zostać wzięte pod uwagę w celu przeprowadzenia poprawnej analizy ilościowej z wykorzystaniem ablacji laserowej jako techniki próbkowania. Straty energii w układzie optycznym należy uwzględnić przy wyznaczaniu energii lub fluencji docierającej do próbki, zwłaszcza w analizach półilościowych i ilościowych [66]. Płaski (jednorodny) rozkład gęstości energii umożliwia wysoce precyzyjną korelację objętości materiału usuniętego w procesie ablacji z konkretnym punktem pomiarowym w przestrzeni 3D (wokselem).

1.3. Obrazowanie spektrometrią mas w trzech wymiarach

Obrazowanie spektrometrią mas w trzech wymiarach ma na celu umożliwić rekonstrukcję przestrzennych map molekularnych całych tkanek biologicznych, a nawet narządów. Łączy informacje o dystrybucji przestrzennej analitów uzyskiwane w technice MSI z informacją o położeniu analizowanych związków w głąb obiektu (w osi *Z*) przez przypisanie sygnałom współrzędnej Z w trakcie pomiaru lub komputerową rekonstrukcję 3D. Wyniki analiz 3D-MSI umożliwiają analizę przestrzennej dystrybucji leków i ich metabolitów w tkankach [67,68]. Wyniki analiz 3D-MSI mogą również umożliwić ocenę wpływu ekspozycji na ksenobiotyki (substancje szkodliwe) na zmiany w profilu molekularnym tkanek [69,70]. Zastosowanie analiz 3D-MSI w proteomice, metabolomice i lipidomice może okazać się kluczowe w pełnym zrozumieniu procesów biologicznych zachodzących w organizmie pod wpływem czynników stresowych.

Główne strategie MSI pozwalające na wizualizację rozmieszczenia związków chemicznych w 3D z rozróżnieniem na sposób rejestrowania informacji w osi Z to: rekonstrukcja modelu trójwymiarowego na podstawie przekrojów seryjnych próbki oraz profilowanie wgłębne (ang. depth profiling) oparte na kontrolowanym usuwaniu kolejnych warstw materiału.

Rekonstrukcja trójwymiarowa na podstawie serii przekrojów 2D

Większość dotychczasowych badań z wykorzystaniem 3D-MSI przedstawia rekonstrukcję wykonaną na podstawie wyników 2D-MSI serii kolejnych skrawków tego samego obiektu [7]. Seria obrazów jonowych jest następnie generowana i składana w trójwymiarowy model zgodnie z ich kolejnością oraz pierwotną orientacją przestrzenną (rys. 2). Wiąże się to z długim czasem pomiaru, rzędu kilku dni dla objętości 0,5 mm^3 [71] lub nawet kilku tygodni przy analizach większych objętości próbki. Wieloetapowy proces przygotowania próbki wpływa również na zwiększenie prawdopodobieństwa zanieczyszczenia próbki przez wprowadzenie na powierzchnię skrawków medium używanego do zatapiania tkanek (podczas kriosekcji), co skutkować może występowaniem na widmach silnych sygnałów artefaktowych pochodzących od tego polimeru [72]. Długi czas analizy może sprzyjać powstawaniu deformacji morfologicznych tkanki, związanych z odwodnieniem tkanki lub dyfuzją związków [17]. Występuje również wysokie ryzyko postępującej degradacji enzymatycznej i zmian metabolicznych pomiędzy kolejnymi pomiarami [73]. Zachowanie dokładnie takiej samej orientacji oraz grubości skrawków jest technicznie trudne, co wpływa na jakość rekonstrukcji trójwymiarowej. Rozdzielczość przestrzenna w osi Z jest ograniczona przez grubość skrawków, co może prowadzić do utraty informacji o gradientowych zmianach intensywności sygnałów w głąb tkanki. Różnice w przygotowaniu i analizie kolejnych skrawków mogą wpływać na intensywność sygnałów jonów, co ogranicza wiarygodność porównań ilościowych w osi Z. Badania dystrybucji związków małocząsteczkowych metodą 3D-MSI przez analizę przekrojów seryjnych opisane w literaturze zazwyczaj wykonywane są przy użyciu technik DESI [74] i MALDI [75–77].

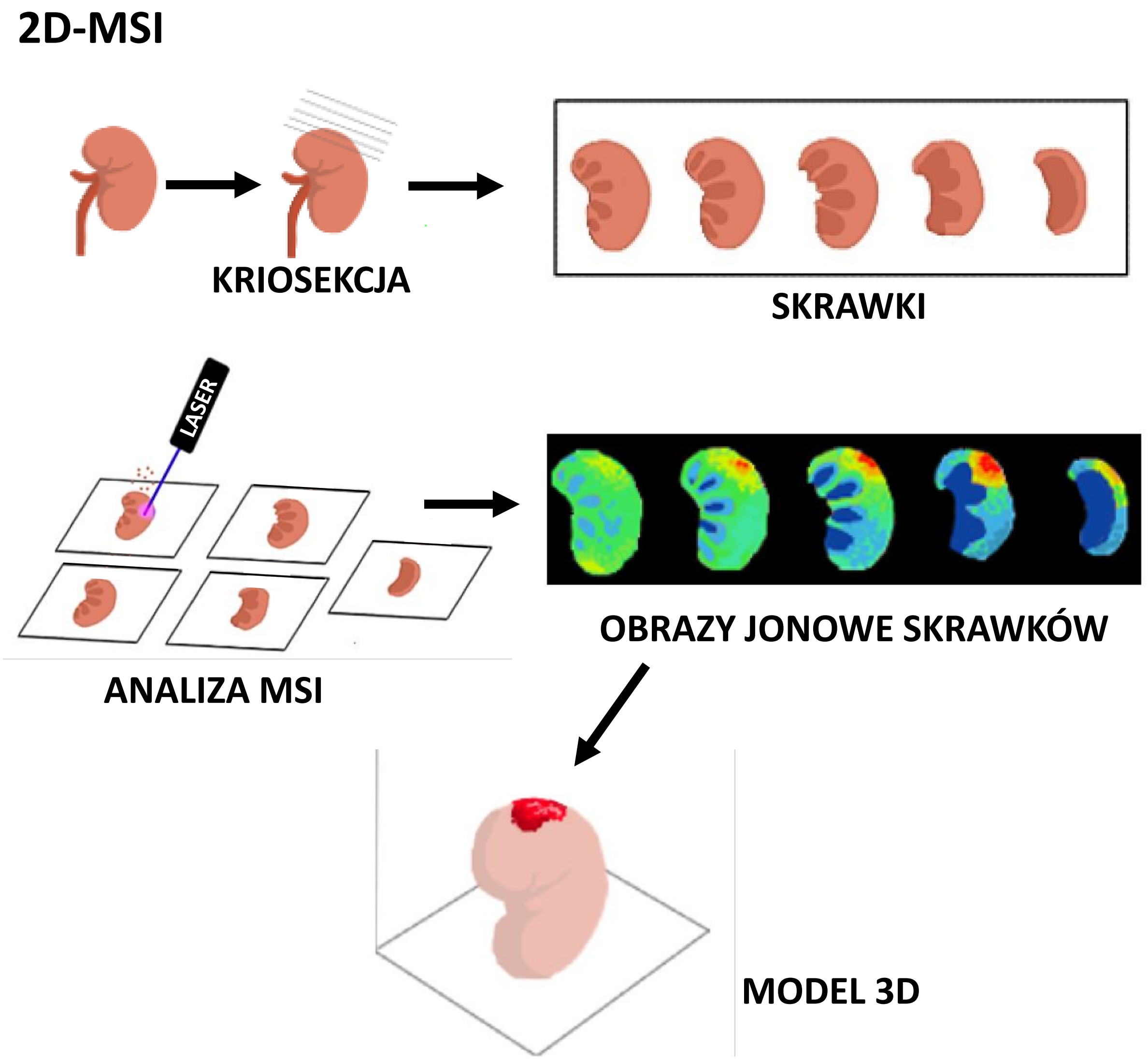

Rys. 2. Schematyczne przedstawienie kolejnych etapów analizy metodą 3D-MSI opartą na rekonstrukcji na podstawie 2D-MSI serii kolejnych skrawków.

Bezpośrednie obrazowanie 3D techniką profilowania wgłębnego

Alternatywnym podejściem stosowanym w 3D-MSI jest sekwencyjne usuwanie kolejnych warstw materiału w głąb wybranego obszaru próbki. Podejście to całkowicie eliminuje konieczność wykonywania kriosekcji, co sprawia, że całkowity czas preparatyki ulega drastycznemu skróceniu w porównaniu do czasu przygotowania próbki w podejściu opartym na trójwymiarowej rekonstrukcji z przekrojów seryjnych. Model 3D nadal rekonstruowany jest na podstawie wyników analiz 2D dla każdej kolejnej usuniętej warstwy analizowanego obszaru, jednak podejście to w sposób naturalny rozwiązuje problem przestrzennego dopasowywania obrazów i zachowania pierwotnej orientacji analizowanego obiektu. Ta technika nazywana jest profilowaniem wgłębnym (rys. 3).

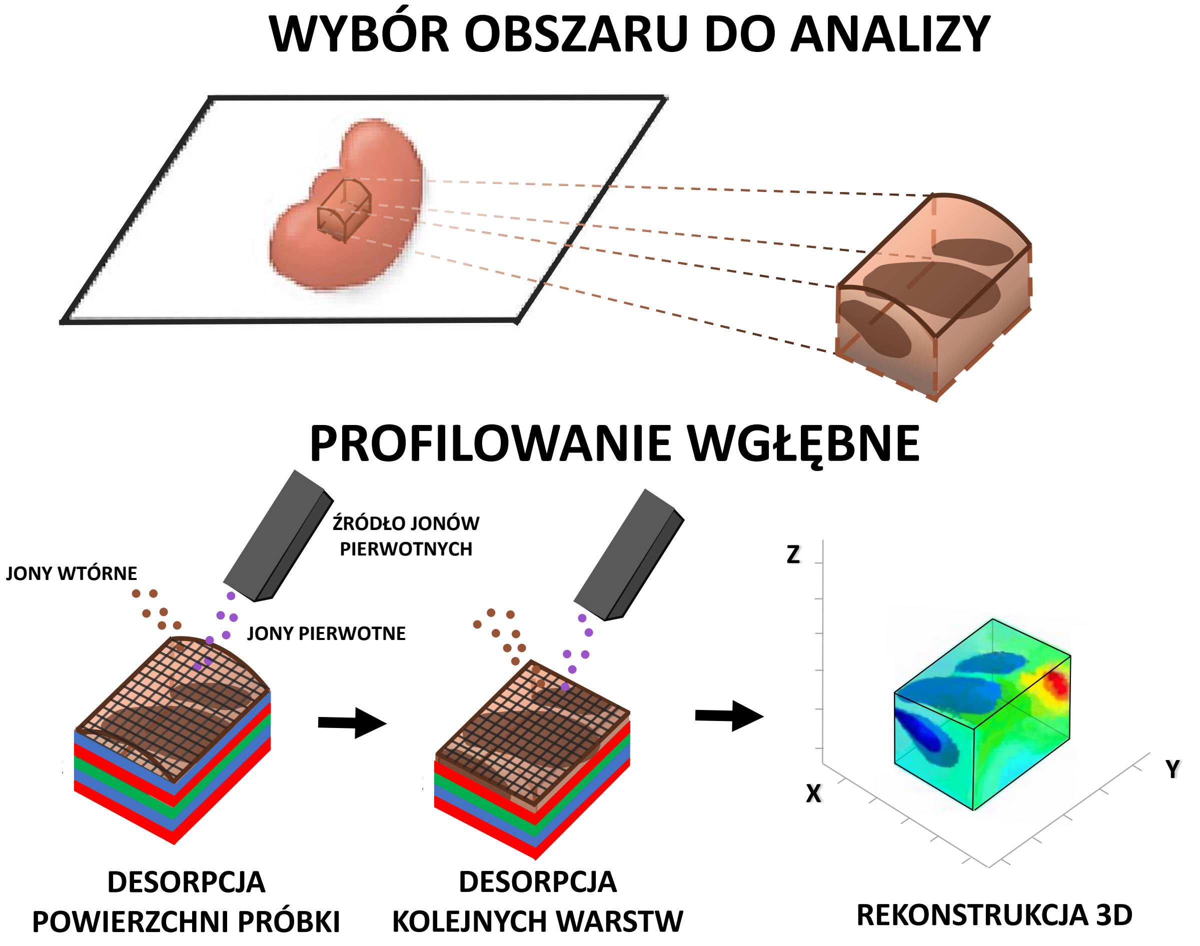

Rys. 3. Schematyczne przedstawienie kolejnych etapów bezpośredniej analizy 3D-MSI techniką profilowania wgłębnego na przykładzie techniki SIMS.

Jednym z najważniejszych parametrów wpływających na możliwość przeprowadzenia profilowania wgłębnego daną techniką jest zdolność do równomiernego usuwania materiału z próbki. W MALDI-MSI istotnym czynnikiem utrudniającym przeprowadzenie profilowania wgłębnego jest konieczność pokrycia powierzchni próbki matrycą przed każdym skanowaniem. W klasycznym DESI usuwanie związków z powierzchni próbki ma charakter ekstrakcyjny i zależy od składu rozpuszczalnika oraz właściwości analitów, dlatego technika ta nie jest standardowo wykorzystywana do kontrolowanego profilowania wgłębnego warstwa po warstwie [78]. Profilowanie wgłębne jest metodą najczęściej stosowaną w obrazowaniu 3D-SIMS [9,10], które pozwala na obrazowanie rozmieszczenia m.in. pierwiastków w obrębie próbki. W technice SIMS próbka jest bombardowana wiązką jonów, ten proces usuwania materiału w SIMS określa się jako erozja jonowa (ang. sputtering). W technice SIMS głębokość usuwania materiału z powierzchni próbki w wyniku rozpylania jonowego wynosi od kilku do kilkudziesięciu nanometrów [79] co sprawia, że znajduje zastosowanie w analizie 3D-MSI obiektów w skali komórkowej i subkomórkowej. Wysokoenergetyczna (tzw. twarda) jonizacja charakterystyczna dla techniki SIMS związana jest jednak z niekontrolowaną fragmentacją związków chemicznych, co może utrudniać analizę metabolomiczną tkanek biologicznych. Technikami, które wykorzystano do profilowania wgłębnego, a jonizacja powoduje minimalną fragmentację, są również metody wykorzystujące laserową ablację jako metodę próbkowania, m.in. LAESI [80] i IR-MALDESI [81]. W celu osiągnięcia większej głębokości ablacji materiału biologicznego stosowany jest laser emitujący promieniowanie w zakresie mid-IR, którego długość fali odpowiada pasmom silnej absorpcji wody, co umożliwia efektywną ablację tkanek uwodnionych.

Szerokie zastosowanie MSI w analizie tkanek biologicznych uzasadnia rozwój metod umożliwiających uzyskanie informacji przestrzennej również w osi Z. Mimo znacznego postępu, zastosowanie dotychczasowych technik pracujących w warunkach ciśnienia atmosferycznego do profilowania wgłębnego ograniczało się niemal wyłącznie do analizy punktowej. Obecnie nie istnieją metody 3D-MSI, które pozwalałyby bezpośrednią, jednoetapową analizę 3D MSI całej wybranej objętości makroskopowych obiektów biologicznych strategią warstwa po warstwie. Żadna z zaprezentowanych do tej pory metod nie umożliwia precyzyjnej ablacji całych skrawków tkanek o wymiarach rzędu od kilku milimetrów w akceptowalnie krótkim czasie. Kompleksowa ewaluacja analityczna, rygorystyczna optymalizacja oraz wdrożenie do badań biologicznych nowatorskiego rozwiązania instrumentalnego (zdefiniowanego w niniejszej pracy jako LARAPPI/CI), pozwalającego na zrealizowanie powyższych założeń przy jednoczesnym zachowaniu wysokiej rozdzielczości i czułości, stanowiły główny cel badawczy rozprawy doktorskiej.

2. Cel i zakres pracy

Głównym celem niniejszej rozprawy doktorskiej była optymalizacja systemu LARAPPI/CI oraz walidacja analityczna opracowanych z jego wykorzystaniem metod, stanowiących nowe rozwiązanie techniczne w obrazowaniu spektrometrią mas (MSI). Praca obejmowała opracowanie parametrów tego układu do celów bezpośredniej analizy związków małocząsteczkowych w złożonych matrycach o zróżnicowanej gęstości i strukturze, prowadzonej w warunkach ciśnienia atmosferycznego. Celem uzupełniającym była ocena przydatności analitycznej podejść opartych na nanocząstkach srebra-109 (^{109}AgNPs-LDI-MS/MSI) oraz porównanie ich parametrów analitycznych w jakościowej, ilościowej oraz przestrzennej analizie związków małocząsteczkowych. Zakres rozprawy doktorskiej obejmuje następujące zagadnienia:

1. Krytyczny przegląd literatury w tematyce obrazowania spektrometrią mas w dwóch i trzech wymiarach
2. Analiza stanu wiedzy dotyczącego wykorzystania metalicznych nanostruktur w technikach LDI-MS/MSI do analizy związków małocząsteczkowych **[P1]**
3. Optymalizacja parametrów i walidacja analityczna metod ilościowego oznaczania i obrazowania wybranych związków małocząsteczkowych z wykorzystaniem nanocząstek metalicznych jako materiałów wspomagających desorpcję i jonizację laserową [**P2, P3]**
4. Adaptacja parametrów pracy systemu LARESI do bezpośredniego obrazowania i detekcji związków małocząsteczkowych w trybie monitorowania wybranych reakcji (SRM) w matrycach roślinnych **[P4]**
5. Optymalizacja konfiguracji układu optyczno-ablacyjnego oraz parametrów ablacji i jonizacji systemu LARAPPI/CI-3D/2D-MSI do bezpośredniej analizy związków małocząsteczkowych w materiałach biologicznych **[P5]**
6. Połączenie systemu LARAPPI/CI-MSI z techniką szerokopasmowej dysocjacji indukowanej zderzeniami (bbCID) w celu jednoczesnej rejestracji danych MS/MS oraz przestrzennej lokalizacji związków małocząsteczkowych **[P6]**
7. Wykorzystanie systemu LARAPPI/CI do trójwymiarowego mapowania (3D-MSI) składu chemicznego matryc złożonych:
    - wyznaczenie przestrzennej dystrybucji związków małocząsteczkowych w modelowych matrycach roślinnych (owoc kiwi, korzeń rzodkiewki) **[P5, P8]**

  - trójwymiarowa analiza różnic metabolicznych w obszarach tkanki normalnej i nowotworowo zmienionej ludzkiej nerki **[P5]**
  - wolumetryczna analiza interakcji w wielowarstwowych układach mikrobiologicznych (bakterie glebowe, fitopatogeny) **[P7]**

8. Zastosowanie systemu LARAPPI/CI w analizach powierzchniowych (2D-MSI) zmian składu chemicznego w matrycach o zróżnicowanej strukturze:
   - monitorowanie transportu i kumulacji ksenobiotyków (pestycydów) w strukturach roślinnych **[P8]**
   - badanie chemicznych mechanizmów interakcji w układach typu „biokontrola–patogen" na powierzchni podłoży stałych **[P7]**
9. Analiza porównawcza parametrów analitycznych systemu LARAPPI/CI oraz technik wykorzystujących nanocząstki metaliczne do obrazowania dystrybucji związków małocząsteczkowych **[P9]**

Realizacja przedstawionych założeń wymagała nie tylko opracowania i walidacji metod analitycznych, lecz również optymalizacji parametrów pracy układu pomiarowego oraz oceny ich wpływu na jakość uzyskiwanych danych. Obejmowała ona także dobór i ocenę właściwości nanocząstek metalicznych stosowanych do wspomagania procesów desorpcji i jonizacji, co stanowi dodatkowy element wiążący rozprawę z zagadnieniami inżynierii chemicznej.

3. Omówienie cyklu publikacji

3.1. Nanocząstki metaliczne jako materiały wspomagające desorpcję i jonizację laserową w analizie związków małocząsteczkowych

W analizie związków małocząsteczkowych, techniki oparte na spektrometrii mas z laserową desorpcją/jonizacją oferują istotne zalety przede wszystkim w aplikacjach wymagających wysokiej przepustowości analiz (tzw. high-throughput screening). Techniki LDI-MS umożliwiają bezpośrednią desorpcję/jonizację cząsteczek z powierzchni próbki, co pozwala na znaczne skrócenie czasu pomiaru serii próbek w porównaniu do standardowych metod wykorzystujących czasochłonny rozdział chromatograficzny.. W wielu przypadkach próbki często mogą być analizowane z pominięciem procedur ekstrakcji, przy ograniczonym zużyciu rozpuszczalników oraz bez konieczności stosowania czasochłonnych procesów chromatograficznych. W rezultacie rejestracja danych może następować w krótkim czasie, co umożliwia prowadzenie wysokoprzepustowych analiz dużej liczby próbek. LDI-MS jest szczególnie przydatna w szybkich analizach przesiewowych oraz w bezpośredniej analizie powierzchni, natomiast LC-MS pozostaje techniką preferowaną w analizie złożonych mieszanin, zwłaszcza gdy wymagany jest rozdział chromatograficzny, większa selektywność oznaczeń oraz bardziej wiarygodna identyfikacja związków [82]. Warto również zaznaczyć, że przewaga LC-MS w tym zakresie wiąże się zwykle z bardziej złożonym przygotowaniem próbki, dłuższym czasem analizy i znacznie wyższym tłem chemicznym.

Metody SALDI wspomagane nanomateriałami, określane w przypadku zastosowania nanocząstek również jako nano-PALDI, często generują znacznie niższą intensywność sygnałów tła w zakresie małych wartości m/z w porównaniu z konwencjonalnymi metodami wspomaganymi matrycą, co poprawia wykrywalność związków małocząsteczkowych, takich jak metabolity, w tym wybrane klasy lipidów. Techniki laserowej desorpcji/jonizacji wspomaganej nanomateriałami stanowią obecnie istotną alternatywę dla powszechnie stosowanej metody MALDI, szczególnie w obrazowaniu próbek biologicznych, w tym tkanek. Według danych literaturowych z roku 2022 około połowa eksperymentów SALDI-MSI wykonywana była z wykorzystaniem nanomateriałów metalicznych [25]. Ze względu na szerokie zastosowanie nanostruktur metalicznych oraz ich korzystne właściwości fizykochemiczne przeprowadzono przegląd literaturowy poświęcony ich właściwościom fizykochemicznym oraz zastosowaniom w MSI **[P1]**. Sporządzony należał do pierwszych opracowań poświęconych dogłębnej analizie efektowi wykorzystania nanomateriałów metalicznych w kontekście analiz SALDI-MSI. Właściwości optyczne i elektromagnetyczne nanocząstek metalicznych silnie zależą od ich rozmiaru, kształtu i otaczającego środowiska [53]. Właściwości te są przede wszystkim uwarunkowane wysokim stosunkiem powierzchni do objętości nanomateriałów, który zwiększa energię powierzchniową. Ta cecha sprzyja efektywnej adsorpcji analitów na powierzchni oraz ich późniejszej desorpcji i jonizacji. Wśród nanomateriałów metalicznych w analizowanych zastosowaniach MSI dominowały nanomateriały oparte na złocie (43%) i srebrze (32%), przede wszystkim nanocząstki. Nanocząstki złota i srebra wykazują właściwości związane ze zjawiskiem zlokalizowanego powierzchniowego rezonansu plazmonowego (LSPR), takie jak wzmocnienie lokalnego pola elektromagnetycznego w otoczeniu nanostruktury oraz zwiększenie absorpcji światła. Nanocząstki złota są chemicznie obojętne i wysoce stabilne, co czyni je odpornymi na utlenianie, dzięki czemu pozwalają na analizy próbek biologicznych bez wchodzenia w reakcję z analitem [83]. Pomimo tych zalet, nanocząstki złota wykazują często niższą wydajność kationizacji w porównaniu z z nanocząstkami srebra, co może przekładać się na niższą efektywność desorpcji/jonizacji niektórych analitów [84]. Dzięki korzystnej absorpcji promieniowania UV , w tym w zakresie zbliżonym do 355 nm, AgNPs ułatwiają efektywny transfer energii i oferują wyższą czułość dla określonych analitów w porównaniu z AuNPs. AgNPs są szczególnie skuteczne w przypadku analiz związków aromatycznych, związków olefinowych i węglowodorów o długich łańcuchach. Właściwość ta została wykorzystana do wykrywania szerokiej gamy lipidów, steroli i estrów woskowych, a także peptydów, kwasów tłuszczowych, węglowodanów i aminokwasów [85]. Przedstawione w przeglądzie literaturowym **[P1]** informacje obrazują, że skuteczność metalicznych nanostruktur nie ma charakteru uniwersalnego. Mimo dużego potencjału analitycznego metalicznych nanostruktur, ich zastosowanie może wiązać się z problemami dotyczącymi ich stabilności, heterogeniczności próbek oraz ograniczonej skalowalności procedur. Opisane zostały również metody nanoszenia nanostruktur na analizowaną powierzchnię, co jest szczególnie istotne ze względu na to, że jednorodne pokrycie powierzchni bezpośrednio wpływa na jakość analizy ilościowej i obrazowania. Z tego względu przeprowadzone zostały testy mające na celu eksperymentalną weryfikację konkretnych konfiguracji parametrów pomiarowych oraz typu nanostruktur.

Ze względu na szerokie zainteresowanie wykorzystaniem AgNPs i AuNPs postanowiono przetestować możliwości ^{109}AgNPs i AuNPs, syntezowane metodą LASiS, konkretnie z użyciem impulsowego lasera światłowodowego z głowicą 2D skanera galwanometrycznego, oraz nanoszone na płytkę przez rozpylanie zawiesiny według wcześniej opracowanej procedury

[41], w analizie ilościowej LDI-MS i -MSI **[P2]**. Analizę ilościową metodą ^{109}AgNPs-LDI-MS/MSI wykonano uprzednio dla grup związków małocząsteczkowych takich jak aminokwasy [86], kwasy karboksylowe [87] i kwasy 3-hydroksykarboksylowe [88]. Publikacja **[P2]** stanowiła pierwszy etap badań eksperymentalnych w ramach niniejszej rozprawy doktorskiej, mających na celu rozszerzenie wcześniejszych badań o porównawczą ocenę nanocząstek srebra-109 i złota w ilościowej analizie hormonów steroidowych w warunkach analizy LDI-MS i LDI-MSI. Publikacja nie ograniczała się do porównania dwóch nanomateriałów, lecz obejmowała także porównanie manualnych pomiarów LDI-MS z półautomatycznym LDI-MSI prowadzonym w rastrze punktów pomiarowych. Celem nie była wyłącznie automatyzacja pomiaru, ale przede wszystkim uzyskanie bardziej reprezentatywnej odpowiedzi analitycznej z całej powierzchni próbki i ograniczenie błędu wynikającego z losowego wyboru kilku punktów. Wyniki uzyskane w ramach przeprowadzonych badań **[P2]** wykazały przewagę obrazowania MSI nad pomiarem manualnym w warunkach niejednorodnego rozmieszczenia analitu.

Analizy ilościowe LDI-MS i LDI-MSI z użyciem ^{109}AgNPs i AuNPs przeprowadzono dla czterech hormonów: kortykosteronu, prednizolonu, estronu i progesteronu w zakresie stężeń od 1 mg/ml do 1 ng/ml. Precyzyjne oznaczanie hormonów steroidowych ma znaczenie diagnostyczne, ponieważ nawet niewielkie zaburzenia hormonalne mogą prowadzić do zmian fizycznych i psychicznych, a monitorowanie zmian ich stężeń jest istotne dla wczesnej diagnostyki chorób związanych z zaburzeniami hormonalnymi. Analiza obojętnych hormonów steroidowych metodą MALDI-MS jest utrudniona z powodu niskiej efektywności jonizacji i interferencji od matrycy organicznej.

Widma uzyskane metodą ^{109}AgNPs-LDI-MS dla roztworów wzorców hormonów ujawniały obecność adduktów srebra-109 dla wszystkich badanych hormonów steroidowych przy braku sygnałów odpowiadających jonom $[M+H]^+$, $[M+Na]^+$, $[M+K]^+$, $[M+^{109}Ag_3]^+$ lub $[M+^{109}Ag-H_2O]^+$. W widmach uzyskanych dla AuNPs-LDI-MS zaobserwowano sygnały adduktów protonowych, sodowych i potasowych, przy czym dla estronu dominował addukt potasu, dla prednizolonu i kortykosteronu addukt sodu, natomiast progesteron obserwowano wyłącznie w postaci adduktu protonowego. Intensywności sygnałów zarejestrowane dla poszczególnych adduktów przedstawione zostały na rysunku 4.

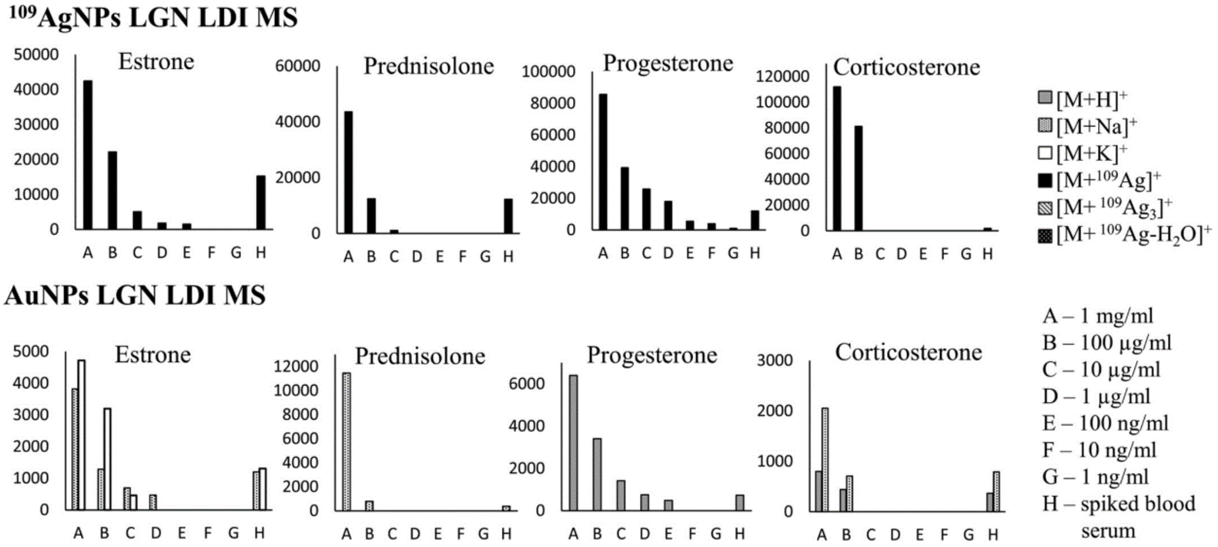

Rys. 4. Wykresy słupkowe przedstawiające zależność intensywności sygnału wybranych jonów od stężenia badanych hormonów steroidowych dla ^{109}AgNPs i AuNPs. Rysunek pochodzi z publikacji **[P2]**.

Analiza z wykorzystaniem ^{109}AgNPs zapewniała wyższe wartości S/N niż analiza z wykorzystaniem AuNPs, a w większości przypadków również lepszą dokładność masową. Świadczy to o większym potencjale dokładnej identyfikacji analizowanych hormonów w wieloskładnikowych mieszaninach wykorzystując ^{109}AgNPs. Wyjątek stanowił estron, dla którego nieco mniejszy błąd masy uzyskano przy użyciu AuNPs. W publikacji **[P2]** porównano również wartości LOD uzyskiwane w manualnych pomiarach LDI-MS, wykonywanych w czterech losowo wybranych punktach próbki, oraz w półautomatycznej analizie LDI-MSI prowadzonej w rastrze punktów pomiarowych na wyznaczonym obszarze.

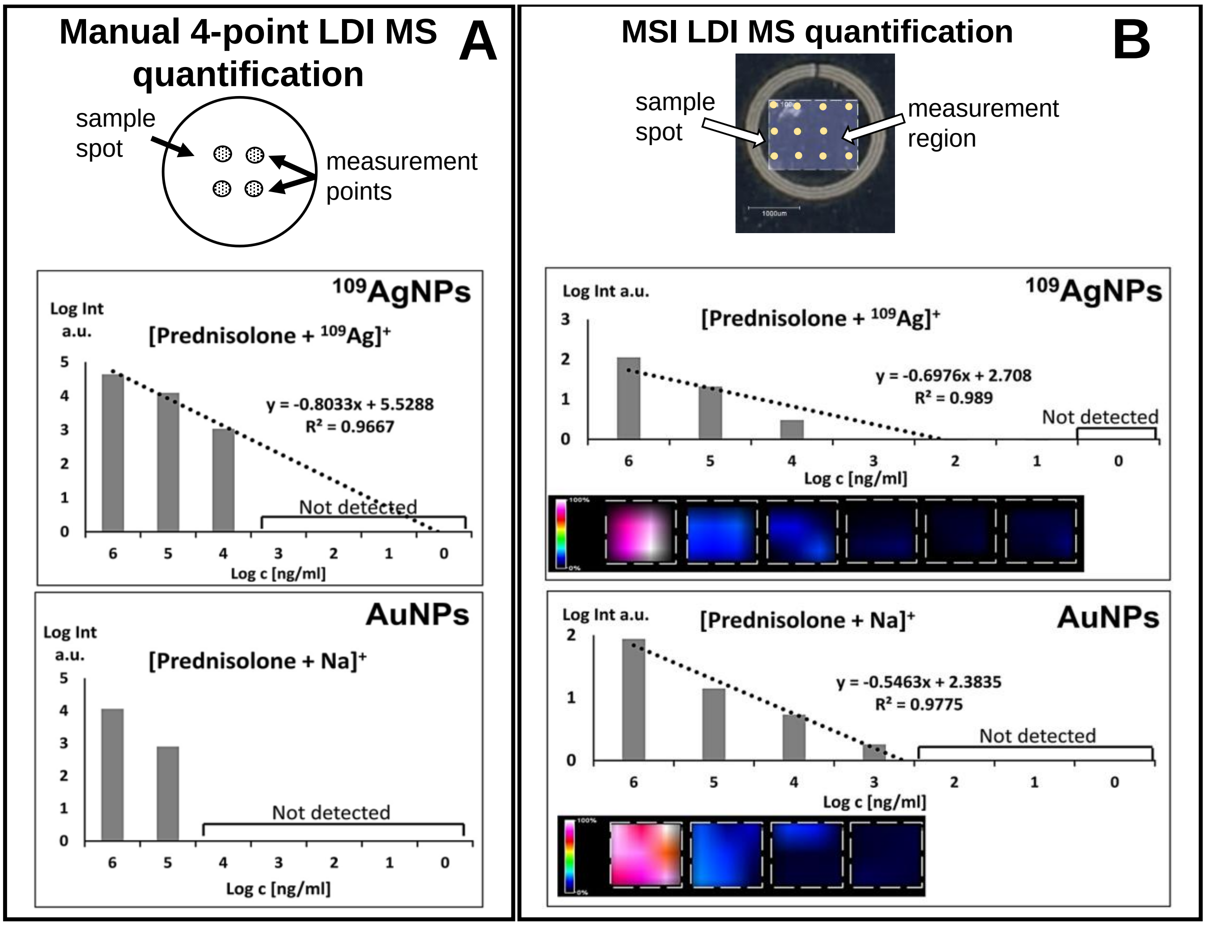

Rys.5. Porównanie analizy ilościowej prednizolonu metodami manualnego LDI-MS (A) i LDI-MSI (B) z wykorzystaniem ^{109}AgNPs i AuNPs. Wykresy przedstawiają zależność logarytmu intensywności sygnału wybranych jonów od logarytmu stężenia, natomiast obrazy jonowe umieszczone pod wykresami w panelu B ilustrują powierzchniowy rozkład sygnału na powierzchni próbki. Rysunek zaadaptowany został z publikacji **[P2]**.

Porównanie wyników uzyskanych dla analizy MS i MSI dwoma typami nanocząstek wykonane dla prednizolonu przedstawione zostało na rysunku 5. Wartości LOD i dolnego limitu oznaczania ilościowego (LLOQ, z ang. lower limit of quantification) dla wykonanych pomiarów przedstawione zostały w tabeli 1. Możliwa do uzyskania mała wartość LOD i LLOQ świadczy o potencjale wykorzystania metody do oznaczania wybranych związków w mieszaninach, w których zawarta jest niewielka ilość tych związków. W przypadku większości badanych hormonów, MSI umożliwiło uzyskanie wartości LOD równych lub niższych niż w manualnych pomiarach LDI-MS. Najkorzystniejsze wyniki, oceniane na podstawie najniższych wartości LOD, uzyskano dla ^{109}AgNPs. Podsumowując, metoda LDI-

MSI z wykorzystaniem ^{109}AgNPs zapewniła najlepsze ogólne wyniki ilościowe oraz najwyższą czułość detekcji spośród badanych układów.

Do kolejnych analiz wybrano metodę ^{109}AgNPs-LDI-MS, ze względu na wyniki poprzednich analiz **[P2]**, wskazujące na większy zakres stężeń możliwy do oznaczenia wykorzystując nanocząstki srebra-109 niż nanocząstki złota. Badania w ramach publikacji **[P3]** wykonane zostały w oparciu o koncepcję analizy ilościowej LDI-MS do szybkiej analizy w szerokim zakresie stężeń substancji psychoaktywnych z grup kannabioidów i opioidów. Badanie tych związków i produktów ich metabolizmu może pozwolić zrozumieć ich skutki toksykologiczne. Ponadto, podejścia metabolomiczne mogą ujawnić, jak narkotyki zmieniają endogenne szlaki metaboliczne, co może przyczyniać się do niekorzystnych skutków zdrowotnych lub długotrwałych zmian fizjologicznych.

Analizie ^{109}AgNPs-LDI-MS poddano tetrahydrokannabinol (THC), jego metabolity 11-OH-THC i 11-COOH-THC oraz wybrane opioidy: fentanyl, kodeinę, metadon, tramadol, heroinę i 6-monoacetylomorfinę (6-MAM). Pomiary wzorców przeprowadzono w zakresie stężeń od 100 µg/ml do 10 pg/ml.

Spośród wszystkich analizowanych związków jedynie dla metadonu nie obserwowano jonu adduktu $[M+^{109}Ag]^+$. Znacząca wysokość sygnału została zaobserwowana dla jonów $[\text{fentanyl}+^{109}Ag]^+$, $[\text{11-OH-THC}+^{109}Ag]^+$ i $[\text{11-COOH-THC}+^{109}Ag]^+$. Odnotowano specyficzny przebieg jonizacji: widma masowe kodeiny, heroiny, 6-MAM i tramadolu pozwoliły na oznaczenie stosunkowo rzadko spotykanych jonów $[M–H]^+$ o znacznie większych intensywnościach sygnału niż jony $[M+^{109}Ag]^+$ w danej próbce. Zjawisko to przypisano fotojonizacji wywołanej przez laser UV stosowany w źródle jonów MALDI-MS. Mechanizm tego procesu jest w literaturze przedstawiony jako początkowa protonacja atomu N, a następnie deprotonacja i utworzenie podwójnego wiązania C═N (rys. 6) [89,90].

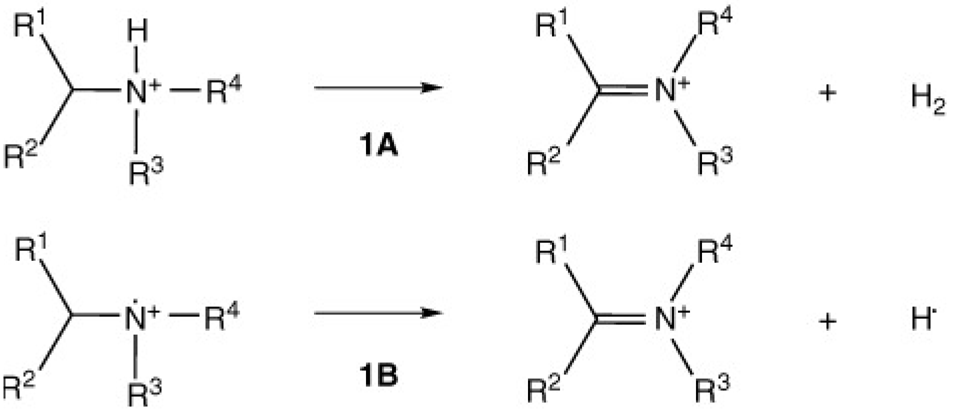

Rys. 6. Możliwe drogi tworzenia się jonu $[M–H]^+$ dla amin trzeciorzędowych [89].

W przypadku metabolitów THC obecne były również sygnały odpowiadające adduktom trójatomowych klastrów srebra-109 $[M+{}^{109}Ag_3]^+$. Addukty te odnotowano wcześniej dla aminokwasów [91] i innych związków [92]. Mimo że występowanie tych adduktów zostało udokumentowane wcześniej dla kodeiny [93], pik $[\text{kodeina}+{}^{109}Ag_3]^+$ w widmie masowym uzyskanym w ramach niniejszych badań nie wykazywał istotnej intensywności. Sugeruje to, że występowanie jonów $[M+{}^{109}Ag_3]^+$ nie jest powiązane z budową związku, a zależy od warunków analizy. Zmiany względnej abundancji wybranych jonów w kolejnych rozcieńczeniach przedstawiono na rysunku 7.

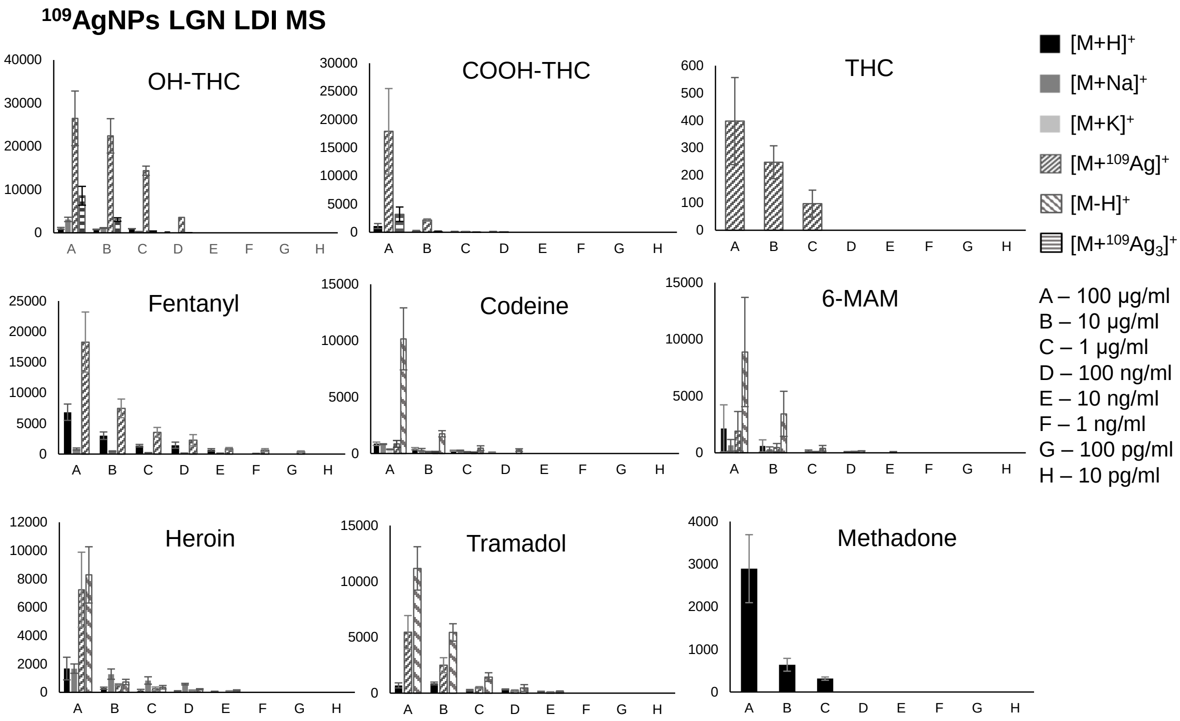

Rys.7. Wykresy słupkowe przedstawiające zależność względnej abundancji wybranych jonów od stężenia analizowanych związków. Rysunek pochodzi z publikacji **[P3]**.

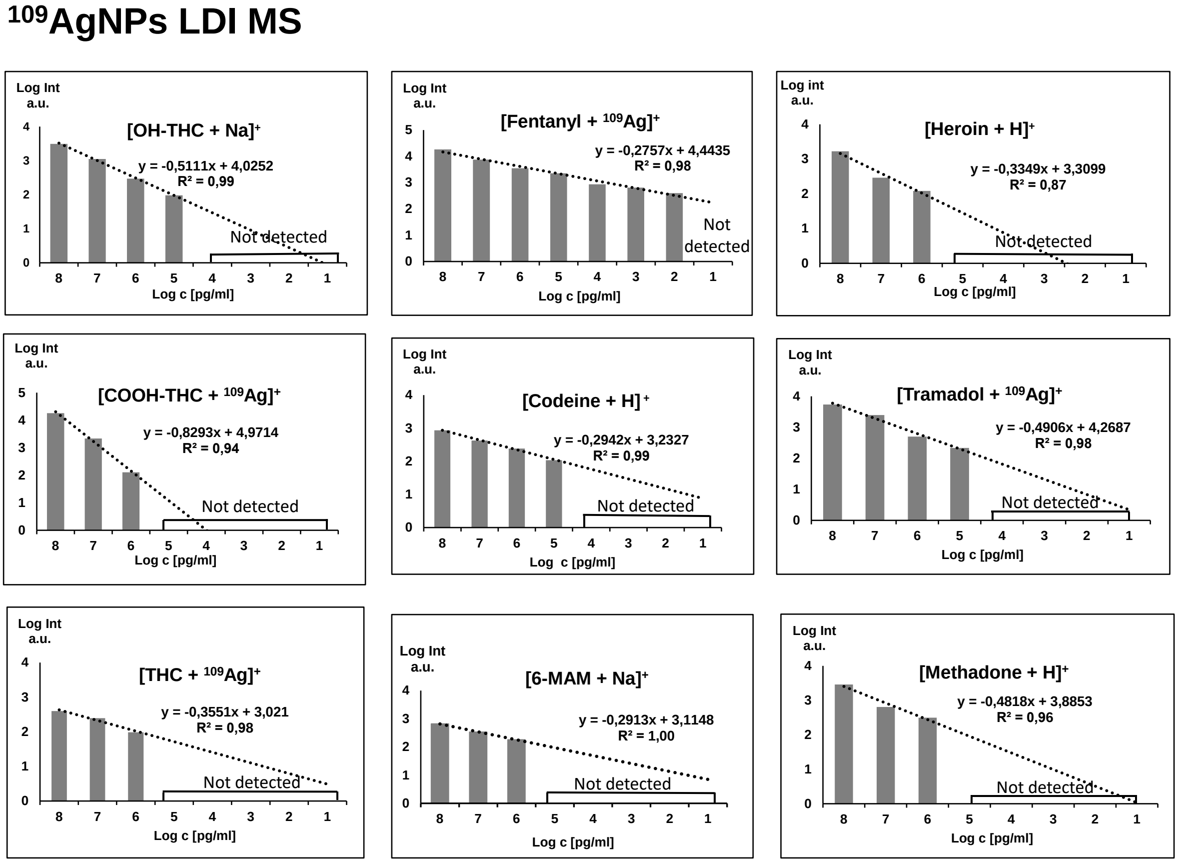

^{109}AgNPs LDI MS

Rys. 8. Zależność sygnału od stężenia, liniowość i jakość kalibracji uzyskane w analizie ^{109}AgNPs-LDI-MS. Rysunek zaadaptowany został z publikacji **[P3]**.

Wartość granicy wykrywalności (LOD, z ang. limit of detection) dla fentanylu wyniosła 1,03 pg/ml (ilość w plamce pomiarowej - 0,515 fg). W pracy Angi i in. [94] technikę UHPLC sprzężoną z pojedynczą kwadrupolową spektrometrią mas wykorzystano do oznaczenia 19 analogów fentanylu. Autorom udało się uzyskać LOD wynoszący 3 ng/ml dla fentanylu. Uzyskana w pracy **[P3]** granica wykrywalności fentanylu była około 3000 razy niższa. Granica wykrywalności heroiny wyniosła 8,22 ng/ml (4,11 pg/punkt pomiarowy). Wykresy przedstawiające wyniki analizy granicy wykrywalności narkotyków przedstawione zostały na rysunku 8. Uzyskane wyniki wskazują, że metoda ^{109}AgNPs-LDI-MS może być szczególnie użyteczna w analizie przesiewowej fentanylu, dla którego uzyskano wyjątkowo niską wartość LOD, oraz przydatna w oznaczaniu wybranych opioidów, w tym heroiny. Wysoka wartość LOD uzyskana dla THC świadczy jednak o braku uniwersalności metody do oznaczania substancji psychoaktywnych o bardzo zróżnicowanych strukturach w szerokim zakresie stężeń.

W ramach badań opisanych w publikacji **[P3]** zbadany został również wpływ matrycy na zakres wykrywalności fentanylu metodą ^{109}AgNPs-LDI-MS. Efekty matrycowe w próbkach biologicznych mogą wpływać na dokładność i czułość. Wykorzystano rozcieńczone próbki moczu i surowicy, do których dodano wzorzec analityczny fentanylu, w kolejnych rozcieńczeniach. Wynik analizy próbek porównano z intensywnością jonów tych samych adduktów dla widm pochodzących z roztworów w czystym rozpuszczalniku. Badanie intensywności sygnałów w całym spektrum badanych stężeń pokazuje, że addukt fentanylu utworzony z jonem srebra-109 był najpowszechniejszą formą jonową dla tego związku. Wyniki wskazują na wysoki stopień czułości metody w wykrywaniu fentanylu, zarówno w roztworze standardowym, jak i w próbkach surowicy wzbogaconych fentanylem, o czym świadczą wartości LOD wynoszące odpowiednio 3,36 ± 0,68 pg/ml i 3,04 ± 0,81 pg/ml. W przypadku moczu wzbogaconego fentanylem, granica wykrywalności wynosiła 4,05 ± 0,76 pg/ml.. Chociaż wyniki dla matrycy biologicznej są porównywalne z wynikami badań LC-MS, granica wykrywalności fentanylu dla roztworu wzorca w metanolu jest nadal jedną z najniższych dotychczas opisanych. Zhang i in. [95] osiągnęli jedną z najniższych odnotowanych wartości LOD dla fentanylu, osiągając 2,5 ng/ml w rozcieńczonych próbkach moczu i 0,5 ng/ml w rozcieńczonych próbkach krwi, stosując chromatografię cieczową połączoną ze spektrometrią mas o wysokiej rozdzielczości. Busardo i in. zanotowali wartości LOD w zakresie pikogramów na mililitr dla fentanylu, ale przy użyciu spektrometru masowego z potrójnym kwadrupolem o niskiej rozdzielczości [96]. Oba przywołane przypadki obejmowały złożone etapy przygotowania próbek, w tym wytrącanie białek, które były znacznie bardziej czasochłonne w porównaniu z metodą ^{109}AgNPs-LDI-MS. Wyniki analiz ^{109}AgNPs-LDI-MS świadczą o dużych możliwościach tej metody do szybkiej analizy toksykologicznej wybranych narkotyków. Szczególnie istotne wyniki uzyskane dla analizy fentanylu sugerują potrzebę dalszego rozwoju metody opartej na analizie LDI-MS opartej o monoizotopowe nanocząstki srebra.

3.2. Obrazowanie spektrometrią mas z wykorzystaniem ablacji laserowej w warunkach ciśnienia atmosferycznego

Wcześniejsze publikacje wchodzące w skład niniejszej rozprawy wykazały przydatność nanostruktur opartych na srebrze i złocie w analizie związków małocząsteczkowych oraz obrazowaniu MSI **[P1-P3]**. Jednocześnie w klasycznych metodach LDI-MSI próbkowanie zazwyczaj zachodzi w warunkach wysokiej próżni, a przygotowanie próbki często wymaga nanoszenia dodatkowej matrycy, istnieje ryzyko zaburzenia pierwotnego rozmieszczenia związków na skutek lateralnego przemieszczania analitów (rozdział 1.2.1). Dodatkowo, kilkuetapowy proces przygotowania próbki (rozdział 1.2.2) wymaga specjalistycznego sprzętu, utrudnia rozwój metod opartych na profilowaniu wgłębnym i obrazowaniu MSI w trzech wymiarach (rozdział 1.3). Wykorzystanie ablacji laserowej jako metody próbkowania w MSI, w połączeniu z jonizacją pod ciśnieniem atmosferycznym, umożliwia prowadzenie analiz w warunkach ciśnienia atmosferycznego oraz dostosowanie techniki do profilowania wgłębnego. Z tego względu w kolejnym etapie badań wykorzystano wcześniej opracowaną platformę LARESI-MSI [47], umożliwiającą próbkowanie w warunkach ciśnienia atmosferycznego oraz zwiększenie selektywności identyfikacji dzięki sprzężeniu z tandemową spektrometrią mas w trybie SRM **[P4]**. Szczegółowe uzasadnienie zastosowania ablacji laserowej w warunkach ciśnienia atmosferycznego oraz zakresu mid-IR przedstawiono wcześniej w rozdziałach 1.2 i 1.3.

Po wstępnej identyfikacji związków w ekstraktach metodą UHPLC-UHRMS wybrane metabolity poddano celowanemu obrazowaniu LARESI-SRM-MSI. Jako metodę próbkowania zastosowano ablację laserową laserem o długości fali 2940 nm. Ta długość fali odpowiada pasmu mid-IR, którego wykorzystanie w MSI opisane zostało w rozdziale 1.2.2 niniejszej rozprawy doktorskiej. Przedstawiona platforma była wcześniej stosowana do celowanej analizy metabolitów w tkance ludzkiej [47] oraz do oznaczania mykotoksyn w zakażonych ziarnach [97], przy wykorzystaniu trybu SRM zwiększającego selektywność identyfikacji na podstawie fragmentacji jonów. W ramach niniejszej rozprawy doktorskiej kontynuowane były badania testujące możliwości opracowanego systemu, tym razem w celowanej analizie nienaruszonych tkanek roślinnych **[P3]**. Jako obiekty testowe wybrano tkanki dwóch odmian banana odmiany Red Dacca (*Musa acuminata*) oraz banana odmiany Cavendish z grupy odmian AAA (*Musa acuminata*). Do analiz LARESI-SRM-MSI przygotowano skrawki tkanek owocu banana o grubości 100 μm wykonane za pomocą mikrotomu. Skrawki umieszczono na stoliku wyposażonym w moduł Peltiera utrzymujący temperaturę −18°C, co miało ograniczyć lateralne przemieszczanie związków na powierzchni oraz degradacje enzymatyczną próbki. Obrazowanie MS wykonano z rozdzielczością 200 × 200 μm dla próbki Cavendish oraz 300 × 300 μm dla próbki Red Dacca.

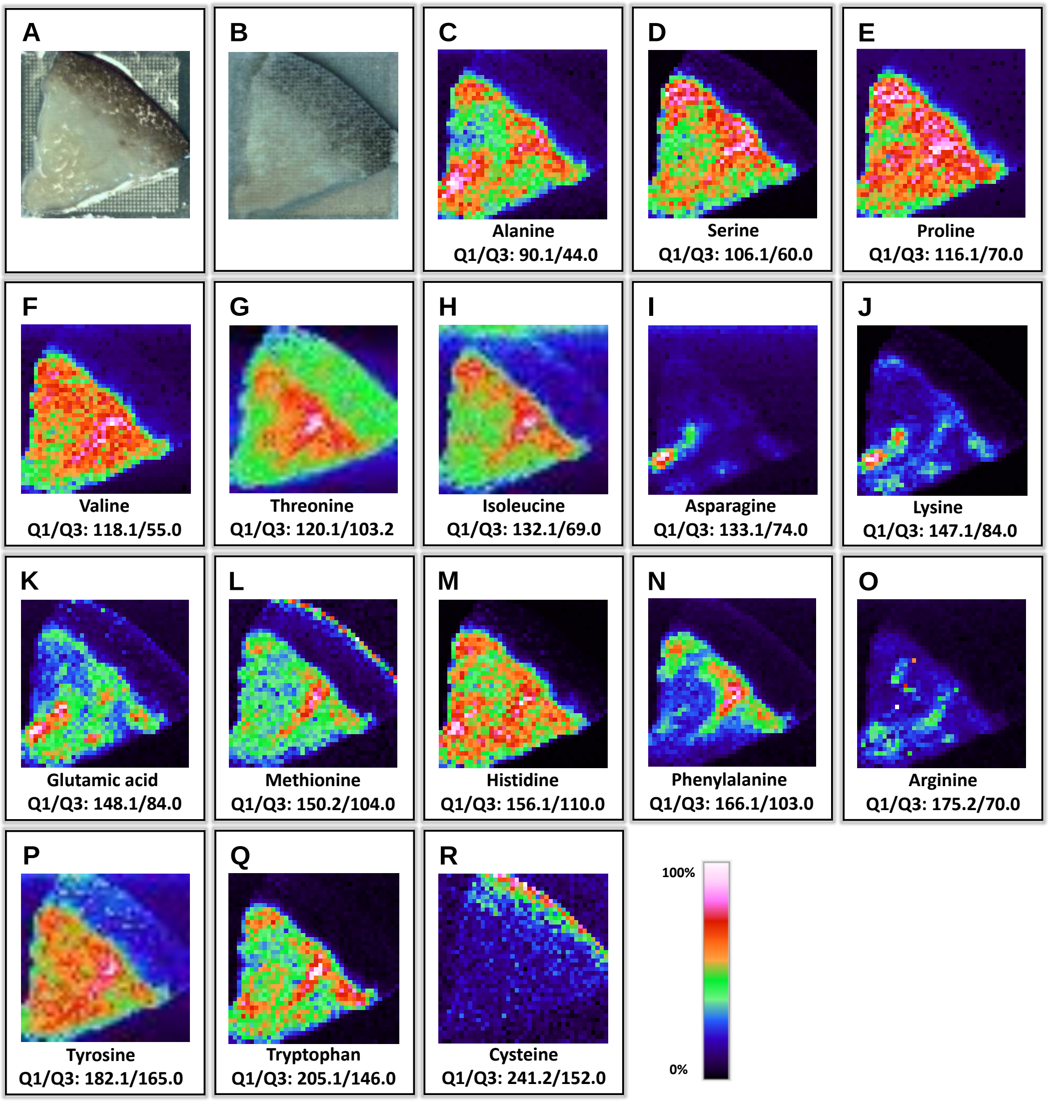

Rys. 9. Fotografie optyczne obrazowanej powierzchni tkanki banana przed (A) i po obrazowaniu (B). Obrazy jonowe LARESI SRM MSI tkanki bananowca Cavendish (C–R). Rysunek pochodzi z publikacji **[P4]**.

Dzięki analizie LARESI-MSI w trybie SRM zlokalizowano 12 metabolitów w tkance banana Cavendish (rys. 9) oraz 16 aminokwasów w tkance banana Red Dacca. Rozmieszczenie przestrzenne niektórych z tych związków występujących w bananach zostało zaprezentowane po raz pierwszy. Wyniki badań potwierdziły przydatność LARESI-SRM-MSI do celowanego obrazowania związków małocząsteczkowych w nienaruszonych tkankach roślinnych. Jednak ma tym etapie rozwoju systemu uzyskana konfiguracja nie umożliwiała wiarygodnego bezpośredniego obrazowania 3D MSI warstwa po warstwie, głównie ze względu na kształt krateru poablacyjnego i wynikające z niego niejednorodne usuwanie materiału. Niekorzystny wpływ tego zjawiska na analizy 2D i 3D MSI opisany został w rozdziale 1.2 (2D MSI) i 1.3 (3D MSI). Analiza opisana w publikacji **[P4]** stanowiła pierwsze zastosowanie platformy LARESI sprzężonej z MS/MS w trybie SRM do celowanego obrazowania metabolitów w nienaruszonych tkankach roślinnych a zarazem pierwszym doniesieniem dotyczącym obrazowania MSI tkanek banana z wykorzystaniem identyfikacji opartej na analizie MS/MS.

3.3. Obrazowanie spektrometrią mas związków małocząsteczkowych w dwóch i trzech wymiarach w warunkach ciśnienia atmosferycznego – metoda LARAPPI/CI-MSI

W pracy **[P4]** wykorzystano układ LARESI-SRM-MSI do dwuwymiarowego obrazowania związków małocząsteczkowych w tkankach roślinnych. Rozwiązanie to umożliwiało analizę powierzchniową próbki w warunkach ciśnienia atmosferycznego, jednak nie było przystosowane do kontrolowanego usuwania warstw badanego materiału, a tym samym do bezpośredniego obrazowania trójwymiarowego. Ograniczenie to wynikało z braku rozwiązań pozwalających na precyzyjne kształtowanie obszaru ablacji i powtarzalne usuwanie kolejnych warstw próbki przy zachowaniu odpowiedniej rozdzielczości przestrzennej oraz akceptowalnego czasu analizy. Z tego względu konieczne było opracowanie zmodyfikowanego układu **[P5]**, umożliwiającego bezpośrednią analizę 3D związków małocząsteczkowych w makroskopowych obiektach biologicznych w warunkach ciśnienia atmosferycznego. Do tego celu wykorzystany został system laserowej ablacji ze zdalną fotojonizacją/jonizacją chemiczną do obrazowania spektrometrią mas (LARAPPI/CI-MSI) **[P5]** wywodzący się koncepcyjnie z rozwiązania zastosowanego w technice LARESI-SRM-MSI **[P4]**, jednak istotnie zmodyfikowany i rozszerzony o funkcjonalność obrazowania trójwymiarowego.

Aby uzyskać równomierne usuwanie materiału z każdej warstwy zastosowany został homogenizator optyczny w postaci optycznego elementu dyfrakcyjnego (DOE) przekształcającego wiązkę o przekroju kołowym i gaussowskim profilu energii w wiązkę o przekroju kwadratowym z rozkładem energii typu „top-hat”, rozwiązanie to zaproponowano wcześnie w technice IR-MALDESI do 3D-MSI [65]. Zastosowanie elementu DOE umożliwiło uzyskanie płaskiego dna krateru poablacyjnego oraz kontrolę objętości pojedynczego woksela, co stanowi kluczowy warunek realizacji obrazowania 3D. Ponieważ pojedynczy woksel w tej metodzie stanowi część sześcianu z zaokrąglonymi krawędziami bocznymi, a nie idealny sześcian, zastosowane zostały dodatkowe założenia techniczne mające zapewnić jednorodną ablację warstwy. Tymi rozwiązaniami były minimalny oversampling oraz schemat ablacji w układzie odwróconej piramidy (rys.10). Model odwróconej piramidy zakłada, że ze względu na nieidealnie sześcienny kształt obszaru poablacyjnego powstałego w wyniku ablacji pojedynczego punktu pomiarowego, materiał z warstwy na wyższym poziomie pozostawałby w miejscu poddawanym ablacji na kolejnym, niższym poziomie. Z tego względu, w tym modelu, każda kolejna warstwa poddawana ablacji ma obszar ablacji mniejszy o jeden rząd wokseli w osi X i jeden rząd wokseli w osi Y, a powstałe nowe rastry są wyśrodkowane względem pierwszej usuwanej warstwy. Rozwiązanie to pozwoliło uniknąć ponownej ablacji materiału z warstw wyższych oraz zminimalizować artefakty związane z nieidealnym profilem ablacji, co stanowi jedno z głównych wyzwań w bezpośrednim obrazowaniu 3D MSI. zastosowanie modelu odwróconej piramidy całkowicie likwidowało problem ablacji materiału pochodzącego z warstw wyższych w sygnale rejestrowanym dla warstw głębszych, mogący wynikać z osuwania się materiału ze ścian krateru ablacyjnego. Rozwiązanie było zgodne z fizycznymi uwarunkowaniami warstwowego usuwania materiału.. Ważnym elementem układu był zintegrowany czujnik odległości pełniący funkcję profilometru powierzchni, umożliwiający kontrolę głębokości ablacji i wyznaczanie położenia kolejnych poziomów analizy.

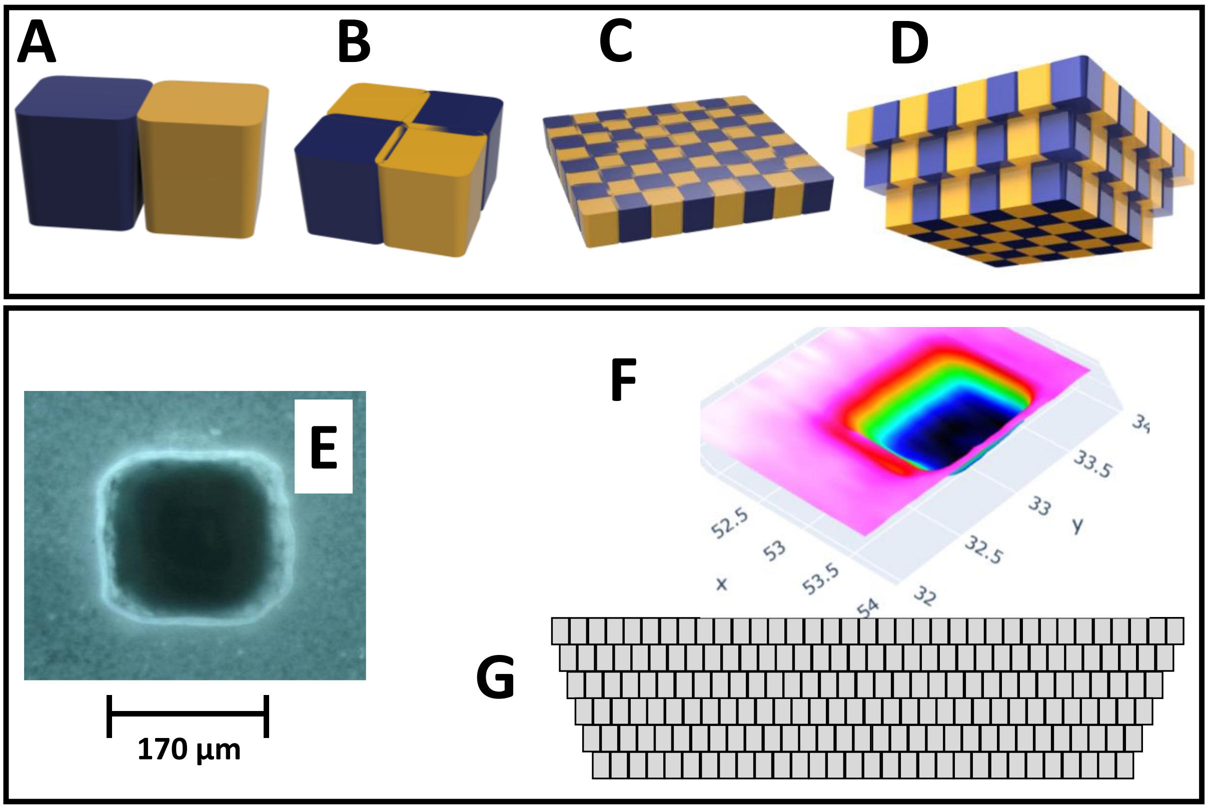

Rys. 10. Modele 3D przestrzeni ablacji: (A) nieoptymalne rozmieszczenie dwóch wokseli; (B) oversampling czterech wokseli umożliwiający całkowitą ablację przestrzeni; (C) przykład oversamplingu dla jednej warstwy tablicy 8 × 8 wokseli; (D) układ odwróconej piramidy dla wokseli poddanych oversamplingowi; (E) obraz z mikroskopu optycznego pojedynczego woksela po ablacji w żelu agarowym z użyciem 20 impulsów laserowych; (F) wynik skanowania profilometrem obszaru po ablacji w żelu agarowym o wymiarach 7 × 7 × 1 wokseli i rozdzielczości 140 × 140 µm; (G) uproszczony układ odwróconej piramidy wokseli w eksperymentach 3D MSI widziany z boku obiektu. Rysunek pochodzi z publikacji **[P5]**.

W badaniach wykorzystano spektrometr mas Bruker Impact II wyposażony w źródło jonów VIP-HESI. W ramach optymalizacji porównano konfiguracje jonizacji ESI i APCI, pod kątem ich kompatybilności z opracowanym systemem. W ramach testów wykorzystana została również lampa VUV emitująca promieniowanie w zakresie 110–160 nm, mające służyć do fotojonizacji. Szereg testów, polegających na porównaniu wybranych konfiguracji, pozwolił na określenie źródła jonów oraz składu i szybkości przepływu cieczy wspomagającej jonizację pozwalających na uzyskanie sygnałów o największych intensywnościach dla użytych związków modelowych: rybozy, histydyny, tymidyny i uracylu oraz lipidów z grup kwasów tłuszczowych oraz karnityn. Jako najlepsza metoda jonizacji wybrana została kombinacja jonizacji chemicznej przy ciśnieniu atmosferycznym (APCI) oraz fotojonizacji wspomaganej dopantem (DA-APPI), z wykorzystaniem mieszaniny metanol/toluen (99:1, v/v) jako cieczy wspomagającej jonizację. Największe wartości stosunku S/N uzyskano dla jonizacji APCI/APPI z pomiarem w trybie jonów ujemnych. Optymalizacja składu cieczy wspomagającej jonizację i natężenia jej przepływu wskazały, że jonizacja z największą efektywnością zachodzi dla mieszaniny metanol/toluen 99:1 (v/v) wprowadzanej do emitera APCI z natężeniem 200 µL/min. Opracowany system był pierwszym przykładem skutecznego zastosowania połączonego źródła DA-APPI/APCI w obrazowaniu spektrometrią mas.

Proces optymalizacji systemu opisanego w publikacji **[P5]** obejmował również dobór rozdzielczości przestrzennej odpowiedniej dla analiz LARAPPI/CI-3D-MSI, z uwzględnieniem geometrii plamki laserowej oraz warunków oversamplingu. Jako optymalną dla obrazowania 3D-MSI z wykorzystaniem systemu LARAPPI/CI przyjęto rozdzielczość 140 × 140 µm odpowiadającą odległości między środkami sąsiednich wokseli. Rozdzielczość ta umożliwiała usuwanie całego materiału z warstwy, co było warunkiem koniecznym do bezpośredniego obrazowania (direct3D-MSI). W konsekwencji umożliwiła ona wielopoziomową analizę makroskopowych obiektów biologicznych przy zachowaniu informacji o przestrzennym rozmieszczeniu związków w obrębie najważniejszych struktur badanych tkanek. Istotną zaletą opracowanego podejścia jest możliwość prowadzenia analiz bez konieczności przygotowania serii przekrojów tkankowych, co eliminuje artefakty związane z rekonstrukcją danych 3D oraz migracją metabolitów pomiędzy warstwami.

Walidację możliwości metody do analiz 3D-MSI wykonano z wykorzystaniem dwóch tkanek roślinnych: fragmentu korzenia rzodkiewki i fragmentu owocu kiwi (rys. 11), oraz tkanki ludzkiej nerki obejmującej obszar przejścia pomiędzy tkanką prawidłową a nowotworową. Wizualizacja 3D pozwoliła na uzyskanie dokładnych informacji na temat globalnego rozmieszczenia związków oraz bardziej precyzyjne przypisanie ich do poszczególnych struktur korzenia rzodkiewki. Szczególnie dobrze ilustrują to jony różnicujące epidermę, korę pierwotną i miękisz badanej próbki. W wizualizacji rozmieszczenia jonów związków w owocu kiwi akumulacja wybranych metabolitów widoczna była w ścianach lokuli oraz nasionach owocu (rys. 11). Przeprowadzone eksperymenty stanowią pierwszą demonstrację możliwości bezpośredniego obrazowania 3D związków małocząsteczkowych w tkankach biologicznych w warunkach ciśnienia atmosferycznego. Dzięki dedykowanemu oprogramowaniu do wizualizacji danych trójwymiarowych oraz analizy współlokalizacji jonów możliwe było przedstawienie lokalizacji kilku jonów w tej samej wizualizacji, co umożliwiło analizę ich wzajemnych relacji przestrzennych. Opracowana metoda direct3D-LARAPPI/CI-MSI stanowi istotny postęp w dziedzinie obrazowania spektrometrią mas, umożliwiając bezpośrednią analizę objętościową próbek biologicznych z zachowaniem informacji przestrzennej, bez konieczności rekonstrukcji danych z przekrojów 2D.

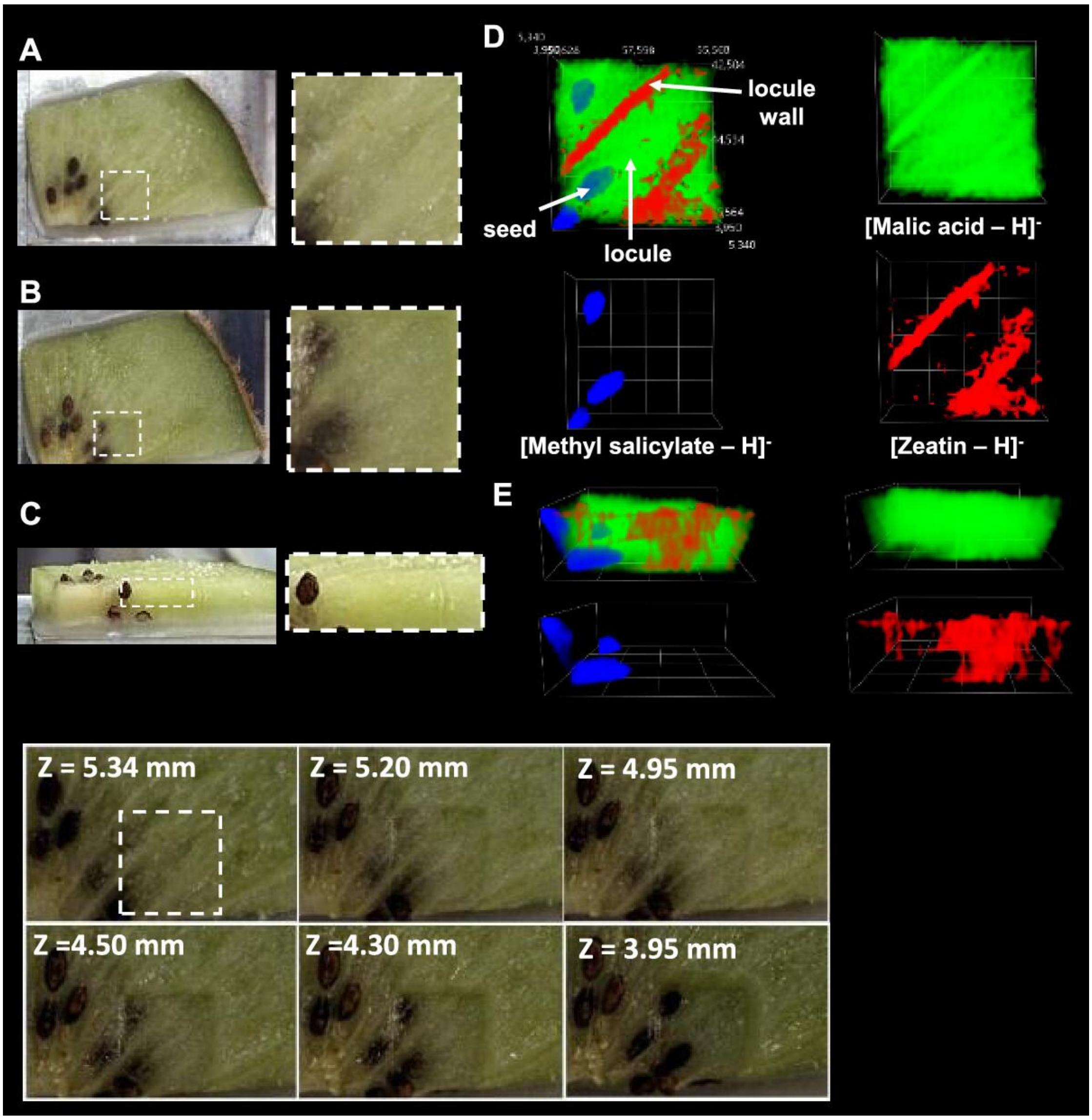

Rys. 11. Fotografie badanego obiektu (przekrój poprzeczny owocu kiwi) oraz wybrane wyniki 3D MSI. (A) Fotografie optyczne obiektu początkowego i obszaru analizy oznaczone białą linią przerywaną; (B) fotografie optyczne obiektu po analizie; (C) widok z boku obiektu. (D) Obrazy jonów 3D MSI dla trzech jonów reprezentowanych przez różne kolory – widoki z góry; (E) widoki z boku obrazów jonów 3D dla jonów o różnych kolorach. Intensywność sygnału jonowego jest reprezentowana przez stopień nieprzezroczystości chmury 3D w danym kolorze. Dolny panel zawiera fotografie optyczne obszaru przed ablacją i po kolejnych etapach ablacji. Wartość Z wyznaczano z wykorzystaniem precyzyjnego czujnika odległości. Rysunek pochodzi z publikacji **[P5]**.

Technika LARAPPI/CI-MSI opracowana została z myślą o wydajnej niecelowanej analizie, rozszerzono ją o tryb bbCID (z ang. broadband collision induced dissociation) w celu poprawy identyfikacji związków na podstawie jednoczesnej rejestracji jonów prekursorowych i fragmentacyjnych **[P6]**.

W tandemowej spektrometrii mas (MS/MS) różne tryby akwizycji danych determinują sposób selekcji i fragmentacji jonów prekursorowych, wpływając zarówno na zakres uzyskiwanej informacji strukturalnej, jak i wydajność analityczną. W konwencjonalnym trybie MS/MS przeprowadzana jest ukierunkowana analiza, w której wcześniej wybrany jon prekursorowy jest poddawany fragmentacji, często poprzez dysocjację indukowaną zderzeniami (CID) przy ustalonej energii zderzeń, w celu wygenerowania jonów fragmentacyjnych, mogących posłużyć do charakterystyki strukturalnej. To podejście zapewnia wysoką specyficzność i czułość w analizie związków będących przedmiotem zainteresowania. Wymaga ono jednak wcześniejszej wiedzy na temat występujących w próbce związków chemicznych, co sprawia, że jest nieodpowiednie do analiz niecelowanych [98].

Strategią akwizycji niezależną od danych jest szerokopasmowa dysocjacja indukowana zderzeniami (bbCID), w której stosuje się szybkie, cykliczne przełączanie między niską a podwyższoną energią zderzeń, co umożliwia uzyskanie danych MS i MS/MS w ramach pojedynczej analizy dla wszystkich jonów wchodzących do komory zderzeniowej, bez wcześniejszej selekcji i izolacji poszczególnych jonów prekursorowych [99].

Ze względu na niepraktyczność klasycznych trybów MS/MS i auto-MS/MS w obrazowaniu MSI, do walidacji sprawności metody LARAPPI/CI-MSI w analizie niecelowanej połączonej z kontrolowaną fragmentacją wybrano tryb bbCID. Strategię tę po raz pierwszy opisano w połączeniu z analizą MSI, a także jako pierwszy raz zastosowano w połączeniu z systemem LARAPPI/CI-MSI. Porównanie obrazu jonowego jonu prekursorowego uzyskanego z danych MS z obrazami jonowymi przypisanych mu jonów fragmentacyjnych generowanych z danych bbCID, wspomagane odniesieniem do widm ESI MS/MS dostępnych w bazach NIST i HMDB, może stanowić dodatkowe potwierdzenie identyfikacji związków w analizie MSI **[P6]**.

W celu walidacji metody pod kątem możliwości rejestracji jonów fragmentacyjnych metodą bbCID-LARAPPI/CI MSI wykorzystano próbkę papieru z trzema obszarami pokrytymi barwnikami oraz jednym obszarem zawierającym tymidynę (rys. 12). Dzięki temu możliwe było bezpośrednie porównanie lokalizacji jonów prekursorowych i fragmentacyjnych na obrazach jonowych z rzeczywistą lokalizacją naniesionych związków. Na próbkę naniesiony został również bezbarwny roztwór tymidyny jako przykład istotnego biologicznie metabolitu endogennego, stanowiącego modelowy związek dla badań prowadzonych metodą LARAPPI/CI-MSI. Próbkę poddano analizie 2D-MSI w trybie dodatnim oraz ujemnym. Analiza w trybie ujemnym pozwoliła na uzyskanie sygnałów o wyższej intensywności, dlatego tryb ten wybrano do dalszych analiz. W publikacji **[P6]** pokazano, że wszystkie cztery związki były identyfikowane na podstawie jonu $[M-H]^-$ i że dla każdego uzyskano co najmniej jeden jon fragmentacyjny. Najwyższe sygnały oraz najwięcej sygnałów jonów fragmentacyjnych uzyskano dla fluoresceiny.

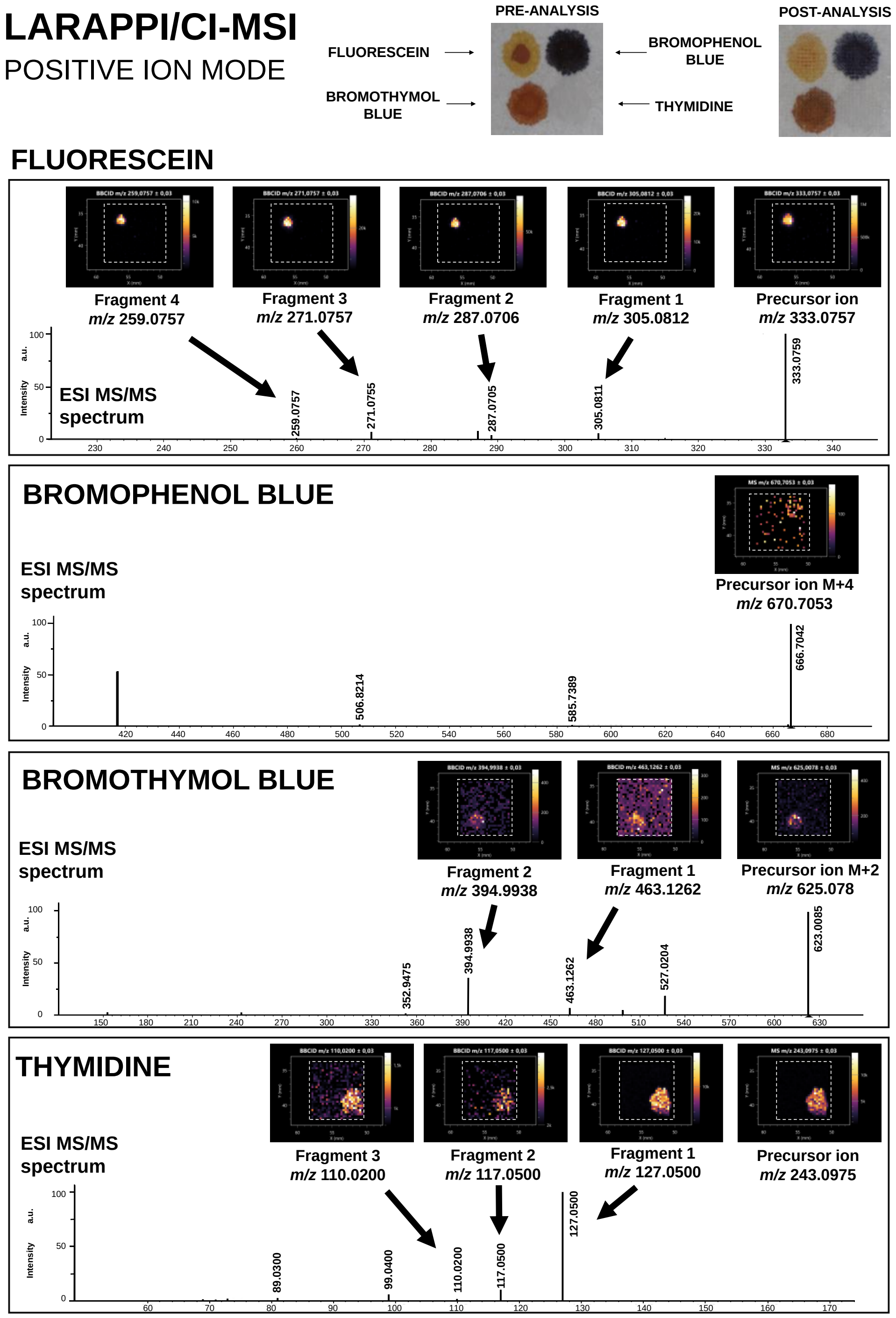

Rys. 12. Wyniki analizy papieru z obszarami, na które naniesiono roztwory fluoresceiny (lewy górny róg), błękitu bromofenolowego (prawy górny róg), błękitu bromotymolowego (lewy dolny róg) i tymidyny (prawy dolny róg), wykonanej metodą LARAPPI/CI-MSI z wykorzystaniem bbCID w trybie jonów ujemnych: (A) zdjęcie optyczne wykonane przed analizą; (B) zdjęcie optyczne wykonane po analizie; (C–F) panele z obrazami jonowymi (górna część panelu) i widmem MS/MS (dolna część panelu) dla danego związku. Rysunek pochodzi z publikacji **[P6].**

Po zweryfikowaniu możliwości metody w zakresie obrazowania MS i MS/MS związków małocząsteczkowych technika bbCID-LARAPPI/CI-MSI wykorzystana została do analizy tkanek ludzkich pęcherza i nerki **[P6]**. Metodyka analizy była analogiczna do metodyki stosowanej w analizach MSI ukierunkowanych na identyfikację potencjalnych biomarkerów nowotworowych. Różnice w profilu metabolicznym tkanki normalnej i nowotworowej pęcherza możliwe były do zaobserwowania na podstawie pięciu związków, przy czym dla nienasyconych kwasów tłuszczowych FA(22:6) i FA(22:5) dopasowano po sześć jonów fragmentacyjnych. W tkance nerki ludzkiej czterem związkom różnicującym tkankę zdrową od nowotworowej przypisano od jednego do dwóch jonów fragmentacyjnych.

Zastosowanie metody LARAPPI/CI-MSI do dwu- i trójwymiarowej analizy mikroorganizmów środowiskowych. Metoda LARAPPI/CI-MSI wykorzystana została do analiz interakcji pomiędzy grzybami patogennymi roślin a mikroorganizmami o właściwościach przeciwgrzybicznych **[P7]**. Analiza interakcji między mikroorganizmami opierała się na obserwacji zwiększonej produkcji metabolitów lub migracji metabolitów wytwarzanych przez jeden organizm w kierunku drugiego w żelu. Celem analiz próbek kolonii bakteryjnych i grzybowych było przetestowanie możliwości metody LARAPPI/CI-MSI w oznaczaniu metabolitów o małych masach cząsteczkowych produkowanych przez mikroorganizmy, które mogą mieć znaczenie w walce z patogenami roślin.

Materiał mikrobiologiczny wykorzystany do analiz pozyskany został od grupy badawczej z Katedry Biotechnologii Środowiskowej na Wydziale Biotechnologii i Nauk o Żywności Politechniki Łódzkiej. Aby umożliwić dokładną identyfikację związków małocząsteczkowych w analizie MSI, na początku badań przeprowadzona została analiza UHPLC-UHRMS ekstraktu każdego z badanych mikroorganizmów wraz z odpowiadającym mu fragmentem żelu agarowego.

Próbki do analizy LARAPPI/CI-MSI zawierające kolonie mikroorganizmów uzyskane zostały przez wycięcie fragmentu żelu agarowego zawierającego obie znajdujące się na szalce kolonie, tak, aby były w niewielkiej odległości od siebie, co umożliwiło jednoznaczne określenie źródła sygnału na obrazie jonowym. Analizy direct3D-LARAPPI/CI-MSI przeprowadzono w celu zbadania interakcji bakterii glebowych *Paenibacillus amylolyticus* oraz *Bacillus cereus* z fitopatogenem *Fusarium graminearum* **[P7]**.

Kluczową zaletą LARAPPI/CI-3D-MSI jest możliwość generowania wizualizacji 3D na podstawie wyników analiz bez poddawania próbki działaniu próżni lub suszeniu. Zastosowanie obrazowania 3D jest szczególnie istotne, aby umożliwić analizę dyfuzji pionowej do pożywki agarowej związków syntezowanych przez mikroorganizmy. Poprzez ablację kolejnych warstw, LARAPPI/CI-3D-MSI ujawniać może ukryte gradienty związków mające znaczenie przeciwdrobnoustrojowe lub sygnalizacyjne, które mogą wpływać na rozwój kolonii drobnoustrojów lub supresję wzrostu fitopatogenów. Podejście direct3D-MSI może być szczególnie przydatne do badania skomplikowanych struktur mikrobiologicznych, takich jak biofilmy.

Wyniki analiz hodowli mikroorganizmów przedstawione w publikacji **[P7]** wskazują na 11 związków małocząsteczkowych różnicujących *Fusarium graminearum* i *Paenibacillus amylolyticus* (rys. 13) oraz 38 metabolitów różnicujących *Fusarium graminearum* i *Bacillus cereus* (rys. 14). Oznaczone związki należą do klas aminokwasów, dipeptydów, kwasów organicznych, cukrów oraz kwasów tłuszczowych. Dzięki analizie LARAPPI/CI-MSI pierwszy raz wykryta została obecność kwasu elaidynowego na skraju obszaru wzrostu kolonii *Bacillus*. Kwas ten prawdopodobnie został zsyntetyzowany w wyniku obecności wysokich stężeń substancji toksycznych z *F. graminearum*[100]. Intensywna synteza kwasu elaidynowego na skraju hodowli może wpływać na zmianę płynności błony komórkowej jako mechanizm obronny.

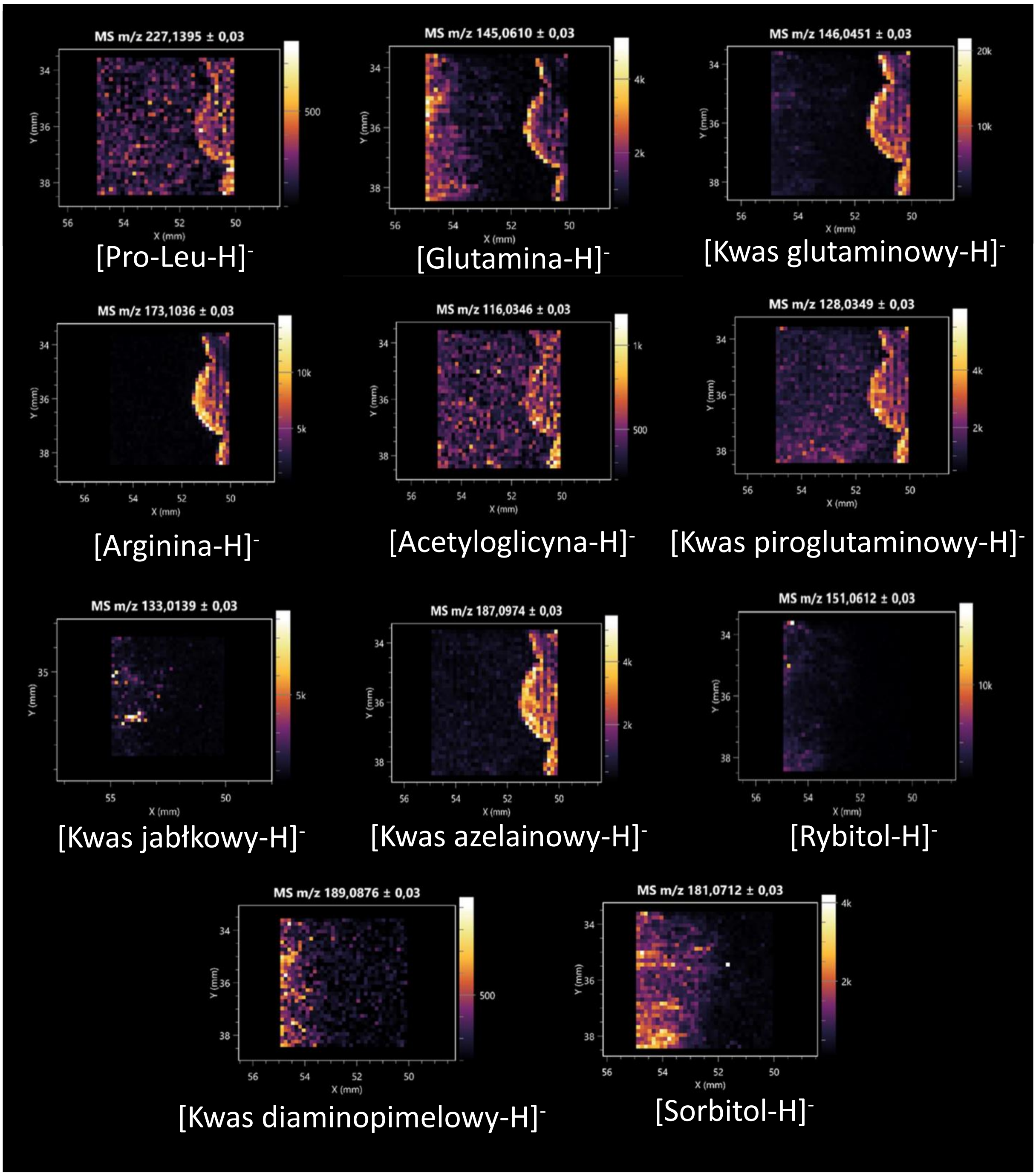

Rys. 13. Obrazy jonowe uzyskane dla związków oznaczonych w hodowli *Fusarium graminearum* i *Paenibacillus amylolyticus*. Rysunek zaadaptowany został z wyników pochodzących z publikacji **[P7]**.

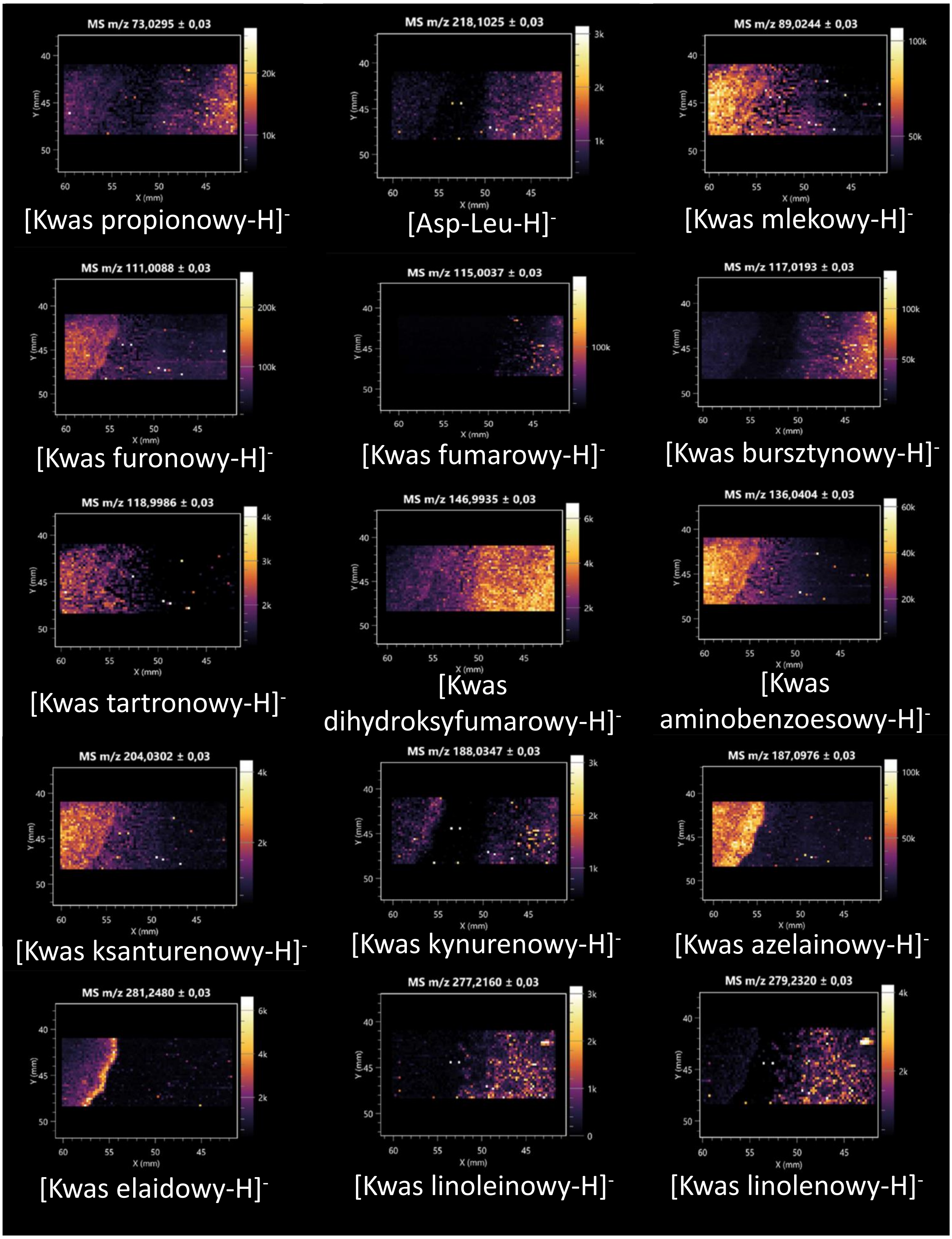

Rys. 14. Obrazy jonowe uzyskane dla związków oznaczonych w hodowli *Fusarium graminearum* i *Bacillus cereus.* Rysunek zaadaptowany został z wyników pochodzących z publikacji **[P7]**.

W ramach realizacji badań do publikacji **[P7]** pierwszy raz przeprowadzona została analiza 3D-LARAPPI/CI-MSI hodowli mikroorganizmów. Umożliwiło to wizualizację rozmieszczenia związków chemicznych oraz ich abundancji na wybranej głębokości w agarze hodowlanym w hodowli *F. graminearum* i *P. amylolyticus*. Różnica w abundancji związków w zakresie osi Z uwidoczniona została na rysunku 15. W ramach publikacji wykonana została również analiza statystyczna szlaków metabolicznych analizowanych mikroorganizmów.

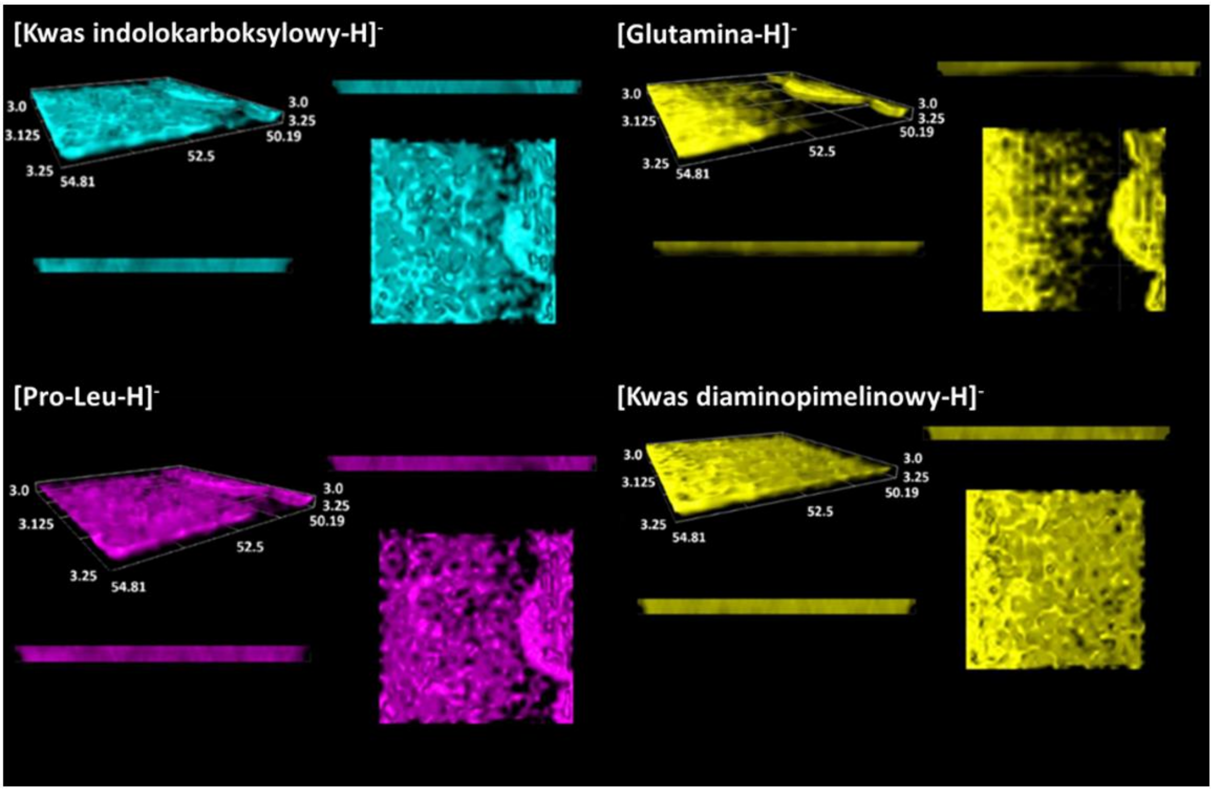

Rys. 15. Wizualizacje 3D uzyskane dla związków oznaczonych w hodowli *F. graminearum* i *P. amylolyticus.* Rysunek zaadaptowany został z wyników pochodzących z publikacji **[P7]**.

Uzyskane wyniki analiz LARAPPI/CI-MSI w dwóch i trzech wymiarach obrazują możliwości systemu do oznaczania różnorodnych klas związków zarówno w miejscu ich syntezy, jak i w wyniku ich przemieszczania się, m.in. w żelu agarowym będącym pożywką hodowlaną mikroorganizmów. Dzięki zachowaniu ciśnienia atmosferycznego na etapie próbkowania, LARAPPI/CI-MSI należy do najbardziej obiecujących metod obrazowania wysoko uwodnionych obiektów w trzech wymiarach metodą profilowania wgłębnego.

3.4. Zastosowanie LARAPPI/CI-MSI do dwu- i trójwymiarowego obrazowania metabolitów rzodkiewki (*Raphanus sativus)* w analizie wpływu pestycydów na jej metabolizm

Obrazowanie korzeni rzodkiewek miało na celu ocenę zmian w metabolizmie rzodkiewki pod wpływem ekspozycji na pestycydy, ze szczególnym uwzględnieniem warunków wysokiego stresu abiotycznego wywołanego ekspozycją na dawkę 100-krotnie wyższą od zalecanej **[P8]**. Analiza LARAPPI/CI-MSI umożliwiła ocenę przestrzennego rozmieszczenia metabolitów w tkance, natomiast niecelowana analiza UHPLC-, wspomagana analizą statystyczną, pozwoliła na szerszą identyfikację związków oraz ocenę zmian w szlakach metabolicznych rzodkiewki w zależności od dawki i składu zastosowanych środków ochrony roślin. Analizy MSI ograniczono do próbki kontrolnej oraz próbki eksponowanej na mieszaninę pestycydów w dawce 100×, aby zwiększyć prawdopodobieństwo uchwycenia przestrzennie zróżnicowanych zmian metabolicznych bezpośrednio w tkance. Rośliny poddano działaniu mieszaniny fungicydów (Scorpion 325 SC, azoksystrobina, difenkonazol), insektycydu (Belem 0.8 MG, cypermetryna) oraz środka ślimakobójczego (Snacol 3G, metaldehyd) w stężeniu 100-krotnie większym niż zalecane przez producenta. Analizowane obszary obejmowały cały korzeń palowy rzodkiewki, hipokotyl oraz część podstawną pędu wraz z liścieniami. Obrazowany obszar obejmujący próbkę kontrolną miał wymiary 19 × 7 mm, natomiast obszar obejmujący próbkę poddaną działaniu pestycydów miał wymiary 21 × 7 mm. Rozdzielczość MSI wybrana do analiz wynosiła 250 µm (X i Y).

Na podstawie dopasowania wartości *m/z* wstępnie przypisano łącznie 88 związków w obu próbkach. 28 z 88 związków wykryte zostało w próbce kontrolnej ze znacząco wyższą intensywnością sygnału, natomiast 23 związki zlokalizowane zostały w próbce poddanej działaniu pestycydów. Pozostałe oznaczone związki wykazywały intensywność sygnału porównywalną dla obu próbek. Rozmieszczenie przestrzenne związków oceniono w czterech obszarach anatomicznych: epidermie, walcu osiowym (steli), tkance korzenia palowego i łodydze. 32 z 88 związków było obecnych stosunkowo równomiernie na całej analizowanej powierzchni przekroju korzenia. 10 związków zaobserwowano głównie w obszarze łodygi, 8 było zlokalizowanych głównie w samej steli, a 19 było obecnych wyłącznie w obszarze korzenia palowego. Kilka jonów było zlokalizowanych w przeważającej mierze w epidermie, zwłaszcza kwas arachidowy, kwas behenowy, kwas α-eleostearynowy i kwas oleinowy. Niektóre obrazy były trudne do sklasyfikowania ze względu na nakładanie się obszarów anatomicznych, szczególnie między łodygą a walcem osiowym. Obecność 30 z tych związków została dodatkowo potwierdzona metodą UHPLC-UHRMS+MS/MS. Wyniki o najwyższym stopniu identyfikacji przedstawione zostały na rysunku 16. Na podstawie porównania obrazów jonowych zidentyfikowanych związków zauważona została zmniejszona intensywność sygnałów przypisanych do aminokwasów i ich pochodnych oraz zwiększone intensywności sygnałów wybranych kwasów karboksylowych, kwasów tłuszczowych i metabolitów wtórnych w rzodkiewce poddanej działaniu pestycydów w trakcie hodowli.

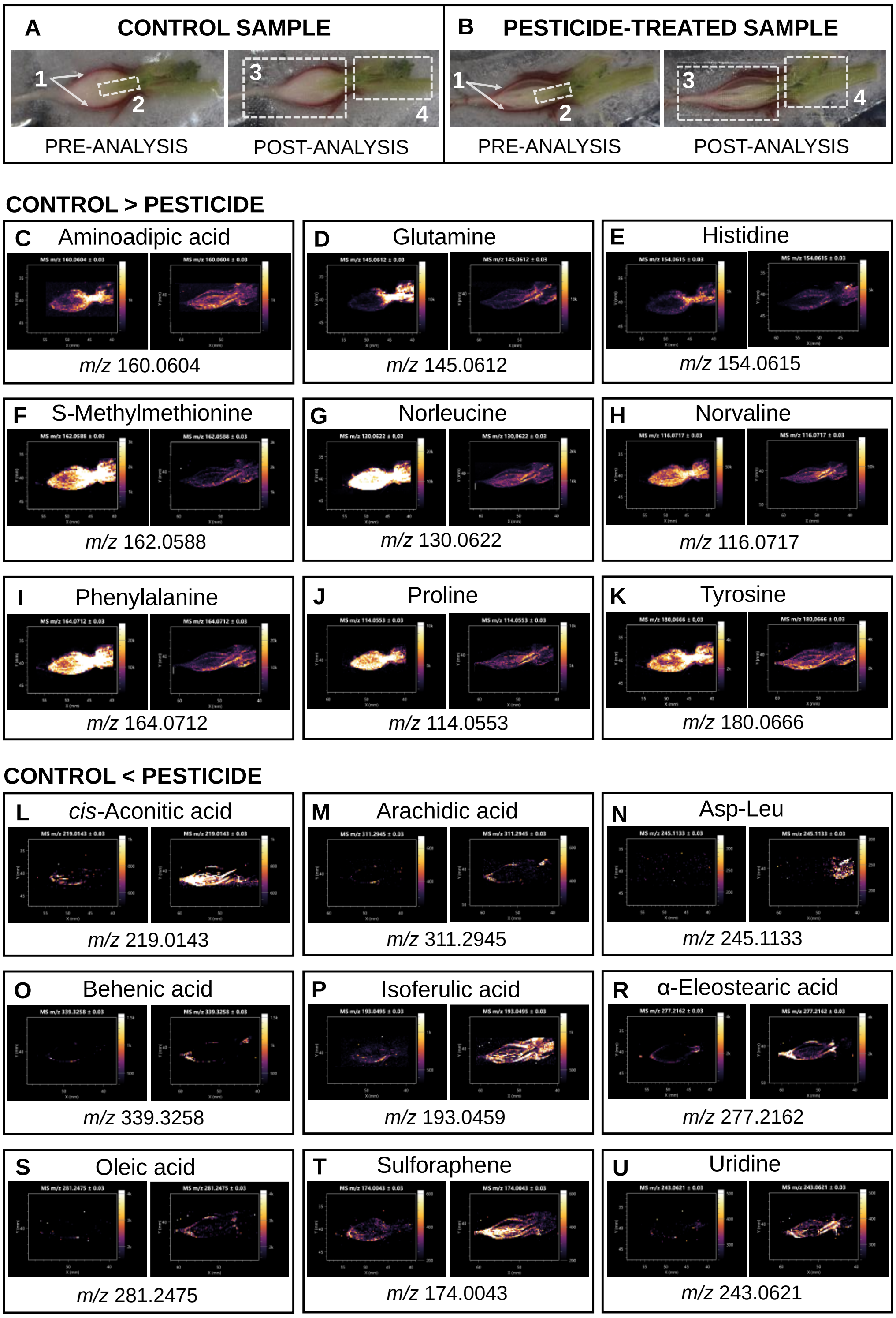

Rys. 16. Wyniki LARAPPI/CI-MSI dla próbki kontrolnej rzodkiewki (A) oraz próbki poddanej działaniu pestycydów (B) przed i po analizie. Panele C–K przedstawiają związki o istotnie wyższej intensywności sygnału w próbce kontrolnej, natomiast panele L–U — związki o istotnie wyższej intensywności sygnału w próbce poddanej działaniu pestycydów. W każdym panelu zastosowano identyczne skale intensywności dla próbki kontrolnej i próbki poddanej działaniu pestycydów. Rysunek pochodzi z publikacji **[P8]**.

Uzupełnieniem analiz MSI była niecelowana analiza UHPLC-UHRMS ekstraktów korzeni rzodkiewek, wykorzystana do rozszerzenia identyfikacji związków oraz interpretacji zmian metabolicznych. Analizie UHPLC-UHRMS poddane zostały ekstrakty korzeni rzodkiewek ze wszystkich sześciu wariantów doświadczalnych, obejmujących próbę kontrolną, mieszaninę pestycydów w stężeniu zalecanym przez producenta, mieszaninę pestycydów w stężeniu 100-krotnie wyższym oraz działanie pojedynczych wykorzystanych środków ochrony roślin w stężeniu 100-krotnie wyższym. Analiza statystyczna uzyskanych danych pozwoliła na dokładniejsze zrozumienie wpływu poszczególnych związków aktywnych środków ochrony roślin oraz efektu dawki na zmiany w szlakach metabolicznych zaobserwowanych w rzodkiewce.

Wyniki wskazały, że ekspozycja rzodkiewki na dawkę zalecaną w rolnictwie wywoływała mierzalną, lecz ograniczoną odpowiedź metaboliczną, objawiającą się przede wszystkim hamowaniem syntezy metabolitów z centralnego metabolizmu węgla i szlaków metabolizmu wtórnego.

Analizy wpływu poszczególnych pestycydów wskazały zróżnicowaną i związaną z daną substancją aktywną odpowiedź rośliny, ściśle zależną od rodzaju zastosowanej substancji aktywnej. Wysoka dawka Snacolu (metaldehyd) w porównaniu z kontrolą wywołała intensywne, lecz ukierunkowane zaburzenie centralnego metabolizmu węgla i lipidów, wraz z aktywacją szlaków reagowania na stres powiązanych z azotem i argininą [101]. Wykorzystanie jedynie Snacolu wywoływało zmiany metaboliczne w węższym zakresie niż mieszanina pestycydów. Zastosowanie samego środka Scorpion (difenkonazol i azoksystrobina) powodowało wzrost stężenia metabolitów związanych z odpowiedzią stresową i metabolizmem aminokwasów, przy jednoczesnym spadku części metabolitów flawonoidowych i lipidowych obserwowanym w porównaniu z kontrolą. W porównaniach między wariantami, w których zastosowano pestycydy, obserwowano zmiany stężenia niacynamidu i kwasu pipekolowego, co może wskazywać na zaburzenia homeostazy NAD^+ [102], oraz aktywację szlaków związanych z nabytą odpornością systemową [103]. W przypadku wykorzystania samego środka Belem (cypermetryna) klasy takie jak tiolaktamy i niektóre acyle tłuszczowe były silniej indukowane w porównaniu do próbki kontrolnej. Flawonoidy, nukleozydy pirymidynowe, ketokwasy i wiele acyli tłuszczowych były intensywniej syntezowane w próbce kontrolnej. Porównanie z zastosowaniem mieszaniny pestycydów wskazuje, że jej zastosowanie wywołuje szerszą i bardziej złożoną reakcję metabolitów wtórnych i lipidów niż tylko Belem. Wyniki sugerują, że rośliny poddane jednoczesnemu działaniu stresu wynikającego z wykorzystania pestycydów reorganizują swój metabolizm tak, że nie można przewidzieć go jako prostej sumy odpowiedzi na pojedyncze substancje aktywne, co niesie ze sobą istotne implikacje zarówno dla oceny toksykologicznej, jak i dla zrozumienia strategii adaptacyjnych roślin. Profil metaboliczny najbardziej zbliżony do wyników uzyskanych przy zastosowaniu mieszaniny pestycydów o 100-krotnie wyższym od zalecanego stężeniu wykazała próbka poddana działaniu pestycydu Scorpion, co sugeruje dominujący udział fungicydów w sygnaturze mieszaniny przy wysokiej dawce.

W pracy **[P8]** wykonano również analizę direct3D-LARAPPI/CI-MSI niepoddanej działaniu pestycydów rzodkiewki, prowadzoną w sześciu kolejnych warstwach ablacji przy rozdzielczości 140 µm (rys. 17). Analiza ta wykazała, że rozmieszczenie metabolitów zmienia się istotnie wraz z głębokością, dzięki czemu wyniki 2D-MSI mogły zostać uzupełnione o dodatkowy kontekst przestrzenny. Wyniki sugerują, że część sygnałów słabo widocznych w 2D może być lepiej widoczna w analizie trójwymiarowej, zwłaszcza gdy metabolity wykazują wyraźne rozmieszczenie pionowe w tkance.

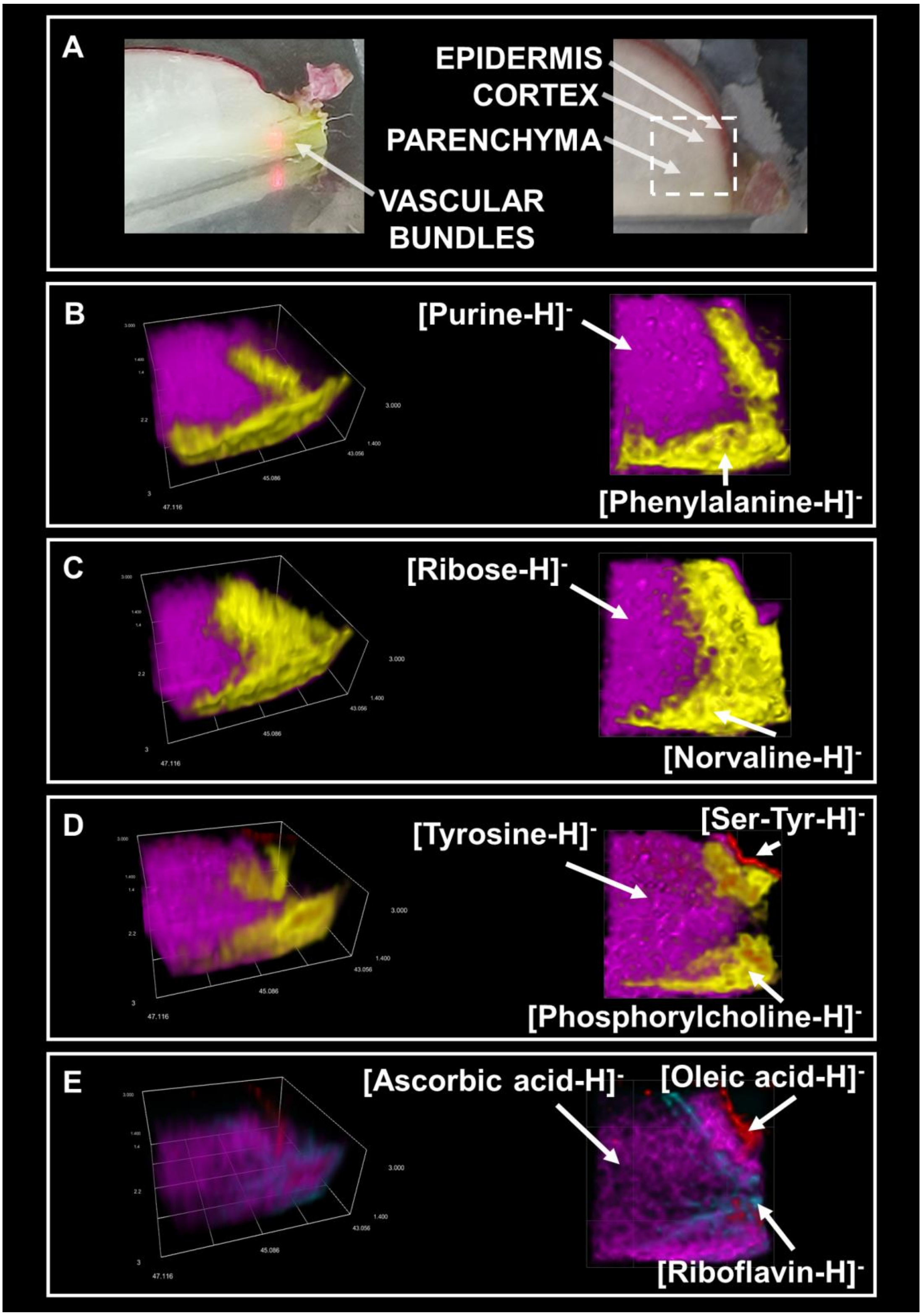

Rys. 17. Wybrane wizualizacje uzyskane na podstawie analizy LARAPPI/CI-3D-MSI. (A) Zdjęcia analizowanego fragmentu korzenia rzodkiewki z opisem położenia zróżnicowanych tkanek, (B-E) wizualizacje 3D przedstawiające rozmieszczenie kilku jonów równocześnie. Rysunek pochodzi z publikacji **[P8]**.

3.5. Porównanie wyników obrazowania spektrometrią mas z wykorzystaniem metody LARAPPI/CI i ^{109}AgNPs-LDI

Optymalizowana w ramach rozprawy doktorskiej metoda LARAPPI/CI-MSI porównana została pod kątem zdolności detekcyjnej i przydatności do obrazowania związków małocząsteczkowych z metodą ^{109}AgNPs-LDI-MSI **[P9]**. Praca **[P9]** stanowiła pierwsze porównanie obrazowania tkanek roślinnych metodą ^{109}AgNPs-LDI-MSI oraz metodą LARAPPI/CI-MSI. Analizie 2D-MSI poddany został imprint przekroju liścia aloesu metodą ^{109}AgNPs-LDI-MSI oraz wycinek liścia o grubości 3,75 mm metodą LARAPPI/CI-MSI.

W analizie ^{109}AgNPs-LDI-MSI uzyskano 179 obrazów jonowych, które po uwzględnieniu możliwości tworzenia różnych adduktów przypisano 129 związkom, natomiast metodą LARAPPI/CI-MSI uzyskano 122 obrazy jonowe. Obie techniki umożliwiły wykrycie 24 wspólnych związków, z czego 8 zidentyfikowano również metodą UHPLC-UHRMS (rys. 18). Analizy MSI pozwoliły na detekcję porównywalnej liczby aminokwasów i węglowodanów. Wyniki ^{109}AgNPs-LDI-MSI sugerowały większy potencjał metody do oznaczania związków lipidowych, ponieważ za jej pomocą wykryto ich ponad dwukrotnie więcej niż LARAPPI/CI-MSI, podczas gdy LARAPPI/CI-MSI przewyższyło ^{109}AgNPs-LDI-MSI w wykrywaniu związków aromatycznych, fenoli i kwasów organicznych. LARAPPI/CI-MSI zapewniło znacznie wyższą rozdzielczość spektralną, co pozwoliło na większą dokładność identyfikacji.

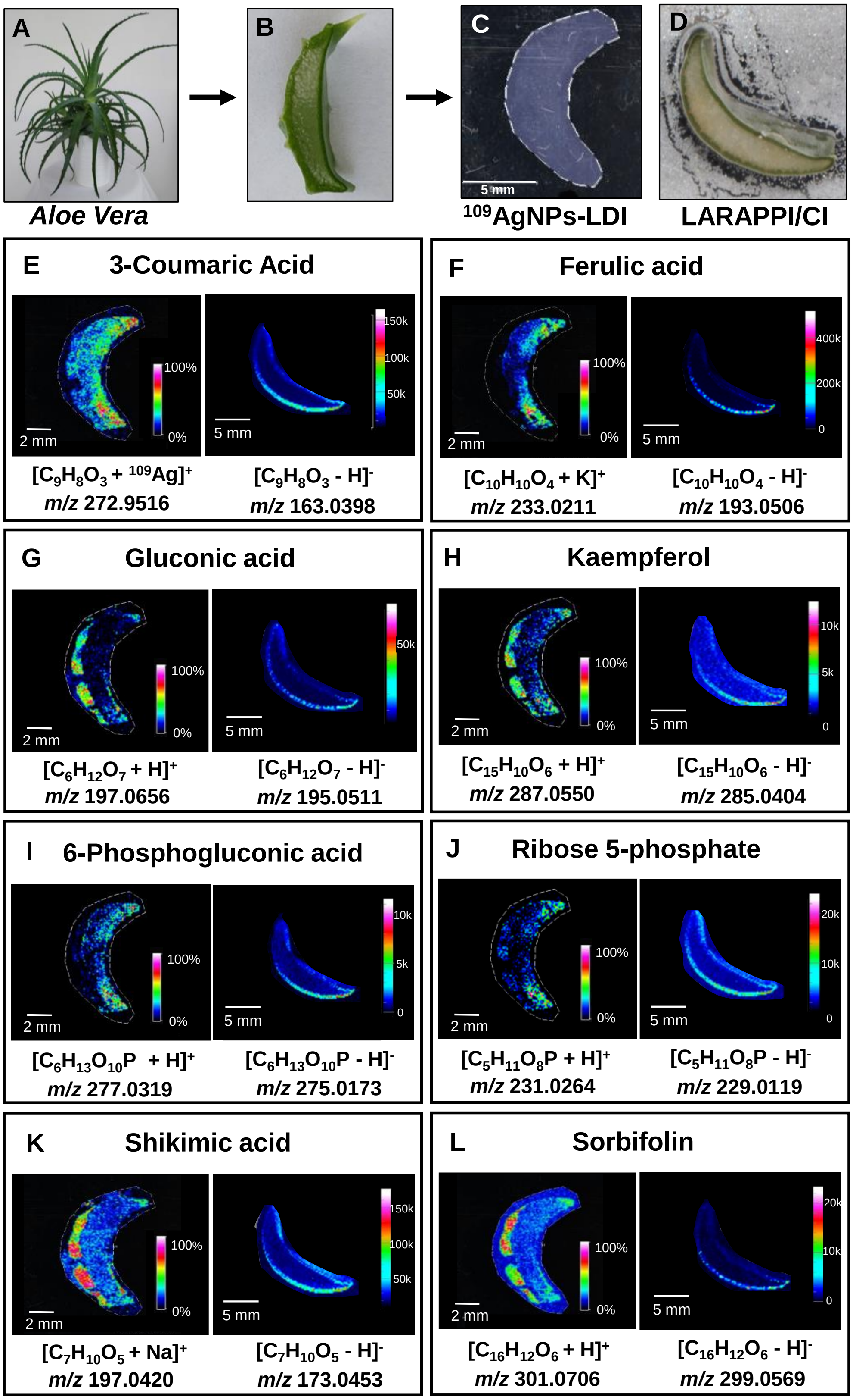

Rys. 18. Porównanie obrazów jonowych dla związków zidentyfikowanych w liściu aloesu metodą UHPLC-UHRMS oraz LARAPPI/CI-MSI (prawa część panelu) i ^{109}AgNPs-LDI-MSI (lewa część panelu). Rysunek pochodzi z publikacji **[P9]**.

Metoda ^{109}AgNPs-LDI-MSI wykorzystuje nanocząstki metali do zwiększania efektywności desorpcji/jonizacji, opierając się na zjawisku zlokalizowanego powierzchniowego rezonansu plazmonowego w celu wzmocnienia właściwości absorpcyjnych. Zjawisko to zwiększa intensywność sygnału dla cząsteczek zaadsorbowanych na powierzchni nanocząstek, co czyni ją szczególnie skuteczną w analizie małych cząsteczek. W kontekście liści *A. vera*, metoda ta wykazuje wyższą czułość, umożliwiając detekcję związków niewidocznych w metodzie LARAPPI/CI-MSI. ^{109}AgNPs-LDI-MSI wykazywała większą skuteczność w detekcji lipidów i innych małych cząsteczek adsorbowanych na powierzchni nanocząstek, a dla niektórych związków ujawniała również ich obecność w regionie żelu liścia, co stanowiło cechę uzupełniającą względem obrazowania LARAPPI/CI-MSI. Porównanie dwóch metod MSI pokazuje, że większość wykrytych związków była obecna w naskórku. Było to zgodne z oczekiwaniami, jako że pozostałą część liścia aloesu stanowi żel składający się przede wszystkim z wody (95-98%) [104]. Ze względu na wyższą rozdzielczość spektralną i lepszą zdolność wykrywania metabolitów specyficznych dla roślin metoda LARAPPI/CI-MSI została wybrana do mapowania szlaków metabolicznych, ze skupieniem na biosyntezie flawonoidów, szlaku pentozofosforanowym i biosyntezie fenylopropanoidów.

Metoda LARAPPI/CI-MSI została również porównana z ^{109}AgNPs-LDI pod względem procesu przygotowania próbki. W obu zastosowanych metodach obrazowania spektrometrią mas wstępne przygotowanie próbki było minimalne i nie wymagało zatapiania tkanki w medium do kriosekcji ani pokrywania próbki matrycą organiczną. W badaniu techniką ^{109}AgNPs-LDI-MSI analizie poddany został imprint przekroju liścia aloesu. Alternatywnym rozwiązaniem w przypadku ^{109}AgNPs-LDI-MSI byłoby wykorzystanie skrawka uzyskanego metodą kriosekcji, jednak prowadzenie analizy w warunkach wysokiej próżni mogłoby sprzyjać odwodnieniu i deformacji tak silnie uwodnionej tkanki. Z tego względu wybrano metodę imprintu, która była lepiej dostosowana do charakterystycznej budowy liścia aloesu, składającego się w większości z silnie uwodnionego żelu.. Głównymi zaletami metody imprintu, oprócz prostoty i szybkości, są: zmniejszone ryzyko uszkodzenia próbki oraz ograniczenie liczby artefaktów analitycznych. Metoda imprintu ma ograniczenia, szczególnie w przypadku bardzo twardych lub miękkich tkanek, mogące wiązać się z delokalizacją związków w obrębie imprintu lub niepełnym przeniesieniem związków na powierzchnię analizowaną [105]. Przygotowanie próbki do MSI metodą LARAPPI/CI wymagało jedynie umieszczenia tkanki o grubości 1 - 10 000 μm na płytce i jej zamrożenia, co zapewniało stabilność próbki podczas analizy

Pomimo różnic, lokalizacja przestrzenna wielu związków między dwiema wykorzystanymi metodami była w dużej mierze spójna, co potwierdza komplementarny charakter obu podejść. Uzupełniające się zalety tych technik umożliwiają bardziej kompleksową analizę tkanek roślinnych. W połączeniu, obie metody te dostarczają cennych informacji na temat aktywności metabolicznej i organizacji strukturalnej liści *A. vera*.

Przedstawione wyniki mają znaczenie nie tylko dla rozwoju wiedzy z zakresu spektrometrii mas oraz metabolomiki, lecz również dla praktyki inżynierskiej, ponieważ odnoszą się do optymalizacji warunków pracy układu, kontroli parametrów wpływających na jakość danych oraz oceny przydatności opracowanego rozwiązania w analizie złożonych materiałów biologicznych. Dotyczy to również badań nad nanocząstkami srebra-109 i złota, których właściwości oraz zastosowanie w LDI-MS/MSI stanowią istotny element rozwoju metod analitycznych o charakterze inżynieryjno-technicznym.

4. Podsumowanie i wnioski

Celem niniejszej rozprawy doktorskiej było opracowanie, optymalizacja oraz walidacja nowoczesnych metod spektrometrii mas, ze szczególnym uwzględnieniem analizy związków małocząsteczkowych. Realizacja tego celu wymagała połączenia badań literaturowych, rozwoju nowych metod eksperymentalnych oraz opracowania ich charakterystyki w analizach materiałów biologicznych o złożonej strukturze. Badania wykonane w ramach rozprawy doktorskiej należą do obszaru współczesnej metabolomiki, dostarczając nowych narzędzi do obrazowania rozmieszczenia metabolitów i innych związków małocząsteczkowych w tkankach roślinnych, ludzkich oraz w hodowlach mikroorganizmów.

W pierwszym etapie pracy przeprowadzono szczegółową analizę literatury dotyczącej obrazowania spektrometrią mas w dwóch i trzech wymiarach, ze szczególnym uwzględnieniem metod laserowej jonizacji, takich jak MALDI, SALDI i nanoPALDI z wyszczególnieniem metod LDI opartych na nanocząstkach metalicznych **[P1]**. Analiza literatury pozwoliła określić główne wyzwania dotychczas stosowanych technik, w tym ograniczenia w zakresie czułości oraz selektywności. W tym kontekście istotne znaczenie miało zastosowanie nanocząstek metalicznych, które zwiększają wydajność jonizacji oraz pozwalają na wydajne analizy obejmujące obrazowanie związków małocząsteczkowych **[P1]**.

W kolejnych etapach pracy skupiono się na testowaniu metod obrazowania związków małocząsteczkowych. Analizy ilościowe wykonano przy użyciu metody ^{109}AgNPs-LDI-MS/MSI **[P2, P3]**, która umożliwia bezpośrednią analizę próbek biologicznych bez konieczności stosowania czasochłonnych procedur ekstrakcji. Metoda ta charakteryzuje się wysoką czułością i selektywnością wobec badanych metabolitów, co pozwala na dokładne odwzorowanie ich przestrzennego rozmieszczenia w materiałach biologicznych. Wyniki tych badań wskazały na potencjał wykorzystania nanocząstek srebra jako wspomagających jonizację dla analizy małocząsteczkowej w środowisku LDI-MS/MSI.

Wykonano szerokie badania w celu optymalizacji oraz zbadania charakterystyki metody LARAPPI/CI opartej na laserowej ablacji w warunkach ciśnienia atmosferycznego **[P4]** i poddano optymalizacji parametry, takie jak budowa toru optycznego lasera w celu zwiększenia rozdzielczości obrazowania i umożliwienia bezpośredniego 3D-MSI wykorzystując metodę profilowania wgłębnego **[P5]**. Ponadto metoda LARAPPI/CI-MSI została połączona z szerokopasmową dysocjacją indukowaną zderzeniami,, umożliwiając dokładniejszą identyfikację strukturalną badanych związków **[P6]**. Takie połączenie technik jonizacji i fragmentacji pozwoliło na uzyskanie danych zarówno o rozmieszczeniu przestrzennym, jak i charakterystyce strukturalnej analizowanych metabolitów.

Następnie przeprowadzono weryfikację skuteczności analiz 3D-MSI metodą LARAPPI/CI na różnych materiałach biologicznych. Obrazowano fragmenty owocu kiwi oraz korzenia rzodkiewki **[P5, P8]**, a także obszary przejścia pomiędzy tkanką normalną a nowotworową ludzkiej nerki **[P5]**. Dodatkowo wykonano obrazowanie hodowli bakterii glebowych i fitopatogenów **[P7]**, co umożliwiło ocenę możliwości metody w badaniach mikrobiologicznych. W przypadku analiz 2D-MSI z użyciem LARAPPI/CI zbadano wpływ pestycydów na fragmenty korzenia rzodkiewki **[P8]** oraz obrazowano hodowle mikroorganizmów o właściwościach przeciwgrzybicznych i fitopatogenów **[P7]**. Uzyskane wyniki potwierdziły możliwość zastosowania systemu do oznaczania szerokiego zakresu klas związków chemicznych. Potwierdzone zostały również możliwości obrazowania różnorodnych obiektów, w tym wysoko uwodnionego materiału biologicznego i hodowli na podłożu agarowym w dwóch i trzech wymiarach z minimalną możliwością zmian w rozmieszczeniu metabolitów, dzięki zamrożeniu tkanki oraz warunkom ciśnienia atmosferycznego na etapie próbkowania.

Ostatnim etapem badań była ocena porównawcza opracowanej metody LARAPPI/CI-MSI z metodą ^{109}AgNPs-LDI-MSI **[P9]**. Porównanie wykazało, że metoda ^{109}AgNPs-LDI-MSI pozwala na obrazowanie związków małocząsteczkowych z wyższą rozdzielczością powierzchniową oraz większą skutecznością detekcji związków lipidowych , z kolei metoda LARAPPI/CI-MSI charakteryzuje się prostszym przygotowaniem próbki, niewymagającym nanoszenia dodatkowej matrycy, oraz możliwością prowadzenia analizy pod ciśnieniem atmosferycznym i szeroką kompatybilnością z różnymi instrumentami, oraz pozwala na oznaczenie większej liczby związków będących produktami wtórnego metabolizmu roślin. Wyniki analiz wskazują na komplementarny charakter obu metod, umożliwiający wybór odpowiedniego podejścia w zależności od rodzaju próbki oraz celu analizy.

Podsumowując, niniejsza rozprawa doktorska przyczyniła się do rozwoju nowoczesnych metod spektrometrii mas w analizie związków małocząsteczkowych w materiałach biologicznych. Zoptymalizowana technika LARAPPI/CI-MSI oraz zastosowana technika ^{109}AgNPs-LDI-MSI umożliwiają czułe i selektywne obrazowanie metabolitów w tkankach biologicznych. Uzyskane wyniki stanowią solidną podstawę do dalszych badań w zakresie metabolomiki przestrzennej, biologii roślin, toksykologii, farmakologii, a także badań mikrobiologicznych. Uzyskane wyniki mają również wyraźne znaczenie dla dyscypliny inżynierii chemicznej. Rozprawa obejmuje bowiem rozwój, optymalizację i walidację złożonych metod oraz układów analityczno-pomiarowych, w których kluczowe znaczenie ma kontrola parametrów procesu wpływających na efektywność ablacji, desorpcji, jonizacji oraz na jakość danych analitycznych. Dotyczy to także badań nad technologią syntezy nanocząstek metalicznych jako materiałów wspomagających desorpcję i jonizację, których właściwości fizykochemiczne determinują efektywność procesu analitycznego. Praca pokazuje, że narzędzia i podejście właściwe dla inżynierii chemicznej mogą być z powodzeniem stosowane do projektowania i doskonalenia metod instrumentalnych przeznaczonych do analizy złożonych układów biologicznych.

Bibliografia

[1] A.R. Buchberger, K. DeLaney, J. Johnson, L. Li, Mass Spectrometry Imaging: A Review of Emerging Advancements and Future Insights, Anal. Chem. 90 (2018) 240–265. https://doi.org/10.1021/ACS.ANALCHEM.7B04733

[2] N.S.K. Achanta, A.N.V. Haritha, R.K. Tekade, Mass spectrometry imaging in lipid and proteomic profiling: an emerging tool for cancer diagnosis, The Future of Pharmaceutical Product Development and Research (2020) 259–295. https://doi.org/10.1016/B978-0-12-814455-8.00008-6

[3] R.M. Caprioli, T.B. Farmer, J. Gile, Molecular imaging of biological samples: localization of peptides and proteins using MALDI-TOF MS, Anal. Chem. 69 (1997) 4751–4760. https://doi.org/10.1021/AC970888I

[4] G.J. Van Berkel, V. Kertesz, Automated sampling and imaging of analytes separated on thin-layer chromatography plates using desorption electrospray ionization mass spectrometry, Anal. Chem. 78 (2006) 4938–4944. https://doi.org/10.1021/AC060690A

[5] T.P. Roddy, D.M. Cannon, C.A. Meserole, N. Winograd, A.G. Ewing, Imaging of freeze-fractured cells with in situ fluorescence and time-of-flight secondary ion mass spectrometry, Anal. Chem. 74 (2002) 4011–4019. https://doi.org/10.1021/AC0255734

[6] P. Nemes, A. Vertes, Laser ablation electrospray ionization for atmospheric pressure, in vivo, and imaging mass spectrometry, Anal. Chem. 79 (2007) 8098–8106. https://doi.org/10.1021/AC071181R

[7] D. Li, Y. Qian, H. Yao, W. Yu, X. Ma, DeepS: Accelerating 3D Mass Spectrometry Imaging via a Deep Neural Network, Anal. Chem. 95 (2023) 10879–10886. https://doi.org/10.1021/ACS.ANALCHEM.2C05785

[8] C. Zhao, Z. Cai, Three-dimensional quantitative mass spectrometry imaging in complex system: From subcellular to whole organism, Mass Spectrom. Rev. 41 (2022) 469–487. https://doi.org/10.1002/MAS.21674

[9] E.H. Seeley, R.M. Caprioli, 3D Imaging by Mass Spectrometry: A New Frontier, Anal. Chem. 84 (2012) 2105. https://doi.org/10.1021/AC2032707

[10] J. Zhang, J. Brown, D.J. Scurr, A. Bullen, K. Maclellan-Gibson, P. Williams, M.R. Alexander, K.R. Hardie, I.S. Gilmore, P.D. Rakowska, Cryo-OrbiSIMS for 3D Molecular Imaging of a Bacterial Biofilm in Its Native State, Anal. Chem. 92 (2020) 9008–9015. https://doi.org/10.1021/ACS.ANALCHEM.0C01125

[11] T. Fukai, J. Kuroda, T. Nomura, Accurate mass measurement of low molecular weight compounds by matrix-assisted laser desorption/ionization time-of-flight mass spectrometry, J. Am. Soc. Mass Spectrom. 11 (2000) 458–463. https://doi.org/10.1016/S1044-0305(00)00109-4

[12] F. Hadacek, G. Bachmann, Low-molecular-weight metabolite systems chemistry, Front. Environ. Sci. 3 (2015) 128574. https://doi.org/10.3389/FENVS.2015.00012

[13] D. Stettin, R.X. Poulin, G. Pohnert, Metabolomics Benefits from Orbitrap GC–MS—Comparison of Low- and High-Resolution GC–MS, Metabolites 2020, Vol. 10, 10 (2020). https://doi.org/10.3390/metabo10040143

[14] V.C. Onwujiogu, S.I. Orjiocha, E.F. Chinonso, M.A. Salem, A.S. Bhat, R. Mehandi, A.H. Onyeka, Chromatography Hyphenated Techniques for the Analysis of Natural Products (A Review), Archives of Case Reports 9 (2025) 383–406. https://doi.org/10.29328/journal.acr.1001177

[15] H. Chen, J. Kong, P. Du, Q. Wang, T. Jiang, X. Hou, T. Feng, J. Duan, C. Liu, Functional metabolomics: unlocking the role of small molecular metabolites, Front. Mol. Biosci. 12 (2025) 1542100. https://doi.org/10.3389/fmolb.2025.1542100

[16] K. Chandra, S. Al-Harthi, S. Sukumaran, F. Almulhim, A.H. Emwas, H.S. Atreya, Ł. Jaremko, M. Jaremko, NMR-based metabolomics with enhanced sensitivity, RSC Adv. 11 (2021) 8694–8700. https://doi.org/10.1039/d1ra01103k

[17] A. Körber, I.G.M. Anthony, R.M.A. Heeren, Mass Spectrometry Imaging, Anal. Chem. 97 (2025) 15517–15549. https://doi.org/10.1021/ACS.ANALCHEM.4C05249

[18] M. Vats, B. Cillero-Pastor, E. Cuypers, R.M.A. Heeren, Mass spectrometry imaging in plants, microbes, and food: a review, (2024) 4553–4582

[19] X. Zhu, T. Xu, C. Peng, S. Wu, Advances in MALDI Mass Spectrometry Imaging Single Cell and Tissues, Front. Chem. 9 (2022) 782432. https://doi.org/10.3389/fchem.2021.782432

[20] A.N. Joignant, K.T. Knizner, Y. Xi, D.C. Muddiman, Evaluating the optimal tissue thickness for mass spectrometry imaging using infrared matrix-assisted laser desorption electrospray ionization, Rapid Communications in Mass Spectrometry 37 (2023) e9638. https://doi.org/10.1002/rcm.9638

[21] X. Wang, L. Zhang, Y. Xiang, N. Ye, K. Liu, Systematic study of tissue section thickness for MALDI MS profiling and imaging, Analyst 148 (2023) 888–897. https://doi.org/10.1039/d2an01739c

[22] R. Lemaire, A. Desmons, J.C. Tabet, R. Day, M. Salzet, I. Fournier, Direct Analysis and MALDI Imaging of Formalin-Fixed, Paraffin-Embedded Tissue Sections, J. Proteome Res. 6 (2007) 1295–1305. https://doi.org/10.1021/pr060549i

[23] I. Spears, G. Lagdameo, A. Black, D.R. Brown, C.C. Johnson, T.H. Hahm, W. Wang, A. Creissen, K. Glunde, C.M. Tressler, To Spray or To Sublimate: Considerations for the Matrix Application of Three Common Positive Ion Mode Matrices, Anal. Chem. 97 (2025) 19001. https://doi.org/10.1021/acs.analchem.5c01767

[24] H. Xie, R. Wu, Y.L.W. Hung, X. Chen, T.W.D. Chan, Development of a Matrix Sublimation Device with Controllable Crystallization Temperature for MALDI Mass Spectrometry Imaging, Anal. Chem. 93 (2021) 6342–6347. https://doi.org/10.1021/acs.analchem.1c00260

[25] W.H. Müller, A. Verdin, E. De Pauw, C. Malherbe, G. Eppe, Surface-assisted laser desorption/ionization mass spectrometry imaging: A review, Mass Spectrom. Rev. 41 (2022) 373–420. https://doi.org/10.1002/MAS.21670

[26] R. Arakawa, H. Kawasaki, Functionalized Nanoparticles and Nanostructured Surfaces for Surface-Assisted Laser Desorption/Ionization Mass Spectrometry, Analytical Sciences 26 (2010) 1229–1240. https://doi.org/10.2116/analsci.26.1229

[27] R.L. Hansen, M.E. Dueñas, Y.J. Lee, Sputter-Coated Metal Screening for Small Molecule Analysis and High-Spatial Resolution Imaging in Laser Desorption Ionization

Mass Spectrometry, J. Am. Soc. Mass Spectrom. 30 (2019) 299–308. https://doi.org/10.1007/S13361-018-2081-0

[28] Q. Wu, J.L. Chu, S.S. Rubakhin, M.U. Gillette, J. V. Sweedler, Dopamine-modified TiO2 monolith-assisted LDI MS imaging for simultaneous localization of small metabolites and lipids in mouse brain tissue with enhanced detection selectivity and sensitivity, Chem. Sci. 8 (2017) 3926–3938. https://doi.org/10.1039/c7sc00937b

[29] K.P. Law, Laser desorption/ionization mass spectrometry on nanostructured semiconductor substrates: DIOS^{TM} and QuickMass^{TM}, Int. J. Mass Spectrom. 290 (2010) 72–84. https://doi.org/10.1016/j.ijms.2009.12.006

[30] J. Sekuła, J. Nizioł, M. Misiorek, P. Dec, A. Wrona, A. Arendowski, T. Ruman, Gold nanoparticle-enhanced target for MS analysis and imaging of harmful compounds in plant, animal tissue and on fingerprint, Anal. Chim. Acta 895 (2015) 45–53. https://doi.org/10.1016/J.ACA.2015.09.003

[31] N. McLaughlin, T.M. Bielinski, C.M. Tressler, E. Barton, K. Glunde, K.A. Stumpo, Pneumatically Sprayed Gold Nanoparticles for Mass Spectrometry Imaging of Neurotransmitters, J. Am. Soc. Mass Spectrom. 31 (2020) 2452–2461. https://doi.org/10.1021/JASMS.0C00156

[32] T.M. Guinan, O.J.R. Gustafsson, G. McPhee, H. Kobus, N.H. Voelcker, Silver Coating for High-Mass-Accuracy Imaging Mass Spectrometry of Fingerprints on Nanostructured Silicon, Anal. Chem. 87 (2015) 11195–11202. https://doi.org/10.1021/ACS.ANALCHEM.5B02567

[33] T. Ikeda, M. Kotani, Thin-section- and matrix-free mass spectrometry imaging: Reproducible sample transfer using novel platinum-coated porous plate formed of glass beads, Rapid Communications in Mass Spectrometry 38 (2024) e9697. https://doi.org/10.1002/rcm.9697

[34] M. Du, D. Chen, Y. Chen, Y. Huang, L. Ma, Q. Xie, Y. Xu, X. Zhu, Z. Chen, Z. Yin, H. Xu, X. Wu, Plasmonic Gold Nanoshell-Assisted Laser Desorption/Ionization Mass Spectrometry for Small-Biomolecule Analysis and Tissue Imaging, ACS Appl. Nano Mater. 5 (2022) 9633–9645. https://doi.org/10.1021/ACSANM.2C01850

[35] C. Gao, Y. Wang, H. Zhang, W. Hang, Titania Nanosheet as a Matrix for Surface-Assisted Laser Desorption/Ionization Mass Spectrometry Analysis and Imaging, Anal. Chem. 95 (2023) 650–658. https://doi.org/10.1021/ACS.ANALCHEM.2C01878

[36] Q. Xie, Z. Li, Y. Chen, Y. Zhao, Y. Xu, Z. Hong, Z. Chen, Z. Zhang, H. Xu, Z. Yin, X. Wu, Mass Spectrometry Imaging Reveals the Morphology-Dependent Toxicological Effects of Nanosilvers on Multiple Organs of Adult Zebrafish (Danio rerio), Environ. Sci. Technol. 58 (2024) 10015–10027. https://doi.org/10.1021/acs.est.4c00655

[37] X.N. Wang, B. Li, Monolithic Gold Nanoparticles/Thiol-β-cyclodextrin-Functionalized TiO2 Nanowires for Enhanced SALDI MS Detection and Imaging of Natural Products, Anal. Chem. 94 (2022) 952–959. https://doi.org/10.1021/ACS.ANALCHEM.1C03764

[38] L.B. Scaffardi, D.C. Schinca, M. Lester, F.A. Videla, J.M.J. Santillan, R.M. Abraham Ekeroth, Size-Dependent optical properties of metallic nanostructures, UV-VIS and Photoluminescence Spectroscopy for Nanomaterials Characterization (2013) 179–229. https://doi.org/10.1007/978-3-642-27594-4_5

[39] A. Kołodziej, A. Płaza-Altamer, Advances in the synthesis and application of silver nanoparticles for laser mass spectrometry: A mini-review, Talanta 277 (2024) 126347. https://doi.org/10.1016/J.TALANTA.2024.126347

[40] A. Płaza-Altamer, A. Kołodziej, J. Nizioł, T. Ruman, LASER GENERATED GOLD NANOPARTICLES FOR MASS SPECTROMETRY OF LOW MOLECULAR WEIGHT COMPOUNDS, Chemical Technology & Biotechnology 2022 (2022) 61–69. https://doi.org/10.7862/RC.2022.1

[41] A. Płaza, A. Kołodziej, J. Nizioł, T. Ruman, Laser Ablation Synthesis in Solution and Nebulization of Silver-109 Nanoparticles for Mass Spectrometry and Mass Spectrometry Imaging, ACS Measurement Science Au 2 (2021) 14–22. https://doi.org/10.1021/acsmeasuresciau.1c00020

[42] M. Muthu, J. Gopal, S. Chun, Nanopost array laser desorption ionization mass spectrometry (NAPA-LDI MS): Gathering moss?, TrAC Trends in Analytical Chemistry 97 (2017) 96–103. https://doi.org/10.1016/j.trac.2017.08.016

[43] L.X. Jiang, E. Hernly, H. Hu, R.T. Hilger, H. Neuweger, M. Yang, J. Laskin, Nanospray Desorption Electrospray Ionization (Nano-DESI) Mass Spectrometry Imaging with High Ion Mobility Resolution, J. Am. Soc. Mass Spectrom. 34 (2023) 1798–1804. https://doi.org/10.1021/jasms.3c00199

[44] J.A. Fincher, A.R. Korte, B. Reschke, N.J. Morris, M.J. Powell, A. Vertes, Enhanced sensitivity and metabolite coverage with remote laser ablation electrospray ionization-mass spectrometry aided by coaxial plume and gas dynamics, Analyst 142 (2017) 3157–3164. https://doi.org/10.1039/c7an00805h

[45] B. Bartels, A. Svatoš, Spatially resolved in vivo plant metabolomics by laser ablation-based mass spectrometry imaging (MSI) techniques: LDI-MSI and LAESI, Front. Plant Sci. 6 (2015) 1–7. https://doi.org/10.3389/fpls.2015.00471

[46] A. Vogel, V. Venugopalan, Mechanisms of Pulsed Laser Ablation of Biological Tissues, Chem. Rev. 103 (2003) 577–644. https://doi.org/10.1021/CR010379N.

[47] J. Nizioł, J. Sunner, I. Beech, K. Ossoliński, A. Ossolińska, T. Ossoliński, A. Płaza, T. Ruman, Localization of Metabolites of Human Kidney Tissue with Infrared Laser-Based Selected Reaction Monitoring Mass Spectrometry Imaging and Silver-109 Nanoparticle-Based Surface Assisted Laser Desorption/Ionization Mass Spectrometry Imaging, Anal. Chem. 92 (2020) 4251–4258. https://doi.org/10.1021/ACS.ANALCHEM.9B04580

[48] J.C. Jurchen, S.S. Rubakhin, J. V. Sweedler, MALDI-MS imaging of features smaller than the size of the laser beam, J. Am. Soc. Mass Spectrom. 16 (2005) 1654–1659. https://doi.org/10.1016/j.jasms.2005.06.006

[49] A.P. Bowman, J.F.J. Bogie, J.J.A. Hendriks, M. Haidar, M. Belov, R.M.A. Heeren, S.R. Ellis, Evaluation of lipid coverage and high spatial resolution MALDI-imaging capabilities of oversampling combined with laser post-ionisation, Anal. Bioanal. Chem. 412 (2020) 2277–2289. https://doi.org/10.1007/S00216-019-02290-3

[50] M. Kompauer, S. Heiles, B. Spengler, Atmospheric pressure MALDI mass spectrometry imaging of tissues and cells at 1.4-μm lateral resolution, Nat. Methods 14 (2016). https://doi.org/10.1038/nmeth.4071

[51] H. Zhang, K.H. Lu, M. Ebbini, P. Huang, H. Lu, L. Li, Mass spectrometry imaging for spatially resolved multi-omics molecular mapping, Npj Imaging 2024 2:1 2 (2024) 20-. https://doi.org/10.1038/s44303-024-00025-3

[52] D.I. Campbell, C.R. Ferreira, L.S. Eberlin, R.G. Cooks, Improved spatial resolution in the imaging of biological tissue using desorption electrospray ionization, Analytical and Bioanalytical Chemistry 2012 404:2 404 (2012) 389–398. https://doi.org/10.1007/s00216-012-6173-6

[53] M. Yang, D. Unsihuay, H. Hu, F. Nguele Meke, Z. Qu, Z.Y. Zhang, J. Laskin, Nano-DESI Mass Spectrometry Imaging of Proteoforms in Biological Tissues with High Spatial Resolution, Anal. Chem. 95 (2023) 5214–5222. https://doi.org/10.1021/acs.analchem.2c04795

[54] M. Iqfath, S.N. Wali, S. Amer, E. Hernly, J. Laskin, Nanospray Desorption Electrospray Ionization Mass Spectrometry Imaging (nano-DESI MSI): A Tutorial Review, ACS Measurement Science Au 4 (2024) 475–487. https://doi.org/10.1021/acsmeasuresciau.4c00028

[55] G. da S. Lima, I. Pereira, L.I.L. Maciel, N.M. Lima, G.L. Araujo, D.V.A. de Aguiar, G.F. Dos Santos, B.G. Vaz, Combining LAESI Imaging and Tissue Spray Ionization Mass Spectrometry To Unveil Pesticides Contaminants in Fruits, J. Am. Soc. Mass Spectrom. 34 (2023) 2461–2468. https://doi.org/10.1021/jasms.3c00169

[56] B. Bartels, A. Svatoš, Influence of Ion Source Geometry on the Repeatability of Topographically Guided LAESI-MSI, J. Am. Soc. Mass Spectrom. 33 (2022) 265–272. https://doi.org/10.1021/jasms.1c00262

[57] M.W.F. Nielen, T.A. Van Beek, Macroscopic and microscopic spatially-resolved analysis of food contaminants and constituents using laser-ablation electrospray ionization mass spectrometry imaging, Analytical and Bioanalytical Chemistry 2014 406:27 406 (2014) 6805–6815. https://doi.org/10.1007/s00216-014-7948-8

[58] J. Zou, F. Talbot, A. Tata, L. Ermini, K. Franjic, M. Ventura, J. Zheng, H. Ginsberg, M. Post, D.R. Ifa, D. Jaffray, R.J.D. Miller, A. Zarrine-Afsar, Ambient Mass Spectrometry Imaging with Picosecond Infrared Laser Ablation Electrospray Ionization (PIR-LAESI), Anal. Chem. 87 (2015) 12071–12079. https://doi.org/10.1021/ACS.ANALCHEM.5B02756

[59] J.P. Hieta, J. Kopra, H. Räikkönen, T.J. Kauppila, R. Kostiainen, Sub-100 µm Spatial Resolution Ambient Mass Spectrometry Imaging of Rodent Brain with Laser Ablation Atmospheric Pressure Photoionization (LAAPPI) and Laser Ablation Electrospray Ionization (LAESI), Anal. Chem. 92 (2020) 13734–13741. https://doi.org/10.1021/acs.analchem.0c01597

[60] M.J. Taylor, A. Liyu, A. Vertes, C.R. Anderton, Ambient Single-Cell Analysis and Native Tissue Imaging Using Laser-Ablation Electrospray Ionization Mass Spectrometry with Increased Spatial Resolution, J. Am. Soc. Mass Spectrom. 32 (2021) 2490–2494. https://doi.org/10.1021/JASMS.1C00149

[61] H. Gross, Plano-Optical Components, Handbook of Optical Systems (2005) 569–645. https://doi.org/10.1002/9783527699223.CH13

[62] K. Thyagarajan, A. Ghatak, Lasers, (2011). https://doi.org/10.1007/978-1-4419-6442-7.

[63] S. Arba-Mosquera, P. Naubereit, S. Sobutas, Simple Estimate of the Impact of M2 and Strehl Ratio on the Effective Focusable Spot Size, Optics 2024, Vol. 5, Pages 56-65 5 (2024) 56–65. https://doi.org/10.3390/OPT5010004

[64] D.J. Hwang, C.P. Grigoropoulos, T.Y. Choi, Efficiency of silicon micromachining by femtosecond laser pulses in ambient air, J. Appl. Phys. 99 (2006). https://doi.org/10.1063/1.2187196/292640

[65] H. Bai, J.G. Manni, D.C. Muddiman, Transforming a Mid-infrared Laser Profile from Gaussian to a Top-Hat with a Diffractive Optical Element for Mass Spectrometry Imaging, J. Am. Soc. Mass Spectrom. 34 (2023) 10–16. https://doi.org/10.1021/JASMS.2C00203

[66] H. Gross, Interfaces, Handbook of Optical Systems (2005) 61–109. https://doi.org/10.1002/9783527699223.CH3

[67] S. Giordano, L. Morosi, P. Veglianese, S.A. Licandro, R. Frapolli, M. Zucchetti, G. Cappelletti, L. Falciola, V. Pifferi, S. Visentin, M. D'Incalci, E. Davoli, 3D Mass Spectrometry Imaging Reveals a Very Heterogeneous Drug Distribution in Tumors, Sci. Rep. 6 (2016) 1–8. https://doi.org/10.1038/SREP37027

[68] M.K. Passarelli, C.F. Newman, P.S. Marshall, A. West, I.S. Gilmore, J. Bunch, M.R. Alexander, C.T. Dollery, Single-Cell Analysis: Visualizing Pharmaceutical and Metabolite Uptake in Cells with Label-Free 3D Mass Spectrometry Imaging, Anal. Chem. 87 (2015) 6696–6702. https://doi.org/10.1021/ACS.ANALCHEM.5B00842

[69] C. Zhao, P. Xie, T. Yong, H. Wang, A.C.K. Chung, Z. Cai, MALDI-MS Imaging Reveals Asymmetric Spatial Distribution of Lipid Metabolites from Bisphenol S-Induced Nephrotoxicity, Anal. Chem. 90 (2018) 3196–3204. https://doi.org/10.1021/ACS.ANALCHEM.7B04540

[70] C. Zhao, P. Xie, T. Yong, W. Huang, J. Liu, D. Wu, F. Ji, M. Li, D. Zhang, R. Li, C. Dong, J. Ma, Z. Dong, S. Liu, Z. Cai, Airborne fine particulate matter induces cognitive and emotional disorders in offspring mice exposed during pregnancy, Sci. Bull. (Beijing). 66 (2021) 578–591. https://doi.org/10.1016/J.SCIB.2020.08.036

[71] L. Kuett, R. Catena, A. Özcan, A. Plüss, H.R. Ali, M. Al Sa'd, S. Alon, S. Aparicio, G. Battistoni, S. Balasubramanian, R. Becker, B. Bodenmiller, E.S. Boyden, D. Bressan, A. Bruna, M. Burger, C. Caldas, M. Callari, I.G. Cannell, H. Casbolt, N. Chornay, Y. Cui, A. Dariush, K. Dinh, A. Emenari, Y. Eyal-Lubling, J. Fan, A. Fatemi, E. Fisher, E.A. González-Solares, C. González-Fernández, D. Goodwin, W. Greenwood, F. Grimaldi, G.J. Hannon, S. Harris, C. Jauset, J.A. Joyce, E.D. Karagiannis, T. Kovačević, L. Kuett, R. Kunes, A.K. Yoldaş, D. Lai, E. Laks, H. Lee, M. Lee, G. Lerda, Y. Li, A. McPherson, N. Millar, C.M. Mulvey, I. Nugent, C.H. O'Flanagan, M. Paez-Ribes, I. Pearsall, F. Qosaj, A.J. Roth, O.M. Rueda, T. Ruiz, K. Sawicka, L.A. Sepúlveda, S.P. Shah, A. Shea, A. Sinha, A. Smith, S. Tavaré, S. Tietscher, I. Vázquez-García, S.L. Vogl, N.A. Walton, A.T. Wassie, S.S. Watson, J. Weselak, S.A. Wild, E. Williams, J. Windhager, C. Xia, P. Zheng, X. Zhuang, P. Schraml, H. Moch, N. de Souza, B. Bodenmiller, Three-dimensional imaging mass cytometry for highly multiplexed molecular and cellular mapping of tissues and the tumor microenvironment, Nature Cancer 2021 3:1 3 (2021) 122–133. https://doi.org/10.1038/s43018-021-00301-w

[72] Y.X. Zhang, Y. Da Zhang, Y.P. Shi, A reliable and effective sample preparation protocol of MALDI-TOF-MSI for lipids imaging analysis in hard and dry cereals, Food Chem. 398 (2023) 133911. https://doi.org/10.1016/j.foodchem.2022.133911

[73] T.S. Høiem, M.K. Andersen, M. Martin-Lorenzo, R. Longuespée, B.S.R. Claes, A. Nordborg, F. Dewez, B. Balluff, M. Giampà, A. Sharma, L. Hagen, R.M.A. Heeren, T.F. Bathen, G.F. Giskeødegård, S. Krossa, M.B. Tessem, An optimized MALDI MSI protocol for spatial detection of tryptic peptides in fresh frozen prostate tissue, Proteomics 22 (2022) 2100223. https://doi.org/10.1002/pmic.202100223

[74] I. Lanekoff, K. Burnum-Johnson, M. Thomas, J. Cha, S.K. Dey, P. Yang, M.C. Prieto Conaway, J. Laskin, Three-dimensional imaging of lipids and metabolites in tissues by nanospray desorption electrospray ionization mass spectrometry, Anal. Bioanal. Chem. 407 (2015) 2063. https://doi.org/10.1007/S00216-014-8174-0

[75] A.C. Crecelius, D.S. Cornett, R.M. Caprioli, B. Williams, B.M. Dawant, B. Bodenheimer, Three-Dimensional Visualization of Protein Expression in Mouse Brain Structures Using Imaging Mass Spectrometry, J. Am. Soc. Mass Spectrom. 16 (2005) 1093–1099. https://doi.org/10.1016/J.JASMS.2005.02.026

[76] M.R.L. Paine, J. Liu, D. Huang, S.R. Ellis, D. Trede, J.H. Kobarg, R.M.A. Heeren, F.M. Fernández, T.J. MacDonald, Three-Dimensional Mass Spectrometry Imaging Identifies Lipid Markers of Medulloblastoma Metastasis, Scientific Reports 2019 9:1 9 (2019) 2205-. https://doi.org/10.1038/s41598-018-38257-0

[77] L.S. Eberlin, D.R. Ifa, C. Wu, R. Graham Cooks, Three-Dimensional Vizualization of Mouse Brain by Lipid Analysis using Ambient Ionization Mass Spectrometry, Angew. Chem. Int. Ed Engl. 49 (2010) 873. https://doi.org/10.1002/ANIE.200906283

[78] C. Wu, A.L. Dill, L.S. Eberlin, R.G. Cooks, D.R. Ifa, Mass spectrometry imaging under ambient conditions, Mass Spectrom. Rev. 32 (2013) 218–243. https://doi.org/10.1002/MAS.21360

[79] O. De Castro, J.N. Audinot, H.Q. Hoang, C. Coulbary, O. Bouton, R. Barrahma, A. Ost, C. Stoffels, C. Jiao, M. Dutka, M. Geryk, T. Wirtz, Magnetic Sector Secondary Ion Mass Spectrometry on FIB-SEM Instruments for Nanoscale Chemical Imaging, Anal. Chem. 94 (2022) 10754–10763. https://doi.org/10.1021/acs.analchem.2c01410

[80] P. Nemes, A.A. Barton, A. Vertes, Three-dimensional imaging of metabolites in tissues under ambient conditions by laser ablation electrospray ionization mass spectrometry, Anal. Chem. 81 (2009) 6668–6675. https://doi.org/10.1021/AC900745E

[81] H. Bai, S. Khodjaniyazova, K.P. Garrard, D.C. Muddiman, Three-Dimensional Imaging with Infrared Matrix-Assisted Laser Desorption Electrospray Ionization Mass Spectrometry, J. Am. Soc. Mass Spectrom. 31 (2019) 292–297. https://doi.org/10.1021/jasms.9b00066

[82] D. Aebisher, I. Rudy, K. Rogóż, D. Bartusik-Aebisher, The MALDI Method to Analyze the Lipid Profile, Including Cholesterol, Triglycerides and Other Lipids, Current Issues in Molecular Biology 2026, Vol. 48, 48 (2026) 59. https://doi.org/10.3390/cimb48010059

[83] A. Gupta, D.F. Moyano, A. Parnsubsakul, A. Papadopoulos, L.S. Wang, R.F. Landis, R. Das, V.M. Rotello, Ultrastable and Biofunctionalizable Gold Nanoparticles, ACS Appl. Mater. Interfaces 8 (2016) 14096–14101. https://doi.org/10.1021/ACSAMI.6B02548

[84] B. Unnikrishnan, C.Y. Chang, H.W. Chu, A. Anand, C.C. Huang, Functional gold nanoparticles coupled with laser desorption ionization mass spectrometry for bioanalysis, Analytical Methods 8 (2016) 8123–8133. https://doi.org/10.1039/C6AY02378A

[85] T. Hayasaka, N. Goto-Inoue, N. Zaima, K. Shrivas, Y. Kashiwagi, M. Yamamoto, M. Nakamoto, M. Setou, Imaging mass spectrometry with silver naeoparticles reveals the distribution of fatty acids in mouse retinal sections, J. Am. Soc. Mass Spectrom. 21 (2010) 1446–1454. https://doi.org/10.1016/J.JASMS.2010.04.005

[86] A. Arendowski, J. Nizioł, T. Ruman, Silver-109-based laser desorption/ionization mass spectrometry method for detection and quantification of amino acids, Journal of Mass Spectrometry 53 (2018) 369–378. https://doi.org/10.1002/JMS.4068

[87] A. Kołodziej, A. Płaza-Altamer, J. Nizioł, T. Ruman, Infrared pulsed fiber laser-produced silver-109-nanoparticles for laser desorption/ionization mass spectrometry of carboxylic acids, Int. J. Mass Spectrom. 474 (2022) 116816. https://doi.org/10.1016/J.IJMS.2022.116816

[88] A. Kołodziej, A. Płaza-Altamer, J. Nizioł, T. Ruman, Infrared pulsed fiber laser-produced silver-109 nanoparticles for laser desorption/ionization mass spectrometry of 3-hydroxycarboxylic acids, Rapid Communications in Mass Spectrometry 36 (2022) e9375. https://doi.org/10.1002/rcm.9375

[89] X. Lou, A.J.H. Spiering, B.F.M. De Waal, J.L.J. Van Dongen, J.A.J.M. Vekemans, E.W. Meijer, Dehydrogenation of tertiary amines in matrix-assisted laser desorption/ionization time-of-flight mass spectrometry, Journal of Mass Spectrometry 43 (2008) 1110–1122. https://doi.org/10.1002/JMS.1395

[90] C. Kang, Y. Zhou, Z. Du, Z. Bian, J. Wang, X. Qiu, L. Gao, Y. Sun, Dehydrogenation and dehalogenation of amines in MALDI-TOF MS investigated by isotopic labeling, Journal of Mass Spectrometry 48 (2013) 1318–1324. https://doi.org/10.1002/JMS.3296

[91] V. Prysiazhnyi, F. Dycka, J. Kratochvil, V. Stranak, Gas aggregated Ag NPs as a matrix for small molecules: a study on natural amino acids, Journal of Nanoparticle Research 2020 22:11 22 (2020) 351-. https://doi.org/10.1007/S11051-020-05082-4

[92] S. Kéki, L. Nagy, G. Deák, M. Zsuga, L. Somogyi, A. Lévai, Cationization of simple organic molecules by singly-charged Ag3+ cluster ions in matrix-assisted laser desorption/ionization mass spectrometry: Metal cluster-molecule interactions, J. Am. Soc. Mass Spectrom. 15 (2004) 879–883. https://doi.org/10.1016/J.JASMS.2004.03.002

[93] J. Nizioł, W. Rode, B. Laskowska, T. Ruman, Novel Monoisotopic 109AgNPET for Laser Desorption/Ionization Mass Spectrometry, Anal. Chem. 85 (2013) 1926–1931. https://doi.org/10.1021/AC303770Y

[94] C. Angi, I.S. Lurie, I. Marginean, Analysis of fentanyl derivatives by ultra high performance liquid chromatography with diode array ultraviolet and single quadrupole mass spectrometric detection, J. Sep. Sci. 42 (2019) 1686–1694. https://doi.org/10.1002/JSSC.201801098

[95] Y. Zhang, J.C. Halifax, C. Tangsombatvisit, C. Yun, S. Pang, S. Hooshfar, A.H.B. Wu, K.L. Lynch, Development and application of a High-Resolution mass spectrometry method for the detection of fentanyl analogs in urine and serum, Journal of Mass Spectrometry and Advances in the Clinical Lab 26 (2022) 1–6. https://doi.org/10.1016/J.JMSACL.2022.07.005

[96] F.P. Busardò, J. Carlier, R. Giorgetti, A. Tagliabracci, R. Pacifici, M. Gottardi, S. Pichini, Ultra-high-performance liquid chromatography-tandem mass spectrometry assay for

quantifying fentanyl and 22 analogs and metabolites in whole blood, urine, and hair, Front. Chem. 7 (2019) 447886. https://doi.org/10.3389/FCHEM.2019.00184

[97] J. Szulc, T. Ruman, Laser Ablation Remote-Electrospray Ionisation Mass Spectrometry (LARESI MSI) Imaging—New Method for Detection and Spatial Localization of Metabolites and Mycotoxins Produced by Moulds, Toxins (Basel). 12 (2020). https://doi.org/10.3390/TOXINS12110720

[98] E. de Hoffmann, V. Stroobant, Tandem Mass Spectrometry (MS/MS), Mass Spectrometry: Principles and Applications (2013) 189–216

[99] Y. Dubrovskii, T. Krivul'ko, L. Gavrilenko, N. Solovyev, Targeted proteomics for the analysis of cultural heritage: application of broadband collision-induced dissociation mass spectrometry, Analytical and Bioanalytical Chemistry 2021 414:4 414 (2022) 1723–1737. https://doi.org/10.1007/s00216-021-03805-7

[100] H. Keweloh, H.J. Heipieper, Trans unsaturated fatty acids in bacteria, Lipids 31 (1996) 129–137. https://doi.org/10.1007/bf02522611

[101] H.T. Shi, Z.L. Chan, In vivo role of Arabidopsis arginase in arginine metabolism and abiotic stress response, Plant Signal. Behav. 8 (2013). https://doi.org/10.4161/PSB.24138

[102] A. Matsui, Y. Yin, K. Yamanaka, M. Iwasaki, H. Ashihara, Metabolic fate of nicotinamide in higher plants, Physiol. Plant. 131 (2007) 191–200. https://doi.org/10.1111/J.1399-3054.2007.00959

[103] F. Bernsdorff, A.C. Döring, K. Gruner, S. Schuck, A. Bräutigam, J. Zeier, Pipecolic Acid Orchestrates Plant Systemic Acquired Resistance and Defense Priming via Salicylic Acid-Dependent and -Independent Pathways, Plant Cell 28 (2016) 102–129. https://doi.org/10.1105/TPC.15.00496

[104] M. Chelu, M. Popa, E.A. Ozon, J. Pandele Cusu, M. Anastasescu, V.A. Surdu, J. Calderon Moreno, A.M. Musuc, High-Content Aloe vera Based Hydrogels: Physicochemical and Pharmaceutical Properties, Polymers 2023, Vol. 15, 15 (2023). https://doi.org/10.3390/polym15051312

[105] W. Hu, Y. Han, Y. Sheng, Y. Wang, Q. Pan, H. Nie, Mass spectrometry imaging for direct visualization of components in plants tissues, J. Sep. Sci. 44 (2021) 3462–3476. https://doi.org/10.1002/JSSC.202100138

Streszczenie

Niniejsza rozprawa doktorska poświęcona jest zagadnieniom obrazowania spektrometrią mas w dwóch i trzech wymiarach, ze szczególnym uwzględnieniem analizy związków małocząsteczkowych w tkankach biologicznych. Zaprezentowany cykl publikacji dotyczy metod MSI wykorzystywanych do analizy związków małocząsteczkowych oraz optymalizacji nowoczesnych metod do obrazowania spektrometrią mas w trzech wymiarach.

Przedstawione zostały wyniki przeglądu literaturowego dotyczącego wykorzystania nanocząstek metalicznych w analizach MSI oraz wyniki własnych analiz ilościowych metodą ^{109}AgNPs-LDI-MS wykorzystując substancje psychoaktywne z grup kannabinoidów i opioidów oraz analiz ilościowych metodą ^{109}AgNPs-LDI-MS/MSI i AuNPs-LDI-MS/MSI.

Kolejne przedstawione wyniki dotyczą zastosowania metody LARESI-MSI z pomiarem w trybie SRM. Na bazie systemu LARESI zoptymalizowano system zakładający 3D-MSI tkanek biologicznych w warunkach ciśnienia atmosferycznego. Optymalizacja tego systemu oraz jego dalsza walidacja była kluczowym aspektem prac wykonanych w ramach niniejszej rozprawy doktorskiej. Po zakończeniu optymalizacji system poddany został testom zakresu zastosowania wykorzystując dwa obiekty roślinne – korzeń rzodkiewki oraz fragment owocu kiwi, a także tkankę ludzką obejmującą obszary normalne i nowotworowe.

Opracowany system LARAPPI/CI wykorzystany został do analiz obiektów mikrobiologicznych, tkanek roślinnych oraz ludzkich. Badane tkanki ludzkie zawierały obszary zdrowe i nowotworowe. Dodatkowo, tkanki ludzkiego pęcherza moczowego oraz nerki obrazowane były z równoczesnym wykorzystaniem metody fragmentacyjnej bbCID, co pozwoliło na opracowanie nowej metody identyfikacji oznaczanych związków. Przeprowadzone zostały analizy mające na celu obserwację interakcji bakterii glebowych z fitopatogenami grzybowymi. Analiza direct3D-MSI pozwoliła również na zaobserwowanie rozmieszczenia związków syntezowanych przez mikroorganizmy w podłożu hodowlanym. Badania syntezy i dyfuzji związków chemicznych wytwarzanych przez mikroorganizmy stanowią istotny wkład w obszar biotechnologii pozwalający na charakterystykę organizmów i ich wpływu na otoczenie. Analiza 2D-MSI korzenia rzodkiewki poddanego działaniu pestycydów w czasie hodowli pozwoliła na porównanie profilu metabolicznego roślin eksponowanych na pestycydy z profilem metabolicznym roślin kontrolnych. 2D-MSI wykorzystane zostało również do analizy przekroju liścia aloesu. Wyniki analizy LARAPPI/CI-

MSI porównane zostały z wynikami analizy ^{109}AgNPs-LDI-MSI, alternatywnej metody obrazowania związków małocząsteczkowych w badanych obiektach.

Rozprawa wykazuje wyraźne powiązanie z dyscypliną inżynieria chemiczna, obejmując opracowanie, optymalizację i walidację złożonego układu analityczno-pomiarowego oraz analizę wpływu parametrów jego pracy na jakość i wiarygodność oznaczeń w złożonych matrycach biologicznych. Powiązanie to wzmacniają również badania dotyczące otrzymywania oraz zastosowania nanocząstek srebra-109 i złota jako materiałów wspomagających procesy desorpcji i jonizacji w technikach LDI-MS/MSI jako przykład badań w obszarze nanotechnologii.

Abstract

This doctoral dissertation is devoted to two- and three-dimensional mass spectrometry imaging, with particular emphasis on the analysis of low molecular weight compounds in biological tissues. The presented publication series covers MSI methods used for the analysis of low molecular weight compounds and the optimization of modern methods for three-dimensional mass spectrometry imaging.

The results of a literature review on the use of metallic nanoparticles in MSI analyses are presented, as well as the results of our own quantitative analyses using the ^{109}AgNPs-LDI-MS method using psychoactive substances from the cannabinoid and opioid groups, and quantitative analyses using the ^{109}AgNPs-LDI-MS/MSI and AuNPs-LDI-MS/MSI methods.

The next presented results concern the application of the LARESI-MSI method with measurement in SRM mode. Based on the LARESI system, a system for 3D-MSI of biological tissues under atmospheric pressure conditions was optimized. The optimization of this system and its further validation were key aspects of the work performed as part of this doctoral dissertation. After optimization, the system was subjected to field testing using two plant objects – a radish root and a kiwi fruit fragment, as well as human tissue containing both normal and cancerous areas.

The developed LARAPPI/CI system was used to analyze microbiological objects, plant tissues, and human tissues. The human tissues examined included both healthy and cancerous areas. Additionally, human bladder and kidney tissues were imaged simultaneously using the bbCID fragmentation method, which allowed for the development of a new method for identifying the assayed compounds. Analyses were conducted to observe the interactions of soil bacteria with fungal phytopathogens. Direct3D-MSI analysis also allowed for the observation of the distribution of compounds synthesized by microorganisms in the culture medium. Studies on the synthesis and diffusion of chemical compounds produced by microorganisms constitute a significant contribution to biotechnology, allowing for the characterization of organisms and their impact on the environment. 2D-MSI analysis of radish roots treated with pesticides during cultivation allowed for a comparison of the metabolic profile of plants exposed to pesticides with that of control plants. 2D-MSI was also used to analyze aloe leaf cross-sections. The results of the LARAPPI/CI-MSI analysis were compared with those of ^{109}AgNPs-LDI-MSI, an alternative method for imaging low molecular weight compounds in the studied objects.

The dissertation demonstrates a clear connection to the discipline of chemical engineering, encompassing the development, optimization, and validation of a complex analytical and measurement system and an analysis of the impact of its operating parameters on the quality and reliability of determinations in complex biological matrices. This connection is also strengthened by research on the preparation and application of silver-109 and gold nanoparticles as materials supporting desorption and ionization processes in LDI-MS/MSI techniques, as an example of research in the field of nanotechnology.

Wykaz pozostałych osiągnięć naukowych

Wykaz artykułów naukowych należących do dorobku naukowego niewchodzących w skład cyklu publikacji:

1. A. Płaza-Altamer, A. Kołodziej, **S. Krupa**, J. Nizioł, T. Ruman, Infrared pulsed fiber laser-produced gold and silver-109 nanoparticles for laser desorption/ionization mass spectrometry of steroid hormones, *Rapid Communications in Mass Spectrometry*, **2023**, 37, e9621

2. J. Nizioł, M. Misiorek, **S. Krupa**, T. Ruman, Infrared Laser-Based Selected Reaction Monitoring Mass Spectrometry Imaging of Banana (Musa spp.) Tissue—New Method for Detection and Spatial Localization of Metabolites in Food, *Food Analytical Methods*, **2024**, 17, 236-250

3. J. Nizioł, K. Ossoliński, A. Płaza-Altamer, A. Kołodziej, A. Ossolińska, T. Ossoliński, **S. Krupa**, T. Ruman, Untargeted Metabolomics of Bladder Tissue using Liquid Chromatography and Quadrupole Time-of-Flight Mass Spectrometry for Cancer Biomarker Detection, *Journal of Pharmaceutical and Biomedical Analysis*, **2024**, 240, 115966

4. K. Ossoliński, T. Ruman, V. Copié, B. P. Tripet, A. Kołodziej, A. Płaza-Altamer, A. Ossolińska, T. Ossoliński, **S. Krupa**, J. Nizioł, Metabolomic profiling of human bladder tissue extracts, *Metabolomics*, **2024**, 20, 14

5. **S. Krupa**, J. Nizioł, UHPLC-UHRMS and ^{109}AgNPs-assisted laser desorption/ionization mass spectrometry imaging of pesticide residues in Solanum lycopersicum L., *Chemical Technology & Biotechnology*, **2024**, 96-101

6. **S. Krupa**, J. Nizioł, Fiber laser-generated silver-109 nanoparticles for laser desorption/ionization mass spectrometry of illicit drugs, *Journal of the American Society for Mass Spectrometry*, **2024**, 35, 1156-1167

7. A. Frydrych, S. Krupa, A. Płaza-Altamer, Detection of metabolomic changes in beetroot tissues under the influence of glyphosate, *Chemical Technology and Biotechnology*, **2025**, 178-190

8. J. Nizioł, S. Krupa, W. Szuberla, T. Ruman, Advances in metallic nanostructures-assisted laser desorption/ionization mass spectrometry imaging of biological samples: A review, *Analytica Chimica Acta*, **2025**, 1366, 344256

Konferencje naukowe:

1. Joanna Nizioł, **Sumi Krupa**, Wiktoria Szuberla, Tomasz Ruman, wystąpienie ustne pt. „Analiza metabolomu mikroorganizmów z wykorzystaniem obrazowania spektrometrią mas" na XII Polskiej Konferencji Chemii Analitycznej (PoKoChA 2025), 1–4 lipca 2025, Gdańsk.

2. Tomasz Ruman, Joanna Nizioł, **Sumi Krupa**, wystąpienie ustne pt. „Obrazowanie spektrometrią mas obiektów biologicznych w dwóch i trzech wymiarach” na Konwersatorium Spektrometrii Analitycznej (KOSAT 2025), 10–12 września 2025, Białystok.

3. Wiktoria Szuberla, **Sumi Krupa**, Justyna Szulc, Tomasz Grzyb, Joanna Nizioł, Tomasz Ruman, poster pt. „Mass spectrometry imaging in localization of metabolites in microorganism cultures on gel substrate”. International Conference „Science and industry – challenges and opportunities”, 24–26 czerwca 2025, Lublin–Puławy, Poland.

4. Justyna Szulc, Tomasz Grzyb, Joanna Nizioł, **Sumi Krupa**, Wiktoria Szuberla, Tomasz Ruman, wystąpienie ustne pt. „3D-MSI for the analysis of microorganism interactions” na konferencji Metabolomics Circle 2025 – 11th International Conference of Polish Metabolomic Society / Modern Pharmaceutical and Biomedical Analytics in Health Care (5th Poznan Scientific Conference), 5–7 listopada 2025, Poznań, Poland

Materiały pokonferencyjne:

1. **S. Krupa**, J. Nizioł, T. Ruman, Laser ablation remote ionisation mass spectrometry imaging for detection of biomarkers and metabolites, Science and Industry – challenges and opportunities, Wydawnictwo Uniwersytetu Marii Curie-Skłodowskiej, Lublin 2024

2. **S. Krupa**, J. Nizioł, W. Szuberla, J. Szulc, T. Grzyb, T. Ruman, Analiza metabolomu mikroorganizmów z wykorzystaniem obrazowania spektrometrią mas w dwóch i trzech wymiarach, XII Polska Konferencja Chemii Analitycznej (PoKoChA 2025), Gdańsk 2025

3. J. Szulc, T. Grzyb, J. Nizioł, **S. Krupa,** W. Szuberla, T. Ruman**,** 3D-MSI for the analysis of microorganism interactions, Metabolomics Circle 2025, Modern Pharamaceutical and Biomedical Analytics in Health Care, Poznań 2025

KOPIE PUBLIKACJI STANOWIĄCYCH ROZPRAWĘ DOKTORSKĄ

Analytica Chimica Acta 1366 (2025) 344256

Contents lists available at ScienceDirect

Analytica Chimica Acta

journal homepage: www.elsevier.com/locate/aca

Advances in metallic nanostructures-assisted laser desorption/ionization mass spectrometry imaging of biological samples: A review

Joanna Nizioł [a,*], Sumi Krupa [b], Wiktoria Szuberla [a], Tomasz Ruman [a]

[a] Rzeszów University of Technology, Faculty of Chemistry, 6 Powstańców Warszawy Ave., 35-959, Rzeszów, Poland
[b] Doctoral School of Engineering and Technical Sciences at the Rzeszów University of Technology, 8 Powstańców Warszawy Ave., 35-959, Rzeszów, Poland

HIGHLIGHTS

- Applications of metallic nanostructures in mass spectrometry imaging are reviewed.
- The advantages of metallic nanomaterials for enhancing ionization efficiency are discussed.
- Recent methods for preparing and applying nanostructures in MSI are reviewed.
- Benefits and challenges of metallic nanostructures in biological imaging are discussed.
- Emerging trends in functionalized and hybrid nanomaterials for MSI are highlighted.

GRAPHICAL ABSTRACT

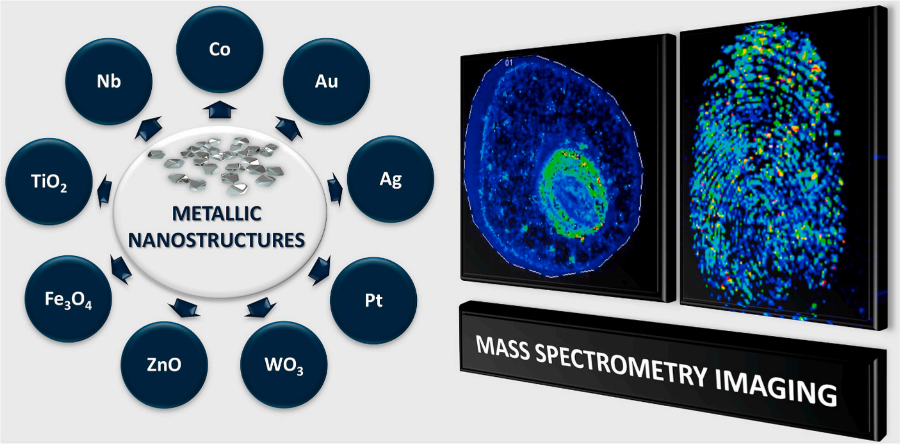

ARTICLE INFO

Keywords:
Metallic nanostructures
Nanoparticles
Mass spectrometry imaging
Mass spectrometry
MSI
LDI-MS

ABSTRACT

Background: Mass spectrometry imaging (MSI) has emerged as a powerful tool for the spatial visualization of biomolecules, driving advances in diverse fields such as biomedical research, plant metabolomics, and forensic science. Incorporating nanostructures, particularly metallic and metal oxide nanoparticles, has revolutionized laser desorption/ionization (LDI)-MSI by enhancing ionization efficiency, spatial resolution, and sensitivity.
Results: This review focuses on the preparation, application, and performance of various metallic nanostructures (e.g., gold, silver, platinum, and metal oxides) in LDI-MSI, emphasizing both fundamental physicochemical properties and their role in improving sensitivity, spatial resolution, and data reproducibility.
Significance: We provide a comparative assessment of metallic nanostructures versus other types of nanomaterials (quantum dots, carbon-based materials), highlight key advantages and current limitations, and offer a roadmap for future developments in nanomaterial-assisted MSI, including prospective strategies for stabilizing and functionalizing surfaces, exploring alternative laser wavelengths, and ensuring robust analytical workflows.

---

[*] Corresponding author.
E-mail address: jniziol@prz.edu.pl (J. Nizioł).

https://doi.org/10.1016/j.aca.2025.344256
Received 16 January 2025; Received in revised form 26 May 2025; Accepted 27 May 2025
Available online 31 May 2025
0003-2670/© 2025 The Author(s). Published by Elsevier B.V. This is an open access article under the CC BY license (http://creativecommons.org/licenses/by/4.0/).

1. Introduction

Advanced analytical methods for the examination of biomolecular structure and function are currently being intensively developed. In recent years, special attention has been paid to the development of mass spectrometry imaging (MSI) techniques, which enable obtaining ion images of the spatial distribution of molecules in biological samples. One of the key tools underpinning MSI is mass spectrometry (MS), an analytical technique that identifies and quantifies chemical compounds based on their molecular masses. Among the various ionization methods available in MSI, the laser desorption/ionization (LDI) method offers unique opportunities for studying low molecular weight compounds (LMWC), i.e. compounds below the molecular weight of 1500 Da [1,2].

Nanostructures, due to their unique physicochemical properties, have found wide application in many fields of science and technology [3]. The first reported use of metallic nanostructures in mass spectrometry, which is also considered the first application of an inorganic nanostructured matrix in LDI-MS, dates back to 1988 [4]. Koichi Tanaka and his co-workers used cobalt nanoparticles suspended in glycerol as a matrix to detect polymers and proteins greater than 100 kDa. They demonstrated that ultrafine metal particles could enhance the desorption and ionization of proteins, significantly advancing modern mass spectrometry techniques. This pioneering work, for which Tanaka was awarded the Nobel Prize in Chemistry in 2002, marked a breakthrough in the field and established the groundwork for future research on nanostructured matrices in LDI-MS.

The MSI method is a versatile technique that provides visualization of the spatial distribution of compounds in complex biological systems. Unlike other methods, such as fluorescence microscopy [5], it does not require chemical labeling. Compared to FT-IR and Raman microscopy [6], MSI offers high chemical specificity, comprehensive molecular analysis, and high spatial resolution. Additionally, it enables quantitative analysis. The three main ionization approaches employed for MSI have been secondary ion mass spectrometry (SIMS) [7], desorption electrospray ionization (DESI) [8], and matrix-assisted laser desorption/ionization (MALDI) [9]. Among those, the latter tends to be the method of choice and was also the first ionization technique employed in MSI [10,11].

The MALDI MS technique is widely used in the molecular imaging of large molecules such as proteins and peptides because of the softest ionization and minimal fragmentation of macromolecules, high ionization efficiency, and label-free detection capability. Additionally, this technique is characterized by high throughput, sensitivity, and tolerance to salts and requires minimal sample amounts, making it ideal for analyzing biological samples [12,13].

The primary limitations of using MALDI ionization in both MS and MSI are associated with the necessity of using a matrix, which traditionally refers to small organic molecules used in large excess relative to the analyte. These molecules co-crystallize with the analyte, forming a layer of small crystals. When exposed to pulsed laser radiation, typically from a neodymium-doped solid-state laser at a wavelength range of 350–355 nm (earlier nitrogen laser of 337 nm), these crystals are evaporated into the gas phase. The primary function of the matrix is to absorb the laser radiation and transfer the energy to the analyte molecules, facilitating their desorption and ionization. The majority of matrices utilized in MALDI-MS consist of a linear conjugated π system or/an aromatic rings, which facilitate UV absorption and assist in the ionization of the desired analytes. α-Cyano-4-hydroxycinnamic acid (CHCA), 2,5-dihydroxybenzoic acid (DHB), and sinapinic acid (SA) are commonly used matrices for macromolecule analysis, such as peptides, proteins, lipids, and polymers [14]. However, while MALDI-MSI is highly effective for such biomolecules, its application to LMWC is limited by intense background signals from the matrix in the low mass range (<1000 Da) [15]. In addition, choosing the optimal matrix and its quantity is often a time-consuming process that can significantly affect the reproducibility and sensitivity of the analysis [16].

The maximum spatial resolution in MALDI-MSI depends not only on the laser waist diameter but also on the matrix crystal size and the redistribution of analytes during matrix crystallization. Inhomogeneous crystallization of the organic matrix can result in poorly reproducible peaks and the occurrence of ‘sweet spots’ where analyte molecules aggregate and generate strong signals, leading to inconsistent detection and limiting accurate quantification of analytes [17].

To address the limitations of organic matrices in MALDI-MS for low-molecular-weight compounds, two main strategies have been proposed [18]. The first approach involved creating high molecular weight matrices to prevent interferences in the lower mass range, but the disadvantages of high molecular weight matrices in MALDI include potential difficulties in ionizing small molecules and the possibility of generating background signals due to fragmentation of the matrix itself [19]. One of these alternatives is carbon nanotubes [20] and graphene structures [21], which act as substrates that capture analytes on their surface. Despite their high efficiency in absorbing laser energy, they can be challenging to prepare and apply. Their surfaces may exhibit heterogeneity, leading to variability in the results. Additionally, they can introduce their background noise into the mass spectrum [22]. Another approach is the use of porous silicon surfaces (DIOS - desorption/ionization on porous silicon) [23]. However, porous silicon surfaces are prone to oxidation, which can affect their performance and lead to a lack of reproducibility. Their preparation is demanding and requires precise control of production conditions, increasing both cost and technical difficulty [23]. Sol-gels are another alternative, where a polymer structure (usually based on siloxane) is used to incorporate matrix molecules into their structure [24]. Although sol-gels can efficiently absorb laser energy, their preparation is complicated and time-consuming. They also introduce minimal, but still present, background signals that can interfere with the analysis of LMWC. There is also an approach involving direct desorption and ionization without using a matrix, where analytes themselves absorb laser energy and undergo ionization.

One of the most intensively developed alternatives to traditional matrices in the analysis of small molecules using LDI-MS is metallic nanostructures [25]. Like other nanomaterials such as carbon nanotubes, graphene or quantum dots metallic nanostructures provide high surface area and strong UV absorption, which are essential for laser energy capture in LDI-MS/MSI. What sets metallic nanostructures apart is their ability to support localized surface plasmon resonance (LSPR), enhance metal-adduct formation, and maintain excellent thermal and chemical stability, which together improve desorption and ionization efficiency particularly in small molecule analysis. Metallic nanostructures offer several advantages over conventional matrices, including tolerance to salts and much simpler, faster sample preparation, resulting in significantly higher throughput and repeatability. Their nanometric dimensions contribute to low heat capacity and efficient thermal energy transfer, further facilitating the rapid desorption of analytes. Additionally, these nanostructures are distinguished by their limited background interference and exceptional chemical stability and physical durability. Such properties not only lower detection limits but also improve signal clarity and enable consistent ionization across repeated measurements, which is beneficial for reliable analysis of LMWC. Some of the approaches discussed in this review generate intense and well-defined signals from metallic nanoparticles, which can be utilized for internal mass calibration [26].

The rapid advancement of nanomaterials has led to numerous innovative proposals for their application in LDI-MS [27,28]. Over the past 30 years, nanomaterials-based methods have acquired various names depending on either the nanostructures used or their application techniques. The proper use and standardization of nomenclature for different LDI-MS methods have often been topics of discussion within the scientific community [29]. Today, the most widely used term for the technique of employing nanomaterials in LDI-MS is surface-assisted laser desorption/ionization mass spectrometry (SALDI-MS). The term was first used by Sunner et al. [30] to describe the LDI-MS method assisted by a graphite particle-enhanced surface. In SALDI, the surface to which samples are applied is coated with nanostructures that facilitate the desorption and ionization of analytes. Another frequently used name that uses nanoparticles in a wider scope is nanoparticle-assisted laser desorption/ionization mass spectrometry (nano-PALDI-MS). In nano-PALDI-MS, nanoparticles can be applied both to the surface on which the sample is placed and directly to the sample itself. The name NALDI-MS (nanostructure-assisted laser desorption/ionization mass spectrometry), which is a trading name used by Bruker to designate commercial, patented plates covered with silicon wires, may be slightly misleading. However, this abbreviation is sometimes found in the literature but refers not to Bruker's product but to other solutions with nanostructures.

The emergence of LDI methods has significantly contributed to advances in MSI. This approach utilizes a broad spectrum of nanomaterials, ranging from unmodified nanoparticles composed of a single material to more complex nanostructures functionalized with various chemical groups. In recent years, several studies have explored the potential of nanomaterials to enhance ionization efficiency in LDI-MS and MSI. However, most of these reports cover a broad spectrum of nanomaterials and often emphasize nonmetallic nanomaterials [25,29,31–40]. To the best of our knowledge, there are currently no dedicated reviews that focus exclusively on metallic nanomaterials for SALDI-based MSI of biological specimens. Hence, the present review aims to address this gap by providing an in-depth examination of the application of metallic nanostructures in SALDI-MSI, with a particular focus on their role in the imaging analyses of biological systems.

2. Metallic nanostructures

2.1. Definition and classification of nanostructures

According to the International Organization for Standardization (ISO), a nanostructure is defined as a material that has any external nanoscale dimension or internal nanoscale surface structure, where nanoscale refers to dimensions in the range of 1–100 nm [41]. In this review, we concentrate on nanostructures composed of metals or metal-like materials (such as metal oxides or composites), as they display unique physicochemical characteristics associated with free conduction electrons, LSPR, which are crucial for laser desorption/ionization processes.

Nanostructures are classified according to dimension, shape, size, composition, and origin [42]. In the context of metallic nanostructures, the dimensional classification system proposed by Pokropivny and Skorokhod is particularly pertinent [43]. Zero-dimensional (0D) metallic nanostructures, such as metallic nanoparticles and nanoclusters, have all spatial dimensions confined within the nanoscale. In these systems, electrons are restricted in all three dimensions and exhibit quantized energy levels. One-dimensional (1D) metallic nanostructures, including nanorods and nanowires, have two dimensions within the nanoscale and one extended dimension. Electrons in 1D systems are constrained in two axes but retain mobility along the elongated axis. Two-dimensional (2D) metallic nanostructures, such as metal nanofilms or nanosheets, are confined in one dimension while allowing electron motion across the remaining two. In contrast, three-dimensional (3D) metallic nanostructures, often formed by interconnected 0D, 1D, or 2D elements, such as nanowire bundles or certain metal–organic frameworks, enable electron mobility in all spatial directions and may support collective plasmonic phenomena.

Metallic and metal-like nanomaterials can also be classified based on their composition. This includes pure metal nanoparticles (e.g., gold, silver, platinum), metal oxide nanostructures (e.g., titanium dioxide, zinc oxide), and composite nanostructures [44]. Composite nanostructures [45] are hybrid materials that combine materials from the above categories to create multifunctional properties. For example, organic-inorganic composites or metal-carbon hybrids can be tailored for specific applications such as catalysis, sensors, and coatings.

2.2. Properties of metallic nanostructures

Noble metal and metal oxide nanostructures have gained significant attention in various scientific disciplines, including SALDI-MS. This interest is driven by their unique chemical and physical properties, such as optical, electronic, and structural characteristics, which distinguish them from individual metal atoms, bulk metals, and larger-scale oxide materials.

One of the most important properties of metallic nanostructures is their ability to exhibit LSPR, which refers to the resonant collective oscillation of free electrons in metallic nanostructures when exposed to light [46]. When photons interact with metallic nanostructures at specific wavelengths, conduction electrons on the metal surface collectively oscillate in resonance with the light's electric field [47]. This phenomenon enhances the local electromagnetic field near the nanoparticle surface and modifies its optical properties, resulting in significant light absorption, scattering, and local electromagnetic field intensification, making LSPR a highly valuable property in analytical applications, including SALDI-MS.

LSPR is particularly advantageous due to its exceptional sensitivity to molecular interactions and local refractive index changes [48]. The localized enhancement of the electromagnetic field can amplify molecular signals through mechanisms such as surface-enhanced Raman scattering (SERS). This amplification not only improves the efficiency of the desorption and ionization processes but also enhances the detection sensitivity, which is critical for ionization in SALDI-MS. The spectral tunability of LSPR further increases its versatility. Although resonance typically occurs in the visible spectrum, it can be shifted into the near-infrared (NIR) region by modifying nanoparticle size, shape, aspect ratio, shell thickness, and composition [49].

Chemical stability is another crucial factor for practical applications. Silver exhibits strong plasmonic properties; however, its tendency to oxidize can lead to diminished plasmonic performance. To mitigate this, strategies such as gold alloying or coating with stabilizing ligands or polymers are used to enhance stability and maintain reproducibility in long-term applications [49]. Furthermore, metallic nanostructures can be functionalized with biomolecules or chemical ligands to enable selective binding to target analytes. This functionalization improves specificity and expands their utility in applications such as biosensors, diagnostics, and targeted drug delivery, where precise molecular recognition is critical [50].

An important aspect of LSPR is the plasmonic coupling effect between closely spaced NPs. These interactions can lead to shifts in resonance wavelengths, enhanced signal intensities, and the formation of localized electromagnetic 'hotspots'. Such hotspots dramatically increase the detection sensitivity, enabling the identification of trace analytes with extremely low detection limits. The dynamic properties of LSPR, such as its sensitivity to changes in the refractive index of the surrounding medium, make it ideal for detecting molecular interactions in real-time. For example, shifts in resonance wavelength can be used to monitor binding events in biosensors or to detect structural changes in nanoparticles caused by external stimuli [51,52].

Metallic nanoparticles exhibit optical and electromagnetic properties that strongly depend on their size, shape, and surrounding environment [53]. These properties are primarily influenced by the high surface-to-volume ratio of nanoparticles, which enhances surface energy and reactivity. This characteristic facilitates the efficient adsorption and desorption of analytes, critical steps in the ionization process. Smaller nanoparticles (<30 nm) predominantly exhibit dipole resonances, resulting in intense light absorption and scattering in the visible range. In contrast, larger nanoparticles (>60 nm) display additional quadrupole resonances, increased scattering effects, and a redshift in the SPR. This size-dependent behavior allows optimization of nanoparticle performance based on specific analytical requirements [54].

The shape of nanoparticles also plays a crucial role in determining their optical properties.

[55]. For instance, ellipsoidal particles exhibit multiple plasmon resonances that shift depending on the polarization axis. Elongated particles tend to display redshifted resonances, while flattened shapes exhibit blueshifts. Irregularly shaped particles, such as triangular prisms, generate plasmonic "hotspots" at sharp edges as a result of the lightning rod effect, further enhancing electromagnetic field intensity [56]. The surrounding environment significantly influences the optical properties of nanoparticles. Placing them on substrates such as glass or mica or embedding them in dielectric media alters their plasmon resonance wavelengths. Specifically, increasing the dielectric constant of the surrounding medium induces a redshift in the resonance [57].

Nanoparticles also provide a high analyte-loading capacity due to their large surface area, which supports uniform surface coverage and improved interaction with target molecules. Unlike traditional organic matrices used in MALDI, metallic nanoparticles minimize matrix-related ion interference, offering cleaner spectra and higher detection sensitivity.

In SALDI-MS, the thermal capacity of the material is a critical factor. Metals such as gold and silver, commonly used in SALDI-MSI, are particularly well-suited for this application due to their relatively low heat capacity, which allows for efficient and rapid energy transfer from the nanoparticle to the analyte during laser irradiation, enhancing the desorption/ionization process [58].

2.3. Methods of metallic nanostructures synthesis

Producing metallic nanostructures with controllable sizes and morphologies is critical because their size and shape significantly influence their physical and chemical properties [59]. Both top-down and bottom-up approaches are commonly employed for this purpose, each offering unique advantages and limitations [60].

Top-down methods involve reducing bulk materials to nanoscale dimensions. Common techniques include ball milling, thermal evaporation, laser ablation, and sputtering. Ball milling uses mechanical attrition to reduce particle size, while thermal evaporation and laser ablation rely on heat to vaporize material, which then condenses into nanoparticles [61]. Sputtering involves the ejection of material atoms using ionized gas under controlled conditions, which can result in thin metal films or colloidal suspensions [62]. Despite their simplicity, top-down methods often yield nanoparticles with limited control over size uniformity and irregular shapes, which may reduce their applicability for specific tasks. In the context of MS and MSI, laser ablation and sputtering are widely used for metallic nanoparticle synthesis. Laser ablation synthesis in solution (LASiS) is a "green" method that requires no chemical reducing or stabilizing agents. This technique utilizes a metal plate immersed in a solvent, where laser pulses vaporize the material, forming nanoparticles directly in the liquid phase. LASiS has been applied for the MS analysis of metabolites, drugs, and other low-molecular-weight compounds [63–68]. In sputtering, atoms are ejected from a metal target through ion bombardment, forming nanoparticles that can be arranged as thin films or colloidal suspensions. Magnetron sputtered nanoparticles have been successfully used in the MS analysis of lipids, amino acids, and metabolites [69,70].

In contrast to top-down methods, bottom-up approaches build nanostructures atom by atom or molecule by molecule. These methods provide precise control over the size, shape, and chemical composition of the nanoparticles. Techniques include chemical vapor deposition (CVD), hydrothermal synthesis, co-precipitation, the sol-gel process, and chemical reduction. CVD deposits thin films on substrates through gas-phase chemical reactions, offering precise control over film composition and thickness [71]. Hydrothermal synthesis involves high temperature and pressure to form nanoparticles in aqueous solutions, enabling tailored morphology and crystallinity [72]. Co-precipitation produces nanoparticles by adding a precipitating agent to a solution containing metal ions, facilitating controlled nucleation and growth. The sol-gel method converts colloidal solutions (sols) into three-dimensional networks (gels), which are subsequently dried and annealed to produce nanostructures with specific properties [73]. Chemical reduction uses reducing agents, such as citric acid, oxalic acid, or borohydrides, to shift metal ions to a reduced state suitable for nanoparticle formation, with stabilizing agents typically employed to prevent aggregation [74]. Although bottom-up methods are less commonly used in MS, chemical reduction has shown significant potential. It has been applied in cancer metabolite analysis [75–79] detection of mycotoxins [80,81] and quantification of amino acids and carboxylic acids [82].

3. Mechanistic insights into desorption and ionization processes mediated by metallic nanostructures in SALDI

Although various nanomaterials such as carbon nanotubes, graphene, quantum dots, and metal oxides, have been explored as SALDI substrates, metallic nanostructures exhibit a unique set of properties that make them especially effective in enhancing desorption and ionization efficiency. While many of these materials share general features like high surface area, UV absorption, and favorable thermal conductivity, metals distinguish themselves through LSPR, which amplifies local electromagnetic fields. This enhancement reduces the laser fluence required for desorption and significantly improves ionization efficiency in SALDI-MS, especially for low-abundance analytes. Additionally, their reduced heat capacity at the nanoscale favors rapid and localized thermal spikes, while noble metals like silver and gold possess melting points and phase-transition thresholds that enable partial substrate melting or vaporization under moderate irradiation, enhancing analyte ejection. Furthermore, noble metals exhibit high chemical and thermal stability, minimizing background signals, and their well-documented affinity for forming metal-adduct ions improves sensitivity for small, polar, or underivatized analytes. These combined features contribute to lower detection limits, improved reproducibility, and cleaner spectra, particularly in the low-mass range relevant to metabolite imaging.

Unlike classical LDI, which primarily relies on direct absorption of laser energy by analyte molecules, SALDI explicitly requires substrate surface participation to mediate analyte desorption and ionization [34, 83–85]. Numerous experimental and computational studies indicate that these processes involve both thermal and nonthermal mechanisms [23,29].

The thermal component arises from the absorption of the laser pulse by the substrate, which elevates the local temperature and initiates the desorption of analytes [86]. Metallic nanoparticles exhibit lower thermal conductivity and reduced melting points compared to their bulk counterparts, which strongly influence the SALDI process by intensifying localized heating and enabling phase transitions at moderate laser fluences [86,87]. These effects are further enhanced by electronic inter- and intraband transitions that govern laser energy absorption and heat conversion. The absorption efficiency, described by the absorption cross-section (Q_{abs}), is strongly influenced by the dielectric properties of the nanoparticles. Noble metals such as Ag and Au, which possess high Q_{abs} values, reach elevated local temperatures that promote thermal desorption and modulate energy transfer to adsorbed molecules.

Molecular dynamics simulations have demonstrated that events such as nanoparticle melting, vaporization, and phase explosion (e.g., Au nanoparticles reaching ~5800 K) significantly enhance ion yield while influencing analyte fragmentation [86]. For example, Ag and Au can undergo phase transitions under moderate laser fluences, improving desorption efficiency while also increasing the risk of fragmentation or metal cluster formation. In contrast, high-melting-point metals such as Pt or Pd require higher energy inputs, resulting in different desorption dynamics [87]. When the energy input exceeds the threshold for melting or vaporization, nonthermal effects such as nanoparticle restructuring and Coulomb-explosion-like behavior may further boost desorption efficiency [88,89].

To assess the energy imparted to analyte ions, preformed benzylpyridinium (BP) ions are frequently used as “thermometer molecules” [90]. Their fragmentation patterns, quantified *via* survival yield (SY), offer insight into energy transfer during laser irradiation. Studies employing metallic nanoparticles have shown that increasing laser fluence raises ion intensities while altering SY, reflecting greater thermal energy deposition. However, fragmentation also depends on nanoparticle composition, with factors such as photoabsorption efficiency, density, and heat capacity playing crucial roles [87,91].

In metallic nanomaterials, conduction-band electrons transfer absorbed energy to the lattice on picosecond timescales, generating a localized “thermal spike” that can desorb molecules before they undergo degradation. Low nanoscale thermal conductivity confines this heat to the surface, preventing dissipation into the bulk [92]. While thermal spikes are generally surface-localized, deeper substrate layers may also participate, leading to bulk phenomena such as partial ablation and ejection of charged clusters [93,94].

Alongside these heat-driven processes, nonthermal mechanisms, particularly in plasmonic metals, play a prominent role [87]. LSPR leads to the generation of intense local electromagnetic fields and results in the formation of “hot electrons” and electron–hole pairs. Energetic electrons can migrate toward adsorbed molecules, promoting the formation of cationized or deprotonated species without requiring radical-based pathways [86]. Simultaneously, the positive charges remaining on the metal surface may weaken analyte-surface interactions, facilitating desorption. This helps explain why SALDI spectra are typically dominated by closed-shell ions such as $[M + H]^+$, $[M + Na]^+$, $[M + Ag]^+$, and $[M + Au]^+$ rather than radical species [23]. The mechanism thus appears to be governed primarily by energy- or charge-mediated cationization and protonation processes, resembling MALDI rather than radical-driven LDI.

Surface modifications and controlled aggregation of metallic nanoparticles can further enhance SALDI-MS performance by optimizing heat distribution and minimizing undesired metal cluster formation. For instance, closely packed Ag nanoparticles with interparticle gaps below 10 nm generate intense plasmonic “hot-spots,” amplifying SERS and SALDI-MS responses. However, excessive aggregation disrupts plasmon coupling and diminishes performance [95,96].

Substrate morphology also exerts a significant influence on desorption efficiency. Laser-induced reshaping, such as the transition of Au nanoparticles into more spherical forms, can further enhance light absorption and thermal confinement. To prevent undesirable aggregation and ensure uniform thermal behavior, nanoparticles may be coated with organic ligands or stabilizing polymers, which also improve heat transfer [96].

Partial substrate ablation constitutes another factor contributing to desorption and ionization. At sufficiently high laser fluences, metal and metal oxide nanostructures can melt, vaporize, or fragment in Coulomb-explosion-like events [97,98]. Processes result in the ejection of charged clusters and electrons that enhance ion formation. However, excessive ablation may introduce metal clusters into the mass spectrum, which can be undesirable due to spectral interferences, although in some cases they can be intentionally utilized for internal calibration [99].

In addition to promoting energy transfer, certain metals enhance ion yield through their inherent ability to form stable adducts with small molecules. Silver, in particular, effectively forms adducts with lipids, sterols, and other unsaturated or heteroatom-containing analytes [25,100] while noble metals rely heavily on plasmonic resonance and efficient charge transfer, non-metallic substrates such as titanium dioxide, zinc oxide, or iron oxide utilize broadband UV absorption or electron–hole pair generation *via* bandgap excitation [101,102]. These oxide-based substrates often support alternative ionization pathways and exhibit different selectivity profiles, depending on their specific chemical and physical properties [27,103]. Functionalized surfaces can further enhance SALDI performance by enabling specific analyte-substrate interactions, thereby improving ion yields, selectivity, and spectral clarity [104,105].

Collectively, these findings highlight that the SALDI mechanism is neither purely thermal nor strictly governed by plasmonic or photochemical effects. Instead, substrate composition, morphology, and size, together with laser wavelength and fluence, jointly determine the dominant desorption and ionization pathways. When nanoparticle diameter is smaller than the laser thermal diffusion length, more uniform heating occurs, reducing the fluence threshold for desorption. Smaller nanoparticles reach higher peak temperatures under the same laser energy, enhancing analyte ejection. However, excessively small particles may lack sufficient thermal capacity, limiting their efficiency under some conditions [106]. Experimental studies with various materials, including Au and GaP nanoparticles, confirm that desorption and ionization efficiency are highly size-dependent [86,87,107].

4. Types of metallic nanostructures used in mass spectrometry imaging

Metallic nanostructures employed in SALDI-MS must efficiently absorb laser energy, rapidly convert it into localized heat, and exhibit low heat capacity to ensure effective analyte desorption and ionization. Their high surface-to-volume ratio facilitates analyte adsorption, enhancing ion yield. Morphological features such as shape, size, and surface roughness further influence desorption efficiency by improving laser energy transfer and analyte-surface interactions [29,35].

Common materials include noble metals (e.g., Au, Ag, Pt), transition metals (e.g., Co), and metal oxides (e.g., TiO_2, Fe_3O_4, ZnO, WO_3), which have demonstrated varying performance depending on the analyte’s polarity, mass, and functional groups. Fig. 1 illustrates the overview of various metallic nanostructures used in MSI, highlighting the dominance of noble metals such as AuNPs (43 %) and AgNPs (32 %), followed by metal oxides like TiO_2 (9 %) and Fe_2O_3/Fe_3O_4 (7 %).

The morphology of nanoparticles also affects their interaction with laser energy. Common shapes include nanospheres, nanorods, nanostars, and nanocubes, each offering different absorption maxima [108–110]. However, for SALDI applications using UV lasers (∼355 nm), such differences are typically secondary to surface uniformity and thermal response [35].

Particle size strongly influences SALDI performance. Smaller nanoparticles increase surface contact and desorption efficiency, while larger ones may generate higher total ion intensities. For example, 2 nm AuNPs reduce spectral noise, whereas 10 nm AuNPs produce stronger signals [107]. In addition, thin layers of metallic nanostructures (e.g., Au or Pt) can act as conductive coatings to mitigate charging on non-conductive

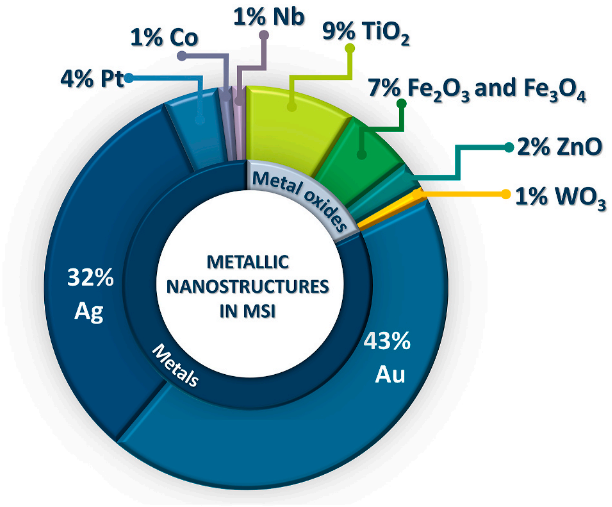

Fig. 1. Overview of metallic nanostructures in MSI applications.

Table 1
Comparison of metallic nanostructures used in LDI-MSI.

Particle size (nm)	Gold (Au)	Silver (Ag)	Platinum (Pt)	Niobium (Nb)	Cobalt (Co)	Titanium Dioxide (TiO_2)	Iron Oxide (Fe_3O_4)	Zinc Oxide (ZnO)	Tungsten Oxide (WO_3)
	2–100	2–100	10–50	25	2	5–700	3–161	70–100	23–65
Morphology	Nanoclusters, nanocomposite, nanolayers, nanoparticles, nanorods, nanoshells, nanospheres, nanotubes	Nanolayers, nanoparticles nanocomposites	Nanolayers, nanoparticles	Nanoparticles	Nanolayers	Monoliths, nanoparticles, nanowires, nanosheets	Nanoparticles	Nanoparticles, nanoshells	Nanoparticles
Ease of functionalization	Very easy	Easy	Moderate	Moderate	Moderate	Easy	Moderate	Difficult	Difficult
Chemical stability	Very high	High	Very high	High	Low	High	Moderate	Moderate	High
Thermal stability	High	Moderate	Very high	Very high	Moderate	Very high	High	Moderate	Very high
UV absorption	Moderate	Strong	Weak	Moderate	Moderate	Strong	Moderate	Strong	Moderate
Plasmonic resonance (LSPR)	Strong	Strong	None	None	Weak	None	None	None	None
Ionization efficiency	High	Very high	Moderate	Moderate	Moderate	Moderate	High	Moderate	High
Adduct formation	Low	Very high	Moderate	High	Moderate	Low	Low	Low	Moderate
Ionization ability	High	Very high	Moderate	High	Moderate	High	Moderate	High	High
Nanocluster ions calibration	Yes	Yes	No	No	No	No	No	No	No
Signals in low *m*/*z* region	Moderate	High to moderate for single isotope	Low	Moderate	High	Low	Moderate	Low	Moderate
Aggregation tendency	Moderate	High	Low	Low	High	Low	Moderate	Low	Low
Electrical conductivity	High	High	High	Moderate	Moderate	Low	Moderate	Low	Moderate
Chemical reactivity	Inert	Low	Very low	High	High	Low	Moderate	Moderate	Low
Target analytes	Lipids, peptides, sterols	Aromatic and olefinic compounds, lipids, sterols, fatty acids, carbohydrates	Lipids, peptides, carbohydrates, polymers	Lipids	Lipids, amino acids, peptides, organic acids, nucleotides	Lipids, peptides, amino acids, nucleotides, organic acids, polyamines, nitrogenous compounds	Lipids, peptides, small metabolites	Amino acids, amines, neurotransmitters, lipids (moderate)	Amino acids, carbohydrateslipids (TAG)
Cost	High	Moderate	Very high	Moderate	Low	Low	Low	Low	Moderate
Availability	High	High	Low	Low	Medium	High	High	Very High	Medium

surfaces, improving MSI resolution—especially for plant or ink-rich samples [111].

To facilitate the selection of an optimal metallic substrate, Table 1 summarizes the key characteristics of various metal-based materials used in SALDI-MSI. It highlights how factors such as molecular weight, polarity, and specific functional groups influence ionization efficiency, the tendency to form clusters, and relative cost.

4.1. Metal nanoparticles

Gold, silver, platinum, and copper nanoparticles demonstrate distinctive optical and thermal properties that make them effective in SALDI-MS applications. Their strong light absorption primarily due to LSPR in AuNPs and AgNPs enables efficient energy transfer to analytes upon laser irradiation. Moreover, their relatively low heat capacity at the nanoscale promotes localized heating and contributes to enhanced desorption and ionization of a variety of analytes without the extensive background noise typically associated with organic matrices.

Studies have shown that Pt nanoparticles (PtNPs) can outperform AuNPs in ionizing certain peptides (e.g., angiotensin I), due to their lower thermal conductivity and higher melting point, which reduce heat dissipation [112]. In turn, AuNPs often provide stronger signals for some high-molecular-weight species, while AgNPs can be more prone to oxidation yet excel in forming stable cationized adducts (e.g., $[M+Ag]^+$) with certain lipids and aromatic compounds. Transmission electron microscopy (TEM) images frequently show that PtNPs are smaller (~2–5 nm) and less prone to aggregation than AgNPs (10–30 nm) or CuNPs (10–20 nm).

Despite their advantages, noble metal nanoparticles can aggregate if stabilizing agents (e.g., surfactants) are not applied, potentially compromising ionization efficiency. However, such agents may produce interfering peaks. An alternative is to employ bare nanoparticles synthesized by laser ablation, which avoid stabilizer-related signals and provide cleaner mass spectra [113]. Moreover, the inherent affinity of sulfur-containing analytes (e.g., methionine) for Au and Pt surfaces can be exploited for selective desorption.

Although later sections address additional metal types and detailed mechanistic considerations, noble metal nanoparticles remain central to many SALDI-MS workflows due to their broad UV absorbance, relatively high stability, and capacity for generating intense, reproducible signals with minimal background interference. Their selection ultimately depends on analyte properties, required sensitivity, and operational constraints such as cost and nanoparticle stability.

4.1.1. Gold nanostructures

Gold nanoparticles (AuNPs) exhibit unique properties that make them particularly useful in SALDI techniques [114]. Their exceptional ability to absorb laser radiation, attributed to plasmonic properties and high absorption coefficients above 400 nm, facilitates efficient energy transfer to analytes, enhancing desorption and ionization processes [115]. Additionally, AuNPs are chemically inert and highly stable, making them resistant to oxidation and suitable for biological sample analysis without interfering with analytes [116].

Their high stability also makes them ideal for use in complex biological matrices such as serum and urine, where they tolerate salts and chemical additives without requiring extensive sample preparation. Their high surface-to-volume ratio enhances analyte adsorption, further improving sensitivity in mass spectrometric analyzes [117]. The efficiency of AuNPs in SALDI is strongly linked to their SPR properties, which depend on particle size, shape, and the surrounding dielectric environment [118]. For AuNPs ranging from 2 to 100 nm, the SPR peak is observed between approximately 515 and 580 nm. Smaller nanoparticles (~2–5 nm) typically exhibit SPR peaks around 515–520 nm, whereas larger particles (~100 nm) shift toward 580 nm due to size-dependent plasmonic effects [119]. Moreover, the stable gold ion peaks in mass spectra provide reliable internal calibration points, enhancing mass accuracy [120].

Despite these advantages, AuNPs exhibit lower cationization efficiency compared to other metallic nanoparticles, such as AgNPs [121]. AuNPs primarily facilitate ionization through thermal desorption and laser energy absorption rather than direct cationization [68]. The relatively weaker cationization efficiency of AuNPs can limit sensitivity for certain compounds, especially those that rely on metal-assisted ionization. However, functionalization of AuNPs with specific ligands can improve their ionization performance by reducing unwanted gold cluster signals and promoting selective analyte interactions [122].

Gold cluster cations Au_n^+ ($n = 1$–11) are frequently observed in LDI-MS spectra when AuNPs are used as a matrix. These ion peaks can serve as reliable internal calibration points due to their high stability and reproducibility [107]. However, in certain cases, these signals may overlap with those of the analytes, potentially interfering with their detection. Compared to AgNPs, AuNPs generate fewer interfering signals due to their monoisotopic nature (^{197}Au), whereas AgNPs produce multiple isotope peaks (^{107}Ag and ^{109}Ag), leading to more complex spectral patterns [65]. This difference makes AuNPs particularly advantageous for applications requiring minimal background interference and precise spectral interpretation.

AuNPs have demonstrated high efficiency in LDI-MS for the analysis of lipids, peptides, and sterols in complex biological matrices [114]. In peptide analysis, AuNPs provide high chemical stability and reduced fragmentation, resulting in improved spectral resolution and reproducibility [123]. Additionally, sterols, which require efficient desorption mechanisms, are effectively ionized with AuNPs due to their strong plasmonic absorption and energy transfer capabilities [124]. However, for certain sterols and highly polar lipids, AgNPs may exhibit superior cationization efficiency, facilitating enhanced ionization and detection sensitivity.

4.1.2. Silver nanostructures

Silver nanoparticles (AgNPs) have similarly garnered interest due to their unique optical and electronic properties [125]. AgNPs exhibit LSPR, with the absorption peak position highly dependent on particle size [126]. For AgNPs ranging from 2 nm to 100 nm in diameter, the LSPR absorption band is observed between approximately 400 nm and 450 nm. Smaller AgNPs (2–20 nm) typically show a maximum absorption around 400–420 nm, whereas larger nanoparticles (~100 nm) exhibit a red-shifted peak above 450 nm [127]. This size-dependent optical behavior arises from retardation effects and the increased mass inertia of conduction electrons in larger nanoparticles. With UV absorption closer to the 355 nm wavelength of typical SALDI lasers, AgNPs facilitate efficient energy transfer and offer higher sensitivity for specific analytes compared to AuNPs [128,129]. AgNPs are particularly effective for aromatic compounds, olefinic species, and long-chain hydrocarbons due to their Lewis acid properties, which allow them to form adducts with π-electron-rich molecules. This property has been leveraged to detect a wide range of lipids, sterols, and wax esters, as well as peptides, fatty acids, carbohydrates, and amino acids [130]. AgNP-based substrates have also proven effective in molecular imaging, particularly for lipid analysis in tissue sections. For example, colloidal AgNPs sprayed onto tissue samples enhance the imaging of cerebrosides [131].

Despite their shared utility in SALDI-MS, AuNPs and AgNPs excel in different contexts. AuNPs are preferred for biological sample analysis due to their inertness and biocompatibility, while AgNPs are superior for aromatic and olefinic compounds due to their strong π-electron interactions [100]. Additionally, AgNPs offer enhanced ionization efficiency through cationization, forming stable $[M+Ag]^+$ adducts, which improves detection sensitivity for certain polar metabolites and lipids [132]. However, AgNPs are more prone to oxidation, which can affect their long-term stability and ionization performance. Moreover, their broad isotopic distribution results in more complex mass spectra, potentially complicating spectral interpretation. The use of monoisotopic silver-109 nanoparticles could eliminate this spectral complexity, providing clearer and more interpretable mass spectra [133]. However, the limited commercial availability of ^{109}Ag and its high cost significantly restrict its widespread application.

Moreover, AgNPs are prone to aggregation during preparation, which can lead to uneven distribution and inconsistent ionization efficiency in SALDI-MS. To mitigate this issue, various deposition techniques have been developed, including thermal evaporation and sputter coating, which help achieve more uniform metal layers [134,135]. Sputter coating, in particular, ensures even nanoparticle deposition, improving spectral reproducibility and enhancing imaging resolution in both forensic and biomedical applications [136,137]. Despite these advances, challenges related to AgNP stability and ionization variability remain, requiring further refinement of synthesis and application methods [138–140].

4.1.3. *Platinum nanostructures*

Platinum nanostructures, including nanolayers (PtNLs) and nanoparticles (PtNPs), are less commonly used in MSI compared to gold or silver nanostructures, but they offer unique advantages in specific applications. PtNPs exhibit key features that make them highly suitable for SALDI-MSI. Unlike other metals, platinum does not produce cluster peaks in mass spectra, eliminating interference with analyte signals [95, 141]. Additionally, PtNPs generate cleaner spectra due to their low cationization efficiency, minimizing adduct formation and ion suppression effects [93,142].

Their homogeneous surface distribution further enhances spatial resolution and reproducibility in MSI [141]. Platinum's low thermal conductivity and high melting point (~2045 K) promote rapid localized heating and effective soft desorption/ionization, while minimizing analyte and metal fragmentation [112,143]. Moreover, their broad UV absorption spectrum (~216–264 nm) supports efficient ionization in MALDI and SALDI-MS under UV laser excitation [144].

Despite these benefits, PtNPs also have limitations. They lack strong LSPR peaks, making them less effective in plasmon-enhanced ionization compared to AuNPs and AgNPs [145]. Additionally, platinum is costly, limiting large-scale applications [146], and its synthesis often requires high temperatures (>800 °C), complicating fabrication [147]. Pt coatings also enhance conductivity on insulating substrates like paper or glass, enabling efficient SALDI-MSI for applications such as ink analysis on documents and fruit imprints in positive and negative ion modes [148].

4.1.4. *Niobium nanostructures*

Niobium nanoparticles (NbNPs) have recently emerged as cost-effective alternatives to traditional metallic nanomaterials for SALDI-MSI [149]. Their unique physicochemical properties, including a monoisotopic composition (^{93}Nb), make them highly suitable for precise mass spectrometric analyses. Niobium's affordability compared to Au and Ag makes it ideal for large-scale or high-throughput experiments. Additionally, gas aggregation sputtering (GAS) allows solvent- and stabilizer-free deposition, avoiding chemical contamination and enhancing analytical sensitivity [150].

Niobium's rapid formation of a passivating Nb_2O_5 layer ensures resistance to oxidation and preserves nanoparticle integrity [151]. The naturally formed Nb_2O_5 layer on Nb nanoparticles significantly influences their physicochemical properties, including surface stability and reactivity. Owing to its wide band gap (3.1–5.3 eV), Nb_2O_5 effectively absorbs UV light at 355 nm, which contributes to laser energy uptake in SALDI-MS [152].

Thermal properties, including a molar heat capacity comparable to Au and Ag, enable efficient energy transfer under laser irradiation, facilitating robust desorption and ionization of thermolabile and low-molecular-weight compounds [153]. Notably, NbNPs form stable adducts ($[\text{analyte} + \text{Nb}]^+$), enhancing analyte specificity and reducing noise levels in MSI. Their ability to form Nb adducts also extends to a wide range of biomolecules, improving detection of metabolites and lipid species that are poorly ionized using conventional organic matrices. In particular, the naturally formed Nb_2O_5 shell facilitates specific analyte–surface interactions and contributes to the efficient and selective ionization of multiple phospholipid classes—including phosphatidylcholines, phosphatidylethanolamines, phosphatidic acids, phosphatidylserines, and galactoceramides—that are often undetectable with conventional MALDI matrices. This broadened ionization capacity enhances lipidomics studies and supports detailed molecular profiling. NbNPs excel in lipid profiling, providing extensive coverage of phospholipid classes such as phosphatidylcholines and galactoceramides, with minimal fragmentation. Moreover, the oxide layer may influence lipid–surface interactions, potentially stabilizing or enhancing the ionization efficiency of specific lipid subclasses. Uniform NbNP layers deposited via GAS achieve high spatial resolution (30 μm), enabling reproducible imaging of biomolecules across tissue sections [149].

4.1.5. *Cobalt nanostructures*

Cobalt nanoparticles (CoNPs) have shown promise in MSI when integrated into Ti_3C_2 MXene platforms, forming Co–N–Ti_3C_2 films [154]. This composite material enhances photocatalytic activity, facilitating sensitive analyte detection and efficient ionization. Co–N–Ti_3C_2 films absorb UV–visible laser wavelengths (337 nm and 355 nm) and exhibit superior photothermal conversion, improving desorption/ionization processes. Compared to other metallic nanoparticles such as AgNPs, AuNPs, and PtNPs, CoNPs provide higher photothermal efficiency and catalytic activity, making them particularly useful in SALDI-MS.

Fabricated *via* an in situ self-assembly method, the Co–N–Ti_3C_2 platforms achieve consistent performance with a coefficient of variation (CV) below 4 %, addressing the uneven nanoparticle distribution seen with other SALDI substrates. Compared to other SALDI substrates, Co–N–Ti_3C_2 films offer exceptional signal uniformity and minimal variability, supporting high-resolution and reproducible imaging across biological samples. Additionally, CoNPs exhibit strong surface plasmon resonance, contributing to their high ionization efficiency. Their magnetic properties enable efficient sample separation and enrichment, which is beneficial in complex biological matrices [155]. Moreover, they maintain high performance in complex biological samples with high salt concentrations.

Despite their advantages, CoNPs face aggregation, oxidation, and toxicity issues [156]. Unlike AgNPs and AuNPs, they require stabilization to prevent cobalt oxide formation, which can reduce ionization efficiency. Graphene coatings or polymer encapsulation help maintain stability. While CoNPs improve ionization, their catalytic activity may induce analyte interactions, leading to signal artifacts or diffusion effects in MSI. Surface functionalization is often required to ensure high-resolution imaging and prevent unintended chemical interferences [93].

4.2. *Metal oxide nanoparticles*

Metal oxide nanoparticles exhibit distinct thermal, optical, and chemical characteristics that complement or surpass the properties of noble metals in certain SALDI-MS applications. Commonly used metal oxides, such as TiO_2, Fe_3O_4, ZnO, and WO_3, all of which provide efficient energy absorption, broad UV–visible responsiveness, and relatively low background noise. In particular, they enable the analysis of small molecules and lipids with high signal intensity, often outperforming conventional organic matrices [157]. Furthermore, their inherent stability and minimal cluster formation can produce cleaner spectra, especially in positive-ion mode.

Despite these benefits, metal oxides may introduce challenges, such as the risk of aggregation and possible oxidative stress in biological contexts [158]. Experimental workflows employing metal oxide nanoparticles also need to address issues like nozzle clogging (e.g., when spraying nanoparticle suspensions) or unwanted analyte adsorption on partially charged oxide surfaces. Notably, the potential formation of adduct ions (e.g., $[M + Na]^+$) or partial chemical modification of certain analytes must be carefully assessed to ensure accurate spectral interpretation.

When compared with noble metal nanoparticles metal oxides often rely on bandgap excitation rather than localized surface plasmon resonance. As a result, they can be advantageous for specific compound classes or for reducing spectral interferences from metal cluster ions. At the same time, their compatibility with diverse sample types (including harsh chemical environments or tissue sections requiring moderate laser fluences) makes them highly versatile SALDI substrates. Nevertheless, the optimal choice of material remains dependent on analyte properties, laser wavelength, and practical considerations like cost and long-term storage stability.

Subsequent subsections will discuss TiO_2, Fe_3O_4, ZnO, and WO_3 nanoparticles in more detail, highlighting their specific absorption characteristics, ionization efficiencies, and potential applications in imaging distinct metabolite classes.

4.2.1. *Titanium dioxide nanoparticles*

TiO_2 NPs are widely applied in SALDI-MS due to their strong UV absorption and photoexcitation properties. Their absorption occurs primarily in the UV range (320–430 nm), with smaller particles absorbing at shorter wavelengths, enabling efficient energy transfer for analyte desorption and ionization [159]. Their ability to generate electron–hole pairs under laser irradiation facilitates ionization without significant background interference [160,161]. Additionally, their high chemical and thermal stability allows their use in a broad range of sample types, including those requiring harsh analytical conditions [162]. Unlike some metal oxide nanoparticles, TiO_2 NPs generally do not form significant adducts with analytes, minimizing spectral interference and improving ionization efficiency. However, studies indicate that under certain conditions, TiO_2 NPs can bind sodium ions, potentially leading to adduct formation and affecting spectral interpretation [163,164].

TiO_2-coated surfaces enable uniform laser energy absorption, improving reproducibility and reducing spectral contamination, particularly in imaging applications requiring high spatial resolution [165,166]. Despite these advantages, TiO_2 NPs exhibit a tendency to aggregate, which can impact homogeneity and reproducibility in MSI experiments. The formation of nanoparticle clusters may lead to uneven ionization across the sample surface, introducing variability in spectral data [167]. Functionalized TiO_2 materials, such as TiO_2-DA (dopamine-modified TiO_2) or TiO_2-MOF (metal–organic framework-based TiO_2), further enhance ionization efficiency and selectivity for specific analytes such as lipids and alkaloids [168,169].

These modifications also help mitigate some of TiO_2 NPs' inherent limitations, such as aggregation and selective ion suppression, by improving surface homogeneity and charge transfer efficiency [170]. These modifications expand TiO_2's utility for metabolite detection across complex biological matrices.

4.2.2. *Iron oxide nanoparticles*

Fe_3O_4 NPs have demonstrated superior performance in MSI for lipids, peptides, and low-molecular-weight metabolites due to their thermal desorption properties and high surface area which facilitate analyte ionization [171,172]. In early studies, functionalized Fe_3O_4 nanoparticles achieved high spatial resolution (15 μm) and minimized background signals [171]. Their broadband absorption spectrum (330–700 nm) allows effective laser energy absorption, ensuring stable ionization of small molecules, particularly metabolites and organic acids, with minimal spectral interference [173]. Unlike gold and silver nanoparticles, Fe_3O_4 NPs do not rely on surface plasmon resonance (SPR), making them less sensitive to specific laser wavelengths while maintaining stable ionization efficiency. Combining Fe_3O_4 with binary matrices, such as DHB, has further improved ionization efficiency for lipids, glycoconjugates, and certain oligosaccharides, enabling detection across a broad mass range (*m/z* 100–2000) with enhanced sensitivity [173]. Additionally, their high thermal and chemical stability prevents spectral contamination, making them particularly advantageous for lipidomics and metabolomics applications. However, their tendency to aggregate can impact homogeneity and reproducibility in MSI experiments, potentially leading to variability in ionization efficiency [167]. While Fe_3O_4 NPs generally exhibit low adduct formation, some studies indicate that sodium ion (Na^+) adducts may form under specific conditions, affecting spectral interpretation [164].

A key advantage of Fe_3O_4 NPs is their superparamagnetic properties, which enable additional applications such as analyte preconcentration, enrichment, and separation prior to MS analysis, expanding their functionality in bioanalytical workflows. However, the strong thermal desorption mechanism of Fe_3O_4 can induce degradation of thermally labile compounds, limiting its applicability for certain metabolite classes. Additionally, its relatively lower ionization efficiency for proteins and other large biomolecules compared to noble metal nanoparticles restricts its use in proteomic studies.

4.2.3. *Zinc oxide nanoparticles*

ZnO NPs have shown promise in MSI for both polar and nonpolar analytes, such as PEG 200 and methyl stearate, offering low background noise and efficient cationization-assisted ionization [174,175]. ZnO exhibits a strong UV absorption band in the 360–380 nm range, making it well-suited for use with UV lasers in LDI-MS but limiting its compatibility with lasers operating at longer wavelengths [176]. Although ZnO requires higher laser fluence compared to TiO_2 or Fe_3O_4, its dissolution in dilute acids simplifies substrate preparation and minimizes deposition-related issues [177]. However, despite its ability to support the ionization of both polar and nonpolar analytes, ZnO exhibits lower ionization efficiency for certain compound classes and limited compatibility with alternative laser wavelengths, which restricts its broader applicability compared to more versatile oxides like TiO_2 and Fe_3O_4 [166,178]. Specifically, ZnO predominantly facilitates ionization *via* Na^+ and K^+ adduction adduction rather than protonation, enhancing the detection of certain metabolites and lipids, but potentially reducing sensitivity for analytes favoring protonation [179]. While effective for small biomolecules (<500 Da), its performance declines for larger molecules due to limited absorption cross-section and suboptimal energy transfer efficiency [157]. Furthermore, ZnO's aggregation tendencies, while lower than those of TiO_2, still require optimized dispersion conditions to maintain reproducibility in MSI experiments [180].

4.2.4. *Tungsten oxide nanoparticles*

WO_3 NPs exhibit a broad absorption band in the visible spectrum, typically ranging from 400 to 500 nm, corresponding to their bandgap energy of approximately 2.6–3.0 eV. This enables efficient absorption of laser energy in LDI-MS, particularly when using UV or visible lasers, enhancing desorption and ionization efficiency. Compared to other metal oxide nanoparticles such as Fe_3O_4 or TiO_2, WO_3 NPs demonstrate superior ionization efficiency for certain metabolite classes, particularly neutral lipids and carbohydrates. However, they are generally less effective for nucleotides and phospholipids, where Fe_3O_4 outperforms them [181]. Their ability to localize metabolites associated with energy-related pathways (e.g., glycolysis, TCA cycle) makes them valuable for metabolomics imaging. However, the performance is highly dependent on experimental conditions and is less effective for larger oligosaccharides and other complex analytes, for which DHB or Fe_3O_4 may be preferred.

One of the key advantages of WO_3 NPs over noble metal nanoparticles (e.g., Ag and Au NPs) is their lower background noise in the low *m/z* region, making them particularly useful for detecting low-mass metabolites with minimal spectral interference. Unlike AgNPs, which preferentially enhance fatty acid ionization, WO_3 NPs provide a more balanced ionization across lipid classes, including glycerides and free sterols. However, they exhibit a lower signal intensity for polyunsaturated fatty acids compared to AgNPs [182].

A notable limitation of WO_3 NPs in LDI-MSI is their tendency to aggregate, which can lead to spatial heterogeneity in ionization efficiency. This aggregation may be mitigated through surface modifications or dispersing agents, but further optimization is required for consistent performance across biological tissue samples [157]. Additionally, WO_3 NPs have shown a weaker performance in detecting amino acids and small organic acids compared to Fe_3O_4 and TiO_2 nanoparticles, suggesting that their application may be best suited for lipidomics and carbohydrate-focused studies [183].

5. Sample preparation for mass spectrometry imaging

Proper sample preparation is critical for MSI, as it preserves the native distribution of analytes and minimizes artifacts introduced during handling. One primary challenge in MSI, especially for organic tissues, is the rapid metabolic alteration of cells once the tissue is removed from its natural environment. These changes, along with possible compound redistribution, can undermine the accuracy of MSI results by altering the molecular landscape [184]. Consequently, the goal is to stabilize tissues promptly and uniformly, ensuring that MSI reflects the in vivo molecular state as closely as possible.

Although different ionization methods exist in MSI (e.g., SIMS, DESI, LDI), fundamental sample-handling principles are consistent across most platforms. In SALDI-MSI, two main preparation methods are commonly employed: sectioning and imprinting [185]. The choice depends on the analyte of interest, the ionization technique, and practical considerations such as operator expertise or sample fragility.

The most widely used approach involves slicing frozen tissue into thin sections (5–20 μm) with a cryostat microtome. Freezing, often achieved by snap-freezing in dry-ice-chilled isopentane [186], liquid nitrogen [187], or dry ice in hexane [188], is crucial to halt enzymatic activity and preserve molecular composition. Temperatures during sectioning typically range between 5 and −20 °C, depending on the composition of the tissue. To secure the sample during cutting, it may be embedded in carboxymethylcellulose or an optimal cutting temperature polymer (OCT). However, one must ensure that these embedding agents do not contaminate the imaging region, as they can ionize readily and interfere with analyte signals [189].

For animal tissues, sections between 2 and 20 μm thickness are generally reported, with thinner sections sometimes offering enhanced detection of higher molecular weight molecules. For plant samples, sections around 50 μm are common, reflecting the different cellular structures encountered in botanical specimens. After sectioning, the tissue is typically mounted on a conductive plate (e.g., stainless steel or ITO-coated glass) *via* a thaw-mounting procedure. Although this minimizes the risk of contamination, prolonged thawing can degrade tissue components, so rapid and consistent handling is essential. In SALDI, the majority of MSI analyses are conducted by applying a suspension of metallic or metal oxide nanoparticles, often introduced through spraying or deposition directly onto the tissue surface. This process forms a nanostructured layer that facilitates efficient desorption and ionization [189,190].

Imprinting is a simpler alternative where the tissue is gently pressed onto a pretreated substrate. In SALDI-MSI, this substrate often contains permanently bound metallic nanoparticles, eliminating the need to prepare thin sections or apply matrix solutions. The contact transfer of molecules from the tissue to the substrate typically requires only a few seconds, reducing the risk of sample damage. The imprint is then analyzed directly, which speeds up sample throughput and lowers the chance of artifact introduction. Imprinting excels for low molecular weight compounds (<1500 Da) due to minimal interference from traditional matrices. Metal ions and their clusters on the substrate can serve as convenient internal calibrants, enhancing mass accuracy. This method has proven effective for fragile or soft tissues—common in many plant studies—where standard cryosectioning is challenging [191]. Examples include using silver-109 nanoparticles for analyzing distribution of LMW metabolites in Mentha piperita stems and Fragaria × ananassa fruits [192], or gold nanoparticles deposited on paper to study pesticide migration in fruit and vegetable imprints [193]. Additionally, titanium dioxide (TiO_2) nanowires [194] and platinum-coated porous surfaces [148] have enabled sensitive, high-resolution metabolite imaging in multiple imprint of plant species. The same approach is also advantageous in fingerprint analysis, capturing endogenous compounds (lipids, amino acids, and metabolites) in ridge patterns without destroying evidence [195]. Nevertheless, imprinting can be suboptimal for very hard or very soft tissues, which may compromise spatial fidelity during pressing. Certain volatile or unstable metabolites may also be lost or unevenly transferred, influencing the accuracy of the data. Furthermore, surface hydrophobicity and morphology can selectively influence which compounds adhere to the substrate, leading to incomplete metabolite profiles [196].

6. Methods of deposition of metallic nanostructures for mass spectrometry imaging

The method of nanoparticle application in SALDI-MSI is a critical determinant of analytical accuracy, spatial resolution, and reproducibility. The uniform distribution of the nanoparticles on the sample surface ensures high spatial fidelity, precise quantitative analyzes, and detailed visualization of analyte localization. Uneven coverage or nanoparticle aggregation can introduce “hotspots” and reduce the reliability of MSI results. Additionally, the method of nanoparticle deposition may influence sample integrity, chemical interactions, and analyte recovery. Five primary methods are currently employed for applying nanostructured substrates in SALDI-MSI: spraying [197], sputtering [136], immobilization [198], deposition [199], and implantation [131]. Each approach offers unique advantages and limitations depending on the nature of the tissue, the properties of the analyte, and the availability of instruments.

Spraying is one of the earliest and most widely used methods for nanoparticle application in SALDI-MSI. In this technique, metallic nanoparticles are suspended in a volatile solvent (e.g., methanol or acetonitrile) to ensure colloid stability. The suspension is then sprayed onto the tissue surface manually (eg, with an airbrush or thin-layer chromatography sprayer) or automatically using robotic systems [197]. Automated spraying offers precise control over deposition parameters, such as flow rate and spray pattern, improving reproducibility. However, solvent-based delivery systems pose a risk of analyte delocalization, especially for small molecules prone to diffusion. To mitigate this, researchers often apply multiple thin coatings, allowing each layer to dry uniformly to minimize aggregation and maintain nanoparticle distribution.

Sputtering is a more advanced method that involves depositing a thin metal layer onto the tissue surface by bombarding a solid metal target with argon plasma in a vacuum chamber. This process generates metal nanoclusters that form a uniform coating on the sample surface. Magnetron sputtering is preferred for SALDI-MSI due to its precise control over deposition parameters, such as coating thickness and nanoparticle density [200]. Proper optimization of sputtering conditions such as vacuum pressure, substrate temperature, and argon gas purity ensures reproducibility and prevents variations in particle morphology or size. Unlike solvent-based methods, sputtering eliminates the risk of analyte delocalization, making it ideal for thick or nonconductive samples. However, sputtering requires specialized equipment, which may not be accessible to all laboratories.

Imprinting involves transferring analytes from the sample tissue onto a pre-modified substrate, such as a metal plate coated with immobilized nanoparticles. The metallic nanoparticle-based imprinting method was first introduced by Ruman’s team in 2013 [195]. In this approach, the sample is briefly pressed against the substrate, leaving a “molecular

Table 2
Applications of metallic nanostructures in mass spectrometry imaging of brain tissues.

Type	Nanostructures			Brain tissue sample		MSI		Classes of compounds	Ref.
	Clasification	Deposition	Size [nm]	Source	Preparation	Spatial resolution	Ion mode		
Gold (Au)	Nanoparticles	Spraying	5.5	Rat	Cryosectioning	200 µm	(+)	Cer	[215]
	Nanoparticles	Spraying	4.3	Mouse	Cryosectioning	200 µm	(−)	GM, ST	[214]
	Nanoparticles	Spraying	10	Fly	Cryosectioning	20 µm	(+)	DAG, Nitrogenous Bases, TAG	[219]
	Nanoparticles	Spraying	30	Mouse	Cryosectioning	120 µm	(+) (−)	HexCer, PA, PE, PG, SHexCer	[221]
	Nanoparticles	Spraying	2	Rabbit	Cryosectioning	20 µm	(+)	Dopamine/Octopamine, Norepinephrine, GABA/Choline	[197]
	Nanoparticles	Sputtering	5	Mouse	Cryosectioning	60 µm	(+) (−)	Amines and Derivatives, FA	[216]
	Nanoparticles	Immersion	20	Mouse	Cryosectioning	10 µm	(+)	Cer, MAG, Purines, Sph, ST	[220]
	Nanolayers	Sputtering	2–10	Mouse	Cryosectioning	80 µm	(+)	TAG, ST	[287]
	Nanoclusters	Deposition	2	Mouse	Cryosectioning	100 µm	(+)	CE, Cer, CPA, DAG, FA, GalCer, PA, PC, PE, Peptides, PG, PS, Phosphorylated Metabolites, SM, TG, dopamine derivatives	[218]
	Functionalized Nanoparticles	Deposition	4-6 (f-AuNPs)	Mouse	Cryosectioning	100 µm	(−)	AA, DHA, HA	[217]
	Functionalized Nanorods	Immersion	41.9 × 12.2 (mPEG-AuNRs)	Mouse	Cryosectioning	2.9 µm	(+)	Cer, MAG, Purines, Sph, ST	[217]
	Functionalized Nanoshells	Spraying	100 (SiO_2) 2-3 (Au)	Mouse	Cryosectioning	50 µm	(+)	Cer, PC, PE, PG	[246]
	Functionalized Nanospheres	Spraying	20 (AuNps) 400 (TiO_2)	Mouse	Cryosectioning	200 µm	(+)	AAs, GA, PA, PC, PE	[223]
	Functionalized nanotubes	Immobilization	64,1 (AuNp-hPDA-TDNT)	Mouse	Cryosectioning	50 µm	(+)	PC, PE	[222]
	Functionalized nanolayers	Sputtering	10 (AuBSi)	Mouse	Imprinting[a]	60 µm	(+)	PG, Sulfo-Galβ-Cer	[245]
Silver (Ag)	Nanoparticles	Implantation	6	Mouse	Cryosectioning	50 µm	(+)	Cer, SM	[204]
	Nanoparticles	Implantation	6	Mouse	Cryosectioning	50 µm	(+) (−)	CE, Cer, DAG, PC, ST PE, PI, SM	[228]
	Nanoparticles	Implantation	8	Rat	Cryosectioning	50 µm	(+) (−)	CE, Cer, DAG, GalCer, PC, PE PE, PI, SM, ST	[203]
	Functionalized nanoparticles	Spraying	1-10 (AgNPs) 41.49 ± 14.40 (PVP)	Mouse	Cryosectioning	150 µm	(+)	Cer, CPA, FA, Gal/GluCer, LPE, PA, PC, PE, PE(P), PS, SM, ST	[229]
				Rat	Cryosectioning	200 µm	(+)	Carnitines, Cer, Cholesterol, CPA, FA, Gal/GluCer, LPA, LPC, LPE, PA, PC, PE, PS, PG, SM, Stearaldehyde, ST, Vitamin A	
	Functionalized nanoparticles	Spraying	95 ± 15 (AgNps@PDA) 3–5 (agnps)	Mouse	Cryosectioning	120 µm	(+)	CDP-DG, Cer, CerP, CPA, DG, FA, GA1, HexCer, LPA, LPE, PA, PC, PE, PG, PI, PIP, PS, SM, ST	[230]
						85 µm	(+)	AAs and Derivatives, Carnitines and CoA Derivatives, CDP-DG, CE, Cer, CerP, CPA, DG, FA, GA1, HexCer, MG, PA, PC, PE, PG, PI, PIP, PIP2, PS, Phosphoethanolamine, Phosphoric Acid, SM, ST, Taurine, Glucose	
	Nanolayers	Sputtering	28	Mouse	Cryosectioning	20 µm	(+)	FA, ST	[231]
						100 µm	(+)	ST	
	Nanolayers	Sputtering	20	Mouse	Cryosectioning	100 µm	(+)	FA, ST	[134]
	Nanolayers	Sputtering	23	Mouse	Cryosectioning	100 µm	(+)	GS, ST	[136]
	Nanolayers	Deposition	6	Mouse	Cryosectioning	20 µm	(+)	GalCer, PC	[135]
Niobium (Nb)	Nanoparticles	Sputtering	25	Mouse	Cryosectioning	30 µm	(+)	PS, Sulfatide	[149]
							(−)	GalCer, PC, PE, PG, PS	
Iron(III) oxide (Fe_2O_3)	Nanoparticles	Spraying	3.7 ± 0.1	Rat	Cryosectioning	15 µm	(+)	FA, PE, PI, ST	[171]
	Nanoparticles	Spraying	3.7 ± 0.1	Rat	Cryosectioning	15 µm	(−)	AA, Nucleotides and Nitrogenous Bases, Amines and Polyamines, Organic Acids, Sulfur-containing Compounds, Vitamins and Derivatives	[172]
Titanium oxide (TiO_2)	Nanoparticles	Spraying	<10	Mouse	Cryosectioning	70 µm	(+)	AA and Peptides, Cer, DAG, FA, PC, PE, ST, Creatinine	[166]
	Monolith	Spraying	500–700	Mouse	Cryosectioning	30 µm 100 µm	(+)	Cer, PE	[232]
	Monolith	Immersion	500–700	Rat	Imprinting[a]	100 µm	(+)	CB, Cer, CH, DAG	[168]
	Monolith	Immobilization	5	Mouse	Cryosectioning	200 µm	(+)	AA, PC, PE, PICer, SM,HA, Nitrogenous Compounds and Amines, Polyamines	[233]
	Nanosheets	Spraying	30–60	Mouse	Cryosectioning	50 µm	(+)	AA, Amines and Polyamines, Carbohydrates and Sugar Derivatives, FA, ST, Nucleotides and Nucleosides, Phosphates and Phospholipid Derivatives, Sulfur-Containing Compounds, Organic Acids	[234]

(continued on next page)

Table 2 (*continued*)

Type	Nanostructures			Brain tissue sample		MSI		Classes of compounds	Ref.
	Clasification	Deposition	Size [nm]	Source	Preparation	Spatial resolution	Ion mode		
Zinc oxide (ZnO)	Nanoparticles	Spraying	<100	Mouse	Cryosectioning	40 μm 17 μm 100 μm	(+)	AA, Amines and Neurotransmitters	[179]
				Rat	Cryosectioning	80 μm	(+)	FA	
				Rat	Cryosectioning	70 μm	(−)	Cer	

[a] -tissue imprint on a surface covered with nanoparticles; AA – Amino Acids; CB – Cerebrosides, CAR – Carnitines; CDP-DG – Cytidine Diphosphate Diacylglycerol; CE – Cholesterol Esters; Cer – Ceramides; CerP – Ceramide-1-Phosphates; CPA – Cyclic Phosphatidic Acid; DAG – Diacylglycerols; DHA – Docosahexaenoic Acid; FA – Fatty Acids; GA – Glycolipids; GA1 – Gangliosides (Subtype GM1); GABA – Gamma-Aminobutyric Acid; GalCer – Galactosylceramides; Gal/GluCer – Galactosyl/Glucosylceramides; GM – Gangliosides; GS – Guanosine Sugars; HA – Hydroxy acids.

imprint" that can be analyzed directly. The technique is simple, fast, and avoids the need for complex sample preparation, making it suitable for high-throughput analyses [123,201].

Deposition methods involve the direct application of nanoparticle suspensions onto tissue samples [194]. This includes incubating the sample in a nanoparticle solution or depositing nanoparticles synthesized in situ on a submerged target plate. For example, gold nanoparticles have been synthesized directly onto tissue sections during SALDI-MSI analysis. Although straightforward, deposition techniques face challenges in achieving uniform nanoparticle coverage. Factors such as solvent composition, pH, and drying conditions must be carefully optimized to prevent aggregation or uneven distribution [202].

Implantation is a specialized technique in which nanoparticles are introduced into the tissue sample using advanced instrumentation. For instance, silver nanoparticles can be deposited onto a sample surface via a magnetron sputtering-based "NPlanter" system, which accelerates size-selected nanoparticles onto the target [131]. This dry implantation technique prevents analyte diffusion and provides exceptional spatial resolution.

However, implantation requires highly specialized equipment and is less commonly used than other methods. Its primary advantage lies in the elimination of solvent-related artifacts and the guarantee of a consistent nanoparticle distribution [203–205].

7. Application of metallic nanostructures in mass spectrometry imaging

Metallic nanostructures have brought significant improvements to MSI by expanding its analytical capabilities beyond the constraints of traditional matrix-based approaches. Researchers had harnessed the high ionization efficiencies of gold, silver, titanium dioxide, and other metal-based materials to expand MSI analyses beyond traditional lipids and peptides, successfully probing otherwise intractable molecules such as sterols, pesticides, and exogenous chemicals in various tissue types. This expanded molecular coverage had exposed new facets of pathology, toxicology, and plant physiology, while also highlighting the importance of careful deposition protocols, surface functionalization strategies, and analytical calibration to mitigate issues like ion suppression or fragment-ion misinterpretation. Although metallic nanostructures had advanced MSI sensitivity and spatial resolution, investigations have underscored ongoing challenges related to nanoparticle stability, tissue heterogeneity, and practical scalability for clinical or industrial applications. Consequently, the following sections evaluate these developments across multiple biological contexts including brain tissue, cancer models, animal organs, forensic specimens, plant material, and cultured cells to illustrate the versatility and limitations of metal-enhanced MSI in delineating molecular distributions at unprecedented resolution.

7.1. *Imaging of brain tissues*

The mouse brain is a widely used tissue sample for assessing various MSI techniques because of its complex structure and abundance of diverse metabolites, with lipids being the most prevalent among them. Lipids in the brain are central to membrane stability, cellular signaling, energy metabolism, and cognitive function, and their altered distribution is often linked to neurological diseases [206,207]. Disruptions in the composition or distribution can have severe consequences for the nervous system, including neurodegenerative diseases, tumorigenic processes, and inflammatory responses [208,209]. Consequently, MSI of lipids in brain tissues is increasingly recognized not only for fundamental neurobiological studies but also for exploring new diagnostic and therapeutic strategies [210]. By examining the spatial distribution of various lipid classes, it can gain a deeper understanding of pathological mechanisms at the molecular level, ultimately guiding the development of targeted interventions. Additionally, MSI enables the simultaneous investigation of structural lipids essential for cellular architecture and those implicated in neurotransmission or immunological processes, thereby providing a more holistic view of brain function and pathology [211].

Metallic nanostructures have emerged as powerful tools for MSI of lipids in brain tissues [212]. By offering enhanced ionization efficiency and more uniform sample coverage, nanoparticles such as gold, silver, titanium dioxide, and zinc oxide have enabled researchers to detect both small metabolites and higher-mass lipids with improved spatial resolution [207,213,214]. Table 2 summarizes the applications of metallic nanostructures in mass spectrometry imaging of brain tissues, highlighting their types, preparation methods, and specific target compounds.

Gold nanoparticles (AuNPs), applied via sputtering, significantly improved detection of challenging lipid species such as cerebrosides, glycosphingolipids (GSL), and sulfatides that are poorly visualized with traditional organic acid matrices due to the strong signals from lipids such as phosphatidylcholines (PCs) and sphingomyelins (SMs) [214,215]. Sensitivity improvements of up to 20-fold were observed in negative ion mode using AuNPs compared to the conventional 2,5-dihydroxybenzoic acid (DHB) matrix [214].

Argon ion sputtering of AuNPs improved the spatial resolution of lipid MSI in mouse brain tissue by enabling uniform, solvent-free nanoparticle deposition, which prevented analyte delocalization [216]. Functionalization of AuNPs with fluorinated ligands further enhanced detection of polar and lipophilic analytes by lowering the energy thresholds required for desorption and ionization processes [213]. Surface-modified AuNPs were also successfully combined with complementary imaging modalities, such as micro-computed tomography (μCT) and electron microscopy, enabling the acquisition of multimodal datasets from a single sample [213]. Other adaptations, like mPEG-modified gold nanorods have focused on improving subcellular resolution, down to a few micrometers, although scaling up to larger tissue areas remains problematic [217]. Water-soluble gold nanoclusters

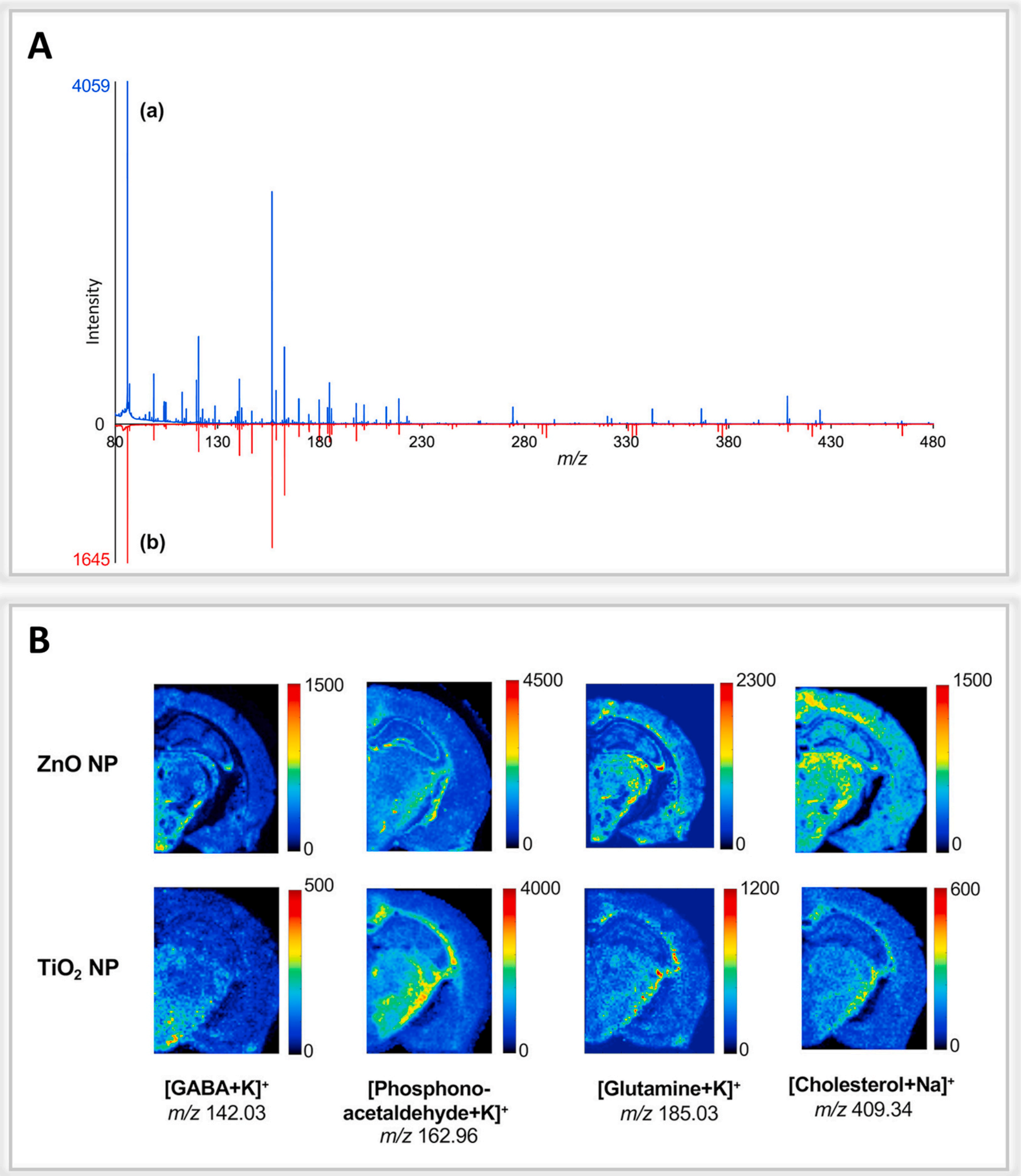

Fig. 2. Comparison of ZnO NP- and TiO_2 NP-assisted LDI-MSI performance in mouse coronal brain hemisphere sections. (A) Ion images obtained with different nanoparticles (raster step size: 70 μm). (B) Averaged mass spectra from all pixels: (a) ZnO NP-assisted and (b) TiO_2 NP-assisted LDI-MSI [179]. Reprinted with permission from the American Chemical Society.

(AuNCs) have been shown to provide more homogeneous deposition and improved signal-to-noise ratios compared to larger gold nanoparticles and traditional organic matrices. Stabilized by ligands such as thiolates, AuNCs enabled enhanced detection of a broader range of metabolites particularly lipids in mouse brain tissue, significantly increasing molecular coverage in MSI [218].

Although AuNP-based techniques offer unique advantages in terms of resolution and the number and types of molecules detected, certain limitations remain. Ion suppression continues to hinder the detection of higher-mass compounds when multiple small molecules and salts accumulate in the same region [219]. Similarly, achieving consistent tissue coverage while avoiding redistribution effects can require sophisticated application strategies, ranging from pneumatic spraying to drop-wise deposition, each carrying trade-offs in terms of throughput and uniformity [197,213]. Adjustments to laser power, type of laser (femtosecond pulsed vs. continuous wave), and the nanoparticle-to-analyte ratio are also necessary to balance efficient desorption with minimal tissue damage [220]. More recent efforts have centered on dual-polarity MSI, enabling complementary detection of different lipid classes within the same sample [221].

Hybrid nanomaterials such as gold-titanium dioxide nanostructures (Au–TiO_2) and silica-gold hybrids (SiO_2@Au) enhanced sensitivity and specificity in MSI of neutral and polar lipids. Optimizing their composition and shell thickness improved ionization efficiency and spatial resolution while reducing background interference [222,223].

Advancements in imprinting techniques have also reduced tissue preparation complexity, allowing for metabolite mapping on plasmonic chips with high photothermal capabilities and strong ion production efficiency [224].

AgNPs are widely used in LDI-MSI due to their strong cationization efficiency, especially for olefinic lipids like cholesterol and fatty acids [225–227]. Achieving uniform AgNP coatings required careful

Table 3

Applications of metallic nanostructures in mass spectrometry imaging of cancer tissues.

Type	Nanostructures			Cancer tissue sample		MSI		Differentiating compounds/ions (fold change)		Ref.
	Clasification	Size	Deposition	Source	Preparation	Spatial resolution	Ion mode	Tumor	Normal	
Gold (Au)	Nanoparticles	<10	Sputtering	Murine colon cancer	Cryosectioning	60 µm	(+) (−)	Taurine, Adenine	[216]	
	Nanoparticles	13	Chemical reduction and deposition prior to imprinting	Human kidney tumor and adjacent normal	Imprinting	150 µm	(+)	DAG(18:1/20:0), Octadecanamide (300–500)	–	[239]
	Nanoparticles	4–6	Deposition	Mouse lung	Cryosectioning	100 µm	(−)	–	PC	[213]
	Functionalized nanoparticles	13 (AuNPs) 235 (GO)	Incubation	Human breast tumor and normal	Cryosectioning	80 µm	(+)	$[Au_1]^+$ (>10)	–	[238]
	Functionalized nanoparticles	60-80 (AuNPs) 40–60 (PC)	Incubation	Human breast tumor and normal	–	150 µm	(+)	$[Au_1]^+$ (>20)	–	[202]
Silver (Ag)	Nanoparticles	100	Chemical reduction and deposition prior to imprinting	Human RCC and adjacent normal	Imprinting	200 µm	(+)	Sulfinpyrazone sulphide, octadecanamide, arachidonic acid, riboflavin, eicosenic acid, adenosyl-L-methionine, N-(2-hydroxypentadecanoyl)-4,8-sphingadienine	Glucose, phenylacetylglycine	[288]
	Nanoparticles	102	Chemical reduction and deposition prior to imprinting	Human RCC and adjacent normal	Imprinting	250 µm	(+)	Arginine (1.1), inosine (1.7), lactate (1.0), thymine (1.3), vitamin E (1.1)	Alanine (0.7), glutamic acid (0.6), guanine (0.7), histidine (0.7), lysine (0.8), methionine (0.6), phenylalanine (0.8), serine (0.7), threonine (0.8), tryptophan (0.8), uridine (0.9)	[241]
	Nanoparticles	102	Spraying	Human bladder cancer and normal	Imprinting	250 µm	(+)	Glycine, 3-methylbutanal, ethylphosphate, glutamine, myosmine, aminopentanal, proline betaine methylguanidine, PI(22:0/0:0)	Hypotaurine	[242]

DAG – Diacylglycerols; PC – Phosphatidylcholine; PI – Phosphatidylinositol.

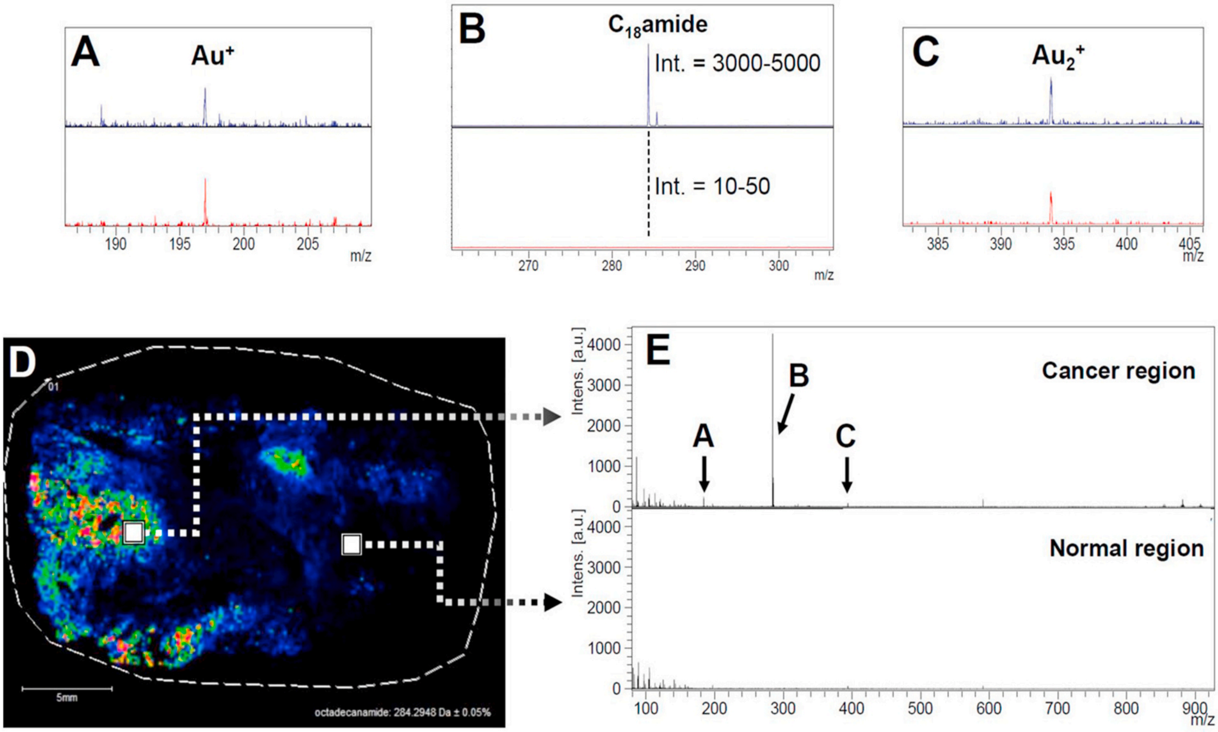

Fig. 3. Ion image of the renal cancer carcinoma (RCC) tissue generated for protonated octadecanamide ion, *m/z* 284.29 (D). Parts A–C and E of the figure present extracted spectra for areas marked with white squares for both cancer (B, upper spectrum) and normal regions (B, lower spectrum) of the sample [239]. Reprinted with permission from the American Chemical Society.

optimization of sputtering parameters or alternative deposition methods to ensure consistent imaging [136]. Later studies highlighted the need to control coating thickness and laser settings, especially for specific brain regions like the cortex, hippocampus, and corpus callosum.

The complex lipid changes in conditions like chronic alcohol exposure or traumatic brain injury pose analytical challenges. AgNP-assisted matrix implanted laser desorption/ionization mass spectrometry imaging (MILDI-MSI) has revealed significant, region-specific alterations in ceramide (CER) and sphingomyelin (SM) levels [204]. Using the NPlanter system for controlled AgNP deposition ensured consistent tissue coverage, helping to overcome sample heterogeneity and improve the accuracy of comparisons between healthy and diseased tissues [228].

Although AgNPs enhance MSI, careful interpretation is required due to the formation of fragment ions like $[DAG–H_2O + Ag]^+$ and $[Cer–H_2O + Ag]^+$, which can misrepresent lipid diversity and distribution, especially in complex tissues like the brain [203]. To improve lipid detection and reduce phosphatidylcholine suppression, researchers modified AgNP surfaces with coatings like polyvinylpyrrolidone (PVP). PVP-capped AgNPs showed superior ionization efficiency and broader lipid class coverage compared to other silver-based matrices, proving especially useful in models of ischemic stroke and brain injury involving diverse metabolic pathways [229]. Polydopamine-coated AgNPs (AgNPs@PDA) enhanced detection of phosphatidylethanolamines and hexosylceramides, while preserving resolution down to 10 μm. In contrast, simpler methods like $AgNO_3$ spraying, though more cost-effective, compromised spatial resolution due to crystal formation and uneven coverage [230,231].

Quantifying cholesterol and sterols in situ using sputtered AgNPs with calibration standards like stigmasterol or cholesterol-D7 improved signal normalization and comparability [134]. In Alzheimer's research, this approach revealed minimal co-localization of cholesterol with amyloid plaques, contrasting with ganglioside distributions and suggesting a limited direct role of cholesterol in plaque formation [135].

TiO_2 nanostructures have shown promise in SALDI-MSI by enhancing small-molecule detection and reducing background noise, though performance varied with particle properties and conditions. Early studies using ~10 nm TiO_2 NPs outperformed conventional matrices due to minimal background signals, though spatial inhomogeneity remained problematic [166]. Functionalization with dopamine (TiO_2-DA) improved surface properties and boosted signal-to-noise ratios, especially for lipids and Lewis basic species, though synthesis complexity limited broader use [232]. The imprint MSI (iMS) approach later improved quantitation by integrating standards on the TiO_2-DA surface to correct for matrix effects [168].

Photocatalytic UV treatment of TiO_2 surfaces has been shown to reduce ion suppression from abundant phospholipids, enhancing detection of less abundant lipids like cerebrosides and ceramides, though it adds procedural complexity and may not be universally applicable [233]. Alternative TiO_2 forms, such as nanosheets, improved desorption and ionization through greater surface area and optimized charge transfer [234]. Comparisons with other metal oxides revealed that ZnO outperformed TiO_2 for some small metabolites, while TiO_2 remained advantageous for certain lipids (Fig. 2) [179]. Other materials like niobium and iron oxide nanoparticles also showed promise, offering stable ion formation, cost efficiency, and high-resolution mapping of specific lipid classes [149,171,172].

7.2. *Imaging of metabolites in cancer tissues*

Tumor heterogeneity encompasses genetic, epigenetic, and phenotypic variability both between patients and within individual tumors, driven by mutations, regulatory changes, and environmental pressures. This results in spatially and temporally distinct subpopulations with diverse metabolic and functional profiles, affecting tumor progression, drug resistance, and treatment outcomes, and complicating diagnosis and personalized therapy [235]. Table 3 summarizes the applications of metallic nanostructures in MSI of cancer tissues, detailing their types,

Table 4
Applications of metallic nanostructures in mass spectrometry imaging of diverse biological tissues.

Nanostructures				Biological tissue sample		MSI		Class compounds	Ref.
Type	Clasification	Size	Deposition	Source	Preparation	Spatial resolution	Ion mode		
Gold (Au)	Nanolayer	28 nm	Sputtering	Mouse liver	Cryosectioning	10 µm	(+)	TAG, PC	[243]
						25 µm	(+)	TAG	
				Rabbit adrenal gland	Cryosectioning	25 µm	(+)	CE, Cholesterol, TAG	
				Midsagittal mouse kidney	Cryosectioning	30 µm	(+)	TAG	
	Nanolayer	10 nm	Immobilization	Mouse kidney	Cryosectioning	100 µm	(+)	FA, PE	[245]
	Nanospheres	10 nm	Spraying	Zebrafish	Cryosectioning	60 µm	(−)	LPE, LPI, PC, PE, PI, PS, SM	[289]
	Nanoflakes	24 nm	Spraying	Zebrafish	Cryosectioning	60 µm	(−)	LPE, LPI, PC, PE, PI, PS, SM	
	Nanowires	0.7 µm	Spraying	Zebrafish	Cryosectioning	60 µm	(−)	LPE, LPI, PC, PE, PI, PS, SM	
	Functionalized Nanoparticles	~20 (AuNPs)	Spraying	Mouse kidney	Cryosectioning	200 µm	(+)	PA, PC, TAG	[223]
		~400 nm ($Au–TiO_2@GA$)		Mouse liver	Cryosectioning	200 µm	(+)	TAG	
	Functionalized Nanoparticles	100 nm (SiO_2) and 2–3 nm (AuNPs)	Spraying	Zebrafish whole body	Cryosectioning	55 µm	(+)	AA, AA derivative, DAG, LPC, PC, TAG.	[246]
				Honeybee whole body	Cryosectioning	30 µm	(+)	Cer, LPC, LPE, LPI, PC, TAG	
	Functionalized Nanoparticles	10 nm (AuNPs)	Spraying	Zebrafish whole body	Cryosectioning	100 µm	(−)	fipronil and its metabolites	[247]
	Functionalized Nanolayers	2–4 nm	Deposition	Mouse colon	Cryosectioning	30 µm.	(+)	AA derivatives, Carbohydrate and derivative, inorganic acid, organic acid, PE, Sterol	[244]
Silver (Ag)	Nanoparticles	3.84 nm	Spraying	Mouse liver	Cryosectioning	100 µm	(−)	FA	[130]
				Mouse retinal	Cryosectioning	10 µm	(−)	FA	
	Nanoparticles	0,5–15 nm	Implantation	Rat heart	Cryosectioning	50 µm	(+)	PC, PE, SM, TAG	[131]
							(−)	CL, PE, PI, PG	
	Nanoparticles	0,5–15 nm	Implantation	Rat kidney	Cryosectioning	50 µm	(+)	Cer, cholesterol, DAG, TAG	[205]
							(−)	PE, PG, PI, SM, ST	
	Nanolayer	1.4 nm	Sputtering	Fore-stomach	Imprinting	60 µm	(+)	6-bromoisatin, and its metabolite	[251]
	Nanolayers	16 nm	Sputtering	Mouse kidney	Cryosectioning	150 µm	(+)	FA, TAG	[136]
	Nanolayer	40 nm	Sputtering	Mouse heart aortic sinuses	Cryosectioning	30 µm	(+)	Cholesterol, CE	[248]
				Human carotid atherosclerotic plaque	Cryosectioning	100 µm	(+)	FA, LPC, PC, Steroids, TAG	
	Nanolayer	6 nm	Deposition	Human heart	Cryosectioning	20 µm	(+)	Cholesterol	[103, 135]
Iron oxide (Fe_2O_3)	Nanoparticles	19–161 nm	Spraying	Zebrafish	Cryosectioning	100 µm	(+)	AA, PC, phosphorylated carboxylic acid, TAG, Vitamin D3 metabolite	[103]
Cobalt (Co)	Nanolayer	2 nm ($Co–N–Ti_3C_2$)	Deposition	Human synovial membrane sections)	Cryosectioning	100 µm	(+)	AA, aldehyde, amino acids, antioxidant, FA, LPC, nucleobase, nucleotide, organic acids, PC, PE, peptide, PI, PS, TAG	[154]

AA – Amino Acids; CE – Cholesteryl Esters; DAG – Diacylglycerols; FA – Fatty Acids; LPC – Lysophosphatidylcholine; LPE – Lysophosphatidylethanolamine; PA – Phosphatidic Acid; PC – Phosphatidylcholine; PE – Phosphatidylethanolamine; PG – Phosphatidylglycerol; PI – Phosphatidylinositol; PS – Phosphatidylserine; SM – Sphingomyelins; TAG – Triacylglycerols.

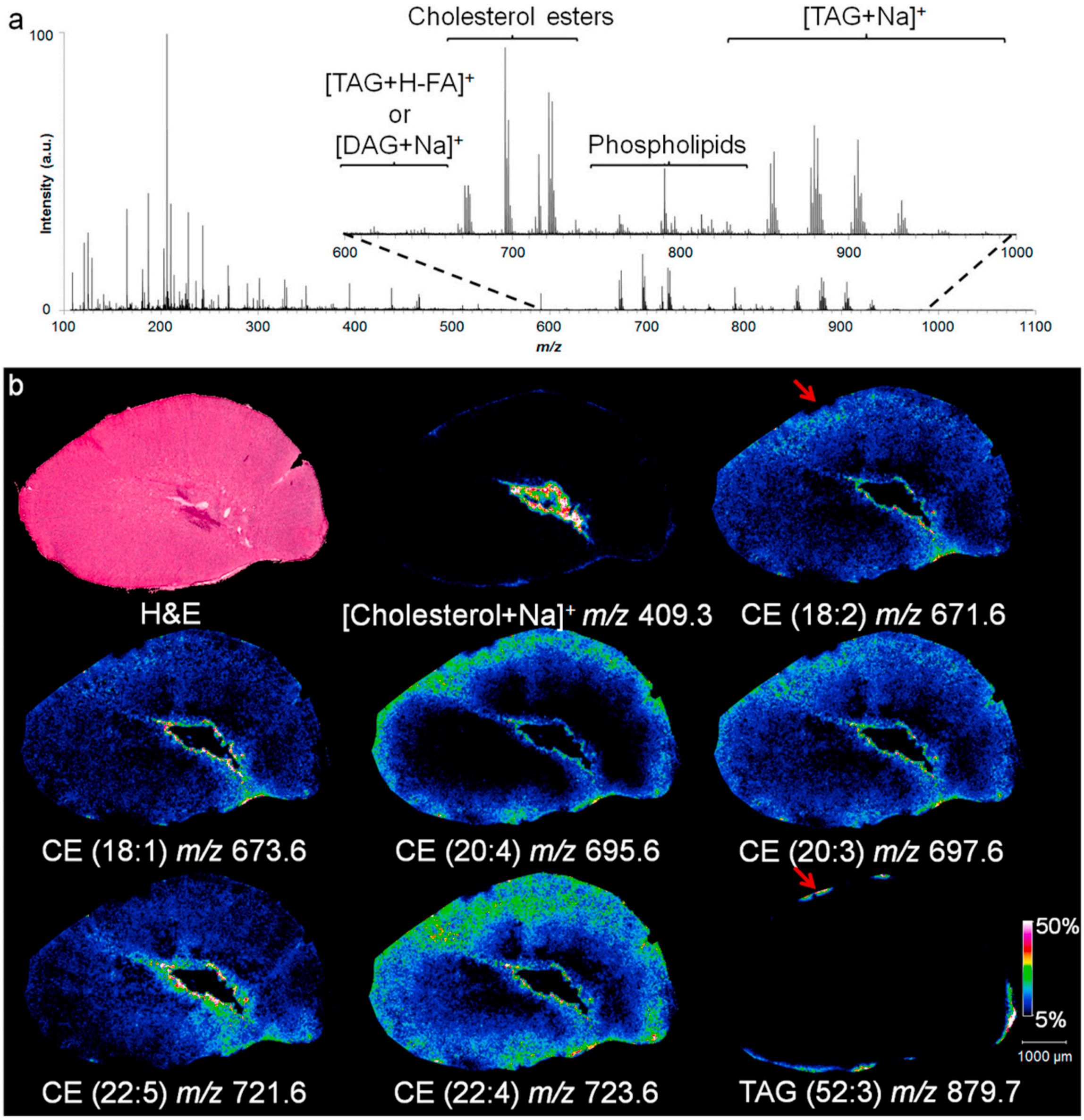

Fig. 4. CBS-Au-LDI (a) MS spectrum and (b) IMS with a lateral resolution of 25 µm, acquired from a rabbit AD tissue section. Based on exactmass and on-tissue MS/MS along with several different CE (*m/z* 671.5, 673.5,695.5, 697.5, 721.5, and 723.5) and TAGs (*m/z* 879.7) where found to be the dominant signals within the adrenal gland. H&E of the next serialsection is provided in the top left corner. The red arrow highlights one of the ion suppression sites of CEs by TAGs [243]. Reprinted with permission from the American Chemical Society. (For interpretation of the references to color in this figure legend, the reader is referred to the Web version of this article.)

Table 5
Applications of metallic nanostructures in mass spectrometry imaging of drugs distribution.

Nanostructures				Imaged tissue sample		MSI		Drugs	Ref.
Type	Classification	Size	Deposition	Source	Preparation	Spatial resolution	Ion mode		
Gold (Au)	Nanoparticles	20	Airbrush spraying	Human malignant pleural mesothelioma tumor tissue	Cryosectioning	100 µm	(+)	paclitaxel, ortataxel, imatinib, lucitanib, doxorubicin, trabectedin	[250]
Silver (Ag)	Nanolayer	1.4	Sputtering	Mouse stomach tissue	Cryosectioning	60 µm	(+) (−)	prostaglandin, cholesterol, oleic acid, stearic acid, 6,6′-DBI, phosphatidylcholine head group	[251]
Titanium oxide (TiO_2)	Nanoparticles	25	Spraying	Mouse liver tissue Ovarian tumors	Cryosectioning Cryosectioning	75 µm 75 µm	(+) (−)	paclitaxel (PTX) paclitaxel (PTX)	[165]

Table 6
Applications of metallic nanostructures in mass spectrometry imaging in forensic medicine/analysis.

Type	Nanostructures			Imaged sample		MSI		Classes of compounds	Ref.
	Classification	Size	Deposition	Source	Preparation	Spatial resolution	Ion mode		
Gold (Au)	Nanoparticles	40	sputtering	Banknotes and checks	Raw sample	140 μm	(+)	Printing and pen ink compounds	[254]
	Nanoparticles	<100	Immobilization	Fingerprint	Imprinting	90 μm	(+)	CerP, Illicit drugs	[120]
	Nanoparticles	<100	Immobilization	fingerprint	Imprinting	50 μm	(+)	AA and derivatives, CerP, FA, Inorganic salts, MG, organic acids, Nitrogen-containing compounds, PC, Phenolic and aromatic compounds, Sterols, TAG,	
	Functionalized nanoparticles	10 (AuBSi)	Sputtering	Fingerprint	Imprinting	80 μm	(+)	FA, PE	[245]
	Functionalized nanoparticles	2.5 (f-AuNPs)	Inkjet printing	Printed ink on paper	Raw sample	50 μm	(+)	Printing dyes	[290]
	Functionalized nanoparticles	64,1 (AuNp-hPDA-TDNT)	Immobilization	Fingerprint	Imprinting	45 μm	(+)	Cotinine, nicotine, FA, TAG, WE	[222]
Silver (Ag)	Nanoparticles	30 ± 5	Chemical reduction and deposition prior to imprinting	Fingerprint	Imprinting	150 μm	(+)	Pharmaceutical compounds, surfactants	[195]
	Nanoparticles	30	Spraying	Fingerprint	Imprinting	40 μm	(+)	AA and derivatives, FA and derivatives, carboxylic acids and derivatives, carboxyhydrates, inorganic salt, piperazine derivative, urea	[63]
	Nanoparticles	700-1000; 1700	Soft-landing ion mobility	Fingerprint	Imprinting	100 μm	(+)	DAG, FA, TAG	[139]
	Nanolayer	0.4, 0.7, 1.7, 3.2	Sputtering	Fingerprint	Imprinting	60 μm	(+)	Cholesterol, FA, TAG, Surfactants, WE	[138]
	Nanolayer	14 ± 2	sputtering	Fingerprint	Imprinting	75 μm	(+)	Cholesterol, FA, TAG, Surfactants, WE	[255]
	Nanolayer	14 ± 2	sputtering	Fingerprint	Imprinting	75 μm	(+)	DAG, FA, Surfactants, TAG	[256]
	Nanolayer	15	Sputtering	Fingerprint	Imprinting	60 μm	(+)	FA, Illicit drug, TAG, WE	[137]
	Nanolayer	1.4	Sputtering	Fingerprint	Imprinting	60 μm	(+)	Cholesterol, FA, TAG, surfactants, WE	[251]
	Nanolayer	14	Sputtering	Fingerprint	Imprinting	75 μm	(+)	FA, Illicit drugs	[257]
Platinum (Pt)	Nanolayer	20	Sputtering	Printed ink on paper	Raw sample	100 μm	(+)	Ink components, paper components and the degradation products of inkjet ink components	[141]
	Nanolayer	20	Sputtering	TLC silica plate	Raw sample	100 μm	(+)	Sacharides	
Titanium oxide (TiO_2)	Nanoparticles	2 μm	Deposition	Fingerprint	Imprinting	50 μm	(+)	CE. DAG, TAG	[258]

CE – Cholesteryl Ester; CerP – Ceramide-1-Phosphates; DAG – Diacylglycerols; FA – Fatty Acids; FA – Fatty Acids; PE – Phosphatidylethanolamine; WE - wax ester.

deposition methods, and class compounds detected in tumor and normal tissues.

Conventional methods such as immunohistochemistry (IHC) and fluorescence in situ hybridization (FISH) are limited by low multiplexing and reliance on antibody labeling, making them less effective for capturing metabolic diversity. In contrast, MSI provides label-free, spatially resolved detection of thousands of biomolecules per pixel while preserving tissue architecture [236]. It is increasingly applied in oncology to study treatment response, monitor drug efficacy, and stratify tumors. Its capacity to distinguish malignant from healthy regions supports early diagnosis and personalized therapeutic strategies [237].

Early MSI studies with nanostructures highlighted the need to preserve tissue morphology while capturing metabolic profiles. AuNP-based methods distinguished necrotic from non-necrotic tumor areas by detecting small-molecule differences [216]. Later, aptamer-functionalized AuNPs improved tumor targeting by binding specific surface proteins, yielding stronger signals in malignant tissues, though challenges remained with synthesis complexity, spatial resolution, and protein specificity [202,238].

Studies have shown that metallic nanoparticles can aid in identifying metastatic regions and distinguishing healthy from cancerous tissue with minimal preparation. Fluorinated AuNPs delivered to mouse lungs avoided metastatic sites, as confirmed by MSI and μCT [213]. Employing stainless steel plates modified with AuNPs for tissue imprinting had further simplified sample handling, allowing direct comparison of malignant and non-malignant kidney tissue areas (Fig. 3) [239].

A similar imprinting strategy with AgNPs revealed distinct tumor metabolic profiles in kidney carcinoma [240]. Advancements with monoisotopic silver-109 (^{109}AgNPs) improved sensitivity and eliminated isotopic overlap, allowing precise detection of metabolites like amino acids and nucleobases [241]. This approach successfully differentiated healthy and tumor tissues in both kidney and bladder, demonstrating its diagnostic potential and ability to capture tumor heterogeneity with minimal sample disruption [242].

7.3. *Imaging of metabolites in diverse biological tissues*

MSI enables high-resolution spatial analysis of metabolites in biological tissues, combining molecular and histological information. This technique has been instrumental in studying disease mechanisms, assessing drug efficacy, and characterizing physiological processes in

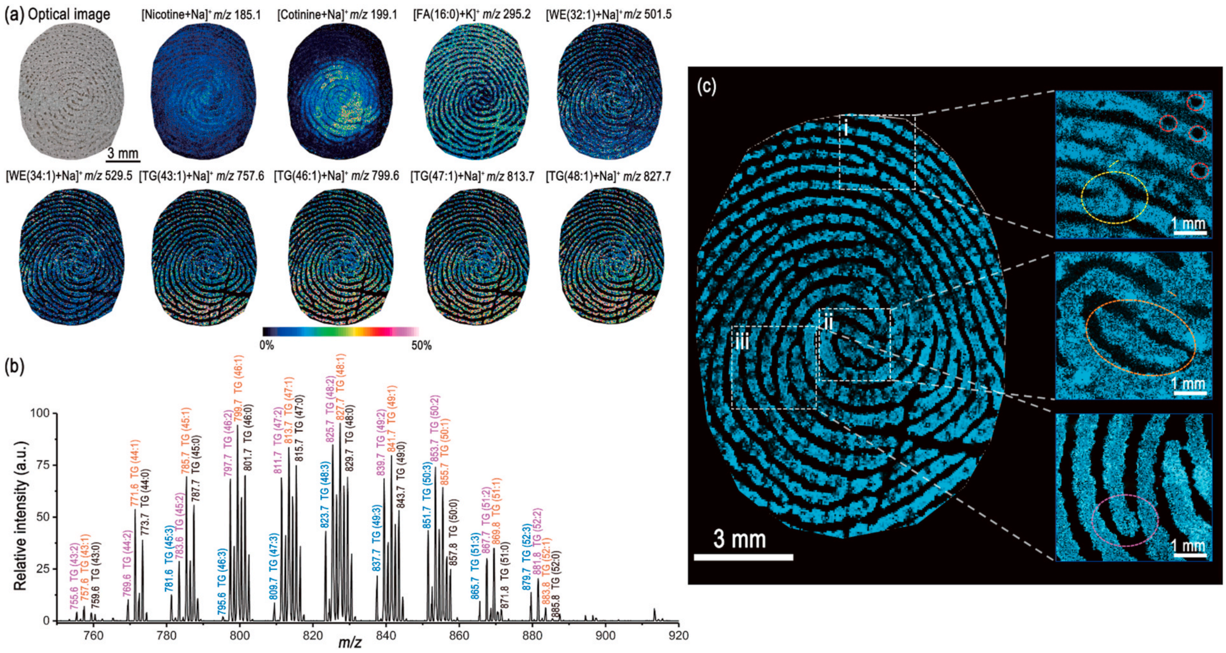

Fig. 5. Visualization of natural skin secretions and exogenous contaminants for LFP imaging acquired using the AuNP-hPDA-TDNT substrate. (a) An optical image of LFP on the AuNP-hPDA-TDNT substrate and representative ion images of nicotine, cotinine, FA(16:0), WE(32:1), WE(34:1), TG(43:1), TG(46:1), TG(47:1), and TG (48:1) with a pixel size of 45 μm. White lines indicate the imaging region, and colored bars indicate the relative signal intensity. Scale bar: 3 mm. (b) Typical SALDI mass spectrum of the TG species for LFP acquired using the AuNP-hPDA-TDNT substrate. The saturated TGs are shown in black, and unsaturated TGs with varying degrees of unsaturation ranging from 1 to 3 are shown in brown, purple, and blue, respectively. (c) The magnified images display the high-resolution fingermark details with a pixel size of 10 μm, including (i) pores and a bifurcation, (ii) an island, and (iii) a termination, as indicated by the white rectangles in the full image [222]. Reprinted with permission from Springer Nature. (For interpretation of the references to color in this figure legend, the reader is referred to the Web version of this article.)

various organs. Advances in sample preparation, instrumentation, and data processing including the use of metallic nanostructures has improved ionization efficiency, sensitivity, and selectivity, enabling precise mapping of diverse compound classes such as lipids, amino acids, and signaling molecules.

As a result, MSI now facilitates detailed profiling of lipids, amino acids, and signaling molecules directly from tissue sections. Table 4 provides an overview of the uses of metallic nanostructures in mass spectrometry imaging applied to diverse biological tissues.

Gold-based MSI approaches have been refined to enhance sensitivity and spatial resolution. Strategies such as sodium salt deposition beneath sputtered gold increased triacylglycerol signal intensity (Fig. 4), [243], while perfluorinated AuNPs expanded metabolite coverage in colon tissue [244]. In kidney imaging, gold-coated black silicon enabled rapid sample prep and clear lipid localization [245].

Other gold nanocomposites, like SiO_2@Au and hexagonal boron nitride (BN) nanosheets doped with AuNPs (Au@BN), improved small-molecule imaging and xenobiotic detection, though some required precise fabrication to maintain performance [246,247].

Silver nanoparticle-based MSI has proven effective for detailed lipid profiling in tissues such as liver, retina, heart, and kidney, enabling detection of low-abundance lipids and spatial mapping of functional regions. Laser-induced fragmentation allowed detection of long-chain fatty acids like DHA in retina revealing tissue-layer specificity and functional compartmentalization in the retina [130], while silver implantation enhanced triacylglycerol ionization in heart tissue [131]. In the kidney, AgNPs mapped cholesterol, ceramides, and sulfatides in different renal compartments [205]. 3D imaging of atherosclerotic plaques identified lysophosphatidylcholines and cholesteryl esters as biomarkers of progression [248]. Iron oxide nanoparticles supported whole-organism imaging while maintaining lower background noise compared to traditional MALDI matrices [103] while cobalt-anchored MXene enabled metabolic profiling in arthritic tissues [154]. Additionally, thermal evaporation of 6 nm silver layers allowed high-resolution cholesterol imaging in cardiac amyloid tissue [135].

7.4. Nanostructures in mass spectrometry imaging of drugs distribution

Metal-based nanostructures have enabled label-free, spatially resolved detection of administered drugs and their metabolites, overcoming the limitations of homogenization-based methods. This approach offers particular value in oncology, where heterogeneous drug distribution affects therapeutic outcomes, and also enhances the detection of poorly soluble compounds that are difficult to recover using traditional extraction techniques [249]. Table 5 outlines the applications of metallic nanostructures in mass spectrometry imaging for drug distribution.

Studies using TiO_2 nanoparticles showed that drug distribution, such as paclitaxel (PTX), varies with dosing regimen and tumor type, though normal tissues exhibited more uniform accumulation [165].

Comparisons of nanomaterials for drug imaging— including AuNPs, titanium, halloysite, and carbon nanotubes—revealed that while AuNPs enhanced signal intensity for standards, their effectiveness in visualizing drugs in tissue remained limited under clinical conditions [250]. Sputtered silver on DIOS substrates further demonstrated low uptake of specific compounds and allowed simultaneous lipid detection [251].

7.5. Imaging in forensics

Metal-based nanostructures had offered a solvent-free strategy for detecting and visualizing characteristic inks, latent fingerprints, and various trace substances on documents or surfaces of forensic interest [252]. This approach had bypassed the destructive aspects of conventional solvent-based extractions and had exhibited substantial potential for unmasking subtle chemical details relevant to forgery and suspect identification. Gold nanoparticle coatings enhanced the detection of

Table 7
Applications of metallic nanostructures in mass spectrometry imaging of plant tissues.

Type	Nanostructures			Plant tissue sample			MSI		Classes of compounds	Ref.
	Clasification	Size	Deposition	Source	Part	Preparation	Spatial resolution	Ion mode		
Gold (Au)	Nanoparticles	10–100	Chemical reduction and deposition prior to imprinting	Onion	Bulb	Imprinting	200 µm	(+)	AA, organic acids, lipids, secondary plant metabolites	[123]
	Nanoparticles	10–100	Chemical reduction and deposition prior to imprinting	Rhubarb	Stalk	Imprinting	40 µm	(+)	AA, organic acids, secondary plant metabolites	[201]
	Nanoparticles	10–100	Chemical reduction and deposition prior to imprinting	Garlic	Clove	Imprinting	100 µm	(+)	AA, dipeptides, FA, organic sulfur compounds, selenoamino acids, sugar phosphates, selenium organic acids	[263]
	Nanoparticles	10–100	Chemical reduction and deposition prior to imprinting	*Taxus baccata*	Twig	Imprinting	40 µm	(+)	AA, alkaloids, diterpenoids, FA, phenolic acids, photosynthetic pigments, polyols	[264]
	Nanoparticles	7–10	Spraying	*Lepidium meyenii*	Root	Cryosectioning	100 µm	(+)	AA, nitriles, amides, pyrrole derivatives, alkaloids, imidazolium compounds	[265]
	Nanoparticles	27	Immersion	Apple	Fruit	Imprinting	120 µm	(+)	Anthranilic diamides, strobilurin fungicides	[193]
				Pepper	Fruit	Imprinting	120 µm	(+)		
				Cucumber	Fruit	Imprinting	120 µm	(+)		
				Plum	Fruit	Imprinting	120 µm	(+)		
				Strawberry	Fruit	Imprinting	120 µm	(+)		
				Carrot	Root	Imprinting	120 µm	(+)		
	Nanoparticles	26	Spraying	*Derris elliptica*	Root	Cryosectioning	60 µm	(+)	Phenolic acids, isoflavones, rotenoids	[266]
	Functionalized Nanolayers	5 (AgNPs)	Immersion in NP solution	*Catharanthus roseus*	Flower	Imprinting	250 µm	(+) (−)	Indole alkaloids Flavonoids	[267]
	Functionalized Nanoshells	100 (SiO_2) and 2–3 (AuNPs)	Spraying	Strawberry	Fruit	Cryosectioning	100 µm	(+)	Nucleobases, amino acids, alkaloids, monosaccharides, terpenoids, disaccharides, proanthocyanidins	[246]
	Functionalized Nanowires	4 (AuNPs)	Immobilization	*Mentha spicata*	Leaf	Imprinting	200 µm	(+)	Diterpenoids, disaccharides, phenolic acids, flavones, flavonoid glycosides	[268]
				Potato	Tuber	Cryosectioning	100 µm	(+)	Steroidal glycoalkaloids	
	Functionalized Nanoparticles	10 (AuNPs)	Spraying	Strawberry	Fruit	Cryosectioning	100 µm	(−)	Phenylpyrazole insecticides and their metabolites.	[247]
	Functionalized nanotubes	66 (TiO_2NTs)	Immobilization	*Catharanthus roseus*	Petal	Imprinting	120 µm	(+)	AA, monosaccharides, coumarins, flavonoids, indole alkaloids, alkaloid iminium ions.	[224]
				Catharanthus roseus	Leaf	Imprinting	120 µm	(+)	AA, monosaccharides, coumarins, flavonoids, indole alkaloids, alkaloid iminium ions, flavonoid glycosides.	
				Strawberry	Fruit	Imprinting	125 µm	(+)	Nucleobases, amino acids, vitamins, phenolic acids, monosaccharides, pentoses, disaccharides, flavonoids, polysaccharides.	
				Ginkgo	Leaf	Imprinting	20, 40, 80, 160 µm	(+)	AA, monosaccharides, flavones, disaccharides, terpene lactones, biflavonoids	
	Functionalized nanotubes	66 (TiO_2NTs)	Immobilization	Strawberry	Fruit	Imprinting	125 µm	(+)	AA, vitamins, monosaccharides, pentoses, phenolic compounds, anthocyanidins, flavones, disaccharides, flavonoid glycosides, triterpenoids, proanthocyanidins	[222]
				Jatropha integerrima	Petal	Imprinting	120 µm	(+)	Nucleobases, terpenoids, coumarins, amino acids, jasmonates, chalcones, flavones, flavonols, disaccharides, flavonoid glycosides, proanthocyanidins, indole alkaloids.	
				Ginkgo	Leaf	Imprinting	120 µm	(+)	AA, monosaccharides, disaccharides, terpene lactones, flavonoid glycosides, biflavonoids	
	Functionalized nanotubes	66 (TiO_2NTs)	Immobilization	*Citrus japonica Thunb.*	Leaf	Imprinting	ND	(+)	Phenylpropanoids, amino acids, coumarins, furanocoumarins, phenolic acids, flavonoids, phthalates, alkaloids, triterpenoids, organic acids, glycosides.	[291]

(*continued on next page*)

Table 7 (*continued*)

Type	Nanostructures			Plant tissue sample			MSI		Classes of compounds	Ref.
	Clasification	Size	Deposition	Source	Part	Preparation	Spatial resolution	Ion mode		
	Functionalized Nanospheres	20 (AuNPs) and 400 (TiO_2)	Spraying	*Gastrodia elata*	Blume	Cryosectioning	100 µm	(+)	Polysaccharides, disaccharides, polyacylglycerophosphates, phosphatidylethanolamines.	[223]
				Potato	Tuber	Cryosectioning	100 µm	(+)	AA, phenolic acids, phosphatidylethanolamines, steroidal glycoalkaloids.	
Silver (Ag)	Nanoparticles	102 ± 3	Immobilization	*Crepis mollis*	Flower	Imprinting	200 µm	(+)	Gibberellins, aldehydes, organic acids, lignans, prostaglandin derivatives, salicinoids, sesquiterpene lactones.	[195]
				Mentha piperita	Stem	Imprinting	50 µm	(+)	Inorganic salts, organohalides, phenoxy herbicides, quinones, sulfur- organic, glutathione conjugates.	
	Nanoparticles	102 ± 3	Chemical reduction and deposition prior to imprinting	Strawberry	Fruit	Imprinting	100 µm	(+)	Aldehydes, ketones, organic acids, alcohols, amino acids, aromatic compounds, esters, vitamins, sugars, phenolic acids, flavonoids, tannins, glycosides.	[192]
	Functionalized Nanospheres	17.6 µm (AgNWs@Mxene)	Immobilization	*Panax ginseng*	Root	Imprinting	200 µm	(+)	Amines, amino acids, organic acids, disaccharides, monosaccharides	[262]
				Panax quinquefolium	root	Imprinting	200 µm	(+)	Choline, oxalic acid, and glycolic acid	
				Scutellaria baicalensis	Root	Imprinting	200 µm	(+)	AA, carbohydrates, flavonoid derivatives, flavones, methoxylated flavonoids.	
				Zingiber officinale	Root	Imprinting	200 µm	(+)	Amines, phenolic ketones, phenolic alcohols, acetates, terpenoids, curcuminoids, lactones.	
				Lonicera japonica Thunb.	Fower	Imprinting	200 µm	(+)	AA, carbohydrates, hydroxycinnamic acids, flavonoids, organic acids	
Platinum (Pt)	Nanolayers	10	Sputtering	*Viola x wittrockiana*	Leaf	Raw sample	150 µm	(+)	Organophosphates, neonicotinoids.	[111]
	Nanoparticles	NA	Sputtering	Wheat	Seed	Cryosectioning	100 µm	(+)	TAG	[269]
	Nanoparticles	NA	Sputtering	Maize	Seed	Cryosectioning	150 µm	(+)	TAG	
	Nanolayers	50	Immobilization	Strawberry	Fruit	Imprinting	200 µm	(+)(−)	Monosaccharides, organic acids, disaccharides	[148]
Iron(III) oxide (Fe_2O_3)	Nanoparticles	10	Spraying	Maize	Seed	Cryosectioning	75 µm	(+)	Glycerophosphocholines, triacylglycerols, glycerophosphoethanolamines, glycerophosphoinositols, digalactosyldiacylglycerols	[173]
	Nanoparticles	3–5	Airbrush spraying	Rice	Root	Cryosectioning	15 µm	(+)	Plant hormones	[270]
	nanoparticles	11	Spraying	Maize	Seed	Cryosectioning	100 µm	(+)	AA, oligosaccharides, TAG	[181]
Titanium oxide (TiO_2)	Nanowires	ND	Immobilization	*Catharanthus roseus*	Flower	Imprinting	250 µm	(+)	Indole alkaloids	[194]
	nanosheets	ND	Deposition	*P. multiflorum*	Root	Cryosectioning	200 µm	(−)	Anthraquinones, stilbenes, naphthoquinones, phenolic acids, carbohydrates.	[169]
Zinc oxide (ZnO)	Functionalized Nanoshells	70	Deposition	*Solanum lycopersicum*	Leaf	Cryosectioning	250 µm		Metalloids (silicon), transition metals (zinc).	[180]
Tungsten oxide (WO_3)	nanoparticles	23–65	Spraying	Maize	Seed	Cryosectioning	100 µm	(+)	AA, oligosaccharides, TAG	[181]

AA – Amino Acids; FA – Fatty Acids; FA – Fatty Acids; ND – no data; TAG – Triacylglycerols.

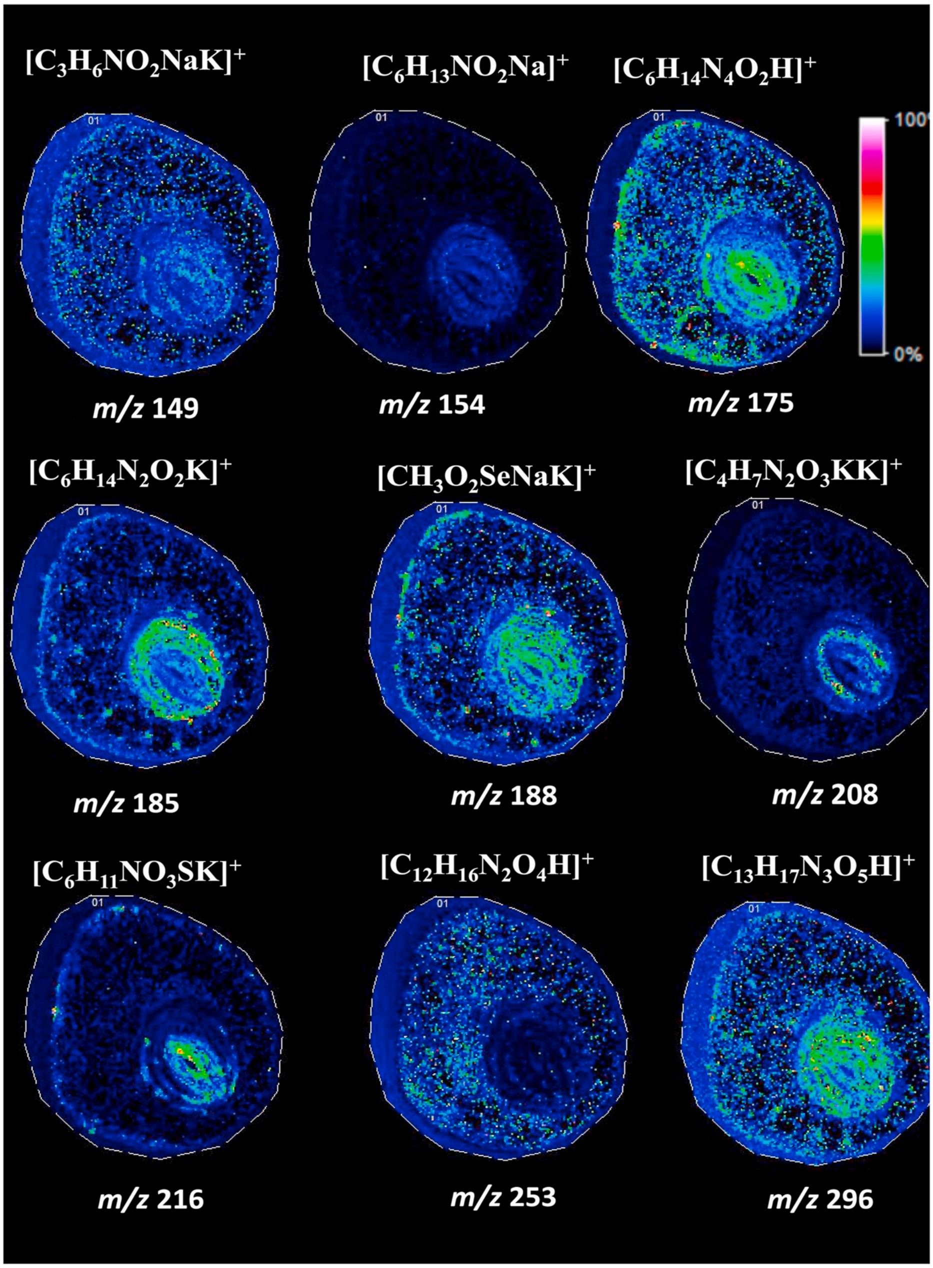

Fig. 6. Ion images of the garlic clove with nominal *m/z* values (bottom). Spatial resolution, 100 μm × 100 μm [263]. Reprinted with permission from Willey.

characteristic ink ions, facilitating the identification of counterfeit alterations. However, their application to worn documents was limited by signal deterioration and optical dulling effects [253]. Additional anticounterfeit strategies had exploited ligand-functionalized AuNPs, generating unique mass spectral signatures upon laser desorption/ionization, although environmental exposure could degrade these ligands and undermine the specificity of printed patterns [254]. Applications of metallic nanostructures in mass spectrometry imaging in forensic science are summarized in Table 6.

Conventional methods for latent fingerprint detection often fail to capture the full chemical complexity of endogenous and exogenous components. Nanoparticle-assisted MSI overcomes these limitations by enabling high-resolution visualization of ridge details and sweat pores, while detecting a broad spectrum of biomolecules including fatty acids, diglycerides, and drugs [120]. Platforms based on sputtered AuNPs on black silicon or glass slides improved sample handling and revealed spatially distinct distributions of hydrophilic and lipophilic compounds [245]. Similar success was achieved with ^{109}AgNPs, which enabled high-resolution fingerprint imaging and detection of pharmaceuticals via distinct adduct signals [63,195]. Advanced SALDI-MS substrates, such as composites of TiO_2 nanotubes with gold and polydopamine (AuNP-hPDA-TDNT), maintained ridge resolution while minimizing matrix effects, allowing detailed imaging of endogenous and exogenous molecules (Fig. 5) [222].

For aged or enhanced prints, stability and uniformity of metallic nanocoatings became crucial. Sputtered Ag layers provided adequate ionization for lipids and drugs across various substrates, though issues like uneven layer thickness and substrate conductivity persisted [255, 256]. Standard chromogenic or fluorescent methods (e.g., ninhydrin, Oil Red O) could interfere with MSI unless mitigated by tailored nanostructures [257].

Alternative deposition methods, including soft-landing of large AgNPs (700–1700 nm), preserved fine ridge details and allowed detection of low-abundance lipids and contaminants, enhancing evidentiary

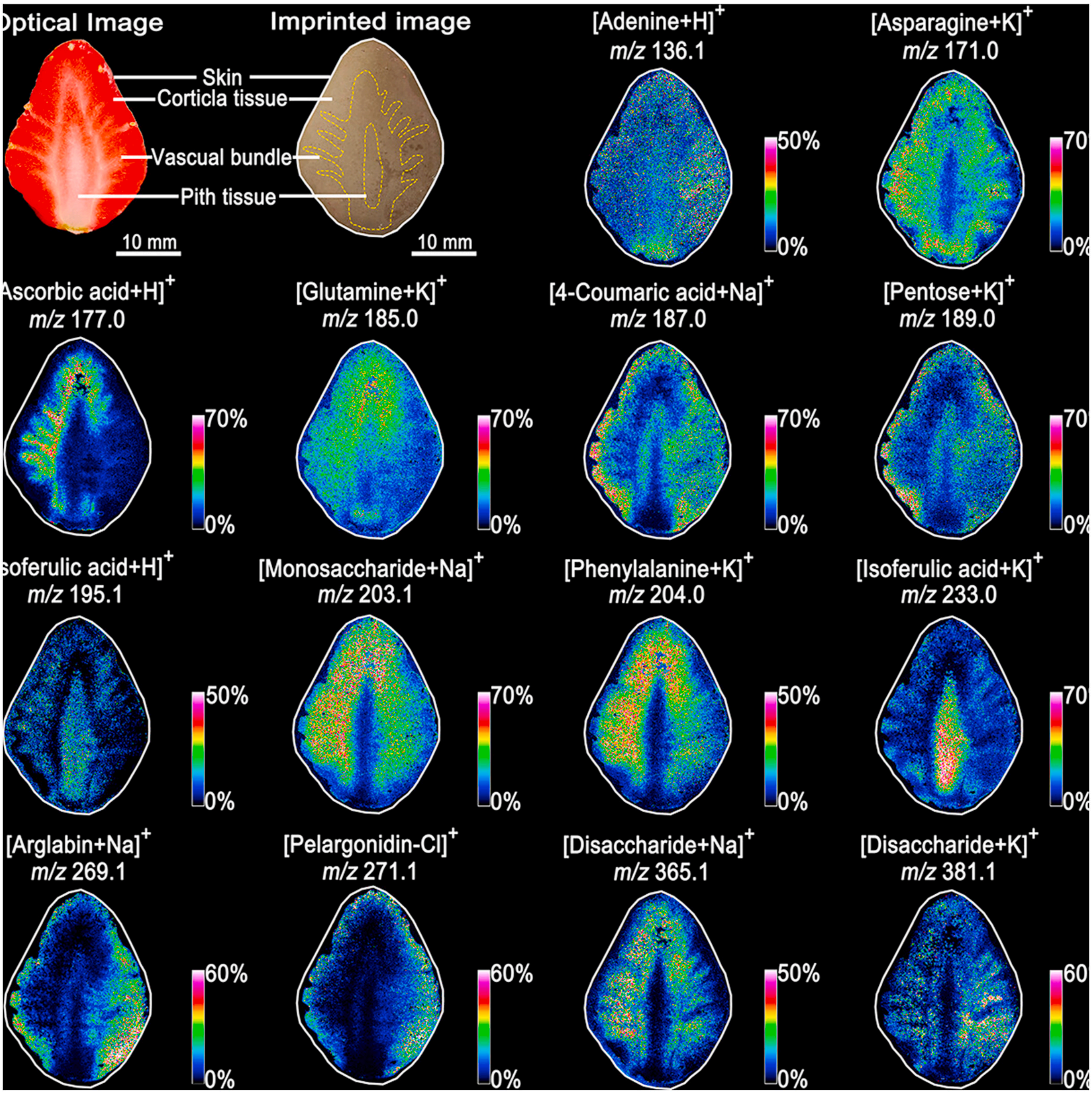

Fig. 7. Spatial distribution of various small-molecule metabolites resulting from a stamped strawberry fruit. An optical image of a strawberry and the corresponding stamped image onto the surface of the AuNP-hPDA-TDNT substrate and the representative ion images of a strawberry using SALDI-MSI with a pixel size of 125 μm. The colored bars indicate the relative intensity of the signal. Scale bar, 10 mm. Reprinted with permission from Ref. [224].

value [139]. However, excessive silver layers could suppress signals of pre-ionized or dissociated compounds and cause matrix effects for heavier lipids. A ~15 nm silver coating enabled fingerprint imaging across diverse surfaces with ~60 μm resolution, capturing both endogenous ions (e.g., potassium) and drug traces [137].

TiO_2 nanoparticles also proved effective for latent print analysis. Electrospray-deposited 2 μm TiO_2 enabled clear ridge patterns and chemical profiling up to 10 days post-deposition, outperforming DHB in lipid sensitivity [258]. Larger 15 μm TiO_2 particles further enhanced detection of fatty acids and cholesterol in positive mode, while negative ion analysis required silver supplementation [259].

7.6. Imaging of plant tissues

Metallic nanoparticles had shown considerable promise in resolving the analytical challenges associated with plant tissue imaging, particularly by improving sensitivity when probing a broad array of organic and inorganic molecules in complex plant matrices [260]. Their efficacy in capturing spatial distributions of both exogenous contaminants (e.g., herbicides) and bioactive metabolites underscored the potential of matrix-free MSI for elucidating physiological mechanisms and guiding the isolation of valuable plant-derived compounds. Nonetheless, the inherent abundance of simple ions in plant sap had complicated MSI analyses, frequently leading to detector saturation or diminished analyte signal intensity, thus necessitating strategies that mitigate competitive ionization events [261]. The applications of metallic nanostructures in the mass spectrometry imaging of plant tissues are summarized in Table 7.

Monoisotopic ^{109}AgNPs enabled sensitive detection of herbicides and metabolites in plant tissues, revealing spatial localization in Mentha piperita [195] and broad metabolite coverage in strawberry fruits [192]. In parallel, AgNWs combined with MXene nanosheets provided a conductive substrate for LDI-MSI of roots and flowers, detecting flavonoids and glycosides even in pathogen-infected ginseng, and outperforming conventional MALDI-MSI in saline matrices [262].

AuNPs have proven effective as a matrix for LDI-MSI of plant tissues, enabling sensitive detection of hormones, flavonoids, and sulfur-containing metabolites. Studies visualized gibberellins and quercetin derivatives in onion peels [123], anthraquinones in rhubarb [201] and organosulfur compounds in garlic (Fig. 6) [263] all without extensive sample preparation. In European yew, gold-assisted MSI localized taxanes and anticancer alkaloids, highlighting its value in analyzing pharmacologically important plants [264].

Gold nanoparticle suspensions and nanocomposites have expanded classical MSI applications in plant analysis. Studies on *Lepidium meyenii* roots revealed chemical changes during drying and zonal distribution of amino acids and alkaloids [265] while AuNP-coated paper enabled real-time monitoring of pesticide migration in produce [193]. Gold nanoshells (SiO_2@Au) improved imaging resolution of sugars and anthocyanins in strawberries [246] and AuNPs mapped rotenone in *Derris elliptica* roots across growth stages [266]. Au@BN substrates enhanced detection of fipronil metabolites [247] while gold-enriched TiO_2 films improved sensitivity for small molecules in *Catharanthus roseus* [267]. Further modifications with thiol-β-cyclodextrin broadened metabolite coverage in spearmint and potato tissues [268].

Chemically modified TiO_2 nanoparticles have enhanced SALDI-MSI of low-molecular-weight metabolites in plant imprints, especially with silane-functionalized TiO_2 nanowires that improved imprint quality and detection limits [194]. Further advances involved the development of AuNP-hPDA-TDNT composites, which enabled precise metabolite mapping in various plant tissues under different stress conditions (Fig. 7) [222,224]. Titanium-based MOFs also revealed dynamic changes in glycosides during Polygonum multiflorum processing, aiding hepatotoxicity assessment [169].

Platinum nanofilms in SALDI-IMS improved compound detection by reducing charge build-up on non-conductive plant surfaces, enabling visualization of pesticides in pansy leaves [111] and mapping sugars and lipids in cereal grains [269]. Porous glass-bead plates coated with platinum further enhanced imaging of sugars and organic acids in strawberries [148]. Iron oxide nanoparticles also proved effective, reducing ion suppression in maize seeds [173] and improving hormone detection in rice roots by minimizing matrix interference [270].

7.7. *MSI of cell lines*

The imaging of cultured cell lines by mass spectrometry offered new perspectives on cellular metabolism and disease pathogenesis by enabling the spatial mapping of biomolecules directly in their native environment. Traditional MS approaches often encountered challenges in detecting certain molecular species, such as sterols, due to low ionization efficiencies and interference from other cellular components. The application of metallic nanostructures, particularly silver nanoparticles, addressed these limitations by facilitating enhanced ionization and improved signal intensity for cholesterol, its precursors, and other recalcitrant compounds. Consequently, these advancements enabled researchers to visualize and quantify metabolic alterations at the cellular level, providing valuable insights into disease mechanisms and potential therapeutic targets.

Silver nanoparticles proved especially effective for analyzing sterols such as cholesterol and 7-dehydrocholesterol (7-DHC) in normal and diseased human fibroblasts, where conventional methods failed [271]. Among various silver-based matrices, sputtered silver nanoparticles provided the lowest detection limits and minimized artifact formation, enabling reliable quantification. This approach also allowed MSI-based detection of elevated 7-DHC/cholesterol ratios in diseased cells, highlighting its utility for characterizing cholesterol metabolism in situ.

8. Limitations and future perspectives

Despite notable advantages and the promise shown by metallic nanoparticles in LDI-MSI, several limitations currently hinder their routine implementation in broader analytical workflows [25,27]. One persistent challenge is the tendency of nanoparticles to aggregate, causing heterogeneity in surface coverage and subsequent fluctuations in ionization efficiency [29]. Although strategies such as gas aggregation sputtering (GAS), chemical reduction approaches, and controlled surface functionalization have been introduced to enhance dispersion stability, ensuring uniform nanoparticle layers across diverse substrates remains difficult [272,273]. Aggregation-related "hot spots" can produce strong signals for selected analytes but reduce reproducibility and undermine quantitative precision.

Moreover, because nanoparticles interact differently with various types of molecules, experiments must be carefully optimized to get reliable results [33,38]. For instance, silver nanoparticles support efficient metal-adduct formation, particularly beneficial for lipid and metabolite detection, but are prone to oxidation [130]. Conversely, gold nanoparticles offer robust chemical stability and cleaner spectra, yet often exhibit weaker cationization efficiency [107]. Metal cluster formation (e.g., with gold) can also confound spectral interpretation and potentially suppress signals from trace analytes [274]. Meanwhile, lower-cost or more reactive metals, such as niobium or cobalt, show promise but require optimization of their oxide layers or other surface properties to balance stability and sensitivity [149,154].

Another important consideration is that the use of metallic nanomaterials as not-binded to surface matrices in LDI-MSI can at times increase demands on mass spectrometer maintenance. Owing to their high ablation efficiency and potential to generate metallic particulates, these nanostructures can lead to more frequent residue buildup on internal instrument components, thereby accelerating the need for cleaning [167,275].

Another barrier is the complexity and cost of nanoparticle synthesis. Methods that rely on high-purity targets or specialized reactors can be expensive and labor-intensive [68]. While top-down techniques, such as laser ablation in liquids, generate stabilizer-free substrates that minimize chemical background, these approaches may require sophisticated instrumentation [276]. Similarly, bottom-up chemical reduction can yield high-quality nanoparticles but may introduce surfactants that interfere with analyte signals [277].

Future work should concentrate on improving synthetic methods and surface engineering strategies that yield homogeneous, durable, and stable nanoparticle coatings of relatively higher thickness. Techniques like precise LASiS, magnetron sputtering, and hybrid chemical routes have already shown potential for reproducible fabrication [278,279]. Exploring composite materials, such as noble metal–metal oxide or noble metal–graphene hybrids, can also enhance both ionization efficiency and chemical stability [280,281].

Elucidating the mechanistic details of nanoparticle–analyte interactions is equally important. Molecular dynamics simulations and advanced modeling approaches could clarify how localized surface plasmon resonance or "hot electron" production affects the energy transfer to specific compound classes. Such insights would guide the rational design of nanomaterials targeted toward challenging analytes [282]. Integrating tailored functionalization—for instance, through selective ligands—may further improve detection limits, enhance specificity in complex biological samples, and reduce background noise [283].

Moreover, the examination of alternative laser wavelengths, particularly in the NIR range, has emerged as a potential solution to decrease photo-induced artifacts and expand molecular coverage [284]. Although UV lasers remain predominant in LDI-MSI, the use of NIR radiation, typically in the range from 700 to 1064 nm, can reduce fragmentation and enhance the detection sensitivity of selected analytes, particularly when combined with plasmonic nanoparticles engineered to resonate at these wavelengths [93].

Finally, robust protocols for automated sample handling, standardized nanoparticle deposition, and reproducible surface treatment are crucial to facilitate method transfer from specialized research contexts to diagnostic and high-throughput applications [285]. Streamlining the integration of metallic nanoparticles into MSI workflows will not only accelerate routine use but also open up opportunities for enhanced clinical diagnostics, drug discovery, plant metabolomics, and forensic analysis [286].

9. Conclusions

Recent progress in SALDI-MSI underscores the pivotal role of metallic nanostructures as enablers of high-resolution, label-free molecular imaging across diverse biological contexts. By capitalizing on unique optical and thermal characteristics, these substrates facilitate robust ion generation under conditions that minimize chemical interferences and preserve spatial accuracy. Their utility has extended beyond conventional target molecules, revealing new opportunities to investigate metabolite distributions, lipid heterogeneity, and other biomolecular features in situ. In particular, strategies that merge nanostructure deposition with automated sample handling have accelerated imaging throughput and reduced variability.

Further refinements in nanofabrication techniques—particularly those that yield uniformly dispersed nanomaterials—will likely amplify analytical reliability while mitigating issues such as uneven analyte desorption. Concurrently, incorporating machine learning tools to process complex spectral datasets may streamline biomarker discovery and quantification in medical diagnostics and environmental studies. By integrating SALDI-MSI data with complementary methods (e.g., structural imaging or spectroscopic techniques), enables spatial correlation of molecular ion distributions with histoarchitectural features, identification of cell-type-specific biochemical signatures, and characterization of microenvironment-dependent variations in metabolite and lipid profiles. Through these multifaceted efforts, the field stands poised to deepen its impact on areas ranging from disease pathogenesis to plant physiology, solidifying SALDI-MSI as a cornerstone in next-generation molecular imaging research.

CRediT authorship contribution statement

Joanna Nizioł: Writing – review & editing, Writing – original draft, Visualization, Supervision, Project administration, Investigation, Funding acquisition, Formal analysis, Data curation, Conceptualization. **Sumi Krupa:** Writing – original draft, Investigation, Data curation. **Wiktoria Szuberla:** Investigation, Data curation. **Tomasz Ruman:** Writing – review & editing.

Declaration of competing interest

The authors declare that they have no known competing financial interests or personal relationships that could have appeared to influence the work reported in this paper.

Acknowledgments

This work was supported by National Science Centre (Poland) research project Sonata Bis number 2022/46/E/ST4/00016.

Data availability

No data was used for the research described in the article.

References

[1] Y. Xiao, J. Deng, Y. Yao, L. Fang, Y. Yang, T. Luan, Recent advances of ambient mass spectrometry imaging for biological tissues: a review, Anal. Chim. Acta 1117 (2020) 74–88, https://doi.org/10.1016/J.ACA.2020.01.052.

[2] S.Q. Gao, J.H. Zhao, Y. Guan, Y.S. Tang, Y. Li, L.Y. Liu, Mass spectrometry imaging technology in metabolomics: a systematic review, Biomed. Chromatogr. 37 (2023) e5494, https://doi.org/10.1002/BMC.5494.

[3] I. Khan, K. Saeed, I. Khan, Nanoparticles: properties, applications and toxicities, Arab. J. Chem. 12 (2019) 908–931, https://doi.org/10.1016/J.ARABJC.2017.05.011.

[4] K. Tanaka, H. Waki, Y. Ido, S. Akita, Y. Yoshida, T. Yoshida, T. Matsuo, Protein and polymer analyses up to m/z 100 000 by laser ionization time-of-flight mass spectrometry, Rapid Commun. Mass Spectrom. 2 (1988) 151–153, https://doi.org/10.1002/rcm.1290020802.

[5] S.W. Hell, Toward fluorescence nanoscopy, Nat. Biotechnol. 21 (11 21) (2003) 1347–1355, https://doi.org/10.1038/nbt895, 2003.

[6] R. Salzer, H.W. Siesler, Infrared and Raman Spectroscopic Imaging: Second, Completely Revised and, Updated Edition, 2014, pp. 57–110. https://www.wiley.com/en-us/Infrared+and+Raman+Spectroscopic+Imaging%2C+2nd%2C+Completely+Revised+and+Updated+Edition-p-9783527336524. (Accessed 16 July 2024).

[7] F. Jia, X. Zhao, Y. Zhao, Advancements in ToF-SIMS imaging for life sciences, Front. Chem. 11 (2023) 1237408, https://doi.org/10.3389/FCHEM.2023.1237408.

[8] T. Soudah, A. Zoabi, K. Margulis, Desorption electrospray ionization mass spectrometry imaging in discovery and development of novel therapies, Mass Spectrom. Rev. 42 (2023) 751–778, https://doi.org/10.1002/MAS.21736.

[9] M. Karas, F. Hillenkamp, Laser desorption ionization of proteins with molecular masses exceeding 10,000 daltons, Anal. Chem. 60 (1988) 2299–2301.

[10] R.M. Caprioli, T.B. Farmer, J. Gile, Molecular imaging of biological samples: localization of peptides and proteins using MALDI-TOF MS, Anal. Chem. 69 (1997) 4751–4760, https://doi.org/10.1021/AC970888I.

[11] M. Tuck, F. Grélard, L. Blanc, N. Desbenoit, MALDI-MSI towards multimodal imaging: challenges and perspectives, Front. Chem. 10 (2022) 904688, https://doi.org/10.3389/FCHEM.2022.904688.

[12] J.L. Norris, R.M. Caprioli, Analysis of tissue specimens by matrix-assisted laser desorption/ionization imaging mass spectrometry in biological and clinical research, Chem. Rev. 113 (2013) 2309–2342, https://doi.org/10.1021/CR3004295.

[13] P. Chaurand, S.A. Schwartz, R.M. Caprioli, Imaging mass spectrometry: a new tool to investigate the spatial organization of peptides and proteins in mammalian tissue sections, Curr. Opin. Chem. Biol. 6 (2002) 676–681, https://doi.org/10.1016/S1367-5931(02)00370-8.

[14] D.S. Peterson, Matrix-free methods for laser desorption/ionization mass spectrometry, Mass Spectrom. Rev. 26 (2007) 19–34, https://doi.org/10.1002/MAS.20104.

[15] S. Francese, F.R. Dani, P. Traldi, G. Mastrobuoni, G. Pieraccini, G. Moneti, MALDI mass spectrometry imaging, from its origins up to today: the state of the art, Comb. Chem. High Throughput Screen. 12 (2009) 156–174, https://doi.org/10.2174/138620709787315454.

[16] E. Gemperline, S. Rawson, L. Li, Optimization and comparison of multiple MALDI matrix application methods for small molecule mass spectrometric imaging, Anal. Chem. 86 (2014) 10030–10035, https://doi.org/10.1021/AC5028534.

[17] H. Qiao, G. Piyadasa, V. Spicer, W. Ens, Analyte distributions in MALDI samples using MALDI imaging mass spectrometry, Int. J. Mass Spectrom. 281 (2009) 41–51, https://doi.org/10.1016/J.IJMS.2008.11.015.

[18] A. Mandal, M. Singha, P.S. Addy, A. Basak, Laser desorption ionization mass spectrometry: recent progress in matrix-free and label-assisted techniques, Mass Spectrom. Rev. 38 (2019) 3–21, https://doi.org/10.1002/MAS.21545.

[19] C.D. Calvano, A. Monopoli, T.R.I. Cataldi, F. Palmisano, MALDI matrices for low molecular weight compounds: an endless story? Anal. Bioanal. Chem. 410 (17 410) (2018) 4015–4038, https://doi.org/10.1007/S00216-018-1014-X, 2018.

[20] S. Xu, Y. Li, H. Zou, J. Qiu, Z. Guo, B. Guo, Carbon nanotubes as assisted matrix for laser desorption/ionization time-of-flight mass spectrometry, Anal. Chem. 75 (2003) 6191–6195, https://doi.org/10.1021/AC0345695.

[21] X. Dong, J. Cheng, J. Li, Y. Wang, Graphene as a novel matrix for the analysis of small molecules by MALDI-TOF MS, Anal. Chem. 82 (2010) 6208–6214, https://doi.org/10.1021/AC101022M.

[22] A. Khajavinia, A. El-Aneed, Carbon-based nanoparticles and their surface-modified counterparts as MALDI matrices, Anal. Chem. 95 (2023) 100–114, https://doi.org/10.1021/ACS.ANALCHEM.2C04537.

[23] J. Wei, J.M. Buriak, G. Siuzdak, Desorption–ionization mass spectrometry on porous silicon, Nature 399 (6733 399) (1999) 243–246, https://doi.org/10.1038/20400, 1999.

[24] Y.S. Lin, Y.C. Chen, Laser desorption/ionization time-of-flight mass spectrometry on sol-gel-derived 2,5-dihydroxybenzoic acid film, Anal. Chem. 74 (2002) 5793–5798, https://doi.org/10.1021/AC020418A.

[25] C.Y. Shi, C.H. Deng, Recent advances in inorganic materials for LDI-MS analysis of small molecules, Analyst 141 (2016) 2816–2826, https://doi.org/10.1039/C6AN00220J.

[26] L. Kolářová, L. Prokeš, L. Kučera, A. Hampl, E. Peña-Méndez, P. Vaňhara, J. Havel, Clusters of monoisotopic elements for calibration in (TOF) mass spectrometry, J. Am. Soc. Mass Spectrom. 28 (2017) 419–427, https://doi.org/10.1007/S13361-016-1567-X.

[27] H.N. Abdelhamid, Nanoparticle-based surface assisted laser desorption ionization mass spectrometry: a review, Microchim. Acta 186 (10 186) (2019) 1–35, https://doi.org/10.1007/S00604-019-3770-5, 2019.

[28] Z. Guo, A.A.A. Ganawi, Q. Liu, L. He, Nanomaterials in mass spectrometry ionization and prospects for biological application, Anal. Bioanal. Chem. 384 (2006) 584–592, https://doi.org/10.1007/S00216-005-0125-3.

[29] W.H. Müller, A. Verdin, E. De Pauw, C. Malherbe, G. Eppe, Surface-assisted laser desorption/ionization mass spectrometry imaging: a review, Mass Spectrom. Rev. 41 (2022) 373–420, https://doi.org/10.1002/MAS.21670.

[30] J. Sunner, E. Dratz, Y.-C. Chen, R.D. Biochem Biophys, Graphite surface-assisted laser Desorption/ionization time-of-flight mass spectrometry of peptides and proteins from liquid solutions, J. Chem. Phys. Lett 67 (1995) 579–585. https://pubs.acs.org/sharingguidelines. (Accessed 12 July 2021).

[31] H. Huang, D. Ouyang, Z.A. Lin, Recent advances in surface-assisted laser desorption/ionization mass spectrometry and its imaging for small molecules, J. Analys.Test. 6 (3 6) (2022) 217–234, https://doi.org/10.1007/S41664-022-00211-5, 2022.

[32] J.Y. Kim, H. Lim, D.W. Moon, Mass spectrometry imaging of small molecules from live cells and tissues using nanomaterials, Surf. Interface Anal. 54 (2022) 381–388, https://doi.org/10.1002/SIA.7070.

[33] C. Lei, K. Qian, O. Noonan, A. Nouwens, C. Yu, Applications of nanomaterials in mass spectrometry analysis, Nanoscale 5 (2013) 12033–12042, https://doi.org/10.1039/C3NR04194H.

[34] W.T. Chen, I. Tomalová, J. Preisler, H.T. Changa, Analysis of biomolecules through surface-assisted laser, desorption/ionization mass spectrometry employing nanomaterials, J. Chin. Chem. Soc. 58 (2011) 769–778, https://doi.org/10.1002/JCCS.201190120.

[35] C.K. Chiang, W.T. Chen, H.T. Chang, Nanoparticle-based mass spectrometry for the analysis of biomolecules, Chem. Soc. Rev. 40 (2011) 1269–1281, https://doi.org/10.1039/C0CS00050G.

[36] H.N. Abdelhamid, Nanoparticle assisted laser desorption/ionization mass spectrometry for small molecule analytes, Microchim. Acta 185 (2018) 1–16, https://doi.org/10.1007/s00604-018-2687-8.

[37] H. He, Z. Guo, Y. Wen, S. Xu, Z. Liu, Recent advances in nanostructure/nanomaterial-assisted laser desorption/ionization mass spectrometry of low molecular mass compounds, Anal. Chim. Acta 1090 (2019) 1–22, https://doi.org/10.1016/J.ACA.2019.08.048.

[38] L.Z. Samarah, A. Vertes, Mass spectrometry imaging based on laser desorption ionization from inorganic and nanophotonic platforms, View 1 (2020) 20200063, https://doi.org/10.1002/VIW.20200063.

[39] Y. Jin, J. Yan, Z. Cai, Z. Lin, Advances in nanomaterials for surface-assisted laser desorption ionization mass spectrometry: applications in small molecule analysis over the past five years, TrAC, Trends Anal. Chem. 183 (2025) 118102, https://doi.org/10.1016/J.TRAC.2024.118102.

[40] X. Du, L. Yuan, S. Gao, Y. Tang, Z. Wang, C.Q. Zhao, L. Qiao, Research progress on nanomaterial-based matrices for matrix-assisted laser desorption/ionization time-of-flight mass spectrometry analysis, J. Chromatogr. A 1712 (2023) 464493, https://doi.org/10.1016/J.CHROMA.2023.464493.

[41] ISO/TS 229, 80004-4:2011, Nanotechnologies — Vocabulary — part 4: nanostructured materials, 201AD, https://www.iso.org/obp/ui/#iso:std:iso:ts:80004:-4:ed-1:v1:en. (Accessed 22 December 2024).

[42] M. Nasrollahzadeh, Z. Issaabadi, M. Sajjadi, S.M. Sajadi, M. Atarod, Types of nanostructures, Interf. Sci. Tech. 28 (2019) 29–80, https://doi.org/10.1016/B978-0-12-813586-0.00002-X.

[43] V.V. Pokropivny, V.V. Skorokhod, Classification of nanostructures by dimensionality and concept of surface forms engineering in nanomaterial science, Mater. Sci. Eng. C 27 (2007) 990–993, https://doi.org/10.1016/J.MSEC.2006.09.023.

[44] S. Bhaviripudi, E. Mile, S.A. Steiner, A.T. Zare, M.S. Dresselhaus, A.M. Belcher, J. Kong, CVD synthesis of single-walled carbon nanotubes from gold nanoparticle catalysts, J. Am. Chem. Soc. 129 (2007) 1516–1517, https://doi.org/10.1021/JA0673332.

[45] L. Oprică, M. Bălăşoiu, Nanoparticles: an overview about their clasifications, synthesis, properties, characterization and applications, J. Experim. Molecul. Biol. 20 (2020) 43–60. https://www.jemb.bio.uaic.ro/index.php/jemb/article/view/39. (Accessed 22 December 2024).

[46] J. Zhao, X. Zhang, C.R. Yonzon, A.J. Hoes, R.P. Van Duyne, Localized surface plasmon resonance biosensors, Nanomedicine 1 (2006) 219–228, https://doi.org/10.2217/17435889.1.2.219.

[47] K.M. Mayer, J.H. Hafner, Localized surface plasmon resonance sensors, Chem. Rev. 111 (2011) 3828–3857, https://doi.org/10.1021/CR100313V.

[48] A. Rabbani, R. Rudacille, K. Hasegawa, Local refractive index sensitivity of localized surface Plasmon resonance biosensors, J. Phys. Chem. C 128 (2024) 11, https://doi.org/10.1021/ACS.JPCC.4C03456.

[49] R. Liu, J. Guo, G. Ma, P. Jiang, D. Zhang, D. Li, L. Chen, Y. Guo, G. Ge, Alloyed crystalline Au-Ag hollow nanostructures with high chemical stability and catalytic performance, ACS Appl. Mater. Interfaces 8 (2016) 16833–16844, https://doi.org/10.1021/ACSAMI.6B03728.

[50] I. Willner, B. Willner, Biomolecule-based nanomaterials and nanostructures, Nano Lett. 10 (2010) 3805–3815, https://doi.org/10.1021/NL102083J.

[51] G.P. Gary, P. Wiederrecht, Handbook of Nanoscale Optics and Electronics, 2010, p. 387.

[52] Y. Xiong, X. Lu, Metallic nanostructures: from controlled synthesis to applications, metallic nanostructures: from controlled synthesis to applications, 1–301, https://doi.org/10.1007/978-3-319-11304-3, 2015.

[53] C. Pabari, Size dependent properties of metallic nanoparticles, Mater. Today Proc. 55 (2022) 98–101, https://doi.org/10.1016/J.MATPR.2021.12.375.

[54] L.B. Scaffardi, D.C. Schinca, M. Lester, F.A. Videla, J.M.J. Santillan, R. M. Abraham Ekeroth, Size-dependent optical properties of metallic nanostructures. UV-VIS and Photoluminescence Spectroscopy for Nanomaterials Characterization, 2013, pp. 179–229, https://doi.org/10.1007/978-3-642-27594-4_5.

[55] L.M. Liz-Marzán, Tailoring surface plasmons through the morphology and assembly of metal nanoparticles, Langmuir 22 (2006) 32–41, https://doi.org/10.1021/LA0513353.

[56] K.L. Kelly, E. Coronado, L.L. Zhao, G.C. Schatz, The optical properties of metal nanoparticles: the influence of size, shape, and dielectric environment, J. Phys. Chem. B 107 (2003) 668–677, https://doi.org/10.1021/JP026731Y.

[57] X. Huang, M.A. El-Sayed, Gold nanoparticles: optical properties and implementations in cancer diagnosis and photothermal therapy, J. Adv. Res. 1 (2010) 13–28, https://doi.org/10.1016/J.JARE.2010.02.002.

[58] N.E. Phillips, Low-temperature heat capacity of metals, Crit. Rev. Solid State Mater. Sci. 2 (1971) 467–553, https://doi.org/10.1080/10408437108243546.

[59] H.M. Chen, R.S. Liu, Architecture of metallic nanostructures: synthesis strategy and specific applications, J. Phys. Chem. C 115 (2011) 3513–3527, https://doi.org/10.1021/JP108403R.

[60] N. Abid, A.M. Khan, S. Shujait, K. Chaudhary, M. Ikram, M. Imran, J. Haider, M. Khan, Q. Khan, M. Maqbool, Synthesis of nanomaterials using various top-down and bottom-up approaches, influencing factors, advantages, and disadvantages: a review, Adv. Colloid Interface Sci. 300 (2022) 102597, https://doi.org/10.1016/J.CIS.2021.102597.

[61] B.W. McMahon, J.P.L. Perez, J. Yu, J.A. Boatz, S.L. Anderson, Synthesis of nanoparticles from malleable and ductile metals using powder-free, reactant-assisted mechanical attrition, ACS Appl. Mater. Interfaces 6 (2014) 19579–19591, https://doi.org/10.1021/AM503845S.

[62] Y. Hatakeyama, K. Onishi, K. Nishikawa, Effects of sputtering conditions on formation of gold nanoparticles in sputter deposition technique, RSC Adv. 1 (2011) 1815–1821, https://doi.org/10.1039/C1RA00688F.

[63] A. Płaza, A. Kołodziej, J. Nizioł, T. Ruman, Laser ablation synthesis in solution and nebulization of Silver-109 nanoparticles for mass spectrometry and mass spectrometry imaging, ACS Measur. Sci. Au 2 (2022) 14–22, https://doi.org/10.1021/ACSMEASURESCIAU.1C00020.

[64] Z. Krupa, J. Nizioł, Fiber laser-generated Silver-109 nanoparticles for laser desorption/ionization mass spectrometry of illicit drugs, J. Am. Soc. Mass Spectrom. 35 (2024) 1156–1167, https://doi.org/10.1021/JASMS.3C00454.

[65] A. Płaza-Altamer, A. Kołodziej, Z. Krupa, J. Nizioł, T. Ruman, Infrared pulsed fiber laser-produced gold and silver-109 nanoparticles for laser desorption/ionization mass spectrometry of steroid hormones, Rapid Commun. Mass Spectrom. 37 (2023) e9621, https://doi.org/10.1002/RCM.9621.

[66] A. Kołodziej, A. Płaza-Altamer, J. Nizioł, T. Ruman, Infrared pulsed fiber laser-produced silver-109 nanoparticles for laser desorption/ionization mass spectrometry of 3-hydroxycarboxylic acids, Rapid Commun. Mass Spectrom. 36 (2022), https://doi.org/10.1002/RCM.9375.

[67] A. Kołodziej, A. Płaza-Altamer, J. Nizioł, T. Ruman, Infrared pulsed fiber laser-produced silver-109-nanoparticles for laser desorption/ionization mass spectrometry of carboxylic acids, Int. J. Mass Spectrom. 474 (2022) 116816, https://doi.org/10.1016/J.IJMS.2022.116816.

[68] V. Amendola, L. Litti, M. Meneghetti, LDI-MS assisted by chemical-free gold nanoparticles: enhanced sensitivity and reduced background in the low-mass region, Anal. Chem. 85 (2013) 11747–11754, https://doi.org/10.1021/AC401662R.

[69] P. Pleskunov, V. Prysiazhnyi, D. Nikitin, T. Košutová, M. Cieslar, I. Gordeev, Z. Krtouš, S. Ali-Ogly, J. Šomvársky, M. Protsak, K. Biliak, K. Kishenina, A. Bednařík, M. Dopita, J. Preisler, A. Choukourov, Magnetron-sputtered niobium nanoparticles for molecular imaging of brain tissues through surface-assisted laser desorption/ionization mass spectrometry, ACS Appl. Nano Mater. 5 (2022) 12865–12875, https://doi.org/10.1021/ACSANM.2C02734.

[70] R.L. Hansen, M.E. Dueñas, Y.J. Lee, Sputter-coated metal screening for small molecule analysis and high-spatial resolution imaging in laser desorption ionization mass spectrometry, J. Am. Soc. Mass Spectrom. 30 (2019) 299–308, https://doi.org/10.1007/S13361-018-2081-0.

[71] K. Nakaso, B. Han, K.H. Ahn, M. Choi, K. Okuyama, Synthesis of non-agglomerated nanoparticles by an electrospray assisted chemical vapor deposition (ES-CVD) method, J. Aerosol Sci. 34 (2003) 869–881, https://doi.org/10.1016/S0021-8502(03)00053-3.

[72] A.N.P. Madathil, K.A. Vanaja, M.K. Jayaraj, Synthesis of Zno Nanoparticles by Hydrothermal Method, 2007, pp. 47–55, https://doi.org/10.1117/12.730364. Doi.Org/10.1117/12.730364 6639.

[73] S. Tokonami, Y. Yamamoto, H. Shiigi, T. Nagaoka, Synthesis and bioanalytical applications of specific-shaped metallic nanostructures: a review, Anal. Chim. Acta 716 (2012) 76–91, https://doi.org/10.1016/J.ACA.2011.12.025.

[74] C. Daruich De Souza, B. Ribeiro Nogueira, M.E.C.M. Rostelato, Review of the methodologies used in the synthesis gold nanoparticles by chemical reduction, J. Alloys Compd. 798 (2019) 714–740, https://doi.org/10.1016/J.JALLCOM.2019.05.153.

[75] A. Arendowski, K. Ossoliński, A. Ossolińska, T. Ossoliński, J. Nizioł, T. Ruman, Serum and urine analysis with gold nanoparticle-assisted laser desorption/ionization mass spectrometry for renal cell carcinoma metabolic biomarkers discovery, Adv. Med. Sci. 66 (2021) 326–335, https://doi.org/10.1016/J.ADVMS.2021.07.003.

[76] J. Nizioł, K. Ossoliński, B.P. Tripet, V. Copié, A. Arendowski, T. Ruman, Nuclear magnetic resonance and surface-assisted laser desorption/ionization mass spectrometry-based serum metabolomics of kidney cancer, Anal. Bioanal. Chem. 412 (2020) 5827–5841, https://doi.org/10.1007/S00216-020-02807-1.

[77] A. Arendowski, K. Ossoliński, J. Nizioł, T. Ruman, Gold nanostructures - assisted laser desorption/ionization mass spectrometry for kidney cancer blood serum biomarker screening, Int. J. Mass Spectrom. 456 (2020) 116396, https://doi.org/10.1016/J.IJMS.2020.116396.

[78] J. Nizioł, K. Ossoliński, B.P. Tripet, V. Copié, A. Arendowski, T. Ruman, Nuclear magnetic resonance and surface-assisted laser desorption/ionization mass spectrometry-based metabolome profiling of urine samples from kidney cancer patients, J. Pharm. Biomed. Anal. 193 (2021) 113752, https://doi.org/10.1016/J.JPBA.2020.113752.

[79] K. Ossoliński, J. Nizioł, A. Arendowski, A. Ossolińska, T. Ossoliński, J. Kucharz, P. Wiechno, T. Ruman, Mass spectrometry-based metabolomic profiling of prostate cancer - a pilot study, J. Cancer Metastas. Treat 5 (2019), https://doi.org/10.20517/2394-4722.2018.63.

[80] J. Szulc, A. Kołodziej, T. Ruman, Silver-109/Silver/Gold nanoparticle-enhanced target surface-assisted laser desorption/ionisation mass spectrometry—the new methods for an assessment of mycotoxin concentration on building materials, Toxins 13 (2021) 45, https://doi.org/10.3390/TOXINS13010045, 13 (2021) 45.

[81] A. Arendowski, J. Szulc, J. Nizioł, B. Gutarowska, T. Ruman, Metabolic profiling of moulds with laser desorption/ionization mass spectrometry on gold nanoparticle enhanced target, Anal. Biochem. 549 (2018), https://doi.org/10.1016/j.ab.2018.03.016.

[82] A. Kołodziej, T. Ruman, J. Nizioł, Gold and silver nanoparticles-based laser desorption/ionization mass spectrometry method for detection and quantification of carboxylic acids, J. Mass Spectrom. 55 (2020) e4604, https://doi.org/10.1002/JMS.4604.

[83] K.P. Law, J.R. Larkin, Recent advances in SALDI-MS techniques and their chemical and bioanalytical applications, Anal. Bioanal. Chem. 399 (2011) 2597–2622, https://doi.org/10.1007/S00216-010-4063-3.

[84] R. Pilolli, F. Palmisano, N. Cioffi, Gold nanomaterials as a new tool for bioanalytical applications of laser desorption ionization mass spectrometry, Anal. Bioanal. Chem. 402 (2012) 601–623, https://doi.org/10.1007/S00216-011-5120-2.

[85] T.X. Dou, J.F. Shi, Y. Li, F.C. Bi, H.J. Gao, C.H. Hu, C.Y. Li, Q.S. Yang, G.M. Deng, O. Sheng, W. Di He, G.J. Yi, T. Dong, Influence of harvest season on volatile aroma constituents of two banana cultivars by electronic nose and HS-SPME coupled with GC-MS, Sci. Hortic. 265 (2020) 109214, https://doi.org/10.1016/J.SCIENTA.2020.109214.

[86] S.K.M. Lai, H.W. Tang, K.C. Lau, K.M. Ng, Nanosecond UV laser ablation of gold nanoparticles: enhancement of ion desorption by thermal-driven desorption, vaporization, or phase explosion, J. Phys. Chem. C 120 (2016) 20368–20377, https://doi.org/10.1021/ACS.JPCC.6B06261.

[87] K.M. Ng, S.L. Chau, H.W. Tang, X.G. Wei, K.C. Lau, F. Ye, A.M.C. Ng, Ion-desorption efficiency and internal-energy transfer in surface-assisted laser desorption/ionization: more implication(s) for the thermal-driven and phase-transition-driven desorption process, J. Phys. Chem. C 119 (2015) 23708–23720, https://doi.org/10.1021/ACS.JPCC.5B05957.

[88] Y.E. Silina, M. Koch, D.A. Volmer, Influence of surface melting effects and availability of reagent ions on LDI-MS efficiency after UV laser irradiation of Pd nanostructures, J. Mass Spectrom. 50 (2015) 578–585, https://doi.org/10.1002/JMS.3564.

[89] J.A. Stolee, B.N. Walker, V. Zorba, R.E. Russo, A. Vertes, Laser–nanostructure interactions for ion production, Phys. Chem. Chem. Phys. 14 (2012) 8453–8471, https://doi.org/10.1039/C2CP00038E.

[90] E. Bertrand, V. Gabelica, Thermometer ions, internal energies, and In-Source fragmentation in ambient ionization, Mass Spectrom. Rev. (2025), https://doi.org/10.1002/MAS.21924.

[91] H.W. Tang, K.M. Ng, W. Lu, C.M. Che, Ion desorption efficiency and internal energy transfer in carbon-based surface-assisted laser desorption/ionization mass spectrometry: desorption mechanism(s) and the design of SALDI substrates, Anal. Chem. 81 (2009) 4720–4729, https://doi.org/10.1021/AC8026367.

[92] M. Herzog, A. von Reppert, J.-E. Pudell, C. Henkel, M. Kronseder, C.H. Back, A. A. Maznev, M. Bargheer, M. Herzog, A. von Reppert, J. Pudell, C. Henkel, M. Bargheer, M. Kronseder, C.H. Back, A.A. Maznev, Phonon-dominated energy transport in purely metallic heterostructures, Adv. Funct. Mater. 32 (2022) 2206179, https://doi.org/10.1002/ADFM.202206179.

[93] R.A. Picca, C.D. Calvano, N. Cioffi, F. Palmisano, Mechanisms of nanophase-induced desorption in LDI-MS. A short review, Nanomaterials 7 (2017) 75, https://doi.org/10.3390/NANO7040075, 7 (2017) 75.

[94] G.H. Vineyard, Thermal spikes and activated processes, Radiat. Eff. 29 (1976) 245–248, https://doi.org/10.1080/00337577608233050.

[95] A. Tarui, H. Kawasaki, T. Taiko, T. Watanabe, T. Yonezawa, R. Arakawa, Gold-nanoparticle-supported silicon plate with polymer micelles for surface-assisted laser desorption/ionization mass spectrometry of peptides, J. Nanosci. Nanotechnol. 9 (2009) 159–164, https://doi.org/10.1166/JNN.2009.J046.

[96] M. Kurita, R. Arakawa, H. Kawasaki, Silver nanoparticle functionalized glass fibers for combined surface-enhanced Raman scattering spectroscopy (SERS)/surface-assisted laser desorption/ionization (SALDI) mass spectrometry via plasmonic/thermal hot spots, Analyst 141 (2016) 5835–5841, https://doi.org/10.1039/C6AN00511J.

[97] L.V. Zhigilei, Z. Lin, D.S. Ivanov, Atomistic modeling of short pulse laser ablation of metals: connections between melting, spallation, and phase explosion, J. Phys. Chem. C 113 (2009) 11892–11906, https://doi.org/10.1021/JP902294M.

[98] D. Werner, A. Furube, T. Okamoto, S. Hashimoto, Femtosecond laser-induced size reduction of aqueous gold nanoparticles: in situ and pump-probe spectroscopy investigations revealing coulomb explosion, J. Phys. Chem. C 115 (2011) 8503–8512, https://doi.org/10.1021/JP112262U.

[99] A. Pento, I. Kuzmin, V. Kozlovskiy, L. Li, P. Laptinskaya, Y. Simanovsky, B. Sartakov, S. Nikiforov, Laser-induced ion formation and electron emission from a nanostructured gold surface at laser fluence below the threshold for plasma formation, Nanomaterials (Basel) 13 (2023) 600, https://doi.org/10.3390/NANO13030600/S1.

[100] S.D. Sherrod, A.J. Diaz, W.K. Russell, P.S. Cremer, D.H. Russell, Silver nanoparticles as selective ionization probes for analysis of olefins by mass spectrometry, Anal. Chem. 80 (2008) 6796–6799, https://doi.org/10.1021/ac800904g.

[101] S. O'Neill, J.M.C. Robertson, V. Héquet, F. Chazarenc, X. Pang, K. Ralphs, N. Skillen, P.K.J. Robertson, Comparison of titanium dioxide and zinc oxide photocatalysts for the inactivation of Escherichia coli in water using slurry and rotating-disk photocatalytic reactors, Ind. Eng. Chem. Res. 62 (2023) 18952–18959, https://doi.org/10.1021/ACS.IECR.3C00508.

[102] Q.M. Al-Bataineh, A.A. Ahmad, A.B. Migdadi, A. Bahti, A. Telfah, Plasmon-exciton interactions in ZnO/AuNPs heterostructure film for high photoconductivity, Phys. B Condens. Matter 685 (2024) 415970, https://doi.org/10.1016/J.PHYSB.2024.415970.

[103] W.W. Wei, Y. Zhong, T. Zou, X.F. Chen, L. Ren, Z. Qi, G. Liu, Z.F. Chen, Z. Cai, Fe3O4-assisted laser desorption ionization mass spectrometry for typical metabolite analysis and localization: influencing factors, mechanisms, and environmental applications, J. Hazard Mater. 388 (2020) 121817, https://doi.org/10.1016/J.JHAZMAT.2019.121817.

[104] B. Yan, Y. Jeong, L.A. Mercante, G.Y. Tonga, C. Kim, Z.J. Zhu, R.W. Vachet, V. M. Rotello, Characterization of surface ligands on functionalized magnetic nanoparticles using laser desorption/ionization mass spectrometry (LDI-MS), Nanoscale 5 (2013) 5063–5066, https://doi.org/10.1039/C3NR01384G.

[105] A. Monopoli, G. Ventura, A. Aloia, F. Ciriaco, A. Nacci, T.R.I. Cataldi, C. D. Calvano, Synthesis and investigation of novel CHCA-derived matrices for matrix-assisted laser desorption/ionization mass spectrometric analysis of lipids, Molecules 27 (2022) 2565, https://doi.org/10.3390/MOLECULES27082565, 27 (2022) 2565.

[106] M. Schürenberg, K. Dreisewerd, F. Hillenkamp, Laser desorption/ionization mass spectrometry of peptides and proteins with particle suspension matrixes, Anal. Chem. 71 (1999) 221–229, https://doi.org/10.1021/AC980634C.

[107] J.A. McLean, K.A. Stumpo, D.H. Russel, Size-selected (2-10 nm) gold nanoparticles for matrix assisted laser desorption ionization of peptides, J. Am. Chem. Soc. 127 (2005) 5304–5305, https://doi.org/10.1021/JA043907W.

[108] O.V. Kharissova, B.I. Kharisov, T.H. Garcia, U.O. Méndez, A review on less-common nanostructures, synthesis and reactivity in inorganic, metal-organic, Nano-Metal Chem. 39 (2009) 662–684, https://doi.org/10.1080/15533170903433196.

[109] D. Melnikau, D. Savateeva, A. Sanchez-Iglesias, M. Grzelczak, L.M. Liz-Marzan, M. K. Schmidt, R. Estiban, J. Aizpurua, Y.P. Rakovich, Strong excitonic-plasmonic coupling in hybrid system of metal nanoparticles and J-aggregates of organic dye. International Conference on Transparent Optical Networks 2015-August, 2015, https://doi.org/10.1109/ICTON.2015.7193582.

[110] A.S.D.S. Indrasekara, R. Thomas, L. Fabris, Plasmonic properties of regiospecific core–satellite assemblies of gold nanostars and nanospheres, Phys. Chem. Chem. Phys. 17 (2015) 21133–21142, https://doi.org/10.1039/C4CP04517C.

[111] T. Ozawa, I. Osaka, S. Hamada, T. Murakami, A. Miyazato, H. Kawasaki, R. Arakawa, Direct imaging mass spectrometry of plant leaves using surface-assisted laser desorption/ionization with sputterdeposited platinum film, Anal. Sci. 32 (2016) 587–591, https://doi.org/10.2116/ANALSCI.32.587.

[112] T. Yonezawa, H. Kawasaki, A. Tarui, T. Watanabe, R. Arakawa, T. Shimada, F. Mafuné, Detailed investigation on the possibility of nanoparticles of various metal elements for surface-assisted laser desorption/ionization mass spectrometry, Anal. Sci. 25 (2009) 339–346, https://doi.org/10.2116/ANALSCI.25.339.

[113] C.L. Su, W.L. Tseng, Gold nanoparticles as assisted matrix for determining neutral small carbohydrates through laser desorption/ionization time-of-flight mass spectrometry, Anal. Chem. 79 (2007) 1626–1633, https://doi.org/10.1021/AC061747W.

[114] A. Płaza-Altamer, A. Kołodziej, Advances in the synthesis and application of gold nanoparticles for laser mass spectrometry: a mini review, Appl. Spectrosc. Rev. (2024), https://doi.org/10.1080/05704928.2024.2346078.

[115] A. Zuber, M. Purdey, E. Schartner, C. Forbes, B. Van Der Hoek, D. Giles, A. Abell, T. Monro, H. Ebendorff-Heidepriem, Detection of gold nanoparticles with different sizes using absorption and fluorescence based method, Sensor. Actuator. B Chem. 227 (2016) 117–127, https://doi.org/10.1016/J.SNB.2015.12.044.

[116] A. Gupta, D.F. Moyano, A. Parnsubsakul, A. Papadopoulos, L.S. Wang, R. F. Landis, R. Das, V.M. Rotello, Ultrastable and biofunctionalizable gold nanoparticles, ACS Appl. Mater. Interfaces 8 (2016) 14096–14101, https://doi.org/10.1021/ACSAMI.6B02548.

[117] P.K. Ngumbi, S.W. Mugo, J.M. Ngaruiya, Determination of gold nanoparticles sizes via surface plasmon resonance, IOSR J. Appl. Chem. (IOSR-JAC 11 (2018) 25–29, https://doi.org/10.9790/5736-1107012529.

[118] V. Amendola, M. Meneghetti, Size evaluation of gold nanoparticles by UV-vis spectroscopy, J. Phys. Chem. C 113 (2009) 4277–4285, https://doi.org/10.1021/JP8082425.

[119] W. Haiss, N.T.K. Thanh, J. Aveyard, D.G. Fernig, Determination of size and concentration of gold nanoparticles from UV-Vis spectra, Anal. Chem. 79 (2007) 4215–4221, https://doi.org/10.1021/AC0702084.

[120] J. Sekuła, J. Nizioł, W. Rode, T. Ruman, Gold nanoparticle-enhanced target (AuNPET) as universal solution for laser desorption/ionization mass spectrometry analysis and imaging of low molecular weight compounds, Anal. Chim. Acta 875 (2015), https://doi.org/10.1016/j.aca.2015.01.046.

[121] A. Kołodziej, T. Ruman, J. Nizioł, Gold and silver nanoparticles-based laser desorption/ionization mass spectrometry method for detection and quantification

of carboxylic acids, J. Mass Spectrom. 55 (2020) e4604, https://doi.org/10.1002/JMS.4604.

[122] B. Unnikrishnan, C.Y. Chang, H.W. Chu, A. Anand, C.C. Huang, Functional gold nanoparticles coupled with laser desorption ionization mass spectrometry for bioanalysis, Anal. Methods 8 (2016) 8123–8133, https://doi.org/10.1039/C6AY02378A.

[123] J. Sekuła, J. Nizioł, M. Misiorek, P. Dec, A. Wrona, A. Arendowski, T. Ruman, Gold nanoparticle-enhanced target for MS analysis and imaging of harmful compounds in plant, animal tissue and on fingerprint, Anal. Chim. Acta 895 (2015) 45–53, https://doi.org/10.1016/j.aca.2015.09.003.

[124] C.D. Sacks, K.A. Stumpo, Gold nanoparticles for enhanced ionization and fragmentation of biomolecules using LDI-MS, J. Mass Spectrom. 53 (2018) 1070–1077, https://doi.org/10.1002/JMS.4282.

[125] A. Kołodziej, A. Płaza-Altamer, Advances in the synthesis and application of silver nanoparticles for laser mass spectrometry: a mini-review, Talanta 277 (2024) 126347, https://doi.org/10.1016/J.TALANTA.2024.126347.

[126] S. Link, M.A. El-Sayed, Spectral properties and relaxation dynamics of surface plasmon electronic oscillations in gold and silver nanodots and nanorods, J. Phys. Chem. B 103 (1999) 8410–8426, https://doi.org/10.1021/JP9917648.

[127] K.B. Mogensen, K. Kneipp, Size-dependent shifts of plasmon resonance in silver nanoparticle films using controlled dissolution: monitoring the onset of surface screening effects, J. Phys. Chem. C 118 (2014) 28075–28083, https://doi.org/10.1021/JP505632N.

[128] B.A. Smith, J.Z. Zhang, U. Giebel, G. Schmid, Direct probe of size-dependent electronic relaxation in single-sized Au and nearly monodisperse Pt colloidal nano-particles, Chem. Phys. Lett. 270 (1997) 139–144, https://doi.org/10.1016/S0009-2614(97)00339-4.

[129] T.W. Roberti, B.A. Smith, J.Z. Zhang, Ultrafast electron dynamics at the liquid–metal interface: femtosecond studies using surface plasmons in aqueous silver colloid, J. Chem. Phys. 102 (1995) 3860–3866, https://doi.org/10.1063/1.468545.

[130] T. Hayasaka, N. Goto-Inoue, N. Zaima, K. Shrivas, Y. Kashiwagi, M. Yamamoto, M. Nakamoto, M. Setou, Imaging mass spectrometry with silver nanoparticles reveals the distribution of fatty acids in mouse retinal sections, J. Am. Soc. Mass Spectrom. 21 (2010) 1446–1454, https://doi.org/10.1016/J.JASMS.2010.04.005.

[131] S.N. Jackson, K. Baldwin, L. Muller, V.M. Womack, J.A. Schultz, C. Balaban, A. S. Woods, Imaging of lipids in rat heart by MALDI-MS with silver nanoparticles, Anal. Bioanal. Chem. 406 (2014) 1377–1386, https://doi.org/10.1007/S00216-013-7525-6.

[132] V. Prysiazhnyi, F. Dycka, J. Kratochvil, V. Stranak, V.N. Popok, Effect of Ag nanoparticle size on ion formation in nanoparticle assisted LDI MS, Appl. Nanosci. 1 (2020) 3–13, https://doi.org/10.3390/APPLNANO1010002.

[133] J. Nizioł, W. Rode, B. Laskowska, T. Ruman, Novel monoisotopic 109AgNPET for laser desorption/ionization mass spectrometry, Anal. Chem. 85 (2013) 1926–1931, https://doi.org/10.1021/ac303770y.

[134] Z.S. Nezhad, J.P. Salazar, R.S. Pryce, L.M. Munter, P. Chaurand, Absolute quantification of cholesterol from thin tissue sections by silver-assisted laser desorption ionization mass spectrometry imaging, Anal. Bioanal. Chem. 414 (2022) 6947–6954, https://doi.org/10.1007/S00216-022-04262-6.

[135] Š. Strnad, V. Vrkoslav, A. Mengr, O. Fabián, J. Rybáček, M. Kubánek, V. Melenovský, L. Maletínská, J. Cvačka, Thermal evaporation as sample preparation for silver–assisted laser desorption/ionization mass spectrometry imaging of cholesterol in amyloid tissues, Analyst 149 (2024) 3152–3160, https://doi.org/10.1039/D4AN00181H.

[136] M. Dufresne, A. Thomas, J. Breault-Turcot, J.F. Masson, P. Chaurand, Silver-assisted laser desorption ionization for high spatial resolution imaging mass spectrometry of olefins from thin tissue sections, Anal. Chem. 85 (2013) 3318–3324, https://doi.org/10.1021/AC3037415.

[137] E.C. Moule, T.M. Guinan, O.J.R. Gustafsson, H. Kobus, K.P. Kirkbride, N. H. Voelcker, Silver-assisted development and imaging of fingermarks on non-porous and porous surfaces, Int. J. Mass Spectrom. 422 (2017) 27–31, https://doi.org/10.1016/J.IJMS.2017.08.001.

[138] T.M. Guinan, O.J.R. Gustafsson, G. McPhee, H. Kobus, N.H. Voelcker, Silver coating for high-mass-accuracy imaging mass spectrometry of fingerprints on nanostructured silicon, Anal. Chem. 87 (2015) 11195–11202, https://doi.org/10.1021/ACS.ANALCHEM.5B02567.

[139] B.L. Walton, G.F. Verbeck, Soft-landing ion mobility of silver clusters for small-molecule matrix-assisted laser desorption ionization mass spectrometry and imaging of latent fingerprints, Anal. Chem. 86 (2014) 8114–8120, https://doi.org/10.1021/AC5010822.

[140] E. Sibińska, J. Walczak-Skierska, A. Arendowski, A. Ludwiczak, A. Radtke, P. Piszczek, D. Gabryś, K. Robotnik, P. Pomastowski, Advances in LDI-MS analysis: the role of chemical vapor deposition-synthesized silver nanoparticles in enhancing detection of low-molecular-weight biomolecules, J. Am. Soc. Mass Spectrom. 35 (2024) 2041–2055, https://doi.org/10.1021/JASMS.4C00071.

[141] H. Kawasaki, T. Ozawa, H. Hisatomi, R. Arakawa, Platinum vapor deposition surface-assisted laser desorption/ionization for imaging mass spectrometry of small molecules, Rapid Commun. Mass Spectrom. 26 (2012) 1849–1858, https://doi.org/10.1002/RCM.6301.

[142] T. Yao, H. Kawasaki, T. Watanabe, R. Arakawa, Effectiveness of platinum particle deposition on silicon surfaces for surface-assisted laser desorption/ionization mass spectrometry of peptides, Int. J. Mass Spectrom. 291 (2010) 145–151, https://doi.org/10.1016/J.IJMS.2010.02.001.

[143] C.K. Chiang, N.C. Chiang, Z.H. Lin, G.Y. Lan, Y.W. Lin, H.T. Chang, Nanomaterial-based surface-assisted laser desorption/ionization mass spectrometry of peptides and proteins, J. Am. Soc. Mass Spectrom. 21 (2010) 1204–1207, https://doi.org/10.1016/J.JASMS.2010.02.028.

[144] E. Gharibshahi, E. Saion, R.L. Johnston, A. Ashraf, Theory and experiment of optical absorption of platinum nanoparticles synthesized by gamma radiation, Appl. Radiat. Isot. 147 (2019) 204–210, https://doi.org/10.1016/J.APRADISO.2019.02.015.

[145] M. Sui, S. Kunwar, P. Pandey, J. Lee, Strongly confined localized surface plasmon resonance (LSPR) bands of Pt, AgPt, AgAuPt nanoparticles, Sci. Rep. 9 (1 9) (2019) 1–14, https://doi.org/10.1038/s41598-019-53292-1, 2019.

[146] M. Xu, J. Huang, X. Yue, S. Huang, Immobilizing ultralow loading platinum nanoparticles onto MXene through defect engineering to enhance the activity of the hydrogen evolution reaction, ACS Appl. Energy Mater. 7 (2024) 2460–2468, https://doi.org/10.1021/ACSAEM.3C03270.

[147] Y. Kimura, D. Abe, T. Ohmori, M. Mizutani, M. Harada, Synthesis of platinum nano-particles in high-temperatures and high-pressures fluids, Colloids Surf. A Physicochem. Eng. Asp. 231 (2003) 131–141, https://doi.org/10.1016/J.COLSURFA.2003.08.015.

[148] T. Ikeda, M. Kotani, Thin-section- and matrix-free mass spectrometry imaging: reproducible sample transfer using novel platinum-coated porous plate formed of glass beads, Rapid Commun. Mass Spectrom. 38 (2024) e9697, https://doi.org/10.1002/RCM.9697.

[149] P. Pleskunov, V. Prysiazhnyi, D. Nikitin, T. Koš, M. Cieslar, I. Gordeev, Z.K. Krtouš, S. Ali-Ogly, J.Š Omvársky, M. Protsak, K. Biliak, K. Kishenina, A. Bednař, M. Dopita, J. Preisler, A. Choukourov, Magnetron-sputtered niobium nanoparticles for molecular imaging of brain tissues through surface-assisted laser desorption/ionization mass spectrometry, ACS PublicationsP Pleskunov, V Prysiazhnyi, D Nikitin, T Košutová, M Cieslar, I Gordeev, Z KrtoušACS Applied Nano Materials, 2022•ACS Publications 2022 (2022) 12865–12875. https://doi.org/10.1021/acsanm.2c02734.

[150] T. Košutová, L. Horák, P. Pleskunov, J. Hanuš, D. Nikitin, P. Kúš, M. Cieslar, I. Gordeev, S. Burazer, A. Choukourov, M. Dopita, Thermally-driven morphogenesis of niobium nanoparticles as witnessed by in-situ x-ray scattering, Mater. Chem. Phys. 277 (2022) 125466, https://doi.org/10.1016/J.MATCHEMPHYS.2021.125466.

[151] R. Olivares-Navarrete, J.J. Olaya, C. Ramírez, S.E. Rodil, Biocompatibility of niobium coatings, Coatings (Oakv.) 1 (2011) 72–87, https://doi.org/10.3390/COATINGS1010072, 1 (2011) 72–87.

[152] R. Pang, Z. Wang, J. Li, K. Chen, Polymorphs of Nb2O5 compound and their electrical energy storage applications, Materials 16 (2023) 6956, https://doi.org/10.3390/ma16216956.

[153] E.D. Gonzalez, C.R.M. Afonso, P.A.P. Nascente, Influence of Nb content on the structure, morphology, nanostructure, and properties of titanium-niobium magnetron sputter deposited coatings for biomedical applications, Surf. Coat. Technol. 326 (2017) 424–428, https://doi.org/10.1016/J.SURFCOAT.2017.03.015.

[154] W. Liang, W. Yan, X. Wang, X. Yan, Q. Hu, W. Zhang, H. Meng, L. Yin, Q. He, C. Ma, A single atom cobalt anchored MXene bifunctional platform for rapid, label-free and high-throughput biomarker analysis and tissue imaging, Biosens. Bioelectron. 246 (2024) 115903, https://doi.org/10.1016/J.BIOS.2023.115903.

[155] F. Mohammadi, A. Gholami, N. Omidifar, A. Amini, S. Kianpour, S. M. Taghizadeh, The potential of surface nano-engineering in characteristics of cobalt-based nanoparticles and biointerface interaction with prokaryotic and human cells, Colloids Surf., B Biointerfaces 215 (2022) 112485, https://doi.org/10.1016/J.COLSURFB.2022.112485.

[156] H. Kawasaki, K. Nakai, R. Arakawa, E.K. Athanassiou, R.N. Grass, W.J. Stark, Functionalized graphene-coated cobalt nanoparticles for highly efficient surface-assisted laser desorption/ionization mass spectrometry analysis, Anal. Chem. 84 (2012) 9268–9275, https://doi.org/10.1021/AC302004G.

[157] G.B. Yagnik, R.L. Hansen, A.R. Korte, M.D. Reichert, J. Vela, Y.J. Lee, Large scale nanoparticle screening for small molecule analysis in laser desorption ionization mass spectrometry, Anal. Chem. 88 (2016) 8926–8930, https://doi.org/10.1021/ACS.ANALCHEM.6B02732.

[158] A. Manuja, B. Kumar, R. Kumar, D. Chhabra, M. Ghosh, M. Manuja, B. Brar, Y. Pal, B.N. Tripathi, M. Prasad, Metal/Metal oxide nanoparticles: toxicity concerns associated with their physical state and remediation for biomedical applications, Toxicol. Rep. 8 (2021) 1970–1978, https://doi.org/10.1016/J.TOXREP.2021.11.020.

[159] K.H. Lee, C.K. Chiang, Z.H. Lin, H.T. Chang, Determining enediol compounds in tea using surface-assisted laser desorption/ionization mass spectrometry with titanium dioxide nanoparticle matrices, Rapid Commun. Mass Spectrom. 21 (2007) 2023–2030, https://doi.org/10.1002/RCM.3058.

[160] X. Chen, S.S. Mao, Titanium dioxide nanomaterials: synthesis, properties, modifications and applications, Chem. Rev. 107 (2007) 2891–2959, https://doi.org/10.1021/CR0500535.

[161] Y. Gholipour, S.L. Giudicessi, H. Nonami, R. Erra-Balsells, Diamond, titanium dioxide, titanium silicon oxide, and barium strontium titanium oxide nanoparticles as matrixes for direct matrix-assisted laser desorption/ionization mass spectrometry analysis of carbohydrates in plant tissues, Anal. Chem. 82 (2010) 5518–5526, https://doi.org/10.1021/AC1003129.

[162] A. Ghareeb, A. Fouda, R.M. Kishk, W.M. El Kazzaz, Unlocking the potential of titanium dioxide nanoparticles: an insight into green synthesis, optimizations, characterizations, and multifunctional applications, Microb. Cell Fact. 23 (1 23) (2024) 1–40, https://doi.org/10.1186/S12934-024-02609-5, 2024.

[163] B. Guan, W. Lu, J. Fang, R.B. Cole, Characterization of synthesized titanium oxide nanoclusters by MALDI-TOF mass spectrometry, J. Am. Soc. Mass Spectrom. 18 (2007) 517–524, https://doi.org/10.1016/J.JASMS.2006.10.021.

[164] M. Radisavljević, T. Kamčeva, I. Vukićević, M. Radoičić, Z. Šaponjić, M. Petković, Colloidal TiO2 nanoparticles as substrates for M(S)ALDI mass spectrometry of transition metal complexes, Rapid Commun. Mass Spectrom. 26 (2012) 2041–2050, https://doi.org/10.1002/RCM.6320.

[165] L. Morosi, P. Spinelli, M. Zucchetti, F. Pretto, A. Carrà, M. D'Incalci, R. Giavazzi, E. Davoli, Determination of paclitaxel distribution in solid tumors by nano-particle assisted laser desorption ionization mass spectrometry imaging, PLoS One 8 (2013) e72532, https://doi.org/10.1371/JOURNAL.PONE.0072532.

[166] K. Shrivas, T. Hayasaka, Y. Sugiura, M. Setou, Method for simultaneous imaging of endogenous low molecular weight metabolites in mouse brain using TiO2 nanoparticles in nanoparticle-assisted laser desorption/ionization-imaging mass spectrometry, Anal. Chem. 83 (2011) 7283–7289, https://doi.org/10.1021/AC201602S.

[167] A.L. Hennemann, H.P. Nogueira, M.D. Ramos, T.C. Correra, B.L. Hennemann, K. Araki, Amorphous titanium dioxide nanoparticles and their unexpected fragmentation in MALDI-TOF/MS, ACS Omega 13 (2024) 28, https://doi.org/10.1021/ACSOMEGA.4C08770.

[168] Q. Wu, S.S. Rubakhin, J.V. Sweedler, Quantitative imprint mass spectrometry imaging of endogenous ceramides in rat brain tissue with kinetic calibration, Anal. Chem. 92 (2020) 6613–6621, https://doi.org/10.1021/ACS.ANALCHEM.0C00392.

[169] F.Y. Kuang, D.J. Hu, L. Wang, F. Chen, G.P. Lv, Ti-based MOF nanosheets as a mass spectrometry imaging matrix for low molecular weight compounds to reveal the spatiotemporal content changes of hepatotoxic components during the processing of Polygonum multiflorum, Analyst (2024), https://doi.org/10.1039/D4AN00964A.

[170] N.R. Kim, Y. Kim, J.M. Yun, S.K. Jeong, S. Lee, B.Z. Lee, J. Shim, Surface coating of titanium dioxide nanoparticles with a polymerizable chelating agent and its physicochemical property, ACS Omega 8 (2023) 18743–18750, https://doi.org/10.1021/ACSOMEGA.3C00734.

[171] S. Taira, Y. Sugiura, S. Moritake, S. Shimma, Y. Ichiyanagi, M. Setou, Nanoparticle-assisted laser desorption/ionization based mass imaging with cellular resolution, Anal. Chem. 80 (2008) 4761–4766, https://doi.org/10.1021/AC800081Z.

[172] H. Ageta, S. Asai, Y. Sugiura, N. Goto-Inoue, N. Zaima, M. Setou, Layer-specific sulfatide localization in rat hippocampus middle molecular layer is revealed by nanoparticle-assisted laser desorption/ionization imaging mass spectrometry, Med. Mol. Morphol. 42 (1 42) (2009) 16–23, https://doi.org/10.1007/S00795-008-0427-6, 2009.

[173] A.D. Feenstra, K.C. O'Neill, G.B. Yagnik, Y.J. Lee, Organic–inorganic binary mixture matrix for comprehensive laser-desorption ionization mass spectrometric analysis and imaging of medium-size molecules including phospholipids, glycerolipids, and oligosaccharides, RSC Adv. 6 (2016) 99260–99268, https://doi.org/10.1039/C6RA20469D.

[174] T. Kinumi, T. Saisu, M. Takayama, H. Niwa, Matrix-assisted laser desorption/ionization time-of-flight mass spectrometry using an inorganic particle matrix for small molecule analysis, J. Mass Spectrom. 35 (2000) 417–422, https://doi.org/10.1002/(SICI)1096-9888(200003)35:3.

[175] T. Watanabe, H. Kawasaki, T. Yonezawa, R. Arakawa, Surface-assisted laser desorption/ionization mass spectrometry (SALDI-MS) of low molecular weight organic compounds and synthetic polymers using zinc oxide (ZnO) nanoparticles, J. Mass Spectrom. 43 (2008) 1063–1071, https://doi.org/10.1002/JMS.1385.

[176] E.Z. Gomaa, Microbial mediated synthesis of zinc oxide nanoparticles, characterization and multifaceted applications, J. Inorg. Organomet. Polym. Mater. 32 (11 32) (2022) 4114–4132, https://doi.org/10.1007/S10904-022-02406-W, 2022.

[177] E. Bae, N. Murakami, M. Nakamura, T. Ohno, Effect of chemical etching by sulfuric acid or H2O2–NH3 mixed solution on the photocatalytic activity of rutile TiO2 nanorods, Appl. Catal. Gen. 380 (2010) 48–54, https://doi.org/10.1016/J.APCATA.2010.03.029.

[178] J. Wang, J. Sun, J. Wang, H. Liu, J. Xue, Z. Nie, Hexagonal boron nitride nanosheets as a multifunctional background-free matrix to detect small molecules and complicated samples by MALDI mass spectrometry, Chemical Communications 53 (2017) 8114–8117, https://doi.org/10.1039/C7CC02957H.

[179] C. Chen, S.R. Laviolette, S.N. Whitehead, J.B. Renaud, K.K.C. Yeung, Imaging of neurotransmitters and small molecules in brain tissues using laser desorption/ionization mass spectrometry assisted with zinc oxide nanoparticles, J. Am. Soc. Mass Spectrom. 32 (2021) 1065–1079, https://doi.org/10.1021/JASMS.1C00021.

[180] X. Gao, A. Kundu, D.P. Persson, A. Szameitat, F. Minutello, S. Husted, S. Ghoshal, Application of ZnO nanoparticles encapsulated in mesoporous silica on the abaxial side of a Solanum lycopersicum leaf enhances Zn uptake and translocation via the phloem, Environ. Sci. Technol. 57 (2023) 21704–21714, https://doi.org/10.1021/ACS.EST.3C06424.

[181] A.D. Feenstra, R.L. Hansen, Y.J. Lee, Multi-matrix, dual polarity, tandem mass spectrometry imaging strategy applied to a germinated maize seed: toward mass spectrometry imaging of an untargeted metabolome, Analyst 140 (2015) 7293–7304, https://doi.org/10.1039/C5AN01079A.

[182] M.C. Bernier, V.H. Wysocki, S. Dagan, Laser desorption ionization of small molecules assisted by tungsten oxide and rhenium oxide particles, J. Mass Spectrom. 50 (2015) 891–898, https://doi.org/10.1002/JMS.3597.

[183] M. Lu, X. Yang, Y. Yang, P. Qin, X. Wu, Z. Cai, Nanomaterials as assisted matrix of laser desorption/ionization time-of-flight mass spectrometry for the analysis of small molecules, Nanomaterials (Basel) 7 (2017) 87, https://doi.org/10.3390/NANO7040087. Page 87 7 (2017.

[184] K. Chughtai, R.M.A. Heeren, Mass spectrometric imaging for biomedical tissue analysis, Chem. Rev. 110 (2010) 3237–3277, https://doi.org/10.1021/CR100012C.

[185] A.R. Buchberger, K. DeLaney, J. Johnson, L. Li, Mass spectrometry imaging: a review of emerging advancements and future insights, Anal. Chem. 90 (2018) 240–265, https://doi.org/10.1021/ACS.ANALCHEM.7B04733.

[186] K.J. Bender, Y. Wang, C.Y. Zhai, Z. Saenz, A. Wang, E.K. Neumann, Sample preparation method for MALDI mass spectrometry imaging of fresh-frozen spines, Anal. Chem. 95 (2023) 17337–17346, https://doi.org/10.1021/ACS.ANALCHEM.3C03672.

[187] S.A. Schwartz, M.L. Reyzer, R.M. Caprioli, Direct tissue analysis using matrix-assisted laser desorption/ionization mass spectrometry: practical aspects of sample preparation, J. Mass Spectrom. 38 (2003) 699–708, https://doi.org/10.1002/JMS.505.

[188] P. Ticha, I. Pilawski, X. Yuan, J. Pan, U.S. Tulu, B.R. Coyac, W. Hoffmann, J. A. Helms, A novel cryo-embedding method for in-depth analysis of craniofacial mini pig bone specimens, Sci. Rep. 10 (2020), https://doi.org/10.1038/S41598-020-76336-3.

[189] R.J.A. Goodwin, Sample preparation for mass spectrometry imaging: small mistakes can lead to big consequences, J. Proteonomics 75 (2012) 4893–4911, https://doi.org/10.1016/J.JPROT.2012.04.012.

[190] Y.X. Zhang, Y. Da Zhang, Y.P. Shi, A reliable and effective sample preparation protocol of MALDI-TOF-MSI for lipids imaging analysis in hard and dry cereals, Food Chem. 398 (2023) 133911, https://doi.org/10.1016/J.FOODCHEM.2022.133911.

[191] J. Li, R. Wei, Y. Meng, R.N. Zare, Evaluation of oil-absorbing film for imprint desorption electrospray ionization mass spectrometry imaging (IDESI-MSI) on biological samples, Metabolites 14 (2024) 160, https://doi.org/10.3390/METABO14030160.

[192] J. Nizioł, M. Misiorek, T. Ruman, Mass spectrometry imaging of low molecular weight metabolites in strawberry fruit (Fragaria x ananassa duch.) cv. primoris with 109Ag nanoparticle enhanced target, Phytochemistry 159 (2019) 11–19, https://doi.org/10.1016/J.PHYTOCHEM.2018.11.014.

[193] R. Qin, P. Li, M. Du, L. Ma, Y. Huang, Z. Yin, Y. Zhang, D. Chen, H. Xu, X. Wu, Spatiotemporal visualization of insecticides and fungicides within fruits and vegetables using gold nanoparticle-immersed paper imprinting mass spectrometry imaging, Nanomaterials (Basel) 11 (2021) 1327, https://doi.org/10.3390/NANO11051327.

[194] E.P. Dutkiewicz, C.H. Su, H.J. Lee, C.C. Hsu, Y.L. Yang, Visualizing vinca alkaloids in the petal of Catharanthus roseus using functionalized titanium oxide nanowire substrate for surface-assisted laser desorption/ionization imaging mass spectrometry, Plant J. 105 (2021) 1123–1133, https://doi.org/10.1111/TPJ.15092.

[195] J. Nizioł, T. Ruman, Surface-transfer mass spectrometry imaging on a monoisotopic silver nanoparticle enhanced target, Anal. Chem. 85 (2013) 12070–12076, https://doi.org/10.1021/ac4031658.

[196] M. Muthu, S. Chun, H.F. Wu, M.W. Duncan, J. Gopal, The ongoing evolution of laser desorption/ionization mass spectrometry: some observations on current trends and future directions, J. Mass Spectrom. 53 (2018) 525–540, https://doi.org/10.1002/JMS.4083.

[197] N. McLaughlin, T.M. Bielinski, C.M. Tressler, E. Barton, K. Glunde, K.A. Stumpo, Pneumatically sprayed gold nanoparticles for mass spectrometry imaging of neurotransmitters, J. Am. Soc. Mass Spectrom. 31 (2020) 2452–2461, https://doi.org/10.1021/JASMS.0C00156.

[198] V. Vidová, P. Novák, M. Strohalm, J. Pól, V. Havlíček, M. Volný, Laser desorption-ionization of lipid transfers: tissue mass spectrometry imaging without MALDI matrix, Anal. Chem. 82 (2010) 4994–4997, https://doi.org/10.1021/ac100661h.

[199] P.J. O'Brien, M. Lee, M.E. Spilker, C.C. Zhang, Z. Yan, T.C. Nichols, W. Li, C. H. Johnson, G.J. Patti, G. Siuzdak, Monitoring metabolic responses to chemotherapy in single cells and tumors using nanostructure-initiator mass spectrometry (NIMS) imaging, Cancer Metabol. 1 (1 1) (2013) 1–14, https://doi.org/10.1186/2049-3002-1-4, 2013.

[200] H. Wender, P. Migowski, A.F. Feil, S.R. Teixeira, J. Dupont, Sputtering deposition of nanoparticles onto liquid substrates: recent advances and future trends, Coord. Chem. Rev. 257 (2013) 2468–2483, https://doi.org/10.1016/J.CCR.2013.01.013.

[201] J. Nizioł, J. Sekuła, T. Ruman, Visualizing spatial distribution of small molecules in the rhubarb stalk (Rheum rhabarbarum) by surface-transfer mass spectrometry imaging, Phytochemistry 139 (2017), https://doi.org/10.1016/j.phytochem.2017.04.006.

[202] Y.T. Tseng, S.G. Harroun, C.W. Wu, J.Y. Mao, H.T. Chang, C.C. Huang, Satellite-like gold nanocomposites for targeted mass spectrometry imaging of tumor tissues, Nanotheranostics 1 (2017) 141, https://doi.org/10.7150/NTNO.18897.

[203] L. Muller, K. Baldwin, D.C. Barbacci, S.N. Jackson, A. Roux, C.D. Balaban, B. E. Brinson, M.I. McCully, E.K. Lewis, J.A. Schultz, A.S. Woods, Laser desorption/ionization mass spectrometric imaging of endogenous lipids from rat brain tissue implanted with silver nanoparticles, J. Am. Soc. Mass Spectrom. 28 (2017) 1716–1728, https://doi.org/10.1007/S13361-017-1665-4.

[204] A. Roux, L. Muller, S.N. Jackson, K. Baldwin, V. Womack, J.G. Pagiazitis, J. R. O'Rourke, P.K. Thanos, C. Balaban, J.A. Schultz, N.D. Volkow, A.S. Woods, Chronic ethanol consumption profoundly alters regional brain ceramide and sphingomyelin content in rodents, ACS Chem. Neurosci. 6 (2015) 247–259, https://doi.org/10.1021/CN500174C.

[205] L. Muller, A. Kailas, S.N. Jackson, A. Roux, D.C. Barbacci, J.A. Schultz, C. D. Balaban, A.S. Woods, Lipid imaging within the normal rat kidney using silver

nanoparticles by matrix-assisted laser desorption/ionization mass spectrometry, Kidney Int. 88 (2015) 186–192, https://doi.org/10.1038/KI.2015.3.

[206] G. Hussain, H. Anwar, A. Rasul, A. Imran, M. Qasim, S. Zafar, M. Imran, S.K. S. Kamran, N. Aziz, A. Razzaq, W. Ahmad, A. Shabbir, J. Iqbal, S.M. Baig, M. Ali, J.L. Gonzalez de Aguilar, T. Sun, A. Muhammad, A. Muhammad Umair, Lipids as biomarkers of brain disorders, Crit. Rev. Food Sci. Nutr. 60 (2020) 351–374, https://doi.org/10.1080/10408398.2018.1529653.

[207] M.M.B. Nielsen, K.L. Lambertsen, B.H. Clausen, M. Meyer, D.R. Bhandari, S. T. Larsen, S.S. Poulsen, B. Spengler, C. Janfelt, H.S. Hansen, Mass spectrometry imaging of biomarker lipids for phagocytosis and signalling during focal cerebral ischaemia, Sci. Rep. 6 (1 6) (2016) 1–14, https://doi.org/10.1038/srep39571, 2016.

[208] L. Yang, M. Li, Y. Shan, S. Shen, Y. Bai, H. Liu, Recent advances in lipidomics for disease research, J. Separ. Sci. 39 (2016) 38–50, https://doi.org/10.1002/JSSC.201500899.

[209] S.R. Ellis, J. Soltwisch, Mass Spectrometry Imaging of Lipids, Mass Spectrometry for Lipidomics: Methods and Applications, 2023, pp. 117–150, https://doi.org/10.1002/9783527836512.CH5.

[210] D. Gode, D.A. Volmer, Lipid imaging by mass spectrometry – a review, Analyst 138 (2013) 1289–1315, https://doi.org/10.1039/C2AN36337B.

[211] R.M. Adibhatla, J.F. Hatcher, Role of lipids in brain injury and diseases, Future Lipidol. 2 (2007) 403, https://doi.org/10.2217/17460875.2.4.403.

[212] D. Jha, K. Blennow, H. Zetterberg, J.N. Savas, J. Hanrieder, Spatial neurolipidomics—MALDI mass spectrometry imaging of lipids in brain pathologies, J. Mass Spectrom. 59 (2024) e5008, https://doi.org/10.1002/JMS.5008.

[213] M.E. Kurczy, Z.J. Zhu, J. Ivanisevic, A.M. Schuyler, K. Lalwani, A.F. Santidrian, J. M. David, A. Giddabasappa, A.J. Roberts, H.J. Olivos, P.J. O'Brien, L. Franco, M. W. Fields, L.P. Paris, M. Friedlander, C.H. Johnson, A.A. Epstein, H.E. Gendelman, M.R. Wood, B.H. Felding, G.J. Patti, M.E. Spilker, G. Siuzdak, Comprehensive bioimaging with fluorinated nanoparticles using breathable liquids, Nat. Commun. 6 (1 6) (2015) 1–8, https://doi.org/10.1038/ncomms6998, 2015.

[214] N. Goto-Inoue, T. Hayasaka, N. Zaima, Y. Kashiwagi, M. Yamamoto, M. Nakamoto, M. Setou, The detection of glycosphingolipids in brain tissue sections by imaging mass spectrometry using gold nanoparticles, J. Am. Soc. Mass Spectrom. 21 (2010) 1940–1943, https://doi.org/10.1016/J.JASMS.2010.08.002.

[215] S.N. Jackson, M. Ugarov, T. Egan, J.D. Post, D. Langlais, J.A. Schultz, A.S. Woods, MALDI-ion mobility-TOFMS imaging of lipids in rat brain tissue, J. Mass Spectrom. 42 (2007) 1093–1098, https://doi.org/10.1002/JMS.1245.

[216] H.W. Tang, M.Y.M. Wong, W. Lam, Y.C. Cheng, C.M. Che, K.M. Ng, Molecular histology analysis by matrix-assisted laser desorption/ionization imaging mass spectrometry using gold nanoparticles as matrix, Rapid Commun. Mass Spectrom. 25 (2011) 3690–3696, https://doi.org/10.1002/RCM.5281.

[217] J.Y. Kim, E.S. Seo, H. Kim, J.W. Park, D.K. Lim, D.W. Moon, Atmospheric pressure mass spectrometric imaging of live hippocampal tissue slices with subcellular spatial resolution, Nat. Commun. 8 (1 8) (2017) 1–13, https://doi.org/10.1038/s41467-017-02216-6, 2017.

[218] J. Li, J. Liu, Z. Liu, Y. Tan, X. Liu, F. Wang, Water-soluble Au nanoclusters for multiplexed mass spectrometry imaging, Chemical Communications 53 (2017) 12688–12691, https://doi.org/10.1039/C7CC07484K.

[219] N.T.N. Phan, A.S. Mohammadi, M. Dowlatshahi Pour, A.G. Ewing, Laser desorption ionization mass spectrometry imaging of drosophila brain using matrix sublimation versus modification with nanoparticles, Anal. Chem. 88 (2016) 1734–1741, https://doi.org/10.1021/ACS.ANALCHEM.5B03942.

[220] J.Y. Kim, E.S. Seo, H.J. Lim, H. Kim, J.W. Park, H.H. Shin, D.K. Lim, D.W. Moon, Nanomaterials and continuous wave laser-based efficient desorption for atmospheric pressure mass spectrometric imaging of live hippocampal tissue slices, RSC Adv. 8 (2018) 8021–8025, https://doi.org/10.1039/C8RA00038G.

[221] W.H. Müller, A. Verdin, C. Kune, J. Far, E. De Pauw, C. Malherbe, G. Eppe, Dual-polarity SALDI FT-ICR MS imaging and Kendrick mass defect data filtering for lipid analysis, Anal. Bioanal. Chem. 413 (2021) 2821–2830, https://doi.org/10.1007/S00216-020-03020-W.

[222] D. Chen, M. Du, Y. Huang, Y. Xu, Y. Chen, L. Ma, Q. Xie, X. Zhu, Z. Chen, H. Xu, X. Wu, Z. Yin, Plasmonic polydopamine-modified TiO2 nanotube substrates for surface-assisted laser desorption/ionization mass spectrometry imaging, Nano Res. 16 (2023) 3028–3039, https://doi.org/10.1007/S12274-022-4924-Z.

[223] R. Sun, W. Tang, B. Li, Gold-TiO2@gallic acid nanospheres for enhanced surface-assisted laser desorption/ionization mass spectrometry imaging, Appl. Mater. Today 26 (2022) 101336, https://doi.org/10.1016/J.APMT.2021.101336.

[224] D. Chen, Y. Xu, Y. Huang, Y. Chen, Y. Zhao, B. Yan, X. Zhu, Z. Chen, H. Xu, Z. Yin, X. Wu, Mapping molecular signatures in plant leaves, flowers, and fruits by a TiO2 nanotube-based plasmonic chip for imprint mass spectrometry imaging, ACS Agricult. Sci. Tech. 3 (2023) 119–130, https://doi.org/10.1021/ACSAGSCITECH.2C00254.

[225] S. Owega, E.P.C. Lai, Silver cationization of thia fatty acids and esters in laser desorption/ionization time-of-flight mass spectrometry, J. Mass Spectrom. 34 (1999) 872–879, https://doi.org/10.1002/(SICI)1096-9888(199908)34:8.

[226] E.P.C. Lai, S. Owega, R. Kulczycki, Time-of-flight mass spectrometry of bioorganic molecules by laser ablation of silver thin film substrates and particles, J. Mass Spectrom. 33 (1998) 554–564, https://doi.org/10.1002/(SICI)1096-9888(199806)33:6.

[227] T. Yalcin, D.C. Schriemer, L. Li, Matrix-assisted laser desorption ionization time-of-flight mass spectrometry for the analysis of polydienes, J. Am. Soc. Mass Spectrom. 8 (1997) 1220–1229, https://doi.org/10.1016/S1044-0305(97)00192-X.

[228] A. Roux, L. Muller, S.N. Jackson, J. Post, K. Baldwin, B. Hoffer, C.D. Balaban, D. Barbacci, J.A. Schultz, S. Gouty, B.M. Cox, A.S. Woods, Mass spectrometry imaging of rat brain lipid profile changes over time following traumatic brain injury, J. Neurosci. Methods 272 (2016) 19–32, https://doi.org/10.1016/J.JNEUMETH.2016.02.004.

[229] M. Guan, Z. Zhang, S. Li, J. Liu, L. Liu, H. Yang, Y. Zhang, T. Wang, Z. Zhao, Silver nanoparticles as matrix for MALDI FTICR MS profiling and imaging of diverse lipids in brain, Talanta 179 (2018) 624–631, https://doi.org/10.1016/J.TALANTA.2017.11.067.

[230] C. Han, S. Li, Q. Yue, N. Li, H. Yang, Z. Zhao, Polydopamine-capped AgNPs as a novel matrix overcoming the ion suppression of phosphatidylcholine for MALDI MS comprehensive imaging of glycerophospholipids and sphingolipids in impact-induced injured brain, Analyst 144 (2019) 6304–6312, https://doi.org/10.1039/C9AN01361J.

[231] E. Yang, F. Fournelle, P. Chaurand, Silver spray deposition for AgLDI imaging MS of cholesterol and other olefins on thin tissue sections, J. Mass Spectrom. 55 (2020) e4428, https://doi.org/10.1002/JMS.4428.

[232] Q. Wu, J.L. Chu, S.S. Rubakhin, M.U. Gillette, J.V. Sweedler, Dopamine-modified TiO 2 monolith-assisted LDI MS imaging for simultaneous localization of small metabolites and lipids in mouse brain tissue with enhanced detection selectivity and sensitivity, Chem. Sci. 8 (2017) 3926–3938, https://doi.org/10.1039/C7SC00937B.

[233] Y. Zhou, Q. Wu, Z. Zhao, Y. Wang, H. Lu, Photocatalytic degradation-based ambient mass spectrometry imaging for enhancing detection coverage of poorly-ionizable lipidomes, Talanta 270 (2024) 125564, https://doi.org/10.1016/J.TALANTA.2023.125564.

[234] C. Gao, Y. Wang, H. Zhang, W. Hang, Titania nanosheet as a matrix for surface-assisted laser desorption/ionization mass spectrometry analysis and imaging, Anal. Chem. 95 (2023) 650–658, https://doi.org/10.1021/ACS.ANALCHEM.2C01878.

[235] J. Hausser, U. Alon, Tumour heterogeneity and the evolutionary trade-offs of cancer, Nat. Rev. Cancer 20 (4 20) (2020) 247–257, https://doi.org/10.1038/s41568-020-0241-6, 2020.

[236] K.D. Duncan, H. Pětrošová, J.J. Lum, D.R. Goodlett, Mass spectrometry imaging methods for visualizing tumor heterogeneity, Curr. Opin. Biotechnol. 86 (2024) 103068, https://doi.org/10.1016/J.COPBIO.2024.103068.

[237] X. Ma, F.M. Fernández, Advances in mass spectrometry imaging for spatial cancer metabolomics, Mass Spectrom. Rev. 43 (2024) 235–268, https://doi.org/10.1002/MAS.21804.

[238] R.C. Huang, W.J. Chiu, I. Po-Jung Lai, C.C. Huang, Multivalent Aptamer/Gold nanoparticle–modified graphene oxide for mass spectrometry–based tumor tissue imaging, Sci. Rep. 5 (1 5) (2015) 1–10, https://doi.org/10.1038/srep10292, 2015.

[239] J. Nizioł, K. Ossoliński, T. Ossoliński, A. Ossolińska, V. Bonifay, J. Sekuła, Z. Dobrowolski, J. Sunner, I. Beech, T. Ruman, Surface-transfer mass spectrometry imaging of renal tissue on gold nanoparticle enhanced target, Anal. Chem. 88 (2016) 7365–7371, https://doi.org/10.1021/ACS.ANALCHEM.6B01859.

[240] A. Arendowski, J. Nizioł, K. Ossoliński, A. Ossolińska, T. Ossoliński, Z. Dobrowolski, T. Ruman, Laser desorption/ionization MS Imaging of Cancer Kidney Tissue on Silver nanoparticle-enhanced Target, vol. 10, 2017, pp. 83–94, https://doi.org/10.4155/BIO-2017-0195, 10.4155/Bio-2017-0195.

[241] J. Nizioł, J. Sunner, I. Beech, K. Ossoliński, A. Ossolińska, T. Ossoliński, A. Płaza, T. Ruman, Localization of metabolites of human kidney tissue with infrared laser-based selected reaction monitoring mass spectrometry imaging and Silver-109 nanoparticle-based surface assisted laser desorption/ionization mass spectrometry imaging, Anal. Chem. 92 (2020) 4251–4258, https://doi.org/10.1021/ACS.ANALCHEM.9B04580.

[242] K. Ossoliński, T. Ruman, T. Ossoliński, A. Ossolińska, A. Arendowski, A. Kołodziej, A. Płaza-Altamer, J. Nizioł, Monoisotopic silver nanoparticles-based mass spectrometry imaging of human bladder cancer tissue: biomarker discovery, Adv. Med. Sci. 68 (2023) 38–45, https://doi.org/10.1016/J.ADVMS.2022.12.002.

[243] M. Dufresne, J.F. Masson, P. Chaurand, Sodium-doped gold-assisted laser desorption ionization for enhanced imaging mass spectrometry of triacylglycerols from thin tissue sections, Anal. Chem. 88 (2016) 6018–6025, https://doi.org/10.1021/ACS.ANALCHEM.6B01141.

[244] A. Palermo, E.M. Forsberg, B. Warth, A.E. Aisporna, E. Billings, E. Kuang, H. P. Benton, D. Berry, G. Siuzdak, Fluorinated gold nanoparticles for nanostructure imaging mass spectrometry, ACS Nano 12 (2018) 6938–6948, https://doi.org/10.1021/ACSNANO.8B02376.

[245] S.A. Iakab, P. Ràfols, M. Tajes, X. Correig-Blanchar, M. García-Altares, Gold nanoparticle-assisted black silicon substrates for mass spectrometry imaging applications, ACS Nano 14 (2020) 6785–6794, https://doi.org/10.1021/ACSNANO.0C00201.

[246] M. Du, D. Chen, Y. Chen, Y. Huang, L. Ma, Q. Xie, Y. Xu, X. Zhu, Z. Chen, Z. Yin, H. Xu, X. Wu, Plasmonic gold nanoshell-assisted laser desorption/ionization mass spectrometry for small-biomolecule analysis and tissue imaging, ACS Appl. Nano Mater. 5 (2022) 9633–9645, https://doi.org/10.1021/ACSANM.2C01850.

[247] Y. Zhao, R. Boukherroub, G. Xu, H. Li, R.S. Zhao, Q. Wei, X. Yu, X. Chen, Au@BN-enhanced laser desorption/ionization mass spectrometry and imaging for determination of fipronil and its metabolites in food and biological samples, Food Chem. 418 (2023) 135935, https://doi.org/10.1016/J.FOODCHEM.2023.135935.

[248] N.H. Patterson, R.J. Doonan, S.S. Daskalopoulou, M. Dufresne, S. Lenglet, F. Montecucco, A. Thomas, P. Chaurand, Three-dimensional imaging MS of lipids

in atherosclerotic plaques: open-source methods for reconstruction and analysis, Proteomics 16 (2016) 1642–1651, https://doi.org/10.1002/PMIC.201500490.

[249] A.N. Al-Thani, A.G. Jan, M. Abbas, M. Geetha, K.K. Sadasivuni, Nanoparticles in cancer theragnostic and drug delivery: a comprehensive review, Life Sci. 352 (2024) 122899, https://doi.org/10.1016/J.LFS.2024.122899.

[250] S. Giordano, V. Pifferi, L. Morosi, M. Morelli, L. Falciola, G. Cappelletti, S. Visentin, S.A. Licandro, R. Frapolli, M. Zucchetti, R. Pastorelli, L. Brunelli, M. D'Incalci, E. Davoli, A nanostructured matrices assessment to study drug distribution in solid tumor tissues by mass spectrometry imaging, Nanomaterials (Basel) 7 (2017) 71, https://doi.org/10.3390/NANO7030071, 7 (2017) 71.

[251] O.J.R. Gustafsson, T.M. Guinan, D. Rudd, H. Kobus, K. Benkendorff, N. H. Voelcker, Metabolite mapping by consecutive nanostructure and silver-assisted mass spectrometry imaging on tissue sections, Rapid Commun. Mass Spectrom. 31 (2017) 991–1000, https://doi.org/10.1002/RCM.7869.

[252] C.M. de Almeida, N.A. dos Santos, V. Lacerda, X. Ma, F.M. Fernández, W. Romão, Applications of MALDI mass spectrometry in forensic science, Anal. Bioanal. Chem. 24 416 (2024) 5255–5280, https://doi.org/10.1007/S00216-024-05470-Y, 2024 416.

[253] M.O. Amin, E. Al-Hetlani, Matrix- and surface-assisted laser desorption/ionization–mass spectrometry analysis of fingermark components for forensic studies: current trends and future prospects, Anal. Bioanal. Chem. 416 (2024) 3751–3764, https://doi.org/10.1007/S00216-024-05297-7.

[254] H.W. Tang, M.Y.M. Wong, S.L.F. Chan, C.M. Che, K.M. Ng, Molecular imaging of banknote and questioned document using solvent-free gold nanoparticle-assisted laser desorption/ionization imaging mass spectrometry, Anal. Chem. 83 (2011) 453–458, https://doi.org/10.1021/AC1020485.

[255] N. Lauzon, M. Dufresne, V. Chauhan, P. Chaurand, Development of laser desorption imaging mass spectrometry methods to investigate the molecular composition of latent fingermarks, J. Am. Soc. Mass Spectrom. 26 (2015) 878–886, https://doi.org/10.1007/S13361-015-1123-0.

[256] N. Lauzon, M. Dufresne, A. Beaudoin, P. Chaurand, Forensic analysis of latent fingermarks by silver-assisted LDI imaging MS on nonconductive surfaces, J. Mass Spectrom. 52 (2017) 397–404, https://doi.org/10.1002/JMS.3938.

[257] N. Lauzon, P. Chaurand, Detection of exogenous substances in latent fingermarks by silver-assisted LDI imaging MS: perspectives in forensic sciences, Analyst 143 (2018) 3586–3594, https://doi.org/10.1039/C8AN00688A.

[258] H. Yang, S. Li, Q. Zhang, Z. Wang, N. Li, C. Han, Q. Huo, Z. Zhao, Combination of electrospray deposition technology of TiO2 nanoparticles and MALDI FTICR MSI for identification of fingerprint morphology and latent components, Talanta 198 (2019) 310–315, https://doi.org/10.1016/J.TALANTA.2019.02.007.

[259] P. Hinners, Y.J. Lee, Mass spectrometry imaging of latent fingerprints using titanium oxide development powder as an existing matrix, J. Mass Spectrom. 55 (2020) e4631, https://doi.org/10.1002/JMS.4631.

[260] Z. Yin, W. Huang, K. Li, A.R. Fernie, S. Yan, Advances in mass spectrometry imaging for plant metabolomics—Expanding the analytical toolbox, Plant J. 119 (2024) 2168–2180, https://doi.org/10.1111/TPJ.16924.

[261] Y.-J. Chen, H.-S. Zeng, H. Jin, H. Wang, Applications of mass spectrometry imaging in botanical research, Advan. Biotech. 2 (1 2) (2024) 1–20, https://doi.org/10.1007/S44307-024-00014-Y, 2024.

[262] G. Zhang, H. Zheng, X. Wang, S. Han, W. Liu, C. Sun, Q. Hu, C. Ma, Flexible substrate-based mass spectrometry platform for in situ non-destructive molecular imaging of living plants, Plant Biotechnol. J. (2024), https://doi.org/10.1111/PBI.14482.

[263] M. Misiorek, J. Sekuła, T. Ruman, Mass spectrometry imaging of low molecular weight compounds in garlic (Allium sativum L.) with gold nanoparticle enhanced target, Phytochem. Anal. 28 (2017) 479–486, https://doi.org/10.1002/PCA.2696.

[264] A. Arendowski, T. Ruman, Laser desorption/ionisation mass spectrometry imaging of European yew (Taxus baccata) on gold nanoparticle-enhanced target, Phytochem. Anal. 28 (2017) 448–453, https://doi.org/10.1002/PCA.2693.

[265] S. Yang, L. Zhan, C. Liu, L. Fu, R. Chen, Z. Nie, Mass spectrometry imaging of small molecule in situ in Lepidium meyenii (Maca) using gold nanoparticles matrix, Microchem. J. 150 (2019) 104190, https://doi.org/10.1016/J.MICROC.2019.104190.

[266] P. Li, Y. Chen, Q. Xie, Y. Xu, Z. Li, Y. Li, Z. Yin, X. Zhu, H. Xu, X. Wu, Spatiotemporal visualization of the synthesis and accumulation of rotenone in Derris elliptica roots using mass spectrometry imaging, Advan. Agrochem. 2 (2023) 340–348, https://doi.org/10.1016/J.AAC.2023.07.002.

[267] X.N. Wang, W. Tang, A. Gordon, H.Y. Wang, L. Xu, P. Li, B. Li, Porous TiO2Film immobilized with gold nanoparticles for dual-polarity SALDI MS detection and imaging, ACS Appl. Mater. Interfaces 12 (2020) 42567–42575, https://doi.org/10.1021/ACSAMI.0C12949.

[268] X.N. Wang, B. Li, Monolithic gold Nanoparticles/Thiol-β-cyclodextrin-Functionalized TiO2 nanowires for enhanced SALDI MS detection and imaging of natural products, Anal. Chem. 94 (2022) 952–959, https://doi.org/10.1021/ACS.ANALCHEM.1C03764.

[269] Y.L. Shen, S.J. Zhuang, F. Yang, C. Gong, X. Xu, Prefabricated platinum nanomaterial matrix for MALDI-MS imaging of oligosaccharides and lipids in plant tissues, Front. Plant Sci. 14 (2023) 1105374, https://doi.org/10.3389/FPLS.2023.1105374.

[270] K. Shiono, S. Taira, Imaging of multiple plant hormones in roots of rice (Oryza sativa) using nanoparticle-assisted laser desorption/ionization mass spectrometry, J. Agric. Food Chem. 68 (2020) 6770–6775, https://doi.org/10.1021/ACS.JAFC.0C00749.

[271] L. Xu, M. Kliman, J.G. Forsythe, Z. Korade, A.B. Hmelo, N.A. Porter, J.A. McLean, Profiling and imaging ion mobility-mass spectrometry analysis of cholesterol and 7-Dehydrocholesterol in cells via sputtered silver MALDI, J. Am. Soc. Mass Spectrom. 26 (2015) 924–933, https://doi.org/10.1007/S13361-015-1131-0.

[272] S.A. Iakab, G. Baquer, M. Lafuente, M.P. Pina, J.L. Ramírez, P. Ràfols, X. Correig-Blanchar, M. García-Altares, SALDI-MS and SERS multimodal imaging: one nanostructured substrate to rule them both, Anal. Chem. 94 (2022) 2785–2793, https://doi.org/10.1021/ACS.ANALCHEM.1C04118.

[273] V.L. Brown, Q. Liu, L. He, Matrix-enhanced surface-assisted laser desorption/ionization mass spectrometry (ME-SALDI-MS) for mass spectrometry imaging of small molecules, Methods Mol. Biol. 1203 (2015) 175–184, https://doi.org/10.1007/978-1-4939-1357-2_17.

[274] J. Sekuła, J. Nizioł, W. Rode, T. Ruman, Gold nanoparticle-enhanced target (AuNPET) as universal solution for laser desorption/ionization mass spectrometry analysis and imaging of low molecular weight compounds, Anal. Chim. Acta 875 (2015) 61–72, https://doi.org/10.1016/J.ACA.2015.01.046.

[275] M.S. Dalgic, S. Weidner, Solvent-free sample preparation for matrix-assisted laser desorption/ionization time-of-flight mass spectrometry of polymer blends, Rapid Commun. Mass Spectrom. 38 (2024), https://doi.org/10.1002/RCM.9756.

[276] P. Szczyglewska, A. Feliczak-Guzik, I. Nowak, Nanotechnology–general aspects: a chemical reduction approach to the synthesis of nanoparticles, Molecules 28 (2023) 4932, https://doi.org/10.3390/MOLECULES28134932, 4932 28 (2023.

[277] S. Verma, R. Gokhale, D.J. Burgess, A comparative study of top-down and bottom-up approaches for the preparation of micro/nanosuspensions, Int. J. Pharm. 380 (2009) 216–222, https://doi.org/10.1016/J.IJPHARM.2009.07.005.

[278] Y. Khan, H. Sadia, S.Z. Ali Shah, M.N. Khan, A.A. Shah, N. Ullah, M.F. Ullah, H. Bibi, O.T. Bafakeeh, N. Ben Khedher, S.M. Eldin, B.M. Fadhl, M.I. Khan, Classification, synthetic, and characterization approaches to nanoparticles, and their applications in various fields of nanotechnology: a review, Catalysts 12 (2022) 1386, https://doi.org/10.3390/CATAL12111386, 1386 12 (2022.

[279] M. Talaikis, L. Mikoliunaite, A.M. Gkouzi, V. Petrikaitė, E. Stankevičius, A. Drabavičius, A. Selskis, R. Juškėnas, G. Niaura, Multiwavelength SERS of magneto-plasmonic nanoparticles obtained by combined laser ablation and solvothermal methods, ACS Omega 8 (2023) 49396–49405, https://doi.org/10.1021/ACSOMEGA.3C08007.

[280] A. Mondal, N.R. Jana, Surfactant-free, stable noble metal-graphene nanocomposite as high performance electrocatalyst, ACS Catal. 4 (2014) 593–599, https://doi.org/10.1021/CS401032P.

[281] M. Iordache, A. Oubraham, I.S. Sorlei, F.A. Lungu, C. Capris, T. Popescu, A. Marinoiu, Noble metals functionalized on graphene oxide obtained by different methods—new catalytic materials, Nanomaterials (Basel) 13 (2023) 783, https://doi.org/10.3390/NANO13040783. Page 783 13 (2023.

[282] C.V. Hoang, K. Hayashi, Y. Ito, N. Gorai, G. Allison, X. Shi, Q. Sun, Z. Cheng, K. Ueno, K. Goda, H. Misawa, Interplay of hot electrons from localized and propagating plasmons, Nat. Commun. 8 (1 8) (2017) 1–8, https://doi.org/10.1038/s41467-017-00815-x, 2017.

[283] P.R. Rauta, P.M. Hallur, A. Chaubey, Gold nanoparticle-based rapid detection and isolation of cells using ligand-receptor chemistry, Sci. Rep. 8 (1 8) (2018) 1–13, https://doi.org/10.1038/s41598-018-21068-8, 2018.

[284] S. Geddes, B. Nichols, S. Flemer, J. Eisenhauer, J. Zahardis, G.A. Petrucci, Near-infrared laser desorption/ionization aerosol mass spectrometry for investigating primary and secondary organic aerosols under low loading conditions, Anal. Chem. 82 (2010) 7915–7923, https://doi.org/10.1021/AC1013354.

[285] J. Radnik, V.D. Hodoroaba, H. Jungnickel, J. Tentschert, A. Luch, V. Sogne, F. Meier, L. Burr, D. Schmid, C. Schlager, T.H. Yoon, R. Peters, S.M. Briffa, E. Valsami-Jones, Automation and standardization—A coupled approach towards reproducible sample preparation protocols for nanomaterial analysis, Molecules 27 (2022) 985, https://doi.org/10.3390/MOLECULES27030985, 985 27 (2022.

[286] X. Ding, K. Liu, Z. Shi, Laser desorption/ablation postionization mass spectrometry: recent progress in bioanalytical applications, Mass Spectrom. Rev. 40 (2021) 566–605, https://doi.org/10.1002/MAS.21649.

[287] P. Ràfols, D. Vilalta, S. Torres, R. Calavia, B. Heijs, L.A. McDonnell, J. Brezmes, E. del Castillo, O. Yanes, N. Ramírez, X. Correig, Assessing the potential of sputtered gold nanolayers in mass spectrometry imaging for metabolomics applications, PLoS One 13 (2018) e0208908, https://doi.org/10.1371/JOURNAL.PONE.0208908.

[288] A. Arendowski, J. Nizioł, K. Ossoliński, A. Ossolińska, T. Ossoliński, Z. Dobrowolski, T. Ruman, Laser desorption/ionization MS imaging of cancer kidney tissue on silver nanoparticle-enhanced target, Bioanalysis 10 (2018), https://doi.org/10.4155/bio-2017-0195.

[289] Q. Xie, Z. Li, Y. Chen, Y. Zhao, Y. Xu, Z. Hong, Z. Chen, Z. Zhang, H. Xu, Z. Yin, X. Wu, Mass spectrometry imaging reveals the morphology-dependent toxicological effects of nanosilvers on multiple organs of adult zebrafish (Danio rerio), Environ. Sci. Technol. 58 (2024) 10015–10027, https://doi.org/10.1021/ACS.EST.4C00655.

[290] B. Creran, B. Yan, D.F. Moyano, M.M. Gilbert, R.W. Vachet, V.M. Rotello, Laser desorption ionization mass spectrometric imaging of mass barcoded gold nanoparticles for security applications, Chemical Communications 48 (2012) 4543–4545, https://doi.org/10.1039/C2CC30499F.

[291] Y. Sun, D. Chen, X. Chen, X. Wu, Stress response of citrus leaves under mechanical damage and huanglongbing disease infection using plasmonic TiO2 nanotube substrate-based imprinting mass spectrometry imaging, Agronomy 14 (2024) 1797, https://doi.org/10.3390/AGRONOMY14081797/S1.

DSc, PhD Joanna Nizioł is an Associate Professor at the Faculty of Chemistry, Rzeszów University of Technology. She earned her habilitation degree in Chemical Technology in 2022. Her current research focuses on advancing laser desorption/ionization mass spectrometry (LDI-MS) and mass spectrometry imaging (MSI), as well as identifying and quantifying small-molecule compounds across various environmental, plant, food, and biological samples. She is also interested in identifying potential small-molecule cancer biomarkers using advanced analytical techniques, including nuclear magnetic resonance (NMR) spectroscopy and mass spectrometry (MS). Additionally, her expertise encompasses multidimensional statistical analysis in lipidomics and metabolomics.

M.Sc. Eng. Sumi Krupa received her master's degree from Rzeszów University of Technology in 2023. She is currently pursuing a Ph.D. in chemical engineering at Rzeszów University of Technology. Her research focuses on the development of new solutions in mass spectrometry imaging, such as nanoparticle-based matrices for laser desorption/ionization and 3D mass spectrometry imaging.

Eng. Wiktoria Szuberla earned her Bachelor's degree in Biotechnology from Rzeszów University of Technology in 2024. She is pursuing her Master's degree in the same field. Her research interests focus on advanced instrumental techniques, particularly their applications in biochemical analysis and diagnostics.

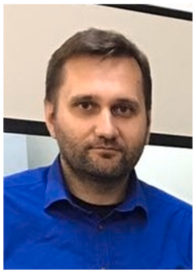

Prof. Dr. Hab. Eng. Tomasz Ruman (born 1980) is a full professor and a research and teaching employee at the Department of Inorganic and Analytical Chemistry at the Faculty of Chemistry of the Rzeszów University of Technology. He specializes, among others, in matrix-free methods for laser mass spectrometry, synthesis and characterization of nanostructures, and mass spectrometry imaging methods. He applies and optimizes new methods for the study of biological material - microbiological systems, physiological fluids, human, animal and plant tissues. This research has been expanded to include the application of new methods for new, small-molecule cancer biomarkers of kidney, prostate and bladder cancer. He has promoted six PhDs, five of whom worked in the area of new methods for laser mass spectrometry and mass spectrometry imaging. He is the designer and creator of the first experimental setup for direct 3D MSI. He published his research results in prestigious journals, for example Journal of Pharmaceutical Analysis, Analytical Chemistry, Scientific Reports, Analytica Chimica Acta, the Analyst, Metabolomics, Journal of Cultural Heritage, International Biodeterioration and Biodegradation. He is also the editor-in-chief of the local scientific journal Chemical Technology & Biotechnology. He is the author or co-author of 107 scientific publications (96 in the SCOPUS database) and his H-index is 22.

ACS Partner Journal

Journal of the American Society for
Mass Spectrometry

Open Access

This article is licensed under CC-BY 4.0

pubs.acs.org/jasms

Article

Fiber Laser-Generated Silver-109 Nanoparticles for Laser Desorption/Ionization Mass Spectrometry of Illicit Drugs

Sumi Krupa and Joanna Nizioł*

Cite This: *J. Am. Soc. Mass Spectrom.* 2024, 35, 1156−1167

Read Online

ACCESS | Metrics & More | Article Recommendations | Supporting Information

ABSTRACT: Cannabinoids and opioids are the most prominently used drugs in the world, with fentanyl being the main cause of drug overdose-related deaths. Monitoring drug use in groups as well as in individuals is an important forensic concern. Analytical methods, such as mass spectrometry (MS), have been found most useful for the identification of drug abuse on a small and large scale. Pulsed fiber laser 2D galvoscanner laser-generated nanomaterial (PFL 2D GS LGN) was obtained from monoisotopic silver-109. Nanomaterial was used for laser desorption/ionization mass spectrometry of selected illicit drug standards with standard high-resolution reflectron-based time-of-flight MALDI apparatus. Δ^9-THC, 11-OH-THC, 11-COOH-THC, fentanyl, codeine, 6-monoacetylmorphine (6-MAM), heroin, tramadol, and methadone were chosen as test compounds. Illicit drugs were tested in a concentration range from 100 μg/mL to 10 pg/mL, equating to 50 μg to 50 fg per measurement spot. For all analyzed compounds, identification and quantification by silver-109-assisted laser desorption/ionization (LDI) MS was possible, with uncommon $[M + {}^{109}Ag_3]^+$ and $[M - H]^+$ ions present for certain structures. The results of the quantitative analysis of drugs using silver-109 PFL 2D GS LGN for LDI MS are presented. Laser-generated NPs are proven to be useful for the analysis of selected drugs, with exceptionally good results for fentanyl monitoring in a broad range of concentrations.

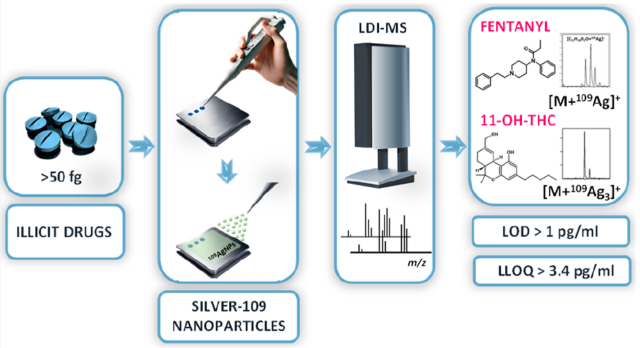

KEYWORDS: *cannabinoids, opioids, monoisotopic silver nanoparticles, mass spectrometry quantification*

Downloaded via RZESZOW UNIV OF TECHNOLOGY on March 30, 2026 at 08:20:28 (UTC).
See https://pubs.acs.org/sharingguidelines for options on how to legitimately share published articles.

1. INTRODUCTION

According to the United Nations Office on Drugs and Crime (UNODC) global estimates of the prevalence of drug use in 2021, the use of opioids, including opiates and prescription opioids, was determined to be 1.18% of the world population (0.72, 1.49),[1] which makes it over 3 times higher than in 2017.[2] The term opioids refers to exogenous compounds, both natural and synthetic, which bind to opioid receptors. Natural opiates, i.e. codeine, are obtained from the poppy plant as alkaloids constituting a substance known as opium.[3] The remaining opioids analyzed in this paper are either of synthetic or semisynthetic origin and metabolites. Among them, fentanyl continues to be the drug of choice due to being relatively easy to produce but most importantly having a high potency, 100 times higher than morphine.[4] The epidemic of fentanyl-induced overdose deaths in the United States started around the year 2015 with 9580 deaths connected to this cause and reached its first peak in 2017, amounting to 28 466 deaths. Since then, as of 2021, the amount of overdose-induced deaths caused by synthetic opioids, primarily fentanyl, increased roughly 2.5 times, with 70 601 deaths.[5,6] In contrast, the European Monitoring Centre for Drugs and Drug Addiction (EMCDDA) reports 49 confirmed deaths linked to fentanyl, with a minimum estimate of 137 deaths overall in Europe in the year 2021.[7]

Opioid use is the second most prevalent illicit drug use reported by UNODC, the first one being cannabis at 4.27% (3.08, 5.38). The most distinctive class of compounds found in cannabis plants are cannabinoids.[8] A part of this group, Δ^9-tetrahydrocannabinol (Δ^9-THC), is considered as the main compound contributing to the psychoactive effect of cannabis use. THC is metabolized in the human body, resulting in the formation of 11-hydroxy-Δ^9-THC (11-OH-THC) and 11-nor-9-carboxy-Δ^9-THC (11-COOH-THC).[9]

Mass spectrometry (MS) coupled with liquid (LC) or gas chromatography (GC) is currently the most widespread analytical technique for illicit drug identification. Several research studies focus on employing LC-MS in estimating illicit drug use in a population rather than in an individual. One of

Received: December 27, 2023
Revised: April 24, 2024
Accepted: April 26, 2024
Published: May 6, 2024

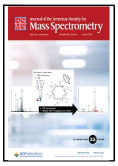

© 2024 The Authors. Published by
American Chemical Society

https://doi.org/10.1021/jasms.3c00454

those approaches is sewage forensics, which focuses on analyzing samples of wastewater from certain living areas.[10−12] For fast identification of illicit drugs in a specific suspect of drug use, approaches such as fluorescence-based lateral flow assay for THC detection in the saliva are used.[13] Another more conclusive technique is electrochemical detection, with a broad spectrum of solutions for various drugs, giving the possibility of testing oral fluids[14] or seized powders.[15]

Table 1. List of Identified Ions with Mean Signal Intensity and Signal-to-Noise Ratios of Analyzed Compounds at 100 μg/mL Concentration

compound	ion type	mean intensity	S/N
11-OH-THC	$[M + H]^+$	1024	7.7
	$[M + Na]^+$	3107	26.5
	$[M + {}^{109}Ag]^+$	26498	298.8
	$[M + {}^{109}Ag_3]^+$	8568	333.1
11-COOH-THC	$[M + H]^+$	1102	9.3
	$[M + {}^{109}Ag]^+$	17908	228.9
	$[M + {}^{109}Ag_3]^+$	3202	83.9
THC	$[M + {}^{109}Ag]^+$	398	7.7
fentanyl	$[M + H]^+$	6835	110.3
	$[M + Na]^+$	830	15.2
	$[M + {}^{109}Ag]^+$	18285	479.8
codeine	$[M + H]^+$	863	18.4
	$[M + Na]^+$	829	14.6
	$[M + K]^+$	369	6.6
	$[M + {}^{109}Ag]^+$	851	22.6
	$[M - H]^+$	10158	190.5
6-MAM	$[M + H]^+$	2154	16.4
	$[M + Na]^+$	660	7.3
	$[M + {}^{109}Ag]^+$	1912	29.4
	$[M - H]^+$	8887	119.8
heroin	$[M + H]^+$	1678	18.7
	$[M + Na]^+$	1687	20.3
	$[M + {}^{109}Ag]^+$	7241	124.2
	$[M - H]^+$	8286	120.2
tramadol	$[M + H]^+$	692	7.2
	$[M + {}^{109}Ag]^+$	5452	101.7
	$[M - H]^+$	11161	151.4
methadone	$[M + H]^+$	2894	32.0

In this study, the applied analytical method allowed for rapid screening for fentanyl and other illicit drugs. The sample preparation for ^{109}AgNP-assisted LDI MS is a matter of minutes, with the spectral data acquisition itself taking even less time.[16−18] Recently, our research has successfully applied this technique for both qualitative and quantitative analysis of low molecular weight compounds, including amino acids,[17−19] carboxylic acids,[20−24] and hormones.[25] Furthermore, this method has shown exceptional utility in analyzing micro-organisms[26−29] and various human biological samples such as serum,[30] urine,[30,31] and tissue. Notably, we have showcased its significant potential in mass spectrometry imaging (MSI), particularly in creating detailed molecular imprints of plant[32,33] and human tissues.[34−36] The resulting limit of detection for fentanyl acquired using silver-109-assisted LDI MS analysis illustrates the advantages of the method for the identification and quantification of fentanyl.

2. MATERIALS AND METHODS

2.1. Materials. All drugs were obtained from Sigma-Aldrich. The steel target was machined from H17 (1.4016) stainless steel. The steel target was cleaned by soaking in boiling solvents: toluene (3 × 100 mL for 30 s), chloroform (3 × 100 mL for 30 s), acetonitrile (3 × 100 mL for 30 s), and deionized water (3 × 100 mL for 30 s) before further use. The plate was dried in a high vacuum (ca. 0.01 mbar, 24 h). Solvents in use were of LC-MS grade, apart from water (18 MΩ·cm water produced locally).

2.2. PFL 2D GS Laser-Generated Nanomaterial (LGN) of Silver-109. Silver-109 foil used to produce nanoparticles (~1 mm thick, 99.7% isotopic purity) was bought from Trace Sciences International (USA). The foil was placed in a glass vessel and covered by acetonitrile, with a total solvent volume of 3 mL.

Laser ablation was conducted with a 1064 nm pulsed fiber laser (Raycus RFL-P20QE/A3). The ^{109}AgNPs suspension was prepared by 2 min of irradiation, with pulse energy of 0.8 mJ (100 ns pulse length) at a repetition rate of 40 kHz and scanning speed of 2000 mm/s. The ablation area was 4 × 4 mm. Suspension was transferred into a syringe immediately after ablation and used in the nebulization step.

2.3. Nebulization of ^{109}AgNPs Suspension. The nebulization process was controlled by dedicated software. The H17 steel plate was placed on the table of a translation system consisting of a motorized XY table powered by closed-loop servomotors. A glass syringe (1 mL) was filled with the suspension of silver-109 nanoparticles prepared earlier and placed in a syringe pump (250 μL/min). The 2D system table was directed by custom-made software with 10 mm/s translation speed using a sequence of movements prepared to uniformly cover a target plate. The nebulizer was a typical, standard flow Bruker ion source nebulizer. Argon at a pressure of 2 bar was used as the nebulizing gas. Studied standards were placed on the target plate before nebulization with an automatic pipet.

2.4. Standard Sample Preparation. Each compound standard was diluted with methanol to give a final concentration of 100 μg/mL. Lower concentrations were prepared by further dilution of ten-times higher concentration ones. Volumes of 0.5 μL (^{109}AgNPs) of selected drug solutions were placed directly on the target plate. After air drying, the target was covered with ^{109}AgNPs suspension as stated previously.

2.5. Human Sample Preparation. The serum and urine samples were obtained from a healthy volunteer during a medical examination conducted at Hospital John Paul II in Kolbuszowa, Poland, with the purpose of detecting urinary tract malignancies. The research project received approval from the Local Bioethics Committee of the University of Rzeszów (Poland), with permit number 2018/04/10. The study was carried out in compliance with relevant rules and legislation. A volume of approximately 2.6 mL of blood was obtained from the patient and thereafter subjected to centrifugation at a speed of 3000 rpm for a duration of 10 min at ambient temperature. Blood workup was performed in the hospital and by a legally entitled medical professional working in the hospital. The serum was subsequently isolated and preserved at a temperature of −80 °C until it was needed again. Blood serum and urine were diluted 500-times with ultrapure water, and then 100 μL of serum or urine or an equal volume of previously prepared fentanyl standard solutions in concentrations from 100 μg/mL to 10 pg/mL was added, resulting in concentrations of fentanyl in spiked

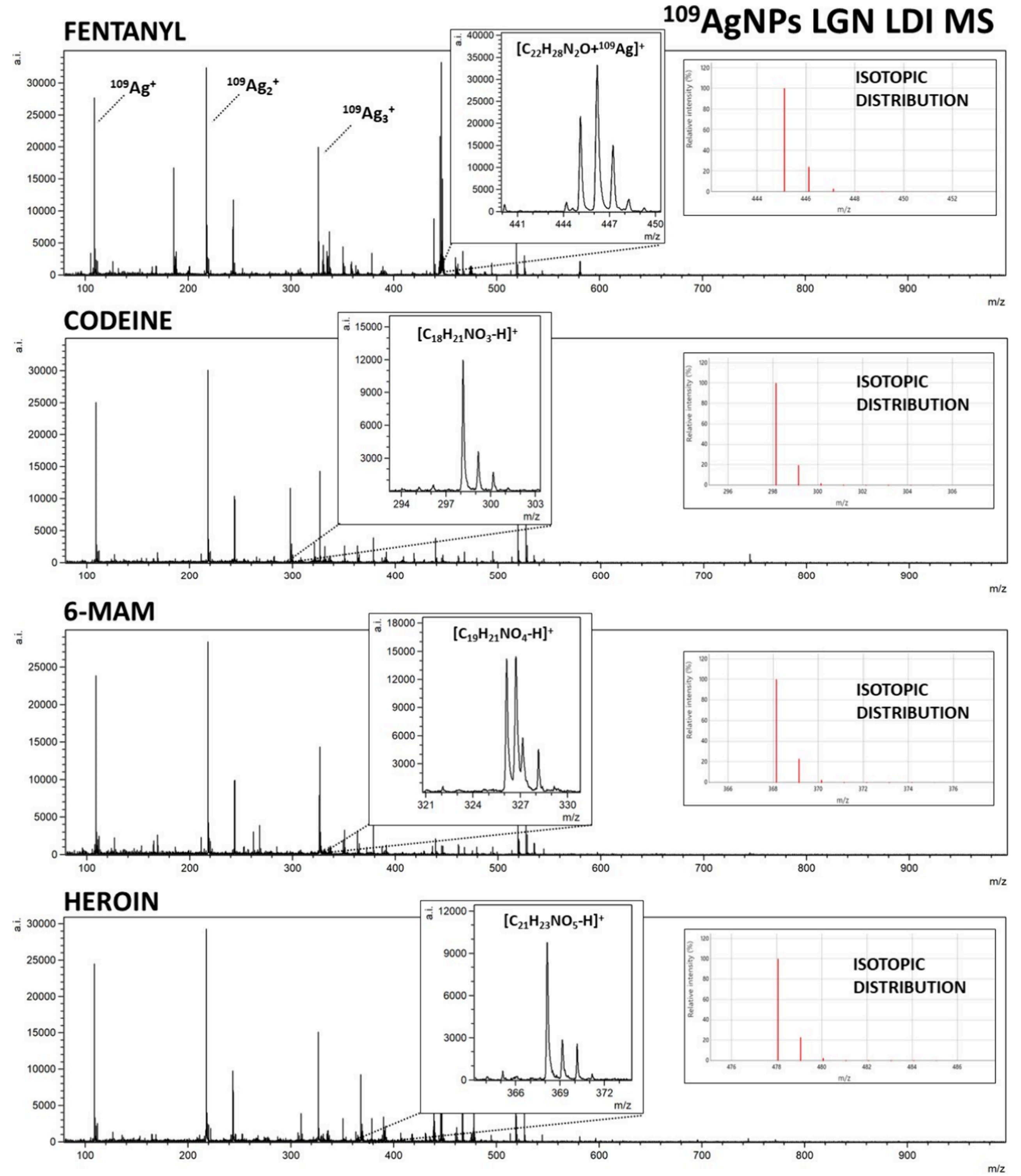

Figure 1. Mass spectra of opioids: fentanyl, codeine, 6-monoacetylmorphine (6-MAM), and heroin, obtained by ^{109}Ag-assisted LDI MS. The spectra correspond to a sample concentration of 100 μg/mL, equating to 50 ng of compound per measurement spot. Selected identified ions and their calculated isotopic distributions are presented on the spectra.

samples from 50 μg/mL to 5 pg/mL. The obtained samples were placed directly on a steel target plate (0.5 μL per spot) previously coated with ^{109}AgNPs.

2.6. LDI Mass Spectrometry. Laser desorption/ionization−time-of-flight (LDI-ToF) mass spectrometry experiments were performed in reflectron mode using a Bruker Autoflex Speed time-of-flight mass spectrometer equipped with a SmartBeam II laser (352 nm). Laser impulse energy was approximately 100 μJ, and the laser repetition rate was 1000 Hz. The total number of laser shots was 9000 for each spot. This amount of laser shots was divided into three, the points positioned at a distance of ca. 1/3 of the spot radius from its center. At each point, 3000 laser shots were made with default random walk applied. The measurement range was m/z 80−

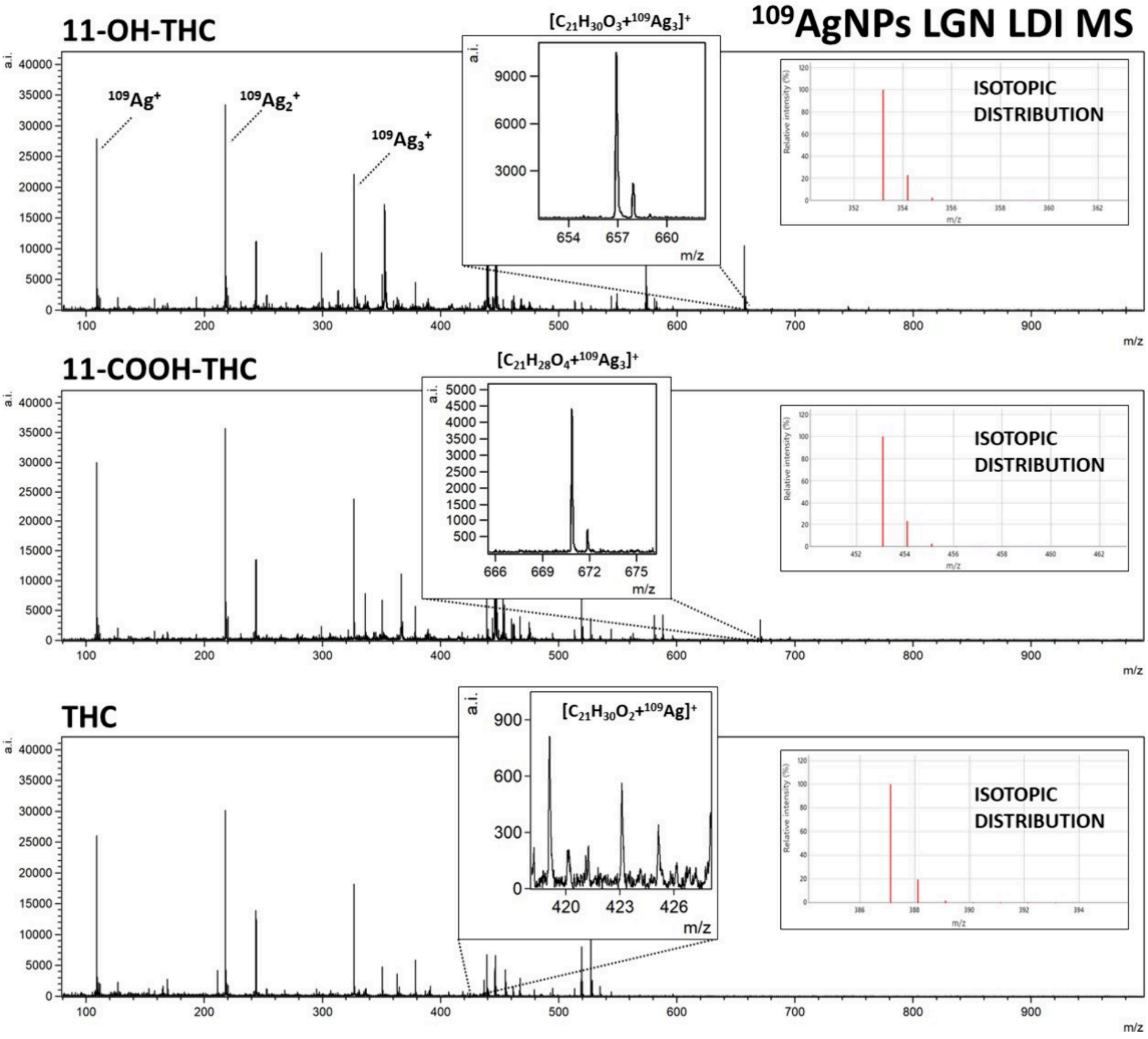

Figure 2. Mass spectra of THC and its metabolites, 11-OH-THC, and 11-COOH-THC, obtained by ^{109}Ag-assisted LDI MS. The spectra correspond to a sample concentration of 100 μg/mL, equating to 50 ng of compound per measurement spot. Selected identified ions and their isotopic distributions are presented on the spectra.

1000. Suppression was turned on typically for ions of m/z lower than 80. Reflector voltages used were 21 kV (the first) and 9.55 kV (the second). The data were calibrated and analyzed with FlexAnalysis (version 3.3) using a centroid calibration model. Mass calibration was performed using internal standards (silver-109 ions and clusters from ^{109}Ag$^+$ to ^{109}Ag$_9$$^+$).

3. RESULTS AND DISCUSSION

In this research, the applicability of ^{109}AgNPs-assisted laser desorption/ionization MS for identification and quantification of fentanyl and other drugs, such as THC and its two metabolites, as well as opioids, including tramadol, 6-monoacetylmorphine (6-MAM), codeine, methadone, and heroin, was presented. Silver-109 nanoparticle-enhanced LDI applicability for samples of various compositions has been presented by our team in the past.[19,21,25] Obtained mass spectra are presented in Figures 1−3. The list of identified ions with the average signal intensity and signal-to-noise ratio of the analyzed compounds at a concentration of 100 μg/mL is presented in Table 1.

For all of the analyzed opioids, except methadone, [M + ^{109}Ag]$^+$ ions were identified in corresponding spectra, which further confirms the validity of silver-109-nanoparticle-assisted LDI as an effective analytical method. Especially high signal intensity has been observed for [fentanyl + ^{109}Ag]$^+$ adduct ions, as well as for [11-OH-THC + ^{109}Ag]$^+$ (Figure 1) and [11-COOH-THC + ^{109}Ag]$^+$ (Figure 2). Nonetheless, the mass spectra of codeine, heroin, 6-MAM, and tramadol allowed for the identification of [M − H]$^+$ ions of significantly higher intensities than [M + ^{109}Ag]$^+$ ions of the given sample (Figures 1 and 3). The formation of deprotonated ions with positive charge is characteristic for tertiary amines. It is believed to be a result of photoionization caused by the UV laser used in the MALDI MS ion source. The mechanism of this process is explained as the

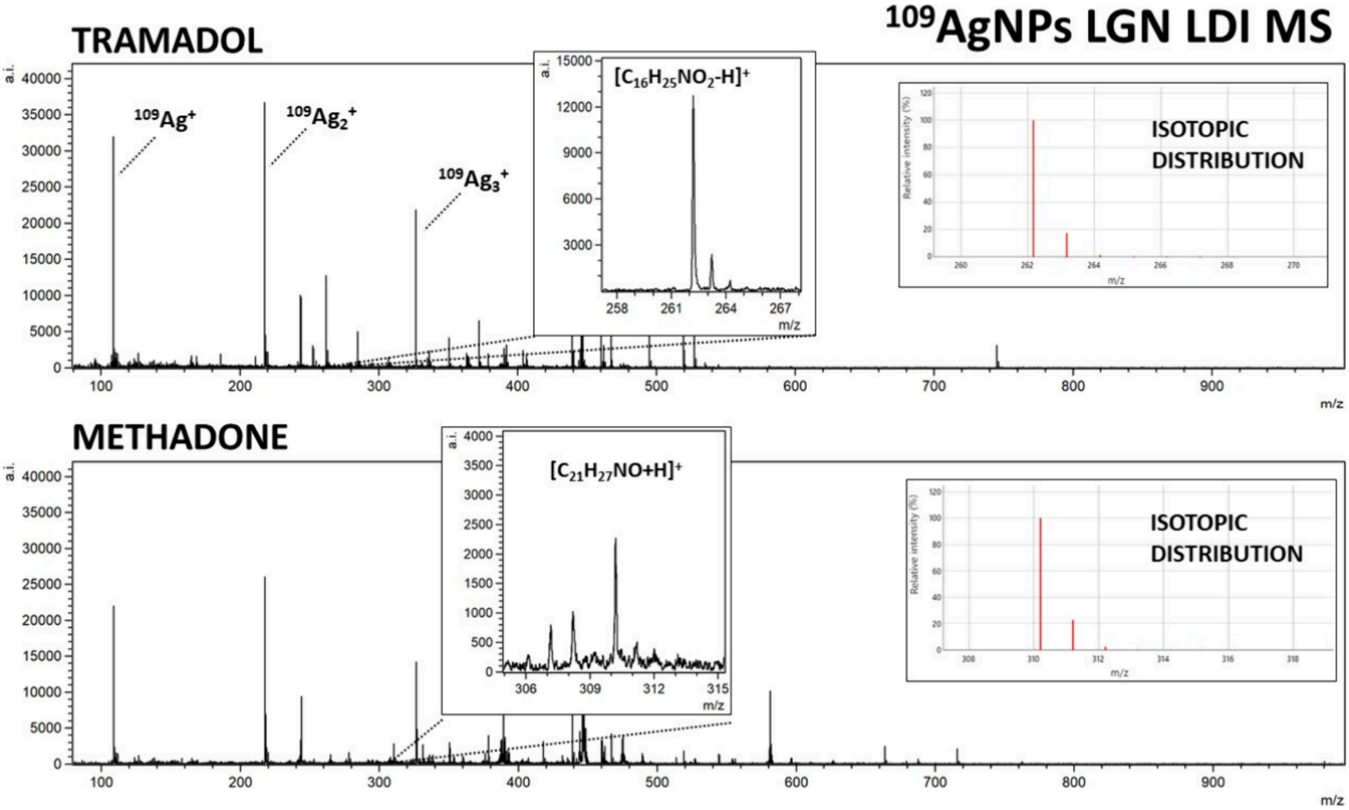

Figure 3. Mass spectra of tramadol and methadone obtained by ^{109}Ag-assisted LDI MS. The spectra correspond to a sample concentration of 100 μg/mL, equating to 50 ng of compound per measurement spot. Selected identified ions and their isotopic distributions are presented on the spectra.

Table 2. Limits of Detection (LOD), Limits of Quantification (LOQ), and Linearity R^2 for Tested Compounds

compound	LOD	LLOQ	R^2
11-OH-THC	538.92 ± 207.47 ng/mL	1796.41 ± 691.57 ng/mL	0.97
11-COOH-THC	6671.61 ± 202.18 ng/mL	22238.7 ± 6739.38 ng/mL	0.96
THC	39.13 ± 20.76 μg/mL	130.43 ± 69.23 μg/mL	0.98
fentanyl	1.03 ± 0.19 pg/mL	3.43 ± 0.66 pg/mL	0.98
codeine	61.22 ± 8.7 ng/mL	204.08 ± 29.01 ng/mL	0.94
6-MAM	57.14 ± 10.16 ng/mL	190.48 ± 33.87 ng/mL	0.97
heroin	8.22 ± 0.16 ng/mL	27.4 ± 0.53 ng/mL	0.86
tramadol	44.55 ± 29.98 ng/mL	148.51 ± 99.92 ng/mL	0.99
methadone	386.27 ± 8.93 ng/mL	1287.55 ± 297.51 ng/mL	0.96

initial protonation of the N atom, followed by deprotonation and formation of the C═N double bond.[37,38]

For THC and its metabolites, 11-OH-THC and 11-COOH-THC, the most prominent identified ion was $[M + {}^{109}Ag]^+$, with $[M + H]^+$ (for OH-THC and COOH-THC) and $[M + Na]^+$ (for OH-THC) also identifiable (Figure 2). Peaks of significant intensity corresponding to rarely appearing triatomic silver-109 cation adducts $[M + {}^{109}Ag_3]^+$ were also present for the two THC metabolites. Mentioned adducts have been recorded previously for amino acids[39] and other compounds.[40] While a distinct occurrence of those adducts has been documented previously for codeine,[41] the $[\text{codeine} + {}^{109}Ag_3]^+$ peak on the mass spectrum acquired in this research was not of significant intensity. An assumption can be made that the occurrence of $[M + {}^{109}Ag_3]^+$ ions has little correlation with the nature of the compound, rather depending on the conditions of the analysis. Sodium and potassium adducts were also identified for selected samples as presented in Table 1.

3.1. Quantification Results.

The measurements of analyzed standards were performed in the concentration range from 100 μg/mL to 10 pg/mL. Samples were placed on the target plate in a 0.5 μL volume equating to 50 ng to 50 fg of compound per spot. The limit of detection (LOD) was calculated based on the S/N ratio of the highest intensity adduct monoisotopic signal of 3, obtained from the mass spectra of the lowest concentration from each sample. The lower limit of quantification (LLOQ) was calculated using an S/N ratio of 10. A regression analysis of mean intensity as a function of sample concentration was conducted. The LOD, LLOQ results, and R^2 values for the linear regressions of the tested compounds are presented in Table 2.

Figure 4 presents the relations of all identified adduct ions' signal intensities against the concentration of the compound in the sample. For Δ^9-THC, the average signal intensity values were rather low, which might cause the quantification of said compound in lower concentrations to be unattainable. Nevertheless, both THC metabolites showed sufficient signal

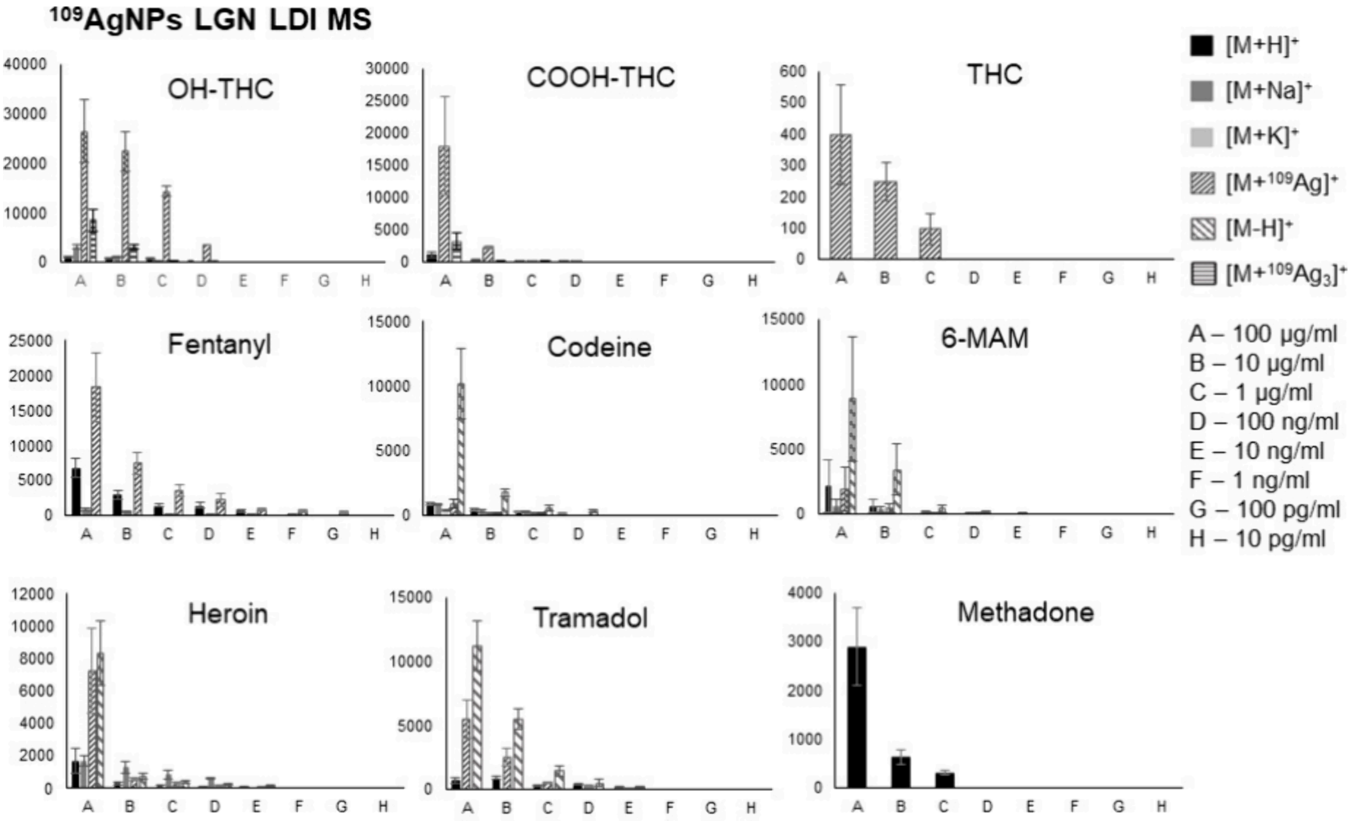

Figure 4. Relation of the mean intensity of adduct ions versus sample concentration, along with standard derivation for each measuring spot presented as bar charts for all tested compounds.

intensity, which suggests that the method might be suitable for the detection of THC-containing drug usage in humans in connection with the reasons stated previously. The results for most of the analyzed standards indicate that using ^{109}AgLGN for LDI MS has its usefulness in illicit drug identification and quantification within the used sample concentration range, making it suitable for regression analysis.

Figure 5 shows bar charts with corresponding linear regression functions. In the case of OH-THC and COOH-THC the $[M + ^{109}Ag_3]^+$ adducts were chosen for analysis; for THC and fentanyl, the $[M + ^{109}Ag]^+$ ions were used, for methadone, $[M + H]^+$ was the selected adduct ion, and for codeine, 6-MAM, heroin, and tramadol the $[M - H]^+$ ions were the most suitable. Additionally, Figures 6 and 7 present the selected ions of each analyzed compound, showcasing the decrease in signal intensity.

The first analyzed opioid was fentanyl, a synthetic analgesic. Despite structurally having traits of a tertiary amine, no significant signal intensities of $[M - H]^+$ ion were observed for said compound. Regardless of that, an exceptional result was obtained for the $[C_{22}H_{28}N_2O + ^{109}Ag]^+$ adduct ion. A logarithmic relationship between intensity and concentration was found for almost all analyzed concentrations, except the lowest one, in a range of 100 μg/mL to 100 pg/mL. LOD value was found to be 1.03 pg/mL (0.515 fg/per spot). The coefficient of determination found for acquired data was 0.98 (Figure 5 A). In the work of Angi et al. from 2019,[42] the UHPLC method coupled with single quadrupole mass spectrometry was used to determine 19 fentanyl analogues also using standard solutions diluted with methanol. The authors managed to obtain an LOD of 3 ng/mL for fentanyl. The LOD in this current research is approximately 3000 times lower than that reported in the LC-MS method, suggesting that ^{109}AgNP-assisted LDI MS is a powerful method of screening for fentanyl.

The 11-OH-THC adduct ion $[C_{21}H_{30}O_3 + ^{109}Ag_3]^+$ was identified in the four highest concentrations, from 100 μg/mL to 100 ng/mL. LOD was calculated to be 0.54 μg/mL (270 pg/per spot). As presented in Figure 5B, the linear regression function gave the coefficient of determination R^2 value of 0.97. For 11-COOH-THC, the triatomic silver cation adduct was also chosen for the regression analysis. The $[C_{21}H_{28}O_4 + ^{109}Ag_3]^+$ ion was found in the three highest sample concentrations, from 100 μg/mL to 1 μg/mL. LOD was found to be 6.67 μg/mL (3.34 ng/per spot). The R^2 value calculated by the regression analysis of this compound is 0.96 as seen in Figure 5B. For Δ^9-THC, only $[C_{21}H_{30}O_2 + ^{109}Ag]^+$ adduct ion has shown the logarithmic relationship of intensity on concentration. It was found in the three highest concentrations. The LOD value was calculated to be 39.13 μg/mL (19.57 ng/per spot) and the R^2 value was determined as 0.98. Referring to the previously mentioned study from Heo et al.,[43] the LOD and LOQ determined for THC were respectively 0.6 ng/mL and 0.0018 in methanol-diluted standard samples using UPLC−MS/MS with a triple quadrupole detector. The corresponding coefficient of determination was 0.9999. In the research conducted by Simões et al.,[44] the LOD values obtained from the calibration curve for standard solutions dissolved in methanol were 0.5 ng/mL for 11-OH-THC and THC-COOH and 0.5 ng/mL for THC.

Codeine, naturally found in opium poppy produced the highest intensity ion assigned to $[C_{18}H_{21}NO_3 - H]^+$ formula. It was identified as the four highest concentrations. The limit of detection calculated for codeine was 61.22 ng/mL (30.6 pg/per

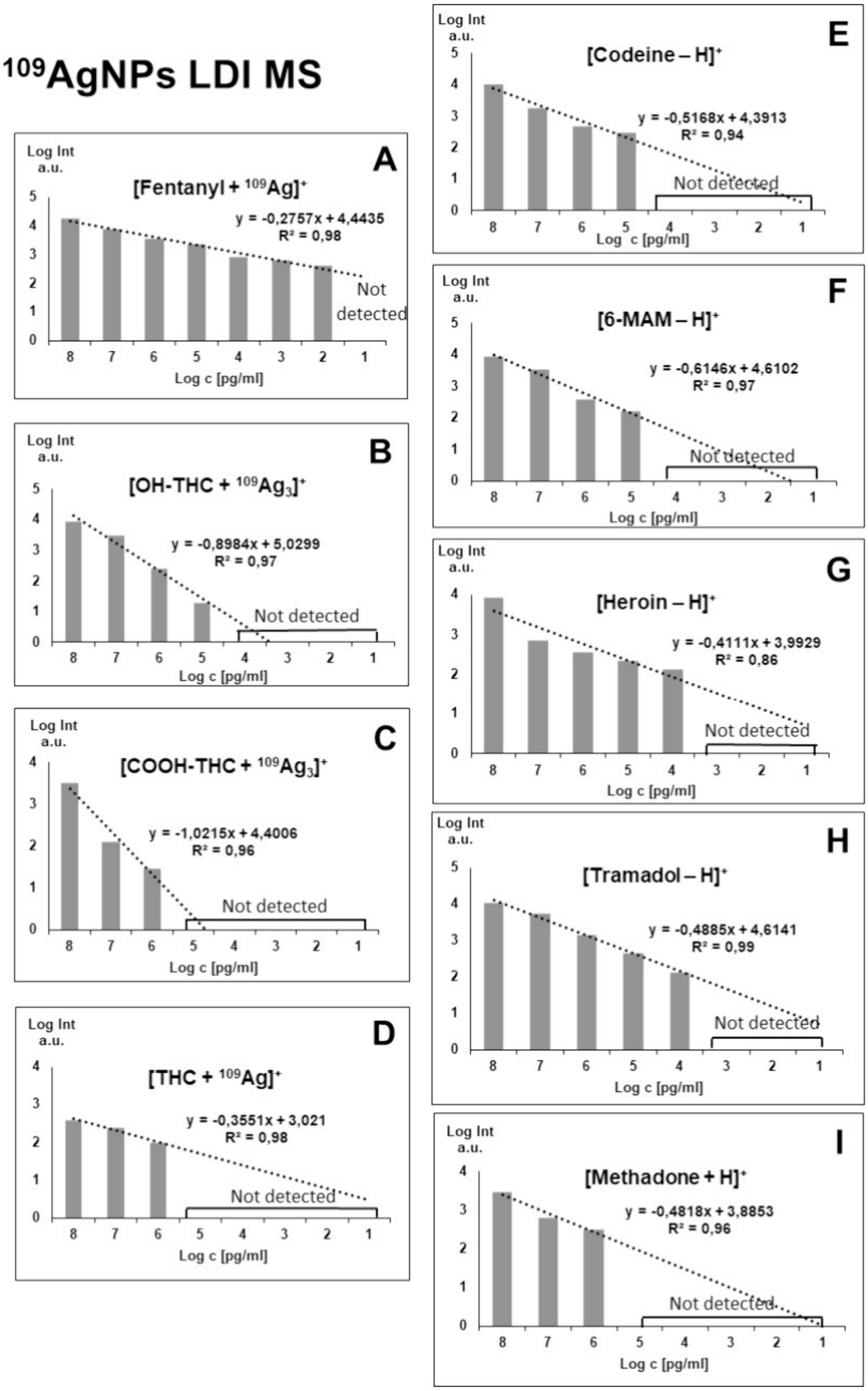

Figure 5. Bar charts presented for the relation of logarithm of signal intensity against the logarithm of concentration, along with regression lines and equations for A: fentanyl, B: 11-OH-THC, C: 11-COOH-THC, D: Δ^9-THC, E: codeine, F: 6-monoacetylmorphine, G: heroin, H: tramadol, I: methadone.

spot). The R^2 value was found to be 0.94. For 6-monoacetylmorphine, which is a metabolite of heroin, a logarithmic relationship of intensity versus concentration was found for the 100 μg/mL to 100 ng/mL range. The ion used for regression analysis was $[C_{19}H_{21}NO_4 - H]^+$. LOD calculated by using the signal-to-noise ratio was found to be 57.14 ng/mL (28.57 pg/per spot). The bar chart used for the analysis of regression is presented in Figure 4F, with an R^2 value of 0.97. In research conducted in 2016 by Gul et al.[45] regarding the analysis of opiates in wastewater using LC-MS/MS, the LOD and LOQ values determined for standard solutions of codeine and 6-MAM were 0.62 ng/mL with an R^2 coefficient of 0.9998.

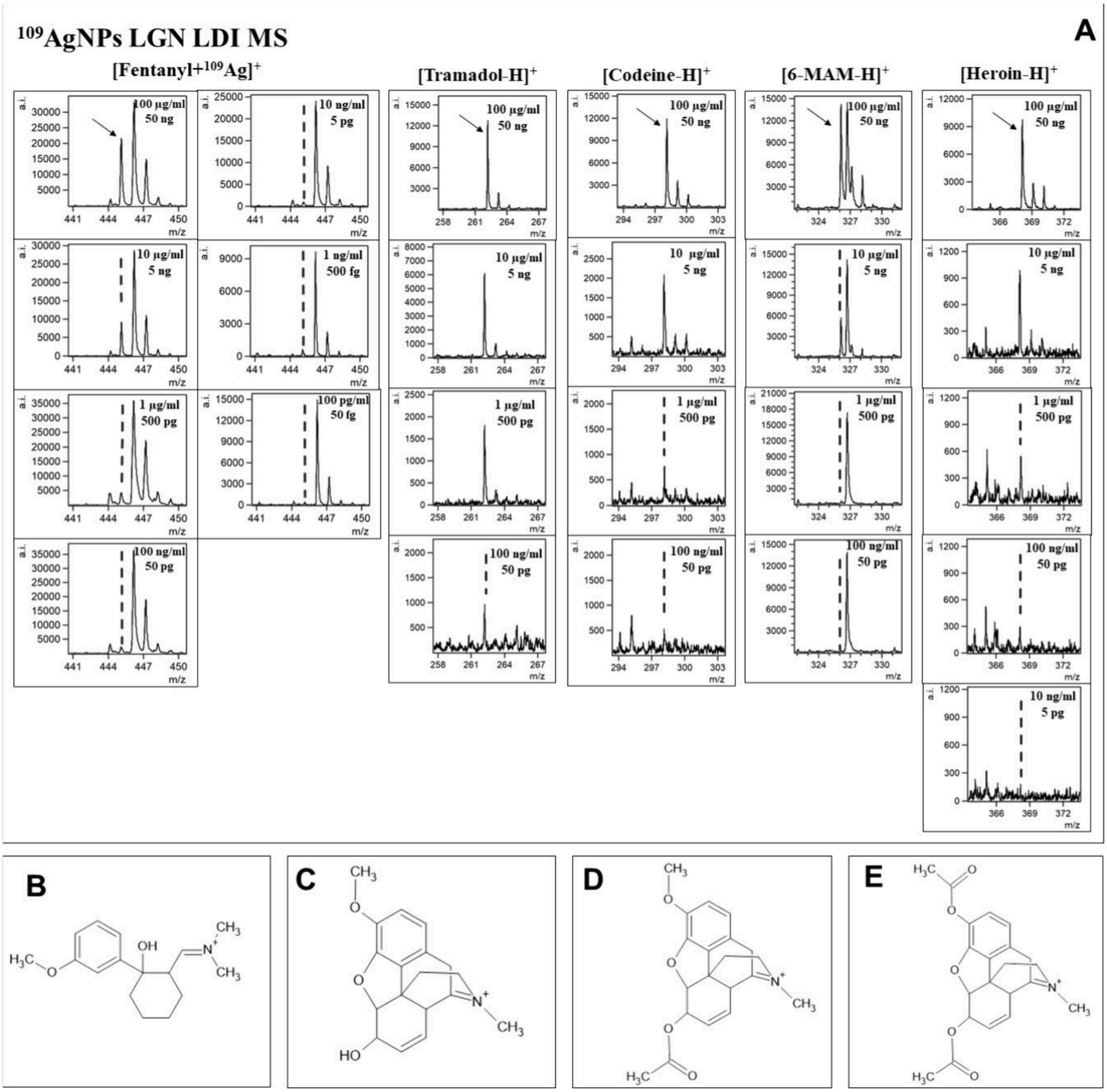

Figure 6. A: Spectra fragments for selected ions of interest presented for different concentrations of fentanyl, tramadol, codeine, 6-MAM, and heroin, with corresponding concentrations and compound mass per spot presented. Proposed structures of uncommon deprotonated ions: B, [tramadol − H]$^+$; C, [codeine − H]$^+$; D, [6-MAM − H]$^+$; E, [heroin − H]$^+$.

The following analyzed compound was heroin, a semi-synthetic opioid. The [$C_{21}H_{23}NO_5$ − H]$^+$ ion was found in the five highest concentrations from 100 μg/mL to 10 ng/mL Limit of detection value for heroin was found to be 8.22 ng/mL (4.11 pg/per spot). As seen in Figure 5G, the coefficient of determination R^2 was 0.86. In a study conducted in 2020 by Jovanov et al.,[46] which presented a rapid method for detecting heroin using HPLC−MS/MS, an LOD and LOQ were obtained from calibration curves of a 0.4 μg/mL heroin standard solution.

The regression analysis of tramadol, a synthetic opioid produced as pain medication, was also based on its [M − H]$^+$ ion. Signals of significant intensity were found in the five highest concentrations, as presented in Figure 5H. LOD was calculated and found to be 44.55 ng/mL (22.28 pg/per spot), and the R^2 coefficient was determined to be 0.99. Abdelshakour et al.[47] conducted a study utilizing UPLC-MS/MS to quantify tramadol in methanol-diluted standard solutions. They achieved a limit of detection (LOD) of 0.015 μg/mL and a limit of quantification (LOQ) of 0.05 μg/mL for tramadol, with an R_2 value of 0.9999.

The last analyzed compound was methadone, also a synthetic opioid, often used for heroin addiction treatment. For this opioid, only the [$C_{21}H_{27}NO$ + H]$^+$ ion has shown linear regression in terms of intensity and concentration relationship, as presented in Figure 4I. It was identified for the three highest concentrations, in the 100 μg/mL to 1 μg/mL range. The calculated LOD value was 386 ng/mL (193 pg/per spot). The

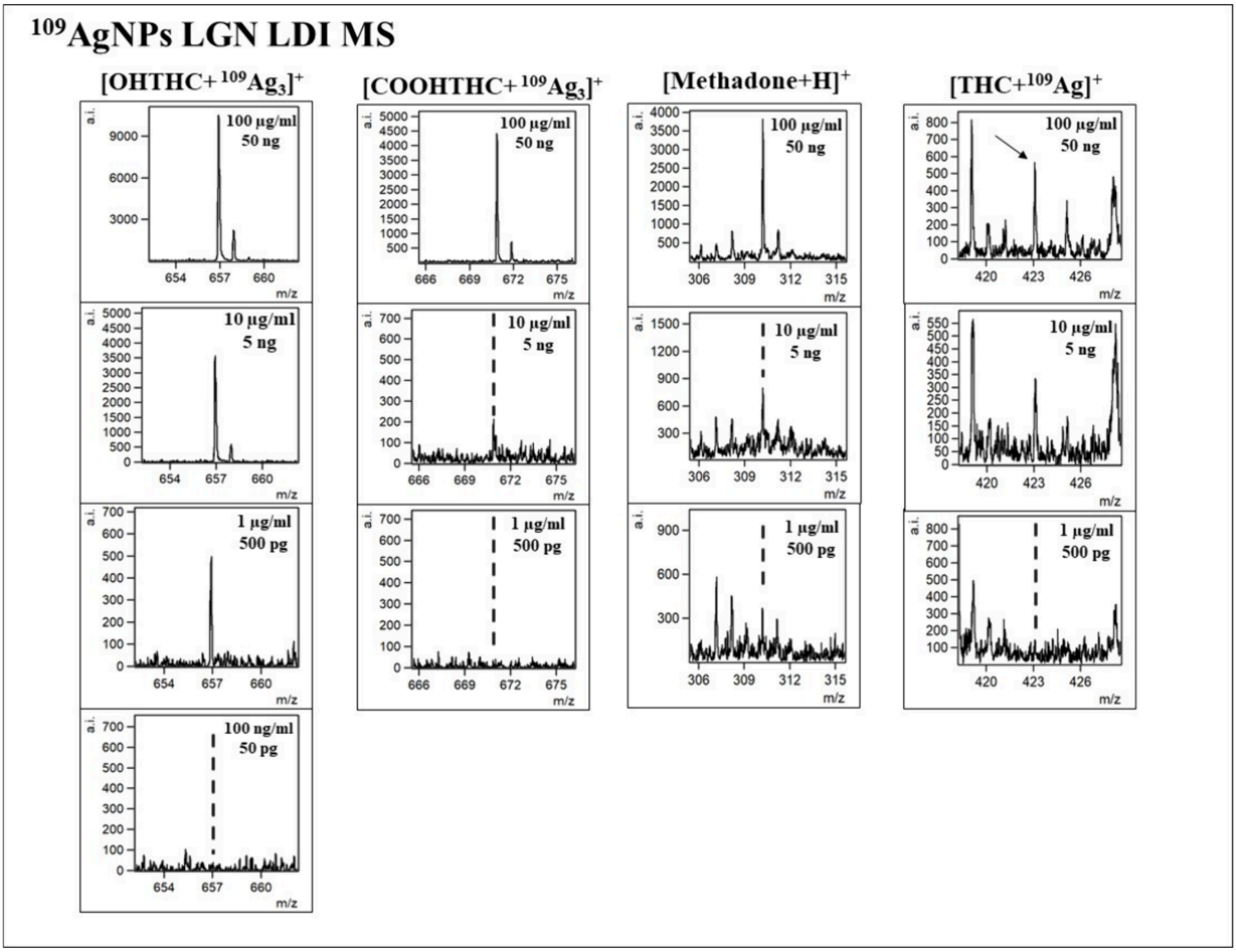

Figure 7. Spectra fragments for selected ions of interest presented for lowering concentrations for 11-OH-THC, 11-COOH-THC, methadone, and Δ^9-THC with corresponding concentrations and compound weight per spot presented.

determination coefficient R^2 value was found to be 0.96. In research conducted by Whitehead et al.[48] in which the LC-MS/MS method was used to detect illicit drugs, the LOD and LOQ values determined for standard solutions were 3.8 pg/mL and 0.1 ng/mL, respectively.

3.2. Matrix Effect. Biological samples, such as tissues or body fluids, are considered to be a complex matrix containing, among others, proteins, peptides, lipids, and other endogenous compounds that may interfere with the detection of illicit drugs. This complexity often requires additional sample preparation steps, such as protein precipitation, solid-phase extraction, or liquid–liquid extraction, to isolate drugs from the biological matrix. Moreover, matrix effects in biological samples can affect the accuracy and sensitivity of detection methods. In contrast, our study, which uses standards diluted in methanol, avoids such matrix effects and can therefore demonstrate the capabilities of the analytical method in an idealized scenario. To validate the effectiveness of ^{109}AgNPs LGN LDI MS in the analysis of illicit drugs in complex mixtures such as biological samples, we conducted additional experiments on samples spiked with illicit drugs

The matrix effect was assessed by evaluating the ion intensity of fentanyl adducts. This involved comparing the intensity of ions from fentanyl in diluted urine and serum samples, which had been spiked with standard compounds, against the ion intensity of corresponding adducts in pure standard solutions diluted in methanol (Figures S1 and S2, Supporting Information). The examination of signal intensities across the entire spectrum of tested fentanyl concentrations reveals that the adduct formed with silver-109 ions ([fentanyl + ^{109}Ag]$^+$) was the most prevalent ion species for this compound. This is evidenced by the significantly stronger signals for the silver adduct in comparison to those of the sodium ion adducts ([fentanyl + Na]$^+$) and the protonated fentanyl ions ([fentanyl + H]$^+$). The prominence of the silver adduct ion was consistent not only in the standard methanol solution but also in the diluted serum and urine samples. The LOD data indicate a high degree of method sensitivity for detecting fentanyl, both in the standard solution and in serum samples spiked with fentanyl, evidenced by LODs of 3.36 ± 0.68 pg/mL and 3.04 ± 0.81 pg/mL, respectively. For spiked urine, LOD was 4.05 ± 0.76 pg/mL. These surprisingly good results are probably results of 1000-times dilution of serum and urine, dilution that is needed in our method mainly due to the formation of thick films of material on the target plate. In this case it would be proper to recalculate LODs to include matrix dilution which gives 3.04 ± 0.81 and 4.05 ± 0.76 ng/mL for serum and urine, respectively. While biological matrix results are comparable to the ones from LCMS studies, still fentanyl LOD for standard solution in methanol is among the lowest to date. Previously, Zhang et al. achieved one of the lowest reported LOD for fentanyl, reaching 2.5 ng/mL in diluted urine samples and 0.5 ng/mL in diluted blood samples, using a liquid chromatography−high resolution mass spectrometry.[49] Meanwhile, Busardo et al. recorded LOD values in the picogram per milliliter range for fentanyl, but with a lower resolution triple quadrupole mass spectrometer.[50] However, both studies involved complicated and time-consuming sample preparation processes, including protein precipitation, that were considerably more time-intensive compared to our rapid method.

3.3. Advantages and Disadvantages of ^{109}AgNPs LGN LDI MS. The laser desorption/ionization mass spectrometry method using silver-109 nanoparticles (^{109}AgNPs-LDI-MS) we've introduced offers considerable advantages over the commonly used atmospheric pressure ionization techniques in toxicological analyses and the detection of new psychoactive substances. A primary benefit of ^{109}AgNPs LGN LDI MS is its capacity for rapid analysis: up to 100 samples on a single 4.5 × 3.5 cm plate; the spectrum is ready typically within seconds per sample, with the potential for automation. This capability significantly enhances throughput. Unlike LC-MS methods, ^{109}AgNPs-LDI-MS is much less affected by matrix effects, reducing sample preparation time. For small molecular analyses in complex biological matrices such as blood or urine, a simple dilution suffices, eliminating the need for elaborate extraction and protein precipitation. While LC-MS often struggles with matrix effects leading to variable reproducibility, ^{109}AgNPs LGN LDI MS achieves superior sensitivity compared to other high-resolution methods under atmospheric pressure. On the other hand, high-performance liquid chromatography coupled with high-resolution mass spectrometry (UHPLC-HRMS) offers a robust advantage for the comprehensive and selective analysis of complex biological mixtures. By separating sample components on a chromatographic column before mass spectrometric analysis, UHPLC-HRMS is essential for the precise identification and quantification of chemical compounds within samples of complex composition. However, the LC-MS method is notably vulnerable to sample contamination; depending on the nature of the sample, contaminants could be introduced, potentially leading to the blockage of columns or tubing. Furthermore, the process of optimizing experimental conditions for LC-MS can be time-intensive, posing challenges when rapid analysis of numerous samples with minute analyte quantities is required. Additionally, sample availability often constrains LC-MS, particularly when the analyte of interest is unidentified and occurs in small amounts in the sample, making it challenging to ascertain the appropriateness of a specific dilution for detection.

4. CONCLUSION

LDI MS with the application of laser-generated silver-109-nanoparticles enabled the detection and quantification of illicit drugs in a broad range of concentrations, from 100 μg/mL to 100 pg/mL in the case of fentanyl. Analyzed standards produced typical adduct ions such as protonated, sodiated ions, and also ions specific to this method, adducts of $^{109}\mathrm{Ag}^+$, and also less known $[\mathrm{M} + {}^{109}\mathrm{Ag}_3]^+$ and uncommon $[\mathrm{M} - \mathrm{H}]^+$ ions. The chosen method turned out to be most suitable for rapid screening for fentanyl, resulting in a low limit of detection, giving exceptional results compared to other published reports. It is therefore a suitable analytical method for the detection and quantification of illicit drug occurrence and use.

■ ASSOCIATED CONTENT

Data Availability Statement

The data sets generated during and/or analyzed during the current study are available from the corresponding author upon request and in the RepOD open data repository (doi: 10.18150/EJLW9K).

Supporting Information

The Supporting Information is available free of charge at https://pubs.acs.org/doi/10.1021/jasms.3c00454.

> Bar graphs showing the relationship between the log intensity of adduct ions and the log concentration of fentanyl in various samples: a methanol standard and diluted serum and urine. Spectra fragments displaying fentanyl ion signals in a standard solution and in fentanyl-spiked diluted serum and urine (PDF)

■ AUTHOR INFORMATION

Corresponding Author

Joanna Nizioł − *Rzeszów University of Technology, Faculty of Chemistry, 35-959 Rzeszów, Poland;* orcid.org/0000-0002-4783-8615; Phone: (+48 17) 865-1310; Email: jniziol@prz.edu.pl

Author

Sumi Krupa − *Doctoral School of Engineering and Technical Sciences at the Rzeszów University of Technology, 35-959 Rzeszów, Poland; Rzeszów University of Technology, Faculty of Chemistry, 35-959 Rzeszów, Poland*

Complete contact information is available at: https://pubs.acs.org/10.1021/jasms.3c00454

Author Contributions

Conceptualization: J.N.; data curation: S.K., J.N.; formal analysis: S.K.; funding acquisition: J.N.; methodology: J.N., S.K.; writing - original draft: S.K.; writing - review and editing: J.N.. All authors read and agreed to the accepted version of the manuscript.

Notes

The authors declare no competing financial interest.

■ ACKNOWLEDGMENTS

The study was supported by National Science Centre (Poland) research project SONATA BIS number 2022/46/E/ST4/00016.

■ REFERENCES

(1) United Nations Office on Drugs and Crime. *Prevalence of drug use.* World Drug Report. https://dataunodc.un.org/dp-drug-use-prevalence (accessed 2023-12-23).

(2) Peacock, A.; Leung, J.; Larney, S.; Colledge, S.; Hickman, M.; Rehm, J.; Giovino, G. A.; West, R.; Hall, W.; Griffiths, P.; Ali, R.; Gowing, L.; Marsden, J.; Ferrari, A. J.; Grebely, J.; Farrell, M.; Degenhardt, L. Global Statistics on Alcohol, Tobacco and Illicit Drug Use: 2017 Status Report. *Addiction* **2018**, *113* (10), 1905−1926.

(3) Duke-Novakovski, T. Opioids. *Pain Management in Veterinary Practice* **2013**, 39−67.

(4) Volpe, D. A.; Tobin, G. A. M. M.; Mellon, R. D.; Katki, A. G.; Parker, R. J.; Colatsky, T.; Kropp, T. J.; Verbois, S. L. Uniform Assessment and Ranking of Opioid Mu Receptor Binding Constants for Selected Opioid Drugs. *Regul. Toxicol. Pharmacol.* **2011**, *59* (3), 385−390.

(5) Hedegaard, H.; Miniño, A. M.; Warner, M. Key Findings Data from the National Vital Statistics System, Mortality. NCHS Data Brief No. 428, December 2021.

(6) Spencer, M. R.; Miniño, A. M.; Warner, M. Drug Overdose Deaths in the United States, 2001−2021. Key Findings Data from the National Vital Statistics System. NCHS Data Brief No. 457, December 2022.

(7) EMCDDA. New Psychoactive Substances - the Current Situation in Europe (European Drug Report 2023). https://www.emcdda.europa.eu/publications/european-drug-report/2023/new-psychoactive-substances_en#level-3-section1, 2023.

(8) Grotenhermen, F.; Russo, E. *Cannabis and Cannabinoids: Pharmacology, Toxicology, and Therapeutic Potential*; Taylor & Francis, 2013; pp 1−439

(9) Wall, M. E.; Perez-Reyes, M. The Metabolism of Δ9-Tetrahydrocannabinol and Related Cannabinoids in Man. *Journal of Clinical Pharmacology* **1981**, *21* (S1), 178S−189S.

(10) Whitacre, D. M. *Reviews of Environmental Contamination and Toxicology*; Springer, 2011; Vol. *210*. DOI: 10.1007/978-1-4419-7615-4.

(11) Zuccato, E.; Castiglioni, S. Assessing Illicit Drug Consumption by Wastewater Analysis: History, Potential, and Limitation of a Novel Approach. *Illicit Drugs in the Environment: Occurrence, Analysis, and Fate Using Mass Spectrometry* **2011**, 291−304.

(12) de Voogt, P.; Emke, E.; Helmus, R.; Panteliadis, P.; van Leerdam, J. A. Determination of Illicit Drugs in the Water Cycle by LC-Orbitrap MS. *Illicit Drugs in the Environment: Occurrence, Analysis, and Fate Using Mass Spectrometry* **2011**, 87−114.

(13) Plouffe, B. D.; Murthy, S. K. Fluorescence-Based Lateral Flow Assays for Rapid Oral Fluid Roadside Detection of Cannabis Use. *Electrophoresis* **2017**, *38* (3−4), 501−506.

(14) Parrilla, M.; Joosten, F.; De Wael, K. Enhanced Electrochemical Detection of Illicit Drugs in Oral Fluid by the Use of Surfactant-Mediated Solution. *Sens Actuators B Chem.* **2021**, *348*, 130659.

(15) De Jong, M.; Sleegers, N.; Kim, J.; Van Durme, F.; Samyn, N.; Wang, J.; De Wael, K. Electrochemical Fingerprint of Street Samples for Fast On-Site Screening of Cocaine in Seized Drug Powders. *Chem. Sci.* **2016**, *7* (3), 2364−2370.

(16) Płaza, A.; Kołodziej, A.; Nizioł, J.; Ruman, T. Laser Ablation Synthesis in Solution and Nebulization of Silver-109 Nanoparticles for Mass Spectrometry and Mass Spectrometry Imaging. *ACS Measurement Science Au* **2022**, *2* (1), 14−22.

(17) Arendowski, A.; Ruman, T. Lysine Detection and Quantification by Laser Desorption/Ionization Mass Spectrometry on Gold Nanoparticle-Enhanced Target. *Analytical Methods* **2018**, *10* (45), 5398−5405.

(18) Arendowski, A.; Nizioł, J.; Ruman, T. Silver-109-Based Laser Desorption/Ionization Mass Spectrometry Method for Detection and Quantification of Amino Acids. *Journal of Mass Spectrometry* **2018**, *53* (4), 369−378.

(19) Płaza-Altamer, A.; Kołodziej, A.; Nizioł, J.; Ruman, T. Infrared Pulsed Fiber Laser-Produced Silver-109-Nanoparticles for Laser Desorption/Ionization Mass Spectrometry of Amino Acids. *J. Mass Spectrom* **2022**, *57* (3), No. 4815, DOI: 10.1002/jms.4815.

(20) Kołodziej, A.; Płaza-Altamer, A.; Nizioł, J.; Ruman, T. Infrared Pulsed Fiber Laser-Produced Silver-109-Nanoparticles for Laser Desorption/Ionization Mass Spectrometry of Carboxylic Acids. *Int. J. Mass Spectrom.* **2022**, *474*, 116816.

(21) Kołodziej, A.; Płaza-Altamer, A.; Nizioł, J.; Ruman, T. Infrared Pulsed Fiber Laser-Produced Silver-109 Nanoparticles for Laser Desorption/Ionization Mass Spectrometry of 3-Hydroxycarboxylic Acids. *Rapid Commun. Mass Spectrom.* **2022**, *36* (21), No. 9375, DOI: 10.1002/rcm.9375.

(22) Kołodziej, A.; Ruman, T.; Nizioł, J. Gold and Silver Nanoparticles-Based Laser Desorption/Ionization Mass Spectrometry Method for Detection and Quantification of Carboxylic Acids. *Journal of Mass Spectrometry* **2020**, *55* (10), No. e4604.

(23) Ciunik, Z.; Ruman, T.; Lukasiewicz, M.; Wolowiec, S. Complexes of Heteroscorpionate Trispyrazolylborate Ligands. Part XI. Weak CH/π Interactions in Crystals of Hydrotris(3-Phenylpyrazolyl)-Boratothallium(I) and Hydrobis(5-Methyl-3-Phenylpyrazolyl)(3,5-Dimethylpyrazol-yl)Boratothallium(I) Studied by X-Ray Crystallography. *J. Mol. Struct.* **2004**, *690* (1−3), 175−180.

(24) Nizioł, J.; Copié, V.; Tripet, B. P.; Nogueira, L. B.; Nogueira, K. O. P. C.; Ossoliński, K.; Arendowski, A.; Ruman, T. Metabolomic and Elemental Profiling of Human Tissue in Kidney Cancer. *Metabolomics* **2021**, *17* (3), 30.

(25) Płaza-Altamer, A.; Kołodziej, A.; Krupa, Z.; Nizioł, J.; Ruman, T. Infrared Pulsed Fiber Laser-Produced Gold and Silver-109 Nanoparticles for Laser Desorption/Ionization Mass Spectrometry of Steroid Hormones. *Rapid Commun. Mass Spectrom.* **2023**, *37* (20), No. e9621.

(26) Szulc, J.; Machnowski, W.; Kowalska, S.; Jachowicz, A.; Ruman, T.; Steglińska, A.; Gutarowska, B. Beeswax-Modified Textiles: Method of Preparation and Assessment of Antimicrobial Properties. *Polymers 2020, Vol. 12, Page 344* **2020**, *12* (2), 344.

(27) Szulc, J.; Ruman, T.; Karbowska-Berent, J.; Kozielec, T.; Gutarowska, B. Analyses of Microorganisms and Metabolites Diversity on Historic Photographs Using Innovative Methods. *J. Cult Herit* **2020**, *45*, 101−113.

(28) Szulc, J.; Kołodziej, A.; Ruman, T. Silver-109/Silver/Gold Nanoparticle-Enhanced Target Surface-Assisted Laser Desorption/Ionisation Mass Spectrometry—The New Methods for an Assessment of Mycotoxin Concentration on Building Materials. *Toxins 2021, Vol. 13, Page 45* **2021**, *13* (1), 45.

(29) Arendowski, A.; Szulc, J.; Nizioł, J.; Gutarowska, B.; Ruman, T. Metabolic Profiling of Moulds with Laser Desorption/Ionization Mass Spectrometry on Gold Nanoparticle Enhanced Target. *Anal. Biochem.* **2018**, *549*, 45.

(30) Nizioł, J.; Ossoliński, K.; Tripet, B. P.; Copié, V.; Arendowski, A.; Ruman, T. Nuclear Magnetic Resonance and Surface-Assisted Laser Desorption/Ionization Mass Spectrometry-Based Serum Metabolomics of Kidney Cancer. *Anal Bioanal Chem.* **2020**, *412* (23), 5827.

(31) Nizioł, J.; Ossoliński, K.; Tripet, B. P.; Copié, V.; Arendowski, A.; Ruman, T. Nuclear Magnetic Resonance and Surface-Assisted Laser Desorption/Ionization Mass Spectrometry-Based Metabolome Profiling of Urine Samples from Kidney Cancer Patients. *J. Pharm. Biomed Anal* **2021**, *193*, 113752.

(32) Misiorek, M.; Sekuła, J.; Ruman, T. Mass Spectrometry Imaging of Low Molecular Weight Compounds in Garlic (Allium Sativum L.) with Gold Nanoparticle Enhanced Target. *Phytochemical Analysis* **2017**, *28* (6), 479−486.

(33) Nizioł, J.; Sekuła, J.; Ruman, T. Visualizing Spatial Distribution of Small Molecules in the Rhubarb Stalk (Rheum Rhabarbarum) by Surface-Transfer Mass Spectrometry Imaging. *Phytochemistry* **2017**, *139*, 72.

(34) Nizioł, J.; Sunner, J.; Beech, I.; Ossoliński, K.; Ossolińska, A.; Ossoliński, T.; Płaza, A.; Ruman, T. Localization of Metabolites of Human Kidney Tissue with Infrared Laser-Based Selected Reaction Monitoring Mass Spectrometry Imaging and Silver-109 Nanoparticle-Based Surface Assisted Laser Desorption/Ionization Mass Spectrometry Imaging. *Anal. Chem.* **2020**, *92* (6), 4251−4258.

(35) Ossoliński, K.; Ruman, T.; Ossoliński, T.; Ossolińska, A.; Arendowski, A.; Kołodziej, A.; Płaza-Altamer, A.; Nizioł, J. Monoisotopic Silver Nanoparticles-Based Mass Spectrometry Imaging of Human Bladder Cancer Tissue: Biomarker Discovery. *Adv. Med. Sci.* **2023**, *68* (1), 38−45.

(36) Arendowski, A.; Nizioł, J.; Ossoliński, K.; Ossolińska, A.; Ossoliński, T.; Dobrowolski, Z.; Ruman, T. Laser Desorption/Ionization MS Imaging of Cancer Kidney Tissue on Silver Nanoparticle-Enhanced Target. *Bioanalysis* **2018**, *10* (2), 83−94.

(37) Lou, X.; Spiering, A. J. H.; De Waal, B. F. M.; Van Dongen, J. L. J.; Vekemans, J. A. J. M.; Meijer, E. W. Dehydrogenation of Tertiary Amines in Matrix-Assisted Laser Desorption/Ionization Time-of-Flight Mass Spectrometry. *Journal of Mass Spectrometry* **2008**, *43* (8), 1110−1122.

(38) Kang, C.; Zhou, Y.; Du, Z.; Bian, Z.; Wang, J.; Qiu, X.; Gao, L.; Sun, Y. Dehydrogenation and Dehalogenation of Amines in MALDI-TOF MS Investigated by Isotopic Labeling. *Journal of Mass Spectrometry* **2013**, *48* (12), 1318−1324.

(39) Prysiazhnyi, V.; Dycka, F.; Kratochvil, J.; Stranak, V. Gas Aggregated Ag NPs as a Matrix for Small Molecules: A Study on Natural Amino Acids. *J. Nanopart. Res.* **2020**, *22* (11), 1−13.

(40) Kéki, S.; Nagy, L.; Deák, G.; Zsuga, M.; Somogyi, L.; Lévai, A. Cationization of Simple Organic Molecules by Singly-Charged Ag3+ Cluster Ions in Matrix-Assisted Laser Desorption/Ionization Mass Spectrometry: Metal Cluster-Molecule Interactions. *J. Am. Soc. Mass Spectrom.* **2004**, *15* (6), 879−883.

(41) Nizioł, J.; Rode, W.; Laskowska, B.; Ruman, T. Novel Monoisotopic ^{109}AgNPET for Laser Desorption/Ionization Mass Spectrometry. *Anal. Chem.* **2013**, *85* (3), 1926−1931.

(42) Angi, C.; Lurie, I. S.; Marginean, I. Analysis of Fentanyl Derivatives by Ultra High Performance Liquid Chromatography with Diode Array Ultraviolet and Single Quadrupole Mass Spectrometric Detection. *J. Sep Sci.* **2019**, *42* (9), 1686−1694.

(43) Heo, S.; Yoo, G. J.; Choi, J. Y.; Park, H. J.; Do, J. A.; Cho, S.; Baek, S. Y.; Park, S. K. Simultaneous Analysis of Cannabinoid and Synthetic Cannabinoids in Dietary Supplements Using UPLC with UV and UPLC-MS-MS. *J. Anal Toxicol* **2016**, *40* (5), 350−359.

(44) Simões, S. S.; Ajenjo, A. C.; Dias, M. J. Qualitative and Quantitative Analysis of THC, 11-Hydroxy-THC and 11-nor-9-Carboxy-THC in Whole Blood by Ultra-Performance Liquid Chromatography/Tandem Mass Spectrometry. *Rapid Commun. Mass Spectrom.* **2011**, *25* (18), 2603−2610.

(45) Gul, W.; Stamper, B.; Godfrey, M.; Gul, S. W.; Elsohly, M. A. LC-MS-MS Method for Analysis of Opiates in Wastewater During Football Games II. *J. Anal Toxicol* **2016**, *40* (5), 330−337.

(46) Jovanov, P.; Petrin-Miličević, M.; Radosavljević-Stevanović, N.; Vraneš, M.; Belić, S.; Sakač, M.; Nikolov, J.; Gadžurić, S. Rapid Determination of the Primary Alkaloids in Illicit Heroin by High-Performance Liquid Chromatography with Tandem Mass Spectrometry (HPLC-MS/MS). *Anal. Lett.* **2021**, *54* (7), 1224−1232.

(47) Abdelshakour, M. A.; Hadad, G. M.; Abdel Salam, R. A.; Abo-ElMatty, D. M.; Abdel Hameed, E. A. HPLC and UPLC-MS/MS Methods for Analyzing TRAMADOL in 70 Medicinal Illegal Products: Application to Counterfeit Study. *Microchemical Journal* **2021**, *161*, 105823.

(48) Whitehead, H. D.; Hayes, K. L.; Swartz, J. A.; Prete, E.; Robison-Taylor, L.; Ellen Mackesy-Amiti, M.; Jimenez, A. D.; Lieberman, M. Validated Method for the Analysis of 22 Illicit Drugs and Their Metabolites via Liquid Chromatography Tandem Mass Spectrometry (LC-MS/MS) in Illicit Drug Samples Collected in Chicago, IL. *Forensic Chemistry* **2023**, *33*, 100475.

(49) Zhang, Y.; Halifax, J. C.; Tangsombatvisit, C.; Yun, C.; Pang, S.; Hooshfar, S.; Wu, A. H. B.; Lynch, K. L. Development and Application of a High-Resolution Mass Spectrometry Method for the Detection of Fentanyl Analogs in Urine and Serum. *Journal of Mass Spectrometry and Advances in the Clinical Lab* **2022**, *26*, 1−6.

(50) Busardò, F. P.; Carlier, J.; Giorgetti, R.; Tagliabracci, A.; Pacifici, R.; Gottardi, M.; Pichini, S. Ultra-High-Performance Liquid Chromatography-Tandem Mass Spectrometry Assay for Quantifying Fentanyl and 22 Analogs and Metabolites in Whole Blood, Urine, and Hair. *Front Chem.* **2019**, *7* (APR), 447886.

Received: 21 April 2023 | Revised: 24 July 2023 | Accepted: 28 July 2023

DOI: 10.1002/rcm.9621

RESEARCH ARTICLE

Rapid Communications in Mass Spectrometry WILEY

Infrared pulsed fiber laser-produced gold and silver-109 nanoparticles for laser desorption/ionization mass spectrometry of steroid hormones

Aneta Płaza-Altamer[1,2] | Artur Kołodziej[1,2] | Zuzanna Krupa[2] |
Joanna Nizioł[2] | Tomasz Ruman[2]

[1]Doctoral School of the Rzeszów University of Technology, Rzeszów, Poland

[2]Faculty of Chemistry, Rzeszów University of Technology, Rzeszów, Poland

Correspondence
A. Płaza-Altamer, Rzeszów University of Technology, Faculty of Chemistry,
6 Powstańców Warszawy Ave., 35-959
Rzeszów, Poland.
Email: a.plaza@prz.edu.pl

Funding information
National Science Centre, Grant/Award Number: SONATA BIS grant no. UMO-2022/46/E/ST4/00016

Rationale: Hormones are compounds that perform many important functions in the human body, but above all their task is to maintain homeostasis by adapting them to the constantly changing environmental conditions. Even minor hormonal disorders have a negative effect on the body, leading to physical or mental changes. Therefore, monitoring these changes and precise quantification of hormones are essential for the early diagnosis of diseases related to hormonal disorders.

Methods: Application of monoisotopic silver-109 and gold nanoparticles obtained by PFL (pulsed fiber laser) 2D GS (galvo-scanner) LGN (laser-generated nanomaterial) for high-resolution laser desorption/ionization mass spectrometry (LDI-MS) and mass spectrometry imaging (MSI) of steroid hormones is presented. Four steroid hormones, estrone, prednisolone, corticosterone and progesterone, were used as test compounds for quantitative analysis with matrix-assisted LDI time-of-flight MS apparatus. Moreover, comparison of manual measurements and semiautomatic MSI with both types of nanoparticles was performed. Methods were also tested on spiked human blood serum for quantification of steroid hormones and for estimation of the matrix effect.

Results: Hormones were directly tested in 1 000 000-fold concentration change conditions ranging from 1 mg/mL to 1 ng/mL which equates to 300 ng to 300 fg of hormone per measurement spot. For almost all tested hormones MSI allowed one to obtain equal or lower limit of detection value than manual LDI-MS. The best results judged by lowest limit of detection values are found for silver-109 nanoparticles.

Conclusion: The results of the quantitative analysis of steroid hormones using silver-109 and gold nanoparticles prepared with PFL 2D GS LGN for LDI-MS and semiautomatic LDI-MSI are presented. It has been proven that nanoparticles obtained by laser synthesis can be successfully used for the analysis of steroid hormones in a wide range of concentrations.

1 | INTRODUCTION

Hormones are compounds found in animals, plants and fungi.[1,2] They have many important functions in the human body, such as regulating metabolism, controlling the reproductive cycle, activating or suppressing the immune system, stimulating or inhibiting growth.[3] In terms of structure, we can distinguish several groups: peptide, amino acid, steroid and eicosanoid hormones. Steroid hormones are a large group of hormones derived from cholesterol backbone.[4,5] This group includes, among others, progesterone, estrone, corticosterone and

https://doi.org/10.1002/rcm.9621
© 2023 John Wiley & Sons Ltd.

prednisolone. For example, progesterone is one of the key female sex hormones influencing fertility, whose dysregulation in expression can lead to infertility and many other disorders in the body.[6,7] Therefore, monitoring of dynamic changes and precise quantification of hormones are necessary for the early diagnosis of diseases related to hormonal disorders such as Cushing's syndrome, congenital adrenal hyperplasia,[8] infertility and premature puberty.[9]

The most popular analytical methods allowing for the identification and quantification of steroid hormones include immunological tests such as radioimmunoassay,[10] chemiluminescent immunoassay[11] and enzyme-linked immunosorbent assay.[12] However, these tests require the use of specific antibodies or markers that affect the accuracy of the result obtained. Moreover, enzyme-based quantification has low reproducibility; whereas measurements based on radioactivity are time-consuming and require many precautions regarding radioactivity during work. Another disadvantage of the use of immunological tests is the inability to measure several hormones at the same time.[6]

Matrix-assisted laser desorption/ionization mass spectrometry (MALDI-MS) is a highly sensitive and accurate method used nowadays. However, MALDI-MS of neutral steroid hormones is difficult because, as neutral molecules, they do not have acidic or basic groups in their structures, which leads to low sensitivity of MS detection.[13] Additionally, the high-intensity ions from the matrix can interfere with or suppress analyte signals. Application of nanoparticles instead of traditional MALDI organic matrices allows solving this problem. The LDI mass spectrum usually obtained using nanoparticles of, for example, silver-109 in the range *m/z* 80–1500 is very simple and clear, containing three main peaks assigned to the silver cations $^{109}Ag^{+}$, $^{109}Ag_2^{+}$ and $^{109}Ag_3^{+}$ and several lower intensity signals of higher monocationic silver aggregates.[14] The lack of additional signals in the low-mass range enables the analysis of low-molecular-weight compounds of complex mixtures. Equally often, gold nanoparticles (AuNPs) are used.[15–19] Similarly to silver-109 nanoparticles (^{109}AgNPs), AuNPs in the low-mass range of the LDI mass spectrum appear in the form of three main peaks assigned to gold cations Au^{+}, Au_2^{+} and Au_3^{+} and several signals of lower intensity of higher cationic gold aggregates. However, compared to ^{109}AgNPs, AuNPs show enhanced cost-effectiveness due to the much lower cost of gold compared to the starting silver-109 compound. Moreover, AuNPs show no reactivity toward oxygen and exhibit better stability, mainly attributed to the lower reactivity of gold compared to silver.[15] Wu et al showed that neutral steroids, which are extremely difficult to ionize using organic chemical matrices, are very efficiently cationized by AuNPs-assisted LDI time-of-flight (TOF) MS, even when present in high-salt solution.[20] Numerous articles have been published showing the usefulness a different type of nanoparticles in MS analysis.[14,21,22]

In this article, we present quantification results of steroid hormones on a steel plate covered with chemically pure silver-109 and gold nanoparticles produced using a recently published method with the use of a 1064 nm pulsed fiber laser (PFL) with 2D galvanometer scanner (GS). We also compare manual LDI-MS and semiautomatic LDI mass spectrometry imaging (MSI) in quantification of steroid hormones along with discussion of results and comparison with various surface-assisted LDI (SALDI) and MALDI methods previously used.

2 | MATERIALS AND METHODS

2.1 | Materials

All hormone analytical standards were purchased from Sigma-Aldrich. Steel targets were machined from H17 (1.4016) stainless steel. Before the LDI-MS and MSI experiments steel targets were cleaned through soaking in boiling solvents: toluene (3 × 100 mL, each plate for 30 s), chloroform (3 × 100 mL, each plate for 30 s), acetonitrile (3 × 100 mL, each plate for 30 s) and deionized water (3 × 100 mL, each plate for 30 s). Every plate was dried in high vacuum (*ca* 0.01 mBar, 24 h). All solvents were of LC/MS grade, except for water (18 MΩ cm water produced locally).

2.2 | PFL 2D GS laser-generated nanomaterial (LGN) of silver-109 and gold nanoparticles

The silver-109 foil (*ca* 1 mm thick, 99.7% isotopic purity) was purchased from Trace Sciences International (USA). The gold foil (*ca* 1 mm thick, 99.9%) was bought from Polish Mint (Poland). Both foils were placed at the bottom of a glass vessel and covered by a solvent layer approximately 3 mm thick. The ^{109}Ag foil was covered with acetonitrile, with a total solvent volume of 3 mL, while for the Au foil, a mixture of isopropanol and water (1:1 v/v) with a total solvent volume of 4 mL was used.

Laser ablation was carried out with a 1064 nm PFL (Raycus RFL-P20QE/A3). The ^{109}AgNPs suspension was obtained after 2 min irradiation with pulse energy of 0.8 mJ (100 ns pulse length) at a repetition rate of 40 kHz. Similarly, a suspension of AuNPs was obtained after 2 min irradiation with pulse energy of 0.7 mJ (100 ns pulse length) at a repetition rate of 60 kHz. Laser ablation was accomplished at a scanning speed of 2000 mm/s for ^{109}AgNPs and 5000 mm/s for AuNPs, with an ablation area of 4 × 4 mm^2. Each suspension was immediately transferred into a syringe and used in the nebulization step.

2.3 | Nebulization of ^{109}AgNPs and AuNPs suspensions

The entire nanoparticle nebulization process was controlled by a computer. The H17 steel plate (laser mass spectrometry target plate) was placed on the table of a translation system consisting of a motorized XY table (powered by closed-loop servomotors). A glass syringe (1 mL) was filled with a previously prepared suspension of silver-109 nanoparticles and placed in a syringe

10970231, 2023, 20, Downloaded from https://analyticalsciencejournals.onlinelibrary.wiley.com/doi/10.1002/rcm.9621 by Rzeszow University Of Tech, Wiley Online Library on [30/03/2026]. See the Terms and Conditions (https://onlinelibrary.wiley.com/terms-and-conditions) on Wiley Online Library for rules of use; OA articles are governed by the applicable Creative Commons License

pump (pumping speed of 250 μL/min). The custom-made software directed the 2D system table with 10 mm/s translation speed using a sequence of movements prepared to uniformly cover a target plate. The nebulizer was a typical, standard flow Bruker ion source "needle" or nebulizer. Argon at a pressure of 2 Bar was used as the nebulizing gas. Studied objects – for MS and MSI – were placed on the target plate before nebulization. The nebulization of the AuNPs suspension was performed in an analogous manner.

2.4 | Sample preparation and handling

Each hormone analytical standard (estrone, prednisolone, corticosterone, progesterone) was dissolved in an isopropanol–water (9:1, v/v) mixture to give a final concentration of 1 mg/mL. Lower concentrations were prepared by diluting of 10-times higher concentration ones. A serum sample was collected from a male volunteer who underwent a medical examination at John Paul II Hospital (Kolbuszowa, Poland). The study was approved by the local bioethics committee (Permission No. 2018/04/10). A 2.6 mL blood sample was drawn from the patient, centrifuged at 3000*g* for 10 min at room temperature, and then separated and stored at −60°C. A volume of 1 μL of serum was diluted with 124 μL of ultrapure water, then 125 μL of 100 μg/mL hormone solution was added. Volumes of 0.5 μL (^{109}AgNPs) or 0.3 μL (AuNPs) of hormones and serum solutions were placed directly on the target plate. After air drying, the target was nebulized with ^{109}AgNPs or AuNPs suspension as stated in the previous subsection.

2.5 | LDI mass spectrometry

LDI-TOFMS experiments were performed in reflectron mode using a Bruker Autoflex Speed TOF mass spectrometer equipped with a SmartBeam II laser (352 nm). Laser impulse energy was approximately 90–140 μJ, with a laser repetition rate of 1000 Hz. The total number of laser shots was 4000 for each spot. This number of laser shots was divided into four, symmetrically positioned points lying at a distance of *ca* 1/3 of the spot radius from its center. At each point, 1000 laser shots were made with default random walk applied (random points with 50 laser shots). Measurement range was *m*/*z* 80–1500. Suppression was turned on typically for ions of *m*/*z* lower than 80. Reflector voltages used were 21 kV (first) and 9.55 kV (second). The data were calibrated and analyzed with FlexAnalysis (version 3.3) using centroid calibration model. Mass calibration (enhanced cubic calibration based on 8–9 calibration points) was performed using internal standards (silver-109 ions and clusters from $^{109}\text{Ag}^+$ to $^{109}\text{Ag}_9^+$ or gold ions Au^+ to Au_7^+).

2.6 | LDI mass spectrometry imaging

Measurements were performed using a Bruker Autoflex Speed TOF mass spectrometer in reflectron positive mode. The apparatus was equipped with a SmartBeam II 1000 Hz, 352 nm laser. Laser impulse energy was approximately 100–120 μJ, laser repetition rate was 1000 Hz and deflection was set on *m*/*z* lower than 80 Da. The *m*/*z* range was 80–1500 and spatial resolution 600 × 600 μm. The imaging experiments were made with 2000 laser shots per individual spot with a default random walk applied (FlexImaging 4.0). All spectra were pre-calibrated (cubic calibration function) with the use of silver-109 ions ($^{109}\text{Ag}^+$ to $^{109}\text{Ag}_9^+$) or gold ions (Au^+ to Au_7^+) as internal standard. The first accelerating voltage was held at 19 kV, and the second ion source voltage was held at 16.7 kV. Reflector voltages used were 21 kV (first) and 9.55 kV (second). All of the shown images are for ±0.05% *m*/*z* window. MSI experiments were performed on all spots of hormone standards and spiked blood serum solution.

3 | RESULTS AND DISCUSSION

Monoisotopic ^{109}AgNPs and AuNPs were prepared using PFL LGN with the use of 2D GS and nebulization. Our recently published articles present characteristics and usefulness of both ^{109}AgNPs and AuNPs obtained for LDI-MS and MSI.[23,24] Both papers present the results obtained through UV–visible spectrophotometry, dynamic light scattering and high-resolution scanning electron microscopy analysis of suspensions containing ^{109}AgNPs or AuNPs. Based on these analyses, the shape and size of the nanoparticles produced by PFL 2D LGN were determined. This method significantly reduces the target preparation time from 48 h to a few minutes compared to producing nanoparticles by chemical synthesis. In addition, it is also cost-effective as no other reducing or stabilizing agents are required and the metal foil can be reused. In general, LGN produces suspensions of a relatively high chemical purity so leading to simple mass spectra with low chemical background.[25] Recent publications reported the results of the quantitative analysis of amino acids and carboxylic acids with the use of monoisotopic AgNPs obtained with the LGN method.[26,27]

3.1 | Quantification results

The LDI-MS and LDI-MSI measurements using both monoisotopic ^{109}AgNPs and AuNPs obtained by PFL 2D GS LGN were performed for four hormones: corticosterone, prednisolone, estrone and progesterone. Direct measurements of hormones were performed in the concentration range from 1 mg/mL to 1 ng/mL, which corresponds to a 1 000 000-fold change in concentration. The limit of detection (LOD) value was calculated using a signal-to-noise (*S*/*N*)

10970231, 2023, 20, Downloaded from https://analyticalsciencejournals.onlinelibrary.wiley.com/doi/10.1002/rcm.9621 by Rzeszow University Of Tech, Wiley Online Library on [30/03/2026]. See the Terms and Conditions (https://onlinelibrary.wiley.com/terms-and-conditions) on Wiley Online Library for rules of use; OA articles are governed by the applicable Creative Commons License

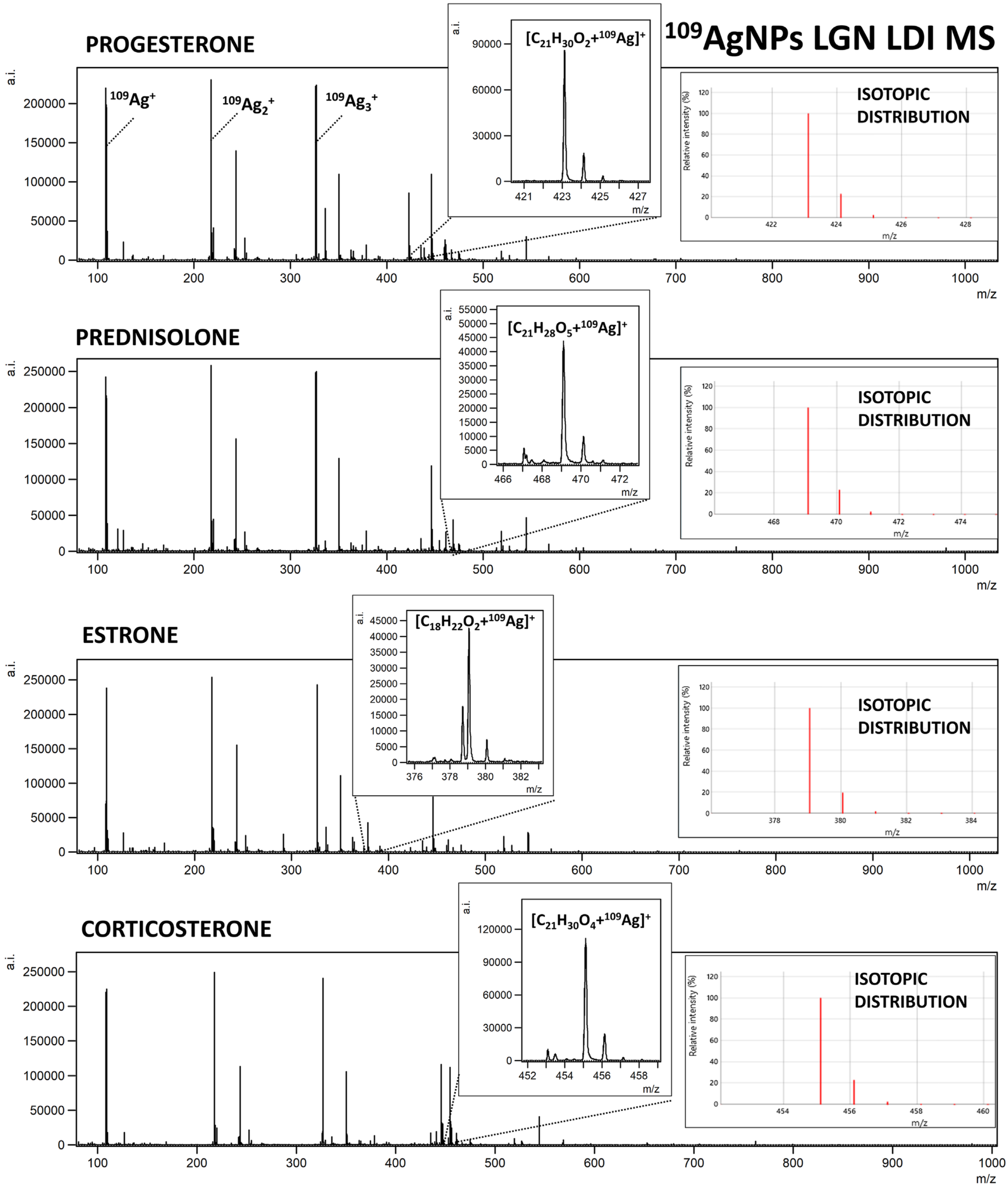

FIGURE 1 Mass spectra of tested steroid hormones obtained by manual LDI-MS measurements with ^{109}AgNPs generated with the PFL 2D GS LGN method. Every sample was placed on the target plate at a concentration of 1 mg/mL, equating to 500 ng of hormones per measurement spot. The isotopic distribution of the identified ions is shown on the right-hand side of each mass spectrum. [Color figure can be viewed at wileyonlinelibrary.com]

10970231, 2023, 20, Downloaded from https://analyticalsciencejournals.onlinelibrary.wiley.com/doi/10.1002/rcm.9621 by Rzeszow University Of Tech, Wiley Online Library on [30/03/2026]. See the Terms and Conditions (https://onlinelibrary.wiley.com/terms-and-conditions) on Wiley Online Library for rules of use; OA articles are governed by the applicable Creative Commons License

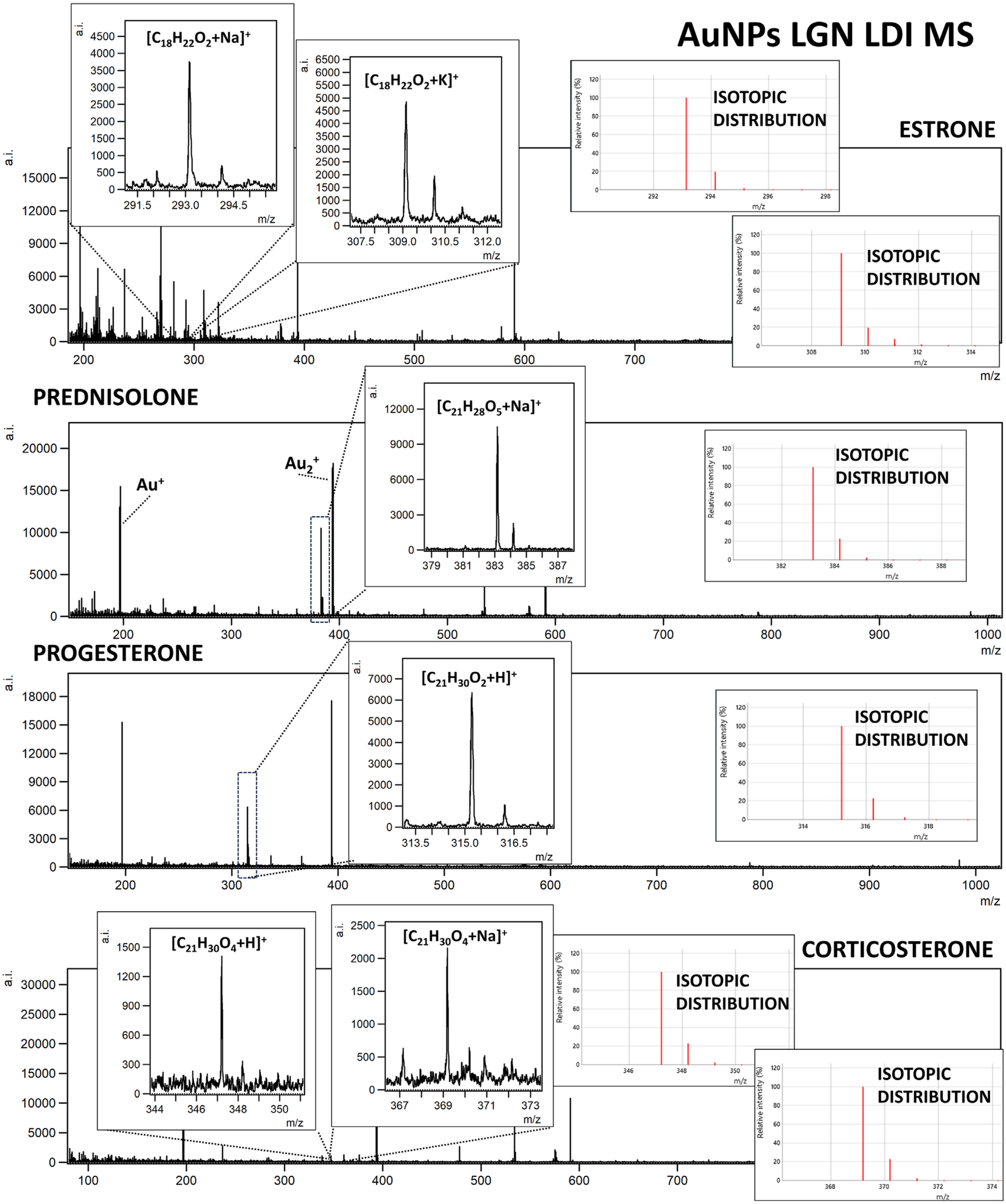

FIGURE 2 Mass spectra of tested steroid hormones obtained by manual LDI-MS measurements with AuNPs generated with the PFL 2D GS LGN method. Every sample was placed on the target plate at a concentration of 1 mg/mL, equating to 300 ng of hormones per measurement spot. The isotopic distribution of the identified ions is shown on the right-hand side of each mass spectrum. [Color figure can be viewed at wileyonlinelibrary.com]

10970231, 2023, 20, Downloaded from https://analyticalsciencejournals.onlinelibrary.wiley.com/doi/10.1002/rcm.9621 by Rzeszow University Of Tech, Wiley Online Library on [30/03/2026]. See the Terms and Conditions (https://onlinelibrary.wiley.com/terms-and-conditions) on Wiley Online Library for rules of use; OA articles are governed by the applicable Creative Commons License

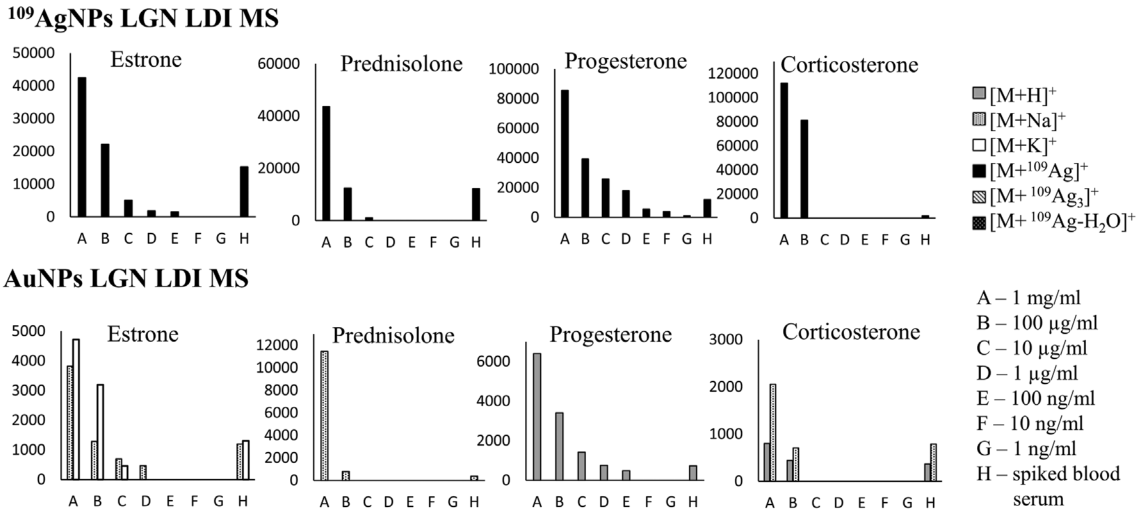

FIGURE 3 Bar charts showing relation of the adduct ion intensity against concentration for the four tested hormones.

TABLE 1 Comparison of mass accuracy and signal-to-noise ratios for manual LDI-MS measurements with gold and silver-109 nanoparticles

	Compound	Calculated *m/z*	Experimental *m/z*	Mass error (ppm)	*S/N*
^{109}AgNPs	[estrone + ^{109}Ag]$^+$	379.06619	379.06698	2.08	182.90
	[prednisolone + ^{109}Ag]$^+$	469.09788	469.09653	−2.87	179.10
	[progesterone + ^{109}Ag]$^+$	423.12879	423.12708	−4.04	386.40
	[corticosterone + ^{109}Ag]$^+$	455.11862	455.12210	7.64	557.80
AuNPs	[estrone + Na]$^+$	293.15120	293.15136	0.55	18.10
	[prednisolone + Na]$^+$	383.18289	383.16832	−15.21	65.70
	[progesterone + H]$^+$	315.23186	315.22048	−36.1	39.00
	[corticosterone + Na]$^+$	369.20363	369.19381	−26.6	12.10

ratio of 3, obtained from the mass spectra of the lowest concentration samples containing the signal of interest. Every sample for ^{109}AgNPs was placed on the target plate in a 0.5 μL volume equating to 500 ng to 500 fg of hormones per measurement spot which is approximately 1.6 nmol to 1.6 fmol respectively calculated for example for the progesterone molar mass. Whereas every sample for AuNPs was placed on the target plate in a 0.3 μL volume equating to 300 ng to 300 fg of hormones per measurement spot which is approximately 0.95 nmol to 0.95 fmol respectively calculated for example for the progesterone molar mass. Additionally, the LDI-MS measurement was performed in five repetitions for both types of nanoparticles and all tested hormones. A regression analysis of the obtained data of mean intensity as a function of concentration was performed.

Figure 1 shows mass spectra of progesterone, prednisolone, estrone and corticosterone obtained by manual LDI-MS measurements with ^{109}AgNPs generated with the PFL 2D GS LGN method. The spectra reveal the presence of silver-109 adducts for all steroid hormones. Notably, no signals of [M + H]$^+$, [M + Na]$^+$, [M + K]$^+$, [M + ^{109}Ag$_3$]$^+$ or [M + ^{109}Ag − H$_2$O]$^+$ adducts were detected, as illustrated in Figure 1. Additionally, the matching theoretical isotopic pattern for each ion is presented adjacent to the corresponding spectrum.

Conversely, the spectra obtained with AuNPs obtained with the PFL 2D GS LGN LDI-MS method contain signals of proton, sodium and potassium adducts for the steroid hormones. In the case of estrone, the mass spectra are dominated by the potassium adduct signal, although the sodium adduct was chosen for quantitative analysis due to its superior detection parameters across a wide range of concentrations. For prednisolone and corticosterone, the sodium adducts dominate in their mass spectra. Progesterone, on the other hand, is exclusively observed as a proton adduct signal. The results are presented in Figure 2.

Furthermore, Figure 3 shows bar graphs depicting the relationship between signal intensity of a specific adduct against concentration in the solution. Table 1 additionally presents the *S/N* ratios for the selected ions chosen for subsequent quantitative analysis. The signal intensities with the *S/N* ratio values clearly highlight the superior analytical performance of ^{109}AgNPs over AuNPs. For instance, the signal intensity of [progesterone + ^{109}Ag]$^+$ reaches 80 000, while the corresponding *S/N* ratio value is 386 in experiments employing ^{109}AgNPs. In contrast, experiments utilizing

10970231, 2023, 20, Downloaded from https://analyticalsciencejournals.onlinelibrary.wiley.com/doi/10.1002/rcm.9621 by Rzeszow University Of Tech, Wiley Online Library on [30/03/2026]. See the Terms and Conditions (https://onlinelibrary.wiley.com/terms-and-conditions) on Wiley Online Library for rules of use; OA articles are governed by the applicable Creative Commons License

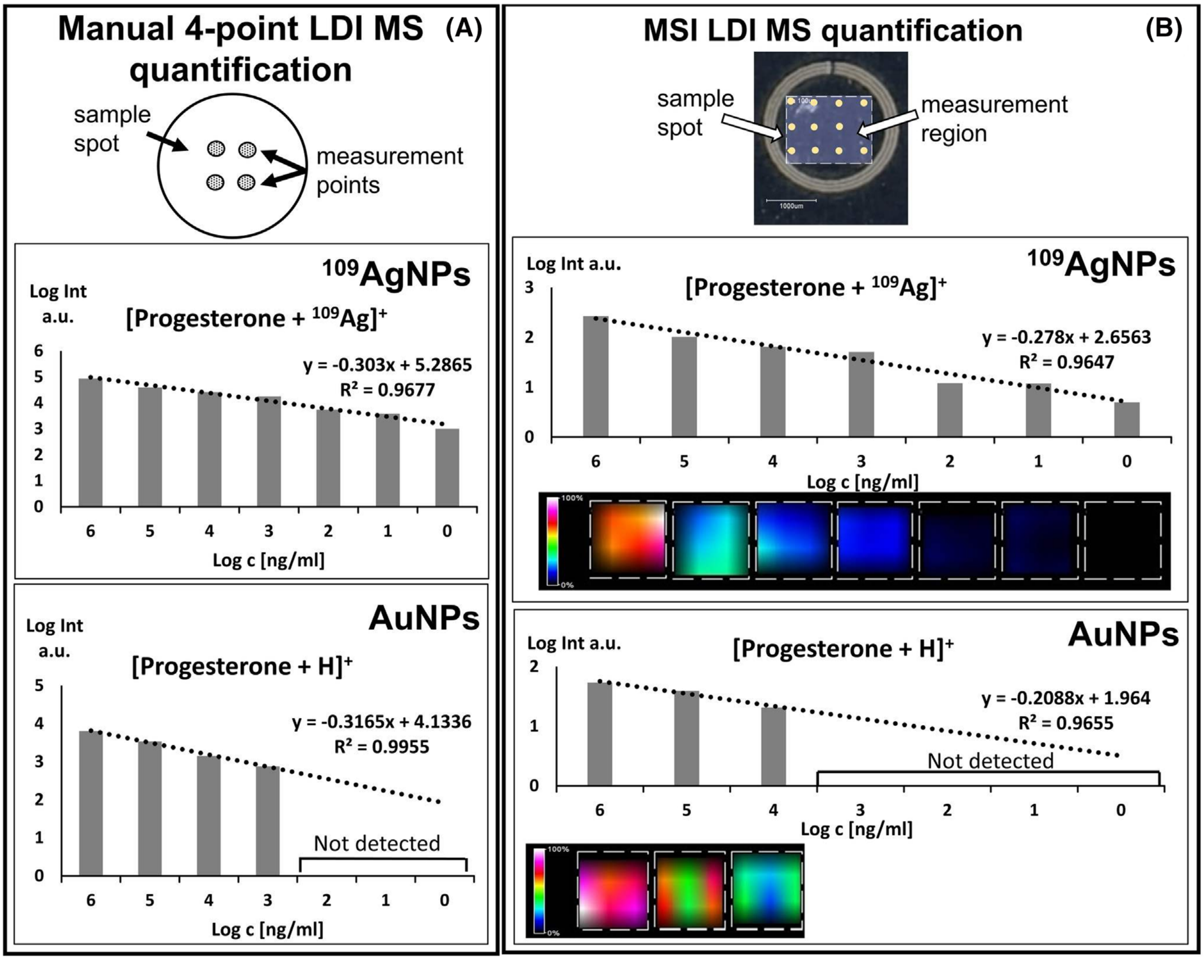

FIGURE 4 (A) Scheme of manual LDI-MS measurement with four random measure points. Bar charts present the average results obtained from five measurements of the same sample spot for progesterone with ^{109}AgNPs and AuNPs. The upper part of (B) presents a photograph of the measurement region with overlaid grid of measurement points. The lower part of (B) contains column charts with regression lines and equations for logarithm of the intensity versus logarithm of the concentration for progesterone analyzed with ^{109}AgNPs and AuNPs. Ion images below bar charts present spatial distributions of stated ions. [Color figure can be viewed at wileyonlinelibrary.com]

AuNPs yield signals with approximately 13-times lower intensity and 10-times lower *S*/*N* values. Table 1 also presents data on the mass accuracy of the LDI-MS measurements for all tested steroid hormones using either silver-109 or gold nanoparticles. The results indicate that the most accurate measurements were obtained using the ^{109}AgNPs from PFL 2D GS LGN for LDI-MS of progesterone, prednisolone and corticosterone. However, for estrone, LDI-MS measurements utilizing AuNPs from PFL 2D GS LGN provided slightly better accuracy, with a measurement mass error of 0.55 ppm. Better overall results for silver-109 are surely an effect of higher *S*/*N* ratios of silver adduct signals and better calibration made with the use of higher amount of calibration ions.

Figure 4 presents results of manual measurements (LDI-MS) and semiautomatic MSI for progesterone with ^{109}AgNPs and AuNPs produced using PFL 2D GS LGN. Progesterone was found in mass spectra mainly as silver-109 adduct of $[C_{21}H_{30}O_2 + {}^{109}Ag]^+$ at *m*/*z* value of 423.1288. The results of manual measurements for progesterone are shown in the bar graph in Figure 4A. Signals of progesterone were found for four highest concentrations in the case of monoisotopic ^{109}AgNPs. In comparison, the use of AuNPs allowed for the detection of progesterone only in concentrations of 1 and 0.1 mg/mL. LOD was found to be 326 pg (1.04 pmol) for ^{109}AgNPs and 2172 pg (6.91 pmol) for AuNPs of progesterone per measured spot. The bar charts of logarithm of signal intensity versus logarithm of concentration obtained with MSI with a series of ion images for the progesterone ions are shown in Figure 4B. Application of ^{109}AgNPs in MSI allowed observation of progesterone–silver-109 signals in all concentrations, which could not be achieved using AuNPs generated in the same manner. MSI ion images proved nonuniform compound localization that is the reason for much better MSI results compared to manual measurements.

Linear regression function for ^{109}AgNPs LDI-MS and LDI-MSI gave similar R^2 values equal to 0.967 and 0.965 respectively. However, MSI allowed the detection of progesterone in a wider

10970231, 2023, 20, Downloaded from https://analyticalsciencejournals.onlinelibrary.wiley.com/doi/10.1002/rcm.9621 by Rzeszow University Of Tech, Wiley Online Library on [30/03/2026]. See the Terms and Conditions (https://onlinelibrary.wiley.com/terms-and-conditions) on Wiley Online Library for rules of use; OA articles are governed by the applicable Creative Commons License

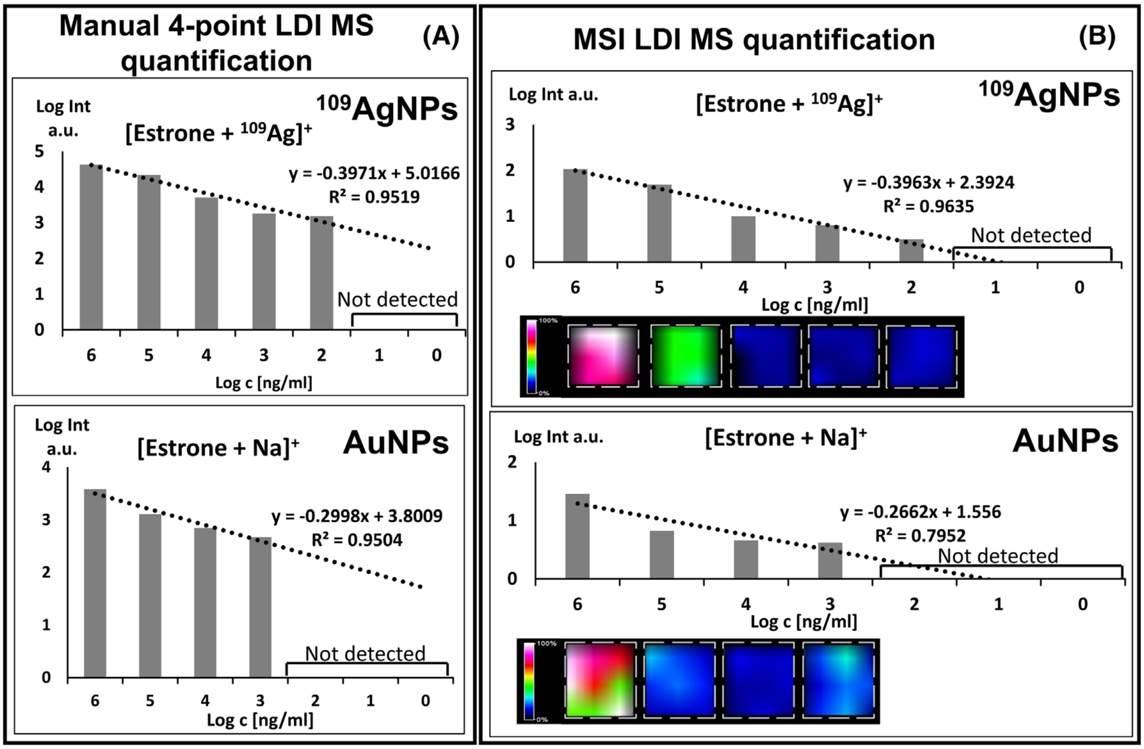

FIGURE 5 (A) Scheme of manual LDI-MS measurement with four random measure points. Bar charts present the average results obtained from five measurements of the same sample spot for estrone with ^{109}AgNPs and AuNPs. The upper part of (B) presents a photograph of the measurement region with overlaid grid of measurement points. Lower part of (B) contains column charts with regression lines and equations for logarithm of the intensity versus logarithm of the concentration for estrone analyzed with ^{109}AgNPs and AuNPs. Ion images below bar charts present spatial distributions of stated ions. [Color figure can be viewed at wileyonlinelibrary.com]

concentration range than LDI-MS, where the lowest amount per spot was 1.6 fmol. Using AuNPs for MSI, signals of progesterone for three of the highest concentrations were obtained.

In 2009, Wu et al used citrate-capped AuNPs as MALDI templates to quantify natural hormones in urine samples. The method showed excellent linearity (5–1000 μM) with a correlation coefficient of 0.9992 and a LOD of 398.9 nM.[20] In 2021, Yang et al presented the MALDI-TOFMS method for the quantification of serum progesterone. Those authors used the quantitative isotope dilution test with the determined ratio of the mass of the ion to the load of progesterone and its fragment. $^{13}C_3$-progesterone was used as an internal standard, which contributed to obtaining precise results as evidenced by the value of the correlation coefficient equal to 0.972. This value relates to the very narrow concentration range (from 0.1 to 80 ng) for which the measurements have been made.[28]

Another studied hormone was estrone being one of the estrogens. Figure 5 presents results analysis for LDI-MS and MSI for estrone with ^{109}AgNPs and AuNPs produced using PFL 2D GS LGN. The method of LDI measurement of estrone with results is presented in Figure 5A. Estrone was found in spectra mainly as silver-109 adduct of $[C_{18}H_{22}O_2 + {}^{109}Ag]^+$ with adduct monoisotopic *m/z* value of 379.0662 or sodium adduct with *m/z* value 293.1512 in the case of using AuNPs. LOD was found to be 938 pg (3.5 pmol) for ^{109}AgNPs and 5897 pg (21.8 pmol) for AuNPs of estrone per measured spot. Signals of estrone were found in spectra in three or two highest concentrations with ^{109}AgNPs or AuNPs, respectively.

The bar charts in Figure 5 show the logarithm of the signal intensity versus the logarithm of the concentration of the test compound. For regression analysis with a linear trend line, *the* R^2 value was found to be 0.996 for ^{109}AgNPs. Moreover, the use of MSI with ^{109}AgNPs allowed the detection of estrone in a wider concentration range, with a slightly lower R^2 coefficient of 0.964. Again, MSI ion images (Figure 5B) proved nonuniform compound localization which is the reason for much better MSI results compared to manual measurements.

This compound was previously studied by Chiu and co-workers who applied AgNPs as a matrix for directly analyzing estrogens using SALDI-MS. Results obtained for estrone were presented with LOD value equal to 2.23 μM.[29]

The next analyzed compound was prednisolone being a synthetic glucocorticoid, which belongs to a class of steroid hormones. Figure 6 presents results of LDI-MS and MSI analysis for prednisolone with ^{109}AgNPs and AuNPs produced using PFL 2D GS LGN. Similar to estrone, measurements of prednisolone were taken at four random locations for the two kinds of nanoparticles, as presented in Figure 6A. Prednisolone was found in spectra mainly as silver-109 adduct of $[C_{21}H_{28}O_5 + {}^{109}Ag]^+$ ion formula in 1 mg/mL to 10 μg/mL samples. LODs were 11 μg/mL (5.3 ng/spot) for ^{109}AgNPs and 52 μg/

10970231, 2023, 20, Downloaded from https://analyticalsciencejournals.onlinelibrary.wiley.com/doi/10.1002/rcm.9621 by Rzeszow University Of Tech, Wiley Online Library on [30/03/2026]. See the Terms and Conditions (https://onlinelibrary.wiley.com/terms-and-conditions) on Wiley Online Library for rules of use; OA articles are governed by the applicable Creative Commons License

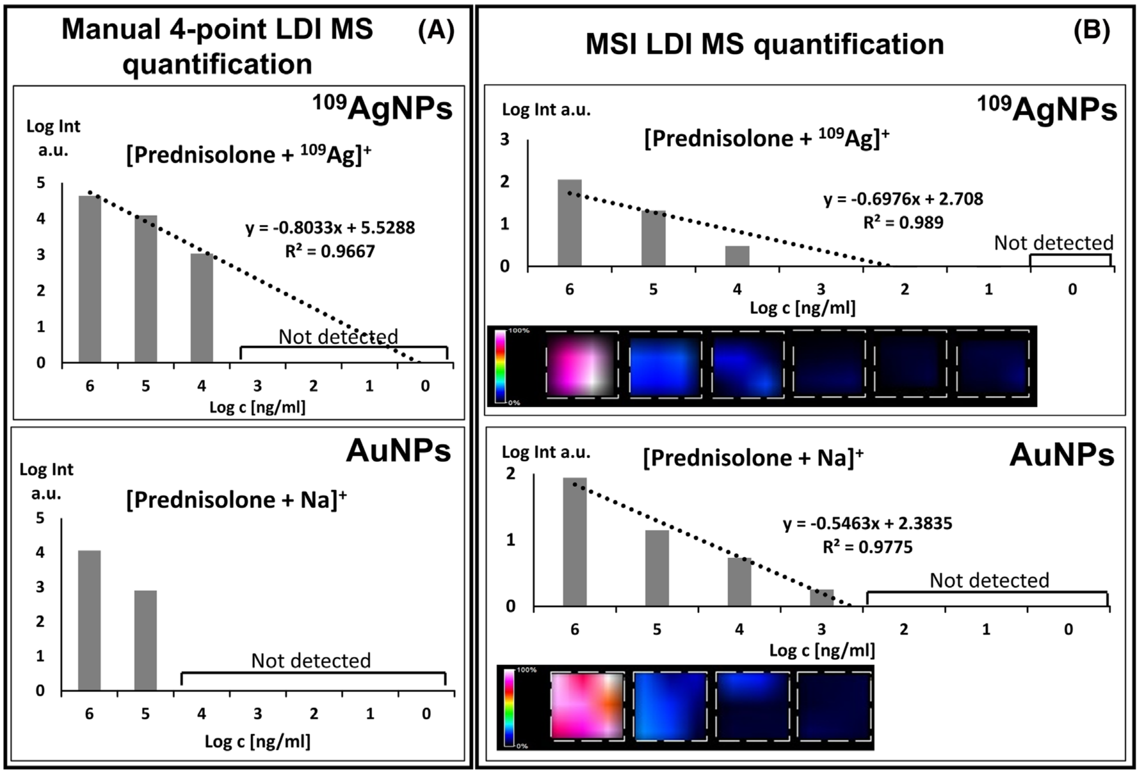

FIGURE 6 (A) Scheme of manual LDI-MS measurement with four random measure points. Bar charts present the average results obtained from five measurements of the same sample spot for prednisolone with ^{109}AgNPs and AuNPs. The upper part of (B) presents a photograph of the measurement region with overlaid grid of measurement points. Lower part of (B) contains column charts with regression lines and equations for logarithm of the intensity versus logarithm of the concentration for prednisolone analyzed with ^{109}AgNPs and AuNPs. Ion images below bar charts present spatial distribution of stated ions. [Color figure can be viewed at wileyonlinelibrary.com]

mL (16.0 ng/spot) for AuNPs. Regression analysis linear trend line was fitted with R^2 value of 0.806 for ^{109}AgNPs in LDI-MS. In the case of using AuNPs generated by PFL 2D GS LGN, signals from prednisolone were identified as sodium adducts only at the three highest concentrations, but the results obtained do not show linearity.

Lack of signal in lower concentration spots is surely an effect of manual placement of measurement points that was again solved by using MSI with a raster of measurement points with specified resolution, as shown in Figure 6B. Application of MSI allowed finding signals of prednisolone–silver-109 in 10 ng/mL concentration sample. The use of AuNPs in MSI allowed the detection of prednisolone signals from a concentration of 1 mg/mL down to a 1000-fold diluted sample. Moreover, results obtained using ^{109}AgNPs with LDI-MSI have much better fit than for manual measurements as proved by R^2 value equal to 0.989. As can be seen in Figure 6B, ion images prove that the studied hormone is deposited nonuniformly throughout of all studied sample spots.

In 2004, Frerichs and Tornatore used liquid chromatography coupled with tandem MS to determine glucocorticoids in human serum. The lower limit of quantification (LLOQ) for prednisolone has been shown to be 10.7 ng/mL. In turn, the LOD value is 225 pg/mL.[30]

The last studied hormone is one of the corticosteroids, namely corticosterone. Figure 7 presents results LDI-MS and MSI analysis for corticosterone with ^{109}AgNPs as well as AuNPs obtained using PFL 2D GS LGN. Manual measurements were made at four random locations, as presented in Figure 7A. Corticosterone was found in spectra mainly as silver-109 adduct of $[C_{21}H_{30}O_4 + {}^{109}Ag]^+$ ion formula in amounts of 500 to 5 ng per sample spot. Average intensities of corticosterone–silver-109 adduct peaks were 2.5×10^4 for the highest concentration, 1.9×10^4 for 100 μg/mL and 2.3×10^3 for 10 μg/mL. The signals obtained using AuNPs were found also in three highest concentrations, but the signal intensities were lower and do not show linearity.

MSI uses a grid or raster of measurement points with specified resolution, as shown in Figure 7B. Application of MSI for analysis of the same samples allowed detection of signal of corticosterone–silver-109 or sodium adduct at the same concentrations as in the case of LDI-MS. Regression analysis of these MSI data provided trend line with R^2 values of 0.835 and 0.969 for ^{109}AgNPs and AuNPs, respectively. LOD based on *S*/*N* ratio was found to be 3 ng (8.82 pmol) or 48 ng (139.81 pmol) of corticosterone per measured spot for ^{109}AgNPs or AuNPs in LDI-MS respectively. In contrast, LOD per measured spot for LDI-MSI was found to be 3 ng (8.76 pmol) for ^{109}AgNPs and 31 ng (90.67 pmol) for AuNPs. As can be seen, measurements at randomly selected sites make the quantitative analysis useless. Moreover, ^{109}AgNPs showed greater utility for quantitative analysis of corticosterone than AuNPs.

10970231, 2023, 20, Downloaded from https://analyticalsciencejournals.onlinelibrary.wiley.com/doi/10.1002/rcm.9621 by Rzeszow University Of Tech, Wiley Online Library on [30/03/2026]. See the Terms and Conditions (https://onlinelibrary.wiley.com/terms-and-conditions) on Wiley Online Library for rules of use; OA articles are governed by the applicable Creative Commons License

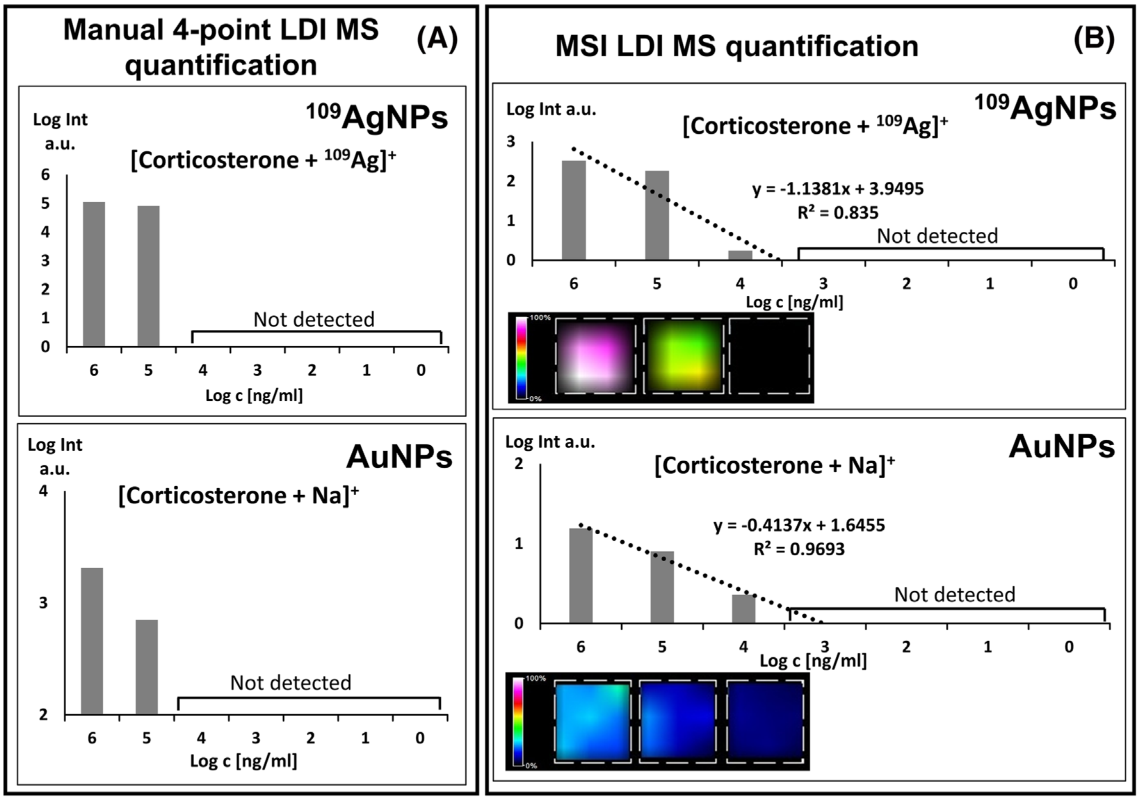

FIGURE 7 (A) Scheme of manual LDI-MS measurement with four random measure points. Bar charts present the average results obtained from five measurements of the same sample spot for corticosterone with ^{109}AgNPs and AuNPs. The upper part of (B) presents a photograph of the measurement region with overlaid grid of measurement points. Lower part of (B) contains column charts with regression lines and equations for logarithm of the intensity versus logarithm of the concentration for corticosterone analyzed with ^{109}AgNPs and AuNPs. Ion images below bar charts present spatial distribution of stated ions. [Color figure can be viewed at wileyonlinelibrary.com]

TABLE 2 Comparison of LOD and LLOQ values for manual and LDI-MSI measurements with using two types of nanoparticles

		LDI-MS		LDI-MSI	
		LOD (ng/mL)	LLOQ (ng/mL)	LOD (ng/mL)	LLOQ (ng/mL)
	Compound	µM		µM	
^{109}AgNPs	[estrone + ^{109}Ag]$^+$	1880 ± 1440 7	3130 ± 2400	1440 ± 970 5	2400 ± 1620
	[prednisolone + ^{109}Ag]$^+$	10 530 ± 4570 30	17 550 ± 7620	11 940 ± 4700 33	19 910 ± 7830
	[progesterone + ^{109}Ag]$^+$	650 ± 725 2	1090 ± 1210	760 ± 830 2	1270 ± 1380
	[corticosterone + ^{109}Ag]$^+$	6110 ± 4520 18	10 190 ± 7530	6070 ± 4800 18	10,110 ± 8,000
AuNPs	[estrone + Na]$^+$	19 660 ± 20 140 70	32 760 ± 33 560	16350 ± 18 110 54	27 240 ± 30 180
	[prednisolone + Na]$^+$	51,680 ± 6,020 140	17 550 ± 7620	22 240 ± 13 180 55	37 070 ± 21 970
	[progesterone + H]$^+$	7240 ± 7160 23	12 070 ± 11 930	4760 ± 5090 14	7940 ± 8480
	[corticosterone + Na]$^+$	161 470 ± 86 470 465	269 110 ± 144 110	104 710 ± 98 200 272	174 520 ± 163 660

10970231, 2023, 20, Downloaded from https://analyticalsciencejournals.onlinelibrary.wiley.com/doi/10.1002/rcm.9621 by Rzeszow University Of Tech, Wiley Online Library on [30/03/2026]. See the Terms and Conditions (https://onlinelibrary.wiley.com/terms-and-conditions) on Wiley Online Library for rules of use; OA articles are governed by the applicable Creative Commons License

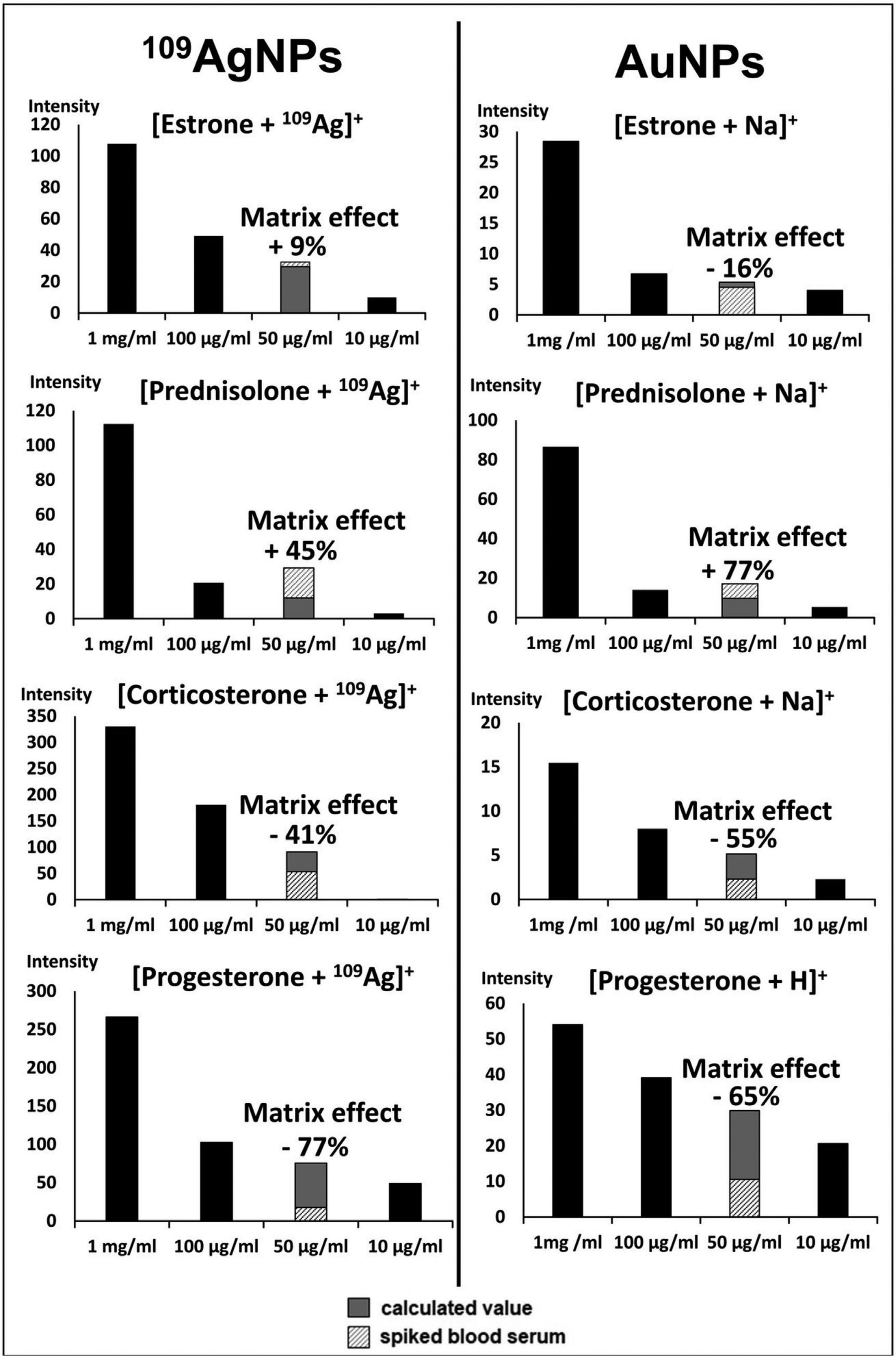

FIGURE 8 Comparison results of quantitative analysis of selected steroid hormones in human blood serum by LDI-MSI with ^{109}AgNPs and AuNPs. For a concentration of 50 μg/mL the calculated intensity of signal (gray bar) was compared with experimental intensity from spiked human blood serum (white bar with dashes).

10970231, 2023, 20, Downloaded from https://analyticalsciencejournals.onlinelibrary.wiley.com/doi/10.1002/rcm.9621 by Rzeszow University Of Tech, Wiley Online Library on [30/03/2026]. See the Terms and Conditions (https://onlinelibrary.wiley.com/terms-and-conditions) on Wiley Online Library for rules of use; OA articles are governed by the applicable Creative Commons License

The quantitative analysis of corticosterone with a concentration range of 0.1–100 μg/mL using the MALDI-MS/MS method was performed by Kim and co-workers. The results showed linearity with R^2 value of 0.997 and LOD value of 45.7 ng/mL.[31] Moreover, Gulid et al presented results of applicability of the SALDI method with an activated carbon surface for the rapid detection of underivatized steroids, i.e. for corticosterone. The authors showed LOD obtained for progesterone in the range 3.14–36.2 μg/mL as LOD for other steroids including for corticosterone.[32]

Table 2 presents the LOD and LLOQ values obtained for the hormones tested by manual MS measurements and MSI with the use of the two types of nanoparticles generated by PFL 2D GS LGN. For almost all hormones, MSI allowed one to obtain equal or lower LOD values than manual LDI-MS. The best results judged by lowest LOD values are found for ^{109}AgNPs. In conclusion, the method based on PFL 2D GS LGN ^{109}AgNPs and MSI gave the best overall results of quantification and highest sensitivity of detection. It should be emphasized that the measurements were performed in a wide range of concentrations.

3.2 | Detection of hormones in spiked human blood serum

The results obtained for hormone solutions were compared with those obtained from spiked human blood serum to estimate the suppression effect of the biological matrix. The serum sample was diluted in deionized water and suitable steroid was then added. The two kinds of nanoparticles were tested for quantitative analysis of hormones in human blood serum. In the case of MSI measurements with the use of ^{109}AgNPs, the highest signals were silver-109 adducts. For AuNPs, these were mainly sodium adducts or, in the case of progesterone, proton adducts.

In order to estimate the suppression effect of biological matrix, results obtained for water solutions of hormones were compared to the ones based on human blood serum (Figure 8). After spiking, each blood serum sample contained 50 μL/mL of the appropriate hormone. The analysis results obtained for all hormones demonstrated a difference in MSI signal response when comparing analyte in standard solution versus the same analyte in a biological matrix such as blood serum.

The difference in estrone signal intensity between the analytical standard solution and the spiked blood sample is small when using both ^{109}AgNPs and AuNPs. The results obtained for prednisolone with ^{109}AgNPs as well as AuNPs show significantly higher (+45% for ^{109}AgNPs and +77% for AuNPs) signal intensities for spiked serum. This difference may be due to the presence of prednisolone in the test sample or its structural similarity to the naturally occurring hormones in the blood produced by the adrenal cortex, which interfere with the signals. The matrix effect significantly reduces the signal intensity for corticosterone by 41% for ^{109}AgNPs and 55% for AuNPs; in the case of progesterone by 77% (^{109}AgNPs) and 65% (AuNPs). In the case of MSI analysis using ^{109}AgNPs for estrone, a smaller matrix effect was observed.

The presented results clearly show that a biological matrix such as human blood serum has a significant impact on the intensity value of the steroid hormones during the MSI experiment. Quantitative analysis of biological samples by LDI-MSI is complicated by the presence of matrix components that can interfere with the assay, resulting in ion suppression or enhancement.[33]

4 | CONCLUSION

The application of monoisotopic silver and gold nanoparticles, generated by the PFL 2D GS LGN method, for manual LDI-MS and semiautomatic LDI-MSI enabled the detection and quantification of hormones across a broad concentration range from 1 mg/mL to 1 ng/mL. An advantage in the analytical performance of ^{109}AgNPs over AuNPs was demonstrated in the quantitative analysis of the tested steroid hormones. LOD and R^2 values obtained indicate that ^{109}AgNPs used in MSI measurement mode for MSI methods allow much better quantification than for commonly used MALDI manual measurements. Ion images obtained in MSI experiments indicated highly nonuniform analyte deposition that makes semiautomatic, multi-pixel MSI a modern requirement rather than an improvement.

AUTHOR CONTRIBUTIONS

Aneta Płaza-Altamer: Data curation; formal analysis; investigation; visualization; writing—original draft; writing—review and editing. **Artur Kołodziej:** Data curation; investigation. **Zuzanna Krupa:** Data curation. **Joanna Nizioł:** Funding acquisition; project administration. **Tomasz Ruman:** Conceptualization; methodology; resources; supervision; writing—original draft; writing—review and editing.

ACKNOWLEDGMENTS

This work was supported by the National Science Centre (NCN), SONATA BIS grant no. UMO-2022/46/E/ST4/00016.

DATA AVAILABILITY STATEMENT

The data that support the findings of this study are available on request from the corresponding author. The data are not publicly available due to privacy or ethical restrictions.

ORCID

Aneta Płaza-Altamer https://orcid.org/0000-0003-1719-8730
Artur Kołodziej https://orcid.org/0000-0002-9222-0937

REFERENCES

1. Chanclud E, Morel JB. Plant hormones: A fungal point of view. *Mol Plant Pathol*. 2016;17(8):1289-1297. doi:10.1111/mpp.12393
2. Kumar A, Kumar P, Faiq MA, Sharma VK, Sesham K, Kulandhasamy M. Hormones and behavior. In: Vonk J, Shackelford T, eds. *Encyclopedia of Animal Cognition and Behavior*. Springer International Publishing; 2018:1-22. doi:10.1007/978-3-319-47829-6_476-2

10970231, 2023, 20, Downloaded from https://analyticalsciencejournals.onlinelibrary.wiley.com/doi/10.1002/rcm.9621 by Rzeszow University Of Tech, Wiley Online Library on [30/03/2026]. See the Terms and Conditions (https://onlinelibrary.wiley.com/terms-and-conditions) on Wiley Online Library for rules of use; OA articles are governed by the applicable Creative Commons License

3. Temerdashev A, Dmitrieva E, Podolskiy I. Analytics for steroid hormone profiling in body fluids. *Microchem J*. 2021;168:106395. doi:10.1016/j.microc.2021.106395
4. Kleine B, Rossmanith WG. *Hormones and the Endocrine System*. Springer International Publishing; 2016. doi:10.1007/978-3-319-15060-4
5. Campbell M, Jialal I. *Physiology, Endocrine Hormones*. StatPearls Publishing; 2021. Accessed December 29, 2021. https://www.ncbi.nlm.nih.gov/books/NBK538498/
6. Taraborrelli S. Physiology, production and action of progesterone. *Acta Obstet Gynecol Scand*. 2015;94(S161):8-16. doi:10.1111/aogs.12771
7. Schumacher M, Akwa Y, Guennoun R, et al. Steroid synthesis and metabolism in the nervous system: Trophic and protective effects. *J Neurocytol*. 2000;29(5):307-326. doi:10.1023/A:1007152904926
8. Speiser PW, White PC. Congenital adrenal hyperplasia. *N Engl J Med*. 2003;349(8):776-788. doi:10.1056/NEJMra021561
9. Song Z, Gao H, Xie W, Sun Q, Liang K, Li Y. Quantitative MALDI-MS assay of steroid hormones in plasma based on hydroxylamine derivatization. *Anal Biochem*. 2021;616:114089. doi:10.1016/j.ab.2020.114089
10. Nieschlag E, Wickings EJ. A review of radioimmunoassay for steroids. *Clin Chem Lab Med*. 1975;13(7). doi:10.1515/cclm.1975.13.7.261
11. Pizzolo F, Corgnati A, Guarini P, et al. Plasma aldosterone assays: Comparison between chemiluminescence-based and RIA methods. *Clin Chem*. 2006;52(7):1431a-11432a. doi:10.1373/clinchem.2005.061184
12. Lequin RM. Enzyme immunoassay (EIA)/enzyme-linked immunosorbent assay (ELISA). *Clin Chem*. 2005;51(12):2415-2418. doi:10.1373/clinchem.2005.051532
13. Son J, Cha S. MALDI mass spectrometric analysis of nonderivatized steroids using cyclodextrin-supported 2,5-dihydroxybenzoic acid as matrix. *Bull Korean Chem Soc*. 2014;35(5):1409-1412. doi:10.5012/bkcs.2014.35.5.1409
14. Nizioł J, Rode W, Laskowska B, Ruman T. Novel monoisotopic ^{109}AgNPET for laser desorption/ionization mass spectrometry. *Anal Chem*. 2013;85(3):1926-1931. doi:10.1021/ac303770y
15. Sekuła J, Nizioł J, Rode W, Ruman T. Gold nanoparticle-enhanced target (AuNPET) as universal solution for laser desorption/ionization mass spectrometry analysis and imaging of low molecular weight compounds. *Anal Chim Acta*. 2015;875:61-72. doi:10.1016/j.aca.2015.01.046
16. Nizioł J, Ossoliński K, Ossoliński T, et al. Surface-transfer mass spectrometry imaging of renal tissue on gold nanoparticle enhanced target. *Anal Chem*. 2016;88(14):7365-7371. doi:10.1021/acs.analchem.6b01859
17. Abdelhamid HN, Wu HF. Gold nanoparticles assisted laser desorption/ionization mass spectrometry and applications: From simple molecules to intact cells. *Anal Bioanal Chem*. 2016;408(17):4485-4502. doi:10.1007/s00216-016-9374-6
18. Tang HW, Lu W, Che CM, Ng KM. Gold nanoparticles and imaging mass spectrometry: Double imaging of latent fingerprints. *Anal Chem*. 2010;82(5):1589-1593. doi:10.1021/ac9026077
19. Su CL, Tseng WL. Gold nanoparticles as assisted matrix for determining neutral small carbohydrates through laser desorption/ionization time-of-flight mass spectrometry. *Anal Chem*. 2007;79(4):1626-1633. doi:10.1021/ac061747w
20. Wu HP, Yu CJ, Lin CY, Lin YH, Tseng WL. Gold nanoparticles as assisted matrices for the detection of biomolecules in a high-salt solution through laser desorption/ionization mass spectrometry. *J Am Soc Mass Spectrom*. 2009;20(5):875-882. doi:10.1016/j.jasms.2009.01.002
21. Arendowski A, Nizioł J, Ruman T. Silver-109-based laser desorption/ionization mass spectrometry method for detection and quantification of amino acids. *J Mass Spectrom*. 2018;53(4):369-378. doi:10.1002/jms.4068
22. Szulc J, Kołodziej A, Ruman T. Silver-109/silver/gold nanoparticle-enhanced target surface-assisted laser desorption/ionisation mass specTromeTry – The new methods for an assessment of mycotoxin concentration on building materials. *Toxins*. 2021;13(1):45. doi:10.3390/toxins13010045
23. Płaza A, Kołodziej A, Nizioł J, Ruman T. Laser ablation synthesis in solution and nebulization of silver-109 nanoparticles for mass spectrometry and mass spectrometry imaging. *ACS Meas Sci Au*. 2022;2(1):14-22. doi:10.1021/acsmeasuresciau.1c00020
24. Rzeszow University of Technology, Faculty of Chemistry, Department of Inorganic and Analytical Chemistry, Płaza-Altamer A, Kołodziej A, Nizioł J, Ruman T. Laser generated gold nanoparticles for mass spectrometry of low molecular weight compounds. *CT&B*. 2022;61-69. doi:10.7862/rc.2022.1
25. Płaza A, Kołodziej A, Nizioł J, Ruman T. Laser ablation synthesis in solution and nebulization of silver-109 nanoparticles for mass spectrometry and mass spectrometry imaging. *ACS Meas Sci Au*. 2021;2(1):14-22. doi:10.1021/acsmeasuresciau.1c00020
26. Kołodziej A, Płaza-Altamer A, Nizioł J, Ruman T. Infrared pulsed fiber laser-produced silver-109-nanoparticles for laser desorption/ionization mass spectrometry of carboxylic acids. *Int J Mass Spectrom*. 2022;474:116816. doi:10.1016/j.ijms.2022.116816
27. Płaza-Altamer A, Kołodziej A, Nizioł J, Ruman T. Infrared pulsed fiber laser-produced silver-109-nanoparticles for laser desorption/ionization mass spectrometry of amino acids. *J Mass Spectrom*. 2022;57(3):e4815. doi:10.1002/jms.4815
28. Yang MH, Chen SC, Chen KC, et al. Quantitative analysis of progesterone using isotope dilution-matrix-assisted laser desorption ionization-time of flight mass spectrometry as a reference procedure for radioimmunoassay. *Clin Chim Acta*. 2021;512:106-111. doi:10.1016/j.cca.2019.11.020
29. Chiu TC, Chang LC, Chiang CK, Chang HT. Determining estrogens using surface-assisted laser desorption/ionization mass spectrometry with silver nanoparticles as the matrix. *J Am Soc Mass Spectrom*. 2008;19(9):1343-1346. doi:10.1016/j.jasms.2008.06.006
30. Frerichs VA, Tornatore KM. Determination of the glucocorticoids prednisone, prednisolone, dexamethasone, and cortisol in human serum using liquid chromatography coupled to tandem mass spectrometry. *J Chromatogr B*. 2004;802(2):329-338. doi:10.1016/j.jchromb.2003.12.015
31. Kim SJ, Jung HJ, Chung BC, Choi MH. Screening analysis of 10 adrenal steroids by matrix-assisted laser desorption ionization-tandem mass spectrometry. *Mass Spectrom Lett*. 2011;2(3):69-72. doi:10.5478/MSL.2011.2.3.069
32. Guild GE, Lenehan CE, Walker GS. Surface-assisted laser desorption ionisation time-of-flight mass spectrometry with an activated carbon surface for the rapid detection of underivatised steroids. *Int J Mass Spectrom*. 2010;294(1):16-22. doi:10.1016/j.ijms.2010.04.001
33. Matuszewski BK, Constanzer ML, Chavez-Eng CM. Strategies for the assessment of matrix effect in quantitative bioanalytical methods based on HPLC−MS/MS. *Anal Chem*. 2003;75(13):3019-3030. doi:10.1021/ac020361s

How to cite this article: Płaza-Altamer A, Kołodziej A, Krupa Z, Nizioł J, Ruman T. Infrared pulsed fiber laser-produced gold and silver-109 nanoparticles for laser desorption/ionization mass spectrometry of steroid hormones. *Rapid Commun Mass Spectrom*. 2023;37(20):e9621. doi:10.1002/rcm.9621

10970231, 2023, 20, Downloaded from https://analyticalsciencejournals.onlinelibrary.wiley.com/doi/10.1002/rcm.9621 by Rzeszow University Of Tech, Wiley Online Library on [30/03/2026]. See the Terms and Conditions (https://onlinelibrary.wiley.com/terms-and-conditions) on Wiley Online Library for rules of use; OA articles are governed by the applicable Creative Commons License

Food Analytical Methods (2024) 17:236–250
https://doi.org/10.1007/s12161-023-02561-x

RESEARCH

Infrared Laser-Based Selected Reaction Monitoring Mass Spectrometry Imaging of Banana (*Musa* spp.) Tissue—New Method for Detection and Spatial Localization of Metabolites in Food

Joanna Nizioł[1] · **Maria Misiorek**[1] · **Zuzanna Krupa**[2] · **Tomasz Ruman**[1]

Received: 19 October 2023 / Accepted: 30 November 2023 / Published online: 13 December 2023
© The Author(s) 2023

Abstract

In this study, for the first time, we present the application of an infrared (IR) laser ablation-remote-electrospray ionization (LARESI) platform coupled to a tandem mass spectrometer (MS/MS) operated in selected reaction monitoring (SRM) mode for targeted metabolite imaging in intact plant tissues. We examined the distribution of specific metabolites in two banana varieties: Red Dacca and Cavendish. To support MSI results, an extensive analysis of banana tissue extracts was conducted using ultra-high-performance liquid chromatography and ultra-high-resolution mass spectrometry (UHPLC-UHRMS). In the Cavendish banana, 12 metabolites were successfully identified, while Red Dacca bananas were found to contain 16 amino acids. The spatial distribution of some of these compounds found in bananas was presented for the first time. This approach eliminates the need for high vacuum conditions and the pretreatment of biological materials, making it an efficient and promising tool for studying metabolites in plant tissues.

Keywords Mass spectrometry imagining · Laser ablation · Ambient mass spectrometry imaging · Metabolites · Banana

Introduction

Banana (*Musa L.*) stands as a highly favored tropical fruit due to its exceptional nutritional value (Singh et al. 2016a; Qamar and Shaikh 2018; Yun et al. 2022). Banana belongs to the monocot plants in the banana family (*Musaceae Juss.*), and its origins trace back to Southeast Asia. This tropical fruit has garnered attention for its remarkable antioxidant and antimicrobial capabilities, attributed to the presence of widespread polyamines and bioactive amines (Adão and Glória 2005; Lima et al. 2008). Moreover, banana pulp serves as a rich source of valuable nutraceuticals and bioactive compounds, including carbohydrates, amino acids (AAs), carotenoids, polyphenols, and phytosterols (Singh et al. 2016b; Sidhu and Zafar 2018; Maduwanthi and Marapana 2021; Mondal et al. 2021). Banana enjoys the status of being one of the most widely consumed fruits worldwide, not only due to its popularity as a nutritional source but also its significant contribution to the global economy and trade, with many countries depending partially or entirely on their banana production (Hussein et al. 2020). Despite their commercial importance, bananas often encounter challenges from various diseases caused by fungi, bacteria, viruses, nematodes, and insects (Shi Ming et al. 2021). The examination of these plant infections is typically conducted using microscopic techniques. However, determining the spatial distribution of chemical compounds necessitates careful examination of the diseased areas in plant tissues.

To gain deeper insights into the intricate processes within living organisms, the ability to examine the spatial distributions of molecules in biological tissues is of paramount importance. While analytical techniques like conventional liquid chromatography mass spectrometry (LC-MS) (Gedük and Zengin 2021) and gas chromatography mass spectrometry (GC–MS) (Dou et al. 2020) have been proven effective in identifying non-volatile and volatile metabolites, respectively, in plant tissue extracts including banana peels and pulps, they offer averaged information for each compound.

✉ Joanna Nizioł
jniziol@prz.edu.pl

[1] Faculty of Chemistry, Rzeszów University of Technology, 6 Powstańców Warszawy Ave., 35-959 Rzeszów, Poland

[2] Doctoral School of Engineering and Technical Sciences at the Rzeszów University of Technology, 8 Powstańców Warszawy Ave., 35-959 Rzeszów, Poland

Mass spectrometry imaging (MSI) is a powerful analytical tool that provides simultaneous spatial distribution information of up to thousands of molecules in a variety of samples in a single experiment without the necessity for labeling or altering the structure of the original molecules (Stoeckli et al. 2001; Chaurand et al. 2004). This is crucial because labeling interferes with the molecule's properties and behavior or the label itself might react with multiple types of molecules, leading to ambiguous results (McDonnell and Heeren 2007). MSI has been the subject of extensive research in recent decades due to its high sensitivity and ability to precisely quantify the spatial distribution of a variety of chemical compounds in various samples such as tissue sections, which can be of great value in biological research (Gao et al. 2023). Mapping ions on the surface of such specimens can reveal intricate details about how compounds are compartmentalized, the localized metabolic activity, and specific binding regions for an extensive range of both natural and man-made compounds (Caprioli et al. 1997). The undoubted advantage of MSI is that it does not require the homogenization of samples, which is necessary in GC/LC-MS. This means that samples can be analyzed in state close to natural conditions and avoid potential changes to the sample caused by the extraction process. MSI allows the analysis of compounds directly in tissue, which is particularly important in biomedical and pharmacological research, where the location of the compound may be important for its function or toxicity (Cornett et al. 2007). In the case of MSI, samples often require only simple preparation such as freezing and cutting into thin sections with minimal risk of tissue degradation. While LC-MS also allows for the analysis of multiple compounds simultaneously, MSI allows the spatial distribution of multiple compounds to be visualized simultaneously without the need to separate them first (Norris and Caprioli 2013).

MSI can also be useful in quickly assessing food safety (Zou et al. 2022). MSI can detect specific peptides or other biomarkers that are characteristic of specific pathogens with high sensitivity and specificity. Information regarding the location of pathogens in a sample may be crucial to understanding their spread and interactions with food (dos Santos et al. 2017; Rocha et al. 2017). MSI is advantageous for food samples where additional processing may lead to the spread or degradation of pathogens (Araújo et al. 2017).

Among the most commonly utilized techniques for investigating the spatial distribution of compounds in biological samples, matrix-assisted laser desorption ionization (MALDI) (Sarabia et al. 2018), secondary ion mass spectrometry (SIMS) (Eswara et al. 2019), and desorption electrospray ionization (DESI) hold prominence (Yin et al. 2018). These cutting-edge approaches have paved the way for a deeper understanding of the molecular composition and localization within biological systems.

SIMS boasts high efficiency in MS imaging owing to its exceptional sensitivity, highest lateral resolution (10 nm), wide dynamic range, and ability to detect all elements along with their isotope order ($m/z < 1000$) (Audinot et al. 2021). However, known issue with SIMS is moderate-to-heavy fragmentation of compounds of interest. MALDI is a much softer ionization method which enables the determination of compounds with a higher practical mass range (>10,000 Da) but with coarser resolution (30–200 µm).

Nevertheless, both methods require specialized and time-consuming sample preparation. In the MALDI method, thin tissue slices are coated with a matrix solution. However, a significant limitation lies in the need for a laser energy-absorbing matrix solution, which can alter the original spatial distribution of molecules through lateral mixing. Moreover, the requirement for a high vacuum environment restricts the range of materials that can be analyzed using this method, and it is not suitable for in vivo measurements. Furthermore, MALDI may encounter interference from the matrix in the low mass region ($m/z < 1000$), making it challenging to measure the $m/z < 600$ domain (Kaspar et al. 2011; Calvano et al. 2018).

Recent developments in MSI have led to the emergence of ambient ionization techniques, providing new avenues for analyzing biological materials (Wu et al. 2013a; Cabral et al. 2013). DESI stands as one such technique, enabling the imaging of low molecular compounds in plant tissues (Tata et al. 2015). However, DESI has certain limitations, including relatively low spatial resolution (usually around 100–200 µm), low ionization efficiency for specific molecules, and shallow sampling depth, which restricts the amount of material available for analysis. Among ambient environment MS methods, those employing a mid-IR laser for sampling show promise in analyzing metabolites within biological tissues (Bartels and Svatoš 2015). An advantage of using an IR laser is its ability to effectively couple energy into the O–H stretching mode of hydrogen-bonded water, commonly present in hydrated biological materials. This facilitates greater depth of sampling, making it suitable for imaging various tissues including non-flat samples (Joignant et al. 2023).

In recent years, there has been a growing interest in developing MSI technologies to map metabolite abundances in various fruits and vegetables. Researchers have successfully applied MSI to study strawberries and apples (da Silva et al. 2022), rhubarb stalk (Nizioł et al. 2017), and garlic (Misiorek et al. 2017). To the best of our knowledge, there have been only a few published reports investigating banana tissue sections biologically. In a significant milestone in 2007, (Li et al. 2007) conducted MSI of banana tissue using a mid-IR laser at atmospheric pressure without the need for an additional matrix. Instead, naturally occurring water in the biological tissue served as the energy-absorbing matrix. The study primarily focused on water-soluble components, such as glucose, fructose, sucrose, citric acid, and potassium ions, which were tentatively identified in the thin (0.2–0.5 mm) sections of the banana tissues. However, it is worth noting that the primary focus of the publication was to introduce the new MSI technique. Consequently, it only presented the average mass spectrum from 300 laser shots measured at randomly selected points on the banana tissues. In 2015, Hölscher et al. (2015) used matrix-free Fourier transform ion cyclotron resonance mass spectrometric imaging (LDI-FT-ICR-MSI) for tentative identification of specific low molecular compounds within the red regions of the ornamental banana *Musa acuminata* spp. *Zebrina* cv "Rowe Red." In another study, Wu et al. used gold nanoparticle (AuNP)-immersed paper imprinting MSI strategy to visualize the spatial distribution of some endogenous compounds within banana corms (Wu et al. 2020). More recently, Yin et al. (2022) proposed AuNPs LDI-MSI for investigating the spatiotemporal distribution and metabolite levels within Brazil and Dongguan banana pulps during postharvest senescence.

Despite these remarkable efforts, one of the main challenges in mass spectrometry imaging (MSI) is the difficulty in unambiguously identifying the compounds being imaged. While MSI provides valuable spatial information about the distribution of molecules in a sample, the identification of these molecules can be complex and challenging. To overcome this limitation, tandem mass spectrometry (MS/MS) imaging can be used.

In this work, we present a new approach to molecular imaging of plant tissue based on laser ablation-remote electrospray ionization (LARESI) in selected reaction monitoring (SRM) mode. It was previously used for targeted analysis of metabolites in human tissue (Nizioł et al. 2020) or mycotoxins in infected grains (Szulc and Ruman 2020), enhancing selectivity through compound-specific ion fragmentation in SRM or MRM modes. MS/MS offers high sensitivity, a wide dynamic range, rapid analysis, and suitability for quantitation, making it valuable for the detection and identification of low-molecular-weight compounds. There are no fragmentation-based mass spectrometry imaging results for banana tissue in the literature published to date.

Experimental

Materials and Equipment

Two species of bananas commercially available were selected. One of the species was Red Dacca Banana (*Musa acuminata*), imported from Colombia. The second was the Cavendish banana from the AAA banana cultivar group (*Musa acuminata*). Fresh banana fruits were purchased from local supermarkets. All solvents were of "LC-MS" or analytical reagent grade. High purity deionized water (> 18 MΩ·cm) was produced locally. Optical photographs of tissue samples were obtained on an Olympus SZ10 microscope, equipped with an 8-MP Olympus camera.

Sample Preparation for MSI Analysis

For the LARESI SRM MSI imaging experiments, 100-μm-thick each banana tissue sections were cut using a microtome. The slices were mounted on the Peltier stage set to −18°C to minimize the lateral mixing of compounds in the sample surface. Two different banana tissue sections recovered from two species (Red Dacca and Cavendish Banana) were examined.

Sample Extraction for LC-MS Analysis

Amount of 60 mg of banana tissue was inserted into 2-mL bead beating lysis tubes. Solvent mixture (900 μL of a 1:2 MeOH/$CHCl_3$) was poured into each tissue tube, three glass beads were then added. Bead homogenizer was then used for 45s and then samples were placed on ice. An amount of 120 μl cold water was added to each tube. Homogenization was repeated for 45 s, and after 5 min—for another 45 s. Samples were placed in −20°C for 1 h to precipitate cell debris and protein matter. After this time, centrifugation for 10 min (14000×*g*) was made, upper phases transferred to 130 μL inserts placed in HPLC vials and inserted into a Bruker Elute autosampler. The thermostated chamber of the autosampler was set at 5°C.

LARESI SRM MSI of Bananas

In this study, we employed an Nd/YAG-pumped, tunable OPO laser (IR Opolette 2731-HE; Opotek, Carlsbad, CA, USA) to generate mid-infrared (mid-IR) laser pulses. The laser system produced 4-ns pulses with a maximum repetition frequency of 20 Hz. Specifically, the laser was tuned to emit at a wavelength of 2.94 μm. During experimentation, the pulse energy of the laser was measured to be 3.5 mJ, and this measurement was conducted using a pyroelectric energy meter (PE25-SH-V2; Ophir-Spiricon, Logan, UT, USA).

In our research, we conducted experiments within a controlled environment using an airtight chamber. The chamber was pressurized with nitrogen gas to create a steady stream flowing at a rate of 2 L/min. To maintain optimal conditions for our sample, we placed it on a 50 × 50 mm sample stage within the chamber. The sample was kept at temperatures as low as –18° C through the use of a Peltier cooling plate (TE-127-1.4-1.5; TE Technology, Traverse City, MI, USA). To manage any excess heat generated by the Peltier element, we implemented a circulating water system coupled with an external radiator. The temperature-controlled sample stage was mounted on a motorized XY-stage (MTS50-Z8; Thorlabs, Newton, NJ, USA) to enable precise movement and positioning. To introduce the laser beam into the sample chamber, we utilized a 1″ Infrasil window (Thorlabs, Newton, NJ, USA), and a gold-plated mirror (PF10-03-M01; Thorlabs) redirected the beam towards the sample stage. A 40-mm focal length CaF_2 spherical lens (Thorlabs, Newton, NJ, USA), mounted on a Z-axis stage (Thorlabs, Newton, NJ, USA), focused the beam onto the sample surface. The incidence angle on the sample was set at 90°, with a laser focus size of 60 ± 10 μm. We measured the pulse energy at the sample surface to be 2.5 mJ. During the imaging process, the laser focal point remained stationary while a computer-controlled XY-stage moved the sample accordingly. To efficiently capture the laser ablation plumes, a funnel connected to a 4-mm I.D. PTFE tube was positioned over the laser ablation site. The pressurized chamber facilitated the entrainment of the laser ablation plumes into the gas, which was then transported to the electrospray ionization (ESI) source of the SCIEX QTRAP 5500 mass spectrometer. For smooth operation and consistent flow, we employed a binary HPLC pump (Agilent G1312A) to provide a steady stream of binary solvent mixture (2:1 IPA:water with 0.5% acetic acid; 20 μL/min) to the electrospray needle. The configuration of this system for LARESI SRM MSI was previously illustrated in our publication, where we successfully applied this method for imaging kidney tissue (Nizioł et al. 2020) and grains (Szulc and Ruman 2020).

To maintain stable conditions for our samples during analysis, we utilized a Peltier module, which kept the samples at a consistent temperature of −18°C. The imaging process focused on square or rectangular areas, encompassing approximately 1 cm^2. With an impressive pixel count of around 1.5×10^3, the spatial resolution ranged from 175 to 300 μm. Each pixel was subjected to the laser for precisely 2 s, and the laser pulse repetition rate was set at 15 Hz. To achieve comprehensive coverage, the sample stage moved at a speed of 2 mm/s between pixels. During the time delay between pixels, which lasted for 4 s, the stage moved along a straight line to position the next pixel accurately. Additionally, there was a time delay of 5 s between lines, ensuring proper alignment during imaging. The total analysis time for an image with an area of 40 × 40 pixels was approximately 3 h excluding tuning and calibration of mass spectrometer. The advanced control and analysis software used in this study have been recently described, guaranteeing reliable and efficient data processing (Brauer et al. 2015).

In MSI analysis, we employed the SCIEX QTRAP 5500 mass spectrometer, operating in positive ion mode, specifically using the SRM measurement mode with Q1/Q3/DP/EP/CE and CXP settings. During SRM mode, we monitored each compound-specific fragmentation for a duration of 10 ms, with a 5-ms delay before monitoring the subsequent fragmentation. This precise timing ensured accurate and comprehensive data acquisition for our analysis. For the ESI source, we set the source temperature at 500°C, with a curtain gas pressure of 20 psi. Additionally, ion source gas 1 was set to 30 psi, while ion source gas 2 was maintained at 20 psi. For positive ion mode, we applied an ion-spray voltage of +5500 V, and for negative mode, it was adjusted to −4500 V. To facilitate collision-induced dissociation, we utilized nitrogen gas as the collision gas, setting it to medium pressure. Detailed settings are presented in Table 1.

UHPLC-Q-ToF-UHRMS of Banana Extracts

UHPLC-Q-ToF-UHRMS analysis was conducted with Bruker Elute UHPLC system operated with Hystar 3.3 software, coupled with a Bruker Impact II mass spectrometer of ESI QToF-MS type (60,000+ resolution version) from Bruker Daltonik GmbH (Bremen, Germany). The UHPLC column used was the Bruker Intensity Solo with C18 silica modification, containing 2-μm particles and having dimensions of 100 × 2.1 mm (length × diameter). To maintain consistent conditions, the UHPLC column was thermostated at 40°C throughout the analysis. For mobile phases, we utilized water with 0.1% HCOOH as phase A and acetonitrile with 0.1% HCOOH as phase B. The injection volume was set at 5 μL, and the percentage of phase B varied as follows: 1% (0–2 min), 99% (17–20 min), and 1% (20.1–30 min). The solvent flow rate was 0.25 mL/min from 0 to 20 min and gradually increased to 0.35 mL/min from 20.1 to 30 min. Internal calibration was carried out using ions from 10 mM sodium formate pumped into the ESI ion source with a syringe pump at an infusion flow rate of 0.12 mL/h (solvent:water:isopropanol 1:1 v/v). High-precision calibration (HPC) mode in Metaboscape was used for the calibration process. The instrument operated in autoMSMS mode, with the *m/z* range set at 50–1500, and the collision-induced dissociation (CID) energy value was maintained at 30 eV. Specific CID settings included an absolute area threshold of 5000 cts, active exclusion 2, and an isolation window for m/z ranges of 100–4, 300–5, 500–6, and 1000–8. For untargeted annotations, we used Metaboscape (ver. 2022b) with a criterion of mass deviation ($\Delta m/z$) under 2 ppm and a mSigma value under 30. MS/MS spectra were automatically matched against MS/MS libraries, such as the Bruker HMDB 2.0 library (with retention times) and the MoNA library (MassBank of North America (MoNA).

Results and Discussion

The MSI method we used in food analysis is a promising technology that, unlike traditional analytical methods such as GC/LC-MS, enables the exact location of various

Table 1 Selected metabolites found in bananas with LARESI-SRM-MSI experiments

No.	Compound name	Plant tissue	Structure	m/z[a]	MS ionization mode	Q1 [*m/z*]	Q3 [*m/z*]	Scan time [ms]	DP [V]	EP [V]	CE [V]	CXP [V]	Ion image
1	Caffeic acid[b]	Cavendish banana	$C_9H_8O_4$	180.0423	Negative	179.0	135.0	5	−48	−8	−21	−11	Fig. 1I
2	Catechin[b]		$C_{15}H_{14}O_6$	290.0790	Negative	289.0	203.0	5	−110	−10	−29	−8	Fig. 1L
					Positive	291.0	139.0	5	16	10	21	10	Fig. 1M
3	Eugenol[b]		$C_{10}H_{12}O_2$	164.0837	Negative	163.0	148.0	5	−49	−5	−19	−13	Fig. 1H
4	Ferulic acid[b,d]		$C_{10}H_{10}O_4$	194.0579	Negative	193.0	134.0	5	−58	−5	−23	−9	Fig. 1J
5	Isobutyl butyrate[b]		$C_8H_{16}O_2$	144.1150	Positive	145.1	71.0	5	70	10	40	10	Fig. 1F
6	Myricetin[b]		$C_{15}H_{10}O_8$	318.0376	Negative	317.0	151.0	20	−20	−10	−26	−8	Fig. 1O
7	Protocatechuic acid[b]		$C_7H_6O_4$	154.0266	Negative	153.0	109.0	5	−64	−5	−22	−9	Fig. 1G
8	Pyruvic acid[b]		$C_3H_4O_3$	88.0160	Negative	87.0	32.0	5	−50	−10	−28	−9	Fig. 1D
					Negative	87.0	43.0						Fig. 1E
9	Quercetin[b]		$C_{15}H_{10}O_7$	302.0427	Negative	301.0	150.9	5	−120	−10	−28	−11	Fig. 1N
10	Sinapic acid[b]		$C_{11}H_{12}O_5$	224.0685	Negative	223.0	192.9	5	−48	−8	−21	−11	Fig. 1K
11	Alanine[b,c]	Red Dacca Banana	$C_3H_7NO_2$	89.0477	Positive	90.1	44.0	30	6	4.5	17	6	Fig. 2C
12	Arginine[b,c,d]		$C_6H_{14}N_4O_2$	174.1117	Positive	133.1	74.0	30	40	11	27	8	Fig. 2O
13	Asparagine[b,c,d]		$C_4H_8N_2O_3$	132.0535	Positive	175.2	70.0	30	50	10	20	15	Fig. 2I
14	Cysteine[b]		$C_3H_7NO_2S$	121.0198	Positive	241.2	152.0	30	20	14	19	10	Fig. 2R
15	Glutamic acid[b]		$C_5H_9NO_4$	147.0532	Positive	148.1	84.0	50	21	14.5	21	10	Fig. 2K
16	Histidine[b,c,d]		$C_6H_9N_3O_2$	155.0695	Positive	156.1	110.0	50	16	13	19	12	Fig. 2M
17	Isoleucine[b]		$C_6H_{13}NO_2$	131.0946	Positive	132.1	69.0	30	8	14.5	23	8	Fig. 2H
18	Lysine[b,c]		$C_6H_{14}N_2O_2$	146.1055	Positive	147.1	84.0	30	15	13.5	23	10	Fig. 2J
19	Methionine[b,d]		$C_5H_{11}NO_2S$	149.0511	Positive	150.2	104.0	50	6	12	15	12	Fig. 2L
20	Phenylalanine[b,d,e]		$C_9H_{11}NO_2$	165.0790	Positive	166.1	103.0	30	11	14	37	12	Fig. 2N
21	Proline[b,c,d]		$C_5H_9NO_2$	115.0633	Positive	116.1	70.0	30	20	13.5	21	10	Fig. 2E
22	Serine[b,c,d]		$C_3H_7NO_3$	105.0426	Negative	106.1	60.0	30	6	10.5	15.5	7	Fig. 2D
23	Threonine[b]		$C_4H_9NO_3$	119.0582	Positive	120.1	103.2	30	105	14.5	25	7	Fig. 2G
24	Tryptophan[b]		$C_{11}H_{12}N_2O_2$	204.0899	Positive	205.1	146.0	30	75	10	25	15	Fig. 2Q
25	Tyrosine[b,d,e]		$C_9H_{11}NO_3$	181.0739	Positive	182.1	165.0	30	20	11	13	8	Fig. 2P
26	Valine[b,d,e]		$C_5H_{11}NO_2$	117.0790	Positive	118.1	55.0	30	11	13.5	27	8	Fig. 2C

CE collision energy, *CXP* cell exit potential, *DP* declustering potential, *EP* entrance potential, *m/z* mass-to-charge ratio, *V* volts, *Q* precursor/parent ion

[a] Theoretical monoisotopic mass

[b] The metabolites identified by high precursor mass accuracy

[c] The metabolites identified by matching retention time

[d] The metabolites identified by matching isotopic pattern

[e] The metabolites identified by matching MS/MS fragment spectra

important plant metabolites such as antioxidants in different sections of plant tissue. This spatial information is critical for understanding how these compounds are dispersed in fruit, which may be useful for basic research as well as enhancing food processing and storage strategies. Unlike extraction methods, MSI can frequently be conducted with minimum sample preparation. This decreases the possibility of sensitive antioxidant chemicals degrading during preparation and avoids potential changes in their natural form during extraction methods. To detect specific antioxidants, traditional quantification may necessitate the use of labels or probes, which can interfere with the compound's activity or modify its concentration. MSI is a label-free technology, which means that it can identify antioxidants in their natural state. MSI provides researchers with not only qualitative but also quantitative data, allowing them to evaluate not only the presence but also the concentration of antioxidants in the geographical context of banana tissue. MSI can capture a comprehensive image of all available antioxidants in a single scan, which can be faster than approaches that require sequential analysis of individual compounds, depending on the setup and the exact MSI technology employed. There is a possibility of losing some molecules or converting them into other ones during traditional extraction and measurement. MSI evaluates chemicals directly in the tissue, lowering these hazards (Yoshimura et al. 2016).

In this publication, we showcased the potential of targeted analysis of low molecular weight compounds (LMWC) through LARESI-MSI in SRM modes, directly applied to intact plant tissues. One of the main advantages of this method is atmospheric pressure ionization that allows for the direct analysis of native or frozen samples without the need for extensive sample preparation or vacuum conditions. This is particularly important for tissue imaging, as it enables researchers to study the spatial distribution of various molecules, including metabolites, lipids, and proteins, without altering their native distribution within the tissue (Wu et al. 2013a). This also makes it possible to perform real-time imaging, providing dynamic information about molecular distributions and changes over time without the need for labeling or staining (Xiao et al. 2020).

The LARESI-SRM-MSI method offers a notable advantage in terms of its straightforward and efficient sample preparation. With this technique, a fragment of the object, measuring up to 5 × 5 cm, is required to be placed directly in the instrument's chamber, eliminating the need for additional coating with MALDI matrix. This streamlined approach simplifies the process, saving time and reducing the risk of introducing artifacts that could alter the sample's original composition (Dong et al. 2016b).

The option of cooling tissue samples is of considerable importance in tissue analysis (Goodwin 2012). In the LARESI method, the tissue sample is securely mounted on the Peltier stage, which can be set to a temperature of −18 °C. This cooling capability offers several advantages during the analysis process. Firstly, it helps to preserve the integrity of the biological material, minimizing any potential degradation or changes in the molecular composition that could occur at higher temperatures. Secondly, the cooling of the tissue sample can slow down metabolite diffusion and thus enhance the spatial resolution and sensitivity of the analysis, allowing for more precise and accurate imaging of the molecules within the tissue.

The key advantage of this method lies in its utilization of a mid-IR laser for the analysis of biological material. Firstly, the IR laser provides enhanced sampling depth, allowing researchers to analyze molecules deeper within the tissue, thereby providing a more comprehensive understanding of the molecular composition (Wu et al. 2013a). Mid-IR lasers with a wavelength around 2.94 μm can effectively couple their energy into the O–H stretching mode of hydrogen-bonded water, which is present in hydrated biological materials. This results in a greater depth of sampling, allowing for analysis of molecules deeper within the tissue, up to about 10 μm for a single laser pulse. Secondly, the IR laser ablation is a non-destructive technique, preserving the integrity of the biological material during analysis and enabling researchers to study the spatial distribution of compounds without altering their native state. Additionally, the IR laser offers high sensitivity and selectivity, allowing for the targeted analysis of specific compounds of interest, while reducing chemical noise (Wu et al. 2013a).

For our study, we utilized commercially available banana tissue slices as the sample material. Figures 1 and 2 depict ion images of 26 selected metabolites found in slices of Cavendish banana and Red Dacca Banana tissue, respectively. Mass spectrometry parameters of LARESI SRM MSI Experiments are listed in Table 1. To further validate the MSI results, an extensive analysis of banana tissue extracts was conducted using ultra-high-performance liquid chromatography and ultra-high-resolution mass spectrometry (UHPLC-UHRMS). The untargeted results of the analysis of banana extracts are listed in Table 2.

Bananas are known for being abundant in various compounds found in the plant world, such as phenolic and polyphenolic substances like catechin, myricetin, quercetin, and phenolic acids like caffeic, protocatechuic acid, ferulic acid, and sinapic acids. Additionally, volatile compounds like isobutyl butyrate, eugenol, and pyruvic acid, representing alpha-keto acids, are also present in significant quantities. Phenolics and polyphenolics are the dominant compounds in banana fruits, and they are widespread throughout the plant kingdom. These secondary metabolites are of utmost importance due to their various health benefits, including antioxidant, antimicrobial, anti-inflammatory, anticancer, anti-mutagenic, and antidiabetic properties. The profiling

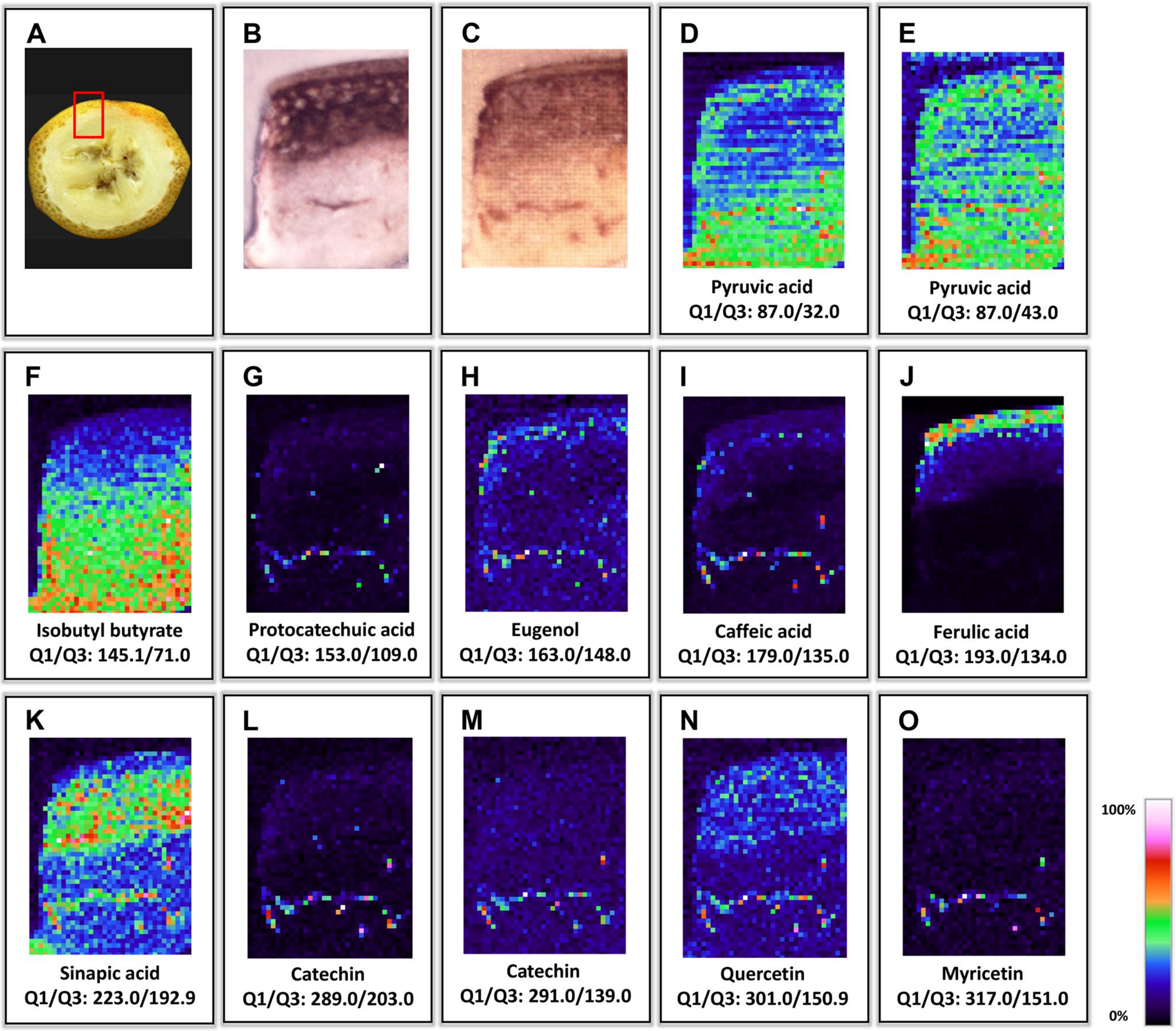

Fig. 1 Photographs and LARESI SRM MSI ion images of selected metabolites in the Cavendish banana tissue section. Optical photographs of the imaged surface of the banana tissue before (**A**, **B**) and following imaging (**C**). LARESI SRM MSI ion images of the Cavendish banana tissue (**D**–**O**). The imaged area is 8 × 8 mm obtained with 40 × 40 pixels and at 200 × 200 µm resolution

of phenolic compounds in different banana varieties was carried out using HPLC–ESI-HR-MS and HPLC-DAD methods (Simirgiotis et al. 2013; Tongkaew et al. 2022). The research findings indicate that bananas serve as an excellent source of phenolic compounds, although their content can vary in different parts of the fruit, such as the pulp and peel.

Among the compounds under analysis, phenolic acids played a prominent role, including protocatechuic acid, caffeic acid, ferulic acid, and sinapic acid. Protocatechuic acid, classified as a dihydroxybenzoic acid, is a naturally occurring phenolic acid widely distributed across the plant kingdom, alongside other plant phenols. In previous studies, both protocatechuic acid and caffeic acid were successfully identified in acetone banana pseudostem extracts using reverse-phase HPLC and ESI-MS, indicating their presence in this plant tissue (Saravanan and Aradhya 2011). Furthermore, quantification of these compounds was performed in banana rhizome extracts from eight commercial banana cultivars, with protocatechuic acid identified as the primary phenolic compound in acetone extracts of banana rhizomes (Kandasamy and Aradhya 2014) Caffeic acid, a common cinnamic acid derivative, is renowned for its antioxidant and antimicrobial properties and was also detected in banana peel extracts using paper spray-mass spectrometry in separate studies (Vu et al. 2018; Silva et al. 2020).

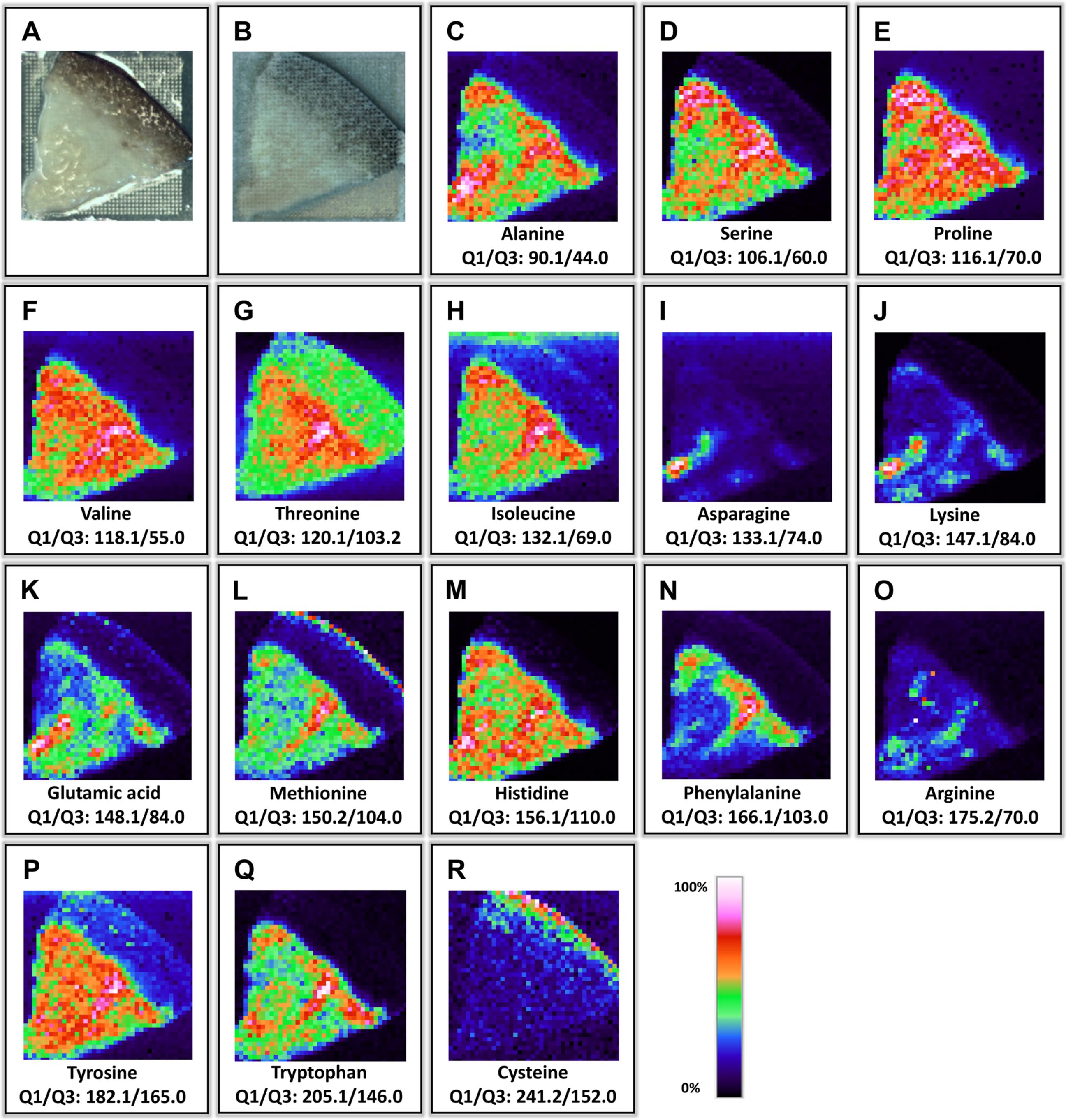

Fig. 2 Photographs and LARESI SRM MSI ion images of selected amino acids in intact Red Dacca Banana tissue section. Optical photographs of the imaged surface of the banana tissue before (**A**) and following imaging (**B**). LARESI SRM MSI ion images of the Red Dacca Banana tissue (**C**–**R**). The imaged area is 12×12 mm obtained with 40 × 40 pixels and at 300 × 300 µm resolution

Bananas are renowned for being rich in compounds with valuable medicinal properties, including ferulic acid. As a phenolic acid and derivative of cinnamic acid, ferulic acid is widely distributed throughout the plant kingdom, naturally occurring in plant cell walls, notably in conifers' leaves, seeds, and bark, as well as in grains like wheat, rice, corn, and rye. The significance of ferulic acid extends to various beneficial biological activities, especially for human health, such as its role as an antioxidant, antimicrobial, anti-inflammatory, anticancer, anti-mutagenic, and antidiabetic agent. Its widespread applicability is reflected in its use across the food, cosmetics, and pharmaceutical industries, owing to its

Table 2 Metabolite identification in Cavendish banana extract using UHPLC-UHRMS Method

No.	Name	Molecular Formula	*m/z*[a]	RT [min]	Ions	Δ*m/z* [ppm]
1	3-Hydroxybutyric acid[b,d]	$C_4H_8O_3$	146.0812	1.10	$[M+H]^+$, $[M+H+CH_3CN]^+$	0.5
2	2,3-Butanediol[b,d]	$C_4H_{10}O_2$	132.1016	18.11	$[M+H]^+$, $[M+H+CH_3CN]^+$	−2.0
3	2-Hydroxyacetanilide[b,d,e]	$C_8H_9NO_2$	152.0703	17.75	$[M+H]^+$	−2.1
4	2-Octenoic acid[b,c]	$C_8H_{14}O_2$	184.1330	17.88	$[M+H]^+$	−1.3
5	2-Oxoarginine[b,d]	$C_6H_{11}N_3O_3$	174.0871	8.45	$[M+H]^+$	−1.2
6	3-Hydroxy-4-methoxycinnamic aicd[b,d]	$C_{10}H_{10}O_4$	236.0912	0.97	$[M+H]^+$	−1.9
7	4-Ethylbenzoic acid[b,c]	$C_9H_{10}O_2$	151.0750	3.94	$[M+H]^+$	−2.4
8	4-Methylcatechol[b,d]	$C_7H_8O_2$	166.0860	0.72	$[M+H+CH_3CN]^+$, $[M+NH_4]^+$	−1.7
9	5α-Androstane-3β,17β-diol[b,d]	$C_{19}H_{32}O_2$	310.2736	8.43	$[M+H]^+$	−2.1
10	5-Aminopentanoate[b,d,e]	$C_5H_{11}NO_2$	118.0861	3.17	$[M+H]^+$	−1.4
11	6-(Methylamino)purine[b]	$C_6H_7N_5$	150.0772	1.64	$[M+H]^+$	−1.8
12	6-Phosphogluconic acid[b,c]	$C_6H_{13}O_{10}P$	277.0318	2.28	$[M+H]^+$	−0.4
13	Acetic acid[b,d]	$C_2H_4O_2$	102.0548	2.89	$[M+H]^+$	−1.2
14	Adenosine[b,d,e]	$C_{10}H_{13}N_5O_4$	268.1033	1.76	$[M+H]^+$, $[M+Na]^+$	−2.3
15	Biotin[b,d]	$C_{10}H_{16}N_2O_3S$	245.0948	0.98	$[M+H]^+$	−1.7
16	Butanal[b,d]	C_4H_8O	114.0910	2.05	$[M+H]^+$	−2.7
17	Cellobiose[b,c,d]	$C_{12}H_{22}O_{11}$	360.1495	5.57	$[M+NH_4]^+$, $[M+H-H_2O]^+$, $[M+H]^+$	−1.5
18	Cytidine[b,c,d]	$C_9H_{13}N_3O_5$	307.1020	6.42	$[M+H]^+$	2.1
19	Alanine[b,c]	$C_3H_7NO_2$	90.0549	6.57	$[M+H]^+$	−0.8
20	Galactose[b,c,d]	$C_6H_{12}O_6$	203.0528	1.17	$[M+H]^+$	0.8
21	Glucose[b,c,d]	$C_6H_{12}O_6$	219.0262	7.93	$[M+H]^+$	−1.9
22	Dimethylglycine[b,c,d]	$C_4H_9NO_2$	142.0261	1.63	$[M+H]^+$	−0.2
23	Maltose[b,c,d]	$C_{12}H_{22}O_{11}$	381.0788	1.15	$[M+H]^+$	−1.8
24	Dodecanoic acid[b,c]	$C_{12}H_{24}O_2$	242.2108	1.07	$[M+H]^+$	−2.8
25	Epigallocatechin[b,d,e]	$C_{15}H_{14}O_7$	307.0805	1.11	$[M+H]^+$	−2.3
26	Erythrose[b]	$C_4H_8O_4$	162.0759	2.33	$[M+H]^+$	−1.3
27	Ethyl isopropyl ketone[b]	$C_6H_{12}O$	139.0517	1.10	$[M+H]^+$	−2.1
28	Formamide[b]	CH_3NO	125.0109	1.41	$[M+H]^+$	−1.9
29	Fructose 6-phosphate[b,c]	$C_6H_{13}O_9P$	298.9925	1.81	$[M+H]^+$	−1.2
30	Glutamylcysteine[b,d]	$C_8H_{14}N_2O_5S$	251.0695	0.98	$[M+H]^+$	−0.9
31	Glycerol[b,c]	$C_3H_8O_3$	134.0812	1.06	$[M+H]^+$	0.1
32	Glycerophosphocholine[b,c,d]	$C_8H_{20}NO_6P$	296.0656	8.09	$[M+H]^+$	−1.2
33	Guanidine[b,d]	CH_5N_3	139.0384	1.84	$[M+H]^+$	2.5
34	Heptadecanoic acidb	$C_{17}H_{34}O_2$	293.2457	1.10	$[M+H]^+$	2.0
35	Homogentisic acid[b,d,e]	$C_8H_8O_4$	169.0490	1.14	$[M+H]^+$	−3.0
36	Imidazole[b,c,d]	$C_3H_4N_2$	110.0711	1.17	$[M+H]^+$	−1.7
37	Indolelactic acid[b,c,d]	$C_{11}H_{11}NO_3$	206.0814	6.31	$[M+H]^+$	0.0
38	Isobutyric acid[b,c]	$C_4H_8O_2$	89.0595	1.17	$[M+H]^+$	−2.6
39	Isocitric acid[b,c,d]	$C_6H_8O_7$	210.0607	1.15	$[M+H]^+$	−0.7
40	Arginine[b,c,d]	$C_6H_{14}N_4O_2$	213.0746	1.31	$[M+H]^+$	−1.0
41	Asparagine[b,c,d]	$C_4H_8N_2O_3$	133.0607	17.87	$[M+H]^+$	−0.7
42	Aspartic acid[b,c]	$C_4H_7NO_4$	134.0447	1.20	$[M+H]^+$	−1.0
43	Levoglucosan[b,d]	$C_6H_{10}O_5$	163.0598	1.74	$[M+H]^+$, $[M+H-H_2O]^+$, $[M+NH_4]^+$	−1.8
44	Fucose[b,d]	$C_6H_{12}O_5$	206.1006	1.03	$[M+H]^+$	−1.3
45	Glutamine[b,c,d]	$C_5H_{10}N_2O_3$	147.0762	1.18	$[M+H]^+$	−1.4
46	Histidine[b,c,d]	$C_6H_9N_3O_2$	194.0326	5.69	$[M+H]^+$	−0.3
47	Linoleic acid[b,d]	$C_{18}H_{32}O_2$	298.2731	1.03	$[M+NH_4]^+$, $[M+Na]^+$	−2.6
48	Lysine[b,c]	$C_6H_{14}N_2O_2$	147.1128	1.01	$[M+H]^+$	−0.3
49	Malic acid[b,c]	$C_4H_6O_5$	152.0551	1.11	$[M+H]^+$	−1.8
50	LPC(16:1)[b,d,e]	$C_{24}H_{48}NO_7P$	494.3218	1.10	$[M+H]^+$	−4.7

Table 2 (continued)

No.	Name	Molecular Formula	*m/z*[a]	RT [min]	Ions	Δ*m/z* [ppm]
51	LPC(18:2)[b,d,e]	$C_{26}H_{50}NO_7P$	520.3374	1.01	$[M+H]^+$, $[M+Na]^+$	−4.5
52	LPC(18:3)[b,d,e]	$C_{26}H_{48}NO_7P$	518.3218	19.70	$[M+H]^+$	−4.5
53	Proline[b,c,d]	$C_5H_9NO_2$	116.0705	1.10	$[M+H]^+$	−1.3
54	Serine[b,c,d]	$C_3H_7NO_3$	106.0496	19.09	$[M+H]^+$	−2.1
55	Sorbose[b,c,d]	$C_6H_{12}O_6$	163.0598	17.44	$[M+H-H_2O]^+$, $[M+H]^+$	−1.7
56	Mannose 6-phosphate[b,c,d]	$C_6H_{13}O_9P$	261.0367	8.12	$[M+H]^+$	−1.4
57	Methionine[b,d]	$C_5H_{11}NO_2S$	191.0849	1.09	$[M+H]^+$	0.2
58	Trimethyllysine[b,d,e]	$C_9H_{20}N_2O_2$	189.1596	16.38	$[M+H]^+$	−1.1
59	Oenanthic ether[b,c,d]	$C_9H_{18}O_2$	200.1640	13.15	$[M+H]^+$	−2.1
60	Oxoglutaric acid[b,c]	$C_5H_6O_5$	147.0287	12.93	$[M+H]^+$	−0.9
61	Pantothenic acid[b,d]	$C_9H_{17}NO_5$	220.1174	7.39	$[M+H]^+$, $[M+Na]^+$	−2.5
62	Coumaric acid[b,d,e]	$C_9H_8O_3$	165.0542	1.12	$[M+H]^+$	−2.4
63	Pentadecanoic acid[b,d]	$C_{15}H_{30}O_2$	243.2311	1.16	$[M+H]^+$	−1.9
64	Phenylacetaldehyde[b,d,e]	C_8H_8O	121.0646	1.08	$[M+H]^+$, $[M+NH_4]^+$	−1.6
65	Phenylacetic acid[b,d,e]	$C_8H_8O_2$	137.0594	10.51	$[M+H]^+$, $[M+NH_4]^+$, $[M+H-H_2O]^+$	−2.3
66	Phenylalanine[b,d,e]	$C_9H_{11}NO_2$	166.0858	15.53	$[M+H]^+$, $[M+Na]^+$	−2.8
67	Phenylglyoxylic acid[b,c]	$C_8H_6O_3$	168.0658	0.90	$[M+H]^+$	1.8
68	Phosphocreatine[b,d]	$C_4H_{10}N_3O_5P$	253.0704	1.02	$[M+H]^+$	3.0
69	Propyl alcohol[b]	C_3H_8O	102.0911	1.10	$[M+H]^+$	−2.5
70	Propylene glycol[b,c,d]	$C_3H_8O_2$	118.0861	1.12	$[M+H]^+$	−1.5
71	Putrescine[b,c]	$C_4H_{12}N_2$	89.1073	11.50	$[M+H]^+$	−0.6
72	Pyridoxamineb	$C_8H_{12}N_2O_2$	169.0969	0.93	$[M+H]^+$	−1.7
73	Pyroglutamic acid[b,c,d]	$C_5H_7NO_3$	130.0497	1.23	$[M+H]^+$	−1.6
74	Pyruvaldehyde[b]	$C_3H_4O_2$	114.0548	1.09	$[M+H]^+$	−1.7
75	Quinic acid[b,c]	$C_7H_{12}O_6$	193.0705	1.09	$[M+H]^+$	−0.7
76	Quinone[b,c,d]	$C_6H_4O_2$	109.0283	1.21	$[M+H]^+$	−0.8
77	Raffinose[b,d,e]	$C_{18}H_{32}O_{16}$	522.2032	5.52	$[M+H]^+$	−2.2
78	Raffinose[b,c,d]	$C_{18}H_{32}O_{16}$	543.1313	6.52	$[M+NH_4]^+$, $[M+Na]^+$	−1.9
79	Rhamnose[b,c]	$C_6H_{12}O_5$	206.1021	1.76	$[M+H]^+$	−0.8
80	Salicinb	$C_{13}H_{18}O_7$	309.0938	1.09	$[M+H]^+$	−2.2
81	Salsolinol[b,d,e]	$C_{10}H_{13}NO_2$	180.1015	7.30	$[M+H]^+$	−2.5
82	Senecioic acid[b,c,d]	$C_5H_8O_2$	118.0858	0.87	$[M+H]^+$	−2.8
83	Methylmethionine[b,d,e]	$C_6H_{13}NO_2S$	164.0738	19.73	$[M+H]^+$	−1.0
84	Succinic acid semialdehyde[b,d]	$C_4H_6O_3$	85.0285	14.61	$[M+H-H_2O]^+$, $[M+NH_4]^+$	1.0
85	Sucrose[b,d,e]	$C_{12}H_{22}O_{11}$	360.1494	1.72	$[M+NH_4]^+$, $[M+H]^+$, $[M+H-H_2O]^+$	−2.0
86	Trehalose[b,c,d]	$C_{12}H_{22}O_{11}$	365.1047	1.76	$[M+H]^+$	−2.2
87	Tyrosine[b,d,e]	$C_9H_{11}NO_3$	182.0809	8.84	$[M+H]^+$	−1.9

m/z mass-to-charge ratio, *RT* retention time

[a] Experimental monoisotopic mass

[b] The metabolites identified by high precursor mass accuracy

[c] The metabolites identified by matching retention time

[d] The metabolites identified by matching isotopic pattern

[e] The metabolites identified by matching MS/MS fragment spectra

low toxicity and numerous health benefits (Zduńska et al. 2018) Notably, ferulic acid's potent antioxidant properties surpass even those of vitamins C and E. Previous studies have involved the mechanical extraction of ferulic acid from banana stem waste, aiming to determine kinetic parameters in the production of this compound using HPLC. In our study, ferulic acid is primarily found in the outer part of the banana peel (Fig. 1J). The presence of ferulic acid in the peel of a banana can explain its structural role in cross-linking and strengthening of plant cell wall polysaccharides (Russell et al. 2009). The presence of ferulic acid in banana fruit and stem extracts has been consistently confirmed in numerous publications, with HPLC being the chosen method for its identification (Zainol et al. 2018). Furthermore, ferulic acid was successfully determined among other bioactive compounds in stem juices from banana plants using a tandem high-resolution mass spectrometry (UHPLC-HRMS/MS) method. An investigation into variations in the occurrence of potentially antidiabetic compounds revealed significant differences in the concentration of ferulic acid based on the origin of the bananas, underscoring the influence of growth conditions on its presence (Nguyen et al. 2017). Phenolic compound profiling in various banana varieties was also conducted through two analytical methods, HPLC–ESI-HR-MS and HPLC-DAD. The research findings demonstrated that bananas serve as a rich source of phenolic compounds; however, their content exhibits variations between the pulp and peel of this fruit (Passo Tsamo et al. 2015).

The remarkable antioxidant properties of bananas can be attributed to the presence of various phenolic compounds, including sinapic acid. Similar to ferulic acid, sinapic acid is a derivative of cinnamic acid and is predominantly found in the outer region of the pulp near the peel (Fig. 1K). Sinapic acid has been identified through LC MS/MS analysis in banana roots (Shi Ming et al. 2021). Furthermore, it has been observed that sinapic acid levels increase in bananas treated with artificial ripeners (Tallapally et al. 2020). Previous research on extracts from different morphological parts of bananas indicated that ferulic acid is more abundant in leaf sheaths and floral stalks, whereas rachis contains it in smaller quantities (Oliveira et al. 2006).

Quercetin, catechin, and myricetin are prominent members of the flavonoid family, renowned for their robust antioxidant activity. These naturally occurring phenols and secondary metabolites are widespread among various plants. Structurally, they share similarities and belong to the flavonol class of flavonoids, exhibiting numerous common functions. In our study, all three compounds were detected in close proximity to the fibrovascular bundles (Fig. 1M, N, O). Flavonoids serve vital roles as secondary metabolites synthesized by plants, contributing to various functions, including stress defense, pigmentation, and attraction of pollinators or seed dispersers (Buer et al. 2010). In the context of fruits, flavonoids play a crucial role in pigmentation and safeguarding against environmental factors (Harborne and Williams 2000). The strategic location of flavonoids like quercetin, catechin, and myricetin near fibrovascular bundles can be attributed to their specific transport and localization patterns. Fibrovascular bundles play a pivotal role in facilitating substance movement within fruits, ensuring the efficient distribution of flavonoids to regions where they are needed (Quattrocchio et al. 2006). This localization in proximity to fibrovascular bundles ensures the availability of flavonoids for protective and pigmentation purposes, contributing to the overall health and resilience of the banana fruit. The antioxidant properties of polyphenols such as quercetin, catechin, and myricetin in bananas have been extensively researched. Notably, in a study comparing 15 commonly consumed fruits and vegetables, bananas were found to have the highest phenolic content (Singh et al. 2016a). Catechin has been identified as the primary constituent in both banana peel (Someya et al. 2002) and pulp (Bennett et al. 2010) extracts. Additionally, quercetin has been detected in bananas using UPLC-MS analysis (Septembre-Malaterre et al. 2016). These findings highlight the significant presence of these beneficial polyphenols in bananas and underscore their potential health-promoting effects.

Flavonoids, such as flavanols like quercetin and myricetin, have been successfully identified in the sap of various dessert banana species using HPLC-ESI-MS (Pothavorn et al. 2010). Both quercetin and catechin have been detected in the banana pulp at all stages of fruit development. Among the flavonoids, quercetin emerged as the predominant metabolite in its free soluble form in bananas (Dong et al. 2016a). Furthermore, myricetin has been previously reported in extracts from the banana peel (Zhang et al. 2019).

In this study, pyruvic acid was identified as the compound with the lowest molecular weight, using the LARESI method, and was found in the pulp close to the center of the banana fruit (Fig. 1D, E). Pyruvic acid is a three-carbon carboxylic acid containing both a ketone and a carboxyl functional group. Its significance lies in its crucial role as an intermediate in various metabolic pathways within the cell, including those involving lipids, amino acids, and carbohydrates. In the cell's environment, pyruvic acid dissociates into pyruvate ions (pyruvate). It is produced during glycolysis, where glucose molecules are broken down into two pyruvate ions. Subsequently, in the mitochondria's matrix, pyruvate is converted into acetyl coenzyme A (acetyl CoA), which further participates in the energy-supplying citric acid cycle (Krebs cycle) when oxygen is present. In the absence of oxygen, pyruvate ferments into lactate (lactic acid). Moreover, pyruvate can be converted into alanine via transamination or into oxaloacetate through carboxylation. Previous studies have quantified pyruvic acid in banana pulp extracts using gas-liquid chromatography (GLC) (McHan and Horvat 1987) and high-performance liquid chromatography (HPLC) (Kozukue 1981). These studies also revealed that the level of pyruvic acid slightly decreased during ripening after five months of storing bananas at −20°C. However, the isolation, separation, and identification of pyruvic acid, like other α-keto acids in biological materials, pose challenges due to their instability.

Isobutyl butyrate, a carboxylic acid ester, is a volatile compound that is produced during the ripening of banana fruits. Its identification and quantification in bananas have been extensively studied due to its significant impact on fruit and flavor quality, employing various analytical methods. In our experiment, isobutyl butyrate was detected in the banana pulp, with the highest intensity of the signal observed near the fibrovascular bundles (Fig. 1F). The quantification of isobutyl butyrate in commercial banana fruit and banana essence was achieved using GC-MS (Jordán et al. 2001). This aromatic compound was identified at two stages of banana ripening: during the color-turning and full-ripening stages, using the solid-phase micro-extraction (SPME) coupled with the GS-MS method (Zhu et al. 2018). Moreover, studies on bananas harvested in different seasons demonstrated that only fruits harvested in March contained isobutyl butyrate and exhibited a higher abundance of volatile aroma compounds (Zhang et al. 2020).

Another notable volatile compound in bananas is eugenol, which belongs to the naturally occurring phenylpropanoid class of organic aromatic compounds, featuring a propylbenzene skeleton. Similar to other secondary metabolites, eugenol was also found in close proximity to the fibrovascular bundles (Fig. 1H). It is associated with a phenolic, sweet flavor, contributing to the overall sensory profile of bananas. Eugenol, a significant flavor compound, has been identified in high concentrations in fresh banana fruit paste, banana extracts, and dehydrated banana powder, utilizing various methods coupled with GC-MS (Miranda et al. 2001; Wang et al. 2007; Pino and Febles 2013). Intriguingly, eugenol was not detected in commercial banana essence, highlighting the distinct aromatic profiles between fresh fruit and banana essence (Jordán et al. 2001). It is noteworthy that the flavor compounds in banana extracts are not formed during the growth and time of harvest, but rather during the ripening process of the fruit (Boudhrioua et al. 2003). This implies that the development of characteristic flavors in bananas is a dynamic process, occurring primarily during the ripening stage, which significantly influences the overall sensory experience of consuming this fruit.

In the second experiment, the spatial distribution of 16 amino acids (AAs) in Red Dacca Banana tissue was examined. AAs play several important roles in banana fruit. As essential nutrients, AAs are essential building blocks for protein synthesis, which is crucial for the growth, development, and maintenance of the fruit. Proteins are essential components of various cellular structures and enzymes that regulate biochemical processes within the fruit. Additionally, amino acids are involved in various metabolic pathways within the banana fruit. They participate in energy production through processes like glycolysis and the citric acid cycle (TCA cycle), providing the necessary energy for cellular activities during fruit ripening and development (Wiskich and Dry 1985). AAs also contribute to the flavor and aroma of banana fruit. Certain amino acids are precursors to volatile compounds, which are responsible for the characteristic scent and taste of ripe bananas (Maoz et al. 2022). Furthermore, AAs play a role in stress responses and defense mechanisms in the fruit. During postharvest senescence, amino acids may be utilized to protect the fruit from oxidative damage and maintain cellular integrity (He et al. 2013). The majority of the tested AAs were found in the pulp of the fruit, with the exception of three amino acids, threonine, methionine, and cysteine, which were also present in the peel (Fig. 2G, 2L, 2R). Notably, cysteine accumulated mainly in the outer part of the banana peel, with only a negligible amount detected in the pulp. Furthermore, MS imaging revealed a high content of exogenous amino acids on the entire surface of the banana, such as valine, tryptophan, histidine, and phenylalanine, with their accumulation predominantly occurring between the peel and the pulp. In contrast, the lowest intensities in ionic images were observed for asparagine, lysine, and arginine. These amino acids possess additional amino groups in their side chains, which may contribute to their distribution pattern within the banana tissues. Our findings align with prior studies that shed light on the distribution of threonine, glutamine, and arginine within banana pulps during postharvest senescence (Yin et al. 2022). These studies revealed that these AAs exclusively accumulated in the middle region near the seed zone.

Conclusions

Utilizing mass spectrometry imaging (MSI) for banana analysis offered a detailed visualization of metabolites like antioxidants within the fruit's tissue, providing essential spatial data that traditional GC/LC-MS methods lack. This insight is valuable for research and enhancing food technology. MSI's minimal preparation preserves the integrity of sensitive compounds, avoiding the alterations extraction can cause. As a label-free approach, it detects antioxidants in their true form and delivers both qualitative and quantitative insights rapidly, without the sequential steps needed for individual compound analysis. By analyzing compounds directly in the tissue, MSI also minimizes the risk of compound loss or alteration inherent in conventional extraction techniques. Our research aimed to demonstrate the significant advantages of employing the LARESI method in SRM modes for targeted MSI of LMWC in intact plant tissues. Through this innovative approach, we were able to gain valuable insights into the spatial distribution of various compounds within plant tissues. It was possible to identify and determine the spatial distribution of 12 metabolites and 16 amino acids. The spatial distribution some of these compounds found in bananas was presented for the first time. The results of the studies presented in this publication confirm that LARESI method's efficiency, simplicity, and ability to analyze intact samples without the need for additional coatings or complex sample preparation make it a powerful tool for advancing our knowledge of plant metabolomics and its diverse applications.

Funding The study was supported by National Science Centre (Poland) research project SONATA BIS Number 2022/46/E/ST4/00016.

Data Availability The data that support the findings of this study is available from the corresponding author upon reasonable request.

Declarations

Competing Interests The authors declare no competing interests.

Declaration of Generative AI and AI-Assisted Technologies in the Writing Process During the preparation of this work, the author(s) used ChatGPT3 (OpenAI) in order to improve language and readability. After using this tool/service, the author(s) reviewed and edited the content as needed and take(s) full responsibility for the content of the publication.

Open Access This article is licensed under a Creative Commons Attribution 4.0 International License, which permits use, sharing, adaptation, distribution and reproduction in any medium or format, as long as you give appropriate credit to the original author(s) and the source, provide a link to the Creative Commons licence, and indicate if changes were made. The images or other third party material in this article are included in the article's Creative Commons licence, unless indicated otherwise in a credit line to the material. If material is not included in the article's Creative Commons licence and your intended use is not permitted by statutory regulation or exceeds the permitted use, you will need to obtain permission directly from the copyright holder. To view a copy of this licence, visit http://creativecommons.org/licenses/by/4.0/.

References

Adão RC, Glória MBA (2005) Bioactive amines and carbohydrate changes during ripening of 'Prata' banana (Musa acuminata × M. balbisiana). Food Chem 90:705–711. https://doi.org/10.1016/J.FOODCHEM.2004.05.020

Araújo FDS, Vieira RL, Molano EPL et al (2017) Desorption electrospray ionization mass spectrometry imaging reveals chemical defense of Burkholderia seminalis against cacao pathogens. RSC Adv 7:29953–29958. https://doi.org/10.1039/C7RA03895J

Audinot JN, Philipp P, De Castro O et al (2021) Highest resolution chemical imaging based on secondary ion mass spectrometry performed on the helium ion microscope. Reports Prog Phys 84:105901. https://doi.org/10.1088/1361-6633/AC1E32

Bartels B, Svatoš A (2015) Spatially resolved in vivo plant metabolomics by laser ablation-based mass spectrometry imaging (MSI) techniques: LDI-MSI and LAESI. Front Plant Sci 6:1–7. https://doi.org/10.3389/FPLS.2015.00471

Bennett RN, Shiga TM, Hassimotto NMA et al (2010) Phenolics and antioxidant properties of fruit pulp and cell wall fractions of postharvest banana (Musa acuminata Juss.) cultivars. J Agric Food Chem 58:7991–8003. https://doi.org/10.1021/JF1008692

Boudhrioua N, Giampaoli P, Bonazzi C (2003) Changes in aromatic components of banana during ripening and air-drying. LWT - Food Sci Technol 36:633–642. https://doi.org/10.1016/S0023-6438(03)00083-5

Brauer JI, Beech IB, Sunner J (2015) Mass spectrometric imaging using laser ablation and solvent capture by aspiration (LASCA). J Am Soc Mass Spectrom 26:1538–1547. https://doi.org/10.1007/S13361-015-1176-0

Buer CS, Imin N, Djordjevic MA (2010) Flavonoids: new roles for old molecules. J Integr Plant Biol 52:98–111. https://doi.org/10.1111/J.1744-7909.2010.00905.X

Cabral EC, Mirabelli MF, Perez CJ, Ifa DR (2013) Blotting assisted by heating and solvent extraction for DESI-MS imaging. J Am Soc Mass Spectrom 24:956–965. https://doi.org/10.1007/S13361-013-0616-Y

Calvano CD, Monopoli A, Cataldi TRI, Palmisano F (2018) MALDI matrices for low molecular weight compounds: an endless story? Anal Bioanal Chem 410:4015–4038. https://doi.org/10.1007/S00216-018-1014-X

Caprioli RM, Farmer TB, Gile J (1997) Molecular imaging of biological samples: localization of peptides and proteins using MALDI-TOF MS. Anal Chem 69:4751–4760. https://doi.org/10.1021/AC970888I

Chaurand P, Schwartz SA, Billheimer D et al (2004) Integrating histology and imaging mass spectrometry. Anal Chem 76:1145–1155. https://doi.org/10.1021/AC0351264

Cornett DS, Reyzer ML, Chaurand P, Caprioli RM (2007) MALDI imaging mass spectrometry: molecular snapshots of biochemical systems. Nat Methods 4(10):828–833. https://doi.org/10.1038/nmeth1094

da Silva LG, Franco dos Santos G, Ramalho RRF et al (2022) Laser ablation electrospray ionization mass spectrometry imaging as a new tool for accessing patulin diffusion in mold-infected fruits. Food Chem 373:131490. https://doi.org/10.1016/J.FOODCHEM.2021.131490

Dong C, Hu H, Hu Y, Xie J (2016a) Metabolism of flavonoids in novel banana germplasm during fruit development. Front Plant Sci 0:1291. https://doi.org/10.3389/FPLS.2016.01291

Dong Y, Li B, Malitsky S et al (2016b) Sample preparation for mass spectrometry imaging of plant tissues: A review. Front Plant Sci 7:170331. https://doi.org/10.3389/FPLS.2016.00060

dos Santos FN, Tata A, Belaz KRA et al (2017) Major phytopathogens and strains from cocoa (Theobroma cacao L.) are differentiated by MALDI-MS lipid and/or peptide/protein profiles. Anal Bioanal Chem 409:1765–1777. https://doi.org/10.1007/S00216-016-0133-5

Dou TX, Shi JF, Li Y et al (2020) Influence of harvest season on volatile aroma constituents of two banana cultivars by electronic nose and HS-SPME coupled with GC-MS. Sci Hortic 265:109214. https://doi.org/10.1016/J.SCIENTA.2020.109214

Eswara S, Pshenova A, Yedra L et al (2019) Correlative microscopy combining transmission electron microscopy and secondary ion mass spectrometry: a general review on the state-of-the-art, recent developments, and prospects. Appl Phys Rev 6:21312. https://doi.org/10.1063/1.5064768

Gao SQ, Zhao JH, Guan Y et al (2023) Mass spectrometry imaging technology in metabolomics: a systematic review. Biomed Chromatogr 37:e5494. https://doi.org/10.1002/BMC.5494

Gedük AŞ, Zengin F (2021) LC–MS/MS characterization, antidiabetic, antioxidative, and antibacterial effects of different solvent extracts of Anamur banana (Musa Cavendishii). Food Sci Biotechnol 30:1183–1193. https://doi.org/10.1007/S10068-021-00953-5

Goodwin RJA (2012) Sample preparation for mass spectrometry imaging: small mistakes can lead to big consequences. J Proteomics 75:4893–4911. https://doi.org/10.1016/J.JPROT.2012.04.012

Harborne JB, Williams CA (2000) Advances in flavonoid research since 1992. Phytochemistry 55:481–504. https://doi.org/10.1016/S0031-9422(00)00235-1

He S, Shan W, Kuang JF et al (2013) Molecular characterization of a stress-response bZIP transcription factor in banana. Plant Cell Tissue Organ Cult 113:173–187. https://doi.org/10.1007/S11240-012-0258-Y

Hölscher D, Fuchser J, Knop K et al (2015) High resolution mass spectrometry imaging reveals the occurrence of phenylphenalenone-type compounds in red paracytic stomata and red epidermis tissue of Musa acuminata ssp. zebrina cv. 'Rowe Red'. Phytochemistry 116:239–245. https://doi.org/10.1016/J.PHYTOCHEM.2015.04.010

Hussein Z, Fawole OA, Opara UL (2020) Harvest and postharvest factors affecting bruise damage of fresh fruits. Hortic Plant J 6:1–13. https://doi.org/10.1016/J.HPJ.2019.07.006

Joignant AN, Xi Y, Muddiman DC (2023) Impact of wavelength and spot size on laser depth of focus: considerations for mass spectrometry imaging of non-flat samples. J Mass Spectrom 58:e4914. https://doi.org/10.1002/JMS.4914

Jordán MJ, Tandon K, Shaw PE, Goodner KL (2001) Aromatic profile of aqueous banana essence and banana fruit by gas chromatography-mass spectrometry (GC-MS) and gas chromatography-olfactometry (GC-O). J Agric Food Chem 49:4813–4817. https://doi.org/10.1021/JF010471K

Kandasamy S, Aradhya SM (2014) Polyphenolic profile and antioxidant properties of rhizome of commercial banana cultivars grown in India. Food Biosci 8:22–32. https://doi.org/10.1016/J.FBIO.2014.10.001

Kaspar S, Peukert M, Svatos A et al (2011) MALDI-imaging mass spectrometry – an emerging technique in plant biology. Proteomics 11:1840–1850. https://doi.org/10.1002/PMIC.201000756

Kozukue N (1981) Determination of alpha-keto acids in banana pulp by high performance liquid chromatography. J Food Sci 46:156–160. https://doi.org/10.1111/j.1365-2621.1981.tb14552.x

Li Y, Shrestha B, Vertes A (2007) Atmospheric pressure molecular imaging by infrared MALDI mass spectrometry. https://doi.org/10.1021/AC061577N

Lima GPP, Da Rocha SA, Takaki M et al (2008) Comparison of polyamine, phenol and flavonoid contents in plants grown under conventional and organic methods. Int J Food Sci Technol 43:1838–1843. https://doi.org/10.1111/J.1365-2621.2008.01725.X

Maduwanthi SDT, Marapana RAUJ (2021) Total phenolics, flavonoids and antioxidant activity following simulated gastro-intestinal digestion and dialysis of banana (Musa acuminata, AAB) as affected by induced ripening agents. Food Chem 339:127909. https://doi.org/10.1016/J.FOODCHEM.2020.127909

Maoz I, Lewinsohn E, Gonda I (2022) Amino acids metabolism as a source for aroma volatiles biosynthesis. Curr Opin Plant Biol 67:102221. https://doi.org/10.1016/J.PBI.2022.102221

McDonnell LA, Heeren RMA (2007) Imaging mass spectrometry. Mass Spectrom Rev 26:606–643. https://doi.org/10.1002/MAS.20124

McHan F, Horvat RJ (1987) Insoluble monolayers at liquid-gas interfaces. In: Kinsella JE, Damodaran S (eds) In Criteria of Food Acceptance, vol 35, pp 453–461 American Chemical Society

Miranda EJF, Nogueira RI, Pontes SM, Rezende CM (2001) Odour-active compounds of banana passa identified by aroma extract dilution analysis. Flavour Fragr J 16:281–285. https://doi.org/10.1002/FFJ.997

Misiorek M, Sekuła J, Ruman T (2017) Mass spectrometry imaging of low molecular weight compounds in garlic (Allium sativum L.) with gold nanoparticle enhanced target. Phytochem Anal 28:479–486. https://doi.org/10.1002/PCA.2696

Mondal A, Banerjee S, Bose S et al (2021) Cancer preventive and therapeutic potential of banana and its bioactive constituents: a systematic, comprehensive, and mechanistic review. Front Oncol 11:697143. https://doi.org/10.3389/FONC.2021.697143

Nguyen D, Nováková A, Spurná K et al (2017) Antidiabetic compounds in stem juice from banana. Czech J Food Sci 35:407–413. https://doi.org/10.17221/172/2017-CJFS

Nizioł J, Sekuła J, Ruman T (2017) Visualizing spatial distribution of small molecules in the rhubarb stalk (Rheum rhabarbarum) by surface-transfer mass spectrometry imaging. Phytochemistry 139. https://doi.org/10.1016/j.phytochem.2017.04.006

Nizioł J, Sunner J, Beech I et al (2020) Localization of metabolites of human kidney tissue with infrared laser-based selected reaction monitoring mass spectrometry imaging and Silver-109 nanoparticle-based surface assisted laser desorption/ionization mass spectrometry imaging. Anal Chem 92:4251–4258. https://doi.org/10.1021/ACS.ANALCHEM.9B04580

Norris JL, Caprioli RM (2013) Analysis of tissue specimens by matrix-assisted laser desorption/ionization imaging mass spectrometry in biological and clinical research. Chem Rev 113:2309–2342. https://doi.org/10.1021/CR3004295

Oliveira L, Freire CSR, Silvestre AJD et al (2006) Lipophilic extractives from different morphological parts of banana plant "Dwarf Cavendish". Ind Crops Prod 23:201–211. https://doi.org/10.1016/J.INDCROP.2005.06.003

Passo Tsamo CV, Herent MF, Tomekpe K et al (2015) Effect of boiling on phenolic profiles determined using HPLC/ESI-LTQ-Orbitrap-MS, physico-chemical parameters of six plantain banana cultivars (Musa sp). J Food Compos Anal 44:158–169. https://doi.org/10.1016/J.JFCA.2015.08.012

Pino JA, Febles Y (2013) Odour-active compounds in banana fruit cv. Giant Cavendish. Food Chem 141:795–801. https://doi.org/10.1016/J.FOODCHEM.2013.03.064

Pothavorn P, Kitdamrongsont K, Swangpol S et al (2010) Sap phytochemical compositions of some bananas in Thailand. J Agric Food Chem 58:8782–8787. https://doi.org/10.1021/JF101220K

Qamar S, Shaikh A (2018) Therapeutic potentials and compositional changes of valuable compounds from banana- a review. Trends Food Sci Technol 79:1–9. https://doi.org/10.1016/J.TIFS.2018.06.016

Quattrocchio F, Baudry A, Lepiniec L, Grotewold E (2006) The regulation of flavonoid biosynthesis. Sci Flavonoids:97–122. https://doi.org/10.1007/978-0-387-28822-2_4/COVER

Rocha DFO, Cunha CMS, Belaz KRA et al (2017) Lipid and protein fingerprinting for Fusarium oxysporum f. sp. cubense strain-level classification. Anal Bioanal Chem 409:6803–6812. https://doi.org/10.1007/S00216-017-0638-6

Russell JB, Muck RE, Weimer PJ (2009) Quantitative analysis of cellulose degradation and growth of cellulolytic bacteria in the rumen. FEMS Microbiol Ecol 67:183–197. https://doi.org/10.1111/J.1574-6941.2008.00633.X

Sarabia LD, Boughton BA, Rupasinghe T et al (2018) High-mass-resolution MALDI mass spectrometry imaging reveals detailed spatial distribution of metabolites and lipids in roots of barley seedlings in response to salinity stress. Metabolomics 14:1–16. https://doi.org/10.1007/S11306-018-1359-3

Saravanan K, Aradhya SM (2011) Polyphenols of pseudostem of different banana cultivars and their antioxidant activities. J Agric Food Chem 59:3613–3623. https://doi.org/10.1021/jf103835z

Septembre-Malaterre A, Stanislas G, Douraguia E, Gonthier M-P (2016) Evaluation of nutritional and antioxidant properties of the tropical fruits banana, litchi, mango, papaya, passion fruit and pineapple cultivated in Réunion French Island. https://doi.org/10.1016/j.foodchem.2016.05.147

Shi Ming F, Razali Z, Somasundram C (2021) Involvement of phenolic compounds and their composition in the defense response of Fusarium oxysporum infected Berangan banana plants. Sains Malays 50:23–33. https://doi.org/10.17576/jsm-2021-5001-03

Sidhu JS, Zafar TA (2018) Bioactive compounds in banana fruits and their health benefits. Food Qual Saf 2:183–188. https://doi.org/10.1093/FQSAFE/FYY019

Silva VDM, Arquelau PBF, Silva MR et al (2020) Use of paper spray-mass spectrometry to determine the chemical profile of ripe banana peel flour and evaluation of its physicochemical and antioxidant properties. Quim Nova 43:579–585. https://doi.org/10.21577/0100-4042.20170521

Simirgiotis MJ, Schmeda-Hirschmann G, Bórquez J, Kennelly EJ (2013) The *Passiflora tripartita* (banana passion) fruit: a source of bioactive flavonoid C-glycosides isolated by HSCCC and characterized by HPLC–DAD–ESI/MS/MS. Molecules 18(2):1672–1692. https://doi.org/10.3390/MOLECULES18021672

Singh B, Singh JP, Kaur A, Singh N (2016b) Bioactive compounds in banana and their associated health benefits – a review. Food Chem 206:1–11. https://doi.org/10.1016/J.FOODCHEM.2016.03.033

Singh J, Kaur A, Shevkani K, Singh N (2016a) Composition, bioactive compounds and antioxidant activity of common Indian fruits and vegetables. J Food Sci Technol 53:4056–4066. https://doi.org/10.1007/S13197-016-2412-8

Someya S, Yoshiki Y, Okubo K (2002) Antioxidant compounds from bananas (Musa Cavendish). Food Chem 79:351–354. https://doi.org/10.1016/S0308-8146(02)00186-3

Stoeckli M, Chaurand P, Hallahan DE, Caprioli RM (2001) Imaging mass spectrometry: a new technology for the analysis of protein expression in mammalian tissues. Nat Med 7(4):493–496. https://doi.org/10.1038/86573

Szulc J, Ruman T (2020) Laser ablation remote-electrospray ionisation mass spectrometry (LARESI MSI) imaging—new method for detection and spatial localization of metabolites and mycotoxins produced by moulds. Toxins 12(11):720. https://doi.org/10.3390/TOXINS12110720

Tallapally M, Sadiq AS, Mehtab V et al (2020) GC-MS based targeted metabolomics approach for studying the variations of phenolic metabolites in artificially ripened banana fruits. LWT 130:109622. https://doi.org/10.1016/J.LWT.2020.109622

Tata A, Perez CJ, Hamid TS et al (2015) Analysis of metabolic changes in plant pathosystems by imprint imaging desi-ms. J Am Soc Mass Spectrom 26:641–648. https://doi.org/10.1007/S13361-014-1039-0

Tongkaew P, Tohraman A, Bungaramphai R et al (2022) Kluai Hin (*Musa sapientum* Linn.) peel as a source of functional polyphenols identified by HPLC-ESI-QTOF-MS and its potential antidiabetic function. Sci Rep 12:1–8. https://doi.org/10.1038/s41598-022-08008-3

Vu HT, Scarlett CJ, Vuong QV (2018) Phenolic compounds within banana peel and their potential uses: a review. J Funct Foods 40:238–248. https://doi.org/10.1016/J.JFF.2017.11.006

Wang J, Li YZ, Chen RR et al (2007) Comparison of volatiles of banana powder dehydrated by vacuum belt drying, freeze-drying and air-drying. Food Chem 104:1516–1521. https://doi.org/10.1016/J.FOODCHEM.2007.02.029

Wiskich JT, Dry IB (1985) The tricarboxylic acid cycle in plant mitochondria: its operation and regulation. Higher Plant Cell Respiration:281–313. https://doi.org/10.1007/978-3-642-70101-6_11

Wu C, Dill AL, Eberlin LS et al (2013a) Mass spectrometry imaging under ambient conditions. Mass Spectrom Rev 32:218–243. https://doi.org/10.1002/MAS.21360

Wu X, Qin R, Wu H et al (2020) Nanoparticle-immersed paper imprinting mass spectrometry imaging reveals uptake and translocation mechanism of pesticides in plants. Nano Res 13:611–620. https://doi.org/10.1007/s12274-020-2700-5

Xiao Y, Deng J, Yao Y et al (2020) Recent advances of ambient mass spectrometry imaging for biological tissues: a review. Anal Chim Acta 1117:74–88. https://doi.org/10.1016/J.ACA.2020.01.052

Yin R, Kyle J, Burnum-Johnson K et al (2018) High spatial resolution imaging of mouse pancreatic islets using nanospray desorption electrospray ionization mass spectrometry. Anal Chem 90:6548–6555. https://doi.org/10.1021/acs.analchem.8b00161

Yin Z, Dong T, Huang W et al (2022) Spatially resolved metabolomics reveals variety-specific metabolic changes in banana pulp during postharvest senescence. Food Chem X 15:100371. https://doi.org/10.1016/J.FOCHX.2022.100371

Yoshimura Y, Goto-Inoue N, Moriyama T, Zaima N (2016) Significant advancement of mass spectrometry imaging for food chemistry. Food Chem 210:200–211. https://doi.org/10.1016/J.FOODCHEM.2016.04.096

Yun Z, Gao H, Chen X et al (2022) The role of hydrogen water in delaying ripening of banana fruit during postharvest storage. Food Chem 373:131590. https://doi.org/10.1016/J.FOODCHEM.2021.131590

Zainol N, Masngut N, Jusup MK (2018) Kinetic study on ferulic acid production from banana stem waste via mechanical extraction. IOP Conf Ser Mater Sci Eng 342:012038. https://doi.org/10.1088/1757-899X/342/1/012038

Zduńska K, Dana A, Kolodziejczak A, Rotsztejn H (2018) Antioxidant properties of ferulic acid and its possible application. Skin Pharmacol Physiol 31:332–336. https://doi.org/10.1159/000491755

Zhang JW, Wang JH, Wang GH et al (2019) Extraction and characterization of phenolic compounds and dietary fibres from banana peel. Acta Aliment 48:525–537. https://doi.org/10.1556/066.2019.48.4.14

Zhang XW, Li QH, Di XZ, Dou JJ (2020) Mass spectrometry-based metabolomics in health and medical science: a systematic review. RSC Adv 10:3092–3104. https://doi.org/10.1039/C9RA08985C

Zhu X, Li Q, Li J et al (2018) Comparative study of volatile compounds in the fruit of two banana cultivars at different ripening stages. Molecules 23(10):2456. https://doi.org/10.3390/MOLECULES23102456

Zou Y, Tang W, Li B (2022) Mass spectrometry imaging and its potential in food microbiology. Int J Food Microbiol 371:109675. https://doi.org/10.1016/J.IJFOODMICRO.2022.109675

Publisher's Note Springer Nature remains neutral with regard to jurisdictional claims in published maps and institutional affiliations.

analytical chemistry

Open Access
This article is licensed under CC-BY 4.0

pubs.acs.org/ac
Article

Direct Three-Dimensional Mass Spectrometry Imaging with Laser Ablation Remote Atmospheric Pressure Photoionization/Chemical Ionization

Tomasz Ruman,* Sumi Krupa, and Joanna Nizioł

Cite This: *Anal. Chem.* 2024, 96, 13326−13334

Read Online

ACCESS | Metrics & More | Article Recommendations | Supporting Information

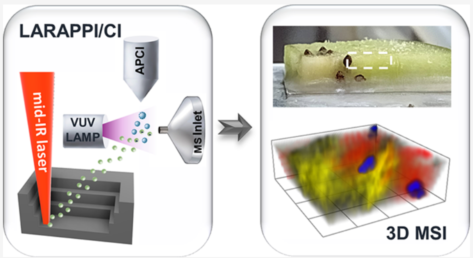

ABSTRACT: The laser ablation remote atmospheric pressure photoionization/chemical ionization (LARAPPI/CI) platform coupled to an ultrahigh resolution quadrupole-time-of-flight (QToF) mass spectrometer was developed and employed for the first direct three-dimensional (3D) mass spectrometry imaging (MSI) of metabolites in human and plant tissues. Our solution for 3D MSI does not require sample modification or cutting into thin slices. Ablation characteristics of an optical system based on a diffraction optical element are studied and used for voxel stacking to directly remove layers of tissues. Agar gel, red radish, kiwi, human kidney cancer, and normal tissue samples were used for the tests of this new system. The 2D and 3D ion images vividly illustrate differences in the abundances of selected metabolites between cancerous and noncancerous regions of the kidney tissue and also between different parts of plant tissues. The LARAPPI/CI MSI setup is also the first example of the successful use of combined dopant-assisted atmospheric pressure photoionization (DA-APPI) and atmospheric pressure chemical ionization (APCI) ion source for mass spectrometry imaging.

Downloaded via RZESZOW UNIV OF TECHNOLOGY on March 30, 2026 at 08:20:39 (UTC).
See https://pubs.acs.org/sharingguidelines for options on how to legitimately share published articles.

INTRODUCTION

Mass spectrometry imaging (MSI) has emerged as an essential technology that offers the simultaneous analysis of a broad spectrum of molecular species with unparalleled chemical specificity.[1] This technique excels in its ability to identify a diverse array of molecules, including endogenous and exogenous compounds, without the need for labels in a single experiment on the same tissue section.[2] It enables the detailed mapping of molecular distributions, the identification of post-translational modifications, and the acquisition of relative quantitative data across various samples.[3] With its high sensitivity and resolution, MSI has been instrumental in profiling element-specific signatures in a range of materials and has propelled forward studies in fields such as medicine, biology, and material science.[4−7]

Three-dimensional (3D) MSI advances beyond 2D MSI by providing the ability to profile the depth of biological samples, thereby enabling the mapping of biomolecules in three dimensions within tissues and organs. It is extremely challenging for mass spectral imaging to map molecular composition in 3D. MS imaging nowadays is performed almost exclusively in 2D mode or by reconstruction of 3D objects by software-stacking of many 2D results.[8] For the realization of 3D software reconstructed MSI, tissues or organs are first sectioned in series. These sections are subsequently imaged in two dimensions and reconstructed into three-dimensional images. Measurement techniques used for the above-mentioned analyses are usually desorption electrospray ionization (DESI),[9] nanospray desorption electrospray ionization (Nano-DESI),[10] laser ablation electrospray ionization (LAESI),[11] and matrix-assisted laser desorption ionization (MALDI).[12]

Most frequently, 3D-reconstructed MSI studies are performed with the use of matrix-assisted laser desorption/ionization mass spectrometry (MALDI MS).[13] MALDI MS has some limitations, such as a crowded chemical background in the low-mass region if low resolving power instrumentation is used[14] or not optimal ionization of neutral organic compounds.[8] Additionally, commercial instruments suitable for MALDI MSI do not have the possibility of sample freezing.

There are also reports of 3D-reconstructed MSI results made with the use of DESI.[9] One of the greatest advantages of sample preparation prior to analysis. Until recently, a major limitation of DESI was its low resolution, typically ranging from tens to hundreds of micrometers.[15] However, the introduction of nano-DESI allowed for achieving resolution up to 6 μm.[16] Controlling the distance between the nano-DESI probe and the sample surface is critical to achieving high resolution but is also technically challenging to maintain, especially for thinner tissue sections.[17] Despite significant improvements, the ionization efficiency in nano-DESI may still

Received: July 2, 2024
Revised: July 24, 2024
Accepted: July 25, 2024
Published: July 30, 2024

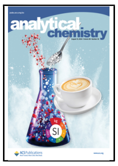

ACS Publications
© 2024 The Authors. Published by American Chemical Society

https://doi.org/10.1021/acs.analchem.4c03402
Anal. Chem. 2024, 96, 13326−13334

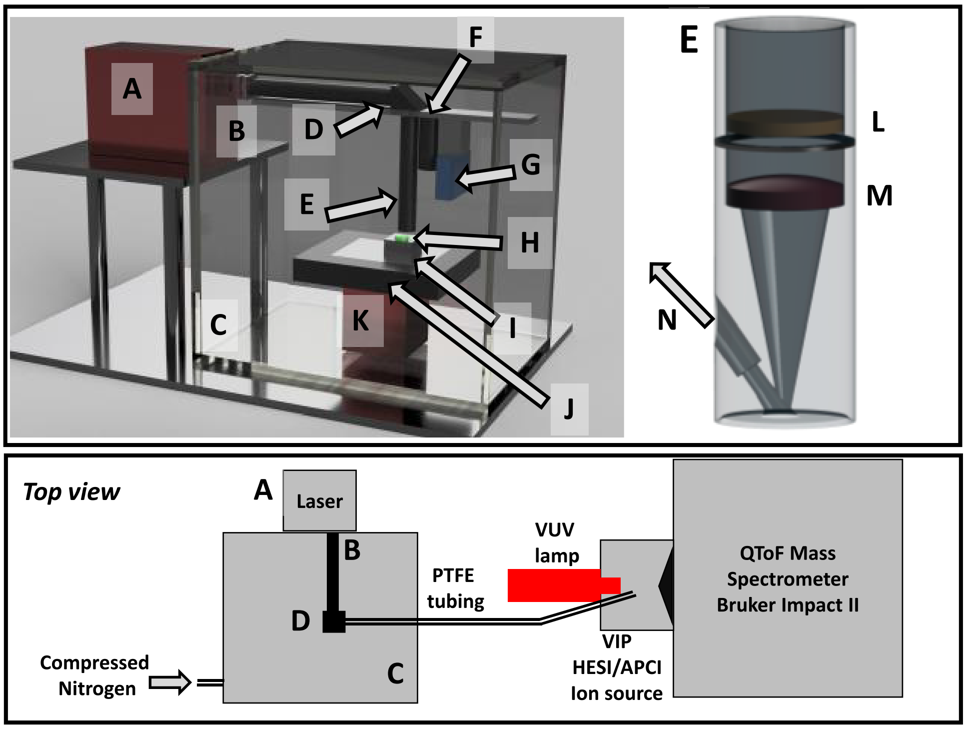

Figure 1. Schematic of the LARAPPI/CI MSI system. The upper panel presents a perspective view of the system without a mass spectrometer; the lower panel contains a simplified top view of the whole system. (A) OPO laser, (B) sapphire window, (C) pressure chamber, (D) gold mirror assembly, (E) laser focus assembly, (F) camera, (G) distance sensor, (H) sample, (I) sample stage with Peltier module and water block, (J) *XY* high-speed stage, (K) *Z* vertical stage, (L) diffractive optical element, (M) aspherical ZnSe lens, and (N) ablated material port connected via PTFE tubing to the ion source.

be insufficient for some types of analysis, particularly when analyzing complex biological matrices. A common issue with nano-DESI is the stability of solvent flow, which is dependent on the inlet vacuum of the mass spectrometer. A major limitation of DESI is the small depth of penetration of liquid into the sample, which is typically limited to a few micrometers. For example, DESI imaging did not cause physical damage to the underlying cells on the algal surfaces.[18] Although the sample removal rate of DESI is similar to that of secondary ion mass spectrometry (SIMS)[19] analytes are removed selectively, which does not allow depth profiling for three-dimensional imaging - a capability that can be achieved with SIMS[20] and LAESI.[21]

Methods reported in the literature as capable of direct, nonsoftware reconstructed 3D MS imaging include SIMS,[22] which uses energetic ion bombardment to erode the surface of a sample.[23] SIMS-based time-of-flight (ToF) MSI is capable of depth profiling molecular content with 10 nm depth resolution. There are also reports of 60 nm depth profiling, but heavy molecular fragmentation is observed.[24,25] In 2020, Zhang et al.[23] presented Cryo-OrbiSIMS for 3D molecular imaging of a frozen bacterial biofilm. It was possible to perform depth profiling by removing up to 30−50 μm of the object. With a shallow ablation depth, it is impossible to obtain a deep profile of macroscopic objects. The necessity of a high vacuum inside the system prevents the analysis of biological objects without risking deformation. Another approach was published with the use of an extreme ultraviolet (EUV) laser.[26] The authors achieved submicrometer resolutions, achieving a lateral resolution of 75 nm and a depth resolution of 20 nm.

The laser ablation remote atmospheric pressure photoionization/chemical ionization (LARAPPI/CI) 2D and 3D MSI platform presented in this work provides a solution to various problems associated with 3D MSI, such as reconstruction of 2D to 3D models, migration of metabolites, sample dehydration, evaporation of metabolites, a large volume of ablated material, and occurrence of artifacts from mechanical section preparations. Also, this allows for control shape and depth of the ablated surface, providing 3D results. The proposed solution should also be compatible with mass spectrometers that use common electrospray ionization (ESI) ion sources; it is not compatible with instruments with vacuum ion sources. The integrated 3D distance sensor acts as a surface profilometer, allowing for ablation control during the experiments.

■ RESULTS AND DISCUSSION

Direct three-dimensional MSI is considered one of the most useful analytical methods today. The possibility of detection of hundreds of compounds within a single microscopic space (voxel) on the surface (2D MSI) or inside (3D MSI) of the studied sample, and then their localization in the object, gives unlimited possibilities to biologists, biochemists, and material chemists. To perform such analysis, the method is capable of removing relatively large volumes of material in a strictly controlled manner, and also on the microscale, and quickly transferring this material to the mass spectrometer. Precise removal of entire layers of material is needed to access the lower parts or layers of the analyzed samples.

Description of the Experimental Setup. In the LARAPPI/CI MSI system, computer-controlled ablation takes place in a pressure chamber working at atmospheric pressure. The sample is placed on a sample stage (Figure 1I) with a built-in Peltier cooling plate that allows for freezing of

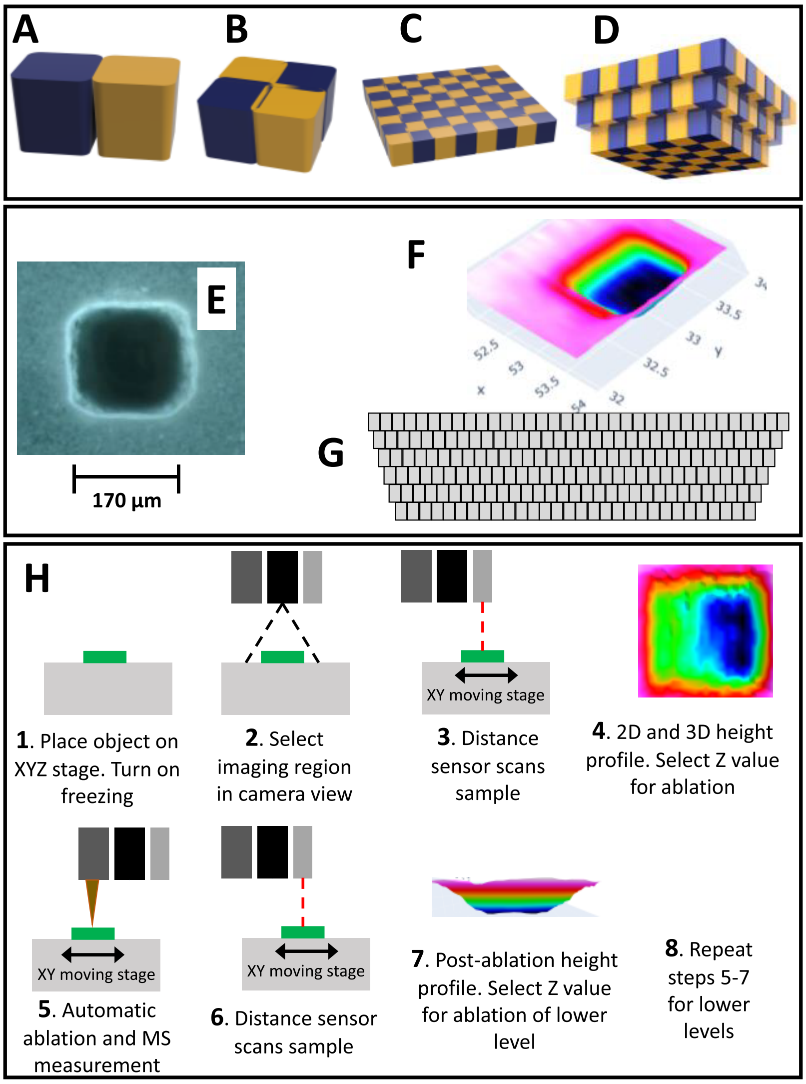

Figure 2. Renderings of 3D models of ablated voxel spaces: (A) not optimal arrangement of two voxels (notice that the lower part of space between voxels is not matching); (B) oversampling of four voxels allows for complete ablation of space; (C) example of oversampling arrangement for one layer of 8 × 8 voxels array; (D) inverted pyramid arrangement for oversampled voxels for three-dimensional ablation of material. The lower panel presents: (E) optical microscope image of a single voxel ablated in an agar gel with 20 laser pulses; (F) profilometer scan result of the ablated space of agar gel for a 7 × 7 × 1 voxel array with 140 × 140 μm resolution (20 laser pulses per voxel). (G) simplified inverted pyramid arrangement of voxels in kiwi and red radish 3D MSI experiments as seen from the side of the object; (H) 2D (steps 1−5) and 3D (steps 1−8) MSI workflow.

the sample for the experiment. The temperature-controlled sample stage is mounted on a motorized high-speed *XY* stage. The pulsed beam from the OPO laser (Figure 1A) of 2930 nm wavelength expanded 3.75 times is redirected toward the sample stage by a gold-plated mirror (Figure 1D), goes through the diffractive optical element, and is focused onto the sample surface by a 50 mm focal length aspherical lens.

The system also contains a camera and a high-precision distance sensor acting as a profilometer. During imaging, the laser focal point remains fixed in space, while the sample (Figure 1H) is moved by the computer-controlled *XY*- and *Z*-stages. A specially designed gas funnel (Figure 1E), also a focusing assembly, is placed on the ablation site. The overpressure in the chamber drives dry nitrogen gas with ablated material to the ion source. The samples are kept at subzero temperatures during analysis to keep their shape unchanged and prevent metabolites from migration.

LARAPPI/CI uses diffractive optical elements produced by HOLO/OR for the generation of a square-focused beam with a flat top profile.[27] The difference in ablation crater shape for the modified beam can be seen in the laser printer paper test results shown in Supporting Information S1.

A graphical representation of the volume removed by this setup is presented in Figure 2A (blue or yellow). As can be seen, a single-voxel shape is part of a pentahedron with rounded side edges. As can be seen in Figure 2A, using laser ablation to remove these shapes leaves some material between them. Oversampling with stacked voxels as presented in Figure 2B improves material removal during multivoxel ablations. To perform ablation without the removal of upper layers due to the fixed shape of the focused laser beam, we introduced an inverted pyramid ablation scheme (Figure 2D).

Single point ablation with 20 laser pulses of agar gel enriched for opacity in titanium dioxide nanopowder produced the desired square shape with rounded edges (170 × 170 μm size) as shown in the optical photograph in Figure 2E. Optimization of oversampling (shown in Supporting Information S7) suggested that 140 μm voxel-center-to-voxel-center (please

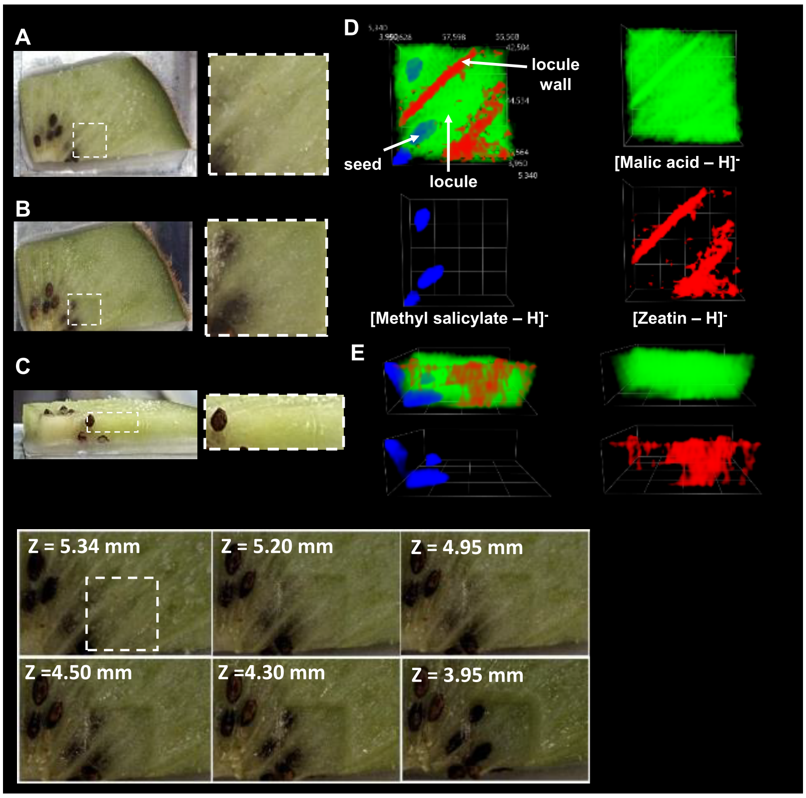

Figure 3. Photographs of the object studied (kiwi fruit cross section) and selected 3D MSI results. (A) Optical photographs of the starting object and analysis region marked with a white dashed line; (B) optical photographs of the postanalysis object; (C) side view of the object; (D) 3D MSI ion images for three ions represented by different colors—top views; (E) side views of 3D ion images of ions of different colors. The intensity of an ion signal is represented by the opacity of the 3D cloud within a given color. The bottom panel contains optical photographs of the preablation region and after the ablation steps. The *Z*-value was measured with the precision distance sensor.

see Figure 2B–D) produced optimal results with a relatively flat bottom of 7 × 7 × 1 voxel ablation area (depth 330 μm) as judged by optical microscope observation and also profiling with a distance sensor (Figure 1F). Additional ablation results of agar gel of 11 × 7 (*X* × *Y*, top-level resolution) space are shown in Supporting Information S2. Figure 2G presents a side view of the inverted pyramid ablation scheme. As can be seen, the layers are ablated with the number of lines in the *X* and *Y* axes reduced by 1 for every ablation layer below the first one (example: first-layer resolution, 40 × 40, second 39 × 39, etc.). Additionally, the voxel pattern of each lower layer is shifted to the center of the ablated region. This ablation scheme allows avoidance of ablation of walls of upper layers, which is one of the biggest problems in 3D MSI.[11] The undesirable ablation of upper layers in SIMS was partially solved by the utilization of two ion beams, the first beam ejects atoms, molecules, and secondary ions from the surface, while the second beam sputters the already analyzed surface to create a new plane for imaging the next layer.[28] Theoretically, a similar solution could be possible for laser systems; however, for complete removal of material, it would still require advanced beam shaping and beam direction control, making it much more complicated and expensive than the solution presented in this work. Each 3D MSI experiment presented below was performed in an inverted pyramid mode (Figure 2D,G). To present the procedure for 2D and 3D imaging in an easily understandable form, a workflow is presented in Figure 2I.

Optimization of LARAPPI/CI Working Conditions. To provide the highest sensitivity for the detection of biological compounds in microscopic-sized ablation voxels, we have modified the Bruker VIP HESI ion source in an APCI configuration to introduce a dopant-assisted APPI ionization by using a vacuum ultraviolet (VUV) lamp producing light of a wavelength in the 110–160 nm range. This ion source irradiates a pulsed stream of ablated material from the chamber that generates low-temperature plasma in the gas phase through direct interaction with biological compounds and, most likely, with toluene vapor from the toluene-methanol mixture pumped to the APCI needle by the HPLC pump (Figure 1 bottom panel). Tests of this ion source showed that ions forming from ablated material are the deprotonated ones of the $[\text{M-H}]^-$ formula, which is in accordance with results from both APPI and APCI ion sources.[29−31] During preliminary experiments, we tested electrospray ionization (ESI), atmospheric pressure chemical ionization (APCI), and atmospheric pressure photoionization (APPI) ionization in both positive and negative ion detection modes. After the optimal ionization type, APCI/APPI, the liquid composition, and the flow rate were also optimized. All optimizations were carried out under conditions similar to the operating mode of the MSI system; therefore, all tests were based on laser ablation of frozen agar gel containing test compounds, each compound at a concentration of 100 μg/mL. The ablated volumes calculated for each voxel were approximately 6.6 × 10^{-6} mL, which equates to 660 pg of each test compound. The test compounds were polar to medium polar biological compounds: ribose, histidine, thymidine, and uracil. The results of the tests mentioned are shown in Supporting

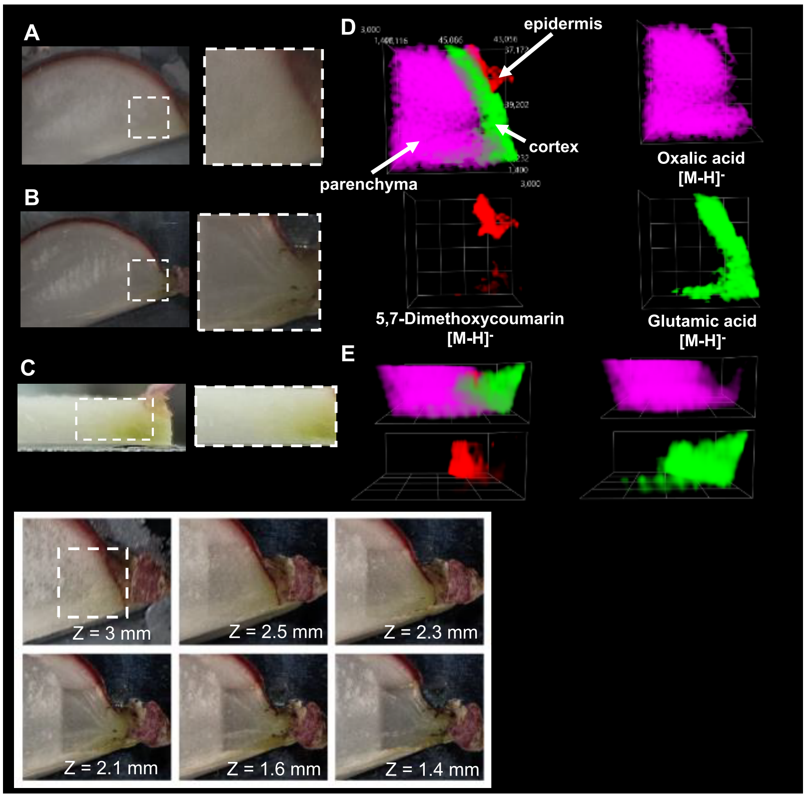

Figure 4. Photographs of the object studied (red radish cross section) and selected 3D MSI results. (A) Optical photographs of the starting object and analysis region marked with a white dashed line; (B) optical photographs of the postanalysis object; (C) side view of the object; (D) 3D MSI ion images for three ions represented by different colors—top views; (E) side views of 3D ion images of ions of different colors. The intensity of an ion signal is represented by the opacity of the 3D cloud within a given color. The bottom panel contains optical photographs of the preablation region and after the ablation steps. The *Z*-value was measured with the precision distance sensor.

Information S4 and S5 and Table S1. As can be concluded from the data in Table S1 and Supporting Information S5, the highest S/N ratios were obtained in the APCI/APPI negative ion mode. All compounds were detected in the APCI, APCI/APPI positive mode, and ESI/APPI negative modes. ESI/APPI results were of lower S/N compared to APCI/APPI in both positive and negative modes, which suggests that the intensity of interactions of charged droplets emitted by the ESI needle with ablated plume material is much lower compared to interactions of plume with more abundant charged gaseous species emitted in the APCI modes.

As the results shown above suggest, the best results were obtained for APCI/APPI. Optimization of the solvent mixture pumped into our modified APCI/APPI ion source was performed in a manner similar to that in the above-described experiments using agar gel laser ablation. In total, eight combinations of solvents (acetonitrile, methanol, acetone), with various dopants (toluene, formic acid) based on the literature were tested (Supporting Information S3) at different flow speeds (0.01 to 0.3 mL/min).[32−38] The highest average S/N value for all four compounds was for 1% toluene in methanol at a flow rate of 200 μL/min flow rate. In conclusion, the optimal ionization conditions in our MSI setup are the combination of APCI with DA-APPI.

Examples of Three-Dimensional Results from the LARAPPI/CI MSI System. The tissue of the kiwi fruit was selected as a real-life biological test for the 3D possibilities of the LARAPPI/CI MSI system. The experiment region was selected as shown in Figure 3A,B due to the placement of the seeds under a thick layer of parenchyma. Published MSI studies of radish taproot, kiwi fruit, and human kidney tissue were carried out only in 2D imaging mode.[39−42] In the case of kiwi fruit, direct 3D MSI was performed in 6 steps or layers. The highest level of ablation was ablated at a resolution of 140 × 140 μm resolution in a 35 × 35 ($X \times Y$) voxel arrangement with a total depth after the six ablation steps of 1.43 mm. The total number of voxels ablated in the experiment was 6355, while the ablation time took only 3 h and 20 min plus 3 min after each level for the ablation region profiling. The entire experiment removed approximately 25−30 mm^3, volume of tissue material, which is a unique characteristic of this system.

It should be noted that the experiment examples shown in each figure with MSI results (Figures 3 to 5) contain ion distributions of just three ions out of hundreds for the sake of clarity. The search provides information that kiwi fruit tissue was studied by MALDI MSI that provided information on differences in compound distribution in pulp, skin, and seeds.[43] In the case of our experiment, one of the 3D-imaged compounds in this fruit was malic acid (Figure 3D,E, green color), widely present as a side product of carbohydrate metabolism in various tissues.[44] The methyl salicylate found in the seeds of kiwi fruit (Figure 3D,E, blue color) was previously found in blended kiwi pulp.[45] It is said to play a role in signaling, and when demethylated to salicylic acid, exhibits anti-inflammatory properties.[46,47] Zeatin, found in the locule walls of the kiwi fruit (Figure 3D,E, red color), is a cytokinin responsible for the regulation of plant growth.[48]

3D MSI of a cross section of red radish is the next example of possibilities of the LARAPPI/CI MSI platform. The compounds identified in the root of the radish stem originate from LC-MS and MS/MS analyses conducted by our team (Supporting Information S6). Oxalic acid (4D,E, purple) is a compound commonly found in almost all plants. The most prominent function suggested for oxalic acid in plants is the retention of ions, specifically calcium, that form calcium oxalate crystals.[49] It has also been associated with plant growth, development regulation, and stress responses.[50] 5,7-Dimethoxycoumarin (Figure 4D,E, red color) has been previously identified in the epidermis of various plants, such as *Citrus aurantifolia* peel, and has been reported to possess antioxidant properties.[51] Glutamic acid (Figure 4D,E, green color) was found in plants to promote callus formation,[52] regulate nitrogen metabolism, serve as a precursor to other amino acids, and is also a building block for proteins.[53]

2D MSI of a red radish root (*Raphanus sativus*) was conducted in 2014 by Seaman et al. by MALDI-MS imaging. The research was focused on the metabolism of nitrogen into amino acids.[54] A different work from 2015 utilized laser ablation and solvent capture by aspiration (LASCA) with an electrospray ion source. The ablation process with an ablation depth of 10−25 μm and volume of approximately 1 nl per pixel allowed differentiation of the spatial distributions in varying structures of the root proved possible, however, the images were still two-dimensional, as stated previously.[55]

Human kidney tissue with visible cancer and normal regions was studied with a 3D MSI system. The identification of compounds found in kidney tissue was performed using previous research. Arachidonic acid (Figure 5D,E, red color) is linked to pro-inflammatory activity in kidney tissue, being released as a result of cell stress. Arachidonic acid then acts as a precursor to bioactive mediators that can lead to renal dysfunction.[56,57] The ways taurine levels (Figure 5D,E, blue color) influence renal processes are many, such as ion reabsorption, antioxidant properties, impact of blood flow, cell apoptosis, and more.[58,59] The taurine transporter gene is down-regulated by the chemotherapeutic agent cisplatin.[60] Malic acid (Figure 5D,E, green color), widely present as a side product of carbohydrate metabolism in various tissues, has also been previously identified in kidney tissue.[61,62]

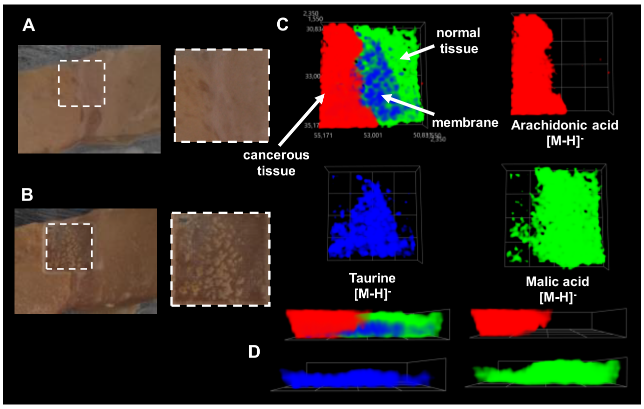

Figure 5. Photographs of the object studied (human kidney tissue) and selected 3D MSI results. (A) Optical photographs of the starting object and analysis region marked with a white dashed line; (B) optical photographs of the postanalysis object; (C) side view of the object; (D) 3D MSI ion images for three ions represented by different colors−top views; (C, D) side views of 3D ion images of ions of different colors. The intensity of an ion signal is represented by the opacity of the 3D cloud within a given color.

2D mass spectrometry imaging of both normal tissue and cancerous tissue of the human kidney has previously been performed for lipidomic, drug, and drug metabolite spatial distribution or proteomic analyses. Zhang et al. have used desorption electrospray ionization mass spectrometry imaging (DESI-MSI) to study metabolic profiles of renal oncocytoma, renal cell carcinoma (RCC), and healthy tissue to utilize the data obtained data for building prediction models.[63] DESI-MSI has also been used as a potential prognostic tool for RCC by Vijayalakshmi et al.[64] Other methods, such as MALDI-MSI for protein and lipid profiling[65] and SALDI-MSI for cancer biomarker identification,[66] have also been performed. Even despite successful results of 2D MSI, two-dimensional methods of profiling can prove unreliable in a tissue of highly varied structure and, therefore, chemical composition, which can only become known by three-dimensional analysis.

■ MATERIALS AND METHODS

All chemicals were analytical reagent grade. All solvents were of LC-MS purity, except water (18 MΩcm water produced locally). Steel plates of 4.5 cm × 3.5 cm size used as sample plates were machined from H17 stainless steel of 0.8 mm thickness. Optical photographs and size/depth measurement results of ablation shapes were obtained with a motorized microscope built locally with three motorized stages in *XYZ* configuration (ThorLabs MTS50), DeltaOptical USB 3.0 camera (DLT Cam Pro 14 MPix) with a 2.5x InfiniFlex HD Compact Lens, and microscope light ring. Syringe filters (PTFA membrane, 0.2 μm-pore) were purchased from Merck Poland.

LARAPPI/CI System Setup. A Nd/YAG-pumped, OPO laser (Opolette HE 2940 model, factory tuned to 2930 ± 1 nm); Opotek, Carlsbad, CA, USA) with a pulse length shorter than 7 ns generated mid-IR laser pulses with a maximum repetition frequency of 20 Hz. The pulse energy measured before the diffractive element was 3.5 mJ (measured using a pyroelectric energy meter, PE25-SH-V2; Ophir, Logan, UT, USA).

The LARAPPI/CI system is based on an airtight chamber, as shown in Figure 1. The chamber (C) is pressurized with nitrogen gas to produce a nitrogen stream of 10 L/min. The sample is placed on a 50 × 50 mm sample stage (I) made of aircraft-grade aluminum alloy; under it, there is a Peltier cooling plate (TE-127−1.4−1.5; TE Technology, Traverse City, MI, USA) that maintains the sample at temperatures as low as −18 °C. The heat generated from the Peltier element is removed using circulating water and an external radiator (not shown in Figure 1).

The temperature-controlled sample stage is mounted on a motorized high-speed *XY*-stage (Figure 1J; MLS203, Thorlabs, Sweden). The pulsed beam from the OPO laser (Figure 1A) enters the sample chamber (Figure 1C) through a 1″ sapphire window (Figure 1B) with both sides with AR-coatings (Thorlabs, Sweden), is then expanded with CaF_2 plano-concave lens of f = −40.0 mm, and collimated with CaF_2 plano-convex lens of f = 150 mm, both are AR-coated for 2−5 μm (not shown in Figure 1). The expanded laser beam is redirected toward the sample stage by a 1 in. gold-plated mirror (Figure 1D; Thorlabs, Sweden) and goes through a diffractive optical element (HM-396, Holo-OR Ltd. Israel), and is focused onto the sample surface by a 50 mm focal length aspherical ZnSe lens with AR coatings (both in Figure 1E, Thorlabs, Sweden).

The optical assembly and also the camera (Figure 1F; FLIR Blackfly S, Color Camera, 6 MPix, Sony IMX178 sensor) with a lens (12 mm C Series Fixed Focal Length Lens, Edmund Optics, UK) and distance sensor (Baumer OM70; Figure 1G) are mounted on locally machined precision aluminum rails and are in a fixed configuration; the only moving parts are *XY* (Figure 1J) and *Z* (Figure 1K) stages that are mounted on a precision aluminum 15 mm plate mounted at the bottom of the pressure chamber. During imaging, the laser focal point remains fixed in space, whereas the sample (Figure 1H) is moved by the computer-controlled *XY*- and *Z*-stages. A specially designed gas funnel (Figure 1E) is also a focusing assembly and is connected to a 6/4 mm (O.D/I.D.) PTFE tube. The gas funnel bottom surface is placed over (~4 mm) the laser ablation site. The overpressure in the chamber drives a 10 L/min nitrogen gas flow through the tube. The nitrogen, chamber lighting, and cooling systems are connected through relays and controlled by a control program.

The laser ablation plumes are entrained into the gas and transported to the modified ion source (Bruker VIP HESI in the APCI configuration) of the Bruker Impact II mass spectrometer. The outlet end of the PTFE tube is mounted at an angle of 30° to the axis of the spectrometer inlet. The ion source also has a VUV source (Hamamatsu L12542) mounted axially to the MS sampling cone inside the ion source. A binary HPLC pump (Agilent G1312A) provided a steady flow of a solvent mixture (1% toluene in methanol; 200 μL/min) to the APCI needle.

Samples are kept at −18 °C during analysis by the Peltier module. The spatial resolution is typically 140 μm with applied oversampling (Figure 2). Each pixel/voxel in 3D MSI experiments was exposed to the laser for 500 ms, at a laser pulse repetition rate of 20 Hz. The delays between pixels were 1000 ms. Between pixels, the sample stage moved at a speed of 50 mm/s. The time delay between lines was 3 s. Time-synchronization of laser pulses with signals recorded by the mass spectrometer is aided by an ethernet-based time server.

Each 3D experiment was carried out in an inverted pyramid scheme (Figure 2D) with the following procedure (Figure 2H):

1. Calibration of the MS instrument.
2. Sample scanning with a distance sensor, generation, and user-analysis of the 2D and 3D profile of the object's top side shape.
3. Setting the ablation region with the camera image.
4. Setting the *Z* level for the first ablation level.
5. Ablation of the layer with the recording of MS or MS + bbCID data.
6. Profiling of ablated object with a distance sensor; visual inspection with the camera image.
7. Setting the *Z* level for the next ablation, etc. It must be noted that the *XY* ablation area of the lower layers is set automatically by software with the same resolution as the first layer but with an ablation area smaller by one *X* and one *Y* row and also centered.

■ CONCLUSIONS

We created a laser ablation remote atmospheric pressure photoionization/chemical ionization (LARAPPI/CI) platform coupled to an ultrahigh resolution quadrupole-time-of-flight (QToF) mass spectrometer. The optics of this system is based on a mid-IR laser and diffractive optical element. We have shown a novel approach, the inverted pyramid ablation scheme that is suitable for the removal of the layers required for three-dimensional MSI. Various optimizations of the MSI system are shown, and the most important one is the modified APCI/dopant-assisted-APPI ion source. The MSI solution was used for the direct three-dimensional (3D) mass spectrometry imaging (MSI) of metabolites in human and plant tissues.

■ ASSOCIATED CONTENT

Data Availability Statement

The data sets generated during and/or analyzed during the current study are available from the corresponding author upon request and in the RepOD open data repository (doi: 10.18150/WWFOHP and 10.18150/UOR5P1).

Supporting Information

The Supporting Information is available free of charge at https://pubs.acs.org/doi/10.1021/acs.analchem.4c03402.

(Figures S1−S10) Additional details on the optimization of the MSI setup, parameters for 3D MSI experiments, LC-MS experimental details, and results (PDF)

■ AUTHOR INFORMATION

Corresponding Author

Tomasz Ruman − *Department of Inorganic and Analytical Chemistry, Faculty of Chemistry, Rzeszów University of Technology, Rzeszów 35-959, Poland;* orcid.org/0000-0002-9899-8627; Phone: +48-17-8651896; Email: tomruman@prz.edu.pl

Authors

Sumi Krupa − *Doctoral School of Engineering and Technical Sciences at the Rzeszów University of Technology, Rzeszów 35-959, Poland*

Joanna Nizioł − *Department of Inorganic and Analytical Chemistry, Faculty of Chemistry, Rzeszów University of Technology, Rzeszów 35-959, Poland;* orcid.org/0000-0002-4783-8615

Complete contact information is available at: https://pubs.acs.org/10.1021/acs.analchem.4c03402

Notes

The authors declare no competing financial interest.

■ ACKNOWLEDGMENTS

The authors gratefully acknowledge support from the National Science Centre (Poland) research project Sonata Bis number 2022/46/E/ST4/00016. We appreciate all the individuals for participating in this study, especially Mr. Dominik Ruman for working on software for this project. We also thank Dr. Krzysztof Ossoliński for providing human kidney tissue samples.

■ REFERENCES

(1) Norris, J. L.; Caprioli, R. M. *Chem. Rev.* **2013**, *113* (4), 2309−2342.

(2) Bednařík, A.; Prysiazhnyi, V.; Bezdeková, D.; Soltwisch, J.; Dreisewerd, K.; Preisler, J. *Anal. Chem.* **2022**, *94* (12), 4889−4900.

(3) Buchberger, A. R.; DeLaney, K.; Johnson, J.; Li, L. *Anal. Chem.* **2018**, *90* (1), 240−265.

(4) Buchberger, A. R.; DeLaney, K.; Johnson, J.; Li, L. *Anal. Chem.* **2018**, *90* (1), 240.
(5) Wang, T.; Cheng, X.; Xu, H.; Meng, Y.; Yin, Z.; Li, X.; Hang, W. *Anal. Chem.* **2020**, *92* (1), 543−553.
(6) Dunham, S. J. B.; Ellis, J. F.; Li, B.; Sweedler, J. V. *Acc. Chem. Res.* **2017**, *50* (1), 96−104.
(7) Neumann, E. K.; Comi, T. J.; Spegazzini, N.; Mitchell, J. W.; Rubakhin, S. S.; Gillette, M. U.; Bhargava, R.; Sweedler, J. V. *Anal. Chem.* **2018**, *90* (19), 11572−11580.
(8) Li, D.; Qian, Y.; Yao, H.; Yu, W.; Ma, X. *Anal. Chem.* **2023**, *95* (29), 10879−10886.
(9) Eberlin, L. S.; Ifa, D. R.; Wu, C.; Cooks, R. G. *Angew. Chem.* **2010**, *122* (5), 885−888.
(10) Lanekoff, I.; Burnum-Johnson, K.; Thomas, M.; Cha, J.; Dey, S. K.; Yang, P.; Prieto Conaway, M. C.; Laskin, J. *Anal Bioanal Chem.* **2015**, *407* (8), 2063−2071.
(11) Nemes, P.; Barton, A. A.; Vertes, A. *Anal. Chem.* **2009**, *81* (16), 6668−6675.
(12) Andersson, M.; Groseclose, M. R.; Deutch, A. Y.; Caprioli, R. M. *Nat. Methods* **2008**, *5* (1), 101−108. *2008 5:1*
(13) Paine, M. R. L.; Liu, J.; Huang, D.; Ellis, S. R.; Trede, D.; Kobarg, J. H.; Heeren, R. M. A.; Fernández, F. M.; MacDonald, T. J. *Sci. Rep.* **2019**, *9* (1), 2205. *2019 9:1*
(14) Nizioł, J.; Ossoliński, K.; Ossoliński, T.; Ossolińska, A.; Bonifay, V.; Sekuła, J.; Dobrowolski, Z.; Sunner, J.; Beech, I.; Ruman, T. *Anal. Chem.* **2016**, *88* (14), 7365−7371.
(15) Eberlin, L. S.; Ifa, D. R.; Wu, C.; Cooks, R. G. *Angew. Chem., Int. Ed.* **2010**, *49* (5), 873−876.
(16) Unsihuay, D.; Hu, H.; Qiu, J.; Latorre-Palomino, A.; Yang, M.; Yue, F.; Yin, R.; Kuang, S.; Laskin, J. *Chem. Sci.* **2023**, *14* (15), 4070−4082.
(17) Jiang, L. X.; Hilger, R. T.; Laskin, J. *J. Mass Spectrom* **2024**, *59* (7), No. e5065.
(18) Lane, A. L.; Nyadong, L.; Galhena, A. S.; Shearer, T. L.; Stout, E. P.; Parry, R. M.; Kwasnik, M.; Wang, M. D.; Hay, M. E.; Fernandez, F. M.; Kubanek, J. *Proc. Natl. Acad. Sci. U. S. A.* **2009**, *106* (18), 7314−7319.
(19) Salter, T. L.; Green, F. M.; Gilmore, I. S.; Seah, M. P.; Stokes, P. *Surf. Interface Anal.* **2011**, *43* (1−2), 294−297.
(20) Wucher, A.; Cheng, J.; Winograd, N. *Anal. Chem.* **2007**, *79* (15), 5529−5539.
(21) Nemes, P.; Barton, A. A.; Vertes, A. *Anal. Chem.* **2009**, *81* (16), 6668−6675.
(22) Seeley, E. H.; Caprioli, R. M. *Anal. Chem.* **2012**, *84* (5), 2105−2110.
(23) Zhang, J.; Brown, J.; Scurr, D. J.; Bullen, A.; Maclellan-Gibson, K.; Williams, P.; Alexander, M. R.; Hardie, K. R.; Gilmore, I. S.; Rakowska, P. D. *Anal. Chem.* **2020**, *92* (13), 9008−9015.
(24) Gunnarsson, A.; Kollmer, F.; Sohn, S.; Höök, F.; Sjövall, P. *Anal. Chem.* **2010**, *82* (6), 2426−2433.
(25) Lechene, C.; Hillion, F.; McMahon, G.; Benson, D.; Kleinfeld, A. M.; Kampf, J. P.; Distel, D.; Luyten, Y.; Bonventre, J.; Hentschel, D.; Park, K.; Ito, S.; Schwartz, M.; Benichou, G.; Slodzian, G. *J. Biol.* **2006**, *5* (6), 20−30.
(26) Kuznetsov, I.; Filevich, J.; Dong, F.; Woolston, M.; Chao, W.; Anderson, E. H.; Bernstein, E. R.; Crick, D. C.; Rocca, J. J.; Menoni, C. S. *Nat. Commun.* **2015**, *6* (1), 6944. *2015 6:1*
(27) Bai, H.; Manni, J. G.; Muddiman, D. C. *J. Am. Soc. Mass Spectrom.* **2023**, *34* (1), 10−16.
(28) Passarelli, M. K.; Pirkl, A.; Moellers, R.; Grinfeld, D.; Kollmer, F.; Havelund, R.; Newman, C. F.; Marshall, P. S.; Arlinghaus, H.; Alexander, M. R.; West, A.; Horning, S.; Niehuis, E.; Makarov, A.; Dollery, C. T.; Gilmore, I. S. *Nat. Methods* **2017**, *14* (12), 1175−1183.
(29) Dousty, F.; Sc, M. *The Use of Dopants in Atmospheric Pressure Ionization Sources of Mass Spectrometers*; University of British Columbia 2015.
(30) Tubaro, M.; Marotta, E.; Seraglia, R.; Traldi, P. *Rapid Commun. Mass Spectrom.* **2003**, *17* (21), 2423−2429.
(31) McEwen, C. N.; Larsen, B. S. *J. Am. Soc. Mass Spectrom.* **2009**, *20* (8), 1518−1521.
(32) Rhourri-Frih, B.; Chaimbault, P.; Claude, B.; Lamy, C.; André, P.; Lafosse, M. *Journal of Mass Spectrometry* **2009**, *44* (1), 71−80.
(33) Himmelsbach, M.; Buchberger, W.; Reingruber, E. *Polym. Degrad. Stab.* **2009**, *94* (8), 1213−1219.
(34) Leinonen, A.; Kuuranne, T.; Kostiainen, R. *Journal of Mass Spectrometry* **2002**, *37* (7), 693−698.
(35) Fredenhagen, A.; Kühnöl, J. *Journal of Mass Spectrometry* **2014**, *49* (8), 727−736.
(36) Itoh, N.; Aoyagi, Y.; Yarita, T. *J. Chromatogr A* **2006**, *1131* (1−2), 285−288.
(37) Riu, A.; Zalko, D.; Debrauwer, L. *Rapid Commun. Mass Spectrom.* **2006**, *20* (14), 2133−2142.
(38) Short, L. C.; Cai, S. S.; Syage, J. A. *J. Am. Soc. Mass Spectrom.* **2007**, *18* (4), 589−599.
(39) Brauer, J. I.; Beech, I. B.; Sunner, J. *J. Am. Soc. Mass Spectrom.* **2015**, *26* (9), 1538−1547.
(40) Kokesch-Himmelreich, J.; Wittek, O.; Race, A. M.; Rakete, S.; Schlicht, C.; Busch, U.; Römpp, A. *Food Chem.* **2022**, *385*, No. 132529.
(41) Martín-Saiz, L.; Mosteiro, L.; Solano-Iturri, J. D.; Rueda, Y.; Martín-Allende, J.; Imaz, I.; Olano, I.; Ochoa, B.; Fresnedo, O.; Fernández, J. A.; Larrinaga, G. *Anal. Chem.* **2021**, *93* (27), 9364−9372.
(42) Nizioł, J.; Sunner, J.; Beech, I.; Ossoliński, K.; Ossolińska, A.; Ossoliński, T.; Płaza, A.; Ruman, T. *Anal. Chem.* **2020**, *92* (6), 4251−4258.
(43) Kokesch-Himmelreich, J.; Wittek, O.; Race, A. M.; Rakete, S.; Schlicht, C.; Busch, U.; Römpp, A. *Food Chem.* **2022**, *385*, No. 132529.
(44) Razgonova, M.; Boyko, A.; Zinchenko, Y.; Tikhonova, N.; Sabitov, A.; Mikhailovich Zakharenko, A.; Golokhvast, K. *Turk. J. Agric. For* **2023**, 155.
(45) Takeoka, G. R.; Güntert, M.; Jennings, W.; Flath, R. A.; Wurz, R. E. *J. Agric. Food Chem.* **1986**, *34* (3), 576−578.
(46) Skypala, I. J.; Reese, I. *Ref. Module Food Sci.* **2023**.
(47) Gondor, O. K.; Pál, M.; Janda, T.; Szalai, G. *J. Plant Physiol* **2022**, *277*, No. 153809.
(48) Lewis, D. H.; Burge, G. K.; Schmierer, D. M.; Jameson, P. E. *Physiol. Plant* **1996**, *98* (1), 179−186.
(49) Álvarez, T.; Ramírez, R. *Turk. J. Zool.* **2000**, *24* (1), 103−106.
(50) Li, P.; Liu, C.; Luo, Y.; Shi, H.; Li, Q.; Pinchu, C.; Li, X.; Yang, J.; Fan, W. *J. Agric. Food Chem.* **2022**, *70* (51), 16037−16049.
(51) Lee, H. S.; Kim, E. N.; Jeong, G. S. *Molecules* **2022**, *27* (14), 4633.
(52) Sun, Y. L.; Hong, S. K. *Plant Cell Tissue Organ Cult* **2010**, *100* (3), 317−328.
(53) Alfosea-Simón, M.; Simón-Grao, S.; Zavala-Gonzalez, E. A.; Cámara-Zapata, J. M.; Simón, I.; Martínez-Nicolás, J. J.; Lidón, V.; García-Sánchez, F. *Front Plant Sci.* **2021**, *11*, No. 581234.
(54) Seaman, C.; Flinders, B.; Eijkel, G.; Heeren, R. M. A.; Bricklebank, N.; Clench, M. R. *Anal. Chem.* **2014**, *86* (20), 10071−10077.
(55) Brauer, J. I.; Beech, I. B.; Sunner, J. *J. Am. Soc. Mass Spectrom.* **2015**, *26* (9), 1538−1547.
(56) Wang, T.; Fu, X.; Chen, Q.; Patra, J. K.; Wang, D.; Wang, Z.; Gai, Z. *International Journal of Molecular Sciences* **2019**, *20* (15), 3683. *2019, Vol. 20, Page 3683*
(57) Schwartzman, M. L.; Martasek, P.; Rios, A. R.; Levere, R. D.; Solangi, K.; Goodman, A. I.; Abraham, N. G. *Kidney Int.* **1990**, *37* (1), 94−99.
(58) Chesney, R. W.; Han, X.; Patters, A. B. *J. Biomed. Sci.* **2010**, *17* (SUPPL. 1), 1−10.
(59) Shankar, V.; Vijayalakshmi, K.; Nolley, R.; Sonn, G. A.; Kao, C.-S.; Zhao, H.; Wen, R.; Eberlin, L. S.; Tibshirani, R.; Zare, R. N.; Brooks, J. D. *JCO Precision Oncology* **2023**, *7*, No. e2200668.
(60) Han, X.; Yue, J.; Chesney, R. W. *Journal of the American Society of Nephrology* **2009**, *20* (6), 1323−1332.

(61) Wettersten, H. I.; Hakimi, A. A.; Morin, D.; Bianchi, C.; Johnstone, M. E.; Donohoe, D. R.; Trott, J. F.; Aboud, O. A.; Stirdivant, S.; Neri, B.; Wolfert, R.; Stewart, B.; Perego, R.; Hsieh, J. J.; Weiss, R. H. *Cancer Res.* **2015**, *75* (12), 2541−2552.

(62) Razgonova, M.; Boyko, A.; Zinchenko, Y.; Tikhonova, N.; Sabitov, A.; Zakharenko, A. M.; Golokhvast, K. *Turk. J. Agric. For.* **2023**, *47* (2), 155−169.

(63) Zhang, J.; Li, S. Q.; Lin, J. Q.; Yu, W.; Eberlin, L. S. *Cancer Res.* **2020**, *80* (4), 689−698.

(64) Vijayalakshmi, K.; Shankar, V.; Bain, R. M.; Nolley, R.; Sonn, G. A.; Kao, C. S.; Zhao, H.; Tibshirani, R.; Zare, R. N.; Brooks, J. D. *Int. J. Cancer* **2020**, *147* (1), 256−265.

(65) Jones, E. E.; Powers, T. W.; Neely, B. A.; Cazares, L. H.; Troyer, D. A.; Parker, A. S.; Drake, R. R. *Proteomics* **2014**, *14* (7−8), 924−935.

(66) Nizioł, J.; Ossoliński, K.; Ossoliński, T.; Ossolińska, A.; Bonifay, V.; Sekuła, J.; Dobrowolski, Z.; Sunner, J.; Beech, I.; Ruman, T. *Anal. Chem.* **2016**, *88* (14), 7365−7371.

CAS BIOFINDER DISCOVERY PLATFORM™

ELIMINATE DATA SILOS. FIND WHAT YOU NEED, WHEN YOU NEED IT.

A single platform for relevant, high-quality biological and toxicology research

Streamline your R&D

CAS
A division of the American Chemical Society

ACS Partner Journal

Journal of the American Society for Mass Spectrometry

pubs.acs.org/jasms

Article

Open Access

This article is licensed under CC-BY 4.0

Downloaded via RZESZOW UNIV OF TECHNOLOGY on March 30, 2026 at 08:21:17 (UTC).
See https://pubs.acs.org/sharingguidelines for options on how to legitimately share published articles.

Broadband Collision-Induced Dissociation Mass Spectrometry Imaging

Sumi Krupa, Wiktoria Szuberla, Joanna Nizioł,* Anna Ossolińska, Krzysztof Ossoliński, and Tomasz Ruman

Cite This: *J. Am. Soc. Mass Spectrom.* 2025, 36, 1443−1455

Read Online

ACCESS | Metrics & More | Article Recommendations | Supporting Information

ABSTRACT: This study demonstrates the first application of broadband collision-induced dissociation (bbCID) to mass spectrometry imaging (MSI) for the identification of untargeted metabolites in human tissues. The methodology integrates bbCID with laser ablation−remote atmospheric pressure photoionization/chemical ionization (LARAPPI/CI), enabling the simultaneous acquisition of precursor and fragment ion distributions during MSI for many compounds simultaneously. In this approach, an infrared (IR) laser is used to ablate biological material, which is then ionized in the gas phase by a combination of photoionization and chemical ionization at atmospheric pressure. The method was validated using reference compounds, including thymidine and commonly used synthetic dyes, to assess ionization efficiency, fragmentation behavior, and spatial colocalization of precursor and fragment ions. Subsequently, bbCID-MSI was applied to clinical tissue samples of human bladder and kidney cancer. For the bladder cancer tissue, higher intensities of heptadecanoic acid, docosahexaenoic acid (FA(22:6)), docosapentaenoic acid (FA(22:5)), and FA(16:0) were observed in tumor regions, whereas proline was more abundant in adjacent nontumorous area. In renal cell carcinoma, cancerous regions exhibited elevated levels of polyunsaturated fatty acids such as arachidonic acid (FA(20:4)) and adrenic acid (FA(22:4)), while creatine and serine were enriched in healthy tissue zones. These findings highlight the utility of bbCID-MSI for spatially resolved metabolite analysis and its potential to reveal biologically relevant metabolic alterations associated with cancer.

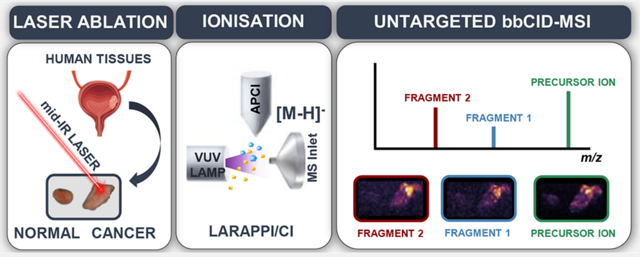

KEYWORDS: *tandem mass spectrometry, mass spectrometry imaging, metabolomics, tissue imaging, molecular imaging*

■ INTRODUCTION

Mass spectrometry imaging (MSI) is a well-established analytical method that presents the spatial distribution of chemical compound ions that occur in biological tissues and synthetic materials. MSI has a plethora of applications in various fields, such as clinical, metabolic pathway research, and also biomarker discovery, microorganism activity, plant research, or forensic analysis.[1]

Most mass-spectrometry-based imaging analyses focus on acquiring results from the MS^1 mass spectrum.[2] The identification of compound ions detected by this method can be challenging for compounds of similar monoisotopic masses and very problematic for isomers. The solution to more accurate identification is the analysis of fragment ions in tandem mass spectrometry (MS/MS).[3]

The identification of detected ions with MSI and MS/MS is usually done by comparing the ion images obtained for precursors with the ion images recorded for fragment ions. The majority of published results present methodologies capable of the fragmentation of only one ion per analysis. These MS/MS analyses are focused on 3 main areas: lipid imaging in animal brain tissues,[4−6] plant-specific metabolites,[7,8] and drug imaging, including already existing drugs, a notable number conducted on brain tissues,[9−18] drug candidates,[19,20] and illicit drugs.[21−23] The commercially available active drug substances studied using MSI range from antibacterial[24−26] and antiviral drugs[12] and allergy drugs[9,25,26] to respiratory system drugs,[17,27,28] anticancer drugs,[16,25,26] and antipsychotic drugs,[10,13,15,25,26,29] drugs on the skin,[30] in rat brain tissue[31] and rat lung tissue,[28] and on disaccharide matrix.[32] MS/MS imaging has also been utilized in forensic research for imaging fingerprints[33] and forgery research.[34]

Selected reaction monitoring (SRM) and multiple reaction monitoring (MRM) are methods that allow mass spectrometry imaging by using multiple fragmentation reactions per analysis as a result of the relatively fast switching of m/z windows by quadrupole analyzers. However, the analysis with SRM/MRM

Received: February 13, 2025
Revised: May 20, 2025
Accepted: June 13, 2025
Published: June 19, 2025

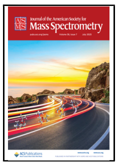

© 2025 The Authors. Published by American Chemical Society

https://doi.org/10.1021/jasms.5c00045

MS or MSI is a targeted approach that requires knowledge of m/z values of precursors and fragment ions of compounds present in the tissue prior to analysis. SRM has been used in MSI analyses of tissues utilizing infrared laser ablation (LA) as the desorption method. SRM analyses of plant tissues, such as banana cross sections and spelled cross sections, have been conducted with MSI, allowing for the identification of amino acids, basic metabolites, plant-specific metabolites, and invading fungi metabolites.[35,36] Objects such as 18th-century silk fabric[37] and historic photographs[38] have also been imaged by the discussed method, allowing the identification of microbial metabolites in negative and positive modes, respectively. Human kidney cancerous and healthy tissue has also been imaged in SRM mode with IR-LA desorption factor, leading to the identification of cancer-normal differentiating compounds.[39]

The use of a dedicated millijoule energy level IR laser as a desorption source is highly effective for biological samples and shows relatively deep penetration of biological material compared to other commonly used desorption methods, such as secondary-ion mass spectrometry (SIMS), matrix-assisted laser desorption/ionization (MALDI), and laser desorption/ionization (LDI) techniques, or desorption electrospray ionization (DESI).[39] The main technique used for MS/MS mass spectrometry imaging reported at present, where infrared-LA is employed, is laser ablation−remote electrospray ionization (LARESI).[39] LARESI is a technique advantageous for MSI due to numerous reasons such as (i) remote nitrogen-filled chamber with the sample, (ii) sample freezing, (iii) deep ablation, (iv) compatibility with all atmospheric ion sources and instruments, and (v) nonfragmenting low photon energy IR laser. Interferences to the composition and structures are minimal because of the minimal sample preparation and the ambient conditions of the analysis. While published studies employed triple quadrupole (QqQ) mass analyzers, which are widely recognized for their exceptional sensitivity and quantification capabilities, these instruments typically operate in a targeted mode and are not inherently designed for high-resolution data acquisition. The spectral resolution is a pivotal parameter in the accurate assignment of m/z value to a specific molecule.

Broadband collision-induced dissociation (bbCID) technology extends traditional CID workflows by employing a wide collision energy range and cycling from low to moderate fragmentation energy, thus generating simultaneous MS and MS/MS data for all suitable ions.[40] Traditional CID typically targets only one selected precursor at a fixed collision energy, whereas bbCID fragments multiple ions and provides multilevel fragmentation, enabling rapid, nontargeted screening of complex mixtures.[41,42] The bbCID as a data-independent approach (DIA) is usually used as a quantitative or qualitative method for metabolomic profiling of biological fluids and comprehensive screening of unknown contaminants.[43−45] By capturing precursors and fragments in a single LC-HRMS run, bbCID allows detection and quantification of numerous analytes without repeated reinjection or sequential MS/MS acquisition steps.[46,47]

In the context of MSI, bbCID should provide several advantages. First, it provides both MS and MS/MS-level data simultaneously, bypassing the need for precursor selection. Second, its nontargeted fragmentation capability is particularly beneficial for detecting and identifying diverse classes of compounds for which fragmentation pathways may be unknown.[48−50] Although wide-energy CID strategies have been successfully demonstrated in nonimaging MS for the characterization of complex biological samples,[51] their adaptation to MSI platforms remains underexplored, highlighting the novelty of this work.

Laser ablation−remote atmospheric pressure photoionization/chemical ionization (LARAPPI/CI) technique provides several analytical advantages over widely adopted MSI platforms such as MALDI, DESI, and SIMS. The use of a mid-infrared (2.93 μm) pulsed laser enables efficient ablation of hydrated biological materials with minimal thermal degradation, allowing for depth profiling without the need for thin sectioning.[52] Importantly, the system operates under ambient conditions and does not require matrix deposition, thereby reducing ion suppression and preserving the native distribution of analytes.[53] Unlike MALDI, which relies on UV-absorbing matrices, and DESI, which requires solvent−surface interaction, LARAPPI/CI minimizes sample preparation while offering high chemical versatility and compatibility with both polar and nonpolar metabolites.[54] Although SIMS achieves submicrometer spatial resolution, it is problematic for centimeter-sized samples and often suffers from low ion yields and limited performance in the high mass range for biomolecules. LARAPPI/CI delivers a practical balance between spatial resolution and ionization efficiency across diverse compound classes.[55]

In this study, we utilize a recently developed LARAPPI/CI system equipped with a high-mass-resolution quadrupole-time-of-flight (QToF) mass spectrometer. The mass spectrometry method employed is bbCID, which continuously cycles very low and high collision energies, enabling the acquisition of both MS and MS/MS-type data for potentially hundreds to thousands of organic compounds within a single MSI experiment. These capabilities are further enhanced by the integration of bbCID with LARAPPI/CI MSI, allowing the simultaneous acquisition of precursor and fragment ion distributions in each voxel, without the need for precursor selection. The resulting nontargeted, multienergy fragmentation profiles facilitate structural elucidation of unknown compounds directly within complex tissue environments, thereby supporting deeper metabolomic interpretation.

While bbCID has been extensively used in nonimaging applications, its adoption for MSI was not previously published. In the first part of this work, the methodology is validated using known reference compounds, while the second part provides results of application to the analysis of human normal and cancerous kidney and bladder tissues. The imaging method presented in this work was developed for Bruker's bbCID but should also be compatible with other properly configured DIA methods, such as Thermo Fisher Scientific's MS/AIF (full scan MS/all ion fragmentation) and Waters' MS^E.

■ MATERIALS AND METHODS

All solvents were LC-MS grade. All chemicals were purchased from Aldrich/Merck Poland and were of analytical purity.

Patient Information. The kidney sample used in the MSI experiment was taken from a 72-year-old male. He was diagnosed with malignant clear cell renal cell carcinoma (ccRCC). The patient underwent a surgical procedure (NSS dex). The tumor size was 22 mm × 20 mm × 20 mm. The cancer stage was classified as pT1aN0M0, indicating an early stage without lymph nodes or distant metastases. The

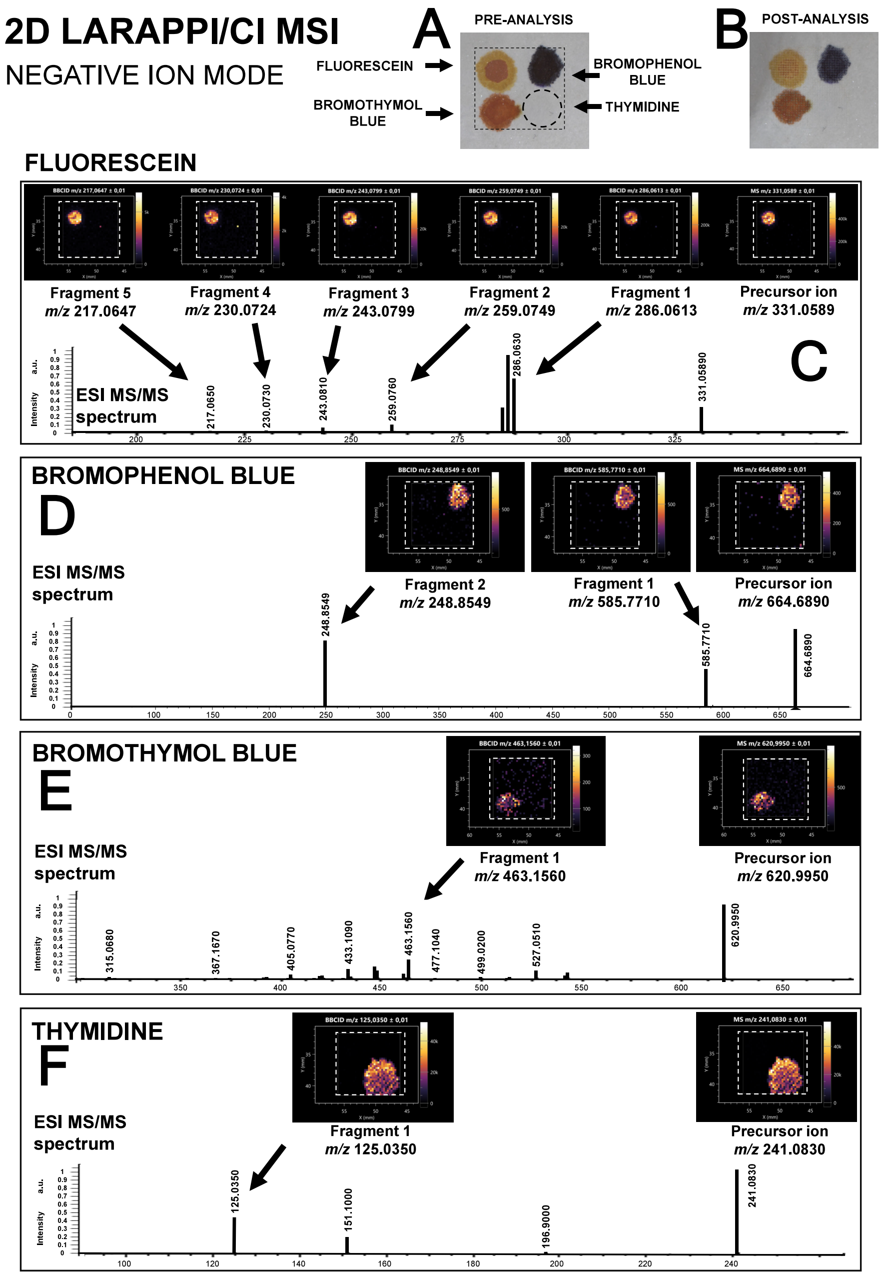

Figure 1. Results of negative ion mode LARAPPI/CI-MSI with bbCID method analysis of paper with fluorescein spots (upper left corner), bromophenol blue (upper right corner), bromothymol blue (lower left corner), and thymidine (lower right corner): (A) preanalysis optical photograph; (B) postanalysis optical photograph; (C−F) panels with ion images (top of the panel) and MS/MS spectra (bottom of the panel) for a given compound.

Fuhrman grade is G1, indicating a low level of cellular aggressiveness.[56]

The bladder cancer (BC) sample used in the MSI experiment originated from a 75-year-old male. The histopathological evaluation indicated the staging classification of pT0, suggesting an early stage of cancer of bladder tissue. The research was approved by the local Bioethics Committee at the University of Rzeszow (Poland, permit number 2018/04/10) and followed all current rules and regulations.

LARAPPI/CI MSI System. The LARAPPI/CI MSI system first described in a recent publication is based on an airtight chamber pressurized with nitrogen gas to produce a nitrogen stream of 10 L/min. The sample is placed on a 50 mm × 50 mm sample stage, with a Peltier cooling plate that sustains the sample at −18 °C. The temperature-controlled sample stage is mounted on a motorized high-speed *XY*-stage The pulsed beam from the OPO laser (2.93 μm, 7 ns, 20 Hz, 2 mJ/pulse measured before the focusing lens) enters the sample chamber through the sapphire window, then the beam is expanded 3.75× and is redirected toward the sample stage by a gold mirror. The beam then goes through a diffractive optical element forming a square-shaped top-hat beam. It is then focused onto the sample surface by a 50 mm focal length aspherical ZnSe lens. The optical assembly and also the camera (FLIR Blackfly S, color camera, 6 MPix, Sony IMX178 sensor, lens, 12 mm C series fixed focal length lens, Edmund Optics, U.K.) with lens and distance sensor are mounted on aluminum rails and are in a fixed configuration; the only moving parts are

XYZ stages. During imaging, the laser focal point remains fixed in space, whereas the sample is moved. A specially designed gas funnel is also a focusing assembly and is connected to a 6/4 mm (O.D/I.D.) PTFE tube. The overpressure in the chamber drives a 10 L/min nitrogen gas flow through the tube. The laser ablation plumes are entrained in the gas and transported to the modified ion source (Bruker VIP HESI in the APCI configuration) of the Bruker Impact II mass spectrometer. The ion source also had a VUV source (Hamamatsu L12542) mounted axially to the MS sampling cone inside the ion source. An HPLC pump (Agilent G1312A) provides a steady flow of a solvent mixture (1% toluene in methanol; 200 μL/min) to the APCI needle [1]. The settings of the ion source were as follows: APCI nebulizer, end plate offset 600 V, capillary 1000 V, corona 6000 nA, nebulizer 3.5 bar, dry gas 0.2 L/min, dry temperature 250 °C, probe gas temperature 350 °C, probe gas 4 L/min, exhaust turned on. Experiments were performed with the following settings: scan range *m/z* 47–1300, 4 Hz MS/bbCID frequency, and CID energy was cycled from 7 to 40 eV. ESI MS/MS spectra presented in Figures 1–3 and S1 are taken from spectral databases: NIST version 2023[57] and HMDB 5.0.[58] The details of software used for registration and visualization of results is described in our previous work.[55]

MSI Experiment: Thymidine and Dyes on Paper. The analyzed compound spots were placed on laser printer paper (two layers, attached to a steel plate with adhesive tape) with automatic pipetting by pipetting 0.2 μL of each solution (thymidine 10 mg/mL in water, bromophenol blue, bromothymol blue, and fluorescein were of 50 mg/mL concentration in methanol).

The 2D MSI experiment in negative ion mode for dyes and thymidine was performed with 300 μm resolution (33 × 33 pixels, *X* × *Y*). Each pixel/voxel in 2D MSI experiments was exposed to the laser for 1 s at a laser pulse repetition rate of 20 Hz. The delays between pixels were 1000 ms. Between pixels, the sample stage moved at a speed of 50 mm/s. The time delay between the lines was 5 s. The starting object was of ca. 0.16 mm thickness and 9.6 mm × 9.6 mm (*X* × *Y*) size. The object was placed on a stainless steel plate, then placed on an ablation table inside the chamber, and frozen. The MS^1 frequency was 3 Hz and the MS to bbCID spectrum recording time ratio was 1:1. The experiment in positive ion mode (Supporting Information Figure S1) was performed similarly to that described above with exceptions: number of pixels, 25 × 27; imaged region size, 7.2 mm × 7.8 mm (*X* × *Y*).

MSI Experiment: Cancer and Normal Human Kidney Tissue. The 2D MSI experiment in negative ion mode for human kidney cancer and normal tissue was performed with a resolution of 150 μm (33 × 37 pixels, *X* × *Y*). Each pixel/voxel in the MSI experiment was exposed to the laser for 1 s at a laser pulse repetition rate of 20 Hz. The delays between pixels were 1000 ms. Between pixels, the sample stage moved at a speed of 50 mm/s. The time delay between lines was 5 s. The starting object was cut with a cryotome with *ca.* 0.5 mm thickness and the imaged area were 4.8 × 5.4 mm (*X* × *Y*) in size. The object was placed on a stainless steel plate and then on an ablation table inside the chamber and frozen. MS^1/bbCID frequency was 4 Hz.

MSI Experiment: Cancer and Normal Human Bladder Tissue. The 2D MSI experiment in negative ion mode for human bladder cancer and normal tissue was performed with 150 μm resolution (43 × 23 pixels, *X* × *Y*). Each pixel/voxel in the MSI experiment was exposed to the laser for 1 s, at a laser pulse repetition rate of 20 Hz. The delays between pixels were 1000 ms. Between pixels, the sample stage moved at a speed of 50 mm/s. The time delay between lines was 5 s. The starting object was cut with a cryotome with *ca.* 0.8 mm thickness and the imaged area were 6.3 mm × 3.3 mm (*X* × *Y*) in size. The object was placed on a stainless steel plate, then on an ablation table inside the chamber, and frozen.

RESULTS AND DISCUSSION

The use of classical fragmentation methods for untargeted MSI such as MS/MS where the precursor ion is selected manually or automatically is extremely impractical in fast imaging setups. In the case of our imaging setup LARAPPI/CI MSI, each ablation spot/voxel is usually ablated for just 0.3 to 1 s; this amount of time for MS/MS-type methods such as AutoMS/MS could allow signal detection, mass selection, and fragmentation of up to few ions with a fast modern instrument. However, the use of automatic MS/MS methods generates another critical problem, which is the differentiation of detection times for different voxels due to different amounts of signals being fragmented, which would artificially vary the MSI intensities of voxels and produce distorted results.

The method of choice for MSI was bbCID, which continuously cycles very low- and medium-high collision energy, allowing recording high-resolution spectra of both MS- and MS/MS type for large amounts of compounds in a single MSI analysis. The methodology in this work assumes improvement of MSI identification with matching of the ion image of precursor generated from MS data with the ion image(s) of fragments generated from bbCID data. Both data types are recorded during each MSI experiment. Four chemical compounds were chosen for preliminary tests: colorless thymidine, colorful bromophenol blue, bromothymol blue, and fluorescein. The choice of dyes allowed for a visual comparison of sample photographs with ion images. As the method was considered for research conducted on biological tissues, the fourth compound, thymidine, was chosen as an important biological compound to confirm the ionization and fragmentation of an endogenous metabolite. Dyes and thymidine samples were tested in 2D MSI in both negative (Figure 1) and positive (Figure S1) ion modes, with the former one chosen due to higher signal intensities. As the LARAPPI/CI MSI system contains a beam-shaping diffractive optical element, the focused laser spot size is a square with dimensions approximately 170 μm. The depth of the ablation of the paper object after 20 laser impulses was measured with a computerized microscope and was 60 μm. The calculated maximum weight of the desorbed material from a single ablation point for fluorescein was 30 ng, for bromophenol and bromothymol blue, 70 ng, and the mass of thymidine per singular spot was 1.5 ng, equating to no more than 1.2 nmol of bromothymol blue, 1.1 nmol of bromophenol blue, 1 nmol of fluorescein, and 60 pmol of thymidine.

All compounds were identified by their precursor ion $[M - H]^-$, and at least one fragment signal was obtained for all compounds. The highest signals were obtained for fluorescein. The bbCID fragmentation of precursor ion of fluorescein of *m/z* 331.0589 produced 5 fragment ions with *m/z* values of 217.0647, 230.0724, 243.0799, 259.0749, and 286.0613 for which ion images are shown in Figure 1. For bromophenol blue, with the precursor ion at *m/z* 664.6890, two fragment ions were found: *m/z* 248.8549 and 585.7710. Both bromothymol blue and thymidine could be identified by one

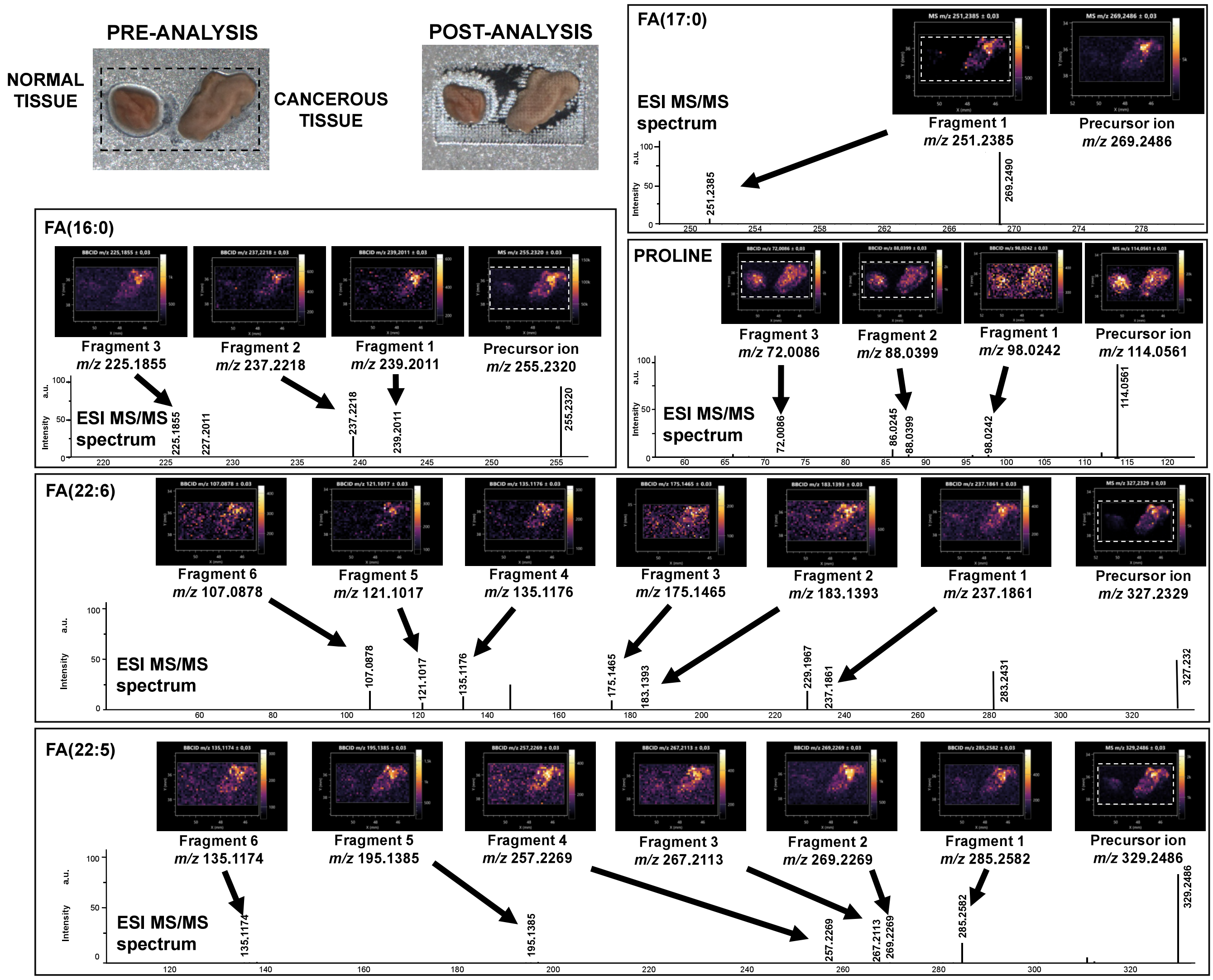

Figure 2. Results of LARAPPI/CI-MSI-bbCID analysis of BC tissue with the bbCID method. Preanalysis and postanalysis optical photographs of the studied object are shown in the top left corner of the figure. The rest of the figure contains panels with ion images (top of the panel) and MS/MS spectra (bottom of the panel) for the given compound. FA: fatty acid.

precursor ion and one fragment ion, m/z 620.9950/463.1560 and m/z 241.0830/125.0350 for precursor/fragment pairs of bromothymol blue and thymidine, respectively. The results obtained were deemed promising for further analysis of complex biological objects.

MSI is currently a key technique that enables the spatial analysis of metabolic changes within the tumor microenvironment.[59,60] Its ability to perform untargeted molecular analysis without the need for labeling makes it particularly well-suited for cancer research, where metabolic reprogramming and tissue heterogeneity are frequently observed.[61] In this study, we selected human bladder and kidney tissues containing both tumor and adjacent normal regions as a model system to evaluate the performance of the LARAPPI/CI-MSI-bbCID method under biologically complex conditions.

BC and normal bladder tissues were analyzed with the LARAPPI/CI-MSI-bbCID method (Figure 2). This type of comparison was chosen to differentiate cancer and normal regions based on possible cancer biomarkers. The compounds identified by comparison of MS and bbCID ion images were heptadecanoic acid (FA(17:0)), hexadecanoic acid (FA(16:0)), FA(22:6), FA(22:5) and proline, all of them can dissociate in water systems and form negative ions. For heptadecanoic acid, the m/z of the precursor and the most intense fragment was 269.2486/251.2385. Palmitic acid FA(16:0) anion at m/z 255.2320 could be identified by its fragment ions m/z 239.2011, 237.2218, and 225.1855. For proline m/z 114.0561 three fragment ions have been also detected: m/z 72.0086, 88.0399, 98.0242. Particularly good results were obtained for unsaturated fatty acids. Ion images of FA(22:6) precursor ion m/z 327.2329 matched ion fragment ion images of six fragments at m/z 107.0878, 121.1017, 135.1176, 175.1465, 183.1393, and 237.1861. FA(22:5) of the m/z 329.2486 of the precursor produced equally as many bbCID fragment ions at m/z 135.1174, 195.1385, 257.2269, 267.2113, 269.2269, and 285.2582 (Figure 2). It should be noted that all fragments discussed in this work are commonly found in CID MS/MS spectra (HMDB spectrum no. 21879, 32181, 21965, 2730, 3445, 2239403, 118936, 278884, 333573). Chemical structures of the precursors and fragments are provided in Figure 4. A study considering the fragmentation of saturated, monounsaturated, and polyunsa-

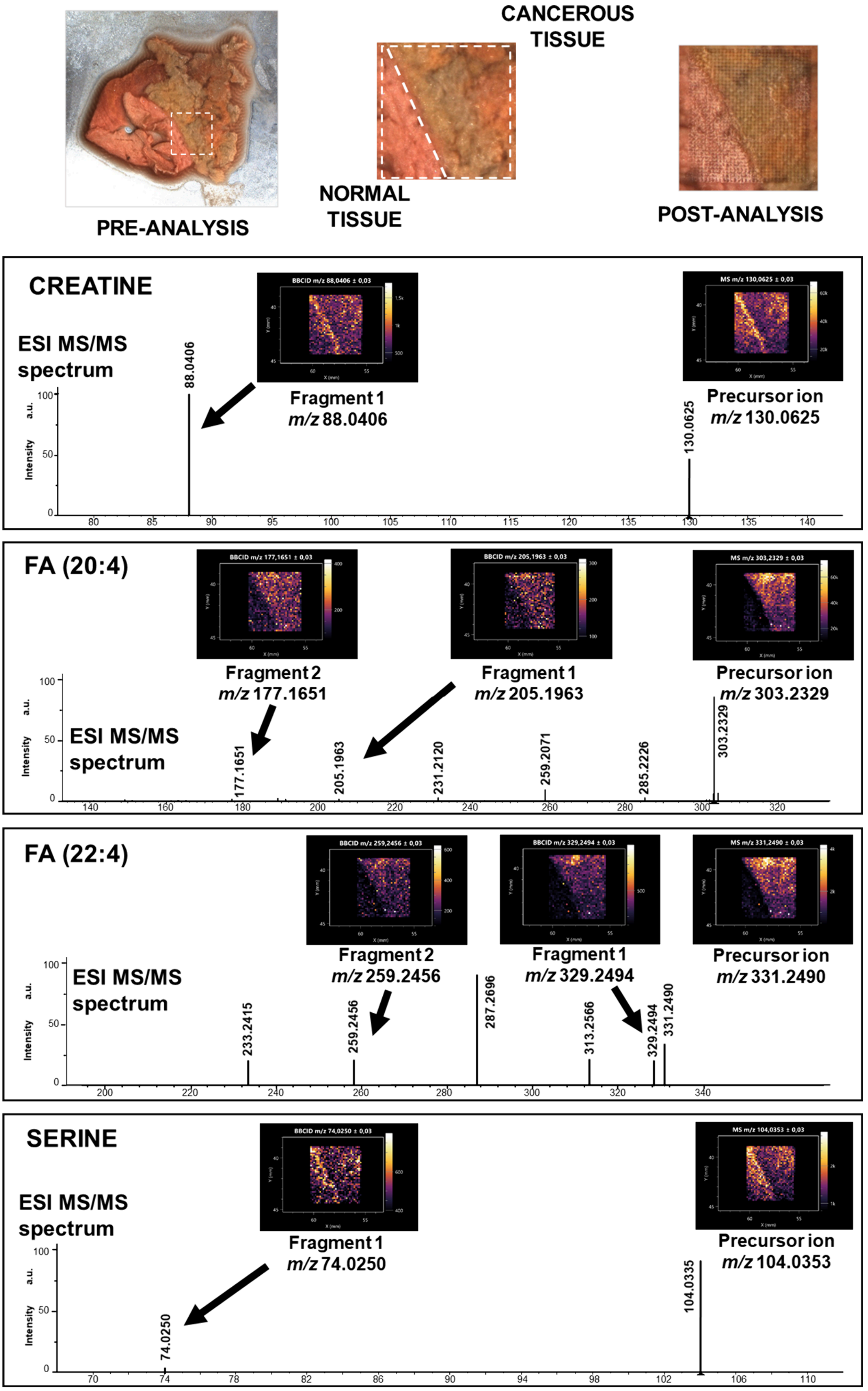

Figure 3. Results of LARAPPI/CI-MSI-bbCID analysis of human RCC tissue. Preanalysis optical photographs of the studied object are shown in the top-left and top-center parts of the figure. The postanalysis optical photograph is shown in the top right corner of the figure. The rest of the figure contains panels with ion images (top of the panel) and MS/MS spectra (bottom of the panel) for the given compound. FA: fatty acid.

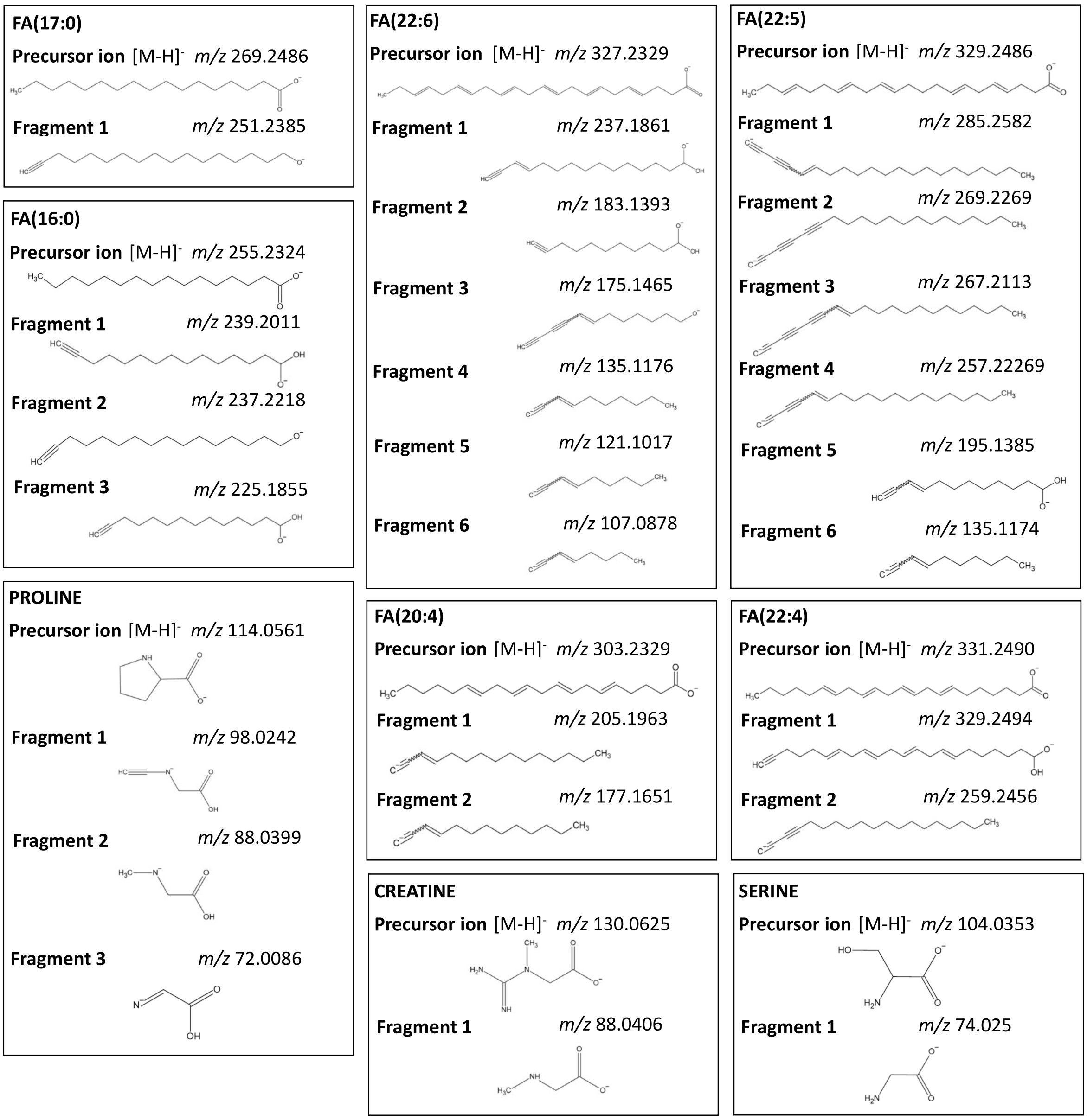

Figure 4. Chemical structures of ions detected in MSI experiments of the RCC and BC tissues. Each panel contains structure and *m/z* for precursor ion found in MS spectra (top of panel) and the same data for fragment ions found in bbCID spectra (middle and lower parts of panel). FA: fatty acid.

turated fatty acids has shown that saturated and monounsaturated FAs produce fragmentation spectra with significantly less distinguishable fragment signals than polyunsaturated acids,[62] which may explain why some of the identified lipid species undergo more abundant fragmentation.

Heptadecanoic acid, although commonly present in human tissues, can be related to the amount of dairy intake in a diet,[63] even though the ratio of pentadecanoic acid and heptadecanoic acid in dairy products versus in plasma of consumers of these products does not correlate in terms of concentration.[64] Although pentadecanoic acid has a concentration about twice higher than that in dairy products, the opposite result is observed in human plasma after consumption. Heptadecanoic acid is sometimes attributed to a lower risk of coronary heart disease or type 2; however, studies show no significant differentiation in the obtained results.[65,66] The ion images of heptadecanoic acid show the highest abundance of the compound in the cancerous tissue. Cancer research shows that heptadecanoic acid occurrence can be associated with a higher risk of prostate cancer,[67] breast cancer,[68] and colorectal cancer.[69] Recent studies also suggest that heptadecanoic acid may induce apoptosis and enhance chemosensitivity in pancreatic cancer cells, further supporting its potential role in tumor pathophysiology.[70]

Palmitic acid (FA(16:0)) is one of the most abundant saturated fatty acids in human tissues, playing a central role in membrane integrity and energy metabolism.[71] Recent studies have shown that elevated levels of palmitic acid can influence various oncogenic processes, including the induction of pro-inflammatory signals, modulation of oxidative stress, and promotion of tumor cell proliferation.[72,73] Several studies have reported elevated levels of palmitic acid (FA(16:0) in cancer patients. In esophageal cancer, patients showed significantly higher plasma levels of FA(16:0) compared to healthy controls, indicating a potential role in tumor-related metabolic changes.[74] Similarly, in colorectal cancer, both cachectic and noncachectic patients had increased plasma FA(16:0) levels compared to controls, suggesting its involvement in inflammation-associated cancer progression.[75] A recent meta-analysis found that elevated blood levels of palmitic acid (FA(16:0)) were significantly associated with an increased risk of several cancers, including breast cancer.[76] In bladder cancer, metabolic profiling has revealed elevated levels of palmitic acid (FA(16:0)) in tumor tissues, particularly in the basal subtype of muscle-invasive cases,[77,78] suggesting its involvement in disease progression. Proposed mechanisms include activation of transcription factors like SREBP1, stimulation of pro-inflammatory pathways such as TLR-4/NF-κB, and epigenetic alterations affecting lipid metabolism, all of which may contribute to a tumor-promoting environment.[79]

The ion images of the proline ion show that the abundance of the compound is similar in both normal and cancerous tissue, with slightly higher levels in normal tissue. Previous metabolomic studies also suggest lower urinary proline concentrations in bladder cancer patients compared to healthy individuals.[80] One possible explanation may involve disrupted proline biosynthesis, which occurs via the P5C reductase pathway and involves three isoforms: PYCR1, PYCR2, and PYCRL. Among these, PYCR1 has been implicated in increasing intracellular proline concentrations and supporting tumor growth in renal cell carcinoma.[81] Beyond biosynthesis, recent studies demonstrate that proline catabolism is actively reprogrammed in cancer cells. Specifically, degradation of proline by proline dehydrogenase (PRODH) has been shown to facilitate metastasis formation in breast cancer models, while pharmacological inhibition of PRODH suppresses lung metastases without significantly impacting primary tumor size.[82] Moreover, recent metabolomic studies of bladder cancer further support the relevance of proline dysregulation. For instance, altered proline levels were identified among metabolites distinguishing low- from high-grade bladder tumors in serum[83] and urinary proline was among key discriminators in a diagnostic panel with high predictive accuracy.[84] These findings highlight the dual regulatory roles of proline turnover (both synthetic and catabolic) in promoting tumor progression in a context-dependent manner.

Polyunsaturated fatty acids (PUFAs), including docosahexaenoic acid (FA(22:6)) and its metabolic precursor FA(22:5), were elevated in bladder cancer tissues compared to those in adjacent normal regions. FA(22:6) plays a multifaceted role in the tumor microenvironment due to its incorporation into membrane phospholipids, which not only enhances fluidity but also increases vulnerability to oxidative stress. This susceptibility contributes to its involvement in ferroptosis, a regulated form of cell death driven by reactive oxygen species (ROS) and iron.[85,86] While elevated FA(22:6) can promote pro-ferroptotic activity and inhibit metastasis in certain cancers tumor cells with strong antioxidant defenses may exploit it to support survival.[87,88] FA(22:5), although less studied, has been linked to immunomodulation and membrane remodeling. These findings align with recent reports on the role of PUFAs in metabolic reprogramming and redox regulation in cancer.[89] Additionally, FA(22:6) has been shown to suppress bladder cancer cell invasiveness by downregulating granzyme B expression,[90] while reduced expression of elongation of very long chain fatty acids protein 2 (ELOVL2), a key enzyme involved in DHA synthesis, has been associated with advanced-stage tumors and poor prognosis.[91]

The second human tissue analyzed in this study was the RCC and adjacent normal kidney tissue (Figure 3). Chemical structures of detected precursors and fragments are listed in Figure 4. Compounds identified with comparison of precursor ion images from MS spectra and fragment ions from bbCID spectra were creatine, FA(20:4), FA(22:4), and serine. Creatine and serine were identified by one precursor ion and one fragment ion, m/z 130.0625/88.0406 and m/z 104.0353/74.0250, respectively. Once again, the best results were obtained for polyunsaturated fatty acids. FA(20:4) m/z 303.2329 was identified by well-fitting ion images of the precursor ion and fragment ions m/z 177.1651 and 205.1963. For FA(22:4) m/z 331.2490, the assigned fragments found were m/z 259.2456 and 329.2494.

In our study, creatine showed the highest levels in the pseudocapsule, the zone between cancerous and healthy kidney tissue. Creatine is important for energy metabolism, and the enzyme creatine kinase helps convert it to phosphocreatine, which stores energy in cells. This enzyme has been linked to cancer progression in several tumor types, including gastric, esophageal, lung, and breast cancer.[92] Higher levels of phosphocreatine can help cancer cells survive in stressful conditions by quickly supplying energy when needed.[93,94] Metabolomic profiling of kidney cancer tissues has shown that creatine levels tend to be lower in malignant regions compared to adjacent noncancerous tissue,[95] supporting the notion that creatine is more abundant in metabolically normal areas. This distribution pattern may result from differences in creatine transport, utilization, or local enzymatic activity. These findings are consistent with studies in other cancers, where MSI has shown an uneven creatine distribution between tumors and surrounding tissues. In breast cancer, energy-buffering pathways involving creatine and related metabolites have been linked to tumor adaptation under metabolic stress.[96] Similarly, brain MSI data indicate that creatine levels shift in response to physiologic challenges, highlighting its role in energy homeostasis.[97]

Serine was also more abundant in noncancerous kidney regions, consistent with reports of altered serine biosynthesis in RCC due to upregulation of enzymes like phosphoglycerate dehydrogenase (PHGDH) and serine hydroxymethyltransferase 2 (SHMT2), which participate in serine−glycine one-carbon metabolism pathways critical for redox balance and biosynthesis.[98] Lower levels of serine in malignant regions were confirmed in two independent RCC tissue samples that contained both cancerous and adjacent normal areas, using two MSI techniques, LARESI-SRM-MSI and ^{109}AgNPET-LDI-MSI.[39] In both cases, serine signals were consistently stronger in the noncancerous regions. This observation supports the notion that serine depletion in tumors may reflect increased utilization for anabolic growth and folate cycle activity. Furthermore, studies have linked elevated expression of serine biosynthetic enzymes with poor prognosis and therapeutic resistance in multiple cancer types, highlighting serine metabolism as a potential therapeutic target. However, previous studies have also highlighted the importance of serine metabolism in cancer, with increased serine levels reported in bladder cancer tissue[99] and leukemia cell lines[100] and decreased levels observed in urine samples of RCC patients,[56] underscoring the importance of sample type when interpreting metabolite distribution.

The renal cancer samples showed increased abundance of arachidonic acid (FA(20:4)) and adrenic acid (FA(22:4)), both ω-6 PUFAs involved in inflammation and tumor progression.[101,102] FA(20:4) serves as a precursor for a variety of eicosanoids, bioactive lipids that modulate angiogenesis, immune responses, and cell proliferation.[103] Its elevated levels have been associated with increased tumor growth and poor prognosis in various malignancies.[104] FA(22:4), synthesized from FA(20:4) via elongation, may amplify these effects by serving as an alternative substrate for lipid signaling or by promoting membrane lipid peroxidation.[105] Notably, both FA(20:4) and FA(22:4) have been identified as potential modulators of ferroptosis sensitivity depending on the cellular oxidative environment, supporting their relevance in tumor pathophysiology.[105] Our findings align with previous MSI-based analyses of RCC tissue, which also demonstrated elevated arachidonic acid levels in tumor regions compared to adjacent normal kidney.[106] Increased FA(20:4) signals were localized specifically within malignant zones, reinforcing its relevance as a spatially resolved metabolic marker of the RCC.

As results of tissue imaging originate from single patients in both RCC and BC cases, the observed metabolic differences should be interpreted with caution as they may not fully capture the biological variability present in larger patient cohorts. Nevertheless, the compounds highlighted in our analysis were systematically cross-validated against the existing literature data. All of the presented metabolites have previously been detected in human biological matrices and reported in association with cancer-related metabolic alterations. Furthermore, our findings are consistent with those of other studies that identified the same compounds in tissues from corresponding tumor types, lending additional support to the biological relevance of our results.

CONCLUSION

A novel approach for untargeted mass spectrometry imaging with improved identification is presented. This method uses an IR laser for deep desorption of the material and atmospheric pressure chemical ionization and photoionization (LARAPPI/CI) for the ionization of ablated material in a gas phase. By simultaneously collecting full-scan (MS) and fragmentation (MS/MS) data for multiple analytes, bbCID maximizes information density in a single MSI experiment and substantially reduces the overall acquisition time, which is crucial for capturing metabolic heterogeneity and potential biomarker candidates in spatially complex tissues. For the first time, bbCID was shown as an MSI-compatible measurement method, allowing untargeted identification of endogenous compounds. The results of the measurements suggested that FA(17:0), FA(16:0), FA(22:6), and FA(22:5) are in higher levels in cancerous bladder cancer tissue, while proline levels are slightly higher in normal tissue. Compounds such as FA(20:4) and FA(22:4) are at higher levels in RCC tissues, and on the contrary, creatine and serine are at lower levels compared to normal kidney tissue.

ASSOCIATED CONTENT

Data Availability Statement

The data sets generated during and/or analyzed during the current study are available from the corresponding author upon request and in the RepOD open data repository (DOI: https://doi.org/10.18150/XSUCCF).

Supporting Information

The Supporting Information is available free of charge at https://pubs.acs.org/doi/10.1021/jasms.5c00045.

Results of positive mode LARAPPI/CI-MSI analysis, with ion images of precursor and fragment ions of each compound shown above the ESI MS/MS spectra (PDF)

AUTHOR INFORMATION

Corresponding Author

Joanna Nizioł − *Department of Polymers and Biopolymers, Faculty of Chemistry, Rzeszów University of Technology, Rzeszów 35-959, Poland;* orcid.org/0000-0002-4783-8615; Phone: (+48 17) 8651550; Email: jniziol@prz.edu.pl

Authors

Sumi Krupa − *Doctoral School at the Rzeszów University of Technology, Rzeszów 35-959, Poland;* orcid.org/0009-0008-8916-0946

Wiktoria Szuberla − *Department of Inorganic and Analytical Chemistry, Faculty of Chemistry, Rzeszów University of Technology, Rzeszów 35-959, Poland*

Anna Ossolińska − *Department of Urology, John Paul II Hospital, Kolbuszowa 36-100, Poland*

Krzysztof Ossoliński − *Department of Urology, John Paul II Hospital, Kolbuszowa 36-100, Poland*

Tomasz Ruman − *Department of Inorganic and Analytical Chemistry, Faculty of Chemistry, Rzeszów University of Technology, Rzeszów 35-959, Poland;* orcid.org/0000-0002-9899-8627

Complete contact information is available at: https://pubs.acs.org/10.1021/jasms.5c00045

Notes

The authors declare no competing financial interest.

ACKNOWLEDGMENTS

This work was supported by the National Science Centre (Poland) research project Sonata Bis number 2022/46/E/ST4/00016.

REFERENCES

(1) Perez, C. J.; Bagga, A. K.; Prova, S. S.; Yousefi Taemeh, M.; Ifa, D. R. Review and Perspectives on the Applications of Mass Spectrometry Imaging under Ambient Conditions. *Rapid Commun. Mass Spectrom.* **2019**, *33* (S3), 27−53.

(2) Sans, M.; Feider, C. L.; Eberlin, L. S. Advances in Mass Spectrometry Imaging Coupled to Ion Mobility Spectrometry for Enhanced Imaging of Biological Tissues. *Curr. Opin Chem. Biol.* **2018**, *42*, 138−146.

(3) Baquer, G.; Sementé, L.; Mahamdi, T.; Correig, X.; Ràfols, P.; García-Altares, M. What Are We Imaging? Software Tools and Experimental Strategies for Annotation and Identification of Small Molecules in Mass Spectrometry Imaging. *Mass Spectrom Rev.* **2023**, *42* (5), 1927−1964.

(4) Müller, M. A.; Kompauer, M.; Strupat, K.; Heiles, S.; Spengler, B. Implementation of a High-Repetition-Rate Laser in an AP-SMALDI MSI System for Enhanced Measurement Performance. *J. Am. Soc. Mass Spectrom.* **2021**, *32* (2), 465−472.

(5) Prentice, B. M.; McMillen, J. C.; Caprioli, R. M. Multiple TOF/TOF Events in a Single Laser Shot for Multiplexed Lipid Identifications in MALDI Imaging Mass Spectrometry. *Int. J. Mass Spectrom.* **2019**, *437*, 30−37.

(6) Fisher, G. L.; Bruinen, A. L.; Ogrinc Potočnik, N.; Hammond, J. S.; Bryan, S. R.; Larson, P. E.; Heeren, R. M. A. A New Method and Mass Spectrometer Design for TOF-SIMS Parallel Imaging MS/MS. *Anal. Chem.* **2016**, *88* (12), 6433−6440.

(7) Angel, P. M.; Caprioli, R. M. Matrix-Assisted Laser Desorption Ionization Imaging Mass Spectrometry: In Situ Molecular Mapping. *Biochemistry* **2013**, *52* (22), 3818−3828.

(8) Korte, A. R.; Yandeau-Nelson, M. D.; Nikolau, B. J.; Lee, Y. J. Subcellular-Level Resolution MALDI-MS Imaging of Maize Leaf Metabolites by MALDI-Linear Ion Trap-Orbitrap Mass Spectrometer. *Anal Bioanal Chem.* **2015**, *407* (8), 2301−2309.

(9) Li, F.; Hsieh, Y.; Kang, L.; Sondey, C.; Lachowicz, J.; Korfmacher, W. A. MALDI-Tandem Mass Spectrometry Imaging of Astemizole and Its Primary Metabolite in Rat Brain Sections. *Bioanalysis* **2009**, *1* (2), 299−307.

(10) Khatib-Shahidi, S.; Andersson, M.; Herman, J. L.; Gillespie, T. A.; Caprioli, R. M. Direct Molecular Analysis of Whole-Body Animal Tissue Sections by Imaging MALDI Mass Spectrometry. *Anal. Chem.* **2006**, *78* (18), 6448−6456.

(11) Prentice, B. M.; Chumbley, C. W.; Caprioli, R. M. High-Speed MALDI MS/MS Imaging Mass Spectrometry Using Continuous Raster Sampling. *Journal of Mass Spectrometry* **2015**, *50* (4), 703−710.

(12) Barry, J. A.; Robichaud, G.; Bokhart, M. T.; Thompson, C.; Sykes, C.; Kashuba, A. D. M.; Muddiman, D. C. Mapping Antiretroviral Drugs in Tissue by IR-MALDESI MSI Coupled to the Q Exactive and Comparison with LC-MS/MS SRM Assay. *J. Am. Soc. Mass Spectrom.* **2014**, *25* (12), 2038−2047.

(13) Wiseman, J. M.; Ifa, D. R.; Zhu, Y.; Kissinger, C. B.; Manicke, N. E.; Kissinger, P. T.; Cooks, R. G. Desorption Electrospray Ionization Mass Spectrometry: Imaging Drugs and Metabolites in Tissues. *Proc. Natl. Acad. Sci. U. S. A.* **2008**, *105* (47), 18120−18125.

(14) Jacobsen, S. C.; Speth, N. R.; Xiong, M.; Herth, M. M.; Kristensen, J. L.; Palner, M.; Janfelt, C. Desorption Electrospray Ionization Mass Spectrometry Imaging of Cimbi-36, a 5-HT2A Receptor Agonist, with Direct Comparison to Autoradiography and Positron Emission Tomography. *Mol. Imaging Biol.* **2021**, *23* (5), 676−685.

(15) Koeniger, S. L.; Talaty, N.; Luo, Y.; Ready, D.; Voorbach, M.; Seifert, T.; Cepa, S.; Fagerland, J. A.; Bouska, J.; Buck, W.; Johnson, R. W.; Spanton, S. A Quantitation Method for Mass Spectrometry Imaging. *Rapid Commun. Mass Spectrom.* **2011**, *25* (4), 503−510.

(16) Marko-Varga, G.; Fehniger, T. E.; Rezeli, M.; Döme, B.; Laurell, T.; Végvári, Á. Drug Localization in Different Lung Cancer Phenotypes by MALDI Mass Spectrometry Imaging. *J. Proteomics* **2011**, *74* (7), 982−992.

(17) Fehniger, T. E.; Végvári, Á.; Rezeli, M.; Prikk, K.; Ross, P.; Dahlbäck, M.; Edula, G.; Sepper, R.; Marko-Varga, G. Direct Demonstration of Tissue Uptake of an Inhaled Drug: Proof-of-Principle Study Using Matrix-Assisted Laser Desorption Ionization Mass Spectrometry Imaging. *Anal. Chem.* **2011**, *83* (21), 8329−8336.

(18) Manier, M. L.; Reyzer, M. L.; Goh, A.; Dartois, V.; Via, L. E.; Barry, C. E.; Caprioli, R. M. Reagent Precoated Targets for Rapid In-Tissue Derivatization of the Anti-Tuberculosis Drug Isoniazid Followed by MALDI Imaging Mass Spectrometry. *J. Am. Soc. Mass Spectrom.* **2011**, *22* (8), 1409−1419.

(19) Goodwin, R. J. A.; MacKay, C. L.; Nilsson, A.; Harrison, D. J.; Farde, L.; Andren, P. E.; Iverson, S. L. Qualitative and Quantitative MALDI Imaging of the Positron Emission Tomography Ligands Raclopride (a D2 Dopamine Antagonist) and SCH 23390 (a D1 Dopamine Antagonist) in Rat Brain Tissue Sections Using a Solvent-Free Dry Matrix Application Method. *Anal. Chem.* **2011**, *83* (24), 9694−9701.

(20) Reyzer, M. L.; Hsieh, Y.; Ng, K.; Korfmacher, W. A.; Caprioli, R. M. Direct Analysis of Drug Candidates in Tissue by Matrix-Assisted Laser Desorption/Ionization Mass Spectrometry. *Journal of Mass Spectrometry* **2003**, *38* (10), 1081−1092.

(21) Beasley, E.; Francese, S.; Bassindale, T. Detection and Mapping of Cannabinoids in Single Hair Samples through Rapid Derivatization and Matrix-Assisted Laser Desorption Ionization Mass Spectrometry. *Anal. Chem.* **2016**, *88* (20), 10328−10334.

(22) Pirman, D. A.; Reich, R. F.; Kiss, A.; Heeren, R. M. A.; Yost, R. A. Quantitative MALDI Tandem Mass Spectrometric Imaging of Cocaine from Brain Tissue with a Deuterated Internal Standard. *Anal. Chem.* **2013**, *85* (2), 1081−1089.

(23) Porta, T.; Grivet, C.; Kraemer, T.; Varesio, E.; Hopfgartner, G. Single Hair Cocaine Consumption Monitoring by Mass Spectrometric Imaging. *Anal. Chem.* **2011**, *83* (11), 4266−4272.

(24) Boudon, S. M.; Morandi, G.; Prideaux, B.; Staab, D.; Junker, U.; Odermatt, A.; Stoeckli, M.; Bauer, D. Evaluation of Sparfloxacin Distribution by Mass Spectrometry Imaging in a Phototoxicity Model. *J. Am. Soc. Mass Spectrom.* **2014**, *25* (10), 1803−1809.

(25) Swales, J. G.; Strittmatter, N.; Tucker, J. W.; Clench, M. R.; Webborn, P. J. H.; Goodwin, R. J. A. Spatial Quantitation of Drugs in Tissues Using Liquid Extraction Surface Analysis Mass Spectrometry Imaging. *Scientific Reports 2016 6:1* **2016**, *6* (1), 1−9.

(26) Swales, J. G.; Tucker, J. W.; Strittmatter, N.; Nilsson, A.; Cobice, D.; Clench, M. R.; Mackay, C. L.; Andren, P. E.; Takáts, Z.; Webborn, P. J. H.; Goodwin, R. J. A. Mass Spectrometry Imaging of Cassette-Dosed Drugs for Higher Throughput Pharmacokinetic and Biodistribution Analysis. *Anal. Chem.* **2014**, *86* (16), 8473−8480.

(27) Nilsson, A.; Fehniger, T. E.; Gustavsson, L.; Andersson, M.; Kenne, K.; Marko-Varga, G.; Andrén, P. E. Fine Mapping the Spatial Distribution and Concentration of Unlabeled Drugs within Tissue Micro-Compartments Using Imaging Mass Spectrometry. *PLoS One* **2010**, *5* (7), No. e11411.

(28) Végvári, Á.; Fehniger, T. E.; Gustavsson, L.; Nilsson, A.; Andrén, P. E.; Kenne, K.; Nilsson, J.; Laurell, T.; Marko-Varga, G. Essential Tactics of Tissue Preparation and Matrix Nano-Spotting for Successful Compound Imaging Mass Spectrometry. *J. Proteomics* **2010**, *73* (6), 1270−1278.

(29) Hsieh, Y.; Casale, R.; Fukuda, E.; Chen, J.; Knemeyer, I.; Wingate, J.; Morrison, R.; Korfmacher, W. Matrix-Assisted Laser Desorption/Ionization Imaging Mass Spectrometry for Direct Measurement of Clozapine in Rat Brain Tissue. *Rapid Commun. Mass Spectrom.* **2006**, *20* (6), 965−972.

(30) Marshall, P.; Toteu-Djomte, V.; Bareille, P.; Perry, H.; Brown, G.; Baumert, M.; Biggadike, K. Correlation of Skin Blanching and Percutaneous Absorption for Glucocorticoid Receptor Agonists by Matrix-Assisted Laser Desorption Ionization Mass Spectrometry Imaging and Liquid Extraction Surface Analysis with Nano-electrospray Ionization Mass Spectrometry. *Anal. Chem.* **2010**, *82* (18), 7787−7794.

(31) Goodwin, R. J. A.; Scullion, P.; MacIntyre, L.; Watson, D. G.; Pitt, A. R. Use of a Solvent-Free Dry Matrix Coating for Quantitative Matrix-Assisted Laser Desorption Ionization Imaging of 4-Bromo-phenyl-1,4-Diazabicyclo(3.2.2) Nonane-4-Carboxylate in Rat Brain and Quantitative Analysis of the Drug from Laser Microdissected Tissue Regions. *Anal. Chem.* **2010**, *82* (9), 3868−3873.

(32) Zhan, L.; Huang, X.; Xue, J.; Liu, H.; Xiong, C.; Wang, J.; Nie, Z. MALDI-TOF/TOF Tandem Mass Spectrometry Imaging Reveals Non-Uniform Distribution of Disaccharide Isomers in Plant Tissues. *Food Chem.* **2021**, *338*, 127984.

(33) Yagnik, G. B.; Korte, A. R.; Lee, Y. J. Multiplex Mass Spectrometry Imaging for Latent Fingerprints. *Journal of Mass Spectrometry* **2013**, *48* (1), 100−104.

(34) Hamid, T. S.; Lostun, D.; Cabral, E. C.; Garrett, R.; Bohme, D. K.; Ifa, D. R. Comparisons of Ambient Spray Ionization Imaging Methods. *Int. J. Mass Spectrom.* **2015**, *377* (1), 736−743.

(35) Nizioł, J.; Misiorek, M.; Krupa, Z.; Ruman, T. Infrared Laser-Based Selected Reaction Monitoring Mass Spectrometry Imaging of Banana (Musa Spp.) Tissue—New Method for Detection and Spatial Localization of Metabolites in Food. *Food Anal Methods* **2024**, *17* (2), 236−250.

(36) Szulc, J.; Ruman, T. Laser Ablation Remote-Electrospray Ionisation Mass Spectrometry (LARESI MSI) Imaging—New Method for Detection and Spatial Localization of Metabolites and Mycotoxins Produced by Moulds. *Toxins* **2020**, *12* (11), 720.

(37) Szulc, J.; Karbowska-Berent, J.; Drążkowska, A.; Ruman, T.; Beech, I.; Sunner, J. A.; Gutarowska, B. Metabolomics and Metagenomics Analysis of 18th Century Archaeological Silk. *Int. Biodeterior Biodegradation* **2021**, *156*, 105120.

(38) Szulc, J.; Ruman, T.; Karbowska-Berent, J.; Kozielec, T.; Gutarowska, B. Analyses of Microorganisms and Metabolites Diversity on Historic Photographs Using Innovative Methods. *J. Cult Herit* **2020**, *45*, 101−113.

(39) Nizioł, J.; Sunner, J.; Beech, I.; Ossoliński, K.; Ossolińska, A.; Ossoliński, T.; Płaza, A.; Ruman, T. Localization of Metabolites of Human Kidney Tissue with Infrared Laser-Based Selected Reaction Monitoring Mass Spectrometry Imaging and Silver-109 Nanoparticle-Based Surface Assisted Laser Desorption/Ionization Mass Spectrometry Imaging. *Anal. Chem.* **2020**, *92* (6), 4251−4258.

(40) Reveglia, P.; Agudo-Jurado, F. J.; Barilli, E.; Masi, M.; Evidente, A.; Rubiales, D. Uncovering Phytotoxic Compounds Produced by Colletotrichum Spp. Involved in Legume Diseases Using an OSMAC-Metabolomics Approach. *J. Fungi* **2023**, *9*, 610.

(41) Edelson-Averbukh, M.; Pipkorn, R.; Lehmann, W. D. Analysis of Protein Phosphorylation in the Regions of Consecutive Serine/Threonine Residues by Negative Ion Electrospray Collision-Induced Dissociation. Approach to Pinpointing of Phosphorylation Sites. *Anal. Chem.* **2007**, *79* (9), 3476−3486.

(42) White, M. E. H.; Sinn, L. R.; Jones, D. M.; de Folter, J.; Aulakh, S. K.; Wang, Z.; Flynn, H. R.; Krüger, L.; Tober-Lau, P.; Demichev, V.; Kurth, F.; Mülleder, M.; Blanchard, V.; Messner, C. B.; Ralser, M. Oxonium Ion Scanning Mass Spectrometry for Large-Scale Plasma Glycoproteomics. *Nature Biomedical Engineering 2023 8:3* **2024**, *8* (3), 233−247.

(43) Chen, Y. C.; Wu, H. Y.; Chang, C. W.; Liao, P. C. Post-Deconvolution MS/MS Spectra Extraction with Data-Independent Acquisition for Comprehensive Profiling of Urinary Glucuronide-Conjugated Metabolome. *Anal. Chem.* **2022**, *94* (6), 2740−2748.

(44) Chang, J. K.; Teo, G.; Pewzner-Jung, Y.; Cuthbertson, D. J.; Futerman, A. H.; Wenk, M. R.; Choi, H.; Torta, F. Q-RAI Data-Independent Acquisition for Lipidomic Quantitative Profiling. *Scientific Reports 2023 13:1* **2023**, *13* (1), 1−15.

(45) van der Laan, T.; Boom, I.; Maliepaard, J.; Dubbelman, A. C.; Harms, A. C.; Hankemeier, T. Data-Independent Acquisition for the Quantification and Identification of Metabolites in Plasma. *Metabolites* **2020**, *10* (12), 514.

(46) Lindemann, V.; Schmidt, J.; Cramer, B.; Humpf, H. U. Detection of Mycotoxins in Highly Matrix-Loaded House-Dust Samples by QTOF-HRMS, IM-QTOF-HRMS, and TQMS: Advantages and Disadvantages. *Anal. Chem.* **2022**, *94* (10), 4209−4217.

(47) Lodge, S.; Litton, E.; Gray, N.; Ryan, M.; Millet, O.; Fear, M.; Raby, E.; Currie, A.; Wood, F.; Holmes, E.; Wist, J.; Nicholson, J. K. Stratification of Sepsis Patients on Admission into the Intensive Care Unit According to Differential Plasma Metabolic Phenotypes. *J. Proteome Res.* **2024**, *23* (4), 1328−1340.

(48) Lioupi, A.; Virgiliou, C.; Walter, T. H.; Smith, K. M.; Rainville, P.; Wilson, I. D.; Theodoridis, G.; Gika, H. G. Application of a Hybrid Zwitterionic Hydrophilic Interaction Liquid Chromatography Column in Metabolic Profiling Studies. *J. Chromatogr A* **2022**, *1672*, 463013.

(49) Rimayi, C.; Chimuka, L.; Gravell, A.; Fones, G. R.; Mills, G. A. Use of the Chemcatcher® Passive Sampler and Time-of-Flight Mass Spectrometry to Screen for Emerging Pollutants in Rivers in Gauteng Province of South Africa. *Environ. Monit Assess* **2019**, *191* (6), 1−20.

(50) Graça, G.; Cai, Y.; Lau, C. H. E.; Vorkas, P. A.; Lewis, M. R.; Want, E. J.; Herrington, D.; Ebbels, T. M. D. Automated Annotation of Untargeted All-Ion Fragmentation LC-MS Metabolomics Data with MetaboAnnotatoR. *Anal. Chem.* **2022**, *94* (8), 3446−3455.

(51) Johnson, A. R.; Carlson, E. E. Collision-Induced Dissociation Mass Spectrometry: A Powerful Tool for Natural Product Structure Elucidation. *Anal. Chem.* **2015**, *87* (21), 10668−10678.

(52) Krupa, S.; Ruman, T.; Szuberla, W.; Nizioł, J. Analysis of the Spatial Distribution of Metabolites in Aloe Vera Leaves by Mass Spectrometry Imaging and UHPLC-UHRMS. *Scientific Reports 2025 15:1* **2025**, *15* (1), 1−15.

(53) Szulc, J.; Grzyb, T.; Gutarowska, B.; Nizioł, J.; Krupa, S.; Ruman, T. 3D Mass Spectrometry Imaging as a Novel Screening Method for Evaluating Biocontrol Agents. *J. Agric. Food Chem.* **2025**, *73*, 8225.

(54) Szulc, J.; Grzyb, T.; Nizioł, J.; Krupa, S.; Szuberla, W.; Ruman, T. Direct 3D Mass Spectrometry Imaging Analysis of Environmental Microorganisms. *Molecules* **2025**, *30* (6), 1317.

(55) Ruman, T.; Krupa, Z.; Nizioł, J. Direct Three-Dimensional Mass Spectrometry Imaging with Laser Ablation Remote Atmospheric Pressure Photoionization/Chemical Ionization. *Anal. Chem.* **2024**, *96* (32), 13326−13334.

(56) Arendowski, A.; Ossoliński, K.; Nizioł, J.; Ruman, T. Screening of Urinary Renal Cancer Metabolic Biomarkers with Gold Nanoparticles-Assisted Laser Desorption/Ionization Mass Spectrometry. *Anal. Sci.* **2020**, *36* (12), 1521−1527.

(57) *NIST Mass Spectral Libraries, 2023 Edition with Search Program, Data Version: NIST23*, software version 3.0.

(58) Wishart, D. S.; Guo, A. C.; Oler, E.; et al. HMDB 5.0: The Human Metabolome Database for 2022. *Nucleic Acids Res.* **2022**, *50*, D622.

(59) Nizioł, J.; Ossoliński, K.; Ossoliński, T.; Ossolińska, A.; Bonifay, V.; Sekuła, J.; Dobrowolski, Z.; Sunner, J.; Beech, I.; Ruman, T. Surface-Transfer Mass Spectrometry Imaging of Renal Tissue on Gold Nanoparticle Enhanced Target. *Anal. Chem.* **2016**, *88* (14), 7365−7371.

(60) Ossoliński, K.; Ruman, T.; Ossoliński, T.; Ossolińska, A.; Arendowski, A.; Kołodziej, A.; Płaza-Altamer, A.; Nizioł, J. Monoisotopic Silver Nanoparticles-Based Mass Spectrometry Imaging of Human Bladder Cancer Tissue: Biomarker Discovery. *Adv. Med. Sci.* **2023**, *68* (1), 38−45.

(61) Zhang, H.; Lu, K. H.; Ebbini, M.; Huang, P.; Lu, H.; Li, L. Mass Spectrometry Imaging for Spatially Resolved Multi-Omics Molecular Mapping. *npj Imaging 2024 2:1* **2024**, *2* (1), 1−15.

(62) Kerwin, J. L.; Wiens, A. M.; Ericsson, L. H. Identification of Fatty Acids by Electrospray Mass Spectrometry and Tandem Mass Spectrometry. *Journal of Mass Spectrometry* **1996**, *31* (2), 184−192.

(63) Golley, R. K.; Hendrie, G. A. Evaluation of the Relative Concentration of Serum Fatty Acids C14:0, C15:0 and C17:0 as Markers of Children's Dairy Fat Intake. *Ann. Nutr Metab* **2014**, *65* (4), 310−316.

(64) Sun, Q.; Ma, J.; Campos, H.; Hu, F. B. Plasma and Erythrocyte Biomarkers of Dairy Fat Intake and Risk of Ischemic Heart Disease. *Am. J. Clin. Nutr.* **2007**, *86* (4), 929−937.

(65) Forouhi, N. G.; Koulman, A.; Sharp, S. J.; Imamura, F.; Kröger, J.; Schulze, M. B.; Crowe, F. L.; Huerta, J. M.; Guevara, M.; Beulens, J. W. J.; van Woudenbergh, G. J.; Wang, L.; Summerhill, K.; Griffin, J. L.; Feskens, E. J. M.; Amiano, P.; Boeing, H.; Clavel-Chapelon, F.; Dartois, L.; Fagherazzi, G.; Franks, P. W.; Gonzalez, C.; Jakobsen, M. U.; Kaaks, R.; Key, T. J.; Khaw, K. T.; Kühn, T.; Mattiello, A.; Nilsson, P. M.; Overvad, K.; Pala, V.; Palli, D.; Quirós, J. R.; Rolandsson, O.; Roswall, N.; Sacerdote, C.; Sánchez, M. J.; Slimani, N.; Spijkerman, A. M. W.; Tjonneland, A.; Tormo, M. J.; Tumino, R.; van der A, D. L.; van der Schouw, Y. T.; Langenberg, C.; Riboli, E.; Wareham, N. J. Differences in the Prospective Association between Individual Plasma Phospholipid Saturated Fatty Acids and Incident Type 2 Diabetes: The EPIC-InterAct Case-Cohort Study. *Lancet Diabetes Endocrinol* **2014**, *2* (10), 810−818.

(66) Warensjö, E.; Jansson, J.-H.; Berglund, L.; Boman, K.; Ahrén, B.; Weinehall, L.; Lindahl, B.; Hallmans, G.; Vessby, B. Estimated Intake of Milk Fat Is Negatively Associated with Cardiovascular Risk Factors and Does Not Increase the Risk of a First Acute Myocardial Infarction. A Prospective Case-Control Study. *Br. J. Nutr.* **2004**, *91* (4), 635−642.

(67) Liss, M. A.; Al-Bayati, O.; Gelfond, J.; Goros, M.; Ullevig, S.; DiGiovanni, J.; Hamilton-Reeves, J.; O'Keefe, D.; Bacich, D.; Weaver, B.; Leach, R.; Thompson, I. M. Higher Baseline Dietary Fat and Fatty Acid Intake Is Associated with Increased Risk of Incident Prostate

Cancer in the SABOR Study. *Prostate Cancer and Prostatic Diseases 2018 22:2* **2019**, *22* (2), 244−251.

(68) Sczaniecka, A. K.; Brasky, T. M.; Lampe, J. W.; Patterson, R. E.; White, E. Dietary Intake of Specific Fatty Acids and Breast Cancer Risk Among Postmenopausal Women in the VITAL Cohort. *Nutr Cancer* **2012**, *64* (8), 1131−1142.

(69) Wu, Q.; Shi, D.; Dong, T.; Zhang, Z.; Ou, Q.; Fang, Y.; Zhang, C. Serum Saturated Fatty Acids Including Very Long-Chain Saturated Fatty Acids and Colorectal Cancer Risk among Chinese Population. *Nutrients* **2023**, *15* (8), 1917.

(70) Kim, H. Y.; Moon, J. Y.; Cho, S. K. Heptadecanoic Acid, an Odd-Chain Fatty Acid, Induces Apoptosis and Enhances Gemcitabine Chemosensitivity in Pancreatic Cancer Cells. *https://home.liebertpub.com/jmf* **2023**, *26* (3), 201−210.

(71) Fajardo, V. A.; McMeekin, L.; Leblanc, P. J. Influence of Phospholipid Species on Membrane Fluidity: A Meta-Analysis for a Novel Phospholipid Fluidity Index. *J. Membr. Biol.* **2011**, *244* (2), 97−103.

(72) Li, S.; Yuan, H.; Li, L.; Li, Q.; Lin, P.; Li, K. Oxidative Stress and Reprogramming of Lipid Metabolism in Cancers. *Antioxidants* **2025**, *14* (2), 201.

(73) Brandi, J.; Dando, I.; Pozza, E. D.; Biondani, G.; Jenkins, R.; Elliott, V.; Park, K.; Fanelli, G.; Zolla, L.; Costello, E.; Scarpa, A.; Cecconi, D.; Palmieri, M. Proteomic Analysis of Pancreatic Cancer Stem Cells: Functional Role of Fatty Acid Synthesis and Mevalonate Pathways. *J. Proteomics* **2017**, *150*, 310−322.

(74) Zemanová, M.; Vecka, M.; Petruželka, L.; Staňková, B.; Žák, A.; Zeman, M. Plasma Phosphatidylcholines Fatty Acids in Men with Squamous Cell Esophageal Cancer: Chemoradiotherapy Improves Abnormal Profile. *Med. Sci. Monit* **2016**, *22*, 4092.

(75) dos Reis Riccardi, D. M.; das Neves, R. X.; de Matos-Neto, E. M.; Camargo, R. G.; Lima, J. D. C. C.; Radloff, K.; Alves, M. J.; Costa, R. G. F.; Tokeshi, F.; Otoch, J. P.; Maximiano, L. F.; de Alcantara, P. S. M.; Colquhoun, A.; Laviano, A.; Seelaender, M. Plasma Lipid Profile and Systemic Inflammation in Patients With Cancer Cachexia. *Front. Nutr.* **2020**, *7*, 477360.

(76) Mei, J.; Qian, M.; Hou, Y.; Liang, M.; Chen, Y.; Wang, C.; Zhang, J. Association of Saturated Fatty Acids with Cancer Risk: A Systematic Review and Meta-Analysis. *Lipids Health Dis* **2024**, *23* (1), 1−16.

(77) Feng, C.; Pan, L.; Tang, S.; He, L.; Wang, X.; Tao, Y.; Xie, Y.; Lai, Z.; Tang, Z.; Wang, Q.; Li, T. Integrative Transcriptomic, Lipidomic, and Metabolomic Analysis Reveals Potential Biomarkers of Basal and Luminal Muscle Invasive Bladder Cancer Subtypes. *Front Genet* **2021**, *12*, 695662.

(78) Pereira, F.; Domingues, M. R.; Vitorino, R.; Guerra, I. M. S.; Santos, L. L.; Ferreira, J. A.; Ferreira, R. Unmasking the Metabolite Signature of Bladder Cancer: A Systematic Review. *Int. J. Mol. Sci.* **2024**, *25* (6), 3347.

(79) Jin, Q.; Qi, D.; Zhang, M.; Qu, H.; Dong, Y.; Sun, M.; Quan, C. CLDN6 Inhibits Breast Cancer Growth and Metastasis through SREBP1-Mediated RAS Palmitoylation. *Cell Mol. Biol. Lett.* **2024**, *29* (1), 1−23.

(80) Li, J.; Cheng, B.; Xie, H.; Zhan, C.; Li, S.; Bai, P. Bladder Cancer Biomarker Screening Based on Non-Targeted Urine Metabolomics. *Int. Urol Nephrol* **2022**, *54* (1), 23−29.

(81) D'Aniello, C.; Patriarca, E. J.; Phang, J. M.; Minchiotti, G. Proline Metabolism in Tumor Growth and Metastatic Progression. *Front Oncol* **2020**, *10*, 544183.

(82) Elia, I.; Broekaert, D.; Christen, S.; Boon, R.; Radaelli, E.; Orth, M. F.; Verfaillie, C.; Grünewald, T. G. P.; Fendt, S. M. Proline Metabolism Supports Metastasis Formation and Could Be Inhibited to Selectively Target Metastasizing Cancer Cells. *Nature Communications 2017 8:1* **2017**, *8* (1), 1−11.

(83) Ossoliński, K.; Ruman, T.; Copié, V.; Tripet, B. P.; Nogueira, L. B.; Nogueira, K. O. P. C.; Kołodziej, A.; Płaza-Altamer, A.; Ossolińska, A.; Ossoliński, T.; Nizioł, J. Metabolomic and Elemental Profiling of Blood Serum in Bladder Cancer. *J. Pharm. Anal* **2022**, *12* (6), 889−900.

(84) Wang, R.; Kang, H.; Zhang, X.; Nie, Q.; Wang, H.; Wang, C.; Zhou, S. Urinary Metabolomics for Discovering Metabolic Biomarkers of Bladder Cancer by UPLC-MS. *BMC Cancer* **2022**, *22* (1), 1−12.

(85) Suda, A.; Umaru, B. A.; Yamamoto, Y.; Shima, H.; Saiki, Y.; Pan, Y.; Jin, L.; Sun, J.; Low, Y. L. C.; Suzuki, C.; Abe, T.; Igarashi, K.; Furukawa, T.; Owada, Y.; Kagawa, Y. Polyunsaturated Fatty Acids-Induced Ferroptosis Suppresses Pancreatic Cancer Growth. *Scientific Reports 2024 14:1* **2024**, *14* (1), 1−16.

(86) Yang, X.; Liu, Y.; Wang, Z.; Jin, Y.; Gu, W. Ferroptosis as a New Tool for Tumor Suppression through Lipid Peroxidation. *Communications Biology 2024 7:1* **2024**, *7* (1), 1−12.

(87) Borgonovi, S. M.; Iametti, S.; Di Nunzio, M. Docosahexaenoic Acid as Master Regulator of Cellular Antioxidant Defenses: A Systematic Review. *Antioxidants* **2023**, *12* (6), 1283.

(88) Tatsumi, Y.; Kato, A.; Niimi, N.; Yako, H.; Himeno, T.; Kondo, M.; Tsunekawa, S.; Kato, Y.; Kamiya, H.; Nakamura, J.; Higai, K.; Sango, K.; Kato, K. Docosahexaenoic Acid Suppresses Oxidative Stress-Induced Autophagy and Cell Death via the AMPK-Dependent Signaling Pathway in Immortalized Fischer Rat Schwann Cells 1. *Int. J. Mol. Sci.* **2022**, *23*, 4405.

(89) Tamura, K.; Horikawa, M.; Sato, S.; Miyake, H.; Setou, M. Discovery of Lipid Biomarkers Correlated with Disease Progression in Clear Cell Renal Cell Carcinoma Using Desorption Electrospray Ionization Imaging Mass Spectrometry. *Oncotarget* **2019**, *10* (18), 1688.

(90) D'Eliseo, D.; Manzi, L.; Merendino, N.; Velotti, F. Docosahexaenoic Acid Inhibits Invasion of Human RT112 Urinary Bladder and PT45 Pancreatic Carcinoma Cells via Down-Modulation of Granzyme B Expression. *J. Nutr Biochem* **2012**, *23* (5), 452−457.

(91) Ding, Y.; Yang, J.; Ma, Y.; Yao, T.; Chen, X.; Ge, S.; Wang, L.; Fan, X. MYCN and PRC1 Cooperatively Repress Docosahexaenoic Acid Synthesis in Neuroblastoma via ELOVL2. *Journal of Experimental and Clinical Cancer Research* **2019**, *38* (1), 1−16.

(92) Li, Y.; Xu, H.; Lin, T.; Zhang, J.; Ai, J.; Zhang, S.; Le, W.; Tan, P.; Zhang, P.; Wei, Q.; Zheng, X.; Yang, L. Preoperative Low Plasma Creatine Kinase Levels Predict Worse Survival Outcomes in Bladder Cancer after Radical Cystectomy. *Int. Urol Nephrol* **2024**, *56* (7), 2215−2225.

(93) Maguire, O. A.; Ackerman, S. E.; Szwed, S. K.; Maganti, A. V.; Marchildon, F.; Huang, X.; Kramer, D. J.; Rosas-Villegas, A.; Gelfer, R. G.; Turner, L. E.; Ceballos, V.; Hejazi, A.; Samborska, B.; Rahbani, J. F.; Dykstra, C. B.; Annis, M. G.; Luo, J. D.; Carroll, T. S.; Jiang, C. S.; Dannenberg, A. J.; Siegel, P. M.; Tersey, S. A.; Mirmira, R. G.; Kazak, L.; Cohen, P. Creatine-Mediated Crosstalk between Adipocytes and Cancer Cells Regulates Obesity-Driven Breast Cancer. *Cell Metab* **2021**, *33* (3), 499−512.

(94) Maqdasy, S.; Lecoutre, S.; Renzi, G.; Frendo-Cumbo, S.; Rizo-Roca, D.; Moritz, T.; Juvany, M.; Hodek, O.; Gao, H.; Couchet, M.; Witting, M.; Kerr, A.; Bergo, M. O.; Choudhury, R. P.; Aouadi, M.; Zierath, J. R.; Krook, A.; Mejhert, N.; Rydén, M. Impaired Phosphocreatine Metabolism in White Adipocytes Promotes Inflammation. *Nature Metabolism 2022 4:2* **2022**, *4* (2), 190−202.

(95) Nizioł, J.; Copié, V.; Tripet, B. P.; Nogueira, L. B.; Nogueira, K. O. P. C.; Ossoliński, K.; Arendowski, A.; Ruman, T. Metabolomic and Elemental Profiling of Human Tissue in Kidney Cancer. *Metabolomics* **2021**, *17* (3), 30.

(96) Sun, C.; Wang, F.; Zhang, Y.; Yu, J.; Wang, X. Mass Spectrometry Imaging-Based Metabolomics to Visualize the Spatially Resolved Reprogramming of Carnitine Metabolism in Breast Cancer. *Theranostics* **2020**, *10* (16), 7070.

(97) Vallianatou, T.; Shariatgorji, R.; Nilsson, A.; Karlgren, M.; Hulme, H.; Fridjonsdottir, E.; Svenningsson, P.; Andrén, P. E. Integration of Mass Spectrometry Imaging and Machine Learning Visualizes Region-Specific Age-Induced and Drug-Target Metabolic Perturbations in the Brain. *ACS Chem. Neurosci.* **2021**, *12* (10), 1811−1823.

(98) Liu, Z.; Fan, M.; Hou, J.; Pan, S.; Xu, Y.; Zhang, H.; Liu, C.; Hao, X.; Li, X.; Wang, H. Serine Hydroxymethyltransferase 2

Knockdown Induces Apoptosis in CcRCC by Causing Lysosomal Membrane Permeabilization via Metabolic Reprogramming. *Cell Death & Disease 2023 14:2* **2023**, *14* (2), 1−11.

(99) Putluri, N.; Shojaie, A.; Vasu, V. T.; Vareed, S. K.; Nalluri, S.; Putluri, V.; Thangjam, G. S.; Panzitt, K.; Tallman, C. T.; Butler, C.; Sana, T. R.; Fischer, S. M.; Sica, G.; Brat, D. J.; Shi, H.; Palapattu, G. S.; Lotan, Y.; Weizer, A. Z.; Terris, M. K.; Shariat, S. F.; Michailidis, G.; Sreekumar, A. Metabolomic Profiling Reveals Potential Markers and Bioprocesses Altered in Bladder Cancer Progression. *Cancer Res.* **2011**, *71* (24), 7376−7386.

(100) Dettmer, K.; Vogl, F. C.; Ritter, A. P.; Zhu, W.; Nürnberger, N.; Kreutz, M.; Oefner, P. J.; Gronwald, W.; Gottfried, E. Distinct Metabolic Differences between Various Human Cancer and Primary Cells. *Electrophoresis* **2013**, *34* (19), 2836−2847.

(101) Zhang, J.; Ruan, K.; Chu, Z.; Wang, X.; Gu, Y.; Jin, H.; Zhang, X.; Liu, Q.; Yang, J. Reprogramming of Fatty Acid Metabolism: A Hidden Force Regulating the Occurrence and Progression of Cholangiocarcinoma. *Cell Death Discovery* **2025**, *11*, 72.

(102) Jin, R.; Dai, Y.; Wang, Z.; Hu, Q.; Zhang, C.; Gao, H.; Yan, Q. Unraveling Ferroptosis: A New Frontier in Combating Renal Fibrosis and CKD Progression. *Biology* **2025**, *14*, 12.

(103) Ortiz-Placin, C.; Castillejo-Rufo, A.; Estaras, M.; Gonzalez, A. Membrane Lipid Derivatives: Roles of Arachidonic Acid and Its Metabolites in Pancreatic Physiology and Pathophysiology. *Molecules* **2023**, *28*, 4316.

(104) Tredicine, M.; Mucci, M.; Recchiuti, A.; Mattoscio, D. Immunoregulatory Mechanisms of the Arachidonic Acid Pathway in Cancer. *FEBS Lett.* **2025**, *599*, 927.

(105) Kim, J. W.; Lee, J. Y.; Oh, M.; Lee, E. W. An Integrated View of Lipid Metabolism in Ferroptosis Revisited via Lipidomic Analysis. *Experimental & Molecular Medicine 2023 55:8* **2023**, *55* (8), 1620−1631.

(106) Arendowski, A.; Nizioł, J.; Ossoliński, K.; Ossolińska, A.; Ossoliński, T.; Dobrowolski, Z.; Ruman, T. Laser Desorption/Ionization MS Imaging of Cancer Kidney Tissue on Silver Nanoparticle-Enhanced Target. *Bioanalysis* **2018**, *10* (2), 83−94.

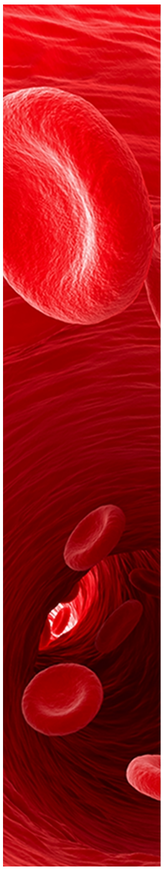

CAS BIOFINDER DISCOVERY PLATFORM™
CAS BIOFINDER HELPS YOU FIND YOUR NEXT BREAKTHROUGH FASTER
Navigate pathways, targets, and diseases with precision
Explore CAS BioFinder
CAS
A division of the American Chemical Society

molecules

MDPI

Article

Direct 3D Mass Spectrometry Imaging Analysis of Environmental Microorganisms

Justyna Szulc [1], Tomasz Grzyb [1,*], Joanna Nizioł [2], Sumi Krupa [2], Wiktoria Szuberla [2] and Tomasz Ruman [2]

[1] Department of Environmental Biotechnology, Faculty of Biotechnology and Food Sciences, Lodz University of Technology, 90-530 Lodz, Poland; justyna.szulc@p.lodz.pl

[2] Department of Inorganic and Analytical Chemistry, Faculty of Chemistry, Rzeszow University of Technology, 35-959 Rzeszow, Poland; jniziol@prz.edu.pl (J.N.); d605@stud.prz.edu.pl (S.K.); 163834@stud.prz.edu.pl (W.S.); tomruman@prz.edu.pl (T.R.)

* Correspondence: tomasz.grzyb@dokt.p.lodz.pl

Abstract: Assessing the spatial distribution of microorganisms' metabolites in growth medium remains a challenge. Here, we present the first use of the newly developed LARAPPI/CI-MSI 3D (laser ablation remote atmospheric pressure photoionization/chemical ionization mass spectrometry imaging) method for direct three-dimensional (3D) mass spectrometry imaging of bacterial and fungal metabolites in solid culture media. Two-dimensional (2D) MSI was also performed, and it indicated the presence of metabolites belonging to, and including, amino acids and their derivatives, dipeptides, organic acids, fatty acids, sugars and sugar derivatives, benzene derivatives, and indoles. Distribution at a selected depth within the culture medium with the estimation of concentration across all dimensions of 16 metabolites was visualized using LARAPPI/CI-MSI 3D. The imaging results were correlated with the results of ultra-high-performance liquid chromatography–ultra-high-resolution mass spectrometry (UHPLC–UHRMS). A total of 351–393 chemical compounds, depending on the tested microorganism, were identified, while 242–262 were recognized in the HMDB database in MetaboAnalyst (v 6.0). The LARAPPI/CI-MSI 3D method enables the rapid screening of the biotechnological potential of environmental strains, facilitating the discovery of industrially valuable biomolecules.

Keywords: 2D/3D microbiological culture imaging; mass spectrometry imaging; microbial interactions; phytopathogens; bioactive compounds; metabolomic analysis

check for updates

Academic Editors: Stefan Tsakovski and Tony Venelinov

Received: 18 February 2025
Revised: 4 March 2025
Accepted: 11 March 2025
Published: 14 March 2025

Citation: Szulc, J.; Grzyb, T.; Nizioł, J.; Krupa, S.; Szuberla, W.; Ruman, T. Direct 3D Mass Spectrometry Imaging Analysis of Environmental Microorganisms. *Molecules* **2025**, *30*, 1317. https://doi.org/10.3390/molecules30061317

Copyright: © 2025 by the authors. Licensee MDPI, Basel, Switzerland. This article is an open access article distributed under the terms and conditions of the Creative Commons Attribution (CC BY) license (https://creativecommons.org/licenses/by/4.0/).

1. Introduction

Microorganisms are a valuable source of primary and secondary metabolites with industrial potential [1,2]. Primary (central) metabolites include amino acids, nucleotides, and fermentation end products such as ethanol and organic acids. They are produced by energy metabolism and are responsible for the growth, development, and reproduction of microorganisms [2]. Secondary metabolites are compounds produced by the modification of primary metabolite synthases, usually at the end of stationary growth. They include pigments, mycotoxins, antibiotics, and others. Numerous secondary metabolites play decisive roles in ecological functions, in particular, mediating antagonistic interactions [1].

Microbial metabolites are key to the production of many food products, dietary supplements, vitamins, amino acids, organic acids, agriculturally important metabolites, enzymes, flavoring agents, coloring agents, and pharmaceutical products [3–5]. Examples of industrially used metabolites include amino acids from *Corynebacterium*, *Brevibacterium* and

Escherichia coli bacteria; vitamins from *Propionibacterium* and *Pseudomonas*; organic acids produced by *Aspergillus*, *Lactobacillus*, *Rhizopus* molds, and enzymes from *Aspergillus* and *Bacillus* [4,6–9]. Secondary metabolites are widely used in health care as anabolic agents, anesthetics, anti-inflammatory agents, antithrombotic agents, hemolytic, vasodilators, hypocholesterolemic agents, antimicrobials, antiparasitics, anticancer agents, enzyme inhibitors, and immunosuppressive drugs [10–12]. Some secondary metabolites show plant growth stimulating effects or herbicide and insecticide activity [13]. Anti-cancer effects have also been demonstrated for adriamycin, bleomycin, daunomycin, and mithramycin, among others [14,15].

The advancement of biotechnological production is driven by its environmental benefits, including a lower pollution burden compared to conventional chemical methods, as well as societal pressure for sustainable resource exploration [4]. Various strategies have been identified for effective overproduction of microbial metabolites through genetic and physiological manipulation [16]. These include the overexpression of genes responsible for the synthesis of metabolites and related coenzymes, the knockdown of genes involved in degradation, and continuous extraction of metabolites from cultures [17]. However, more effective tools are needed for rapid assessment of the metabolic abilities of environmental microorganisms.

Recently, along with the development of other omics methods (genomics and transcriptomics), there has been an expansion of metabolomics, including MSI (mass spectrometry imaging) methods in microbiological studies [18,19]. The most commonly used method is matrix-assisted laser desorption/ionization mass spectrometry imaging (MALDI MSI). This method has been used to identify microorganisms based on the ribosomal protein profile and reference databases [20–22], as well as for the identification and imaging of metabolites of microbiological origin (including mycotoxins) on technical and historical materials [19,23,24].

Since MS imaging of microorganism structures and their growth media is currently performed almost exclusively in 2D, a key challenge remains the development of 3D analysis techniques [25]. So far, 3D imaging has been most often performed using specialized software that stacks multiple 2D results. Recently, Shein et al. [26] proposed a moisture-assisted cryo-section (MACS) modification of MALDI-MSI. However, this method requires sectioning colonies and maintaining appropriate humidity conditions.

The laser ablation remote atmospheric pressure photoionization/chemical ionization (LARAPPI/CI) platform coupled to an ultra-high-resolution quadrupole-time-of-flight (QToF) mass spectrometer (LARAPPI/CI MSI system) was described in a recent publication by Ruman and co-workers [25]. The setup contains an airtight chamber with flowing nitrogen gas (10 L/min). The sample is placed on a sample stage with a Peltier cooling plate for sample freezing. The sample stage is mounted on a motorized XYZ-configuration stage. The pulses from the OPO laser (2.93 µm) passes through a diffractive optical element, forming a square-shaped top-hat beam that is focused onto the sample surface by a 50 mm focal length aspherical ZnSe lens. The system contains also the camera with a lens and distance sensor, the latter for the 3D profiling of the sample shape and dimensions. During MSI, the laser ablation plumes are taken with the gas and transported to the ion source (Bruker VIP HESI in the APCI configuration) of the Bruker Impact II mass spectrometer (Bruker Daltonics, Bremen, Germany). An HPLC pump provides the solvent mixture (1% toluene in methanol; 200 µL/min) to the APCI needle. This system is capable of performing 2D and also direct 3D MSI.

The LARAPPI/CI MSI technique offers several noteworthy advantages over more established methods such as desorption electrospray ionization (DESI), matrix-assisted laser desorption/ionization (MALDI), and surface-assisted laser desorption/ionization

(SALDI). From a practical standpoint, LARAPPI/CI can be performed under ambient conditions—akin to DESI—and does not necessarily require sample slicing into ultra-thin sections or the use of exogenous matrix layers. This feature helps preserve the native configuration of many biological specimens, including plant or animal tissues, especially those that contain regions of markedly different structural integrity (e.g., hydrated gel-like areas). Compared to MALDI, which commonly uses vacuum conditions and an organic or nanoparticle-based matrix, LARAPPI/CI does not require a vacuum system for desorption, minimizing potential sample deformation due to dehydration. This method was recently used by Ruman et al. [25,27] for the first 2D and 3D mass spectrometry imaging (MSI) of metabolites in human and plant tissues.

The aim of this study was to evaluate the usefulness of the newly developed LARAPPI/CI-MSI 3D (laser ablation remote atmospheric pressure photoionization/chemical ionization mass spectrometry imaging) method for direct 3D mass spectrometry imaging of bacterial and fungal metabolites in solid culture media. Two-dimensional (2D) MSI was also performed to study the localization of fungal and bacterial metabolites, including amino acids and their derivatives, dipeptides, organic acids, fatty acids, sugars and sugar derivatives, benzene derivatives, and indoles. Here, we present the first direct 3D MSI of solid bacterial and fungal cultures. We show that direct 3D mass spectrometry imaging analysis can also be used for metabolome analysis of microbial cultures, creating new opportunities for the metabolic profiling of industrially important strains.

2. Results and Discussion

2.1. 2D Mass Spectrometry Imaging of Microbial Cultures

The LARAPPI/CI-MSI 2D was used to visualize numerous metabolites of bacterial and fungal origin in agar cultures, including six dipeptides and one dipeptide derivative (PyroGlu-Ala) (Table 1). Some of the metabolites (Pro-Leu; PyroGlu-Ala; Pro-Asn) occurred with different intensities, depending on whether they originated from bacterial or fungal cultures. Others (Pro-Pro; Pro-Val; Leu-Pro) were associated with a bacterial colony (*B. cereus*). Asp-Leu was associated with a fungal colony (*F. graminarum*).

Table 1. LARAPPI/CI-MSI 2D ion images of dipeptides and their derivatives produced from the tested microbial cultures.

Type	Name (Tested Microorganisms)	Ion Image
Pro-Leu	(left: *F. graminarum*; right: *P. amylolyticus*)	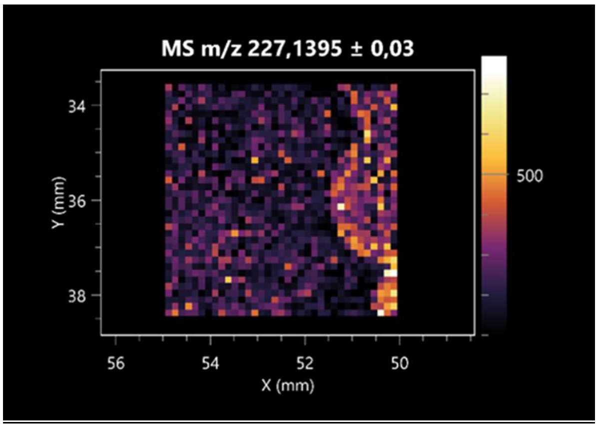

Table 1. *Cont.*

Type	Name (Tested Microorganisms)	Ion Image
PyroGlu-Ala	(left: *B. cereus*; right: *F. graminarum*)	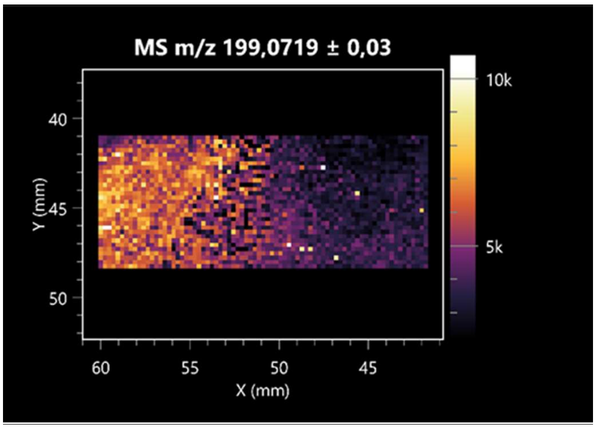
Pro-Pro	(left: *B. cereus*; right: *F. graminarum*)	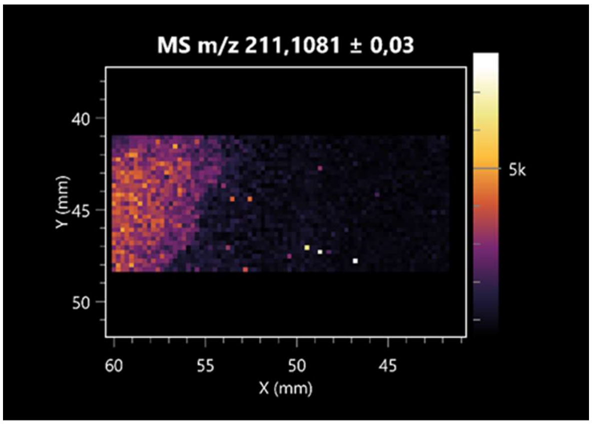
Pro-Val	(left: *B. cereus*; right: *F. graminarum*)	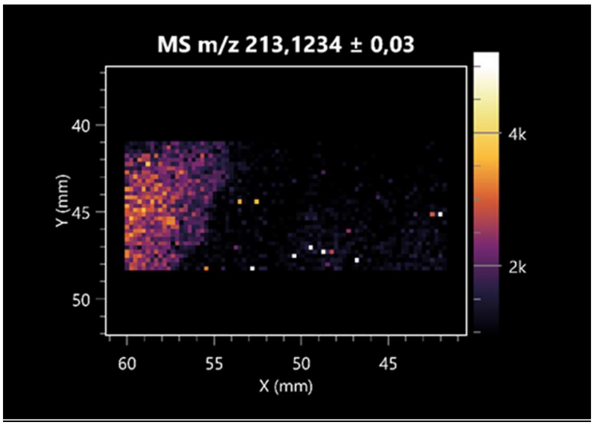
Leu-Pro	(left: *B. cereus*; right: *F. graminarum*)	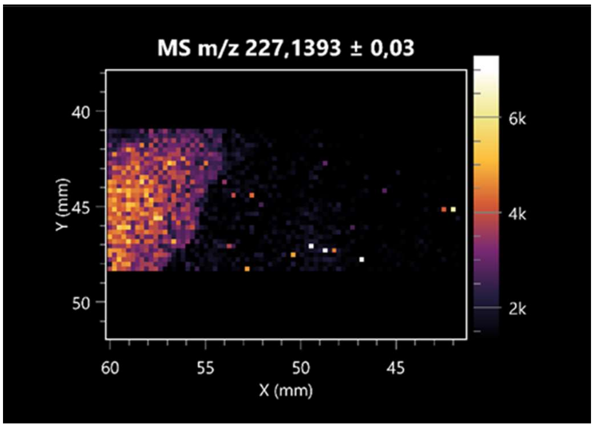

Table 1. *Cont.*

Type	Name (Tested Microorganisms)	Ion Image
Pro-Asn	(left: *B. cereus*; right: *F. graminarum*)	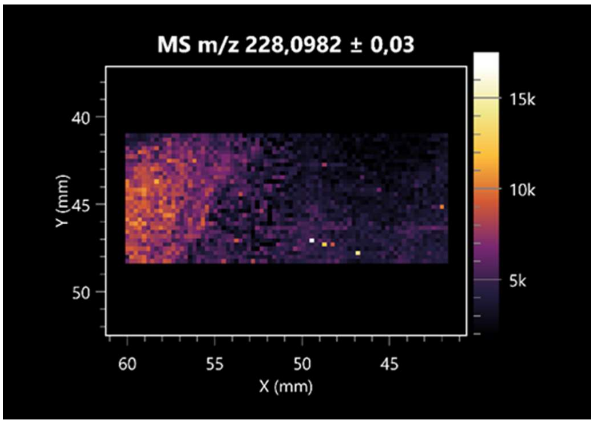
Asp-Leu	(left: *B. cereus*; right: *F. graminarum*)	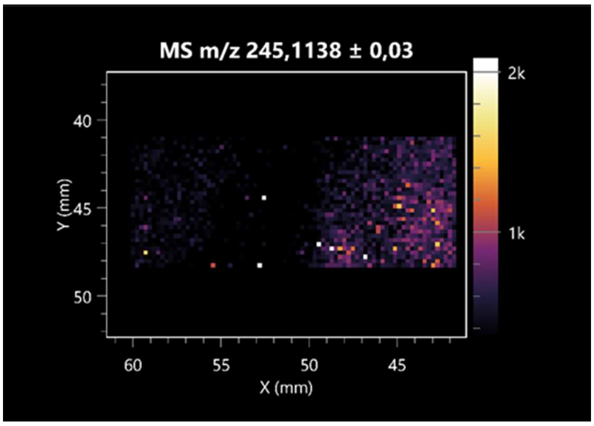

LARAPPI/CI-MSI 2D facilitated the imaging of a wide range of important amino acids from the point of view of biochemistry and medical and industrial biotechnology (Table 2). L-glutamine has many practical applications, primarily in the food and pharmaceutical industries. Glutamine has been shown in laboratory simulations to have numerous benefits in the treatment of critical illnesses, cancer, and cardiac injury. The mechanism of action of glutamine includes improving immune cell function, strengthening the intestinal barrier, increasing stress tolerance, reducing the expression of proinflammatory cytokines, and lowering mortality [28]. Glutamine is an amino acid used as a dietary supplement to support the immune system, increase glycogen synthesis, exert anticatabolic effects, and enhance fluid and electrolyte uptake [29]. L-glutamine is produced using bacteria from the genus *Bacillus* and *Paenibacillus*. Therefore, the presented method can be used to assess the industrial potential of these bacteria for glutamine production. Similarly, L-arginine is currently used in pharmacology for the treatment of liver dysfunction, metabolic alkalosis, ammonia poisoning, asthenic disorders and malnutrition, and growth hormone deficiency. It is also used as a supplement for athletes. It can potentially be used in the treatment of various types of hypertension, heart disease, atherosclerosis, hypercholesterolemia, glaucoma, renal failure, diabetes, and other diseases [30].

Table 2. LARAPPI/CI-MSI 2D ion images of amino acids and their derivatives produced from the tested microbial cultures.

Name (Tested Microorganisms)	**Ion Image**
L-glutamine (left: *F. graminarum*; right: *P. amylolyticus*)	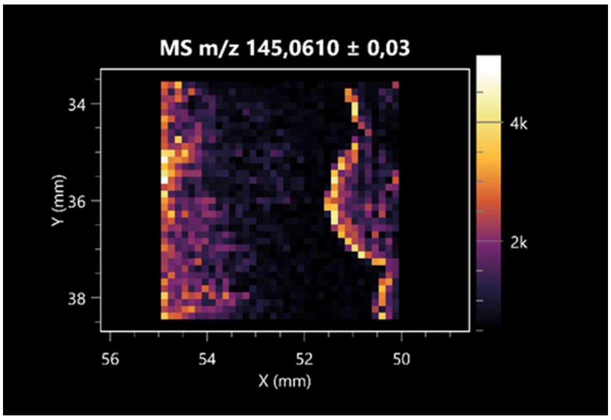
L-glutamic acid (left: *F. graminarum*; right: *P. amylolyticus*)	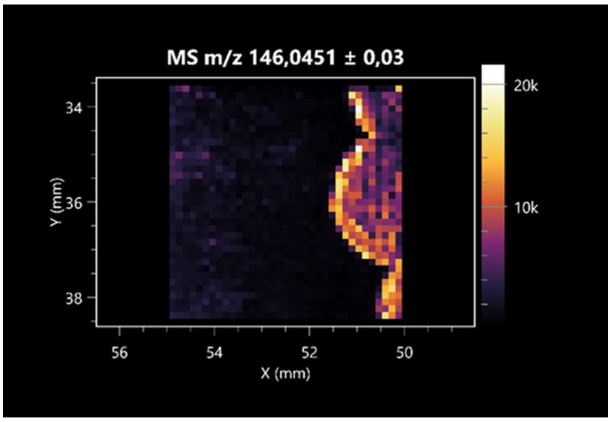
L-arginine (left: *F. graminarum*; right: *P. amylolyticus*)	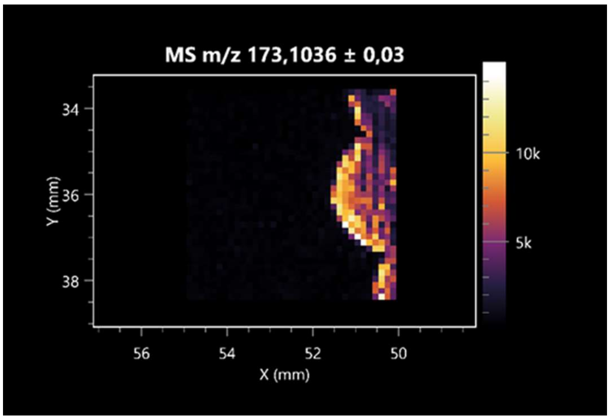
Diaminopimelic acid (left: *F. graminarum*; right: *P. amylolyticus*)	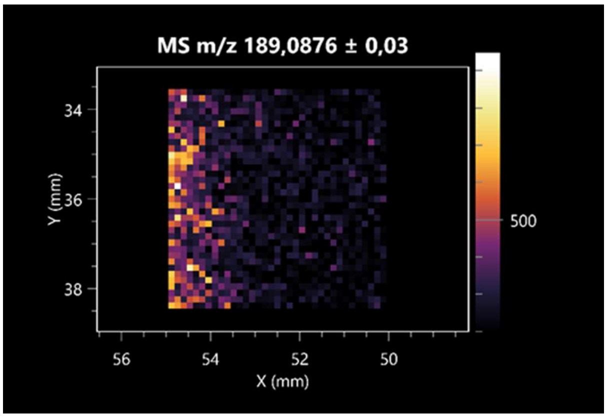

Table 2. *Cont.*

Name (Tested Microorganisms)	Ion Image
L-proline (left: *B. cereus* right: *F. graminarum*)	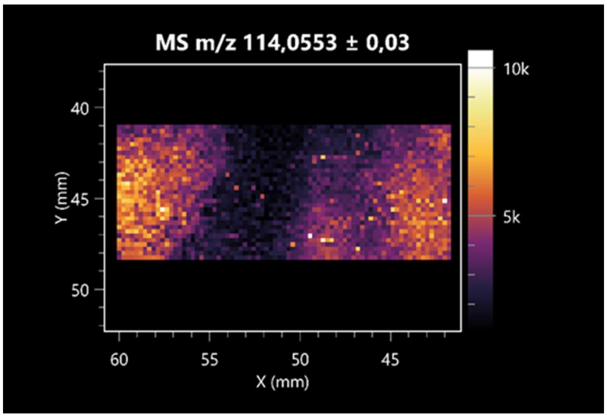
L-aspartic acid (left: *B. cereus*; right: *F. graminarum*)	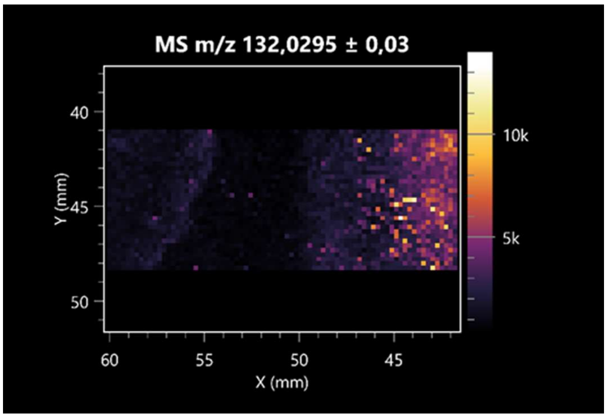
Citrulline (left: *B. cereus*; right: *F. graminarum*)	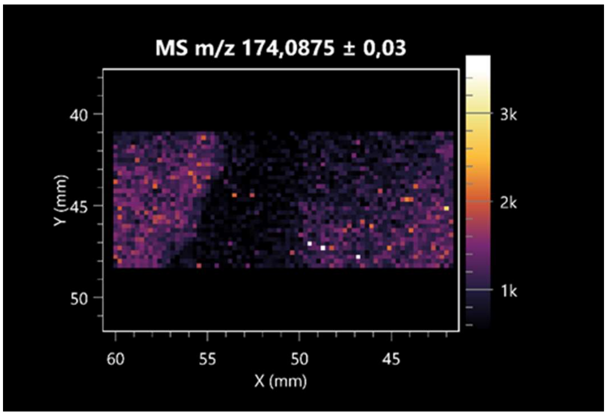
L-tryptophan (left: *B. cereus*; right: *F. graminarum*)	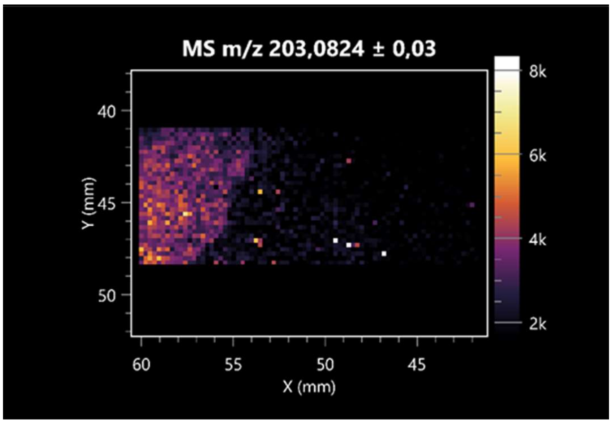

Table 2. *Cont.*

Name (Tested Microorganisms)	Ion Image
N-acetylglycine (left: *F. graminarum;* right: *P. amylolyticus*)	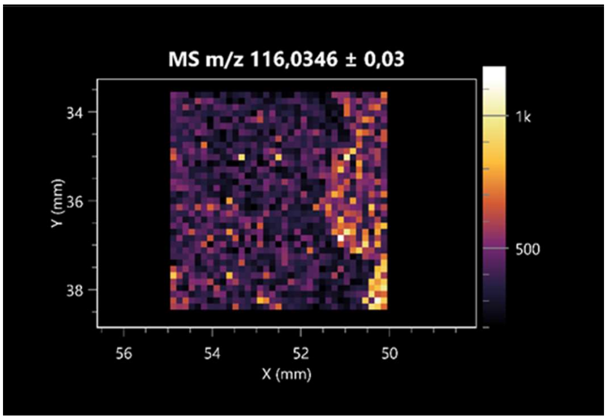
Creatine (left: *B. cereus;* right: *F. graminarum*)	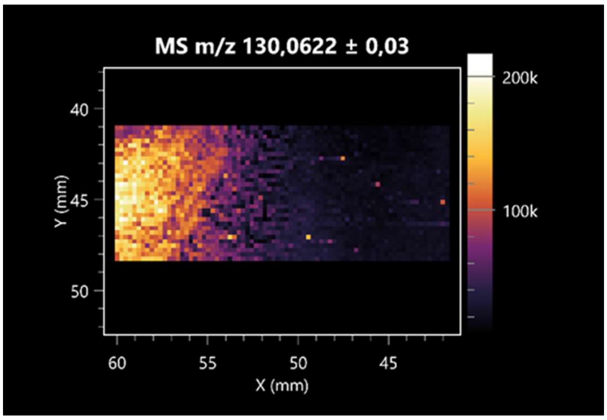
Aminoadipic acid (left: *B. cereus;* right: *F. graminarum*)	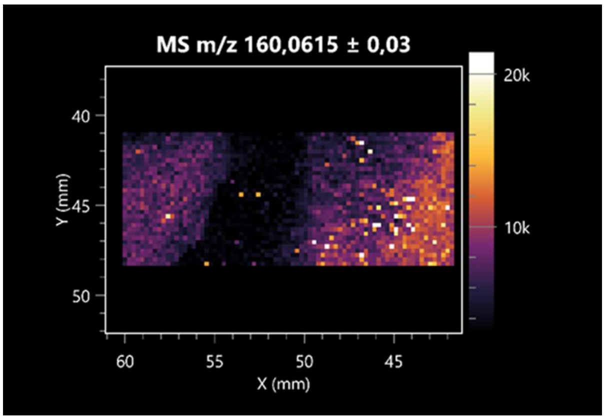
4-acetamidobutanoic acid (left: *B. cereus;* right: *F. graminarum*)	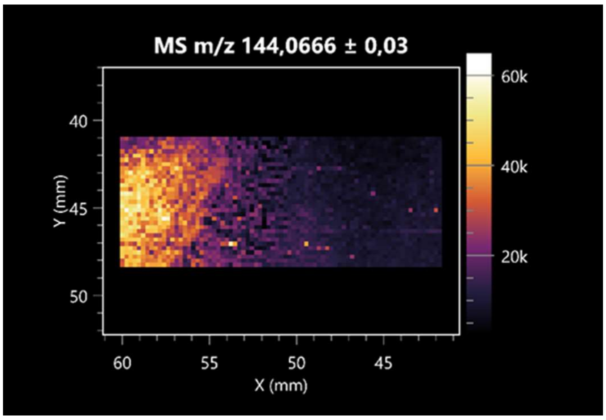

One of the main metabolites of *B. coagulans* R11 is 4-acetamidobutanoic acid, which shows antioxidant and antimicrobial activity [31]. L-glutamic acid can be produced with high yield by environmental isolates of *Bacillus* sp. [32]. L-glutamic acid in the form of monosodium salt is commonly used as a flavor-enhancing compound in food [33]. Similarly, *N*-acetylglycine has been found at low concentrations in various types of food products. It is not genotoxic in in vivo or in vitro assays [34]. Diaminopimelic acid is a constituent of the bacterial and fungal cell wall structure and is found in higher plants [35]. L-proline is an osmoprotectant that takes part in the response of bacteria and plants to osmotic stress. It also has many other functions, including as an antioxidant that captures reactive oxygen species. It increases the stability of proteins and membranes during freezing, dehydration, or heating. Additionally, it can increase the solubility of some proteins and inhibit protein aggregation [36]. Aspartic acid has potential antibacterial and antifungal effects [37]. Citrulline is a precursor of arginine and plays an important role in the metabolism and regulation of nitric oxide. Citrulline supplements may help to control disorders of NO metabolism and improve cardiovascular function [38]. Tryptophan is an essential amino acid in mammals. It is involved in the proper functioning of neurons, the immune system, and the intestines. Tryptophan supplementation may be beneficial for diseases such as autism, cardiovascular disease, chronic kidney disease, depression, inflammatory bowel disease, multiple sclerosis, and bacterial infections, among others [39,40]. Creatine plays a key role in cellular metabolism, especially in states of metabolic stress. Its main practical application is as an ergogenic agent for exercise, training, and sports, improving cellular metabolism and reducing the severity of injuries and/or disease states [41]. In turn, 2-aminoadipic acid is a key intermediary in the biosynthesis of lysine and penicillin in microorganisms producing β-lactams and 3-lactams. Additionally, it plays a role in lysine catabolism in mammals [42]. The remaining amino acids and their derivatives imaged by this method are listed in Supplementary Materials Table S1.

The LARAPPI/CI-MSI 2D technique also revealed a wide range of organic acids produced by the studied microorganisms (Table 3). Organic acids exert antimicrobial activity by lowering the environmental pH and lowering the internal pH of the microbial cells through ionizing undissociated acid molecules. Additionally, they disrupt substrate transport by changing the permeability of the cell membrane or reducing the proton driving force [43]. Pyrrolidone carboxylic acid is a valuable compound used in many cosmetics due to its moisturizing properties and ability to retain moisture (Villeneuve et al., 2003) [44]. It is also known for its antimicrobial properties, including against bacteria of the genera *B. subtilis*, *Escherichia*, *Enterobacter*, *Klebsiella*, and *Pseudomonas* [45]. Malic acid has been shown to have antibacterial activity against food pathogens (*Listeria monocytogenes*, *Salmonella enterica*, and *Escherichia coli*) [46]. It can also stimulate the production of *Fusarium* antagonists in soil [47]. Similarly, citric acid has proven activity against foodborne pathogens including *Shigella* sp., *Listeria*, *Escherichia*, and *Salmonella* [43,48].

Pantothenic acid has many applications in the food, cosmetic, and pharmaceutical industries. Its biotechnological production methods are well established [49]. Propionic acids are weak organic acids, which are commonly used as preservatives in various food products. The antimicrobial activity of succinic acid has been applied for the preservation of poultry and beef meat [50]. Several studies have reported that lactic acid of microbiological origin has antimicrobial activity against bacteria and molds, both in vitro and in foods [51]. Unver [52] showed that fumaric acid has a potent inhibitory effect against pathogenic and opportunistic microorganisms, including bacteria belonging to the genus *Escherichia*, *Enterobacter*, *Klebsiella*, and *Pseudomonas*, as well as *Candida* yeast. It also has potential analgesic, anti-inflammatory, antioxidant, antipsoriatic, chemopreventive, immunomodulatory, and neuroprotective properties. Hydroxypropanedioic acid detected in the present study in the *B. cereus* colony is a primary metabolite directly involved in the growth, development, and reproduction of living organisms. 3-hydroxypropionic acid is an industrially valuable compound used in the chemical synthesis of solvents, cleaning agents, adhesives, paints and coatings, plastics, and fibers. Genetic engineering has been used to enable its microbial production, including from bacteria of the genus *Bacillus* [53].

Table 3. LARAPPI/CI-MSI 2D ion images of organic acids and their derivatives produced from the tested microbial cultures.

Name	Tested Microorganisms	Ion Image
Pyrrolidonecarboxylic acid	(left: *F. graminarum*; right: *P. amylolyticus*)	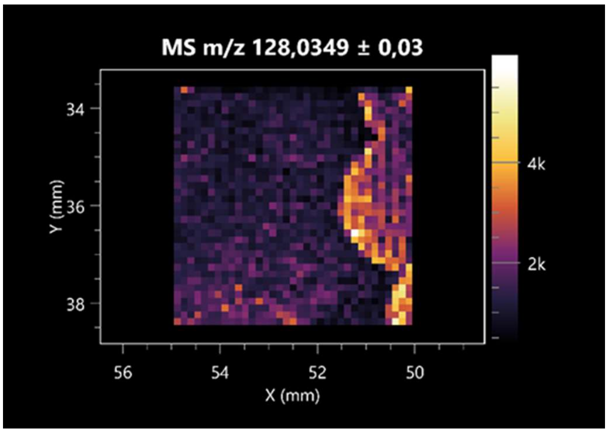
Malic acid	(left: *F. graminarum*; right: *P. amylolyticus*)	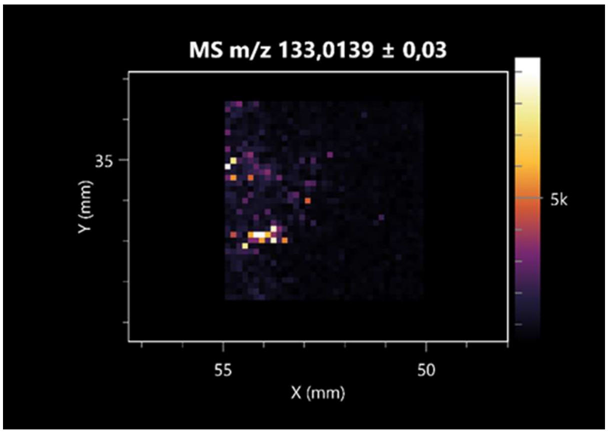
Citric acid	(left: *B. cereus*; right: *F. graminarum*)	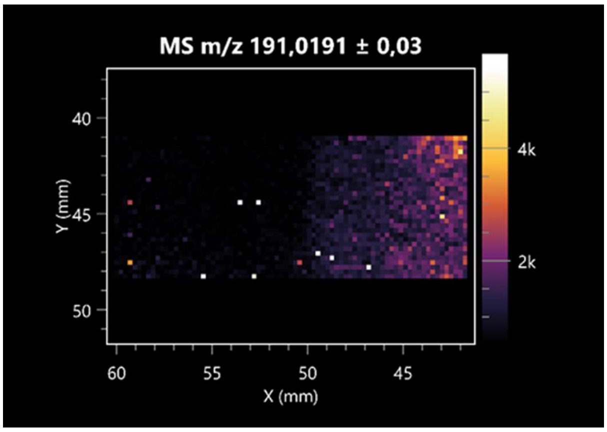

Table 3. *Cont.*

Name	Tested Microorganisms	Ion Image
Sebacic acid	(left: *B. cereus*; right: *F. graminarum*)	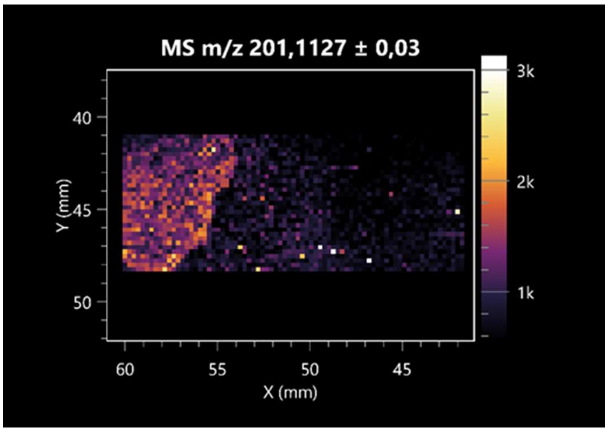
Pantothenic acid	(left: *B. cereus*; right: *F. graminarum*)	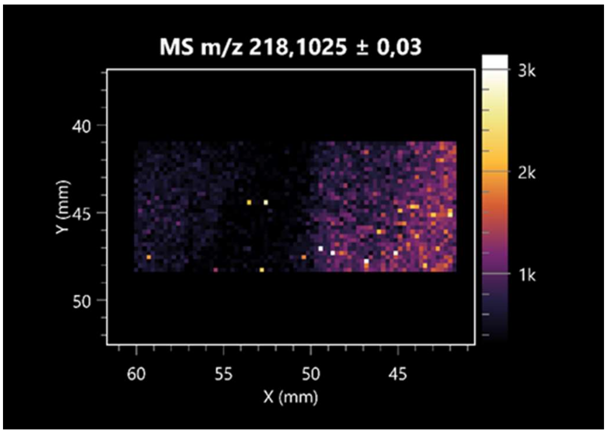
Propionic acid	(left: *B. cereus*; right: *F. graminarum*)	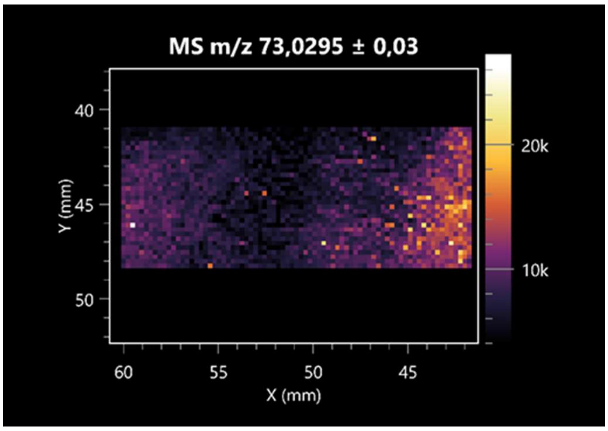
Lactic acid	(left: *B. cereus*; right: *F. graminarum*)	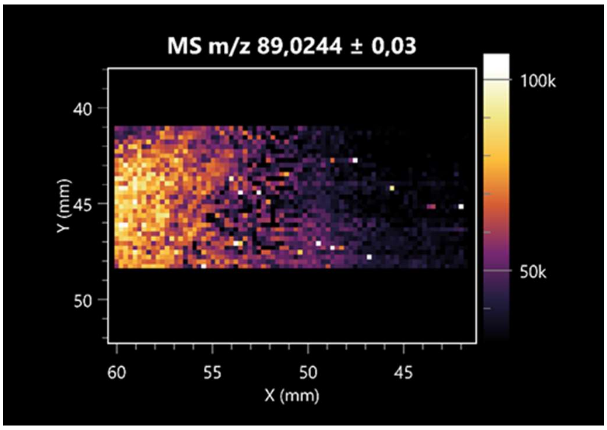

Table 3. *Cont.*

Name	Tested Microorganisms	Ion Image
2-furoic acid	(left: *B. cereus*; right: *F. graminarum*)	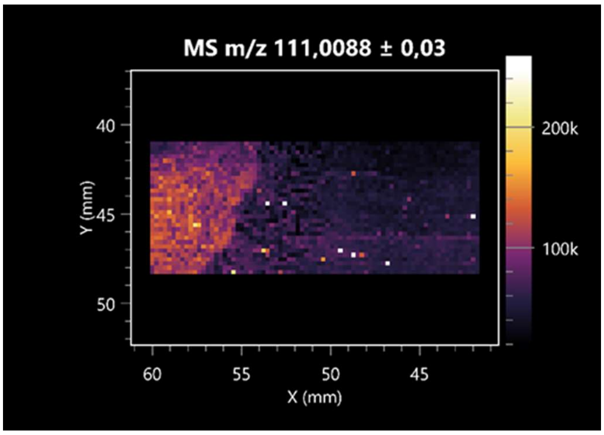
Fumaric acid	(left: *B. cereus*; right: *F. graminarum*)	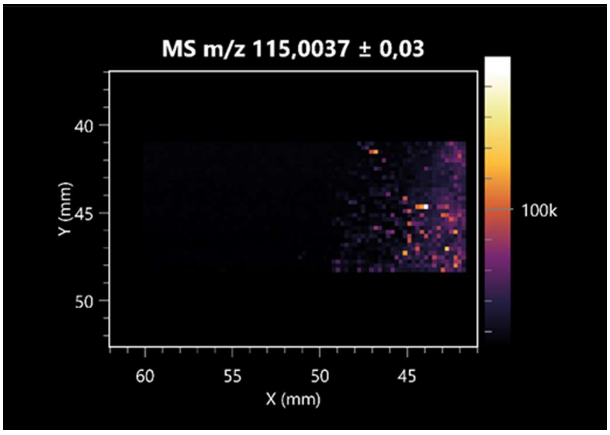
Succinic acid	(left: *B. cereus*; right: *F. graminarum*)	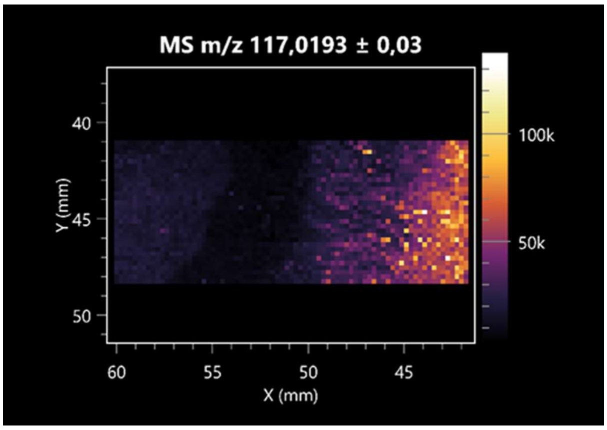
Hydroxypropanedioic acid	(left: *B. cereus*; right: *F. graminarum*)	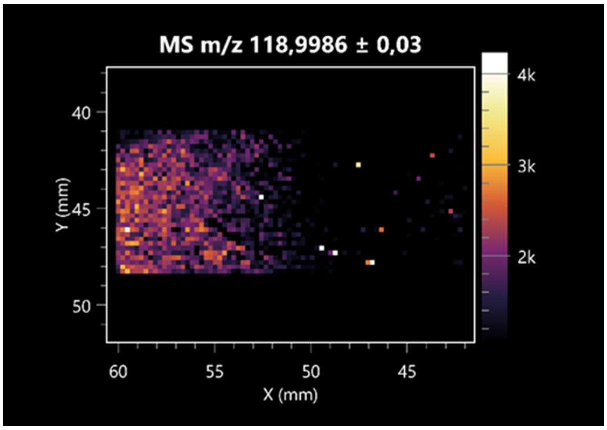

Table 3. *Cont.*

Name	Tested Microorganisms	Ion Image
Dihydroxyfumaric acid	(left: *B. cereus*; right: *F. graminarum*)	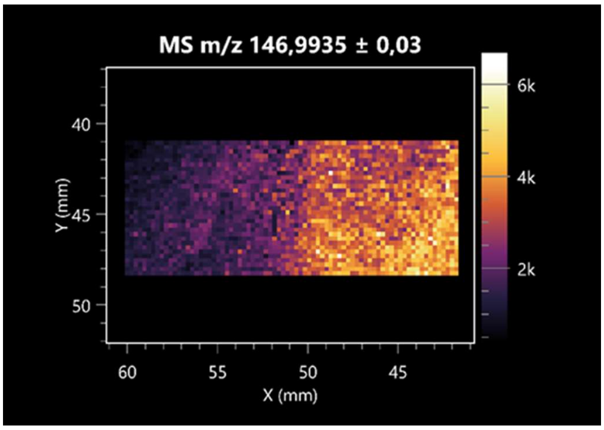
2-Aminobenzoic acid	(left: *B. cereus* right: *F. graminarum*)	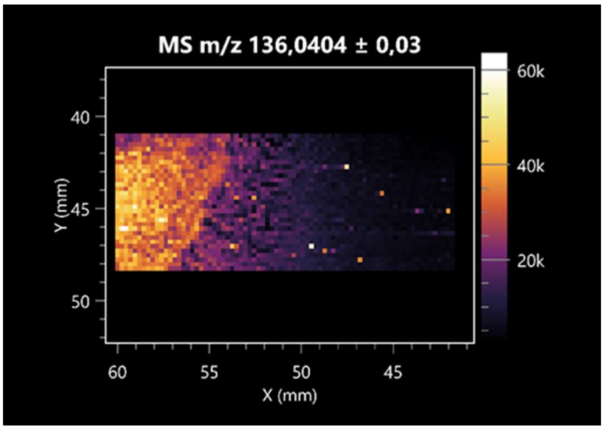
Xanthurenic acid	(left: *B. cereus*; right: *F. graminarum*)	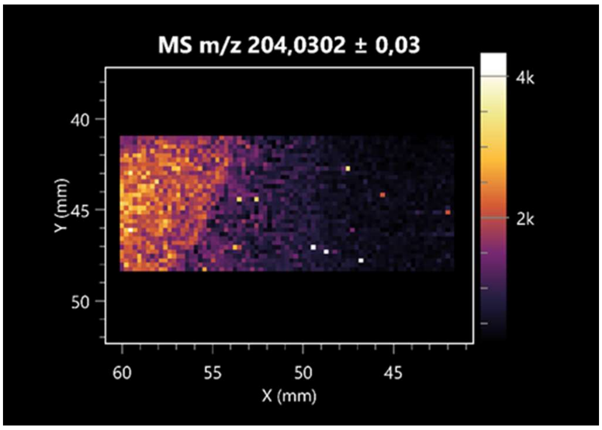
Kynurenic acid	(left: *B. cereus*; right: *F. graminarum*)	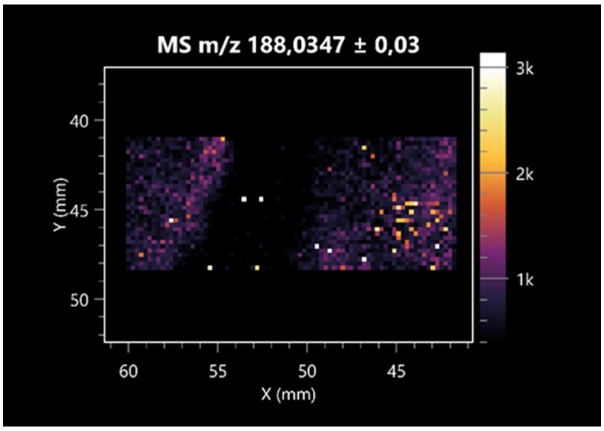

Dihydroxyfumaric acid is used for the biosynthesis of sugars, uronic acids, and vitamin C. Its industrial applications include its use as a disinfectant in contact lenses and as a color-destabilizing agent in cleaning products. It can also be used to treat municipal wastewater or wastewater from the paper or food industries [54]. 2-aminobenzoic acid from *Bacillus* has been identified as compound involved in microbial induced systemic resistance, demonstrating activity against soft-rot disease in tobacco [55]. Sebacic acid (decanedioic acid) has antimicrobial and antifungal activity and has been reported previously in *Bacillus* species. 2-furoic acid demonstrates strong nematicidal activity [56]. Xanthurenic acid is produced by bacteria as part of tryptophan catabolism. It is associated with the endogenous cell death factor, which accelerates the cell-aging process [57]. Depending on the microbe, the function of kynurenic acid is unclear. This compound is considered to play an essential role in the survival of microorganisms, including amino acid synthesis and nitrogen assimilation [58].

Notably, azelaic acid was one of the fatty acids and derivatives detected by LARAPPI/CI-MSI 2D (Table 4). Azelaic acid has anti-inflammatory, antibacterial, antioxidant, anti-comedogenic, and anti-cancer effects. It has been approved by the US Food and Drug Administration as a therapeutic agent for the treatment of acne and rosacea [59]. It is a natural inducer of the plant defense system, capable of stimulating innate resistance in plants and reducing the damage caused by diseases, without the negative effects of fungicides [60]. Azelaic acid is also a valuable bio-based monomer for the synthesis of biodegradable and sustainable polymers, plasticizers, and lubricants [61]. Linoleic and linolenic acids also have broad antibacterial activity [62]. Pentadecanoic acid has anti-biofilm properties, including against *Klebsiella pneumoniae* bacteria and *Candida albicans* fungi [63]. Bacteria of the *Bacillus* genus are known to produce valeric acid [64]. Its effectiveness against phytopathogens of the *Fusarium* genus as well as Gram-negative and Gram-positive bacteria has also been demonstrated [65].

Table 4. LARAPPI/CI-MSI 2D ion images of fatty acids and their derivatives produced from the tested microbial cultures.

Name	Tested Microorganisms	Ion Image
Azelaic acid	(left: *F. graminarum*; right: *P. amylolyticus*)	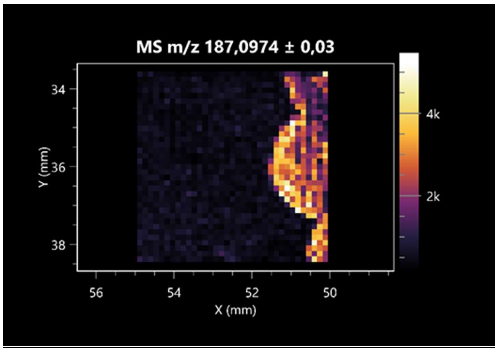
	(left: *B. cereus*; right: *F. graminarum*)	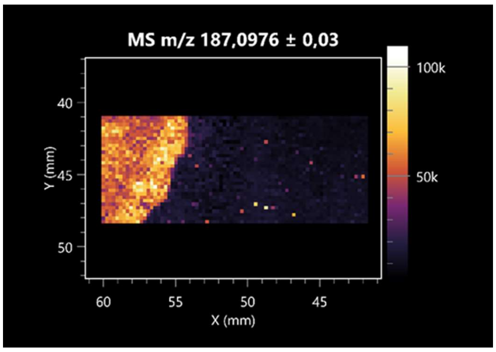

Table 4. *Cont.*

Name	Tested Microorganisms	Ion Image
Elaidic acid	(left: *B. cereus*; right: *F. graminarum*)	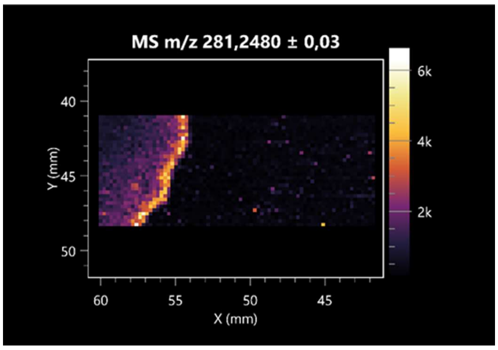
Linolenic acid	(left: *B. cereus*; right: *F. graminarum*)	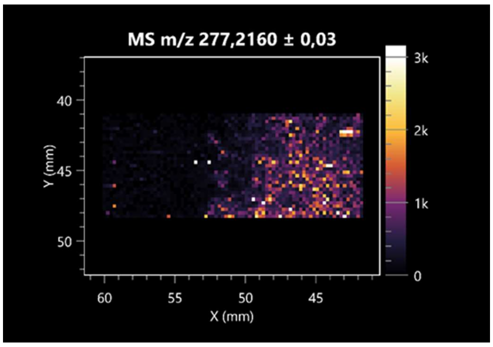
Linoleic acid	(left: *B. cereus*; right: *F. graminarum*)	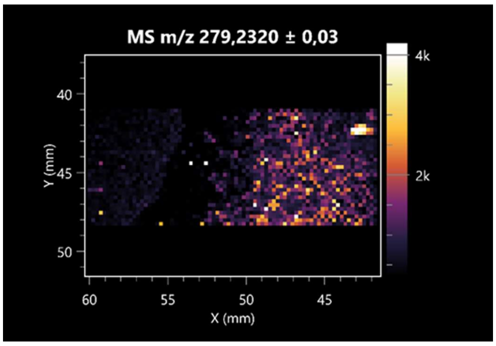
Pentadecanoic acid	(left: *B. cereus*; right: *F. graminarum*)	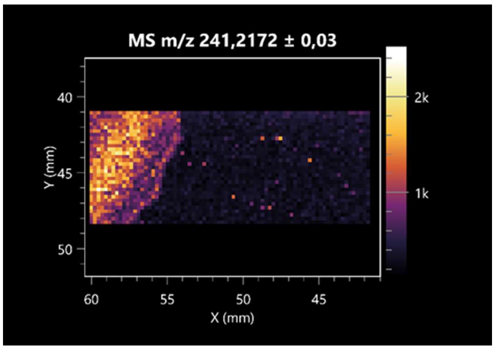
Valeric acid	(left: *B. cereus*; right: *F. graminarum*)	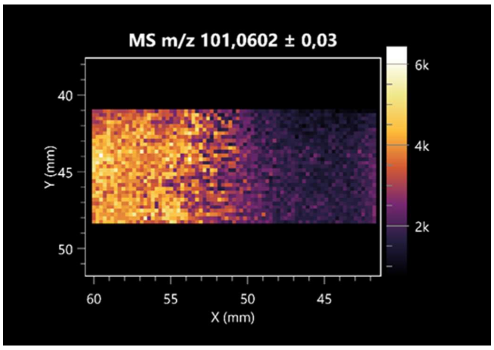

This is the first study to report finding elaidic acid on the edge of the *Bacillus* growth area. The probable explanation is that this acid was synthesized due to the presence of high concentrations of toxic substances from *F. graminarum* [66]. It seems that the secretion of elaidic acid at the edge of the culture modified the membrane fluidity as a defense mechanism. Elaidic acid is known to have an antimalarial effect [67].

Other biotechnologically important sugars and their derivatives were also imaged using LARAPPI/CI-MSI 2D (Table 5).

Table 5. LARAPPI/CI-MSI 2D ion images of sugars and their derivatives produced from the tested microbial cultures.

Name	Tested Microorganisms	Ion Image
Ribitol	(left: *F. graminarum*; right: *P. amylolyticus*)	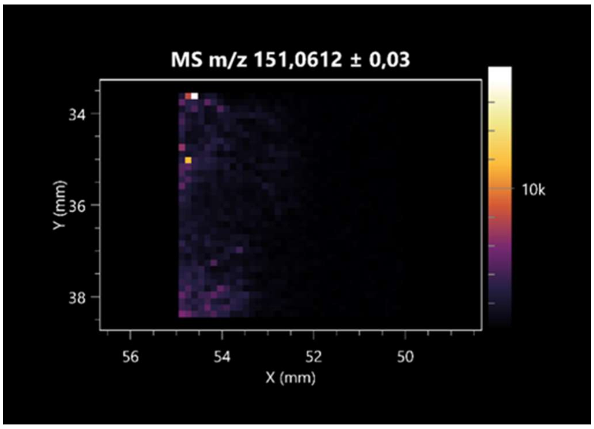
Sorbitol	(left: *F. graminarum*; right: *P. amylolyticus*)	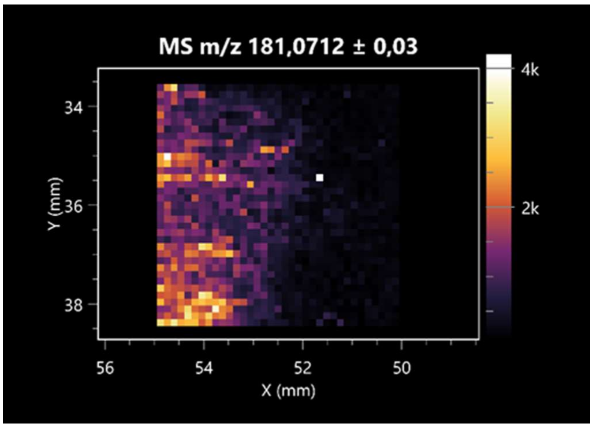
2-amino-2-deoxy-D-mannitol	(left: *B. cereus*; right: *F. graminarum*)	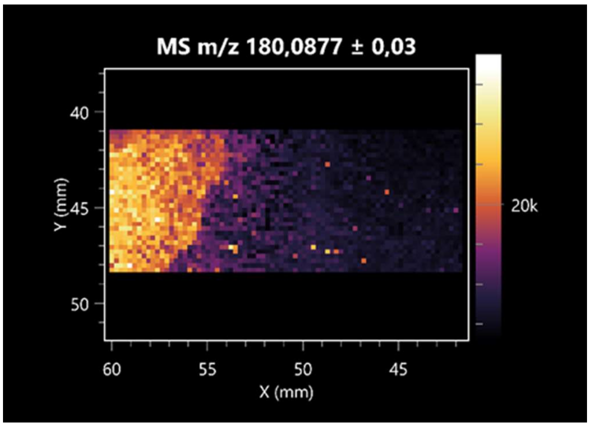

Table 5. *Cont.*

Name	Tested Microorganisms	Ion Image
4-amino-4-deoxy-L-arabinose	(left: *B. cereus*; right: *F. graminarum*)	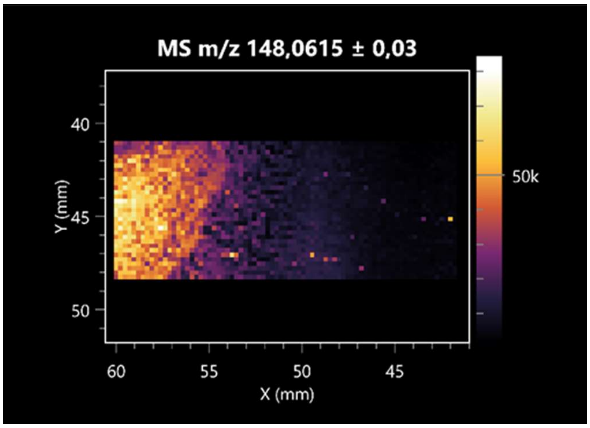
Erythronic acid	(left: *B. cereus*; right: *F. graminarum*)	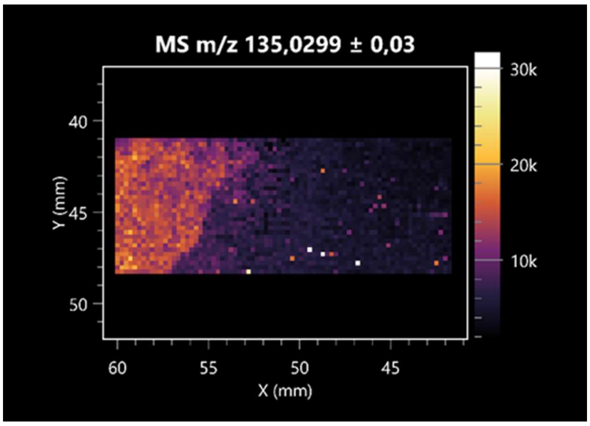
Deoxyribose 5-phosphate	(left: *B. cereus*; right: *F. graminarum*)	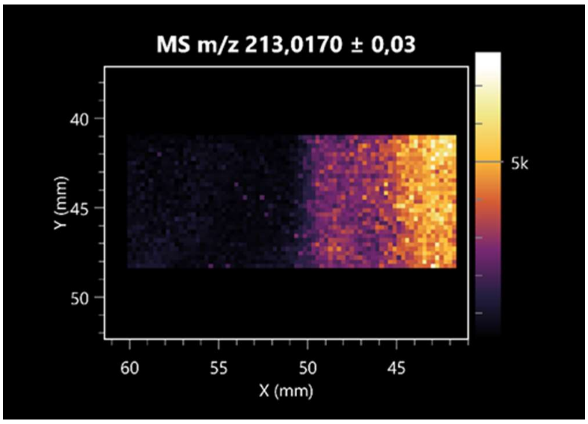
N-acetylmannosamine	(left: *B. cereus*; right: *F. graminarum*)	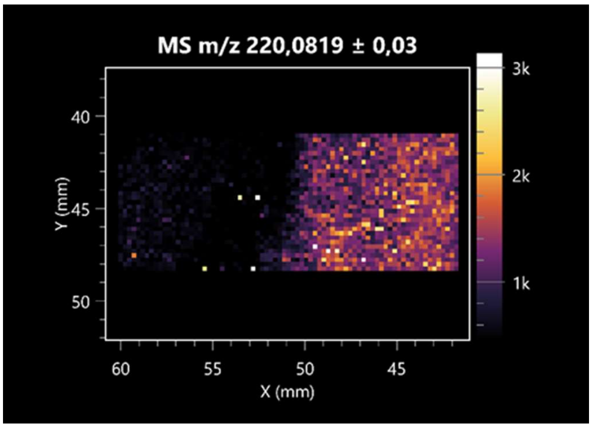

Table 5. *Cont.*

Name	Tested Microorganisms	Ion Image
Trehalose	(left: *B. cereus*; right: *F. graminarum*)	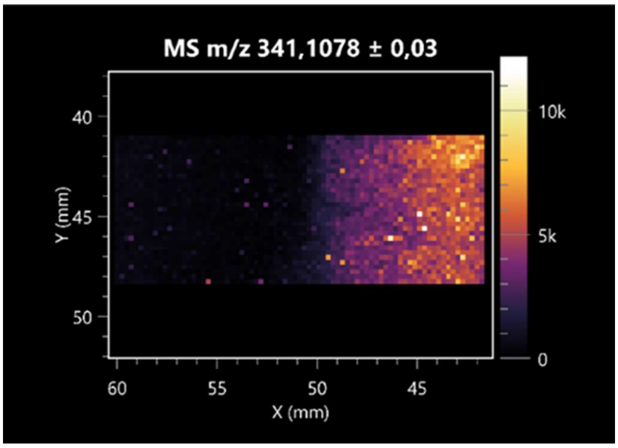

Corona and Munday [68] found ribitol in the mycelium of molds, but, as in the present study, they did not observe any diffusion into the culture medium. Similarly, in our work, the intensity of signals indicates that this compound was produced in small amounts and was concentrated in the colonies rather than in the medium. Onose et al. [69] reported that bacteria of the genus *Bacillus* (*Bacillus amyloliquefaciens* and *Bacillus subtilis*) produce 2-amino-2-deoxy-D-mannitol, which is a precursor of 1-deoxynojirimycin and has therapeutic applications in the treatment of HIV, Gaucher's disease, and diabetes. Interestingly, the level of sorbitol in the culture medium increased with the production of this compound. Sorbitol was one of the metabolites of *F. graminarum* co-cultured with *P. amylolyticus*. It is a natural polyol used as a sweetener, moisturizing agent, and softener. It can be produced chemically or biotechnologically using microorganisms, primarily *Zymomonas mobilis* [70]. Observing the interactions of the metabolites of both groups of microorganisms may be useful for optimizing the production of therapeutic metabolites.

4-amino-4-deoxy-L-arabinose is an important metabolite for the modification of lipid A, which is a component of the lipopolysaccharides of Gram-negative bacteria. It participates in the acquisition of resistance to polymyxin antibiotics [71]. Batovska et al. [72] proposed erythronic acid and other individual metabolites as biomarkers for fungal resistance based on the correlations between GC/MS data and the estimated resistance of leaves towards the etiological agents of powdery mildew and downy mildew. 2-deoxyriobse 5-phosphate is used as a building block for antisense and antiviral drugs, reagents, and reagents for PCR [73]. *N*-acetylmannosamine is a plant primary metabolite precursor with bioprotective features [74]. *N*-acetylmannosamine induces gratuitous β-*N*-acetylhexosaminidase in *C. albicans* and *Mucor fragilis*, which performs an important vegetative function in heterotrophic microorganisms [75]. Trehalose is widely present in bacteria, fungi, plants, and invertebrates. In fungi, trehalose constitutes a source of reserve carbon and agents of adaptation to stress conditions, such as dehydration, oxidative, and heat/cold treatment. Trehalose is capable of stabilizing and protecting membranes and proteins, making it suitable for use as a protective agent during the freeze-drying of microorganisms [76].

The LARAPPI/CI-MSI 3D method also enabled the acquisition of ion images for other bacterial and fungal metabolites, including alcohols, indoles, amines, aldehydes, purines, pyrimidines, benzene derivatives, organic phosphates, carnitines, and sulfur compounds (Table S1).

2.2. 3D Mass Spectrometry Imaging of Microbial Cultures

This is the first study to use the LARAPPI/CI-MSI 3D method to generate ion images of bacterial and fungal metabolites in solid culture media (Table 6). The method facilitated the assessment of chemically diverse metabolites, classified as amino acids and amino acid derivatives, dipeptides, organic acids, fatty acids, sugars and sugar derivatives, benzene derivatives, and indoles. A novelty of the method is that it enables the visualization of chemical compound distribution at a selected depth within the culture agar while also allowing for the estimation of compound concentration across all dimensions. The 3D ion images for L-glutamine, L-glutamic acid, L-arginine, and *N*-acetylglycine match those obtained in the 2D analysis. This indicates the presence of these compounds in both types of colonies (bacterial and fungal), although their distributions are different. The concentration of L-glutamine was higher in the center of the fungal colony and in the outer part of the bacterial colony. The concentration of glutamic acid was higher in *Paenibacillus* than in *Fusarium*. L-arginine was detected only in bacteria. Similar to indole-3-carboxylic acid, 3D analysis showed a better diffusion of diaminopimelic acid into the substrate than 2D analysis and an almost uniform distribution in the culture medium, making it difficult to assign this metabolite (Table 6).

According to the results of 3D analysis, malic acid is characteristic for molds, and pyrrolidonecarboxylic acid dominates in the bacterial colony. Pro-Leu cannot be considered a microorganism-specific dipeptide because it occurred in almost the entire volume of the tested area. In contrast, azelaic acid is closely related to *Paenibacillus,* and the obtained ion image suggests that it is not released into the substrate. The applied method also proved effective for imaging sugars and sugar derivatives from molds, revealing the spatial distribution for ribitol, sorbitol, and deoxyguanosine. As can be seen more clearly from the 3D ion image for *N*-methylbenzamide, this metabolite is primarily associated with the bacterial colony but probably also occurs in the culture medium itself (Table 6). Additionally, 3D ion images were generated for D-α-aminobutyric acid and *N*-acetyl-L-alanine (Table S2). Moreover, MS spectra of the top ablation level of 3D MSI are provided in Supplementary Materials Figure S1.

It is worth emphasizing that the advantage of LARAPPI/CI in the context of comparing MSI methods is its suitability for imaging microbial colonies cultured on agar-based media. Owing to the mid-infrared laser's strong coupling with water, LARAPPI/CI enables efficient desorption of microorganisms and surrounding matrix without requiring the vacuum conditions typical of SIMS (secondary-ion mass spectrometry) or MALDI. The sample can remain in a near-native state—particularly important for microbial colonies whose morphology and metabolite gradients can be distorted by drying, slicing, or excessive handling.

2.3. Pathway Analysis

After LC-MS positive and negative mode analysis, 382 chemical compounds were identified for *P. amylolyticus*, of which 262 metabolites were included in the analysis using the *Bacillus subtilis* subsp. *subtilis 168* (KEGG) library. In turn, 351 chemical compounds were detected for *B. cereus*, of which 242 metabolites were included in the analysis using the same library. For *F. graminarum*, 393 chemical compounds were identified, of which 244 metabolites were included in the analysis using the *Aspergillus clavatus* library (KEGG). Figure 1 shows a pathway impact analysis of metabolites for the tested microorganisms. The most statistically significant pathways for both tested bacteria strains were tyrosine, alanine, aspartate, and glutamate metabolism. For *B. cereus*, only the taurine and hypotaurine metabolism pathway was statistically significant. More significant metabolic pathways were detected for *P. amylolyticus*, including D-amino acid metabolism; arginine biosynthesis; arginine and proline metabolism; glycine, serine and threonine metabolism; purine metabolism; cyanoamino acid metabolism. For *F. graminarum*, the most important pathways were as follows: alanine, aspartate, and glutamate metabolism; arginine biosynthesis; purine metabolism; butanoate metabolism; lysine biosynthesis; glyoxylate and dicarboxylate metabolism; pyruvate metabolism; the citrate cycle (TCA cycle).

Table 6. LARAPPI/CI-MSI 3D ion images of bacterial and fungal metabolites produced from *Paenibacillus amylolyticus* (right) and *Fusarium graminarum* (left) cultures.

Compound		**Ion Images**
Amino acids and derivatives	L-glutamine	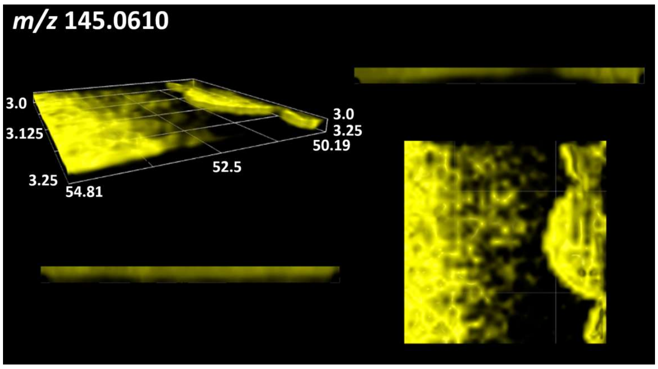
	L-glutamic acid	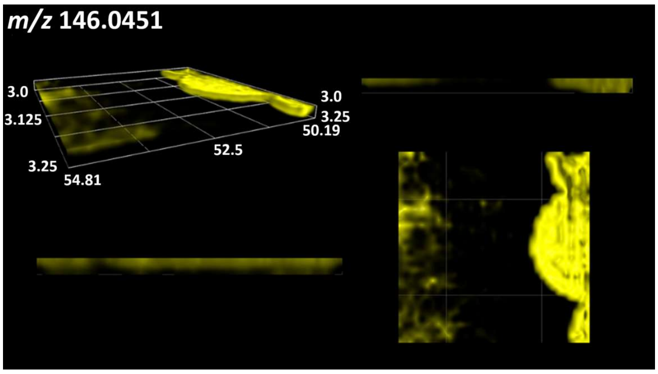
	L-arginine	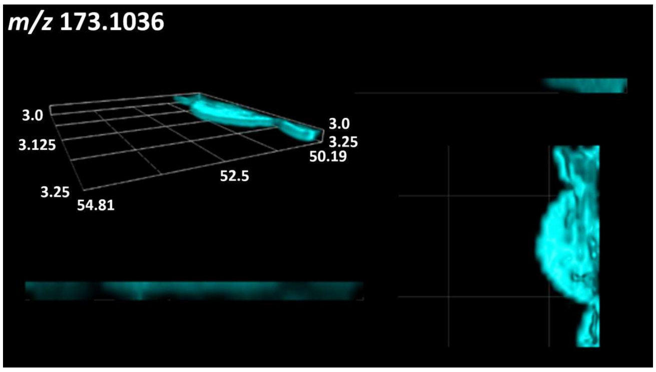
	N-acetylglycine	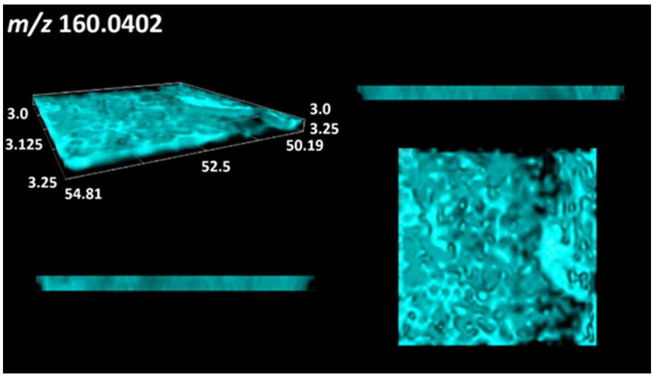

Table 6. *Cont.*

Compound		Ion Images
	Diaminopimelic acid	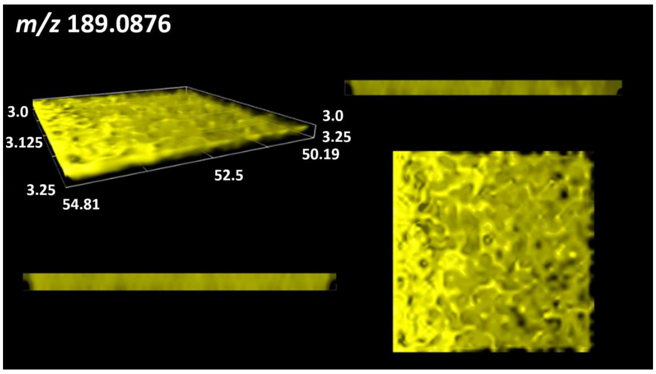
Organic acids	Pyrrolidonecarboxylic acid	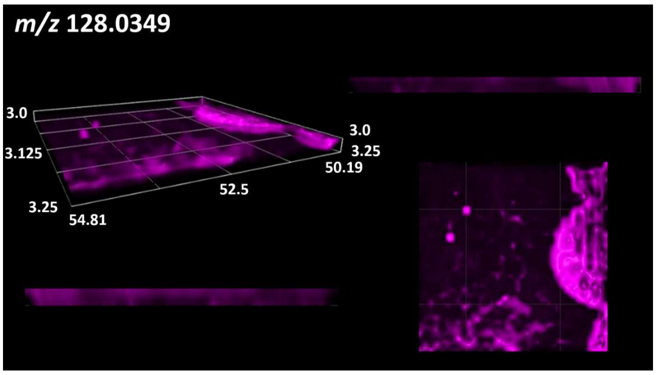
	Malic acid	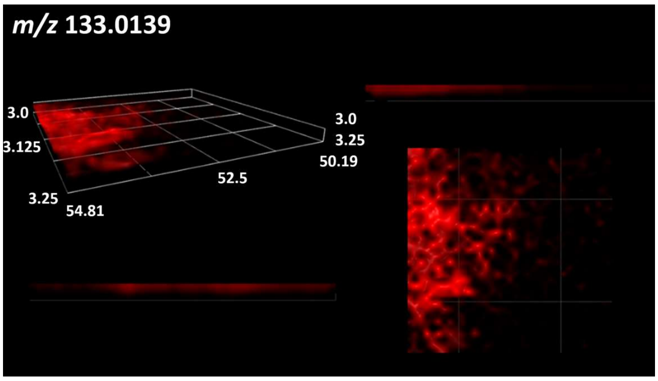
Dipeptides	Pro-Leu	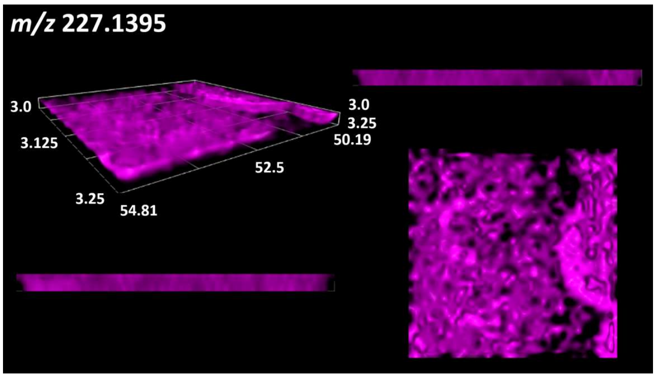

Table 6. *Cont.*

Compound		Ion Images
Fatty acids	Azelaic acid	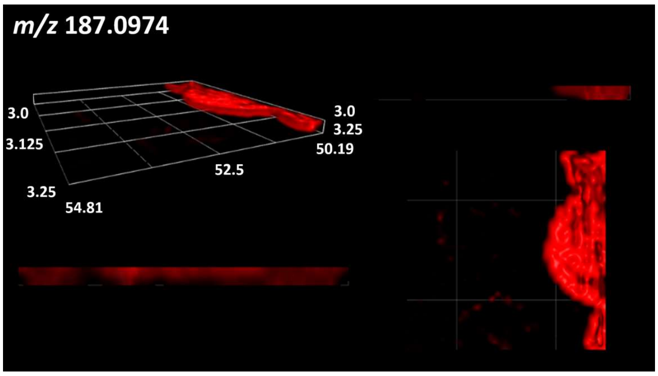
Sugars and sugar derivatives	Ribitol	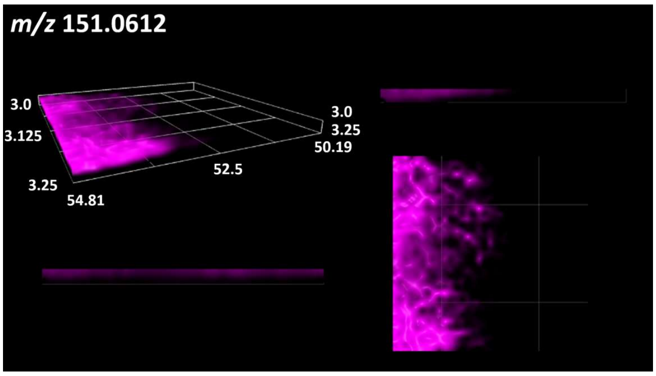
	Sorbitol	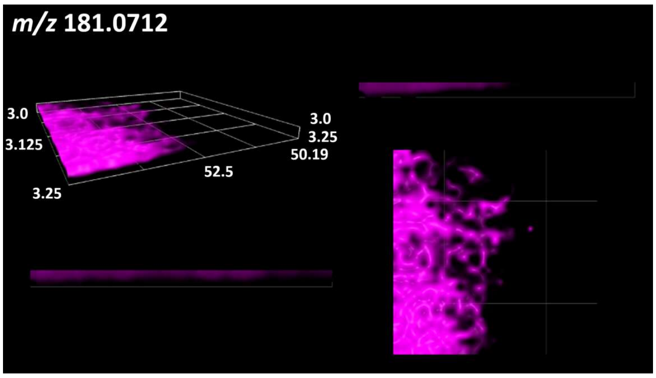
	Deoxyguanosine	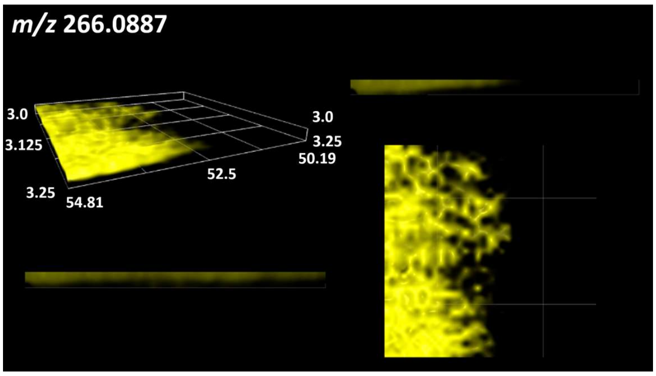

Table 6. *Cont.*

Compound		**Ion Images**
Benzene derivatives	*N*-methylbenzamide	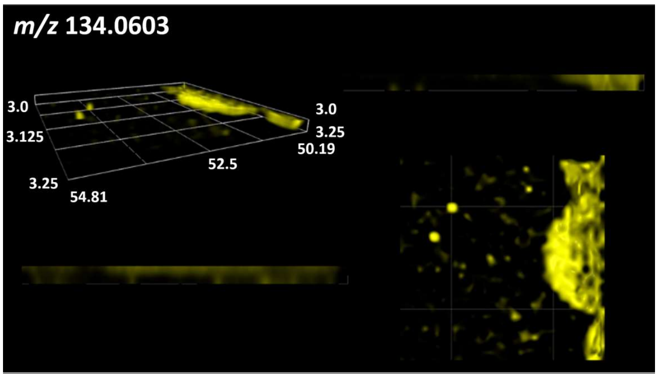
Indoles	Indole-3-carboxylic acid	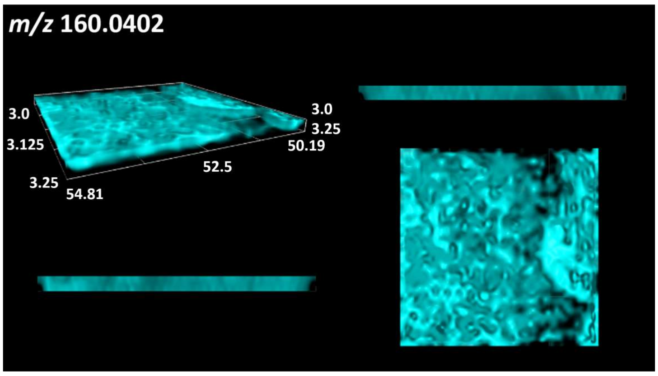

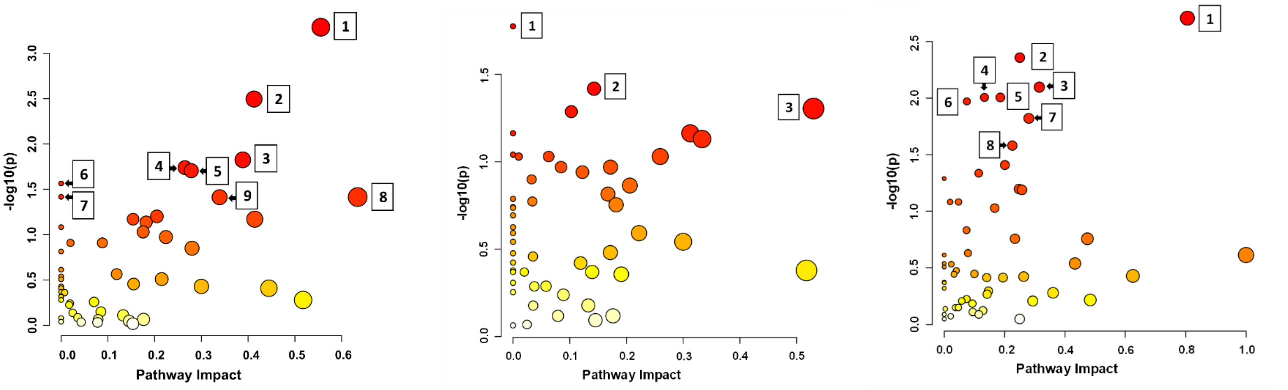

(**A**) (**B**) (**C**)

Figure 1. Pathway impact analysis of metabolites for the tested microorganisms. The bubble plot shows metabolic pathways impacted based on pathway impact scores (*X*-axis) and −log10(*p*) values (*Y*-axis). Larger and more intense red bubbles represent pathways with higher impact and statistical significance. Pathways numbered in the plot have the greatest influence and significance in distinguishing between the groups. (**A**) *Paenibacillus amylolyticus*; 1—D-amino acid metabolism; 2—arginine biosynthesis; 3—arginine and proline metabolism; 4—glycine, serine, and threonine metabolism; 5—purine metabolism; 6—cyanoamino acid metabolism; 7—tyrosine metabolism; 8—alanine, aspartate, and glutamate metabolism; 9—pyrimidine metabolism; (**B**) *Bacillus cereus*, 1—tyrosine metabolism; 2—taurine and hypotaurine metabolism; 3—alanine, aspartate, and glutamate metabolism; (**C**) *Fusarium graminarum*; 1—alanine, aspartate, and glutamate metabolism; 2—arginine biosynthesis; 3—purine metabolism; 4—butanoate metabolism; 5—lysine biosynthesis; 6—glyoxylate and dicarboxylate metabolism; 7—pyruvate metabolism; 8—citrate cycle (TCA cycle).

The identified metabolic pathways, including the key metabolites and their statistical significance, are presented in Tables S3–S5. The results of pathway enrichment analysis results are presented in Figure 2.

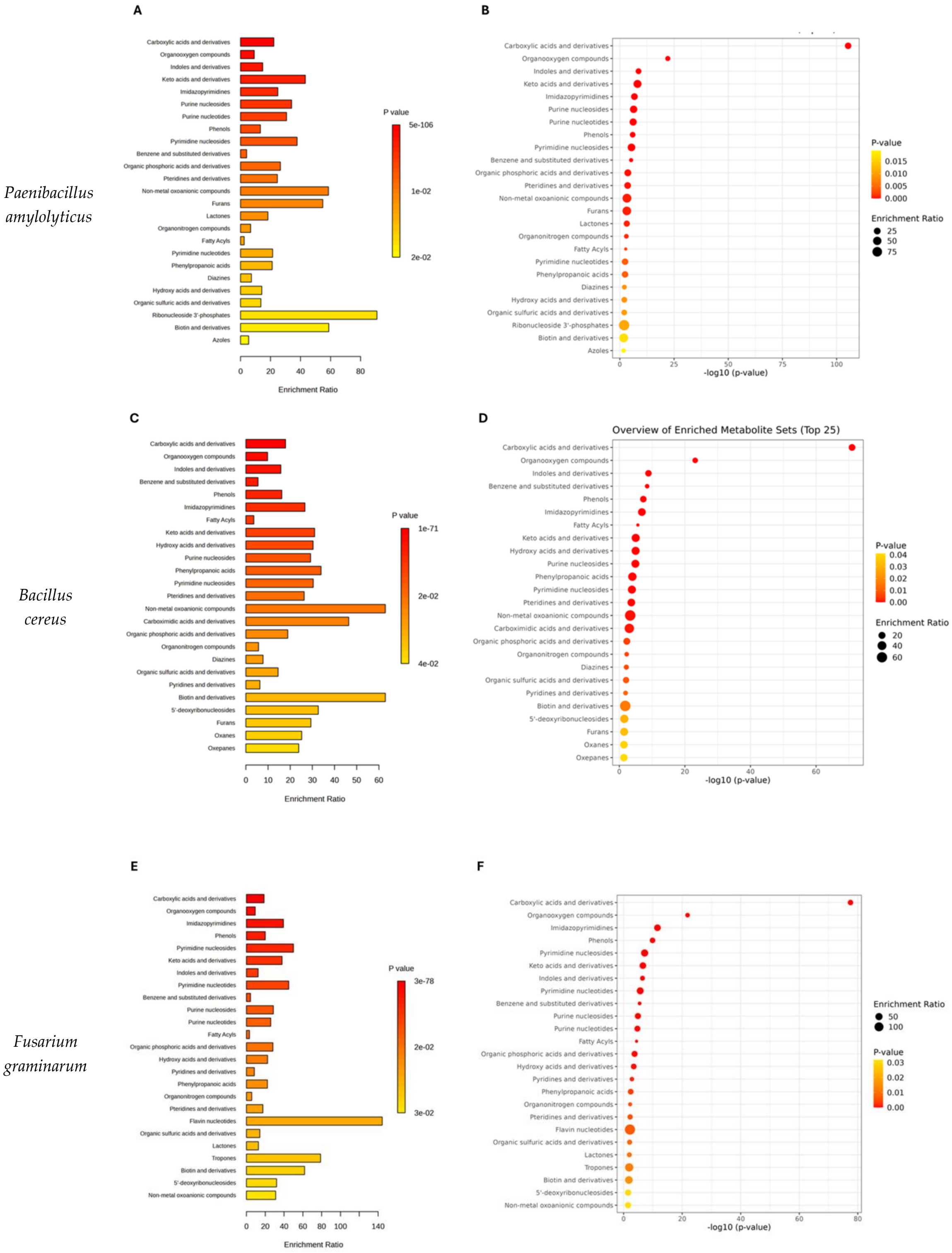

Figure 2. Pathway enrichment analysis results for the tested microorganisms based on chemical compound classes. (**A**,**C**,**E**) Bar plots of enriched chemical classes showing the enrichment ratio for each class. (**B**,**D**,**F**) Bubble plots illustrating the pathway impact with the corresponding −log10(*p*-value). (**A**,**B**) data for *Paenibacillus amylolyticus*, (**C**,**D**) data for *Bacillus cereus*, (**E**,**F**) data for *Fusarium graminarum*. Larger bubbles represent higher enrichment ratios. The color scale indicates statistical significance (*p*-value), with red indicating higher significance.

In total, 34 metabolite sets were identified for *P. amylolyticus*, and 38 sets were identified for *B. cereus* (Supplementary Materials Tables S6 and S7). For *F. graminarum,* 37 metabolite sets were found (Table S8). The bacteria metabolite profile was dominated by carboxylic acids and derivatives (39.9% of detected compounds for *P. amylolyticus* and 32.2% for *B. cereus*), organooxygen compounds (13.8% and 14.8%), benzene and substituted derivatives (5.9% and 8%), fatty acyls (5.5% and 8%), and indoles and derivatives (4.0% and 4.2%). The remaining metabolite sets accounted for less than 2.8% of hits in the *P. amylolyticus* profile and less than 3.4.% for *B. cereus* (Figure 2A,B, Tables S6 and S7). Similarly, the dominant metabolites detected for the mold *F. graminarum* were carboxylic acids and derivatives (33.8%), organooxygen compounds (14.2%), fatty acyls (7.1%), benzene and substituted derivatives (6.2%), and indoles and derivatives (3.3%). Large proportions of phenols (4.2%) and imidazopyrimidines (3.8%) were also detected, while other metabolites accounted for less than 2.1% (Figure 2C, Table S8). The most discriminating compounds between analyzed microorganism sets were visualized using volcano plots (Figures S2 and S3). Furthermore, the differences in the abundance of these compounds are illustrated by box plots (Figures S4 and S5).

3. Materials and Methods

3.1. Microorganisms

The study used two strains of genetically identified environmental bacteria: *Paenibacillus amylolyticus* (NCBI genome assembly number ASM4051371v1) and *Bacillus cereus* (NCBI genome assembly number ASM4309929v1). The strains were isolated from soil (corn plantation located in Central Poland, 2023 year). The strains were deposited in the collection of pure cultures of the Department of Environmental Biotechnology, Lodz University of Technology (Lodz, Poland). The tested mold strain was *Fusarium graminarum* IOR 1540 (one of the most common fungal pathogens of maize). The strains were sourced from the Institute of Plant Protection—National Research Institute in Poznan (Poznan, Poland).

3.2. Microbial Cultures

The bacteria were cultured together with the mold strain (in pairs). Cultures were prepared pointwise with a distance of 5 cm between the bacteria and mold on petri dishes containing TSA agar medium (Tryptic Soy Agar, Merck-Millipore, Poznan, Poland). Samples were prepared in four replicates. The microorganisms were incubated at 30 ± 2 °C for 3 days. Portions of the agar medium with microorganisms measuring 20–30 × 20–30 mm in size (shown in Figure 3) were cut using stainless steel blades and transferred to stainless steel plates (45 × 35 × 0.8 mm) for use in MSI experiments.

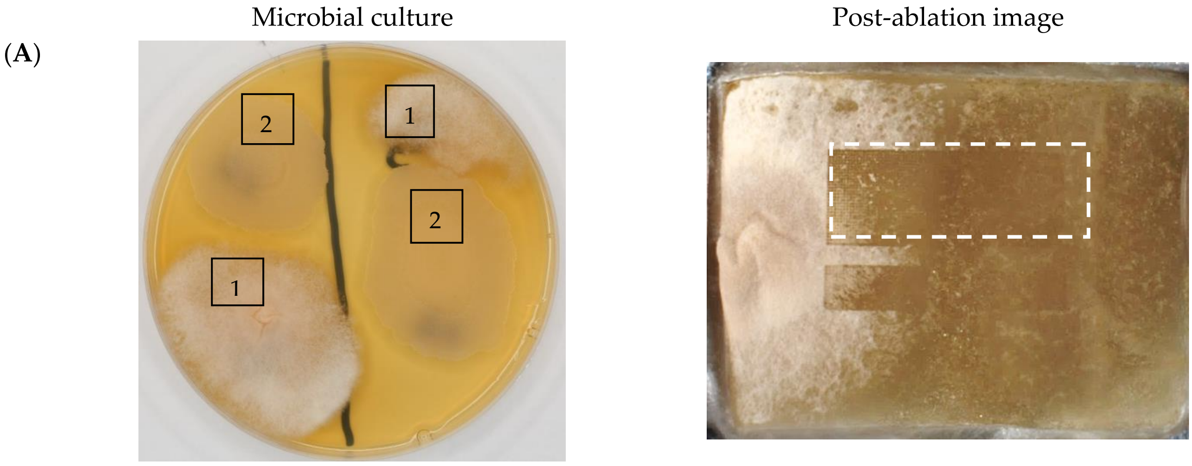

Figure 3. *Cont.*

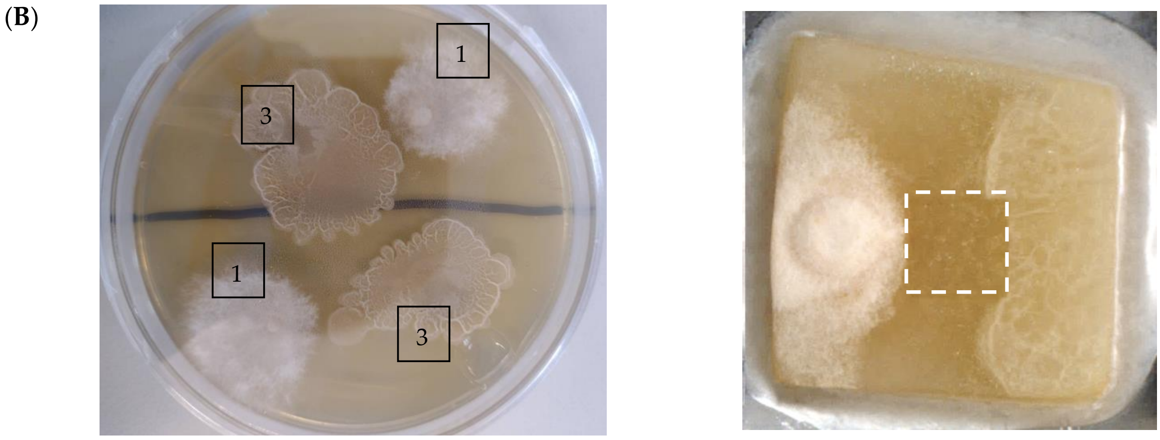

Figure 3. Tested agar medium samples used in MSI experiments: (**A**) *Fusarium graminarum* (1) and *Bacillus cereus* (2); (**B**) *Fusarium graminarum* (1) and *Paenibacillus amylolyticus* (3). Dashed line areas represent imaged regions.

3.3. Mass Spectrometry Imaging (MSI) Experiments

3.3.1. LARAPPI/CI MSI System

The laser ablation remote atmospheric pressure photoionization/chemical ionization (LARAPPI/CI) platform coupled to an ultra-high-resolution quadrupole-time-of-flight (QToF) mass spectrometer (LARAPPI/CI MSI system) first described in a recent publication [25] is based on an airtight chamber pressurized with nitrogen gas to produce a nitrogen stream of 10 L/min. The sample (Figure 3) is placed on a 50 × 50 mm sample stage, with a Peltier cooling plate that sustains the sample at −18 °C. The temperature-controlled sample stage is mounted on a motorized high-speed XY stage. The pulsed beam from the OPO laser (2.93 µm, 7 ns, 20 Hz, 3.5 mJ/pulse) enters the sample chamber through sapphire window. Then, the beam is expanded 3.75× and is redirected toward the sample stage by a gold mirror. The beam then goes through a diffractive optical element forming square-shape top-hat beam. It is then focused onto the sample surface by a 50 mm focal length aspherical ZnSe lens (ThorLabs, Mölndal, Sweden). The optical assembly and also the camera with the lens and distance sensor are mounted on aluminum rails and are in a fixed configuration; the only moving parts are XYZ stages. During imaging, the laser focal point remains fixed in space, whereas the sample is moved. A specially designed gas funnel is also a focusing assembly and is connected to a 6/4 mm (O.D/I.D.) PTFE tube. The overpressure in the chamber drives a 10 L/min nitrogen gas flow through the tube. The laser ablation plumes are entrained into the gas and transported to the modified ion source (Bruker VIP HESI in the APCI configuration) of the Bruker Impact II mass spectrometer (Bruker Daltonik GmbH, Bremen, Germany). The ion source also had a VUV source (Hamamatsu L12542) (Hamamatsu Photonics K.K., Iwata City, Japan) mounted axially to the MS sampling cone inside the ion source. A HPLC pump (Agilent G1312A) (Agilent Technologies, Santa Clara, CA, USA) provides a steady flow of a solvent mixture (1% toluene in methanol; 200 µL/min) to the APCI needle [25]. The settings of the ion source were as follows: APCI nebulizer, end-plate offset 600 V, capillary 1000 V, corona 6000 nA, nebulizer 3.5 bar, dry gas 0.2 L/min, dry temperature 250 °C, probe gas temperature 350 °C, probe gas 4 L/min, exhaust turned on. MS1 experiments were performed with the following settings: scan range *m*/*z* 47–1300.

3.3.2. Direct Three-Dimensional Mass Spectrometry Imaging (MSI 3D)

The spatial resolution for 3D MSI experiment was 140 µm with applied oversampling. Each pixel/voxel in 3D MSI experiments was exposed to the laser for 0.5 s, at a laser pulse repetition rate of 20 Hz. The delays between pixels were 1200 ms. Between pixels, the sample stage moved at a speed of 50 mm/s. The time delay between lines was 3 s. Each 3D experiment was carried out in an inverted pyramid ablation scheme [25].

The 3D MSI experiment (Figure 3B, Table 6) performed on sample containing *Paenibacillus amylolyticus* and *Fusarium graminarum* had a top ablation level of 35 × 35 (X × Y) voxel arrangement, second (lower) level—34 × 34, with ablation levels at 3.25, 3.00 mm for top level and lower levels, respectively. The starting object was of ca. 3.25 mm thickness and 19.2 × 18.6 mm (X × Y) size, while the analyzed area was of 4.8 × 4.8 mm (X × Y) size. The objects were cut with a blade and placed on a stainless-steel plate and then on an ablation table inside the chamber and frozen.

3.3.3. Two-Dimensional Mass Spectrometry Imaging (MSI 2D)

The spatial resolution for 2D MSI experiment was 240 µm without oversampling. Each pixel/voxel in 2D MSI experiments was exposed to the laser for 1 s at a laser pulse repetition rate of 20 Hz. The delays between pixels were 1200 ms. Between pixels, the sample stage moved at a speed of 50 mm/s. The time delay between lines was 5 s [25]. The 2D MSI experiment (Figure 3A) performed on sample containing *Paenibacillus amylolyticus* and *Fusarium graminarum* had a top ablation level of 77 × 31 (X × Y) voxel arrangement, with the ablation level at 4.50 mm. The starting object was of ca. 4.5 mm thickness and 34 × 28 mm size, and the analyzed region was 18.2 × 7.2 mm (X × Y) size. The objects were cut with a blade and placed on a stainless-steel plate and then on an ablation table inside the chamber and frozen.

3.4. Ultra-High-Performance Liquid Chromatography–Ultra-High-Resolution Mass Spectrometry (UHPLC–UHRMS)

3.4.1. LC–MS Sample Preparation

Metabolomic profiling was performed on medium samples from both regions of each Petri dish with microorganism growth. Approximately 200 mg of the sample was weighed and cut into small pieces. To the sample pieces, 150 µL of distilled water and 900 µL of acetone (Sigma-Aldrich, Poznan, Poland LC–MS grade) were added. At the same time, 3 stainless beads were added to this suspension, and the samples were homogenized 3 times for one minute with BeadBug 6 (Benchmark Scientific, Sayreville, NJ, USA) at 4000 rpm. Then, the samples were incubated at temp. 4 °C overnight. The following day, the samples were centrifuged (mySPIN™ 12 Mini Centrifuge, Thermo Fisher Scientific, Waltham, MA, USA; temp. 4°C, 14,000× *g*, 5 min). The supernatant of each sample was transferred, and the samples were left in a speed vac-type apparatus (2 × 10^{-3} mbar vacuum) overnight. The next day, the dried pellet was dissolved in methanol (800 µL). To facilitate dissolution, the samples were sonicated and then centrifuged for 5 min at 14,000× *g*, and the resulting supernatants were transferred to a standard HPLC vials.

3.4.2. LC–MS Metabolomic Analysis

Mass spectrometry–liquid chromatography analyses were performed on a Bruker Elute UHPLC system operated by Hystar 3.3 software and an ultra-high-resolution (60,000+) mass spectrometer Bruker Impact II (Bruker Daltonik GmbH, Bremen, Germany) ESI QTOF-MS equipped with Data Analysis 4.2 (Bruker Daltonik GmbH, Bremen, Germany), TASQ (2022b), and Metaboscape (2022b). The ion source used was a Bruker VIP-HESI with optimized flows and temperatures. The column used for AutoMSMS measurements was Waters Acquity UPLC BEH C18 1.7 µm particles of 2.1 × 50 mm dimensions (Waters Poland, Gdansk, Poland). For AutoMSMS measurements flows and percentages were 0 and 0.56 min 99% A, 4.72 min—1% A, 5.56 min—1% A, and 5.60, 6.34, and 9.45 min—99% A, all flows at 450 µLmin^{-1} (Ossoliński et al., 2024; Szulc et al., 2024; Nizioł et al., 2024) [77–79]. The column was held at 40 °C.

The column exit was connected to the VIP HESI ion source. Internal calibration on 10 mM sodium formate (water–isopropanol 1:1 v/v) ions was performed automatically in Metaboscape with the use of a syringe pump at an infusion flow rate of 0.12 mL h^{-1}, using a high-precision calibration (HPC) mode. The autoMSMS method was used with an m/z range 50–1500; CID (Collision-Induced Dissociation) was used with the following settings: absolute area threshold: 5000 counts; active exclusion 2 spectra; release after 0.3 min, isolation mass: for m/z = 100, the width was 4; for 300, the width was 5; for 500, the width was 6; for 1000, the width was 8; collision energy value was 30 eV.

The untargeted annotations were performed in Metaboscape (ver. 2022b) with a criterion of mass deviation ($\Delta m/z$) under 2 ppm and mSigma value (isotopic fit score based on the relative mean square of the difference of an experimental mass spectrum from the theoretical isotopic pattern of a specific molecular formula) under 30 as the maximum acceptable deviation of the mass of the compound and the isotopic pattern, respectively. All the molecular formulas were obtained using the Smart Formula tool (Metaboscape v. 2022b) and the C, H, N, O, P, S, Cl, Br, I, and F elements. MSMS spectra were automatically matched with MSMS libraries: Bruker HMDB 2.0 library, MassBank of North America (MoNA) library, and NIST ver. 2020 MSMS library. For compounds annotated in Metaboscape, 2D and 3D ion images were generated. Compounds were identified by LARAPPI/CI-MSI based on acquired LC–MS data and basic metabolites from Ideom database and their representing ion images for microorganisms.

3.4.3. Statistical Analysis

All metabolite datasets exported from Metaboscape v.2022b were analyzed using MetaboAnalyst 6.0 (Pang et al., 2024) [80]. Volcano plots were generated with a fold change threshold (>2 or <0.5) and a p-value cutoff (<0.05) to highlight metabolites showing statistically significant differences in abundance. To identify the affected metabolic pathways, pathway impact analysis was performed using the KEGG pathway library of *Bacillus subtilis subsp. Subtilis* for bacteria and the KEGG pathway library of *Aspergillus clavatus* for fungal strain, as well as the Small Molecule Pathway Database (SMPD). Pathways were ranked based on statistical p-values, Holm-adjusted p-values, and FDR from pathway topology analysis.

4. Conclusions

In this study, the LARAPPI/CI-MSI 3D method was used for the first time to generate ion images of bacterial and fungal metabolites in solid culture media. The LARAPPI/CI MSI mass spectrometry imaging method enabled the assessment of the spatial distribution within the colony and in the growth medium. The studied bacteria and fungi produced metabolites belonging to various chemical groups, including amino acids and derivatives, dipeptides, organic acids, fatty acids, sugars and sugar derivatives, benzene derivatives, and indoles. The LARAPPI/CI-MSI 3D method was found to be more precise than LARAPPI/CI-MSI 2D, opening new possibilities for the metabolic profiling of strains in target growth conditions/media, such as depth profiling in the absence/presence of stress factors affecting the metabolic profile. This innovative method can be used for the rapid screening of the biotechnological potential of environmental strains, facilitating the search for industrially valuable biomolecules.

Supplementary Materials: The following supporting information can be downloaded at https://www.mdpi.com/article/10.3390/molecules30061317/s1: Table S1. LARAPPI/CI-MSI 2D ion images of metabolites from the tested microbial culture; Table S2. LARAPPI/CI-MSI 3D ion images of bacterial and fungal metabolites from *Paenibacillus amylolyticus* (right) and *Fusarium graminarum* (left) cultures; Table S3. Pathway enrichment analysis of metabolites in *Paenibacillus amylolyticus*, highlighting the matched pathways, key metabolites, and statistical significance for each metabolic pathway; Table S4. Pathway enrichment analysis of metabolites in *Bacillus cereus*, highlighting the matched pathways, key metabolites, and statistical significance for each metabolic pathway; Table S5. Pathway enrichment analysis of metabolites in *Fusarium graminarum*, highlighting the matched pathways, key metabolites, and statistical significance for each metabolic pathway; Table S6. Enrichment analysis of main-class chemical structures in *Paenibacillus amylolyticus*; Table S7. Enrichment analysis of main-class chemical structures in *Bacillus cereus*; Table S8. Enrichment analysis of main-class chemical structures in *Fusarium graminarum*; Table S9. LC–MS data supporting generated LARAPPI/CI-MSI 2D and LARAPPI/CI-MSI 3D ion images. Figure S1. MS spectra of top ablation level of 3D MSI. Upper spectrum represents one voxel for *P. amylolyticus* area, bottom for *F. graminarum* medium area. Figure S2. Volcano plot displaying the most discriminating compounds between *Paenibacillus amylolyticus* and *Fusarium graminearum*, identified from microbial extracts analyzed using UHPLC–HRMS and visualized by LARAPPI/CI-MSI 3D. Figure S3. Volcano plot displaying the most discriminating compounds between Bacillus cereus and Fusarium graminearum, identified from microbial extracts analyzed using UHPLC–HRMS and visualized by LARAPPI/CI-MSI 3D. Figure S4. Box plots of the most discriminating compounds between *Paenibacillus amylolyticus* (P.A.) and *Fusarium graminearum* (F.G.) identified from microbial extracts analyzed using UHPLC–HRMS and visualized by 3D LARAPPI/CI-MSI. Figure S5. Box plots of the most discriminating compounds between *Fusarium graminearum* (F.G.) and *Bacillus cereus* (B.C.), identified from microbial extracts analyzed using UHPLC–HRMS and visualized by 3D LARAPPI/CI-MSI.

Author Contributions: Conceptualization, T.R. and J.S.; methodology, T.R., J.N. and J.S.; software, T.R. and J.N.; validation, T.R., J.N. and J.S.; formal analysis, J.N. and S.K.; investigation, S.K., J.N., T.R. and W.S.; resources, T.R. and J.N.; data curation, S.K.; writing—original draft preparation, J.S. and T.G.; writing—review and editing, J.S. and T.G.; visualization, T.R., J.N. and T.G.; supervision, J.S. and T.R.; project administration, J.N. and J.S.; funding acquisition, J.N. and J.S. All authors have read and agreed to the published version of the manuscript.

Funding: This work was supported by the Agency for Restructuring and Modernization of Agriculture, Poland, grant number 00077.DDD.6509.000167.2022.05. The authors gratefully acknowledge support from the National Science Centre (Poland) research project Sonata Bis number 2022/46/E/ST4/00016.

Institutional Review Board Statement: Not applicable.

Informed Consent Statement: Not applicable.

Data Availability Statement: The datasets generated during and/or analyzed during the current study are available from the corresponding author upon request and in the RepOD open data repository (DOI: https://doi.org/10.18150/YCUODU).

Acknowledgments: We appreciate all the individuals for participating in this study, especially Dominik Ruman for working on software for this project. This article was completed while the second author was a doctoral candidate at the Interdisciplinary Doctoral School at Lodz University of Technology, Poland.

Conflicts of Interest: The authors declare no conflicts of interest.

Abbreviations

The following abbreviations are used in this manuscript:

UHPLC	Ultra-high-performance liquid chromatography
UHRMS	Ultra-high-resolution mass spectrometry
LARAPPI/CI	Laser ablation remote atmospheric pressure photoionization/chemical ionization
MSI	Mass spectrometry imaging
APCI	Atmospheric pressure chemical ionization
ESI	Electrospray ionization

References

1. Fouillaud, M.; Dufossé, L. Microbial Secondary Metabolism and Biotechnology. *Microorganisms* **2022**, *10*, 123. [CrossRef]
2. Bano, A.; Qadri, T.A.; Mahnoor; Khan, N. Bioactive Metabolites of Plants and Microbes and Their Role in Agricultural Sustainability and Mitigation of Plant Stress. *S. Afr. J. Bot.* **2023**, *159*, 98–109. [CrossRef]
3. Demain, A.L. Reviews: The Business of Biotechnology. *Ind. Biotechnol.* **2007**, *3*, 269–283. [CrossRef]
4. Singh, R.; Kumar, M.; Mittal, A.; Mehta, P.K. Microbial Metabolites in Nutrition, Healthcare and Agriculture. *3 Biotech* **2017**, *7*, 15. [CrossRef]
5. Rusu, A.V.; Trif, M.; Rocha, J.M. Microbial Secondary Metabolites via Fermentation Approaches for Dietary Supplementation Formulations. *Molecules* **2023**, *28*, 6020. [CrossRef]
6. Shimizu, S. Vitamins and Related Compounds: Microbial Production. In *Biotechnology Set*; Rehm, H.-J., Reed, G., Eds.; Wiley: Hoboken, NJ, USA, 2001; pp. 318–340. ISBN 978-3-527-25762-1.
7. Gurung, N.; Ray, S.; Bose, S.; Rai, V. A Broader View: Microbial Enzymes and Their Relevance in Industries, Medicine, and Beyond. *BioMed Res. Int.* **2013**, *2013*, 329121. [CrossRef] [PubMed]
8. Zafar, A.; Mahmood, Z.A. Microbial Amino Acids Production. In *Microbial Biotechnology—Progress and Trends*; CRC Press: Boca Raton, FL, USA, 2015.
9. Sun, X.; Shen, X.; Jain, R.; Lin, Y.; Wang, J.; Sun, J.; Wang, J.; Yan, Y.; Yuan, Q. Synthesis of Chemicals by Metabolic Engineering of Microbes. *Chem. Soc. Rev.* **2015**, *44*, 3760–3785. [CrossRef] [PubMed]
10. Ruiz, B.; Chávez, A.; Forero, A.; García-Huante, Y.; Romero, A.; Sánchez, M.; Rocha, D.; Sánchez, B.; Rodríguez-Sanoja, R.; Sánchez, S.; et al. Production of Microbial Secondary Metabolites: Regulation by the Carbon Source. *Crit. Rev. Microbiol.* **2010**, *36*, 146–167. [CrossRef]
11. Bentley, R. Microbial Secondary Metabolites Play Important Roles in Medicine; Prospects for Discovery of New Drugs. *Perspect. Biol. Med.* **1997**, *40*, 364–394. [CrossRef]
12. Demain, A.L.; Sanchez, S. Microbial Drug Discovery: 80 Years of Progress. *J. Antibiot.* **2009**, *62*, 5–16. [CrossRef]
13. Silva Dias, B.H.; Jung, S.-H.; Castro Oliveira, J.V.D.; Ryu, C.-M. C4 Bacterial Volatiles Improve Plant Health. *Pathogens* **2021**, *10*, 682. [CrossRef] [PubMed]
14. Lee, D.A.; Lee, T.C.; Cortes, A.E.; Kitada, S. Effects of Mithramycin, Mitomycin, Daunorubicin, and Bleomycin on Human Subconjunctival Fibroblast Attachment and Proliferation. *Invest. Ophthalmol. Vis. Sci.* **1990**, *31*, 2136–2144.
15. Deshmukh, S.K.; Prakash, V.; Ranjan, N. Marine Fungi: A Source of Potential Anticancer Compounds. *Front. Microbiol.* **2018**, *8*, 2536. [CrossRef] [PubMed]
16. Tinôco, D.; Seldin, L.; Coutinho, P.L.D.A.; Freire, D.M.G. Strategies to Reduce the Culture Medium Costs for a High-yield and High-selectivity Bio-based 2,3-butanediol Production. *Biofuels Bioprod. Biorefining* **2025**, *19*, 85–108. [CrossRef]
17. Tamano, K. Enhancing Microbial Metabolite and Enzyme Production: Current Strategies and Challenges. *Front. Microbiol.* **2014**, *5*, 718. [CrossRef]
18. Szulc, J.; Otlewska, A.; Ruman, T.; Kubiak, K.; Karbowska-Berent, J.; Kozielec, T.; Gutarowska, B. Analysis of Paper Foxing by Newly Available Omics Techniques. *Int. Biodeterior. Biodegrad.* **2018**, *132*, 157–165. [CrossRef]
19. Szulc, J.; Karbowska-Berent, J.; Drążkowska, A.; Ruman, T.; Beech, I.; Sunner, J.A.; Gutarowska, B. Metabolomics and Metagenomics Analysis of 18th Century Archaeological Silk. *Int. Biodeterior. Biodegrad.* **2021**, *156*, 105120. [CrossRef]
20. Welker, M.; Moore, E.R.B. Applications of Whole-Cell Matrix-Assisted Laser-Desorption/Ionization Time-of-Flight Mass Spectrometry in Systematic Microbiology. *Syst. Appl. Microbiol.* **2011**, *34*, 2–11. [CrossRef]
21. Carbonnelle, E.; Mesquita, C.; Bille, E.; Day, N.; Dauphin, B.; Beretti, J.-L.; Ferroni, A.; Gutmann, L.; Nassif, X. MALDI-TOF Mass Spectrometry Tools for Bacterial Identification in Clinical Microbiology Laboratory. *Clin. Biochem.* **2011**, *44*, 104–109. [CrossRef]
22. Gautier, M.; Ranque, S.; Normand, A.-C.; Becker, P.; Packeu, A.; Cassagne, C.; L'Ollivier, C.; Hendrickx, M.; Piarroux, R. Matrix-Assisted Laser Desorption Ionization Time-of-Flight Mass Spectrometry: Revolutionizing Clinical Laboratory Diagnosis of Mould Infections. *Clin. Microbiol. Infect.* **2014**, *20*, 1366–1371. [CrossRef]
23. Szulc, J.; Ruman, T. Laser Ablation Remote-Electrospray Ionisation Mass Spectrometry (LARESI MSI) Imaging—New Method for Detection and Spatial Localization of Metabolites and Mycotoxins Produced by Moulds. *Toxins* **2020**, *12*, 720. [CrossRef]
24. Szulc, J.; Jablonskaja, I.; Jabłońska, E.; Ruman, T.; Karbowska-Berent, J.; Gutarowska, B. Metabolomics and Metagenomics Characteristic of Historic Beeswax Seals. *Int. Biodeterior. Biodegrad.* **2020**, *152*, 105012. [CrossRef]
25. Ruman, T.; Krupa, Z.; Nizioł, J. Direct Three-Dimensional Mass Spectrometry Imaging with Laser Ablation Remote Atmospheric Pressure Photoionization/Chemical Ionization. *Anal. Chem.* **2024**, *96*, 13326–13334. [CrossRef]
26. Shen, Y.; Wang, Y.; Wang, J.; Xie, P.; Xie, C.; Chen, Y.; Banaei, N.; Ren, K.; Cai, Z. High-Resolution 3D Spatial Distribution of Complex Microbial Colonies Revealed by Mass Spectrometry Imaging. *J. Adv. Res.* **2024**, in press. [CrossRef]
27. Krupa, S.; Ruman, T.; Szuberla, W.; Nizioł, J. Analysis of the Spatial Distribution of Metabolites in Aloe Vera Leaves by Mass Spectrometry Imaging and UHPLC-UHRMS. *Sci. Rep.* **2025**, *15*, 3502. [CrossRef] [PubMed]
28. Wischmeyer, P.E. Clinical Applications of L-Glutamine: Past, Present, and Future. *Nutr. Clin. Pr.* **2003**, *18*, 377–385. [CrossRef]

29. Piattoly, T.; Parish, T.R.; Welsch, M.A. L-Glutamine Supplementation: Effects on Endurance, Power and Recovery. *Curr. Top. Nutraceutical Res.* **2013**, *11*, 55–62.
30. Grady, E.N.; MacDonald, J.; Liu, L.; Richman, A.; Yuan, Z.-C. Current Knowledge and Perspectives of Paenibacillus: A Review. *Microb. Cell Factories* **2016**, *15*, 203. [CrossRef]
31. Xing, S.-C.; Mi, J.-D.; Chen, J.-Y.; Hu, J.-X.; Liao, X.-D. Metabolic Activity of Bacillus Coagulans R11 and the Health Benefits of and Potential Pathogen Inhibition by This Species in the Intestines of Laying Hens under Lead Exposure. *Sci. Total Environ.* **2020**, *709*, 134507. [CrossRef]
32. Thapa, P.; Thapa, A.; Khadka, S.; Sapkota, S.; Panta, O.P.; Sharma, S.; Karki, T.B.; Poudel, P. Screening and Characterization of Potent Poly Glutamic Acid Producing Bacillus Sp. Isolated from Kinema, Water and Soil Samples. *Heliyon* **2021**, *7*, e07715. [CrossRef]
33. Lawal, A.K.; Oso, B.A.; Sanni, A.I.; Olatunji, O.O. L-Glutamic Acid Production by Bacillus Spp. Isolated from Vegetable Proteins. *Afr. J. Biotechnol.* **2011**, *10*, 5337–5345.
34. Harper, M.S.; Amanda Shen, Z.; Barnett, J.F.; Krsmanovic, L.; Dakoulas, E.W.; Delaney, B. Toxicology Studies with N-Acetylglycine. *Food Chem. Toxicol.* **2010**, *48*, 1321–1327. [CrossRef]
35. Dzierzbicka, K. Synthesis of 2,6-Diaminopimelic Acid (DAP) and Its Analogues. *ChemInform* **2007**, *38*. [CrossRef]
36. Bach, T.M.H.; Takagi, H. Properties, Metabolisms, and Applications of l-Proline Analogues. *Appl. Microbiol. Biotechnol.* **2013**, *97*, 6623–6634. [CrossRef]
37. Aiyelabola, T.O.; Isabirye, D.A.; Akinkunmi, E.O.; Ogunkunle, O.A.; Ojo, I.A.O. Synthesis, Characterization, and Antimicrobial Activities of Coordination Compounds of Aspartic Acid. *J. Chem.* **2016**, *2016*, 1–8. [CrossRef]
38. Bahri, S.; Zerrouk, N.; Aussel, C.; Moinard, C.; Crenn, P.; Curis, E.; Chaumeil, J.-C.; Cynober, L.; Sfar, S. Citrulline: From Metabolism to Therapeutic Use. *Nutrition* **2013**, *29*, 479–484. [CrossRef] [PubMed]
39. Friedman, M. Analysis, Nutrition, and Health Benefits of Tryptophan. *Int. J. Tryptophan Res.* **2018**, *11*, 1178646918802282. [CrossRef] [PubMed]
40. Comai, S.; Bertazzo, A.; Brughera, M.; Crotti, S. Tryptophan in Health and Disease. In *Advances in Clinical Chemistry*; Elsevier: Amsterdam, The Netherlands, 2020; Volume 95, pp. 165–218. ISBN 978-0-12-821165-6.
41. Kreider, R.B.; Stout, J.R. Creatine in Health and Disease. *Nutrients* **2021**, *13*, 447. [CrossRef]
42. Esmahan, C.; Alvarez, E.; Montenegro, E.; Martin, J.F. Catabolism of Lysine in Penicillium Chrysogenum Leads to Formation of 2-Aminoadipic Acid, a Precursor of Penicillin Biosynthesis. *Appl. Environ. Microbiol.* **1994**, *60*, 1705–1710. [CrossRef]
43. Eswaranandam, S.; Hettiarachchy, N.S.; Johnson, M.G. Antimicrobial Activity of Citric, Lactic, Malic, or Tartaric Acids and Nisin-incorporated Soy Protein Film Against *Listeria monocytogenes*, *Escherichia coli* O157:H7, and *Salmonella gaminara*. *J. Food Sci.* **2004**, *69*, FMS79–FMS84. [CrossRef]
44. Villeneuve, P.; Barēa, B.; Sarrazin, P.; Davrieux, F.; Boulanger, R.; Caro, Y.; Figueroa-Espinoza, M.C.; Pina, M.; Graille, J. Synthesis of Pyroglutamic Acid Fatty Esters through Lipase-Catalyzed Esterification with Medium Chains Alcohols. *Enzym. Microb. Technol.* **2003**, *33*, 79–84. [CrossRef]
45. Urbanek, A.; Szadziewski, R.; Stepnowski, P.; Boros-Majewska, J.; Gabriel, I.; Dawgul, M.; Kamysz, W.; Sosnowska, D.; Gołębiowski, M. Composition and Antimicrobial Activity of Fatty Acids Detected in the Hygroscopic Secretion Collected from the Secretory Setae of Larvae of the Biting Midge Forcipomyia Nigra (Diptera: Ceratopogonidae). *J. Insect Physiol.* **2012**, *58*, 1265–1276. [CrossRef]
46. Raybaudi-Massilia, R.M.; Mosqueda-Melgar, J.; Martín-Belloso, O. Antimicrobial Activity of Malic Acid against Listeria Monocytogenes, Salmonella Enteritidis and Escherichia Coli O157:H7 in Apple, Pear and Melon Juices. *Food Control* **2009**, *20*, 105–112. [CrossRef]
47. Ling, N.; Raza, W.; Ma, J.; Huang, Q.; Shen, Q. Identification and Role of Organic Acids in Watermelon Root Exudates for Recruiting Paenibacillus Polymyxa SQR-21 in the Rhizosphere. *Eur. J. Soil Biol.* **2011**, *47*, 374–379. [CrossRef]
48. In, Y.; Kim, J.; Kim, H.; Oh, S. Antimicrobial Activities of Acetic Acid, Citric Acid and Lactic Acid against S. *higella* Species. *J. Food Saf.* **2013**, *33*, 79–85. [CrossRef]
49. Tadi, S.R.R.; Nehru, G.; Sivaprakasam, S. Microbial Production of Pantothenic Acid. In *Microbial Production of Food Bioactive Compounds*; Jafari, S.M., Harzevili, F.D., Eds.; Springer International Publishing: Cham, Switzerland, 2022; pp. 1–18. ISBN 978-3-030-81403-8.
50. Mohan, A.; Purohit, A.S. Anti-Salmonella Activity of Pyruvic and Succinic Acid in Combination with Oregano Essential Oil. *Food Control* **2020**, *110*, 106960. [CrossRef]
51. Mani-López, E.; Arrioja-Bretón, D.; López-Malo, A. The Impacts of Antimicrobial and Antifungal Activity of Cell-free Supernatants from Lactic Acid Bacteria in Vitro and Foods. *Comp. Rev. Food Sci. Food Safe* **2022**, *21*, 604–641. [CrossRef]
52. Unver, T. A Preliminary Study of Fumaric Acid, Called Allomaleic Acid, as a Pharmaceutical Antimicrobial Compound. *Med. Sci. Int. Med. J.* **2024**, *13*, 383. [CrossRef]

53. Garg, A.; Jers, C.; Hwang, H.J.; Kalantari, A.; Ventina, I.; Mijakovic, I. Engineering Bacillus Subtilis for Production of 3-Hydroxypropanoic Acid. *Front. Bioeng. Biotechnol.* **2023**, *11*, 1101232. [CrossRef]
54. Secara, N.; Duca, G.; Vlad, L.; Macaev, F. Observations on the Antioxidant Activity of Novel Dihydroxyfumaric Acid Derivatives. *Chem. J. Mold.* **2010**, *5*, 59–67. [CrossRef]
55. Yang, S.Y.; Park, M.R.; Kim, I.S.; Kim, Y.C.; Yang, J.W.; Ryu, C.-M. 2-Aminobenzoic Acid of *Bacillus* sp. BS107 as an ISR Determinant against *Pectobacterium carotovorum* subsp. carotovotrum SCC1 in Tobacco. *Eur. J. Plant Pathol.* **2011**, *129*, 371–378. [CrossRef]
56. Lei, H.-M.; Wang, J.-T.; Hu, Q.-Y.; Li, C.-Q.; Mo, M.-H.; Zhang, K.-Q.; Li, G.-H.; Zhao, P.-J. 2-Furoic Acid Associated with the Infection of Nematodes by *Dactylellina haptotyla* and Its Biocontrol Potential on Plant Root-Knot Nematodes. *Microbiol. Spectr.* **2023**, *11*, e01896-23. [CrossRef]
57. Tangerina, M.M.P.; Furtado, L.C.; Leite, V.M.B.; Bauermeister, A.; Velasco-Alzate, K.; Jimenez, P.C.; Garrido, L.M.; Padilla, G.; Lopes, N.P.; Costa-Lotufo, L.V.; et al. Metabolomic Study of Marine Streptomyces Sp.: Secondary Metabolites and the Production of Potential Anticancer Compounds. *PLoS ONE* **2020**, *15*, e0244385. [CrossRef]
58. Alves, L.D.F.; Moore, J.B.; Kell, D.B. The Biology and Biochemistry of Kynurenic Acid, a Potential Nutraceutical with Multiple Biological Effects. *Int. J. Mol. Sci.* **2024**, *25*, 9082. [CrossRef] [PubMed]
59. Kumar, A.; Rao, R.; Yadav, P. Azelaic Acid: A Promising Agent for Dermatological Applications. *Curr. Drug Ther.* **2020**, *15*, 181–193. [CrossRef]
60. Haghpanah, M.; Jelodar, N.B.; Zarrini, H.N.; Pakdin-Parizi, A.; Dehestani, A. New Insights into Azelaic Acid-Induced Resistance against Alternaria Solani in Tomato Plants. *BMC Plant Biol.* **2024**, *24*, 687. [CrossRef] [PubMed]
61. Todea, A.; Deganutti, C.; Spennato, M.; Asaro, F.; Zingone, G.; Milizia, T.; Gardossi, L. Azelaic Acid: A Bio-Based Building Block for Biodegradable Polymers. *Polymers* **2021**, *13*, 4091. [CrossRef] [PubMed]
62. Yoon, B.; Jackman, J.; Valle-González, E.; Cho, N.-J. Antibacterial Free Fatty Acids and Monoglycerides: Biological Activities, Experimental Testing, and Therapeutic Applications. *Int. J. Mol. Sci.* **2018**, *19*, 1114. [CrossRef]
63. Galdiero, E.; Ricciardelli, A.; D'Angelo, C.; De Alteriis, E.; Maione, A.; Albarano, L.; Casillo, A.; Corsaro, M.M.; Tutino, M.L.; Parrilli, E. Pentadecanoic Acid against Candida Albicans-Klebsiella Pneumoniae Biofilm: Towards the Development of an Anti-Biofilm Coating to Prevent Polymicrobial Infections. *Res. Microbiol.* **2021**, *172*, 103880. [CrossRef]
64. Skorochod, I.; Roy, A.; Kurdish, I.; Erdenezogt, U. Content of Organic Acids in the Cultural Medium of Bacillus Subtilis Imv B-7023 at Cultivation with Different Sources of the Phosphorus Nutrient. *J. Microb. Biotechnol. Food Sci.* **2020**, *10*, 73–77. [CrossRef]
65. Santos, J.E.D.Á.; De Brito, M.V.; Pimenta, A.T.Á.; Da Silva, G.S.; Zocolo, G.J.; Muniz, C.R.; De Medeiros, S.C.; Grangeiro, T.B.; Lima, M.A.S.; Da Silva, C.D.F.B. Antagonism of Volatile Organic Compounds of the *Bacillus* Sp. against Fusarium Kalimantanense. *World J. Microbiol. Biotechnol.* **2023**, *39*, 60. [CrossRef] [PubMed]
66. Keweloh, H.; Heipieper, H.J. *Trans* Unsaturated Fatty Acids in Bacteria. *Lipids* **1996**, *31*, 129–137. [CrossRef] [PubMed]
67. Das, U.N. Arachidonic Acid and Other Unsaturated Fatty Acids and Some of Their Metabolites Function as Endogenous Antimicrobial Molecules: A Review. *J. Adv. Res.* **2018**, *11*, 57–66. [CrossRef]
68. Corina, D.L.; Munday, K.A. Studies on Polyol Function in Aspergillus Clavatus: A Role for Mannitol and Ribitol. *J. Gen. Microbiol.* **1971**, *69*, 221–227. [CrossRef] [PubMed]
69. Onose, S.; Ikeda, R.; Nakagawa, K.; Kimura, T.; Yamagishi, K.; Higuchi, O.; Miyazawa, T. Production of the α-Glycosidase Inhibitor 1-Deoxynojirimycin from Bacillus Species. *Food Chem.* **2013**, *138*, 516–523. [CrossRef]
70. Silveira, M.; Jonas, R. The Biotechnological Production of Sorbitol. *Appl. Microbiol. Biotechnol.* **2002**, *59*, 400–408. [CrossRef]
71. Olaitan, A.O.; Morand, S.; Rolain, J.-M. Mechanisms of Polymyxin Resistance: Acquired and Intrinsic Resistance in Bacteria. *Front. Microbiol.* **2014**, *5*, 643. [CrossRef]
72. Batovska, D.I.; Todorova, I.T.; Nedelcheva, D.V.; Parushev, S.P.; Atanassov, A.I.; Hvarleva, T.D.; Djakova, G.J.; Bankova, V.S.; Popov, S.S. Preliminary Study on Biomarkers for the Fungal Resistance in Vitis Vinifera Leaves. *J. Plant Physiol.* **2008**, *165*, 791–795. [CrossRef]
73. Ogawa, J.; Saito, K.; Sakai, T.; Horinouchi, N.; Kawano, T.; Matsumoto, S.; Sasaki, M.; Mikami, Y.; Shimizu, S. Microbial Production of 2-Deoxyribose 5-Phosphate from Acetaldehyde and Triosephosphate for the Synthesis of 2′-Deoxyribonucleosides. *Biosci. Biotechnol. Biochem.* **2003**, *67*, 933–936. [CrossRef]
74. Li, G.; Jian, T.; Liu, X.; Lv, Q.; Zhang, G.; Ling, J. Application of Metabolomics in Fungal Research. *Molecules* **2022**, *27*, 7365. [CrossRef]
75. Scigelova, M.; Crout, D.H.G. Microbial β-N-Acetylhexosaminidases and Their Biotechnological Applications. *Enzym. Microb. Technol.* **1999**, *25*, 3–14. [CrossRef]
76. Song, X.-S.; Li, H.-P.; Zhang, J.-B.; Song, B.; Huang, T.; Du, X.-M.; Gong, A.-D.; Liu, Y.-K.; Feng, Y.-N.; Agboola, R.S.; et al. Trehalose 6-Phosphate Phosphatase Is Required for Development, Virulence and Mycotoxin Biosynthesis Apart from Trehalose Biosynthesis in Fusarium Graminearum. *Fungal Genet. Biol.* **2014**, *63*, 24–41. [CrossRef]
77. Ossoliński, K.; Ruman, T.; Copié, V.; Tripet, B.P.; Kołodziej, A.; Płaza-Altamer, A.; Ossolińska, A.; Ossoliński, T.; Krupa, Z.; Nizioł, J. Metabolomic Profiling of Human Bladder Tissue Extracts. *Metabolomics* **2024**, *20*, 14. [CrossRef] [PubMed]

78. Szulc, J.; Okrasa, M.; Nowak, A.; Ryngajłło, M.; Nizioł, J.; Kuźniar, A.; Ruman, T.; Gutarowska, B. Uncontrolled Post-Industrial Landfill—Source of Metals, Potential Toxic Compounds, Dust, and Pathogens in Environment—A Case Study. *Molecules* **2024**, *29*, 1496. [CrossRef] [PubMed]
79. Nizioł, J.; Misiorek, M.; Krupa, Z.; Ruman, T. Infrared Laser-Based Selected Reaction Monitoring Mass Spectrometry Imaging of Banana (Musa Spp.) Tissue—New Method for Detection and Spatial Localization of Metabolites in Food. *Food Anal. Methods* **2024**, *17*, 236–250. [CrossRef]
80. Pang, Z.; Lu, Y.; Zhou, G.; Hui, F.; Xu, L.; Viau, C.; Spigelman, A.F.; MacDonald, P.E.; Wishart, D.S.; Li, S.; et al. MetaboAnalyst 6.0: Towards a Unified Platform for Metabolomics Data Processing, Analysis and Interpretation. *Nucleic Acids Res.* **2024**, *52*, W398–W406. [CrossRef]

Disclaimer/Publisher's Note: The statements, opinions and data contained in all publications are solely those of the individual author(s) and contributor(s) and not of MDPI and/or the editor(s). MDPI and/or the editor(s) disclaim responsibility for any injury to people or property resulting from any ideas, methods, instructions or products referred to in the content.

JOURNAL OF
AGRICULTURAL AND
FOOD CHEMISTRY

Metabolic Impact of Pesticides on Radish: 2D and 3D Mass Spectrometry Imaging of Metabolites in *Raphanus sativus*

Sumi Krupa, Tomasz Ruman, and Joanna Nizioł*

Cite This: *J. Agric. Food Chem.* 2025, 73, 29229−29244

Read Online

ACCESS | Metrics & More | Article Recommendations | Supporting Information

Downloaded via RZESZOW UNIV OF TECHNOLOGY on March 30, 2026 at 08:21:32 (UTC).
See https://pubs.acs.org/sharingguidelines for options on how to legitimately share published articles.

ABSTRACT: Pesticides are essential for crop protection but can markedly reshape plant metabolism with implications for food quality and safety. This work introduces an integrated strategy that combines untargeted ultrahigh-performance liquid chromatography−ultrahigh-resolution mass spectrometry (UHPLC-UHRMS) with two- and three-dimensional mass spectrometry imaging using laser ablation remote atmospheric pressure photoionization/chemical ionization (LARAPPI/CI-2D/3D-MSI) to elucidate global and spatial metabolic responses of radish to pesticide exposure. The results reveal compound- and dose-dependent effects: field-relevant concentrations cause minor metabolic perturbations, whereas 100-fold higher doses induce systemic reprogramming of amino acid, carbohydrate, lipid, and secondary metabolism. MSI uncovers distinct tissue- and depth-specific patterns of metabolic alteration, demonstrating nonadditive responses to pesticide mixtures. By linking molecular profiling with spatial metabolite mapping, this work advances the mechanistic understanding of plant stress responses and provides a framework for evaluating the metabolic consequences of pesticide regimes on crop physiology and food safety.

KEYWORDS: *laser ablation, photoionization, untargeted metabolomics, plant metabolomics, environmental stress response, UHPLC-UHRMS*

1. INTRODUCTION

Radishes (*Raphanus sativus* L.), a member of the *Brassicaceae* family, are widely consumed root vegetables and are a model plant for studying secondary metabolism in crucifers. Their characteristic phytochemicals include glucosinolates and their hydrolysis products (isothiocyanates, nitriles, thiocyanates), which play essential roles in plant defense and contribute to biological activities, such as antimicrobial and antiproliferative effects.[1,2] In addition, radishes accumulate diverse phenolic compounds (e.g., vanillic, ferulic, and caffeic acids; flavonoids such as rutin, pelargonidin, and cyanidin) in both leaves and roots, along with vitamins and minerals that support nutritional value.[3−7] These metabolites, particularly glucosinolates and phenolics, represent core elements of the metabolic phenotype of radish and other Brassicaceae crops. In modern agriculture, radish cultivation relies on the use of fungicides, insecticides, and herbicides to maintain yield and quality.[6] However, pesticide application can alter the primary and secondary metabolism of crops, leading to measurable shifts in nutrient content and defense-related compounds.[8] For instance, pesticide exposure has been associated with changes in sugar, protein, chlorophyll, and amino acid levels in legumes and vegetables.[9,10] Beyond their direct toxicological action, pesticides may trigger or suppress metabolic pathways in plants, influencing stress-related responses and modifying the biochemical composition of edible tissues.[11−13] Therefore, investigating how pesticides reshape plant metabolism is essential not only for food safety but also for understanding plant physiological adaptation.

Both nuclear magnetic resonance (NMR) spectroscopy and mass spectrometry-based approaches, such as gas chromatography−mass spectrometry (GC−MS) and liquid chromatography−mass spectrometry (LC−MS), have been widely used to profile radish metabolites[14−16] but they require homogenization and lack spatial information. In contrast, mass spectrometry imaging (MSI) enables the direct visualization of metabolite distributions in plant tissues without extensive sample preparation.[17,18] MSI approaches, such as matrix-assisted laser desorption/ionization mass spectrometry imaging (MALDI-MSI), secondary ion mass spectrometry (SIMS), and laser ablation−surface collision atmospheric pressure mass spectrometry imaging (LASCA-MSI), have been successfully applied to radish leaves and bulbs, revealing the localization of pigments, glucosinolates, and nitrogen-cycle metabolites.[19,20] Recent advances further extend the use of MSI to pesticide tracking, revealing translocation patterns in diverse crops.[21−23]

In this study, we combined untargeted ultra-high-performance liquid chromatography coupled with ultrahigh-resolution mass spectrometry (UHPLC-UHRMS) with laser ablation remote atmospheric pressure photoionization/chemical ionization (LARAPPI/CI)-MSI to investigate the metabolic impact of selected pesticides (cypermethrin, azoxystrobin, difenoconazole, and metaldehyde) on radish roots. LARAPPI/CI-MSI employs mid-IR ablation at 2.93 μm, efficiently coupling to O−H stretching vibrations, and has previously been demonstrated for 2D and 3D imaging of hydrated biological samples, including

Received: September 17, 2025
Revised: October 23, 2025
Accepted: October 23, 2025
Published: October 29, 2025

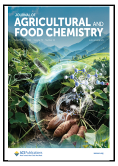

© 2025 American Chemical Society

https://doi.org/10.1021/acs.jafc.5c12445

radish tissues.[24−28] This integrated approach provides both global metabolomic profiling and spatially resolved insights, enabling the evaluation of dose- and pesticide-specific effects on radish metabolism.

2. MATERIALS AND METHODS

2.1. Materials. Radish seeds (*Raphanus sativus* cv. Carmen) were purchased from the online store of PNOS, a Polish seed producer based in Ożarów Mazowiecki, Poland. The radish sample used for 3D-MSI was purchased in a local shop in Rzeszów, Poland, in April 2024. The following plant protection products were used: Belem 0.8 MG (SBM Développement, Escully, France); Scorpion 325 S.C. (Syngenta, Warsaw, Poland), and Snacol 3G (BROS Ltd., Poznań, Poland). The active substances were cypermethrin in Belem 0.8 MG, difenoconazole, and azoxystrobin in Scorpion 325 S.C., and metaldehyde in Snacol 3G. Plastic pots (24 × 12 × 11 cm, polyethylene) and universal potting soil for radish cultivation were also purchased locally. All solvents were LC−MS grade unless stated otherwise: methanol (Supelco, Bellefonte, PA, USA), acetonitrile (Honeywell, Charlotte, NC, USA), toluene (Sigma-Aldrich, St. Louis, MO, USA), and formic acid (Fisher Chemical, Waltham, MA, USA); water (18 MΩ·cm) was produced in-house. 3-Hydroxyoctanoic acid, 3-hydroxydecanoic acid, 3-hydroxydodecanoic acid, 3-hydroxytetradecanoic acid, 3-hydroxyhexadecanoic acid, and 3-hydroxyoctadecanoic acid were purchased as analytical standard grade from Larodan AB (Solna, Sweden). Microscope images were captured using a DeltaOptical USB 3.0 camera (DLT Cam Pro 14 MPix) equipped with a 2.5× InfiniFlex HD Compact Lens and a microscope light ring.

2.2. Plant Cultivation and Pesticide Application. The pesticides selected for this study were metaldehyde (molluscicide), cypermethrin (pyrethroid insecticide), and a mixture of azoxystrobin and difenoconazole (fungicides). These compounds are widely applied in European agriculture, particularly in vegetable cultivation, and represent distinct classes of plant protection products with different modes of action. Their combined use reflects common agricultural practice, where multiple pesticides targeting different groups of pests and pathogens are often applied within the same crop cycle. In addition to their regional importance, azoxystrobin and difenoconazole are also registered and used in other countries, including the United States, underscoring the broader relevance of their inclusion in this study. Radish was chosen as a model crop due to its short growth cycle and its established relevance in ecotoxicological and metabolomic research. Radish (*R. sativus* cv. Carmen) was cultivated in polyethylene pots (24 × 12 × 11 cm, cultivation area 288 cm^2; soil volume ∼ 3.2 L) under controlled conditions. In the initial experiment, two treatment groups were established: an untreated control and radish exposed to a pesticide mixture applied at one hundred times the recommended field dose (named "Mix100×"). Plants from this preliminary cultivation were subjected to MSI analysis, and extracts were additionally evaluated by LC-MS to provide a baseline reference data set.

To enable a systematic comparative analysis across different plant protection products, a subsequent extended experiment was performed. Radish was cultivated in a single polyethylene pot per treatment group, with four seeds planted at a depth of 1 cm and spaced 4 cm apart. From each pot, three mature plants were harvested and analyzed independently, with each plant treated as a separate biological replicate. The experimental design included: (i) untreated control (no pesticide), (ii) radish treated with Snacol 5 GB at one hundred times (100×) the recommended field dose, (iii) radish treated with Scorpion 325 SC at 100× dose, (iv) radish treated with Belem 0.8 MG at 100× dose, (v) radish treated with a mixture of all three pesticides at 100× dose, and (vi) radish treated with a mixture of all three pesticides at the recommended field dose (named "Mix1×").

Pesticides were applied according to manufacturers' recommendations: Snacol 5 GB (granules) was spread on the soil surface between plants, Belem 0.8 MG (microgranules) was placed directly into sowing holes with the seeds, and Scorpion 325 SC (suspension concentrate) was diluted in water and applied using a hand-held spray bottle with an atomizer. Scorpion was sprayed directly onto the soil at sowing, and after plant emergence, it was applied to both the leaves and the soil surface to ensure uniform exposure.

Field doses (1×) were calculated from label recommendations and scaled to the pot surface area, while 100× doses were 100-fold higher. Per pot, this corresponded to 3.5 g of Belem, 0.3 mL of Scorpion, and 1.2 g of Snacol at 100×, and 0.035 g, 0.003 mL, and 0.012 g, respectively, at 1×. Mixture treatments combined the three products in the same application forms.

In both experiments, radish plants were cultivated for 23 days under identical conditions in southeast Poland, with humidity and soil pH levels monitored daily. The average temperature during the cultivation process in Rzeszów was 19 °C; however, the pots were kept indoors with constant access to sunlight during the day. Apart from the day of seeding, Scorpion was added on the tenth day of radish growth, and Snacol was added on the tenth and twentieth days of growth, as recommended by the manufacturers. Radishes were harvested after 23 days of growth, corresponding to their early vegetation stage.

2.3. Sample Preparation for UHPLC-UHRMS and MSI. The untreated (control) radish was 16 cm tall with a 5.2 cm root and an 11.8 cm stem. The analyzed region, which included portions of both the root and the stem, measured 3.1 cm in length. The taproot was 0.4 cm wide at its widest point. The radish affected by pesticides grew to 14 cm tall. The stem was 9.6 cm long, and the root was 4.4 cm in length. The region of the root and stem used for analysis was 2.2 cm long. The widest point of the taproot was also about 0.4 cm wide. Both control and treated samples were cut in half along the proximodistal axis of the root and analyzed within 10 min after collection, without additional storage or preparation. One-half of each sample from the earlier experiment was used for MSI analysis, whereas the remaining halves were processed for UHPLC-UHRMS (data available in the Supporting Information). Radish extracts from all treatment groups were also analyzed by UHPLC-UHRMS and subjected to a statistical evaluation.

For UHPLC-UHRMS analysis, radish samples (59−145 mg of tissue) were placed in Eppendorf tubes and extracted with methanol (10 μL/1 mg of tissue) to ensure proportional extraction across all samples. The samples were homogenized using steel beads three times for 60 s each at 4000 rpm. Following homogenization, the samples were incubated at −20 °C for 12 h and then centrifuged at 10,000*g* for 12 min. The upper phase was transferred to a new 2 mL Eppendorf-type tube. Samples were dried using a SpeedVac vacuum concentrator (≈0.1 mbar) and stored at −60 °C until analysis.

Before UHPLC-UHRMS analysis, the samples were thawed, and methanol was added in a 100 μL per 60 mg dry weight ratio. An ultrasonic bath was used to dissolve any remaining precipitate, and the samples were centrifuged at 9800*g* for 5 min. A total of 80 μL of the final supernatant was transferred to chromatography vials with 130 μL glass inserts for analysis. An extraction blank (methanol) subjected to all of the extraction steps was also made and analyzed.

2.4. LARAPPI/CI-MSI of Radish Taproot Section. LARAPPI/CI-MSI was performed using the technique described in our recent publication.[29] Pesticide-affected and control radish cross sections were separately placed on clean stainless-steel plates. The plates were mounted on the stage with a Peltier cooling plate (TE-127-1.4-1.5; TE Technology, Traverse City, MI, USA) set to −18 °C, and each sample remained frozen throughout the laser ablation process. An Nd:YAG-pumped, tunable, OPO laser (Opolette HE 2940; Opotek, Carlsbad, CA, USA) was used to generate mid-infrared (mid-IR) laser pulses of 7 ns with a maximum repetition frequency of 20 Hz. The laser was tuned to emit at a wavelength of 2.93 μm, and the pulse energy was 3.5 mJ (measured before the diffractive optical element using a pyroelectric energy meter, PE25-SH-V2, Ophir, Logan, UT, USA). Laser ablation was conducted in an airtight chamber pressurized with nitrogen gas at a steady flow of 9.5 L/min. The mass spectrometer used for the analysis was a Bruker Impact II operating in negative-ion mode. The ionization was conducted using a Bruker VIP-HESI ion source in the APCI configuration with the addition of a VUV source (Hamamatsu L12542), a deuterium-based lamp emitting radiation from 115 to 160 nm through an MgF_2 window, mounted axially to the MS sampling cone to induce photoionization. A binary HPLC pump (Agilent G1312A) was used to provide a steady flow of a solvent mixture (1%

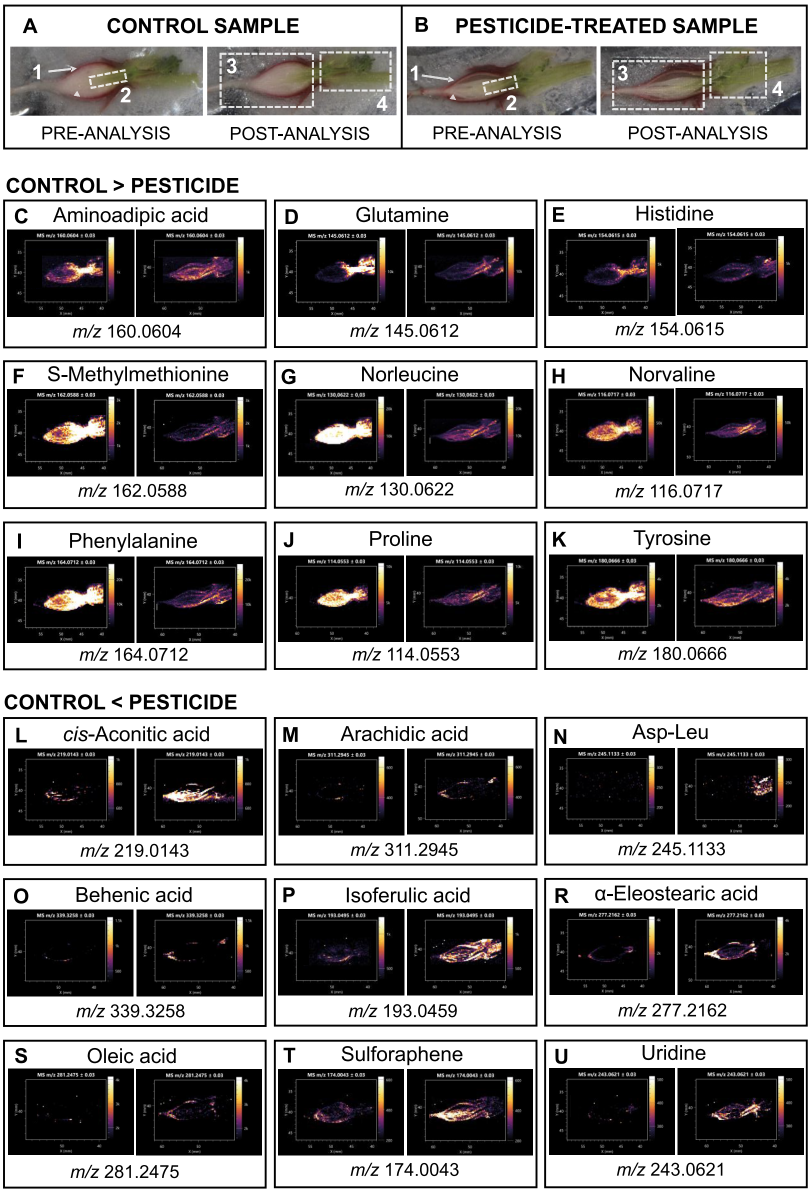

Figure 1. Results of LARAPPI/CI-MSI: control radish sample before and after analysis (A), pesticide-treated radish sample before and after analysis (B); regions of interest were epidermis (A1, B1), stele (A2, B2), taproot (A3, B3), and stem (A4, B4); compounds with significantly higher abundance in the control sample identified using the data from the UHPLC-UHRMS analysis: aminoadipic acid (C), glutamine (D), histidine (E), methylmethionine (F), norleucine (G), norvaline (H), phenylalanine (I), proline (J), and tyrosine (K); compounds with significantly higher abundance in the pesticide-treated sample: *cis*-aconitic acid (L), arachidic acid (M), Asp-Leu (N), behenic acid (O), isoferulic acid (P), α-eleostearic acid (R), oleic acid (S), sulforaphene (T), and uridine (U). Identical intensity scales were applied for control and treated samples within each panel.

toluene in methanol; 200 μL/min) to the APCI needle. The laser ablation plumes were transported to the ion source through a PTFE tube connected to the ablation module. The analyzed rectangular regions encompassed the entire radish taproot, the hypocotyl, and the basal part of the shoot including the cotyledons. The control sample region measured 19 × 7 mm, whereas the pesticide-treated sample region measured 21 × 7 mm. The spatial resolution chosen for the analyses was 250 μm (X and Y). The duration of each laser shot was 1 s, with a delay of 1 s between the shots in one line and 5 s between sequential lines. MSI acquisition and data analysis were performed by using proprietary software developed in-house. Details of the software are provided in Section S1 of the Supporting Information.

2.5. UHPLC-UHRMS of Radish Taproot. UHPLC-UHRMS analysis was conducted in both positive and negative electrospray ionization modes using a Bruker Elute UHPLC system, coupled with a Bruker Impact II ESI QToF-MS mass spectrometer (resolving power ~40,000 fwhm at m/z 400) according to the procedure described previously.[30] The UHPLC column used was the C18 Bruker Intensity Solo with 2-μm particles and dimensions of 100 × 2.1 mm length × diameter. The UHPLC column was thermostated at 40 °C during the analysis. Water with 0.1% HCOOH was used as phase A, and acetonitrile with 0.1% HCOOH was used as phase B. The samples were kept at 4 °C. The injection volume was set at 5 μL, and the percentage of phase B was as follows: 1% (0, 2 min), 99% (17, 20 min), and 1% (20.1−30 min). From 0 to 20 min, the solvent flow rate was 0.25 mL/min, increasing to 0.35 mL/min from 20.1 to 30 min. All measurements were performed thrice. Measurements in autoMSMS mode were carried out using the following parameters: m/z 50−1500; capillary voltage: 4.5 kV; nebulizer: 2.7 bar; dry gas: 12 L min^{-1}; drying gas temperature: 220 °C; hexapole voltage: 50 Vpp; funnel 1:200 Vpp; funnel 2:200 Vpp; prepulse storage time: 5 μs; transfer time: 60 μs. Collision-induced dissociation (CID) was performed with the following settings: absolute threshold (per 100 sum), 200 cts; absolute threshold, 88 cts; active exclusion, 3 spectra; release after 0.3 min;

isolation mass window: width 3 for m/z 100, 4 for m/z 500, 6 for m/z 1000, and 8 for m/z 1300; collision energy, 30 eV. The MS acquisition frequency was 20 Hz, and the MS/MS frequency ranged from 5 to 30 Hz.

Compound annotation was performed in MetaboScape (ver. 2022b) primarily based on accurate mass ($\Delta m/z < 3$ ppm) and MS/MS spectral similarity (cosine score ≥ 0.6). When available, isotopic pattern fit (mSigma < 80) and database-derived or in-house retention times were additionally considered to strengthen identification confidence. MS/MS spectra were automatically matched against multiple spectral libraries, including Bruker HMDB 2.0, MassBank of North America (MoNA), and NIST ver. 2023 MS/MS and GNPS2 (June 2025 version) mass spectral libraries. According to the Metabolomics Standards Initiative.[31] This approach corresponds to MSI Level 2 for most compounds, while selected metabolites confirmed against in-house reference standards reached MSI Level 1. Annotation confidence for each feature is specified in the Supplementary Data.

To ensure analytical reliability, the LC-MS system was stabilized with multiple blank injections before the sample analysis. Extraction blanks (processed without biological material) were included to monitor background contaminants. Solvent blanks were injected after each biological sample to control for potential carry-over. Quality control (QC) pooled samples, prepared by mixing aliquots of all extracts, were injected three times at the beginning of the sequence, then after every ninth injection, and again at the end of the run to monitor instrument stability and analytical drift. A system suitability test (SST) standard mixture of hydroxy acids was analyzed at the beginning, throughout the run, and at the end to confirm the retention time stability and mass accuracy. The SST was prepared by dissolving 3-hydroxyoctanoic, 3-hydroxydecanoic, 3-hydroxydodecanoic, 3-hydroxytetradecanoic, 3-hydroxyhexadecanoic, and 3-hydroxyoctadecanoic acids (Larodan AB) in LC-MS-grade methanol at a final concentration of each compound of 2 μg/mL. Biological samples were injected in randomized order to minimize batch effects. Both extraction and UHPLC-UHRMS procedures were performed identically for all of the experimental series.

2.6. Statistical Analysis. Compounds identified by UHPLC-UHRMS analysis were analyzed using the MetaboAnalyst 6.0 online software.[32] Before analysis, data were log-transformed and autoscaled. The overall variability and grouping trends among pesticide-treated and control radish samples were explored using unsupervised Principal Component Analysis (PCA) and hierarchical clustering, visualized as heatmaps. For univariate analysis, two-sample Student's t tests (unpaired, equal variance) were applied with a raw p-value threshold of 0.05. Metabolites were considered statistically significant when $p < 0.05$ and biologically relevant when the fold change exceeded 2.0 or was below 0.5. Given the limited sample size ($n = 3$ per group), PCA and heatmaps were interpreted as exploratory tools. Metabolite selection, however, was based solely on combined t test and fold-change criteria to ensure robust and conservative identification. Pathway and chemical class enrichment analyses were performed in MetaboAnalyst 6.0. Pathway impact was assessed using topology-based analysis with the KEGG pathway library for *Arabidopsis thaliana*, while enrichment analysis was based on metabolite sets grouped by chemical main classes. Both analyses considered results significant when meeting the dual criterion of statistical significance (p-value < 0.05) and pathway or class impact greater than 0.1.

2.7. 3D-LARAPPI-MSI Analysis of Radish Taproot. The radish root region was analyzed as described in a publication by Ruman et al.[29] 3D-LARAPPI/CI-MSI involved sequential depth profiling of the radish root surface. 3D-LARAPPI/CI-MSI was performed in six sequential ablation layers, starting from a sample height of 3 mm. The spatial resolution was 140 μm. The imaged region at the first step measured 4.76 × 4.76 mm (X × Y). At each subsequent step, the imaged area was reduced by 0.14 × 0.14 mm according to the inverted-pyramid acquisition scheme described in our previous publication. The heights of measurement for the following steps were respectively 2.5, 2.30, 2.16, 1.6, and 1.4 mm. The height of the measurement at each step was determined using a high-precision laser distance sensor (Baumer OM70-P0070.HH0048.EK, Baumer Group, Switzerland). The sensor was used to record the surface profile of the sample and provide the laser focus level for the next ablation step.

3. RESULTS AND DISCUSSION

In this study, two complementary analytical strategies were employed to investigate the metabolic impact of pesticide exposure in radish. MSI was restricted to control plants and high-stress conditions (a hundred-fold overdose) to overcome the limited sensitivity of on-tissue detection and to visualize spatial patterns of metabolite changes under extreme stress. In parallel, UHPLC-UHRMS analysis was performed for all experimental conditions, including environmentally relevant field-dose mixtures and overdose treatments, providing a comprehensive overview of pesticide-induced alterations in the radish metabolome. This dual strategy enabled the combination of proof-of-concept MSI imaging with broader untargeted metabolomic profiling by LC-MS.

3.1. Detection of Metabolic Changes in Radish Roots Using LARAPPI/CI-MSI. In this part of the study, MSI was applied exclusively to control plants and those exposed to the hundred-fold overdose conditions. This design was chosen to maximize the likelihood of detecting spatially resolved metabolic perturbations, as pesticide-induced changes at field-dose levels may remain below the on-tissue detection threshold of MSI. By contrasting control and high-stress treatments, we were able to visualize characteristic patterns of metabolite redistribution in radish root cross sections. Representative ion images are presented in Figure 1, with additional examples provided in the Supporting Information (Figures S1−S6).

First, LARAPPI/CI-MSI of a cross-section of a radish root and stem was performed on a control and a pesticide-treated sample. Using only putative identification, 88 compounds were detected across both samples. Twenty-eight of 28 compounds were found in the control sample with significantly higher signal intensity, while 23 compounds showed higher abundance in the pesticide-treated sample. The remaining detected compounds showed signal intensities similar to those in both samples. The spatial distribution of compounds was evaluated across four anatomical regions: epidermis, stele, central taproot tissue, and stem. 32 of the 88 compounds were present relatively uniformly on the whole cross-section surface. Ten compounds were observed predominantly in the stem region, 8 were located mainly in the stele alone, and 19 were present solely in the taproot region. Several ions showed predominant epidermal localization, notably arachidic acid (Figure 1M), behenic acid (Figure 1O), α-eleostearic acid (Figure 1R), and oleic acid (Figure 1S). Some images were difficult to classify due to overlapping anatomical regions, particularly between the stem and stele. The presence of 30 of these compounds was further confirmed by UHPLC-UHRMS/MS (Table S1, Supporting Information). For both putatively annotated and LC-MS confirmed compounds, ion images at the exact m/z values were generated in MSI software, taking into consideration the predominant ion species produced in the LARAPPI/CI method ($[M-H]^-$). It should be emphasized that, as in all MSI approaches, ion signal intensities may be affected by matrix effects related to the heterogeneous biochemical composition of plant tissue. Therefore, the interpretation of signal differences was restricted to relative comparisons, and metabolite identification was confirmed using UHPLC-UHRMS analysis.

The results of the LARAPPI/CI-2D-MSI analysis indicate that specific pesticides (cypermethrin, azoxystrobin, difenoconazole, and metaldehyde) significantly impact the metabolism of the radish plant, leading to compound-specific decreases or accumulations. Figure 1 presents 2D ion images obtained using LARAPPI/CI-MSI for metabolites identified by both LARAPPI/CI-MSI and UHPLC-UHRMS+MS/MS. Additionally, the Supporting Information (Figures S1−S6) contains ion images of other metabolites detected using LARAPPI/CI-2D-MSI. The compounds with higher signal intensity in the control sample (Figure 1A), compared to the pesticide-treated sample (Figure 1B), include aminoadipic acid, glutamine, histidine, *S*-methylmethionine, norleucine, norvaline, phenylalanine, proline, and tyrosine. As evident from the results, the most pronounced differences were observed for amino acids. Certain herbicides exert their activity by inhibiting the biosynthesis of amino acids, which are essential for protein synthesis in plants. For example, acetohydroxyacid synthase (AHAS) inhibitors block the production of branched-chain amino acids, while glyphosate disrupts the shikimate pathway, affecting the biosynthesis of aromatic amino acids.[33] The results for compounds identified by UHPLC-UHRMS found in higher concentration in the pesticide-treated sample are presented in Figure 1L−U. These compounds are *cis*-aconitic acid, arachidic acid, aspartyl-leucine (Asp-Leu), behenic acid, isoferulic acid, α-eleostearic acid, oleic acid, sulforaphene, and uridine.

Aminoadipic acid (Figure 1C) is a metabolite formed by the degradation of lysine. Lysine (Figure S4E), as well as methionine (Figure S4I) and *S*-methylmethionine (Figure 1F), are obtained from aspartate metabolism.[34,35] Aspartate metabolism is part of the alanine, aspartate, and glutamate metabolic pathways in higher plants. Our MSI results suggest that the metabolism of aspartate-derived amino acids may be affected by pesticide treatment. Specifically, compounds such as aminoadipic acid, *S*-methylmethionine, and pipecolic acid (Figure S5E, Supporting Information) showed decreased intensities in pesticide-treated samples, suggesting a potential disruption of aspartate metabolism. Glutamine (Figure 1D), as well as proline (Figure 1J) and ornithine (Figure S5A, Supporting Information), are synthesized from glutamic acid, a key intermediate in nitrogen metabolism,[36] and one of the main metabolites in the previously mentioned alanine, aspartate, and glutamate metabolism. The levels of these amino acids were lower in pesticide-treated samples, suggesting a potential disruption in nitrogen assimilation and amino acid biosynthesis. Since glutamine plays a central role in nitrogen transport and storage, and proline and ornithine are involved in stress responses and polyamine synthesis, their decreased levels may indicate broader disturbances in nitrogen homeostasis. Although no clear differences in putatively identified glutamic acid (Figure S3F, Supporting Information) intensity were observed between control and pesticide-treated samples, further investigation is needed to validate this result and confirm its metabolic role in response to pesticide exposure.

Additionally, histidine (Figure 1E), phenylalanine (Figure 1I), and tyrosine (Figure 1K), formed via metabolic pathways preceded by the pentose phosphate pathway, also exhibited reduced intensities, indicating broader alterations in nitrogen metabolism and amino acid biosynthesis.

Norleucine (Figure 1G) is a product of the valine, leucine, and isoleucine biosynthesis pathway, which originates from pyruvate. Norleucine has been implicated in the regulation of bacterial growth in plants by substituting for methionine in proteins.[37] Norvaline (Figure 1H) is also produced in this pathway. Derivatives of this compound have been found to accumulate in response to microbial infestation and abiotic stress factors.[38,39]

The synthesis of aromatic amino acids, such as phenylalanine and its derivative, *N*-hydroxy-L-phenylalanine (Figure S4K, Supporting Information), and tyrosine (Figure 1K), occurs via the shikimate pathway, with chorismic acid (Figure S2D, Supporting Information).[40] In our study, a higher signal intensity of chorismic acid was found in the control sample compared to that in the pesticide-treated sample, which may suggest a disruption in the biosynthesis of aromatic amino acids. Amino acids serve structural functions, forming protein, increasing the shoot system and growth of the plant, and enhancing resistance to diseases and abiotic stress factors.[41] A decrease in amino acid abundance not only reduces the nutritional value of plants for human consumption but also may negatively affect their growth and overall crop yield. The MSI results for putative compounds reinforce the observations made for the previously discussed metabolic pathways. The detected changes in erucin (Figure S2M, Supporting Information) suggest alterations in glucosinolate metabolism in response to pesticide exposure.[42] The variation in isoquinoline levels (Figure S4C, Supporting Information) aligns with alterations in tyrosine metabolism, supporting its role as a secondary metabolite affected by chemical stress.[43] The presence of octyl palmitate in the stem region (Figure S6H, Supporting Information) and its spatial co-occurrence with palmitic acid are consistent with pesticide exposure impacting lipid metabolism, potentially influencing plant interactions with insects and microorganisms.[44−47]

One of the key compounds present at higher levels in the pesticide-treated samples is *cis*-aconitate (Figure 1L), which accumulated predominantly in the taproot region of the treated radish and exhibited markedly higher abundance than in the control. This intermediate of the tricarboxylic acid (TCA) cycle participates in the interconversion of citrate and isocitrate. The observed increase in the *cis*-aconitate content relative to the control sample may suggest alterations in TCA flux under chemical stress conditions. Notably, in plants, part of the *cis*-aconitate pool can be converted into its trans isomer, which displays antifungal and antiparasitic properties.[48]

Among the compounds found in higher concentrations in the pesticide-treated sample, arachidic acid (Figure 1M), behenic acid (Figure 1O), α-eleostearic acid (Figure 1R), and oleic acid (Figure 1S) are directly involved in fatty acyl metabolism. Their increased presence may suggest enhanced lipid synthesis, altered membrane composition, or an adaptive response to pesticide-induced stress. These compounds were predominantly localized in the epidermis and in the lower part of the radish root. The reported results of pesticide influence on fatty-acid concentrations in plants are nonuniform and dependent on the stage of growth at the time of the analysis.[49−51] While a direct correlation between pesticide use and fatty-acid composition remains difficult to establish, our findings indicate a significant increase in the signal intensity of identified fatty acids in pesticide-treated radish samples.

Asp-Leu (Figure 1N) is a dipeptide that was detected in high abundance in the stem of the pesticide-treated sample. Studies on asparaginase activity suggest that Asp-Leu may not be efficiently hydrolyzed by plant-type asparaginases,[52] whereas certain bacterial asparaginases, including those from *Escherichia coli* and *Lupinus luteus*, exhibit isoaspartyl dipeptidase activity, which may contribute to Asp-Leu hydrolysis.[53] The observed differences in Asp-Leu levels might reflect variations in microbial

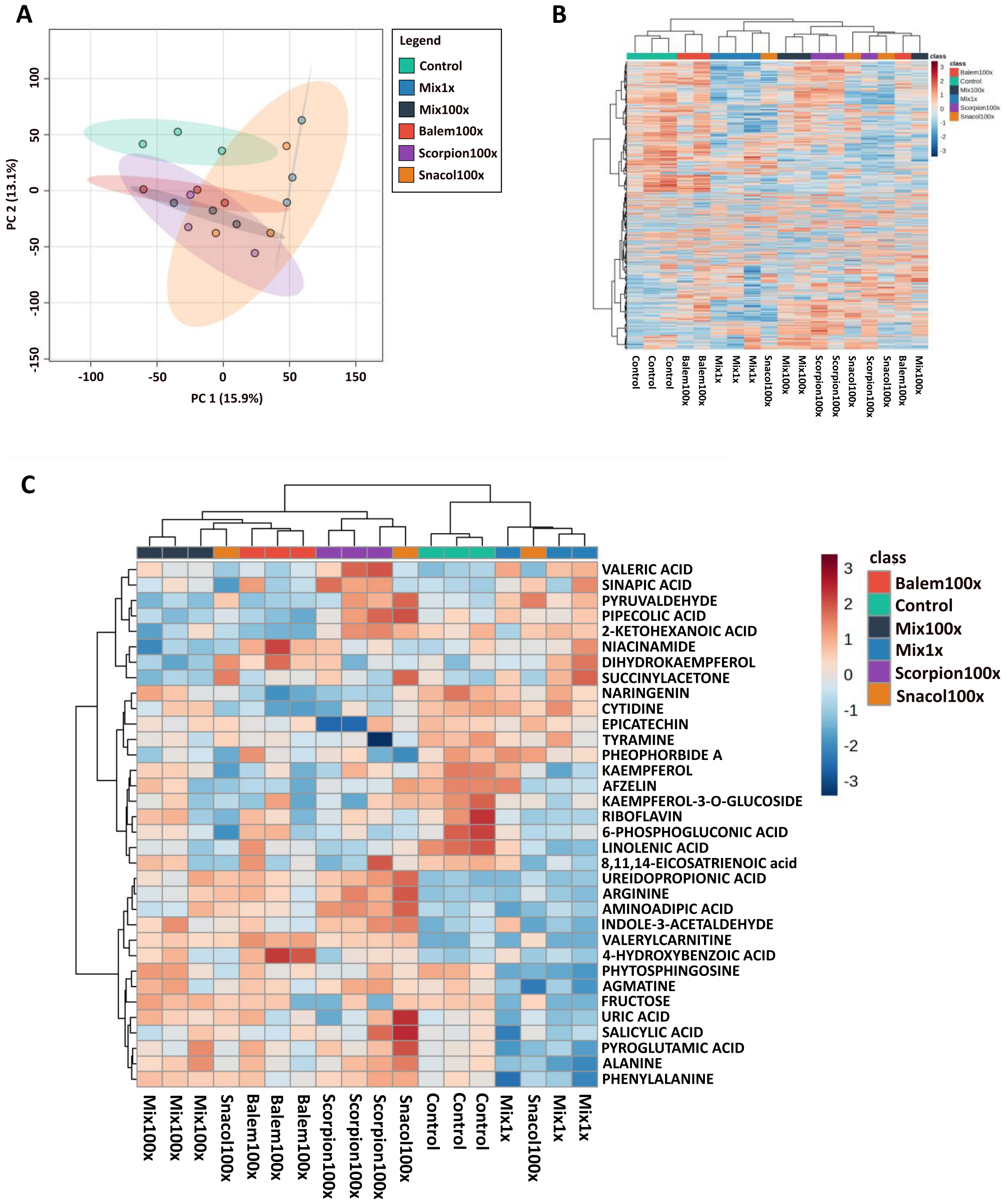

Figure 2. Global and targeted metabolomic differences between control and pesticide-treated radish samples. (A) PCA score plot showing separation of treatment groups based on all detected features from UHPLC-UHRMS data. (B) Hierarchical clustering heatmap of all detected features across six experimental conditions. (C) Heatmap of statistically and biologically significant metabolites, highlighting differences across all treatment groups.

activity between the treated and control samples. Furthermore, some peptides, including certain dipeptides, have been found to possess herbicidal properties.[54]

Isoferulic acid (Figure 1P), a derivative of phenolic acids in the phenylpropanoid pathway, exhibited significantly higher concentrations in the pesticide-treated samples. Isoferulic acid (similar to other cinnamic acid derivatives) may exhibit herbicidal activity,[55] which further suggests an enhanced defensive response or the release of allelopathic compounds in reaction to chemical stress.

Sulforaphene (Figure 1T) is an isothiocyanate derived from glucoraphenin, which is the main glucosinolate in radish. It was mostly found to be present in the taproot region of the pesticide-treated sample. Glucosinolates, including glucoraphenin, are secondary metabolites in the phenylpropanoid pathway that play a crucial role in plant defense. Upon tissue damage, they are enzymatically hydrolyzed into bioactive compounds such as isothiocyanates, which contribute to plant resistance by producing a pungent odor and taste, potentially deterring herbivores and pathogens. The increased abundance of sulforaphene in the pesticide-treated sample may indicate an intensified defensive response or allelopathic interactions triggered by chemical stress.[56]

Table 1. Pathway Enrichment Across Pairwise Pesticide-Treatment Comparisons in Radish[a,b,c,d]

Pathway name	Control vs Mix1×	Control vs Mix100×	Control vs Snacol100×	Control vs Scorpion100×	Control vs Belem100×	Mix1× vs Mix100×	Scorpion100× vs Mix100×	Singles100× vs Mix100×
Alanine, aspartate, and glutamate metabolism	↓	-	-	-	-	↑	-	-
Amino sugar and nucleotide sugar metabolism	↓	↑	-	-	-	↑	-	-
Arginine and proline metabolism	↓	↑	-	↑	↑	↑*	-	-
Arginine biosynthesis	-	↑*	-	↑	↑*	↑	-	-
β-Alanine metabolism	-	↑*	-	↑	↑*	↑	-	-
Biosynthesis of unsaturated fatty acids	↓	↓*	↓*	↓	-	-	-	-
Biosynthesis of various plant secondary metabolites	↓	-	-	-	-	↑	-	-
Carbon fixation by Calvin cycle	↓	-	-	-	-	↑	-	-
Cyanoamino acid metabolism	-	-	-	-	-	↑	-	-
Flavone and flavonol biosynthesis	↓	-	↓*	↓	↓	-	-	-
Flavonoid biosynthesis	↓	-	↓	↓	↓*	↓	-	↓
Fructose and mannose metabolism	↓	↑*	-	-	-	↑	-	-
Galactose metabolism	↓	↑	-	-	-	↑	-	-
Glucosinolate biosynthesis	-	-	-	↑	-	↑	-	-
Glutathione metabolism	↓	-	-	-	-	↑	-	-
Glycine, serine, and threonine metabolism	-	-	-	-	-	↓	-	-
Indole alkaloid biosynthesis	-	-	↓*	-	-	-	-	-
Isoquinoline alkaloid biosynthesis	-	↓*	↓*	-	↓*	-	-	-
Lysine degradation	-	-	-	↑	↓	↓	↓*	-
Nicotinate and nicotinamide metabolism	-	-	-	-	-	↓*	↓*	↓
Pantothenate and CoA biosynthesis	-	↑	-	↑	↑*	↑	-	-
Pentose and glucuronate interconversions	-	-	-	-	-	-	-	↓
Pentose phosphate pathway	-	-	↓	-	-	-	-	-
Phenylalanine metabolism	-	-	-	-	-	↑	-	-
Phenylalanine, tyrosine, and tryptophan biosynthesis	-	-	-	-	-	↑	-	-
Phenylpropanoid biosynthesis	-	-	-	↑	-	↑	↓	-
Porphyrin metabolism	-	↓	-	-	-	-	-	-
Purine metabolism	-	-	-	-	-	↑	-	↓
Pyrimidine metabolism	-	↑	-	↑	↑↓	↑	-	↓*
Pyruvate metabolism	-	-	-	-	-	↓	-	-
Riboflavin metabolism	-	-	↓	-	-	-	-	-
Selenocompound metabolism	↓	-	-	-	-	↑	-	-
Sphingolipid metabolism	↓	-	-	-	-	↑	-	-
Starch and sucrose metabolism	↓	↑	-	-	-	↑	-	-
Tryptophan metabolism	-	↑	↓	↑	-	-	-	-
Tropane, piperidine, and pyridine alkaloid biosynthesis	-	-	-	-	-	↑	-	-
Tyrosine metabolism	-	↓*	↓	-	↓	-	-	-
Ubiquinone and other terpenoid-quinone biosynthesis	-	-	-	-	↑	-	-	-
Valine, leucine, and isoleucine biosynthesis	-	-	-	↑	-	-	-	-
Valine, leucine, and isoleucine degradation	-	-	-	↑	-	-	-	-

[a] Input lists comprise metabolites significantly differing between groups ($p < 0.05$; FC > 2 or < 0.5). [b] Arrow convention: for a column "A vs B", ↑ = enriched in B; ↓ = enriched in A; "−" = not enriched. [c] Statistics: over-representation analysis on annotated metabolites (Fisher's exact test); only pathways with nominal pathway $p \leq 0.05$ are reported (*). [d] Notes on coverage: comparisons Snacol100× vs Mix100× and Belem100× vs Mix100× were omitted due to insufficient hits for pathway testing.

Uridine (Figure 1U) was detected mostly in the stele, although signals of slightly lower intensity were also present in the lower root region. It is a nucleoside made out of uracil and ribose. Overlapping detection areas of uracil and uridine suggest metabolic interconnections within the nucleotide biosynthesis pathway. Uridine diphosphate-glycosyltransferases (UGTs) have been linked to insecticide metabolism, particularly in detoxification processes involving pyrethroids in insects.[57] Some

Table 2. Chemical Class Enrichment Across Pairwise Pesticide-Treatment Comparisons in Radish[a,b,c]

Enriched class	Control vs Mix1×	Control vs Mix100×	Control vs Snacol100×	Control vs Scorpion100×	Control vs Belem100×	Mix1× vs Mix100×	Snacol100× vs Mix100×	Scorpion100× vs Mix100×	Belem100× vs Mix100×	Singles100× vs Mix100×
Benzene and substituted derivatives	↓	↑↓	↓	-	↑↓	↑*	↑	↑↓	↑*	↑*
Carboxylic acids and derivatives	↓*	↑	↑	↑*	↑↓	↑*↓	-	↓	-	↓*
Cinnamic acids and derivatives	-	-	-	↑*	-	-	-	↓*	-	-
Fatty Acyls	↑*↓*	↑*↓*	↑↓	↑*↓*	↑*↓*	↑↓	↑	-	↑↓*	-
Flavonoids	↓*	-	↓	↓	↓*	↓	-	↑*	↑*↓*	↓
Furans	↓*	-	-	-	-	-	-	-	-	-
Glycerolipids	↓	-	-	-	-	-	-	-	-	-
Imidazopyrimidines	-	-	↓*	-	-	↑*	-	-	-	↓*
Indoles and derivatives	↓*	↑*↓*	↓*	↑*	↑*	↑*	↑*↓*	↑*↓*	-	↑*↓*
Keto acids and derivatives	↑*	↑*	-	↑*	↓*	↓*	-	↑*	-	-
Naphthofurans	-	-	-	-	-	-	-	-	↓*	-
Organic carbonic acids and derivatives	-	↑*	-	↑*	↑*	↑*	-	-	-	-
Organonitrogen compounds	↓*	-	-	-	-	↑*	-	-	-	-
Organooxygen compounds	↓*	↑	↑*↓	-	-	↑*↓	↑↓*	-	-	↓*
Phenols	↓*	↓*	-	↓*	-	-	-	↑*	-	-
Pteridines and derivatives	-	-	↓*	-	-	-	-	-	-	-
Purine nucleosides	-	-	↓*	↓*	-	-	-	-	-	-
Pyridines and derivatives	↓	-	-	-	-	↓*	-	↓*	↓*	↓*
Pyrimidine nucleosides	-	-	-	-	↓*	-	-	-	-	↓*
Steroids and steroid derivatives	-	↑	-	-	↑*	↑	-	-	-	↓
Thiolactams	-	-	-	↑*	↑*	-	-	-	-	-

[a] Input list: metabolites that significantly differentiated the two groups ($p < 0.05$; FC > 2 or < 0.5). [b] Arrow convention: for a column "A vs B", ↑ denotes enrichment in B, ↓ denotes enrichment in A, "—" = not enriched. [c] Statistics: over-representation analysis at the chemical class level (Fisher's exact test); * indicates nominal enrichment $p < 0.05$.

pyridine-containing compounds have also been associated with chitin biosynthesis inhibition in insects, ticks, and fungi,[58] suggesting a potential role of related metabolic pathways in plant defense responses against chemical stress.

A qualitative comparison between the most intense MSI voxels and the highest-intensity UHPLC−UHRMS signals for the same 100× samples indicates several consistent trends. The vast majority of endogenous metabolites show a higher signal intensity in LC−MS than in MSI. Notably, a few carboxylic acids and other easily deprotonated compounds exhibited relatively stronger responses in MSI, which is consistent with the negative-ion LARAPPI/CI ionization characteristics. The higher apparent sensitivity of UHPLC−UHRMS is justified by the markedly different sample amounts introduced into each system. Approximately 10 μg of extract was injected onto the LC column, whereas the total amount of biological material removed by the laser and transferred to the ion source in MSI is estimated to be around 3 μg. Considering that the metabolite content in 3 μg of tissue may correspond to only ∼100 ng of analytes, UHPLC−UHRMS effectively analyzes up to 2 orders of magnitude more material. Thus, while UHPLC−UHRMS offers superior sensitivity and broader metabolite coverage, MSI provides unique spatial information and still detects key metabolites at the 100× dose, especially those favored by negative-ion formation.

3.2. UHPLC-UHRMS and Statistical Analysis of the Results.

Extracts obtained from the extended cultivation experiment, comprising six treatment groups (i) untreated control, (ii) mixture of pesticides at field dose (1×), (iii) mixture of pesticides at 100×, (iv) Snacol 5 GB at 100×, (v) Scorpion 325 SC at 100×, and (vi) Belem 0.8 MG at 100× were analyzed by UHPLC-UHRMS and subsequently subjected to statistical evaluation. In total, 7750 m/z features were detected in positive ionization mode, of which 707 were successfully annotated to specific metabolites, and 4581 features were detected in negative mode, of which 351 were annotated. To minimize background interference, extraction blanks were processed identically to biological samples, and average blank signal intensities were compared with those of each treatment group. Features with a sample-to-blank intensity ratio ≤ 3 were excluded from further analysis. This filtering step ensured that only biologically relevant signals with sufficient discrimination from background noise were retained for the statistical evaluation. QC pooled samples clustered closely in the PCA scores plot (Figure S7), confirming analytical stability throughout the run. A slight spread was observed along PC2 (4.8% of total variance), but this effect was negligible compared to that of PC1 (54.9%). System suitability test (SST) standards were clearly separated from the biological samples, as expected. The tight grouping of QC replicates indicates that the variability observed between treatment groups reflects genuine biological differences rather than instrumental drift.

The results were further explored using unsupervised PCA and hierarchical clustering heatmaps to visualize global metabolic differences between groups. PCA was performed on the full data set comprising all detected features (Figure 2). The score plot (Figure 2A) shows that PC1 (15.9%) and PC2 (13.1%) together explain ∼29% of the total variance.[59] Although these values may appear modest, this is typical for untargeted metabolomics data sets with thousands of chemically diverse variables, where variance is distributed across many components. Even with relatively low explained variance, PCA effectively resolves the main biological trends and treatment-related separations. Control samples form a compact and distinct cluster, reflecting their stable baseline metabolome. The pesticide mixture at field dose (Mix1×) overlaps with Snacol100×, suggesting that even environmentally relevant exposures induce a metabolic response resembling that of metaldehyde, albeit in a more homogeneous manner. At high doses, Mix100× (dark blue) clusters with Scorpion100× (purple) and partially overlap with Belem100× (red), indicating that fungicides and cypermethrin dominate the mixture's signature. Snacol100× shows the broadest dispersion, consistent with a strong, but heterogeneous, stress effect. The heatmap (Figure 2B) corroborates these observations. Controls cluster together, though two Belem100× replicates appear closer to the control branch, reflecting variability in the cypermethrin response. Mix100× aligns with Scorpion100×, while Snacol100× forms a separate cluster, confirming its distinct impact.

To further dissect the metabolic impact of pesticide exposure in radish, a series of targeted pairwise comparisons was performed. First, environmentally relevant and dose−response effects were evaluated by comparing the pesticide mixture at the recommended agricultural dose with the control (Mix1× vs Control), representing the most practical scenario, and at an extreme overdose (Mix100× vs Control), serving as a proof-of-concept to reveal the full spectrum of metabolic perturbations. The direct comparison between high- and low-dose mixtures (Mix100× vs Mix1×) enabled the assessment of dose-dependent responses. Second, the contribution of individual active ingredients was examined through comparisons of each pesticide applied at high dose against the control (Snacol100×, Scorpion100×, and Belem100× vs Control), allowing attribution of specific metabolic signatures to metaldehyde, azoxystrobin/difenoconazole, and cypermethrin, respectively. Finally, potential synergistic or nonadditive effects of mixtures were addressed by comparing the high-dose mixture against the pooled single-pesticide treatments (Mix100× vs Singles100×) as well as against each pesticide individually (Mix100× vs Snacol100×, Mix100× vs Scorpion100×, Mix100× vs Belem100×). All performed pairwise comparisons and the corresponding statistical outcomes are presented in Tables 1 and 2, which provide a comprehensive summary for detailed interpretation. For metabolite selection, univariate statistical approaches were applied, including Student's *t* test ($p < 0.05$) combined with fold change thresholds (FC > 2 or FC < 0.5), to identify the most significantly altered compounds between control and pesticide-treated samples. The identification data for all biologically and statistically significant metabolites are provided in Table S2 of the Supporting Information.

3.2.1. Metabolic Alterations under Field-Relevant Pesticide Exposure. At the field-relevant dose (Mix1×), the metabolic response of radish was measurable but restricted in scope, with only a few metabolites meeting both statistical and biological thresholds ($p < 0.05$; FC > 2 or < 0.5). Among the compounds elevated in Mix1×, valeric acid and succinylacetone were the only significant markers (Table S3, Supporting Information). These metabolites belonged to the classes of keto acids and derivatives and fatty acyls (Table S4, Supporting Information). Succinylacetone is not typically reported as a plant metabolite; however, it has been found to accumulate in *Arabidopsis thaliana* short-day sensitive cell death 1 (sscd1) mutants due to disruption of fumarylacetoacetate hydrolase activity associated with the tyrosine degradation pathway.[60] Valeric acid is a metabolite of *Valeriana officinalis*,[61] but was not found to occur in plants of the *Brassicaceae* family. Valeric acid, as a short-chain volatile fatty acid, is used in the production of some pesticides, serving as a stanching agent.[62]

In parallel, comparison with the control revealed a broader and more systematic effect in the opposite direction: many more metabolites were suppressed in Mix1×, with higher abundance in the control group. These decreases included amino acids, such as alanine and 5-oxoproline, carbohydrates, such as fructose, fatty-acid derivatives, including linolenic acid, and secondary metabolites, such as kaempferol-3-*O*-glucoside, epicatechin, indole derivatives, and phytosphingosine. Pathway analyses confirmed that control plants maintained elevated activity of pathways linked to central carbon and nitrogen metabolism (alanine, aspartate, and glutamate metabolism; starch and sucrose metabolism; fructose and mannose metabolism; galactose metabolism) as well as antioxidant and defense-related processes such as glutathione metabolism, flavonoid biosynthesis, and the biosynthesis of various secondary metabolites (Table S5, Supporting Information). However, none of these enrichments reached statistical significance ($p > 0.05$), and therefore, the interpretation should be considered indicative rather than conclusive. Chemical class enrichment further supported this pattern, showing a clear predominance of fatty acyls, phenols, flavonoids, indoles, and organonitrogen compounds in the control group (Table S6, Supporting Information). Similar reductions in sugars and amino acids under abiotic or chemical stress have been widely reported in *Brassicaceae*[63] and in other crops exposed to environmental contaminants.[64] In radish, flavonoid glycosides are known to be environmentally responsive metabolites,[65] supporting the observed decrease in secondary metabolites.

These results indicate that even exposure at the recommended agricultural dose is sufficient to trigger measurable metabolic reprogramming, primarily reflected in the suppression of metabolites from central carbon metabolism and secondary biosynthetic pathways. At the same time, the minimal number of significantly increased metabolites suggests that low-dose exposure primarily affects isolated metabolic nodes rather than entire pathways, which is consistent with the absence of statistically significant enrichment in the treated group and aligns with previous metabolomics studies reporting similarly subtle effects under low-level pesticide exposure.[66]

3.2.2. Metabolic Effects of High-Dose Pesticide Mixture. At the high-dose treatment (Mix100×), the metabolic profile of radish plants was characterized by a markedly stronger and more systemic response compared with the field dose. Several metabolites were significantly elevated in Mix100×, including valerylcarnitine and succinylacetone, but also arginine, 3-ureidopropionate, fructose, and indole-3-acetaldehyde (Table S7, Supporting Information). These changes resulted in the enrichment of amino acid−related pathways, including arginine biosynthesis, arginine and proline metabolism, and β-alanine metabolism, as well as carbohydrate and energy-related pathways such as fructose and mannose metabolism, starch and sucrose metabolism, and pantothenate and CoA biosynthesis (Table S8, Supporting Information). The marked increase of valerylcarnitine likely reflects buffering of acyl-CoA homeostasis (temporary shuttling to acylcarnitines) when lipid catabolism/remodeling is perturbed; evidence for plant acylcarnitines and carnitine acyltransferases exists, whereas direct signaling roles remain unsubstantiated.[67,68] The increased arginine levels in the treated sample are consistent with stress-induced activation of arginine-derived polyamine and nitric oxide biosynthesis in plants.[69] The observed increase in 3-ureidopropionate is consistent with DNA-damage−associated activation of uracil (pyrimidine) catabolism in plants and with engagement of the uracil → β-alanine route under stress.[70] An increase in indole-3-acetaldehyde is consistent with alterations in indolic/auxin-related metabolism (IAA pathway intermediates are proposed to include IAAld in some routes).[71] In contrast to Mix1×, fructose increased, consistent with dose-dependent remodeling of soluble sugar pools under pesticide stress, as reported for multidose chlorpyrifos, where starch/sucrose, galactose, and fructose/mannose pathways shift with increasing dose.[72] Class-level enrichment toward organic acids/keto acids, fatty acyls, and indoles in Mix100× aligns with literature showing accumulation of organic acids and lipid species at higher pesticide doses and enrichment of tryptophan/indole-related metabolism in the high-dose condition,[72] and with foliar nanopesticide studies reporting broad perturbation of central carbon and lipid pathways (Table S9, Supporting Information).[13,64]

Conversely, several compounds were more abundant in control plants, including tyramine, octadecatrienoic acid, and pheophorbide (Table S10, Supporting Information). At the chemical class level, these metabolites mapped to fatty acyls, phenols, indoles, and related derivatives (Table S11, Supporting Information), highlighting the preservation of lipid, phenolic antioxidant, and chlorophyll-related metabolism in unstressed plants.

This comparison thus reveals a clear asymmetry between high-dose stress and the unstressed state. While the control maintains a broad baseline of metabolic diversity, including lipids, phenolic antioxidants, and chlorophyll derivatives, the Mix100× condition induces reprogramming toward amino acid and nitrogen metabolism, carbohydrate mobilization, and signaling molecules derived from indole compounds. This shift indicates that pesticide exposure at supra-field levels overrides basal metabolic homeostasis and enforces a systemic stress program,[63,64] in which resources are redirected from growth and maintenance-related pathways (lipids, chlorophyll, phenolics) toward defense and survival-related ones (arginine/polyamine metabolism, sugar and energy turnover, indolic stress metabolites).

3.2.3. Metabolic Effects of High-Dose Single Pesticides. In plants treated with Scorpion at 100× concentration, increased levels of valerylcarnitine, valeric acid, arginine, 3-ureidopropionate, and indole-3-acetaldehyde were observed, consistent with the metabolic profile of the Mix100× treatment (Table S12, Supporting Information). Additionally, 2-aminoadipate, 3-methyl-2-oxopentanoic acid, and sinapate were more abundant compared to those of the control. The two former compounds are strongly linked to amino acid biosynthesis pathways (Table S13, Supporting Information). 2-Aminoadipic acid accumulation has been linked to stress responses in *Arabidopsis thaliana* (*Brassicaceae*), particularly under glutathione-dependent redox imbalance. An increased GSSG/GSH ratio or the application of exogenous reduced glutathione (GSH) has been shown to elevate 2-aminoadipic acid levels. Furthermore, increased 2-aminoadipic acid has also been reported under hydrogen peroxide treatment and pathogen challenge.[73] Enrichment of phenylpropanoid biosynthesis is consistent with activation of defense-associated pathways in *Brassicaceae* under stress (Table S14, Supporting Information).[74]

Control plants showed a profile centered on lipid and phenolic metabolism, with enrichment of flavone, flavonol, and unsaturated fatty-acid biosynthesis, consistent with the documented abundance of flavonoids and phenylpropanoids in radish; representative metabolites such as afzelin, naringenin, and linolenic acid fall within the established radish metabolome and plant polyunsaturated fatty-acid pools (Tables S15−S16, Supporting Information).[65] Under pesticide stress, multiple studies have reported the suppression of flavonoid pathways. For example, chlorpyrifos drives broad downregulation at higher doses, and triazole fungicides in lettuce have been shown to perturb lipid metabolism. These observations support the decline of flavonoid and lipid-related metabolites observed under Scorpion treatment.[72] The accompanying shift toward nitrogen-intensive defenses is consistent with the activation of arginine-derived polyamine/NO pathways in response to stress.[75]

The comparative analysis of control vs Belem100× reveals similarities with previous comparisons, such as increased levels of 3-ureidopropionate and arginine in the treated sample and higher abundance of tyramine, afzelin, naringenin, and epicatechin in the control sample (Table S17, Supporting Information). A putative impact on coenzyme Q biosynthesis is supported by the elevated level of 4-hydroxybenzoate, a recognized eukaryotic precursor of coenzyme Q, which has been documented in both plants and fungi.[72] In turn, higher pipecolate and cytidine concentrations in the control are consistent with perturbations of amino acid degradation and nucleotide metabolism under pesticide treatment. The levels of valerylcarnitine accumulated in the Belem-treated samples were particularly high and are best interpreted as buffering of acyl-CoA homeostasis (acylcarnitine shuttling) under strong lipid flux perturbation.[67] Pathway analysis indicated contributions of arginine and β-alanine metabolism in Belem100×, while control samples were associated with flavonoid and isoquinoline alkaloid biosynthesis (Tables S18, S20, Supporting Information). Chemical class enrichment further supported these patterns. In Belem100×, only a few classes, such as thiolactams and certain fatty acyls, were more abundant. In contrast, flavonoids, pyrimidine nucleosides, keto acids, and multiple fatty acyls were significantly enriched in the control (Tables S19 and S21, Supporting Information). This pattern, phenolic/lipid prevalence in controls vs nitrogen-/amino acid-centered shifts in treated plants, is in line with stress-metabolome literature for *Brassicaceae* and related species.[63]

In the case of Snacol at the high dose (Snacol100×), the metabolic response of radish plants was portrayed by three metabolites of statistical and biological significance: valerylcarnitine, arginine, and pyruvaldehyde (Table S22, Supporting Information). Although the limited number of hits precluded robust pathway enrichment, their biological relevance is substantial. At the chemical main-class level, these metabolites belonged to organooxygen compounds, carboxylic acids and derivatives, and fatty acyls (Table S23, Supporting Information). As noted earlier, the rise of valerylcarnitine indicates overflow of acyl-CoA/fatty-acid fluxes, while elevated arginine is consistent with activation of arginine-derived polyamine/NO routes.[69] Pyruvaldehyde, also known as methylglyoxal, is an intermediate produced by both enzymatic and nonenzymatic pathways, acting as a signaling molecule at low concentrations but exerting cytotoxic effects when strongly accumulated.[76] Together, these features suggest that a high dose of Snacol triggers a targeted but intense perturbation of central carbon and lipid metabolism along with activation of nitrogen/arginine-linked stress-responsive pathways.

In contrast, the control samples exhibited a broader metabolic profile, with enrichment of pathways associated with primary and secondary metabolism, including biosynthesis of unsaturated fatty acids, tyrosine and tryptophan metabolism, riboflavin metabolism, flavone and flavonol biosynthesis, and biosynthesis of indole and isoquinoline alkaloids (Table S24, Supporting Information). Class-level analysis further highlighted an overrepresentation of fatty acyls, flavonoids, indoles and derivatives, purine nucleosides, imidazopyrimidines, and pteridines (Table S25, Supporting Information), consistent with a metabolically diverse, unstressed baseline.

3.2.4. Metabolomic Analysis of Mixture and Single Pesticides under High-Dose Exposure. The comparative analysis of Mix100× and Snacol100× (Tables S26−S28 Supporting Information) showed that in Mix100×, five metabolites exceeded the dual threshold of statistical significance and biological relevance, indicating a strong metabolic response. These included tryptamine, homoveratric acid, fructose, valeric acid, and dodecanamide. The profile is dominated by a striking accumulation of tryptamine, an indole-related stress metabolite, consistent with activation of tryptophan/indole metabolism.[77] The Snacol100× treatment elicited a more constrained metabolic response. Only two metabolites passed the thresholds: indole-3-lactic acid and methylglyoxal/pyruvaldehyde, both decreased in Snacol relative to the mix. Indole-3-lactic acid is a low-abundance indolic metabolite in plants and indicates redirection within tryptophan catabolism.[78] The difference in the methylglyoxal levels is consistent with a divergent balance of carbonyl stress between treatments. Overall, Snacol alone elicited a signature narrower than that of the mixture.

The comparative analysis of Mix100× and Scorpion100× (Tables S29 and S32, Supporting Information) revealed distinct metabolic signatures between the mixture and the single-pesticide treatment. In Mix100×, seven metabolites exceeded both statistical and biological thresholds, again indicating stronger indolic/phenylpropanoid engagement than with Scorpion alone. These included tryptamine, succinylacetone, homoveratric acid, 6-gingerol, naringenin, 5,7-dihydroxychromen-4-one, and linoleoylglycine. Because succinylacetone is not typically reported in plants, we treat this cautiously, although accumulation under tyrosine catabolism blockade has been shown in *Arabidopsis*.[60] In contrast, nine metabolites were significantly altered in Scorpion100×, including sinapic acid and its glucoside, indole-3-lactic acid, tryptophanol, p-anisic acid, niacinamide, pipecolic acid, and a PI(16:0/18:3) species. Pathway analysis identified contributions from nicotinate/nicotinamide metabolism, lysine degradation, and phenylpropanoid biosynthesis. Although sinapic acid and its derivatives are widely present in *Brassicaceae* vegetables, their accumulation is believed to be a favorable adaptation process under environmental stress.[79] Elevated indolelactic acid and tryptophanol (also known as tryptophol or indole-3-ethanol) suggest shifts in tryptophan metabolism. The presence of niacinamide (nicotinamide) points to perturbations of NAD^+ homeostasis in the nicotinate/nicotinamide pool,[80] and the higher level of pipecolic acid, a regulator of systemic acquired resistance, suggests that Scorpion100× promotes immune-related signaling.[81]

The comparative analysis of Mix100× and Belem100× (Tables S33 and S35, Supporting Information) revealed clear treatment-specific differences. In Mix100×, six metabolites met the statistical criteria, all showing higher levels relative to Belem100×. These include 3-hydroxy-4-ketotorulene, homoveratric acid, methyl-4-hydroxycinnamate, naringenin, and 2-octenoic acid. Because 3-hydroxy-4-ketotorulene is a yeast-associated carotenoid, this annotation should be considered putative and verified by MS/MS; extreme FC values may signal mis-annotation or background.[82] In contrast, Belem100× exposure resulted in significantly lower levels relative to Mix100× for LPI 18:1, sclareolide, dihydrokaempferol, niacinamide, hoveitrichoside C, pentadecanoic acid, and valerylcarnitine. High levels of valerylcarnitine in the Belem treatment were confirmed in the Belem versus Control comparison, suggesting that cypermethrin has a pronounced effect on lipid metabolism. However, in the Mix100× vs Belem contrast, valerylcarnitine levels were lower in the mixture, indicating that this specific effect of Belem was attenuated in the presence of other pesticides. The presence of sclareolide and hoveitrichoside C suggests engagement of additional secondary-metabolite branches under Belem exposure. Together, these patterns indicate that the mixture recruits broader secondary-metabolite and lipid responses than those of Belem alone.

3.2.5. Metabolic Effects of High-Dose Mixture and Pooled Single Pesticides. The comparative analysis of Mix100× versus Singles100× revealed a striking divergence in the metabolic response, indicating that the combined exposure to all pesticides cannot be considered equivalent to the sum of the effects elicited by each pesticide individually (Tables S36 and S38, Supporting Information). In the Mix100× treatment, only two metabolites, tryptamine and homoveratric acid, were statistically and biologically significant. Notably, the exceptionally high fold change of tryptamine indicates a highly selective yet pronounced metabolic reprogramming. In contrast, the Singles100× group, which aggregates the effects of individual pesticide treatments, displayed significant alterations in 19 metabolites spanning diverse chemical classes and pathways, including pyrimidine metabolism, purine metabolism, flavonoid biosynthesis, and nicotinate and nicotinamide metabolism. This discrepancy highlights that exposure to the pesticide mixture does not simply reproduce the additive effects of single compounds but instead triggers a qualitatively distinct metabolic response.

The dominance of tryptamine accumulation in the Mix100× group suggests that the mixture acts as a strong but focused inducer of indole-derived pathways, potentially linked to stress signaling or defense-related metabolic adjustments. Meanwhile, the broad spectrum of changes observed under Singles100× indicates that individual pesticides perturb multiple metabolic nodes. However, when combined, these effects are not additive; instead, they appear to be suppressed, masked, or rechanneled into a narrower set of dominant responses. This observation suggests possible synergistic or compensatory interactions between pesticides, where the simultaneous presence of multiple compounds reshapes the plant's regulatory networks, prioritizing specific pathways while attenuating others. Such nonadditive effects challenge the assumption that mixture toxicity can be extrapolated from single-compound studies. These findings also highlight metabolic plasticity as a critical factor in the response to complex exposures. The results suggest that plants confronted with simultaneous pesticide stressors reorganize their metabolism in a way that is not predictable from the sum of single stress responses, raising important implications for both toxicological assessments and our understanding of plant adaptive strategies.[83,84]

3.2.6. Metabolic Effects of High-Dose Mixture. The comparative analysis of Mix1× and Mix100× revealed a clear dose-dependent effect of pesticide exposure (Tables S39 and S42, Supporting Information). At the recommended dose (Mix1×), the number and extent of metabolic changes were limited, and the magnitude of fold changes remained modest. Significant differences were primarily linked to the relative depletion of nicotinamide in Mix1× and to enrichment signals in the nicotinate/nicotinamide (NAD^+ salvage) pathway. This pattern is consistent with dose-dependent regulation of the pyridine-nucleotide pool (NAD^+/NADH, NADP(H)) in plants.[80] Chemical class enrichment supported this observation, with pyridines/derivatives (nicotinamide) and keto acids/derivatives enriched, aligning with central energy and redox coupling via the TCA cycle.[85] A mild tendency toward flavonoid enrichment further suggests a subtle antioxidant adjustment, as expected in phenolic-rich *Brassicaceae* species.[86] These results indicate that at field-level doses, radish plants primarily engage early adaptive compensatory mechanisms without broad metabolic reprogramming.

In contrast, at the high dose (Mix100×), both the number of altered metabolites and the magnitude of their fold changes were substantially greater, increased significantly, resulting in enrichment of the arginine/proline network, a stress-responsive hub linked to proline biosynthesis, ROS control, and nitrogen metabolism; this is coherent with the tight integration of carbon−nitrogen metabolism and redox control around respiratory/TCA nodes in plants.[85] Additional enrichment was observed for other amino acid pathways (alanine, aspartate, and glutamate metabolism; phenylalanine metabolism) and secondary routes (phenylpropanoid biosynthesis, glucosinolate biosynthesis) driven by elevated precursor pools—particularly, phenylalanine for phenylpropanoids (rather than alanine) and by broader C/N remodeling. Chemical class enrichment was fully consistent: the strongest signals appeared for carboxylic acids/derivatives (amino acids), indoles/derivatives typical of *Brassicaceae* (e.g., indolic glucosinolates), and wider nitrogen- and phenolic-containing classes (organonitrogen compounds; benzene and substituted derivatives).[86]

Consistent with previous studies, our results indicate that high-dose pesticide exposure elicits a broader and more intense metabolic perturbation, recruiting both primary metabolism (amino acids, carboxylic acids) and secondary metabolism (indoles, phenolics, glucosinolates), in a systemic response characteristic of severe toxic stress in plants.[83,84]

3.3. 3D-LARAPPI/CI-MSI of a Radish Taproot Region. In addition to the 2D LARAPPI/CI-MSI and UHPLC-UHRMS analyses performed on the control and pesticide-treated radish samples, a separate 3D-LARAPPI/CI-MSI analysis was conducted on an untreated (control) radish taproot to demonstrate the capability of this method for visualizing the three-dimensional spatial distribution of metabolites throughout the root tissue. The results of the 3D-MSI analysis were interpreted using compounds identified by UHPLC-UHRMS, as well as putatively identified metabolites from plant metabolite databases. This analysis demonstrated that the metabolite distribution varies significantly with depth, even within small sample regions. Consequently, 2D-MSI results can be further validated and supplemented with additional spatial context, particularly in cases in which 2D analysis alone may be inconclusive. Selected results of the 3D-LARAPPI/CI-MSI of the radish sample are shown in Figure 3. The predominant regions where most compound ions were localized are the parenchyma, cortex, vascular bundles, and epidermis. In the parenchyma, key compounds, such as ribose, purine, ascorbic acid, and tyrosine, were localized. These metabolites play fundamental roles in energy metabolism and structural biosynthesis in plants. The cortex region exhibited the highest abundance of amino acids and their metabolites. This is consistent with the 2D-MSI results in Section 3.1, where amino acids were most abundant in the stele region during early development. Another correlation can be drawn between the identification of fatty acids, such as oleic acid, in the epidermal

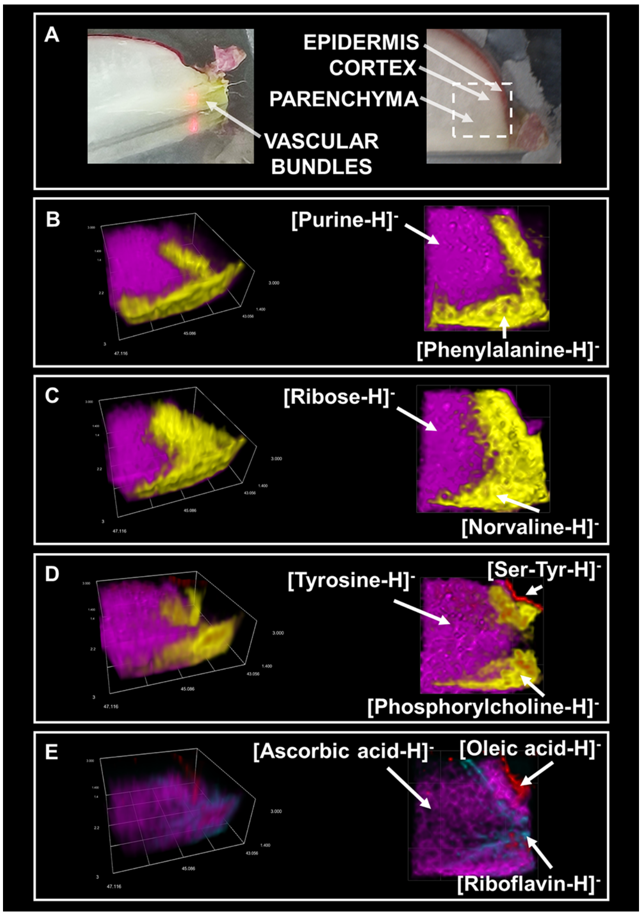

Figure 3. Selected 3D-LARAPPI/CI-MSI visualizations of the 3D-MSI metabolite distribution in radish. (A) Photographs of the analyzed radish sample: an angled view highlighting the cortex and vascular bundles and a top-down image indicating the analyzed region. Visualization of purine and phenylalanine distribution (B), visualization of ribose and norvaline distribution (C), visualization of tyrosine, Ser-Tyr, and phosphorylcholine ions (D), visualization of ascorbic acid, oleic acid, and riboflavin distribution (E). The color scheme indicates tissue-specific localization: magenta (parenchyma), yellow (cortex), red (epidermis), and cyan (vascular bundles).

part, as in the pesticide-treated radish sample. Serine-tyrosine (Ser-Tyr), a dipeptide also identified in the pesticide-affected sample in the 2D imaging, was found in the epidermal region as well. (c) Interestingly, this m/z value was not detected in the 2D-MSI results of either the control or pesticide-treated radish, suggesting that certain metabolites may be more readily visualized in three-dimensional analysis. The 3D visualization may provide a clearly visible volumetric shape of the ion of interest for which individual 2D images may be of low interest; for example, it is possible for vertical compound distributions. Vertically shaped, relatively weak signals may be better visible in 3D to the person performing the analysis.

Overall, the results of 3D-MSI validate and expand upon the findings from 2D-MSI, confirming the spatial distribution of key metabolites in both the pesticide-treated and the control radish.

This work combines untargeted UHPLC-UHRMS with 2D/3D-LARAPPI/CI-MSI to elucidate how radish metabolism responds to pesticide exposure across different doses and compositions. The dataset shows a dose-dependent gradient: field-dose exposure results in modest, node-level adjustments, whereas the high-dose mixture elicits a systemic shift characterized by activation of arginine/proline and β-alanine pathways, indolic and phenylpropanoid branches, carbohydrate remodeling (including fructose), and disturbances in lipid flux, as evidenced by acylcarnitine accumulation. Among the single-compound high-dose treatments, Scorpion most closely recapitulates the mixture's indolic/phenylpropanoid signature. Treatment with Belem results in pronounced lipid perturbation, accompanied by concurrent reductions in phenolics and nucleosides relative to the control, whereas Snacol produces a narrower profile, characterized by alterations in methylglyoxal and arginine. Direct mixture-to-single contrasts indicate non-additive, mixture-specific features (e.g., stronger indole-linked signals such as tryptamine), underscoring that mixture effects are not simply the sum of their parts. MSI complements UHPLC−UHRMS by localizing metabolite changes in tissue space and depth, helping to interpret shifts in central carbon, nitrogen, and secondary pathways under severe stress. Together, these results support a model in which pesticide exposure drives a resource reallocation from lipid/phenolic maintenance toward nitrogen-intensive stress programs and enhanced energy/redox turnover, with the extent of reprogramming scaling with dose and composition. Limitations of this study include a modest number of biological replicates and the use of controlled growth conditions without pest pressure. These data warrant validation in a larger sample set and targeted LC−MS/MS using authentic external standards.

■ ASSOCIATED CONTENT

Data Availability Statement

The data sets generated during and/or analyzed during the current study are available from the corresponding author upon request and in the RepOD open data repository (doi: 10.18150/H9GBGK).

Supporting Information

The Supporting Information is available free of charge at https://pubs.acs.org/doi/10.1021/acs.jafc.5c12445.

> Ion images obtained by 2D LARAPPI/CI-MSI for control and pesticide-treated radish samples (Figures S1−S6), principal component analysis plots (Figure S7), and comprehensive UHPLC-UHRMS metabolomic data sets (Tables S1−S3). It also includes pathway and enrichment analyses for metabolites differentiating various pesticide treatments and doses (Tables S4−S43), as well as a description of the custom-developed software used for LARAPPI/CI-MSI control and visualization (S1) (PDF)

■ AUTHOR INFORMATION

Corresponding Author

Joanna Nizioł − *Department of Polymers and Biopolymers, Faculty of Chemistry, Rzeszów University of Technology, Rzeszów 35-959, Poland;* orcid.org/0000-0002-4783-8615; Email: jniziol@prz.edu.pl

Authors

Sumi Krupa − *Doctoral School at the Rzeszów University of Technology, Rzeszów 35-959, Poland;* orcid.org/0009-0008-8916-0946

Tomasz Ruman − *Department of Inorganic and Analytical Chemistry, Faculty of Chemistry, Rzeszów University of Technology, Rzeszów 35-959, Poland;* orcid.org/0000-0002-9899-8627

Complete contact information is available at: https://pubs.acs.org/10.1021/acs.jafc.5c12445

Author Contributions

Sumi Krupa: methodology, writing—original draft, visualization, investigation, and data curation. **Tomasz Ruman:** methodology, resources, writing—review and editing, and data curation. **Joanna Nizioł:** conceptualization, methodology, investigation, data curation, supervision, investigation, visualization, writing—review and editing, project administration, and funding acquisition.

Notes

The authors declare no competing financial interest.

■ ACKNOWLEDGMENTS

This work was supported by the National Science Centre (Poland) Research Project Sonata Bis number 2022/46/E/ST4/00016.

■ REFERENCES

(1) Prieto, M. A.; López, C. J.; Simal-Gandara, J. Glucosinolates: Molecular Structure, Breakdown, Genetic, Bioavailability, Properties and Healthy and Adverse Effects. *Adv. Food Nutr. Res.* **2019**, *90*, 305−350.

(2) Yi, G.; Lim, S.; Chae, W. B.; Park, J. E.; Park, H. R.; Lee, E. J.; Huh, J. H. Root Glucosinolate Profiles for Screening of Radish (*Raphanus Sativus* L.) Genetic Resources. *J. Agric. Food Chem.* **2016**, *64* (1), 61−70.

(3) Hanlon, P. R.; Barnes, D. M. Phytochemical Composition and Biological Activity of 8 Varieties of Radish (*Raphanus Sativus* L.) Sprouts and Mature Taproots. *J. Food Sci.* **2011**, *76* (1), C185−C192.

(4) Goyeneche, R.; Rodrigues, C. R.; Quispe-Fuentes, I.; Pellegrini, M. C.; Cumino, A.; Di Scala, K. Radish Leaves Extracts as Functional Ingredients: Evaluation of Bioactive Compounds and Health-Promoting Capacities. *Waste Biomass Valorization* **2025**, *16* (2), 1003−1014.

(5) Zieliński, H.; Frias, J.; Piskuła, M. K.; Kozłowska, H.; Vidal-Valverde, C. Vitamin B1 and B2, Dietary Fiber and Minerals Content of Cruciferae Sprouts. *Eur. Food Res. Technol.* **2005**, *221* (1−2), 78−83.

(6) Gamba, M.; Asllanaj, E.; Raguindin, P. F.; Glisic, M.; Franco, O. H.; Minder, B.; Bussler, W.; Metzger, B.; Kern, H.; Muka, T. Nutritional and Phytochemical Characterization of Radish (*Raphanus Sativus*): A Systematic Review. *Trends Food Sci. Technol.* **2021**, *113*, 205−218.

(7) Goyeneche, R.; Roura, S.; Ponce, A.; Vega-Gálvez, A.; Quispe-Fuentes, I.; Uribe, E.; Di Scala, K. Chemical Characterization and Antioxidant Capacity of Red Radish (*Raphanus Sativus* L.) Leaves and Roots. *J. Funct. Foods* **2015**, *16*, 256−264.

(8) Tudi, M.; Ruan, H. D.; Wang, L.; Lyu, J.; Sadler, R.; Connell, D.; Chu, C.; Phung, D. T. Agriculture Development, Pesticide Application and Its Impact on the Environment. *Int. J. Environ. Res. Public Health* **2021**, *18* (3), 1112.

(9) Abd-Alla, M. H.; Omar, S. A.; Karanxha, S. The Impact of Pesticides on Arbuscular Mycorrhizal and Nitrogen-Fixing Symbioses in Legumes. *Appl. Soil Ecol.* **2000**, *14* (3), 191−200.

(10) Parween, T.; Jan, S.; Mahmooduzzafar, S.; Fatma, T.; Siddiqui, Z. H. Selective Effect of Pesticides on Plant—A Review. *Crit. Rev. Food Sci. Nutr.* **2016**, *56* (1), 160−179.

(11) Baskar, V.; Thiruvengadam, M.; Sharma, K.; Govindasamy, R.; Shahid, M.; Singh, U. B.; Khan, M. S. Metabolomics-Based Mechanistic Insights into Revealing the Adverse Effects of Pesticides on Plants: An Interactive Review. *Metabolites* **2023**, *13* (2), 246.

(12) Aliferis, K. A.; Jabaji, S. Metabolomics − A Robust Bioanalytical Approach for the Discovery of the Modes-of-Action of Pesticides: A Review. *Pestic. Biochem. Physiol.* **2011**, *100* (2), 105−117.

(13) Zhao, L.; Ortiz, C.; Adeleye, A. S.; Hu, Q.; Zhou, H.; Huang, Y.; Keller, A. A. Metabolomics to Detect Response of Lettuce (Lactuca Sativa) to Cu(OH)2 Nanopesticides: Oxidative Stress Response and Detoxification Mechanisms. *Environ. Sci. Technol.* **2016**, *50* (17), 9697−9707.

(14) Lin, L. Z.; Sun, J.; Chen, P.; Harnly, J. A. LC-PDA-ESI/MSn Identification of New Anthocyanins in Purple Bordeaux Radish (*Raphanus Sativus* L. Variety). *J. Agric. Food Chem.* **2011**, *59* (12), 6616−6627.

(15) Wang, Y.; Xu, L.; Shen, H.; Wang, J.; Liu, W.; Zhu, X.; Wang, R.; Sun, X.; Liu, L. Metabolomic Analysis with GC-MS to Reveal Potential Metabolites and Biological Pathways Involved in Pb &cd Stress Response of Radish Roots. *Sci. Rep.* **2015**, *5* (1), No. 18296.

(16) Otsuki, T.; Matsufuji, H.; Takeda, M.; Toyoda, M.; Goda, Y. Acylated Anthocyanins from Red Radish (*Raphanus Sativus* L.). *Phytochemistry* **2002**, *60* (1), 79−87.

(17) Boughton, B. A.; Thinagaran, D.; Sarabia, D.; Bacic, A.; Roessner, U. Mass Spectrometry Imaging for Plant Biology: A Review. *Phytochem. Rev.* **2016**, *15* (3), 445−488.

(18) Gemperline, E.; Keller, C.; Li, L. Mass Spectrometry in Plant-Omics. *Anal. Chem.* **2016**, *88* (7), 3422−3434.

(19) Brauer, J. I.; Beech, I. B.; Sunner, J. Mass Spectrometric Imaging Using Laser Ablation and Solvent Capture by Aspiration (LASCA). *J. Am. Soc. Mass Spectrom.* **2015**, *26* (9), 1538−1547.

(20) Seaman, C.; Flinders, B.; Eijkel, G.; Heeren, R. M. A.; Bricklebank, N.; Clench, M. R. "Afterlife Experiment": Use of MALDI-MS and SIMS Imaging for the Study of the Nitrogen Cycle within Plants. *Anal. Chem.* **2014**, *86* (20), 10071−10077.

(21) Lima, G. da S.; Pereira, I.; Maciel, L. I. L.; Lima, N. M.; Araujo, G. L.; de Aguiar, D. V. A.; Dos Santos, G. F.; Vaz, B. G. Combining LAESI Imaging and Tissue Spray Ionization Mass Spectrometry To Unveil Pesticides Contaminants in Fruits. *J. Am. Soc. Mass Spectrom.* **2023**, *34* (11), 2461−2468.

(22) Gerbig, S.; Brunn, H. E.; Spengler, B.; Schulz, S. Spatially Resolved Investigation of Systemic and Contact Pesticides in Plant Material by Desorption Electrospray Ionization Mass Spectrometry Imaging (DESI-MSI). *Anal. Bioanal. Chem.* **2015**, *407* (24), 7379−7389.

(23) Qin, R.; Li, P.; Du, M.; Ma, L.; Huang, Y.; Yin, Z.; Zhang, Y.; Chen, D.; Xu, H.; Wu, X. Spatiotemporal Visualization of Insecticides and Fungicides within Fruits and Vegetables Using Gold Nanoparticle-Immersed Paper Imprinting Mass Spectrometry Imaging. *Nanomaterials* **2021**, *11* (5), 1327.

(24) Ruman, T.; Krupa, Z.; Nizioł, J. Direct Three-Dimensional Mass Spectrometry Imaging with Laser Ablation Remote Atmospheric Pressure Photoionization/Chemical Ionization. *Anal. Chem.* **2024**, *96* (32), 13326−13334.

(25) Krupa, S.; Ruman, T.; Szuberla, W.; Nizioł, J. Analysis of the Spatial Distribution of Metabolites in Aloe Vera Leaves by Mass Spectrometry Imaging and UHPLC-UHRMS. *Sci. Rep.* **2025**, *15* (1), No. 3502.

(26) Krupa, S.; Szuberla, W.; Nizioł, J.; Ossolińska, A.; Ossoliński, K.; Ruman, T. Broadband Collision-Induced Dissociation Mass Spectrometry Imaging. *J. Am. Soc. Mass Spectrom.* **2025**, *36* (7), 1443−1455.

(27) Szulc, J.; Grzyb, T.; Nizioł, J.; Krupa, S.; Szuberla, W.; Ruman, T. Direct 3D Mass Spectrometry Imaging Analysis of Environmental Microorganisms. *Molecules* **2025**, *30* (6), 1317.

(28) Szulc, J.; Grzyb, T.; Gutarowska, B.; Nizioł, J.; Krupa, S.; Ruman, T. 3D Mass Spectrometry Imaging as a Novel Screening Method for Evaluating Biocontrol Agents. *J. Agric. Food Chem.* **2025**, *73*, 8225.

(29) Ruman, T.; Krupa, Z.; Nizioł, J. Direct Three-Dimensional Mass Spectrometry Imaging with Laser Ablation Remote Atmospheric Pressure Photoionization/Chemical Ionization. *Anal. Chem.* **2024**, *96* (32). 13326.

(30) Nizioł, J.; Misiorek, M.; Krupa, Z.; Ruman, T. Infrared Laser-Based Selected Reaction Monitoring Mass Spectrometry Imaging of Banana (Musa Spp.) Tissue—New Method for Detection and Spatial Localization of Metabolites in Food. *Food Anal. Methods* **2023**, *17*, 236−250.

(31) Sumner, L. W.; Amberg, A.; Barrett, D.; Beale, M. H.; Beger, R.; Daykin, C. A.; Fan, T. W. M.; Fiehn, O.; Goodacre, R.; Griffin, J. L.; Hankemeier, T.; Hardy, N.; Harnly, J.; Higashi, R.; Kopka, J.; Lane, A. N.; Lindon, J. C.; Marriott, P.; Nicholls, A. W.; Reily, M. D.; Thaden, J. J.; Viant, M. R. Proposed Minimum Reporting Standards for Chemical Analysis: Chemical Analysis Working Group (CAWG) Metabolomics Standards Initiative (MSI). *Metabolomics* **2007**, *3* (3), 211−221.

(32) Pang, Z.; Lu, Y.; Zhou, G.; Hui, F.; Xu, L.; Viau, C.; Spigelman, A. F.; Macdonald, P. E.; Wishart, D. S.; Li, S.; Xia, J. MetaboAnalyst 6.0: Towards a Unified Platform for Metabolomics Data Processing, Analysis and Interpretation. *Nucleic Acids Res.* **2024**, *52* (W1), W398−W406.

(33) Tan, S.; Evans, R.; Singh, B. Herbicidal Inhibitors of Amino Acid Biosynthesis and Herbicide-Tolerant Crops. *Amino Acids* **2006**, *30* (2), 195−204.

(34) Azevedo, R. A.; Lea, P. J. Lysine Metabolism in Higher Plants. *Amino Acids* **2001**, *20* (3), 261−279.

(35) Cohen, H.; Salmon, A.; Tietel, Z.; Hacham, Y.; Amir, R. The Relative Contribution of Genes Operating in the S-Methylmethionine Cycle to Methionine Metabolism in Arabidopsis Seeds. *Plant Cell Rep.* **2017**, *36* (5), 731−743.

(36) Forde, B. G.; Lea, P. J. Glutamate in Plants: Metabolism, Regulation, and Signalling. *J. Exp. Bot.* **2007**, *58* (9), 2339−2358.

(37) Rowbury, R. J. Resistance to Norleucine and Control of Methionine Synthesis in *Escherichia Coli*. *Nature* **1965**, *206* (4987), 962−963.

(38) Yan, J.; Lipka, A. E.; Schmelz, E. A.; Buckler, E. S.; Jander, G. Accumulation of 5-Hydroxynorvaline in Maize (Zea Mays) Leaves Is Induced by Insect Feeding and Abiotic Stress. *J. Exp. Bot.* **2015**, *66* (2), 593−602.

(39) Skwarecki, A. S.; Schielmann, M.; Martynow, D.; Kawczyński, M.; Wiśniewska, A.; Milewska, M. J.; Milewski, S. Antifungal Dipeptides Incorporating an Inhibitor of Homoserine Dehydrogenase. *J. Pept. Sci.* **2018**, *24* (1), No. e3060, DOI: 10.1002/psc.3060.

(40) Tzin, V.; Galili, G. New Insights into the Shikimate and Aromatic Amino Acids Biosynthesis Pathways in Plants. *Mol. Plant* **2010**, *3* (6), 956−972.

(41) Rai, V. K. Role of Amino Acids in Plant Responses to Stresses. *Biol. Plant* **2002**, *45* (4), 481−487.

(42) Citi, V.; Piragine, E.; Pagnotta, E.; Ugolini, L.; Di Cesare Mannelli, L.; Testai, L.; Ghelardini, C.; Lazzeri, L.; Calderone, V.; Martelli, A. Anticancer Properties of Erucin, an H2S-Releasing Isothiocyanate, on Human Pancreatic Adenocarcinoma Cells (AsPC-1). *Phytother. Res.* **2019**, *33* (3), 845−855.

(43) Singh, S.; Pathak, N.; Fatima, E.; Negi, A. S. Plant Isoquinoline Alkaloids: Advances in the Chemistry and Biology of Berberine. *Eur. J. Med. Chem.* **2021**, *226*, No. 113839.

(44) Mukherjee, A.; Sarkar, N.; Barik, A. Long-Chain Free Fatty Acids from Momordica Cochinchinensis Leaves as Attractants to Its Insect Pest, Aulacophora Foveicollis Lucas (Coleoptera: Chrysomelidae). *J. Asia Pac. Entomol.* **2014**, *17* (3), 229−234.

(45) Kanobe, C.; McCarville, M. T.; O'Neal, M. E.; Tylka, G. L.; MacIntosh, G. C. Soybean Aphid Infestation Induces Changes in Fatty Acid Metabolism in Soybean. *PLoS One* **2015**, *10* (12), No. e0145660.

(46) Fabiyi, O. A.; Baker, M. T.; Olatunji, G. A. Application of Fatty Acid Esters on Meloidogyne Incognita Infected Jew's Mallow Plants. *Pak. J. Nematol.* **2022**, *40* (2), 127−137.

(47) Gonçalves, A. M.; Rocha, C. P.; Marques, J. C.; Gonçalves, F. J. M. Fatty Acids as Suitable Biomarkers to Assess Pesticide Impacts in Freshwater Biological Scales − A Review. *Ecol. Indic.* **2021**, *122*, No. 107299.

(48) Du, C.; Cao, S.; Shi, X.; Nie, X.; Zheng, J.; Deng, Y.; Ruan, L.; Peng, D.; Sun, M. Genetic and Biochemical Characterization of a Gene Operon for Trans-Aconitic Acid, a Novel Nematicide from Bacillus Thuringiensis. *J. Biol. Chem.* **2017**, *292* (8), 3517−3530.

(49) Tayeb, W.; Nakbi, A.; Cheraief, I.; Miled, A.; Hammami, M. Alteration of Lipid Status and Lipid Metabolism, Induction of Oxidative Stress and Lipid Peroxidation by 2,4-Dichlorophenoxyacetic Herbicide in Rat Liver. *Toxicol. Mech. Methods* **2013**, *23* (6), 449−458.

(50) Zhou, J.; Zhang, L.; Chang, Y.; Lu, X.; Zhu, Z.; Xu, G. Alteration of Leaf Metabolism in Bt-Transgenic Rice (Oryza Sativa L.) and Its Wild Type under Insecticide Stress. *J. Proteome Res.* **2012**, *11* (8), 4351−4360.

(51) Campe, R.; Hollenbach, E.; Kämmerer, L.; Hendriks, J.; Höffken, H. W.; Kraus, H.; Lerchl, J.; Mietzner, T.; Tresch, S.; Witschel, M.; Hutzler, J. A New Herbicidal Site of Action: Cinmethylin Binds to Acyl-ACP Thioesterase and Inhibits Plant Fatty Acid Biosynthesis. *Pestic. Biochem. Physiol.* **2018**, *148*, 116−125.

(52) Hejazi, M.; Piotukh, K.; Mattow, J.; Deutzmann, R.; Volkmer-Engert, R.; Lockau, W. Isoaspartyl Dipeptidase Activity of Plant-Type Asparaginases. *Biochem. J.* **2002**, *364* (1), 129−136.

(53) Borek, D.; Michalska, K.; Brzezinski, K.; Kisiel, A.; Podkowinski, J.; Bonthron, D. T.; Krowarsch, D.; Otlewski, J.; Jaskolski, M. Expression, Purification and Catalytic Activity of *Lupinus Luteus* Asparagine β-Amidohydrolase and Its *Escherichia Coli* Homolog. *Eur. J. Biochem.* **2004**, *271* (15), 3215−3226.

(54) Zhang, Y. M.; Ye, D. X.; Liu, Y.; Zhang, X. Y.; Zhou, Y. L.; Zhang, L.; Yang, X. L. Peptides, New Tools for Plant Protection in Eco-Agriculture. *Adv. Agrochem.* **2023**, *2* (1), 58−78.

(55) Xuan, T. D.; Tsuneaki, T.; Masakazu, F.; Tran, D. K.; Shinkichi, T. Chemical Interaction in the Invasiveness of Cogongrass (Imperata Cylindrica (L.) Beauv.). *J. Agric. Food Chem.* **2009**, *57* (20), 9448−9453.

(56) Ishida, M.; Hara, M.; Fukino, N.; Kakizaki, T.; Morimitsu, Y. Glucosinolate Metabolism, Functionality and Breeding for the Improvement of Brassicaceae Vegetables. *Breed Sci.* **2014**, *64* (1), 48.

(57) Liu, X.; Wang, S.; Tang, H.; Li, M.; Gao, P.; Peng, X.; Chen, M. Uridine Diphosphate-Glycosyltransferase RpUGT344D38 Contributes to λ-Cyhalothrin Resistance in Rhopalosiphum Padi. *J. Agric. Food Chem.* **2024**, *72* (10), 5165−5175.

(58) Zakharychev, V. V.; Kuzenkov, A. V.; Martsynkevich, A. M. Good Pyridine Hunting: A Biomimic Compound, a Modifier and a Unique Pharmacophore in Agrochemicals. *Chem. Heterocycl. Compd.* **2020**, *56* (12), 1491−1516.

(59) Aigensberger, M.; Bueschl, C.; Castillo-Lopez, E.; Ricci, S.; Rivera-Chacon, R.; Zebeli, Q.; Berthiller, F.; Schwartz-Zimmermann, H. E. Modular Comparison of Untargeted Metabolomics Processing Steps. *Anal. Chim. Acta* **2025**, *1336*, No. 343491.

(60) Han, C.; Ren, C.; Zhi, T.; Zhou, Z.; Liu, Y.; Chen, F.; Peng, W.; Xie, D. Disruption of Fumarylacetoacetate Hydrolase Causes Spontaneous Cell Death under Short-Day Conditions in Arabidopsis. *Plant Physiol.* **2013**, *162* (4), 1956−1964.

(61) Patočka, J.; Jakl, J. Biomedically Relevant Chemical Constituents of *Valeriana Officinalis*. *J. Appl. Biomed.* **2010**, *8* (1), 11−18.

(62) Krzyżowski, M.; Francikowski, J.; Baran, B.; Babczyńska, A. The Short-Chain Fatty Acids as Potential Protective Agents against Callosobruchus Maculatus Infestation. *J. Stored Prod. Res.* **2020**, *86*, No. 101570.

(63) Jahangir, M.; Abdel-Farid, I. B.; Kim, H. K.; Choi, Y. H.; Verpoorte, R. Healthy and Unhealthy Plants: The Effect of Stress on the Metabolism of Brassicaceae. *Environ. Exp. Bot.* **2009**, *67* (1), 23−33.

(64) Hurtado, C.; Parastar, H.; Matamoros, V.; Piña, B.; Tauler, R.; Bayona, J. M. Linking the Morphological and Metabolomic Response of Lactuca Sativa L Exposed to Emerging Contaminants Using GC × GC-MS and Chemometric Tools. *Sci. Rep.* **2017**, *7* (1), No. 6546.

(65) Zhang, J.; Qiu, X.; Tan, Q.; Xiao, Q.; Mei, S. A Comparative Metabolomics Study of Flavonoids in Radish with Different Skin and Flesh Colors (*Raphanus Sativus* L.). *J. Agric. Food Chem.* **2020**, *68* (49), 14463−14470.

(66) Palaniswamy, S.; Abass, K.; Rysä, J.; Grimalt, J. O.; Odland, J. Ø.; Rautio, A.; Järvelin, M. R. Investigating the Relationship between Non-Occupational Pesticide Exposure and Metabolomic Biomarkers. *Front. Public Health* **2023**, *11*, No. 1248609.

(67) Jacques, F.; Rippa, S.; Perrin, Y. Physiology of L-Carnitine in Plants in Light of the Knowledge in Animals and Microorganisms. *Plant Sci.* **2018**, *274*, 432−440.

(68) Bourdin, B.; Adenier, H.; Perrin, Y. Carnitine Is Associated with Fatty Acid Metabolism in Plants. *Plant Physiol. Biochem.* **2007**, *45* (12), 926−931.

(69) Shi, H. T.; Chan, Z. L. In Vivo Role of Arabidopsis Arginase in Arginine Metabolism and Abiotic Stress Response. *Plant Signal. Behav.* **2013**, *8* (5), No. e24138, DOI: 10.4161/PSB.24138.

(70) Pagano, A.; de Sousa Araújo, S.; Macovei, A.; Dondi, D.; Lazzaroni, S.; Balestrazzi, A. Metabolic and Gene Expression Hallmarks of Seed Germination Uncovered by Sodium Butyrate in Medicago Truncatula. *Plant, Cell Environ.* **2019**, *42* (1), 259−269.

(71) Sugawara, S.; Hishiyama, S.; Jikumaru, Y.; Hanada, A.; Nishimura, T.; Koshiba, T.; Zhao, Y.; Kamiya, Y.; Kasahara, H. Biochemical Analyses of Indole-3-Acetaldoxime-Dependent Auxin Biosynthesis in Arabidopsis. *Proc. Natl. Acad. Sci. U.S.A.* **2009**, *106* (13), 5430−5435.

(72) Mu, Q.; Zhang, M.; Li, Y.; Feng, F.; Yu, X.; Nie, J. Metabolomic Analysis Reveals the Effect of Insecticide Chlorpyrifos on Rice Plant Metabolism. *Metabolites* **2022**, *12* (12), 1289.

(73) Gulyás, Z.; Simon-Sarkadi, L.; Moncsek, B.; Pál, M.; Kocsy, G. α-Aminoadipic Acid Metabolism Is Controlled by the Glutathione-Dependent Redox Environment in Arabidopsis. *J. Plant Biochem. Biotechnol.* **2023**, *32* (1), 204−210.

(74) Lee, B. R.; Park, S. H.; Muchlas, M.; La, V. H.; Al Mamun, M.; Bae, D. W.; Kim, T. H. Differential Response of Phenylpropanoid Pathway as Linked to Hormonal Change in Two Brassica Napus Cultivars Contrasting Drought Tolerance. *Physiol. Plant.* **2023**, *175* (6), No. e14115.

(75) Shi, H.; Ye, T.; Chen, F.; Cheng, Z.; Wang, Y.; Yang, P.; Zhang, Y.; Chan, Z. Manipulation of Arginase Expression Modulates Abiotic Stress Tolerance in Arabidopsis: Effect on Arginine Metabolism and ROS Accumulation. *J. Exp. Bot.* **2013**, *64* (5), 1367−1379.

(76) Li, Z. G. Role of Methylglyoxal and Its Detoxification System in Plant Thermotolerance. *Acta Physiol. Plant* **2022**, *44* (7), No. 69.

(77) Negri, S.; Commisso, M.; Avesani, L.; Guzzo, F. The Case of Tryptamine and Serotonin in Plants: A Mysterious Precursor for an Illustrious Metabolite. *J. Exp. Bot.* **2021**, *72* (15), 5336−5355.

(78) Sprunck, S.; Jacobsen, H. J.; Reinard, T. Indole-3-Lactic Acid Is a Weak Auxin Analogue but Not an Anti-Auxin. *J. Plant Growth Regul.* **1995**, *14* (4), 191−197.

(79) Nguyen, V. P. T.; Stewart, J. D.; Ioannou, I.; Allais, F. Sinapic Acid and Sinapate Esters in Brassica: Innate Accumulation, Biosynthesis, Accessibility via Chemical Synthesis or Recovery From Biomass, and Biological Activities. *Front. Chem.* **2021**, *9*, No. 664602.

(80) Matsui, A.; Yin, Y.; Yamanaka, K.; Iwasaki, M.; Ashihara, H. Metabolic Fate of Nicotinamide in Higher Plants. *Physiol. Plant.* **2007**, *131* (2), 191−200.

(81) Bernsdorff, F.; Döring, A. C.; Gruner, K.; Schuck, S.; Bräutigam, A.; Zeier, J. Pipecolic Acid Orchestrates Plant Systemic Acquired

Resistance and Defense Priming via Salicylic Acid-Dependent and -Independent Pathways. *Plant Cell* **2016**, *28* (1), 102−129.

(82) Breitenbach, J.; Visser, H.; Verdoes, J. C.; van Ooyen, A. J. J.; Sandmann, G. Engineering of Geranylgeranyl Pyrophosphate Synthase Levels and Physiological Conditions for Enhanced Carotenoid and Astaxanthin Synthesis in Xanthophyllomyces Dendrorhous. *Biotechnol. Lett.* **2011**, *33* (4), 755−761.

(83) Lin, Y.; Jia, Y.; Zhou, C.; Wang, H.; Pan, C. Impact of Pesticide Abiotic Stresses on Plant Secondary Metabolism: From Plant Individuals to Ecological Interfaces. *J. Agric. Food Chem.* **2025**, *73* (34), 21247−21263.

(84) Isah, T. Stress and Defense Responses in Plant Secondary Metabolites Production. *Biol. Res.* **2019**, *52* (1), No. 39.

(85) Zhang, Y.; Fernie, A. R. The Role of TCA Cycle Enzymes in Plants. *Adv. Biol.* **2023**, *7* (8), No. 2200238.

(86) Avato, P.; Argentieri, M. P. Brassicaceae: A Rich Source of Health Improving Phytochemicals. *Phytochem. Rev.* **2015**, *14* (6), 1019−1033.

CAS INSIGHTS™

EXPLORE THE INNOVATIONS SHAPING TOMORROW

Discover the latest scientific research and trends with CAS Insights. Subscribe for email updates on new articles, reports, and webinars at the intersection of science and innovation.

Subscribe today

CAS
A division of the American Chemical Society

scientific reports

OPEN

Analysis of the spatial distribution of metabolites in *Aloe vera* leaves by mass spectrometry imaging and UHPLC-UHRMS

Sumi Krupa[1], Tomasz Ruman[2], Wiktoria Szuberla[2] & Joanna Nizioł[3]✉

This study presents an investigation of the chemical composition of *Aloe vera* leaf tissue with a focus on the spatial distribution of compounds. The composition was studied using two mass spectrometry imaging techniques: silver-109 nanoparticles assisted laser desorption/ionization mass spectrometry imaging (^{109}AgNPs-LDI-MSI) and laser ablation-remote atmospheric pressure photoionization/chemical ionization mass spectrometry imaging (LARAPPI/CI-MSI) and the identification was aided by ultra-high-performance liquid chromatography and ultra-high-resolution mass spectrometry (UHPLC-UHRMS) analysis. The results showed an abundance of phenolic compounds with antioxidant, antimicrobial, and anti-inflammatory properties, making it a beneficial food additive and food packaging material. Analysis of the results of mass spectrometry imaging provided information about the potential changes in metabolic pathway expression in different regions of the leaf.

Keywords *Aloe vera*, Mass spectrometry imaging, Laser ablation, Metabolomics, Plant tissue, Ambient ionization

According to market research[1] the value of the global *Aloe vera* market in 2023 was 2.65 billion dollars and is projected to grow to 2.86 billion USD in 2024. The market share connected to using *A. vera* in the food and beverage industry is evaluated at approx. 25% of the global market value. Aloe has been utilized in the human diet in different forms, starting with the consumption of raw parts of the plant. The flowers of *A. vera* have been regarded as edible and their nutritional contents have been studied, revealing the occurrence of β-sitosterol, β-carotene, and tocopherol, as well as lipids, such as palmitic acid[2]. The products made with added aloe extracts include drinks, such as juices or health-promoting beverages[3,4], products of milk fermentation, jams, and jellies[5,6]. *A. vera* gel has been found useful as an edible coating for increasing the shelf-life of perishable foods[7–9].

Due to its properties, *A. vera* has been utilized in other fields. It has found use in cosmetics thanks to the presence of polysaccharides, which stimulate fibroblasts, effectively preventing skin irritation, likewise protecting from UV-B-induced hazards[10]. Oligosaccharides present in *A. vera* gel also exhibit an effect in reduced Interleukin-10 production, which results in UV-induced skin hypersensitivity prevention[11]. This, coupled with the moisturizing, soothing, antibacterial, and anti-inflammatory action of *A. vera* gel resulted in its common use as an ingredient in creams, cleansers, and moisturizers[12]. A wide set of applications for *A. vera* is documented for its medicinal qualities. Mannose-6-phosphate[13], aloesin, emodin, and aloin[14–16] present in *A. vera* are associated with the reduction of inflammation and antioxidant mechanisms, aiding in wound healing. *A. vera* gel used on the skin can also result in glycosaminoglycans and type III collagen production, further promoting tissue healing[17]. *A. vera* can be used in HSV-1 treatment[18], as well as psoriasis[19] and seborrheic dermatitis[20]. Aloe exhibited antidiabetic potential connected to its antioxidant qualities[21].

The analytical methods most commonly used for *A. vera* analysis include chromatography coupled with mass spectrometry, such as gas chromatography (GC-MS)[22] and liquid chromatography (LC-MS)[23], as well as nuclear magnetic resonance spectroscopy (NMR)[24]. Those methods, however, require that the extract of the homogenized sample is used, which results in a loss of information about the location of identified compounds. Mass spectrometry imaging (MSI) allows for the detection of various compounds in the analyzed sample, usually

[1]Doctoral School, Rzeszów University of Technology, 8 Powstańców Warszawy Ave., Rzeszów 35-959, Poland. [2]Department of Inorganic and Analytical Chemistry, Faculty of Chemistry, Rzeszów University of Technology, 6 Powstańców Warszawy Ave., Rzeszów 35-959, Poland. [3]Department of Polymers and Biopolymers, Faculty of Chemistry, Rzeszów University of Technology, 6 Powstańców Warszawy Ave., Rzeszów 35-959, Poland. ✉email: jniziol@prz.edu.pl

a tissue, without previous homogenization, resulting in the acquisition of data in the form of ion images with the spatial location of each compound in the sample.

MSI has been used in plant tissue analyses investigating plant growth and reproduction processes[25]. The metabolic processes in endosperm have been studied, as well as the effect of light availability to specific parts of a leaf on secondary metabolite accumulation. Investigation into the nitrogen cycle and the effect of symbiotic microorganisms in the process has also been conducted. MSI also allowed for the analysis of plant biotic and abiotic stress responses[26]. Due to the possibility of visual comparison of the regions where the compound occurs in the sample in the highest amount, a better understanding of the metabolism and functions of different parts of the organism is possible. The analysis of plant tissues can prove problematic due to the difference in anatomy between different structures of the plant organs. *A. vera* leaf is made up of three differentiable regions. The structured outermost layer is responsible for the transportation of substances due to numerous vascular bundles, a middle layer, close to the epidermis, is made of sap containing glycosides and anthraquinones, and the inner layer – gel – is composed of up to 98% water with various compounds mostly sterols, polyphenols, and alkaloids[27]. The preparation of tissue with highly varying structural integrity regions poses technical difficulties due to differences in sample material desorption, as well as in the ionization of compounds, especially in the gel region where the low concentration of compounds other than water makes it difficult to detect or image certain molecules.

Various techniques provide the possibility of desorption and ionization in MSI analysis, so it's important to choose the method most suitable for the desired results and sample type. The most common techniques are desorption electrospray ionization (DESI), secondary ion mass spectrometry (SIMS), and laser desorption/ionization methods, most notably matrix-assisted laser desorption/ionization (MALDI).

MSI analysis conducted using SIMS produces ion images with the highest resolution of all mentioned MSI techniques[28,29]. This in turn is connected to imaging of a smaller size of the sample region. In this study, the whole cross-section of a leaf was analyzed, which wouldn't be possible for SIMS. The method is also regarded as a hard ionizing one, meaning that fragments of precursor ions are produced alongside molecular ions. For the analysis of complicated biological systems with a variety of compounds, soft ionization methods are preferred.

MALDI is the most common ionization technique for plant tissue MSI. MALDI utilizes an organic matrix as surface assistance[30]. The use of organic matrices interferes with the signals on the spectrum in the lower mass region (< 1000 Da), which is why the use of inorganic matrices, such as nanoparticles (NPs) in surface assisted-laser desorption/ionization (SALDI) became very popular. A considerable problem is the presence of "sweet spots" occurring when conducting a MALDI-MSI analysis. The solution again lies in the use of nanoparticles, as they do not exhibit this effect. Ions emitted from nanoparticles can also serve as internal calibration points[31]. The process of sample preparation for MALDI-MSI is time-consuming and complicated, as the tissue has to be sliced to the width of ~ 10 µm and homogeneously covered with the used matrix.

Both SIMS imaging and LDI-MSI analyses are conducted in vacuum conditions. Biological samples can change their shape in those conditions due to the loss of moisture. The imprinting method can be used to overcome that, as no actual tissue enters the high vacuum conditions[32,33], however, the material that is transferred represents mainly intercellular liquid. DESI-MSI has the advantage of analysis in ambient conditions in contrast to the aforementioned methods, which contributes to sample integrity conservation, however, the resolution achievable in DESI-MSI analysis is the lowest out of the mentioned techniques and the sampling depth is very shallow[34].

Biological samples contain a substantial amount of water, which makes a mid-IR laser perfect for the desorption of the material from the sample for ionization. Mid-IR wavelength, specifically 2930 nm in the case of this study, effectively couples its energy into the stretching mode of the O-H bond, which makes it very effective for the desorption of highly hydrated biological material, such as *A. vera* leaves. Laser ablation-remote atmospheric pressure photoionization/chemical ionization (LARAPPI/CI) that uses this laser is a novel technique used in mass spectrometry, developed by Ruman et al.[35]. This technique allows for MSI analysis of tissues in a close-to-native state after freezing a sample without any previous preparation. The superficial resolution of the technique is 140 µm and the depth of sampling is from 100 to 300 µm depending on the sample and pulse energy. LARAPPI/CI system is capable of 2D as well as 3D imaging.

In this study, two very different MSI methods: 109-silver nanoparticles assisted laser desorption/ionization mass spectrometry imaging (^{109}AgNPs-LDI-MSI) and LARAPPI/CI-MSI were used to determine the *A. vera* leaf location of metabolites. The identification was aided by UHPLC-UHRMS + MS/MS analysis of the extract from the plant tissue. This is the first work that contains the comparison of nanoparticles-based laser mass spectrometry imaging with chemical ionization/photoionization-based imaging of plant tissue.

Experimental

Materials

A silver-109 isotope of 99.7% isotopic purity was bought from Trace Sciences International (USA). All solvents (toluene, chloroform, acetonitrile) were of HPLC quality, except for water (18 MΩcm water produced locally). The plant used in this study was initially purchased from a local store in Rzeszow, Poland. The analyzed samples for MSI analyses were cross-section slices of *A. vera* (L.) leaf obtained from a 5-year-old potted plant, which had been cultivated under indoor conditions in southern Poland for two years following its purchase. Half of a leaf, growing at the midpoint of the trunk, was cut off from the stem. The age of the analyzed leaf fragment is estimated to be 2 years (± 3 months). A leaf was collected from the middle section of the plant and transported at 4 °C. It was analyzed within 10 min of collection, without further storage in the laboratory. Prior to analysis, the *A. vera* leaf was cut at one-third of its length from the tip. For ^{109}AgNPsLDI-MSI, the entire cut section was used to create a cross-sectional imprint on the steel plate (LDI target plate). For LARAPPI/CI-MSI, a 3.75 mm thick slice was prepared by cutting with a blade from the region of the leaf adjacent to the one used for imprinting (for

LDI-MSI), then placed on the stainless steel plate and frozen. For LC-MS analysis, 200 mg of *A. vera* material from the leaf region adjacent to that used for MSI analyses was used.

Steel plates used for LARAPPI/CI-MSI as well as LDI targets were fabricated from H17 stainless steel and underwent a thorough cleaning process prior to MSI. The cleaning involved sequential soaking in boiling solvents, including toluene, chloroform, acetonitrile, and deionized water (each solvent was used three times in 100 mL volumes for 30 s per plate). After cleaning, the plates were dried under high vacuum conditions (approximately 0.01 mbar) for 24 h. Optical photographs were made with the use of an Olympus SZ10 microscope equipped with an 8 MPix. Olympus digital camera and also a Canon 6D camera with a macro-type 90 mm focal length lens.

Sample extraction for LC-MS analysis

A. vera leaf material was homogenized with 1050 µL of 3:1 acetone/water (v/v) mixture in a bead homogenizer. After homogenization, the samples were placed at a temperature of -20 °C for 20 min. After this time, the samples were centrifuged for 10 min at 9800 x g. The supernatant was then transported to Eppendorf vials and dried in a SpeedVac vacuum concentrator for 18 h. The samples were weighted after drying and 100 µL of methanol was added per every 1 mg of the dried extract. Samples were then centrifuged again in 9800 x g for 5 min, 100 µL from each vial was placed in HPLC vial inserts and inserted into a Bruker Elute autosampler. The samples were in a thermostated autosampler at 4 °C during the analysis.

Imaging of *A. vera* leaf cross-section imprint using ^{109}AgNPs-LDI-MSI

Imaging of the cross-section imprint of the *A. vera* leaf was performed following the methodology described in our previous publications[36]. Fresh leaf was cut transversely at one-third of the distance from the tip, and excess liquid from the cut surface was absorbed using filter paper. The leaves were manually imprinted onto the surface of the steel target plate by gently pressing for 3 s. Next, the leaf was removed, and the remaining imprint on the plate was coated with a suspension of silver-109 nanoparticles using the pulsed fiber laser-generated nanomaterial method with a 2D galvo-scanner (PFL 2D GS LGN)[37]. The process of the 109-silver nanoparticles synthesis and application on the surface of the plate was described in our recent publication[38]. Measurements were performed using a Bruker Autoflex Speed time-of-flight mass spectrometer in reflectron positive ion mode. The apparatus was equipped with a Smart Beam II 1000 Hz 352 nm laser. Laser impulse energy was approximately 100–190 µJ, laser repetition rate was 1 kHz, and deflection was set on *m/z* lower than 95. The measured *m/z* range was 100–2000, experiments were made with 2000 laser shots per individual spot. All spectra were calibrated with the use of silver ions of $^{109}\mathrm{Ag}^+$ to $^{109}\mathrm{Ag}_{13}^+$ formula.

LARAPPI/CI-MSI of *A. vera* leaf cross-section

The MSI in ambient conditions was performed using the LARAPPI/CI technique described in our recent publication[35]. For LARAPPI/CI-MSI analysis, a 3.75 mm thick slice from the same region of the *A. vera* leaf was placed on a clean stainless steel plate. The plate was then mounted on the stage with a Peltier cooling plate (TE-127-1.4-1.5; TE Technology, Traverse City, MI, USA) which was set to -18 °C. This ensured the sample remained frozen throughout the laser ablation process, minimizing the risk of compound mixing on the sample surface. An Nd/YAG-pumped, tunable OPO laser (Opolette HE 2940; Opotek, Carlsbad, CA, USA) was used to generate mid-infrared (mid-IR) laser pulses. The laser system produced shorter than 7 ns pulses with a maximum repetition frequency of 20 Hz. The laser was tuned to emit at a wavelength of 2.93 µm. The pulse energy of the laser-measured before focusing lens was 2.0 mJ. The process of laser ablation was conducted in an airtight chamber pressurized with nitrogen gas at a steady flow of 9.5 L/min. The mass spectrometer used for the analysis was Bruker Impact II operating in negative ion mode. The ionization was conducted using Bruker VIP HESI ion source in the APCI configuration. The ion source additionally had a VUV source (Hamamatsu L12542) mounted to the MS sampling cone to induce photoionization. A binary HPLC pump (Agilent G1312A) was used to provide a steady flow of a solvent mixture (1% toluene in methanol; 200 µL/min) to the APCI needle. The laser ablation plumes were transported to the ion source through a PTFE tube connected to the ablation module. The analyzed region encompassed the whole leaf slice. The selected area was irregular in shape, fitting the shape of the slice. The spatial resolution chosen for the analysis was 200 µm. The duration of each laser shot was 1 s. To ensure accurate alignment of each pixel, the delay between the shots in one line was 1 s, and between sequential lines, it was 5 s. The analysis of the results of the imaging was done using software made specifically for the used system.

UHPLC-Q-ToF-UHRMS analysis

UHPLC-Q-ToF-UHRMS analysis was conducted with Bruker Elute UHPLC system, coupled with a Bruker Impact II mass spectrometer of ESI QToF-MS type. The UHPLC column used was the C18 Bruker Intensity Solo with silica functionalized with octadecyl groups, with 2 µm particles and dimensions of 100 × 2.1 mm (length × diameter). To maintain consistent conditions, the UHPLC column was thermostated at 40 °C during the analysis. For mobile phases, water with 0.1% HCOOH as phase A and acetonitrile with 0.1% HCOOH as phase B were used. The injection volume was set at 5 µL, and the percentage of phase B was as follows: 1% (0–2 min), 99% (17–20 min), and 1% (20.1–30 min). From 0 to 20 min, the solvent flow rate was 0.25 mL/min, gradually increasing to 0.35 mL/min from 20.1 to 30 min. All measurements were made in technical triplicates. Measurements in positive autoMSMS mode were carried out using the following parameters: *m/z* 50–1200; capillary voltage: 4.5 kV; nebulizer: 2.7 bar; dry gas: 12 L min^{-1}; drying gas temperature: 220 ºC; hexapole voltage: 50 Vpp; funnel 1: 200 Vpp; funnel 2: 200 Vpp; pre-pulse storage time: 5 µs; transfer time: 60 µs. Collision-induced dissociation (CID) was used with the following settings: absolute threshold (per 100 sum): 200 cts; absolute threshold 88 cts; active exclusion 3 spectra; release after 0.3 min, isolation mass: for *m/z* = 100, the width was 3, for 500 widths was 4, for 1000 was 6 and for 1300 was 8); collision energy value was 30 eV. MS frequency was 20 Hz and for MS/MS - from 5 to 30. The untargeted annotations were performed in Metaboscape (ver. 2022b) with a criterion of mass deviation ($\Delta m/z$) under 2 ppm and mSigma value under 20 as the maximum acceptable deviation of the mass of the compound and the isotopic pattern respectively. For identification and molecular formula generation, the exact mass of parent ions was matched with < 3 ppm error and mSigma value < 50 in most cases. All the molecular formulas were obtained using the Smart Formula tool and the C, H, N, O, P, S, Cl, Br, I, and F elements. MS/MS spectra were automatically matched against MS/MS libraries: Bruker HMDB 2.0 (this database contains retention times that were used as an additional identification factor), MassBank of North America (MoNA) library, and NIST ver. 2020 MS/MS library. The matching of identified compounds with metabolic pathways of the *Arabidopsis thaliana* plant was conducted based on the Kyoto Encyclopedia of Genes and Genomes (KEGG) database. The analysis of metabolic pathways in *A. vera* leaf was conducted in MetaboAnalyst 6.0 software[39].

Results and discussion

The analysis of the composition of *A. vera* leaf was conducted by three analytical methods. The mass spectrometry imaging analyses of the *A. vera* leaf cross section were conducted by two methods: ^{109}AgNPs-LDI-MSI and LARAPPI/CI-MSI. The identification process was initiated through the analysis of *A. vera* leaf extracts using UHPLC-UHRMS and MS/MS detailed in Sect. 2.5. The additional MSI images were also generated for compounds reported for *Aloe* genus plants in published analytical studies. Based on the identified and reported compounds, ion images for exact *m/z* values were generated in MSI software using both methods (^{109}AgNPs-LDI-MSI and LARAPPI/CI-MSI), taking into account various possible adducts. The analyses were performed using high-resolution instruments equipped with a ToF analyzer, which facilitated the accurate determination of molecular masses. Mass-to-charge values as well as isotopic patterns were checked for ions identified in MSI studies of both methods. The full results of the MSI analysis are presented in Fig. S1–S10 and in Table S2 in the Supplementary Information. A detailed description of UHPLC-UHRMS findings is provided in Sect. 3.2, as well as in the Supplementary Information in Table S1 and Fig. S11.

Mass spectrometry imaging results of *A. vera* leaf

In ^{109}AgNPs-LDI-MSI, an imprint of the *A. vera* leaf cross section was analysed. The analysis in total led to obtaining 179 ion images of identified compounds (Fig. 1C). Taking into consideration that multiple adduct types are possible, the number of identified compounds was reduced to 129. For LARAPPI/CI-MSI the number of ion images matching the sample (Fig. 1D) obtained was 122. In this method, only $[M\text{-}H]^-$ ions were considered.

Employing two imaging methods allowed for the comparison of MSI results. Twenty-four compounds were found with both MSI methods including eight identified also by the UHPLC-UHRMS method (Figs. 1, 2 and 3), Supplementary Information, Table S2). The comparison of the ion images of the 8 most relevant compounds, which were detected using all three methods and whose presence in *A. vera* has been corroborated by previous scientific publications, is presented in Fig. 1. The remaining common 16 images from both MSI experiments, representing compounds that were putatively identified and are endogenous, are shown in Figs. 2 and 3. Compounds characteristic of *A. vera*, such as aloesin, aloin, and mannose-6-phosphate, were identified using UHPLC-UHRMS (Supplementary Information, Table S1), and their ion images were obtained through ^{109}AgNPs-LDI-MSI (Supplementary Information, Fig. S1–5) and LARAPPI/CI-MSI (Supplementary Information, Fig. S6–10) along with MSI of other common metabolites. These images are included in the Supplementary Information, as the study focused on comparing the two imaging methods based on compounds detected by both techniques.

The ion images presented in Fig. 1 demonstrate the spatial distribution and signal intensity of eight metabolites in *A. vera* tissue obtained using two complementary MSI methods: ^{109}AgNPs-LDI-MSI and LARAPPI/CI-MSI. The structures of these compounds were confirmed through UHPLC-UHRMS analysis of leaf extracts. The comparison highlights significant differences in the sensitivity and localization capabilities of the two methods.

For 3-coumaric acid (Fig. 1E) and ferulic acid (Fig. 1F), hydroxycinnamic acids that are involved in tissue defense and antioxidative functions as structural components of the cell wall[40], the spatial distribution differs between methods. While ^{109}AgNPs-LDI-MSI shows a strong, localized signal in the adaxial epidermis for both compounds, LARAPPI/CI-MSI demonstrates higher abundance of 3-coumaric acid in the abaxial epidermis and a more even distribution of ferulic acid across the leaf. 3-Coumaric acid plays a key role in the degradation of cinnamate, leading to the formation of citric cycle intermediates such as fumarate and acetyl-CoA[41], and has been identified in various plant species, including *Agave Angustifolia*[42], mulberry[43], olives[44], and *Ilex kaushue*[45]. The observed differences in spatial distribution between the adaxial and abaxial surfaces may result from differential light exposure, which could influence the accumulation of hydroxycinnamic acids based on their photoprotective roles.

In plants, ferulic acid is synthesized *via* the polyphenolic pathway from caffeic acid or coniferaldehyde and serves as a precursor for lignin biosynthesis, contributing to the formation of guaiacyl and syringyl lignins[46]. Ferulic acid has been previously detected in cereals, such as rice, rye, barley, and maize, particularly in the aleurone cells of seeds[47–49], and in Aloe tissue extracts analyzed using HPLC[50] and LC-ESI/MS/MS[51]. Studies using MALDI-MSI[52] have localized ferulic acid predominantly in the epidermis of plant tissues, including both adaxial and abaxial leaf regions. Similarly, DESI-MSI studies[53] have shown ferulic acid distribution throughout the leaf in *Salvia miltiorrhiza*. The ion images obtained in this study confirm these findings, showing the highest ferulic acid abundance in the adaxial epidermis for ^{109}AgNPs-LDI-MSI and in the abaxial epidermis for LARAPPI/CI-MSI, demonstrating consistency with prior reports.

In this study, gluconic acid (Fig. 1G) exhibits higher signal intensity consistently observed on one side of the leaf cross-section in both MSI methods. ^{109}AgNPs-LDI-MSI detected gluconic acid predominantly in the adaxial epidermis with high abundance. In contrast, LARAPPI/CI-MSI revealed a broader distribution concentrated in

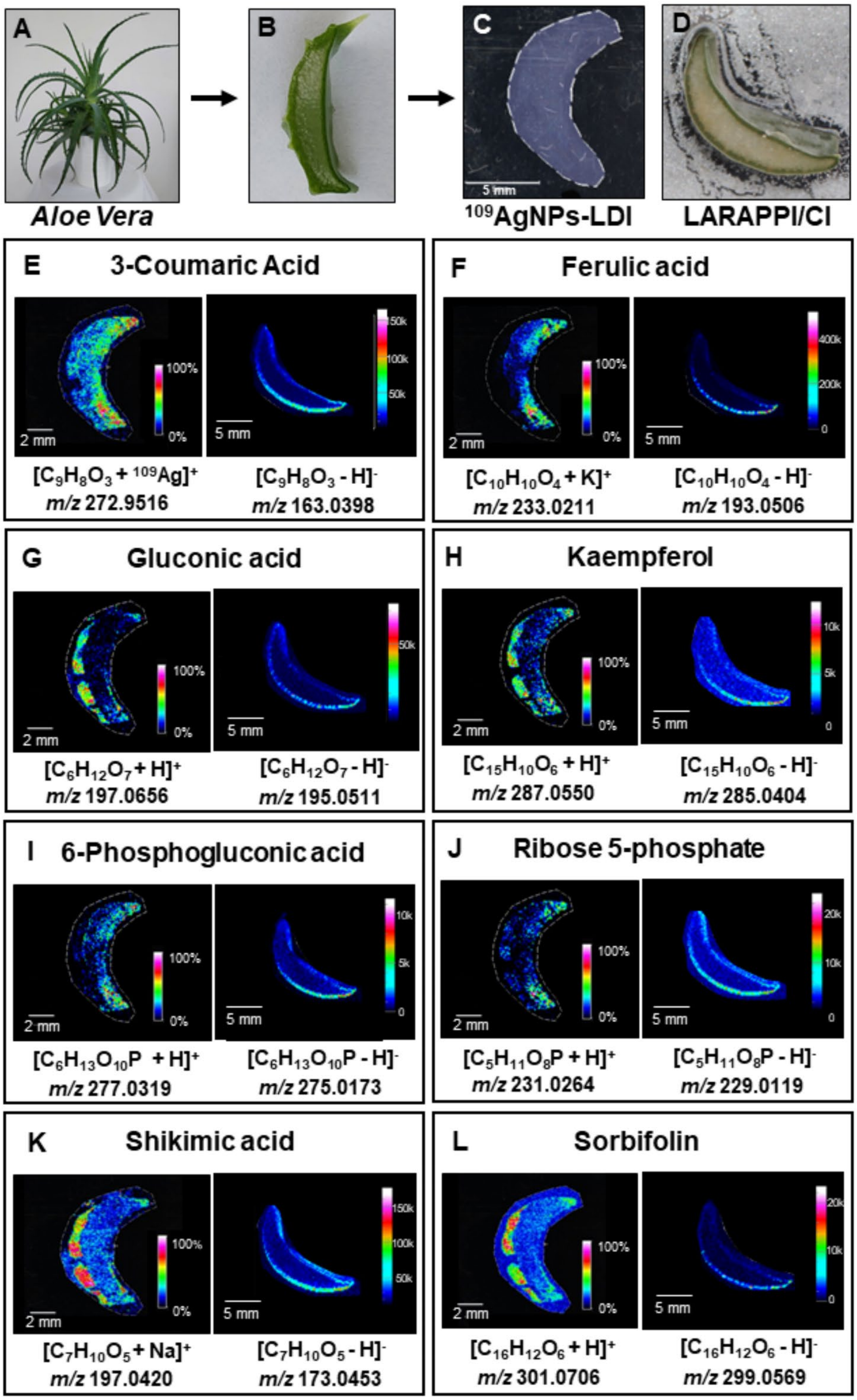

Fig. 1. Metabolites identified by LC-MS, LDI-MSI and LARAPPI/CI-MSI. The photos taken of the sample material: (**A**) The *A. vera* plant used to acquire samples for the study, (**B**) *A. vera* leaf slice used as the sample, (**C**) the image of the imprint used for the ^{109}AgNPs-LDI-MSI analysis, (**D**) the image of leaf slice used in the LARAPPI/CI-MSI analysis. The compounds identified by the three mentioned analytical methods: (**E**) 3-coumaric acid, (**F**) ferulic acid, (**G**) gluconic acid, (**H**) kaempferol, (**I**) 6-phosphogluconic acid, (**J**) ribose 5-phosphate, (**K**) shikimic acid, (**L**) sorbifolin. For each compound, the left-ion image is for the imprint technique and the right-ion image for ablation.

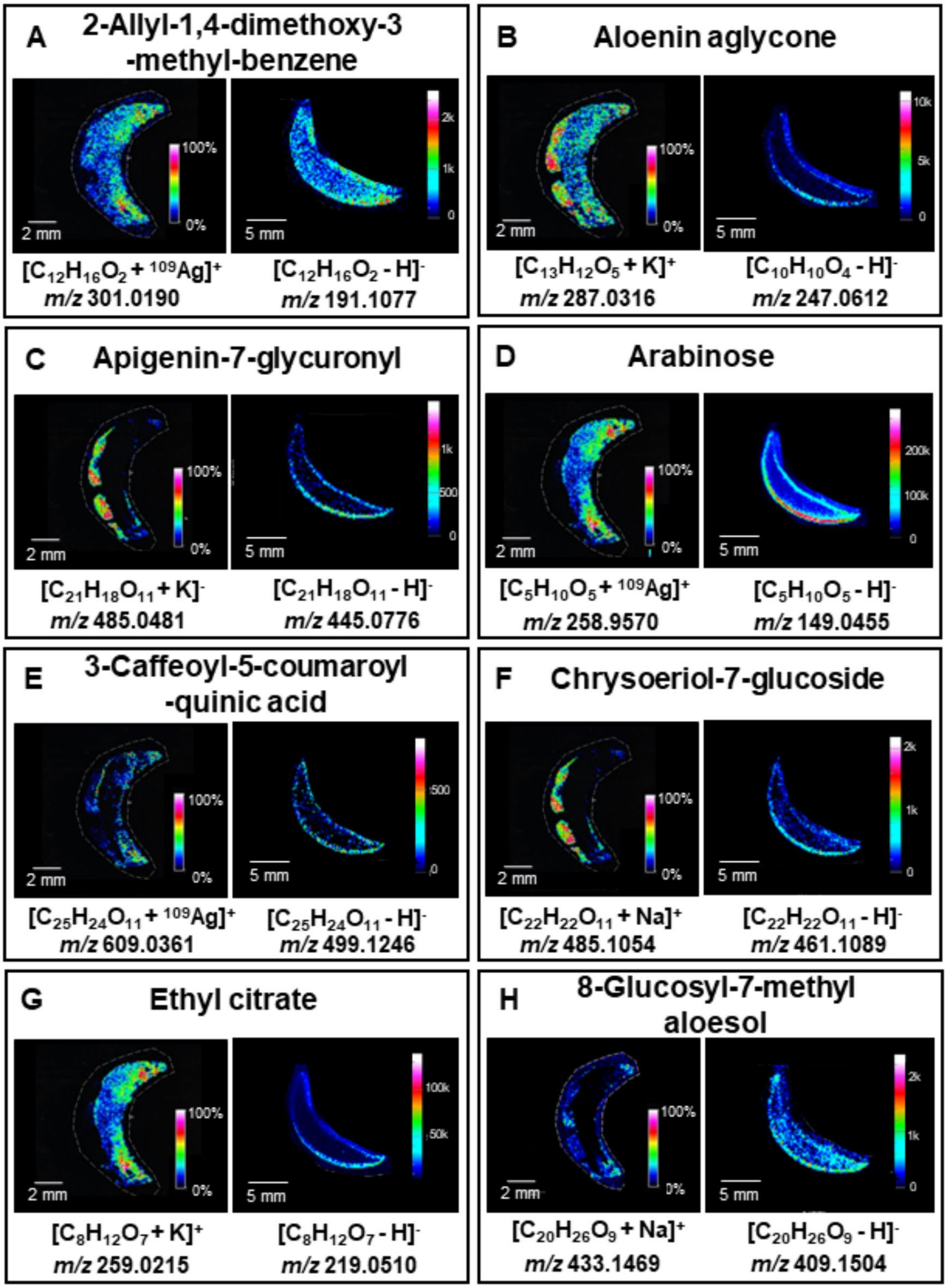

Fig. 2. Metabolites identified by both LDI-MSI and LARAPPI/CI-MSI: (**A**) 2-Allyl-1,4-dimethoxy-3-methyl-benzene, (**B**) aloein aglycone, (**C**) apigenin-7-glycuronyl, (**D**) – arabinose, (**E**) 3-caffeoyl-5-coumaroylquinic acid, (**F**) chrysoeriol-7-glucoside, (**G**) ethyl citrate, (**H**) – 8-glucosyl-7-methyl aloesol. For each compound, the left-ion image is for the imprint technique and the right-ion image for ablation.

the same region, but with moderate signal abundance. Both methods showing the highest abundance confined to the epidermal layers. Gluconic acid is a widely occurring compound formed through the oxidation of glucose and serves as a precursor for 6-phosphogluconic acid. Its elevated levels in plants are often associated with microbial activity, including pathogenic infections or symbiotic interactions[54]. Previous studies using MALDI-

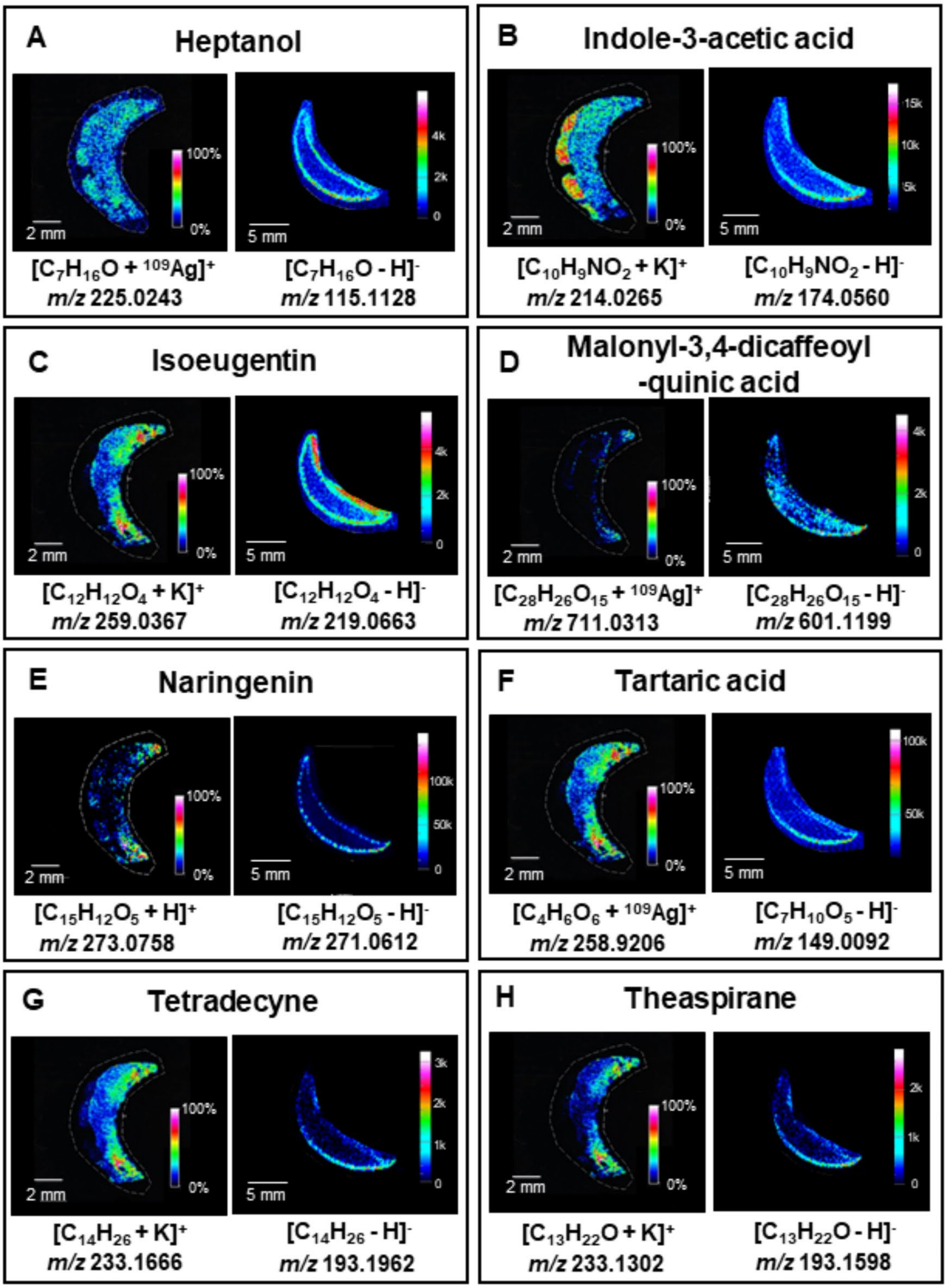

Fig. 3. Metabolites identified by both LDI-MSI and LARAPPI/CI-MSI: (**A**) heptanol, (**B**) indole-3-acetic acid, (**C**) – isoeugentin, (**D**) – malonyl-3,4-dicaffeoylquinic acid, (**E**) – naringenin, (**F**) tartaric acid, (**G**) tetradecyne, (**H**) theaspirine. For each compound, the left-ion image is for the imprint technique and the right-ion image for ablation.

MSI localized gluconic acid in the outer regions of root tissues in species such as *Panax notoginseng* and *Clitoria fairchildana*[55], suggesting its role in microbial interactions. In leaves of *Cyclocarya paliurus*, DESI-MSI analysis revealed its accumulation at the junction between the leaf and stem, with lower concentrations in the veins[56]. In *A. vera*, gluconic acid has been previously identified using HPLC-MS/MS[57]. The findings in this study align with prior reports of gluconic acid distribution in plant tissues, although the unique anatomy of *A. vera* leaves, characterized by distinct epidermal regions and a highly hydrated gel layer, urge to consider the specific context for these observations.

Kaempferol (Fig. 1H) was detected with higher intensity on one side of the leaf, specifically in the abaxial epidermis, as revealed by both ^{109}AgNPs-LDI-MSI and LARAPPI/CI-MSI. Kaempferol is a flavonoid synthesized in the shikimic acid pathway via intermediate compounds like 4-coumaroyl-CoA, naringenin chalcone, and dihydrokaempferol, with flavanol synthase catalyzing the final step[58]. It is abundant in cruciferous vegetables and tea[59] and plays a key role in scavenging reactive oxygen species (ROS)[60], protecting plants from oxidative stress, and regulating ROS and auxin signaling, which influence plant growth. Kaempferol also exhibits antibacterial and antifungal activity[61,62]. In *A. vera*, kaempferol has been previously identified in leaf skin and flower extracts, with higher concentrations in the leaf[63]. Previous MSI studies have localized kaempferol in epidermal tissues in various plants, such as tea and ginkgo leaves[64], consistent with this study's findings, which confirm its predominant localization in the abaxial epidermis of *A. vera*.

6-Phosphogluconic acid (Fig. 1I) and ribose 5-phosphate (Fig. 1J) in ^{109}AgNPs-LDI-MSI, show the highest intensity in the adaxial epidermis. In contrast, LARAPPI/CI-MSI reveals their highest intensity in the abaxial epidermis, with a broader and more diffuse distribution. 6-Phosphogluconic acid is a substrate in the pentose phosphate pathway (PPP), where it provides phosphate groups for ribulose 5-phosphate, ribose 5-phosphate, and xylulose 5-phosphate through oxidation by 6-phosphogluconate dehydrogenase. Its product, ribose 5-phosphate, is essential for the biosynthesis of key biomolecules, including histidine, tryptophan, NAD$^+$, NADP$^+$, purines, and pyrimidines[65]. Both compounds are reported here for the first time in *A. vera*, with their presence consistent with their central role in plant metabolism. The pentose phosphate pathway predominantly occurs in plastids, especially chloroplasts, supporting the observed localization of these compounds in the epidermal tissues, where chloroplasts are abundant[66].

Shikimic acid (Fig. 1K) shows the highest intensity in the abaxial epidermis in both MSI methods. In ^{109}AgNPs-LDI-MSI, the signals are most intense in the epidermal region, while in LARAPPI/CI-MSI, the distribution is broader but still strongest in the abaxial region. Shikimic acid is a key intermediate in the shikimate pathway, which links primary and secondary metabolism in plants. It serves as a precursor for aromatic amino acids (phenylalanine, tyrosine, and tryptophan) and other aromatic compounds, including phenylpropanoids and alkaloids. These downstream metabolites play critical roles as structural components of plant cells and as defenses against environmental stressors, such as UV radiation, herbivores, and pathogens[67]. Previous studies using DESI-MSI in *Cyclocarya paliurus* leaves localized shikimic acid primarily in the veins and at the junction between the leaf and stem[56]. Given the identification of numerous secondary metabolites derived from the shikimate pathway in *A. vera* leaves, the occurrence of shikimic acid in this sample is consistent with its known role in plant metabolism.

Sorbifolin (Fig. 1L) in ^{109}AgNPs-LDI-MSI is observed in specific regions of the abaxial epidermis. In contrast, LARAPPI/CI-MSI shows a broader distribution with moderate intensity, primarily in the abaxial epidermis as well. Sorbifolin, like most flavonoids, exhibits radical scavenging activity and myeloperoxidase inhibitory effects[68]. It has previously been identified in species such as *Spathelia sorbifolia*[69], *Thymus herba-barona*[70], *Mentha x piperita*, and *M. pulegium*[71], but this study displays its first identification in the Aloe genus. Although sorbifolin has not been extensively studied and no prior MSI analyses have been reported, its consistent localization in the abaxial epidermis suggests a protective role against environmental stressors, consistent with the known functions of flavonoids in plants.

Figures 2 and 3 present 16 compounds detected simultaneously using both MSI techniques. 2-Allyl-1,4-dimethoxy-3-methyl-benzene (Fig. 2A) was distributed throughout the sample in LARAPPI/CI-MSI, with higher intensity in the epidermis, while ^{109}AgNPs-LDI-MSI showed it predominantly in the adaxial epidermis, with intensity decreasing centrally. Aloesin aglycone (Fig. 2B) exhibited similar epidermal localization in both methods but was more abundant in the gel region with ^{109}AgNPs-LDI-MSI. Apigenin-7-glucuronyl (Fig. 2C) was localized mainly in the abaxial epidermis, with stronger signals in ^{109}AgNPs-LDI-MSI.

Arabinose (Fig. 2D) showed broader distribution in LARAPPI/CI-MSI, with the highest signal in the abaxial epidermis, whereas ^{109}AgNPs-LDI-MSI localized it at the adaxial epidermis. 3-Caffeoyl-5-coumaroyl-quinic acid (Fig. 2E) was detected in low abundance, particularly on the adaxial side of the leaf, while the signal was absent in some regions of the abaxial epidermis. Chrysoeriol-7-glucoside (Fig. 2F) showed the highest abundance in the abaxial epidermis, with more detailed MSI by ^{109}AgNPs-LDI. Ethyl citrate (Fig. 2G) was found on the adaxial side in ^{109}AgNPs-LDI-MSI and in the lower abaxial region in LARAPPI/CI-MSI. 8-Glucosyl-7-methyl aloesol (Fig. 2H) was localized to the gel region by LARAPPI/CI-MSI and the epidermis by ^{109}AgNPs-LDI-MSI. Heptanol (Fig. 3A) was detected uniformly across the sample by ^{109}AgNPs-LDI-MSI, while LARAPPI/CI-MSI localized it at the epidermal region, with no signal in the gel. Indole-3-acetic acid (Fig. 3B) showed higher abundance and signal-to-noise ratio in ^{109}AgNPs-LDI-MSI, with uniform distribution in the epidermis and additional detection in the gel contrary to the result of LARAPPI/CI-MSI. Isoeugentin (Fig. 3C) was concentrated in the adaxial epidermis in both methods, with lower abundance detected across other epidermal regions by LARAPPI/CI-MSI. Malonyl-3,4-dicaffeoyl-quinic acid (Fig. 3D) was detected at low intensity in the adaxial and abaxial epidermis by ^{109}AgNPs-LDI-MSI but was exclusively localized in the gel and inner epidermis by LARAPPI/CI-MSI. The final compounds—naringenin (Fig. 3E), tartaric acid (Fig. 3F), tetradecyne (Fig. 3G), and theaspirane (Fig. 3H) exhibited complementary patterns. ^{109}AgNPs-LDI-MSI showed the highest intensity in the adaxial epidermis, while LARAPPI/CI-MSI localized them to the abaxial epidermis, with comparable overall intensities. Naringenin showed stronger signals and a better signal-to-noise ratio in ^{109}AgNPs-LDI-MSI, with some detection in the lower leaf region.

The detected compounds presented in Figs. 2 and 3 play key roles in the metabolic and defense mechanisms of *A. vera*. Flavonoids such as apigenin-7-glucuronyl and chrysoeriol-7-glucoside provide antioxidant protection, while aloesin aglycone and 8-glucosyl-7-methyl aloesol are involved in gel maintenance and hydration regulation. Indole-3-acetic acid, a plant hormone, regulates growth and development, and organic acids like tartaric acid support pH balance and metabolic pathways. Compounds such as naringenin and 3-caffeoyl-5-coumaroyl-quinic acid are intermediates in phenolic biosynthesis, enhancing stress resistance and structural integrity. These metabolites reflect *A. vera's* adaptations to environmental stress and its unique biological functions.

Analysis of *A. vera* extracts using the UHPLC-UHRMS method

UHPLC-UHRMS analysis provided 304 identified compounds, 137 in the negative mode and 226 in the positive mode. The results involved essential compounds such as amino acids, organic acids, fatty acyls and other lipids, but a substantial amount of compounds identified were secondary plant metabolites. Among them the main groups would be cinnamic acid derivatives, such as coumaric acid and ferulic acid, polyphenolic secondary metabolites, flavones, flavanones, flavonoles and their glycosides, and metabolites of the shikimate pathway. Additionally, many compound widely associated with the Aloe genus were also detected. Those compounds are aloeresin A, aloeresin D, aloesin and aloin. Except for aloeresin D, all of those compounds were detected in negative mode. Both aloeresin A and aloeresin D were detected in the positive mode. Aloeresin A and aloeresin D have been identified in 7 and 14 aloe species respectively, incudin *A. vera*[72][73]. Both aloesin and aloin have been identified in more than 20 aloe species. Except for aloin, those compounds could be classified as chromones, common plant metabolites. The UHPLC-UHRMS analysis results are summarized in Supplementary Information, Table S1 and Fig. S11.

Comparison of ^{109}AgNPs-LDI-MSI and LARAPPI/CI-MSI

In both methods we employed, preliminary sample preparation was minimal and did not require embedding the tissue in a cryosectioning medium or coating with an organic matrix, as is necessary in MALDI-MSI[74]. In the imprinting method we used, the sample was pressed against the steel target surface for a few seconds, during which chemical compounds were transferred from the sample to the target plate's surface. Its main advantages besides simplicity and rapidness is reduced risk of sample damage, and minimal amount of artifacts. Unlike traditional methods, it mitigates the risks associated with direct sample exposure to high vacuum conditions during analysis, such as dehydration, mechanical stress, or redistribution of analytes. The method is highly effective for low molecular weight compounds (< 1500 Da), providing low background noise, high sensitivity (up to attomole level), and precise mass accuracy through multi-point calibration with silver-109 ions. However, the imprint method has limitations, particularly with very hard or soft tissues, which can affect imprint quality and metabolite detection[25].

When preparing a sample for MSI using the LARAPPI/CI method, the process is significantly simplified, as it only requires placing tissue of nearly any thickness onto the target plate. The sample is frozen using a Peltier module, ensuring stability and immobility throughout the analysis.

Tissue thickness plays a critical role in MSI sample preparation, as it directly influences signal intensity. A study using MALDI-ToF MS on FFPE tissue microarrays demonstrated higher signal intensities for 1 μm sections compared to 5 μm sections, highlighting the sensitivity advantages of thinner samples[75]. However, achieving such thin sections consistently poses challenges due to technical issues like floating and rolling. In traditional MSI techniques, such as MALDI, thin tissue Sects. (5–20 μm) enhance spatial resolution by reducing signal overlap between layers and enabling efficient ionization. In contrast, thicker sections can lead to signal interference from deeper layers, incomplete analyte desorption, and uneven matrix application, which results in localized signal variations and reduced data quality. Furthermore, analyte migration during preparation, caused by mechanical stress during sectioning or water evaporation during drying, can distort the native compound distribution[76].

The LARAPPI/CI system employs a distance sensor functioning as a surface profilometer, enabling precise control of the ablation height during experiments, which ensures accurate removal of tissue layers. The use of a flat-top laser beam profile, achieved through diffractive optical elements, ensures uniform material removal and reduces the formation of artifacts. This beam shape produces shallow, rectangular ablation craters. Unlike conical beams that create deeper craters and can result in overlapping ablation zones, the flat-top profile ensures precise material removal with minimal distortion.

In the imprint method, sample thickness does not significantly affect the resolution of MSI, as the key process is the transfer of chemical compounds from the sample surface to the plate, rather than the analysis of the entire sample volume. It is possible to achieve instruments maximum resolution, however it is not practical for larger objects as imaging time is very long. The common practice in our surface transfers is to observe imprint in high magnification optical microscope to assess practical resolution of the transfer and set MSI resolution accordingly.

The ^{109}AgNPs-LDI-MSI method employs metal nanoparticles as a surface-assistance, utilizing their localized surface plasmon resonance (LSPR) to enhance absorptive properties. This phenomenon increases the signal intensity for molecules absorbed on the nanoparticle surface, making it particularly effective for analyzing small molecules. In the context of *A. vera* leaves, this method demonstrates a higher sensitivity, enabling the detection of compounds not visible with LARAPPI/CI-MSI. For example, ^{109}AgNPs-LDI-MSI reveals the presence of some compounds in lower concentrations in the inner part of the leaf, a feature that complements the more surface-oriented imaging of LARAPPI/CI-MSI.

The comparison of the two MSI methods highlights that most detected compounds are concentrated in the epidermis, as expected given the high water content (95–98%) of the *A. vera* gel. The post-analysis image of the leaf after LARAPPI/CI-MSI analysis suggests that the ablation was uniformly conducted across the whole leaf slice. Both methods operate in a similar *m/z* range and detect a comparable number of amino acids and carbohydrates. However, LDI-MSI excels in the identification of lipid compounds, detecting over twice as many as LARAPPI/CI-MSI, whereas LARAPPI/CI-MSI outperforms in detecting aromatic compounds, phenolics, and organic acids. Importantly, LARAPPI/CI-MSI provides much higher spectral resolution, allowing for much higher quality of identification. By contrast, LDI-MSI provides less extensive data for pathway mapping but excels in detecting lipids and other small molecules absorbed on nanoparticle surfaces. Despite these differences, the spatial localization of compounds between the two methods is largely consistent, underscoring their reliability. The complementary strengths of these techniques enable a more comprehensive analysis of plant tissues, with LARAPPI/CI-MSI offering superior spatial resolution and enhanced precision for plant-specific metabolites and pathway mapping, while LDI-MSI provides deeper insight into lipid distributions and small molecule detection. Together, these methods contribute valuable information on the metabolic activity and structural organization of *A. vera* leaves, with minimal compromise in spatial resolution or accuracy even in highly hydrated tissues.

Metabolic pathways based on the identified compounds

MSI is a key tool for analyzing metabolic pathways in plant tissues, providing high-resolution spatial mapping of metabolite distribution. Ion images generated by MSI reveal the localization of metabolites, which can be used to infer metabolic activity and reconstruct pathways based on spatial correlations between metabolites and their products. MSI offers semi-quantitative analysis by comparing relative signal intensities, which indicate the relative abundance of metabolites across tissue regions. While not fully quantitative, these data provide valuable insights into the localization and dynamics of metabolic processes[77]. Integrating MSI with other "omics" approaches enables a comprehensive understanding of plant metabolism, revealing spatial relationships between metabolites and their roles in stress responses and metabolic interactions[78,79].

For pathway analysis, LARAPPI/CI-MSI was selected over ^{109}AgNPs-LDI-MSI due to its much higher spectral resolution and superior ability to detect plant-specific metabolites, including aromatic compounds, phenolics, and organic acids. The enhanced resolution of QToF instrument used for LARAPPI/CI-MSI enables more detailed visualization of compound localization and intensity, which is essential for accurately reconstructing metabolic pathways and identifying the spatial organization of key reactions.

All identified compounds were used to determine metabolic pathways occurring in *A. vera* leaves using MetaboAnalyst version 6.0. The best fit based on the match status and continuity of the pathway based on the ion images was obtained for pathways of flavonoid biosynthesis, pentose phosphate pathway, and phenylpropanoid biosynthesis. The full results of the matching process are presented in Supplementary Information Table S3.

The compounds identified as part of the pentose phosphate pathway (PPP) using LARAPPI/CI-MSI (Fig. 4) include D-gluconate, 6-phospho-D-gluconate, D-glucono-1,5-lactone 6-phosphate, D-ribose, D-ribose 5-phosphate, and 5-phospho-α-D-ribose 1-diphosphate. These compounds are distributed primarily in the abaxial epidermis, with D-gluconate exhibiting the highest signal intensity. 6-Phospho-D-gluconate and D-glucono-1,5-lactone 6-phosphate show small regions of higher intensity in the adaxial epidermis, suggesting a potential metabolic connection between them. In the pathway, 6-phospho-D-gluconate is metabolized by 6PGD to produce ribulose 5-phosphate, which is further transformed into D-ribose 5-phosphate by RpiA. Both D-ribose 5-phosphate and its precursor, D-ribose, were detected, with D-ribose 5-phosphate showing higher abundance and a more extensive distribution in the epidermis, likely due to multiple synthesis sources. Its product, 5-phospho-α-D-ribose 1-diphosphate, was identified with much lower abundance and a spatial distribution similar, but not identical, to its precursor. PPP is a critical pathway in plants, producing metabolites required for nucleotide biosynthesis and contributing to antioxidant activity through NADPH production[80]. NADPH plays a key role in redox reactions involved in glutathione and thioredoxin activity[81]. In plants, PPP is more active in leaf tissues than in roots, potentially correlating with photosynthetic activity. However, studies suggest that stromal oxidative PPP is inactive during photosynthesis, implying that PPP activity is regulated by non-photosynthetic processes[82]. The higher concentration of compounds such as D-gluconate, 6-phospho-D-gluconate, and D-ribose in the abaxial epidermis and regions with less light exposure suggests that light availability may influence their abundance[66].

The ion images obtained using LARAPPI/CI-MSI revealed the spatial distribution of key metabolites in the phenylpropanoid biosynthesis pathway (Fig. 5A), including phenylalanine, trans-cinnamate, 4-coumaroyl quinic acid, chlorogenate, 4-coumaroyl shikimate, ferulate, and 5-hydroxyferulate. Phenylalanine, abundantly present throughout the epidermal region, serves as the starting compound in this pathway. Through enzymatic deamination by PAL, it is converted to trans-cinnamate, which is further hydroxylated by C4H to form 4-coumarate. This compound undergoes activation by 4CL, producing coumaroyl-CoA, which acts as a precursor for downstream metabolites, including 4-coumaroyl quinic acid and 4-coumaroyl shikimate.

Chlorogenate, derived from 4-coumaroyl quinic acid via CYP98A3, is a key antioxidant and defense compound, abundant in the lower abaxial epidermis, similar to its precursor. Ferulate, another significant product in this pathway, exhibited the highest abundance among the identified compounds, concentrated in the lower leaf regions. This suggests its crucial role in oxidative stress protection. The final metabolite, 5-hydroxyferulate, was more evenly distributed across the epidermis but with lower abundance than its precursor. The phenylpropanoid pathway is pivotal for plant defense, contributing to the synthesis of lignins and flavonoids[83]. Lignins reinforce plant structure, while flavonoids provide UV protection and regulate growth[84,85]. The impact of UV-B radiation has been linked to changes in phenylpropanoid-derived compounds, with extended exposure reducing ferulic acid and hydroxycinnamic acid concentrations[86,87], both of which influence photosynthetic activity[88,89]. In the flavonoid biosynthesis pathway (Fig. 5B), key metabolites, including naringenin, apiforol, dihydrokaempferol, kaempferol, taxifolin, and quercetin, were identified. Naringenin, present in high abundance in the inner epidermis, serves as the central branching point, leading to the synthesis of protective flavonoids. It is converted to dihydrokaempferol by F3H, which then forms kaempferol via FLS or taxifolin via CYP75B1 [93]. Kaempferol and taxifolin are precursors to quercetin, a major flavonoid distributed similarly to naringenin, highlighting its importance in this pathway. The increased abundance of flavonoids in specific epidermal regions correlates with

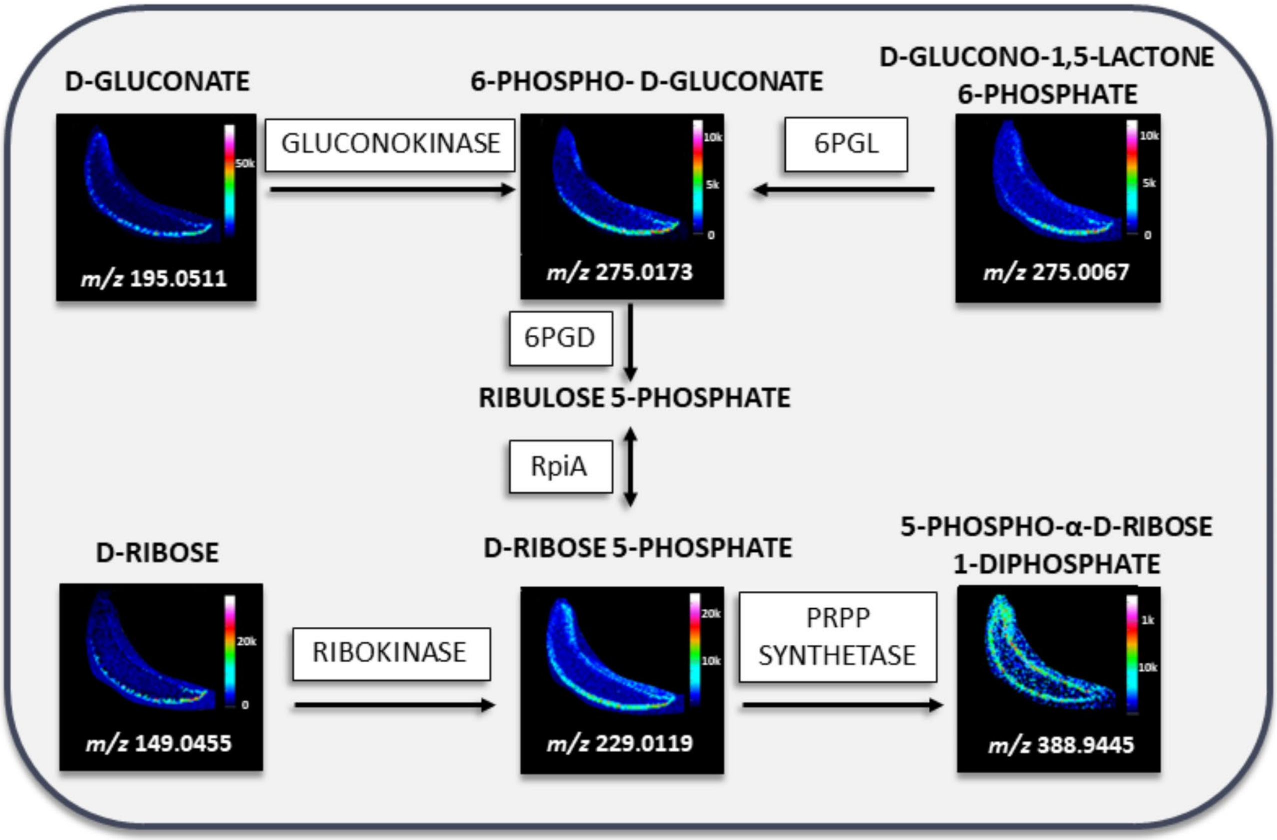

Fig. 4. Ion images obtained by LARAPPI/CI-MSI of compounds present in PPP. The fragment of the pathway was presented for comparison of the location of compounds in the pathway in *A. vera* leaf; 6PGL – 6-phosphogluconolactonase, 6PGD – 6-phosphogluconate dehydrogenase, rpiA – ribose-5-phosphate isomerase A.

their role in plant defense and UV protection[91,92]. While physical handling can impact compound detection, the observed distribution patterns are consistent with active metabolic pathways rather than sample preparation artifacts[93]. Together, the phenylpropanoid and flavonoid biosynthesis pathways illustrate the plant's adaptive mechanisms to environmental stress and its metabolic coordination across different tissue regions.

Conclusions

The study allowed for the identification of key *A. vera* metabolites, such as phenylpropanoids and flavonoids. The identified compounds show properties that confirm the usefulness of Aloe extracts in medicinal, food, and cosmetic uses. The ion images obtained from the two laser ablation-based MSI methods proved that the majority of the compounds were identified in the skin or latex regions of the plant leaf. Further analysis of potential metabolic pathways based on acquired ion images proved the metabolic processes identified undergo in the epidermal part of the *A. vera* leaf. The specific structure of the leaf seems to confirm acquired results. The difference in the used desorption/ionization techniques, as well as sample vs. imprint analysis, showed slight discrepancies in the location of the compounds identified with both methods. Since the majority of the compounds identified with ion images showing their occurrence in the gel region have not been previously identified in that part of the leaf the probable explanation is the effect of drifting of compounds during imprinting due to high moisture levels. The novel LARAPPI/CI-MSI technique proved to be preferential in the detection of plant-related metabolites, and the ^{109}AgNPs-LDI-MSI performed better in lipid detection. The integration of three distinct analytical platforms, ^{109}AgNPs-LDI-MSI, LARAPPI/CI-MSI, and UHPLC-UHRMS, enabled a comprehensive and highly efficient visualization of metabolites in an aloe leaf cross-section, providing deeper insights into its metabolic processes. This multi-platform approach facilitated a more detailed understanding of the tissue's biochemical landscape.

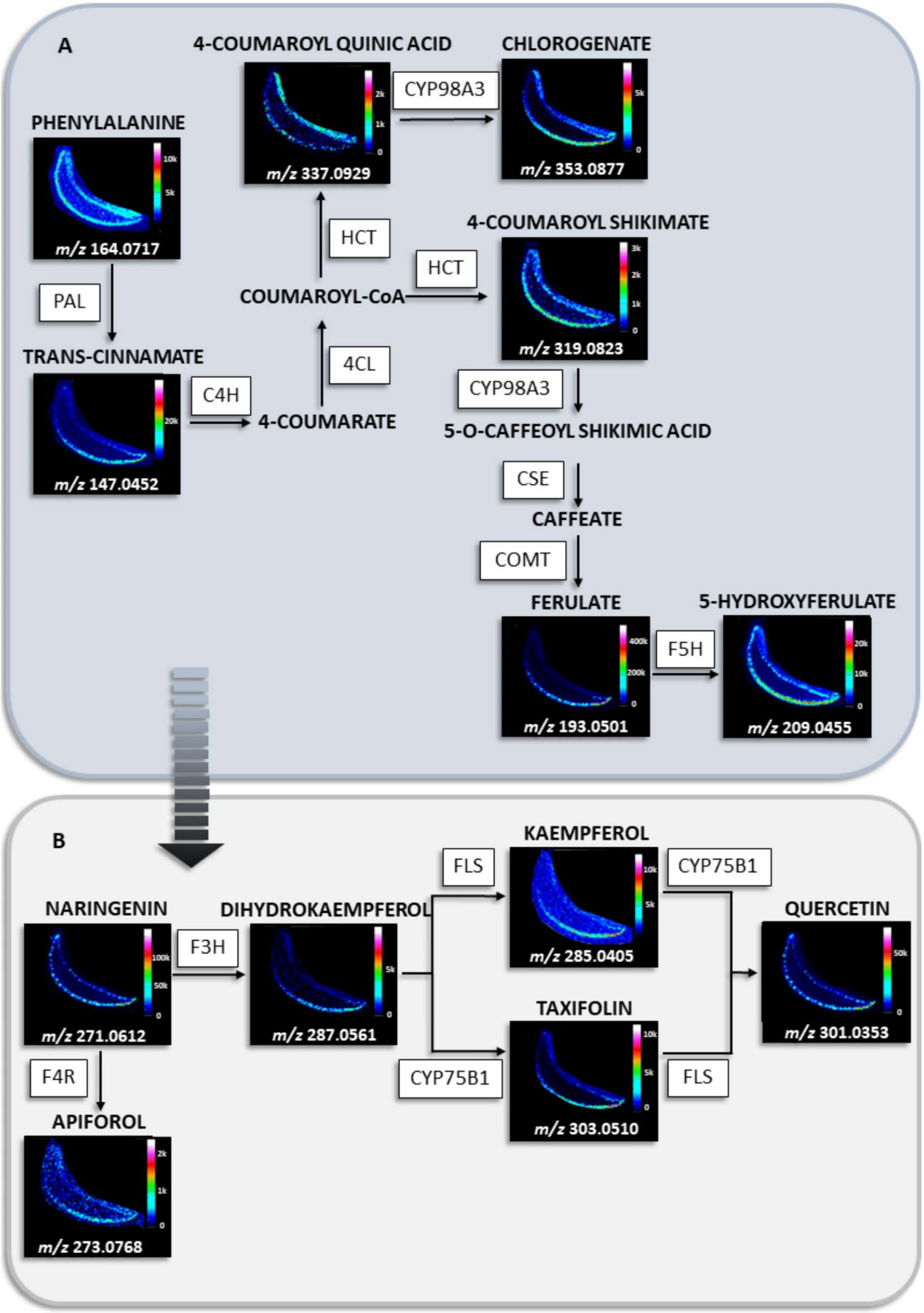

Fig. 5. Ion images obtained by LARAPPI/CI-MSI of compounds present in A - phenylpropanoid biosynthesis pathway and B - flavonoid biosynthesis pathway. The fragments of the pathways were presented for comparison of the location of compounds in the pathway in *A. vera* leaf; 4CL – 4-coumarate–CoA ligase, C4H – trans-cinnamate 4-monooxygenase, COMT – caffeic acid 3-O-methyltransferase, CSE - caffeoylshikimate esterase, CYP75B1 - flavonoid 3'-monooxygenase, CYP98A (C3'H) – 5-O-(4-coumaroyl)-D-quinate 3'-monooxygenase, F3H – flavanone 3-hydroxylase, F4R – flavonone 4-reductase, F5H – ferulate-5-hydroxylase, FLS – flavonol synthase, HCT – shikimate O-hydroxycinnamoyltransferase, PAL – phenylalanine ammonia-lyase.

Data availability

The data sets generated during and/or analyzed during the current study are available from the corresponding author upon request and in the RepOD open data repository (DOI: https://doi.org/10.18150/TNVBKJ).

Received: 13 November 2024; Accepted: 24 January 2025

Published online: 28 January 2025

References

1. Fortune Business Insights. Aloe Vera Extract Market Size, Share & Industry Analysis, By Product Form (Liquid, Gel, Powder, and Others), By Distribution Channel (Offline and Online), By Application (Food & Beverages, Cosmetics, and Pharmaceuticals), and Regional Forecast, 2024–2032. (2024).
2. López-Cervantes, J. et al. Antioxidant capacity, proximate composition, and lipid constituents of Aloe vera flowers. *J. Appl. Res. Med. Aromat. Plants*. **10**, 93–98 (2018).
3. Ramachandra, C. T. & Srinivasa Rao, P. Processing of Aloe Vera Leaf Gel: a review. *Am. J. Agric. Biol. Sci.* **3**, 502–510 (2008).
4. Sharma, R., Tandon, D., Joshi, V. & Attri, S. Development and evaluation of different beverages from Aloe vera (L.) Burm.f. For their nutritional, functional and sensory qualities. *Indian J. Nat. Prod. Resour.* (2015).
5. El-Sayed, S. M. & El-Sayed, H. S. Production of UF-soft cheese using probiotic bacteria and Aloe vera pulp as a good source of nutrients. *Annals Agricultural Sci.* **65**, 13–20 (2020).
6. Basannavar, S., Pothuraju, R. & Sharma, R. K. Effect of Aloe vera (Aloe barbadensis Miller) on survivability, extent of proteolysis and ACE inhibition of potential probiotic cultures in fermented milk. *J. Sci. Food Agric.* **94**, 2712–2717 (2014).
7. Kumar, S. et al. Aloe vera: a contemporary overview on scope and prospects in food preservation and packaging. *Prog Org. Coat.* **166**, (2022).
8. Maan, A. A., Ahmed, R., Iqbal Khan, Z. F., Riaz, M. K., Nazir, A. & A. & Aloe vera gel, an excellent base material for edible films and coatings. *Trends Food Sci. Technol.* **116**, 329–341 (2021).
9. Salama, H. E. & Abdel Aziz, M. S. Optimized alginate and Aloe vera gel edible coating reinforced with nTiO2 for the shelf-life extension of tomatoes. *Int. J. Biol. Macromol.* **165**, 2693–2701 (2020).
10. West, D. P. & Zhu, Y. F. Evaluation of aloe vera gel gloves in the treatment of dry skin associated with occupational exposure. *Am. J. Infect. Control*. **31**, 40–42 (2003).
11. Byeon, S. W. et al. Aloe Barbadensis extracts reduce the production of Interleukin-10 after exposure to Ultraviolet Radiation. *J. Invest. Dermatology*. **110**, 811–817 (1998).
12. Sánchez, M., González-Burgos, E., Iglesias, I. & Gómez-Serranillos, M. P. Pharmacological Update properties of Aloe Vera and its major active constituents. *Molecules* **25**, (2020).
13. Davis, R. H., Donato, J. J., Hartman, G. M. & Haas, R. C. Anti-inflammatory and wound healing activity of a growth substance in Aloe vera. *J. Am. Podiatr. Med. Assoc.* **84**, 77–81 (1994).
14. Li, C. Y. et al. Aloe Metabolites Prevent LPS-Induced Sepsis and Inflammatory Response by Inhibiting Mitogen-Activated Protein Kinase Activation. (2017). https://doi.org/10.1142/*S0192415X17500458* 45, 847–861.
15. Liu, F. W., Liu, F. C., Wang, Y. R., Tsai, H. I. & Yu, H. P. Aloin protects skin fibroblasts from heat stress-Induced oxidative stress damage by regulating the oxidative Defense System. *PLoS One*. **10**, e0143528 (2015).
16. Wahedi, H. M. et al. Aloesin from Aloe vera accelerates skin wound healing by modulating MAPK/Rho and smad signaling pathways in vitro and in vivo. *Phytomedicine* **28**, 19–26 (2017).
17. de Aro, A. A. et al. Effect of Aloe vera application on the content and molecular arrangement of glycosaminoglycans during calcaneal tendon healing. *Microsc Res. Tech.* **77**, 964–973 (2014).
18. Rezazadeh, F., Moshaverinia, M., Motamedifar, M. & Alyaseri, M. Assessment of Anti HSV-1 activity of Aloe Vera Gel Extract: an in Vitro Study. *J. Dent.* **17**, 49 (2016).
19. Syed, T. A. et al. Management of psoriasis with Aloe vera extract in a hydrophilic cream: a placebo-controlled, double-blind study. *Trop. Med. Int. Health*. **1**, 505–509 (1996).
20. Vardy, D. A., Cohen, A. D., Tchetov, T., Medvedovsky, E. & Biton, A. A double-blind, placebo-controlled trial of an Aloe vera (A. barbadensis) emulsion in the treatment of seborrheic dermatitis. *J. Dermatological Treat.* **10**, 7–11 (1999).
21. Mourad, A., Abo-Youssef, H., Anwar, B. & Messiha, S. Beneficial effects of Aloe vera in treatment of diabetes: comparative in vivo and in vitro studies. (2013). https://doi.org/10.1016/j.bfopcu.2012.03.002
22. Yoruk, N. G. Istanbullu Paksoy, Ö. GC/MS evaluation of the composition of the Aloe vera gel and extract. *Food Chem. X*. **23**, 101536 (2024).
23. Bendjedid, S. et al. Analysis of Phytochemical constituents by using LC-MS, antifungal and allelopathic activities of leaves extracts of Aloe vera. *Jordan J. Biol. Sci.* **15**, 21–28 (2022).
24. Monakhova, Y. B., Randel, G. & Diehl, B. W. K. Automated control of the organic and inorganic composition of Aloe vera extracts using 1H NMR spectroscopy. *J. AOAC Int.* **99**, 1213–1218 (2016).
25. Hu, W. et al. Mass spectrometry imaging for direct visualization of components in plants tissues. *J. Sep. Sci.* **44**, 3462–3476 (2021).
26. Dinaiz, B. A. B. et al. Mass spectrometry imaging for plant biology: a review. *Phytochemistry Reviews 2015 15:3* 15, 445–488 (2015).
27. Du, T. L., Van Der Westhuizen, F. H. & Botes, L. Aloe ferox Leaf Gel Phytochemical Content, antioxidant capacity, and possible health benefits. *J. Agric. Food Chem.* **55**, 6891–6896 (2007).
28. Lanni, E. J., Rubakhin, S. S. & Sweedler, J. V. Mass spectrometry imaging and profiling of single cells. *J. Proteom.* **75**, 5036–5051 (2012).
29. Wogelred, L., Höök, F., Agnarsson, B. & Sjövall, P. Toward multiplexed quantification of biomolecules on surfaces using time-of-flight secondary ion mass spectrometry. *Biointerphases* **13**, 3–413 (2018).
30. Sturtevant, D., Lee, Y. J. & Chapman, K. D. Matrix assisted laser desorption/ionization-mass spectrometry imaging (MALDI-MSI) for direct visualization of plant metabolites in situ. *Curr. Opin. Biotechnol.* **37**, 53–60 (2016).
31. Müller, W. H., Verdin, A., De Pauw, E., Malherbe, C. & Eppe, G. Surface-assisted laser desorption/ionization mass spectrometry imaging: a review. *Mass Spectrom. Rev.* **41**, 373–420 (2022).
32. Nizioł, J., Sekuła, J. & Ruman, T. Visualizing spatial distribution of small molecules in the rhubarb stalk (Rheum rhabarbarum) by surface-transfer mass spectrometry imaging. *Phytochemistry* **139**, 72–80 (2017).
33. Arendowski, A. et al. Laser Desorption/Ionization MS imaging of Cancer kidney tissue on silver nanoparticle-enhanced target. *Bioanalysis* **10**, 83–94 (2018).
34. Claude, E., Jones, E. A. & Pringle, S. D. DESI mass spectrometry imaging (MSI). *Methods Mol. Biol.* **1618**, 65–75 (2017).
35. Ruman, T., Krupa, Z. & Nizioł, J. Direct three-Dimensional Mass Spectrometry Imaging with laser ablation Remote Atmospheric pressure Photoionization/Chemical ionization. *Anal. Chem.* **96**, (2024).
36. Nizioł, J. & Ruman, T. Surface-transfer Mass Spectrometry Imaging on a monoisotopic silver nanoparticle enhanced target. *Anal. Chem.* **85**, 12070–12076 (2013).
37. Płaza, A., Kołodziej, A., Nizioł, J. & Ruman, T. Laser ablation synthesis in solution and nebulization of Silver-109 nanoparticles for Mass Spectrometry and Mass Spectrometry Imaging. *ACS Meas. Sci. Au.* **2**, 14–22 (2022).

38. Krupa, Z. & Nizioł, J. Fiber laser-generated Silver-109 nanoparticles for laser Desorption/Ionization Mass Spectrometry of Illicit drugs. *J. Am. Soc. Mass. Spectrom.* **35**, 1156–1167 (2024).
39. Pang, Z. et al. MetaboAnalyst 6.0: towards a unified platform for metabolomics data processing, analysis and interpretation. *Nucleic Acids Res.* **52**, W398–W406 (2024).
40. El-Seedi, H. R. et al. Biosynthesis, natural sources, dietary intake, pharmacokinetic properties, and biological activities of hydroxycinnamic acids. *J. Agric. Food Chem.* **60**, 10877–10895 (2012).
41. Arai, H. et al. Genetic organization and characteristics of the 3-(3-hydroxyphenyl)propionic acid degradation pathway of Comamonas testosteroni TA441. *Microbiol. (N Y).* **145**, 2813–2820 (1999).
42. Aguilar-Méndez, E. D., Monribot-Villanueva, J. L. & Guerrero-Analco, J. A. & De-la-Peña, C. Chlorophyll deficiency in Agave angustifolia Haw.: unveiling the impact on secondary metabolite production. *Planta* **260**, (2024).
43. Altaf, L. et al. Bioactive compounds and antioxidant activity in various parts of Morus alba L. Cv. Ichinose: a comparative analysis. *Discover Life.* **54**, 1–15 (2024).
44. Lozano-Castellón, J. et al. New vacuum cooking techniques with extra-virgin olive oil show a better phytochemical profile than traditional cooking methods: a foodomics study. *Food Chem.* **362**, 130194 (2021).
45. Chen, Y. L. et al. Ilex kaushue and Its Bioactive Component 3,5-Dicaffeoylquinic Acid Protected Mice from Lipopolysaccharide-Induced Acute Lung Injury. *Scientific Reports 2016 6:1* 6, 1–12 (2016).
46. Nair, R. B., Bastress, K. L., Ruegger, M. O., Denault, J. W. & Chapple, C. The Arabidopsis thaliana REDUCED EPIDERMAL FLUORESCENCE1 gene encodes an Aldehyde dehydrogenase involved in Ferulic Acid and Sinapic Acid Biosynthesis. *Plant. Cell.* **16**, 544–554 (2004).
47. Callipo, L. et al. Phenilpropanoate identification in young wheat plants by liquid chromatography/tandem mass spectrometry: monomeric and dimeric compounds. *J. Mass Spectrom.* **45**, 1026–1040 (2010).
48. Renger, A. & Steinhart, H. Ferulic acid dehydrodimers as structural elements in cereal dietary fibre. *Eur. Food Res. Technol.* **211**, 422–428 (2000).
49. Rhodes, D. I., Sadek, M. & Stone, B. A. Hydroxycinnamic acids in walls of wheat aleurone cells. *J. Cereal Sci.* **36**, 67–81 (2002).
50. Kim, D. M., Jung, J. Y., Lee, H. K., Kwon, Y. S. & Choi, Y. M. Determination and profiling of secondary metabolites in Aloe Vera, Aloe Arborescens and Aloe Saponaria. https://doi.org/10.26717/BJSTR.2021.40.006499
51. Lucini, L. et al. Phytochemical constituents and in vitro radical scavenging activity of different Aloe species. *Food Chem.* **170**, 501–507 (2015).
52. Korte, A. R., Yandeau-Nelson, M. D., Nikolau, B. J. & Lee, Y. J. Subcellular-level resolution MALDI-MS imaging of maize leaf metabolites by MALDI-linear ion trap-orbitrap mass spectrometer. *Anal. Bioanal Chem.* **407**, 2301–2309 (2015).
53. Xia, J. et al. Unveiling the spatial distribution and molecular mechanisms of terpenoid biosynthesis in Salvia miltiorrhiza and S. grandifolia using multi-omics and DESI–MSI. *Hortic. Res.* **10**, (2023).
54. Hadas, Y., Goldberg, I., Pines, O. & Prusky, D. Involvement of Gluconic Acid and Glucose Oxidase in the Pathogenicity of Penicillium expansum in Apples.(2007). https://doi.org/10.1094/PHYTO-97-3-0384 97, 384–390.
55. Sun, C. et al. Visualizing the distributions and spatiotemporal changes of metabolites in Panax notoginseng by MALDI mass spectrometry imaging. *J. Ginseng Res.* **45**, 726–733 (2021).
56. Xi, H. et al. Spatial metabolome of biosynthesis and metabolism in Cyclocarya paliurus leaves. *Food Chem.* **443**, 138519 (2024).
57. Tong, X. et al. Aloe vera gel extract: Safety evaluation for acute and chronic oral administration in Sprague-Dawley rats and anticancer activity in breast and lung cancer cells. *J. Ethnopharmacol.* **280**, 114434 (2021).
58. Rommens, C. M. et al. Engineered native pathways for high kaempferol and caffeoylquinate production in potato. *Plant. Biotechnol. J.* **6**, 870–886 (2008).
59. Justesen, U., Knuthsen, P. & Leth, T. Quantitative analysis of flavonols, flavones, and flavanones in fruits, vegetables and beverages by high-performance liquid chromatography with photo-diode array and mass spectrometric detection. *J. Chromatogr. A.* **799**, 101–110 (1998).
60. Onkokesung, N. et al. Modulation of flavonoid metabolites in Arabidopsis thaliana through overexpression of the MYB75 transcription factor: role of kaempferol-3,7-dirhamnoside in resistance to the specialist insect herbivore Pieris brassicae. *J. Exp. Bot.* **65**, 2203 (2014).
61. Taiwo, F. O., Oyedeji, O. & Osundahunsi, M. T. Antimicrobial and antioxidant properties of kaempferol-3-O-glucoside and 1-(4-Hydroxyphenyl)-3-phenylpropan-1-one isolated from the leaves of Annona muricata (Linn). *J. Pharm. Res. Int.* **26**, 1–13 (2019).
62. Ming, D. et al. Kaempferol inhibits the primary attachment phase of biofilm formation in Staphylococcus aureus. *Front. Microbiol.* **8**, 282585 (2017).
63. López, A., De Tangil, M. S., Vega-Orellana, O., Ramírez, A. S. & Rico, M. Phenolic Constituents, Antioxidant and Preliminary Antimycoplasmic Activities of Leaf Skin and Flowers of Aloe vera (L.) Burm. f. (syn. A. barbadensis Mill.) from the Canary Islands (Spain). *Molecules* Vol. 18, Pages 4942–4954 18, 4942–4954 (2013). (2013).
64. Wu, L. et al. Enhanced Coverage and Sensitivity of Imprint DESI Mass Spectrometry Imaging for Plant Leaf metabolites by post-photoionization. *Anal. Chem.* **94**, 15108–15116 (2022).
65. Sharkey, T. D. Pentose phosphate pathway reactions in photosynthesizing cells. *Cells 2021.* **10, Page 1547** (10), 1547 (2021).
66. Kruger, N. J. & Von Schaewen, A. The oxidative pentose phosphate pathway: structure and organisation. *Curr. Opin. Plant. Biol.* **6**, 236–246 (2003).
67. Santos-Sánchez, N. F. et al. Shikimic acid pathway in biosynthesis of Phenolic compounds. *Plant. Physiological Aspects Phenolic Compd.* https://doi.org/10.5772/INTECHOPEN.83815 (2019).
68. Fernandes, D. C. et al. Myeloperoxidase inhibitory and radical scavenging activities of Flavones from Pterogyne Nitens. *Chem. Pharm. Bull. (Tokyo).* **56**, 723–726 (2008).
69. Zaitsev, V. G., Makarova, G. V. & Komissarenko, N. F. Sorbifolin-A new flavone glycoside from Sorbaria sorbifolia. *Chem. Nat. Compd.* **5**, 423–426 (1969).
70. Corticchiato, M. et al. Free flavonoid aglycones from Thymus herba barona and its monoterpenoid chemotypes. *Phytochemistry* **40**, 115–120 (1995).
71. Zaidi, F., Voirin, B., Jay, M. & Viricel, M. R. Free flavonoid aglycones from leaves of mentha pulegium and mentha suaveolens (labiatae). *Phytochemistry* **48**, 991–994 (1998).
72. Saccù, D., Bogoni, P. & Procida, G. Aloe Exudate: characterization by reversed phase HPLC and headspace GC-MS. *J. Agric. Food Chem.* **49**, 4526–4530 (2001).
73. Lv, L. et al. BACE1 (beta-secretase) inhibitory chromone glycosides from Aloe vera and Aloe nobilis. *Planta Med.* **74**, 540–545 (2008).
74. Cuypers, E. Cillero-Pastor Sample Preparation of Biological tissues for MALDI-MSI. in MALDI Mass Spectrometry Imaging: from Fundamentals to Spatial Omics (ed Siegel, P.) T.) vol. 5 87–104 (The Royal Society of Chemistry, (2021).
75. Longuespée, R. et al. In MALDI–Mass Spectrometry Imaging on Formalin-fixed paraffin-embedded tissue specimen section thickness significantly influences m/z peak intensity. *Proteom. Clin. Appl.* **13**, (2019).
76. Dilmetz, B. A. et al. Novel technical developments in mass spectrometry imaging in 2020: a mini review. *Anal. Sci. Adv.* **2**, 225–237 (2021).
77. Horn, P. J. & Chapman, K. D. Imaging plant metabolism in situ. *J. Exp. Bot.* **75**, 1654–1670 (2024).

78. Chen, Y. J., Zeng, H. S., Jin, H. & Wang, H. Applications of mass spectrometry imaging in botanical research. *Advanced Biotechnology 2024 2:1* 2, 1–20 (2024).
79. Bhandari, D. R. et al. High resolution mass spectrometry imaging of plant tissues: towards a plant metabolite atlas. *Analyst* **140**, 7696–7709 (2015).
80. Gupte, R. S. et al. Upregulation of glucose-6-phosphate dehydrogenase and NAD(P)H oxidase activity increases oxidative stress in failing human heart. *J. Card Fail.* **13**, 497–506 (2007).
81. Debnam, P. M. & Emes, M. J. Subcellular distribution of enzymes of the oxidative pentose phosphate pathway in root and leaf tissues. *J. Exp. Bot.* **50**, 1653–1661 (1999).
82. Sharkey, T. D., Preiser, A. L., Weraduwage, S. M. & Gog, L. Source of 12 C in Calvin–Benson cycle intermediates and isoprene emitted from plant leaves fed with 13CO2. *Biochem. J.* **477**, 3237 (2020).
83. Vogt, T. Phenylpropanoid Biosynthesis. *Mol. Plant.* **3**, 2–20 (2010).
84. Sytar, O. et al. Shift in accumulation of flavonoids and phenolic acids in lettuce attributable to changes in ultraviolet radiation and temperature. *Sci. Hortic.* **239**, 193–204 (2018).
85. Xue, J. S. et al. Phenylpropanoid derivatives are essential components of Sporopollenin in vascular plants. *Mol. Plant.* **13**, 1644–1653 (2020).
86. Liu, L., Gitz, D. C. & McClure, J. W. Effects of UV-B on flavonoids, ferulic acid, growth and photosynthesis in barley primary leaves. *Physiol. Plant.* **93**, 725–733 (1995).
87. Schmitz-Hoerner, R. & Weissenböck, G. Contribution of phenolic compounds to the UV-B screening capacity of developing barley primary leaves in relation to DNA damage and repair under elevated UV-B levels. *Phytochemistry* **64**, 243–255 (2003).
88. Hussain, M. I., Reigosa, M. J. & Secondary Metabolites Ferulic acid and p-Hydroxybenzoic Acid Induced toxic effects on photosynthetic process in Rumex acetosa L. *Biomolecules 2021*. **11, Page 233** (11), 233 (2021).
89. Huang, X. & Bie, Z. Cinnamic acid-inhibited ribulose-1,5-bisphosphate carboxylase activity is mediated through decreased spermine and changes in the ratio of polyamines in cowpea. *J. Plant. Physiol.* **167**, 47–53 (2010).
90. Liu, W. et al. The flavonoid biosynthesis network in plants. *Int. J. Mol. Sci. 2021*. **22**, 12824 (2021).
91. Kim, B. G., Kim, J. H., Kim, J., Lee, C. & Ahn, J. H. Accumulation of flavonols in response to Ultraviolet-B irradiation in soybean is related to induction of Flavanone 3-β-Hydroxylase and Flavonol synthase. *Mol. Cells.* **25**, 247–252 (2008).
92. Martínez-Silvestre, K. E. et al. Effect of UV-B Radiation on Flavonoids and Phenols Accumulation in Tempisque (Sideroxylon capiri Pittier) Callus. *Plants* 11, (2022).
93. Cha, S. et al. Direct profiling and imaging of plant metabolites in intact tissues by using colloidal graphite-assisted laser desorption ionization mass spectrometry. *Plant J.* **55**, 348–360 (2008).

Acknowledgements

This work was supported by the National Science Centre (Poland) research project Sonata Bis number 2022/46/E/ST4/00016 and by the Minister of Science and Higher Education Republic of Poland within the program "Regional Excellence Initiative", agreement no. RID/SP/0032/2024/01 for Rzeszow University of Technology, 2024–2027.

Author contributions

Sumi Krupa: Methodology, Writing – original draft, Visualization, Investigation, Data curation. Tomasz Ruman: Methodology, Resources, Writing – review & editing, Supervision, Investigation, Formal analysis, Data curation, Funding acquisition. Wiktoria Szuberla: Investigation, Data curation. Joanna Nizioł: Conceptualization, Methodology, Investigation, Data Curation, Visualization, Supervision, Investigation, Writing – review & editing, Project Administration, Funding acquisition.

Declarations

Competing interests

The authors declare no competing interests.

Additional information

Supplementary Information The online version contains supplementary material available at https://doi.org/10.1038/s41598-025-88144-8.

Correspondence and requests for materials should be addressed to J.N.

Reprints and permissions information is available at www.nature.com/reprints.

Publisher's note Springer Nature remains neutral with regard to jurisdictional claims in published maps and institutional affiliations.

Open Access This article is licensed under a Creative Commons Attribution 4.0 International License, which permits use, sharing, adaptation, distribution and reproduction in any medium or format, as long as you give appropriate credit to the original author(s) and the source, provide a link to the Creative Commons licence, and indicate if changes were made. The images or other third party material in this article are included in the article's Creative Commons licence, unless indicated otherwise in a credit line to the material. If material is not included in the article's Creative Commons licence and your intended use is not permitted by statutory regulation or exceeds the permitted use, you will need to obtain permission directly from the copyright holder. To view a copy of this licence, visit http://creativecommons.org/licenses/by/4.0/.

© The Author(s) 2025

OŚWIADCZENIA WSPÓŁAUTORÓW

POLITECHNIKA
RZESZOWSKA
im. IGNACEGO ŁUKASIEWICZA

al. Powstańców Warszawy 12, 35-029 Rzeszów
tel.: +48 17 865 1100, e-mail: kancelaria@prz.edu.pl
prz.edu.pl

Rzeszów, 30.03.2026 r.

mgr inż. Sumi Krupa

OŚWIADCZENIE

Jako współautorka publikacji wchodzących w skład niniejszej rozprawy doktorskiej oświadczam, że mój indywidualny wkład w powstanie poszczególnych publikacji przedstawia się następująco:

[P1] J. Nizioł, **S. Krupa**, W. Szuberla, T. Ruman**,** Advances in metallic nanostructures-assisted laser desorption/ionization mass spectrometry imaging of biological samples: A review, *Analytica Chimica Acta,* 2025, 1366, 344256

Mój wkład w powstanie tej publikacji obejmował przegląd literatury, udział w krytycznej analizie danych literaturowych, współudział w opracowaniu koncepcji i układu pracy, oraz udział w przygotowaniu pierwszej wersji manuskryptu. Mój udział w powstaniu publikacji oceniam na 30%.

[P2] A. Płaza-Altamer, A. Kołodziej, **S. Krupa**, J. Nizioł, T. Ruman, Infrared pulsed fiber laser-produced gold and silver-109 nanoparticles for laser desorption/ionization mass spectrometry of steroid hormones, Rapid Communications in Mass Spectrometry, 2023, 37, e9621

Mój indywidualny wkład w powstanie tej publikacji obejmował opracowanie i przygotowanie części danych eksperymentalnych przedstawionych w publikacji. Mój udział w powstaniu publikacji oceniam na 20%.

[P3] **S. Krupa**, J. Nizioł, Fiber Laser-Generated Silver-109 Nanoparticles for Laser Desorption/Ionization Mass Spectrometry of Illicit Drugs, *Journal of the American Society for Mass Spectrometry,* 2024, 35, 1156-1167

Mój indywidualny wkład w powstanie tej publikacji obejmował udział w wytwarzaniu nanocząstek srebra-109, przygotowaniu płytki pomiarowej oraz próbek do analiz, współudział w opracowaniu metodyki badań, wykonanie analiz z wykorzystaniem ^{109}AgNPs-LDI-MS przy użyciu spektrometru MALDI-ToF/ToF, opracowanie i interpretację uzyskanych widm masowych, przeprowadzenie formalnej analizy danych, opracowanie graficzne wyników oraz przygotowanie pierwotnej wersji manuskryptu. Mój udział w powstaniu publikacji oceniam na 60%.

Krupa

[P4] J. Nizioł, M. Misiorek, **S. Krupa**, T. Ruman, Infrared Laser-Based Selected Reaction Monitoring Mass Spectrometry Imaging of Banana (Musa spp.) Tissue—New Method for Detection and Spatial Localization of Metabolites in Food, Food Analytical Methods, 2023, 17, 236-250

Mój indywidualny wkład w powstanie tej publikacji obejmował udział w części przeprowadzonych analiz LARESI-SRM-MSI oraz udział w opracowaniu finalnej wersji manuskryptu. Mój udział w powstaniu publikacji oceniam na 25%.

[P5] T. Ruman, **S. Krupa**, J. Nizioł Direct Three-Dimensional Mass Spectrometry Imaging with Laser Ablation Remote Atmospheric Pressure Photoionization/Chemical Ionization, *Analytical Chemistry,* 2024, 96, 13326-13334

Mój indywidualny wkład w powstanie tej publikacji obejmował udział w badaniach optymalizacyjnych ukierunkowanych na dobór elementów układu optycznego toru lasera, konfiguracji źródła jonów, składu cieczy wspomagającej jonizację oraz parametrów pomiarowych, w tym rozdzielczości przestrzennej i czasu trwania impulsów lasera. Obejmował on również wykonanie analiz LARAPPI/CI-MSI z wykorzystaniem obiektów testowych, w tym modeli tkankowych w postaci żelu agarowego, oraz próbek tkanek biologicznych, przygotowanie obiektów testowych i udział w wyborze obiektów walidacyjnych, a także analizę i wizualizację danych uzyskanych w badaniach optymalizacyjnych i walidacyjnych oraz współudział w opracowaniu manuskryptu. Mój udział w powstaniu publikacji oceniam na 33,3%.

[P6] **S. Krupa**, W. Szuberla, J. Nizioł, A. Ossolińska, K. Ossoliński, T. Ruman, Broadband collision-induced dissociation mass spectrometry imaging, *Journal of the American Society for Mass Spectrometry,* 2025, 36, 1443-1455

Mój indywidualny wkład w powstanie tej publikacji obejmował przygotowanie obiektów testowych z naniesionymi związkami referencyjnymi oraz przygotowanie ludzkich tkanek do analiz, wykonanie pomiarów LARAPPI/CI-MSI z wykorzystaniem metody bbCID na obiektach testowych i tkankach biologicznych, udział w optymalizacji warunków analizy, w tym sposobu jonizacji, składu cieczy wspomagającej jonizację oraz parametrów akwizycji danych, analizę uzyskanych danych, przygotowanie ich wizualizacji oraz udział w opracowaniu pierwszej wersji manuskryptu. Mój udział w powstaniu publikacji oceniam na 30%.

[P7] J. Szulc, T. Grzyb, J. Nizioł, **S. Krupa**, W. Szuberla, T. Ruman, Direct 3D Mass Spectrometry Imaging Analysis of Environmental Microorganisms, *Molecules*, 2025, 30, 1317

Mój indywidualny wkład w powstanie tej publikacji obejmował przygotowanie kultur mikroorganizmów do analiz MSI, wykonanie ekstraktów do analizy UHPLC-HRMS, przeprowadzenie pomiarów LARAPPI/CI-MSI w trybie 2D i 3D, udział w doborze i optymalizacji parametrów pomiarowych dla analiz kultur mikroorganizmów, opracowanie uzyskanych widm i obrazów MSI, analizę oraz interpretację wyników MSI, wizualizację wyników, a także udział w opracowaniu manuskryptu publikacji. Mój udział w powstaniu publikacji oceniam na 20%.

[P8] **S. Krupa,** T. Ruman, J. Nizioł, Metabolic Impact of Pesticides on Radish: 2D and 3D Mass Spectrometry Imaging of Metabolites in *Raphanus sativus, Journal of Agricultural and Food Chemistry,* 2025, 73, 29229-29244

Mój indywidualny wkład w powstanie tej publikacji obejmował współudział w opracowaniu metodyki badań, przygotowanie próbek rzodkiewki do analiz MSI oraz wykonanie ekstraktów do analiz UHPLC-HRMS, przeprowadzenie analiz LARAPPI/CI-MSI, opracowanie uzyskanych widm i obrazów jonowych, analizę oraz interpretację danych, przygotowanie wszystkich rysunków i tabel zamieszczonych w publikacji, przeprowadzenie części analizy statystycznej danych UHPLC-HRMS, przygotowanie pierwszej wersji manuskryptu oraz współudział w opracowaniu jego ostatecznej wersji. Mój udział w powstaniu publikacji oceniam na 50%.

[P9] **S. Krupa**, T. Ruman, W. Szuberla, J. Nizioł Analysis of the spatial distribution of metabolites in *Aloe vera* leaves by mass spectrometry imaging and UHPLC-HRMS, *Scientific Reports*, 2025, 15, 3502

Mój wkład w powstanie tej publikacji obejmował współudział w opracowaniu metodyki badań, przygotowanie próbek do analiz, wykonanie pomiarów techniką LARAPPI/CI-MSI, interpretację oraz porównanie danych uzyskanych metodami LARAPPI/CI-MSI, ^{109}AgNPs-LDI-MSI i UHPLC-HRMS, w tym opracowanie obrazów jonowych, analizę przestrzennego rozmieszczenia metabolitów oraz analizę szlaków metabolicznych, przygotowanie wszystkich rysunków i tabel zamieszczonych w publikacji, a także przygotowanie pierwszej wersji manuskryptu i udział w opracowaniu jego wersji ostatecznej. Mój udział w powstaniu publikacji oceniam na 60%.

....

POLITECHNIKA
RZESZOWSKA
im. IGNACEGO ŁUKASIEWICZA

al. Powstańców Warszawy 12, 35-029 Rzeszów
tel.: +48 17 865 1100, e-mail: kancelaria@prz.edu.pl
prz.edu.pl

Rzeszów, 30.03.2026 r.

dr hab. Joanna Nizioł, prof. PRz

OŚWIADCZENIE

Jako współautorka publikacji wchodzących w skład rozprawy doktorskiej Pani mgr inż. Sumi Krupy, oświadczam, że mój wkład w powstanie poszczególnych publikacji przedstawia się następująco:

[P1] **J. Nizioł**, S. Krupa, W. Szuberla, T. Ruman**,** Advances in metallic nanostructures-assisted laser desorption/ionization mass spectrometry imaging of biological samples: A review, *Analytica Chimica Acta,* 2025, 1366, 344256

Mój wkład w powstanie tej publikacji obejmował opracowanie koncepcji i układu pracy, sprawowanie nadzoru merytorycznego nad realizacją publikacji, udział w przeglądzie literatury oraz krytycznej analizie danych literaturowych, przygotowanie rysunków i tabel, udział w przygotowaniu pierwszej wersji manuskryptu, pełnienie funkcji autora korespondencyjnego, w tym opracowanie odpowiedzi na recenzję, opracowanie i redakcję ostatecznej wersji manuskryptu oraz pozyskanie finansowania tych badań w ramach projektu SONATA BIS 12 nr 2022/46/E/ST4/00016, którego jestem kierownikiem, finansowanego przez Narodowe Centrum Nauki. Mój udział w powstaniu publikacji oceniam na 55%.

[P2] A. Płaza-Altamer, A. Kołodziej, S. Krupa, **J. Nizioł**, T. Ruman, Infrared pulsed fiber laser-produced gold and silver-109 nanoparticles for laser desorption/ionization mass spectrometry of steroid hormones, *Rapid Communications in Mass Spectrometry*, 2023, 37, e9621

Mój wkład w powstanie tej publikacji obejmował kierowanie projektem badawczym, w ramach którego finansowane były badania stanowiące podstawę niniejszej pracy. Badania te były realizowane ze środków pozyskanych przeze mnie w ramach projektu SONATA BIS 12 nr 2022/46/E/ST4/00016 finansowanego przez Narodowe Centrum Nauki. Mój udział w powstaniu publikacji oceniam na 20%.

[P3] S. Krupa, **J. Nizioł**, Fiber Laser-Generated Silver-109 Nanoparticles for Laser Desorption/Ionization Mass Spectrometry of Illicit Drugs, *Journal of the American Society for Mass Spectrometry,* 2024, 35, 1156-1167

Mój wkład w powstanie tej publikacji obejmował opracowanie koncepcji pracy, współudział w opracowaniu metodyki badań, pełnienie funkcji autora korespondencyjnego, w tym opracowanie odpowiedzi na recenzje, redakcję ostatecznej wersji manuskryptu oraz pozyskanie finansowania przeprowadzenie pomiarów LARAPPI/CI-MSI w trybie 2D i 3D, udział w doborze i optymalizacji parametrów pomiarowych dla analiz kultur mikroorganizmów, opracowanie uzyskanych widm i obrazów MSI, analizę oraz interpretację wyników MSI, wizualizację wyników, a także udział w opracowaniu manuskryptu publikacji. Mój udział w powstaniu publikacji oceniam na 20%.

[P8] **S. Krupa,** T. Ruman, J. Nizioł, Metabolic Impact of Pesticides on Radish: 2D and 3D Mass Spectrometry Imaging of Metabolites in *Raphanus sativus, Journal of Agricultural and Food Chemistry,* 2025, 73, 29229-29244

Mój indywidualny wkład w powstanie tej publikacji obejmował współudział w opracowaniu metodyki badań, przygotowanie próbek rzodkiewki do analiz MSI oraz wykonanie ekstraktów do analiz UHPLC-HRMS, przeprowadzenie analiz LARAPPI/CI-MSI, opracowanie uzyskanych widm i obrazów jonowych, analizę oraz interpretację danych, przygotowanie wszystkich rysunków i tabel zamieszczonych w publikacji, przeprowadzenie części analizy statystycznej danych UHPLC-HRMS, przygotowanie pierwszej wersji manuskryptu oraz współudział w opracowaniu jego ostatecznej wersji. Mój udział w powstaniu publikacji oceniam na 50%.

[P9] **S. Krupa**, T. Ruman, W. Szuberla, J. Nizioł Analysis of the spatial distribution of metabolites in *Aloe vera* leaves by mass spectrometry imaging and UHPLC-HRMS, *Scientific Reports*, 2025, 15, 3502

Mój wkład w powstanie tej publikacji obejmował współudział w opracowaniu metodyki badań, przygotowanie próbek do analiz, wykonanie pomiarów techniką LARAPPI/CI-MSI, interpretację oraz porównanie danych uzyskanych metodami LARAPPI/CI-MSI, ^{109}AgNPs-LDI-MSI i UHPLC-HRMS, w tym opracowanie obrazów jonowych, analizę przestrzennego rozmieszczenia metabolitów oraz analizę szlaków metabolicznych, przygotowanie wszystkich rysunków i tabel zamieszczonych w publikacji, a także przygotowanie pierwszej wersji manuskryptu i udział w opracowaniu jego wersji ostatecznej. Mój udział w powstaniu publikacji oceniam na 60%.

Joanna Nizioł
....

POLITECHNIKA
RZESZOWSKA
im. IGNACEGO ŁUKASIEWICZA

al. Powstańców Warszawy 12, 35-029 Rzeszów
tel.: +48 17 865 1100, e-mail: kancelaria@prz.edu.pl
prz.edu.pl

Rzeszów, 30.03.2026 r.

prof. dr hab. inż. Tomasz Ruman

OŚWIADCZENIE

Jako współautor publikacji wchodzących w skład rozprawy doktorskiej Pani mgr inż. Sumi Krupy, oświadczam, że mój wkład w powstanie poszczególnych publikacji przedstawia się następująco:

[P1] J. Nizioł, S. Krupa, W. Szuberla, **T. Ruman,** Advances in metallic nanostructures-assisted laser desorption/ionization mass spectrometry imaging of biological samples: A review, *Analytica Chimica Acta,* 2025, 1366, 344256

Mój wkład w powstanie tej publikacji obejmował udział w redakcji ostatecznej wersji manuskryptu. Mój udział w powstaniu publikacji oceniam na 10%.

[P2] A. Płaza-Altamer, A. Kołodziej, S. Krupa, J. Nizioł, **T. Ruman**, Infrared pulsed fiber laser-produced gold and silver-109 nanoparticles for laser desorption/ionization mass spectrometry of steroid hormones, *Rapid Communications in Mass Spectrometry*, 2023, 37, e9621

Mój wkład w powstanie tej publikacji obejmował współudział w opracowaniu koncepcji pracy oraz metodyki badań, nadzór naukowy nad realizacją badań, udział w interpretacji uzyskanych wyników, udział w redakcji manuskryptu, w tym odniesienie się do uwag recenzentów oraz współudział w opracowaniu ostatecznej wersji publikacji. Mój udział w powstaniu publikacji oceniam na 20%.

[P4] J. Nizioł, M. Misiorek, S. Krupa, **T. Ruman**, Infrared Laser-Based Selected Reaction Monitoring Mass Spectrometry Imaging of Banana (*Musa spp.*) Tissue—New Method for Detection and Spatial Localization of Metabolites in Food, *Food Analytical Methods*, 2023, 17, 236-250

Mój wkład w powstanie tej publikacji obejmował współudział w opracowaniu koncepcji pracy oraz metodyki badań, wykonanie analiz z wykorzystaniem techniki LARESI-SRM-MSI i pomiarów UHPLC-HRMS, a także udział w redakcji manuskryptu oraz opracowaniu jego ostatecznej wersji. Mój udział w powstaniu publikacji oceniam na 25%.

[P5] **T. Ruman**, S. Krupa, J. Nizioł Direct Three-Dimensional Mass Spectrometry Imaging with Laser Ablation Remote Atmospheric Pressure Photoionization/Chemical Ionization, *Analytical Chemistry,* 2024, 96, 13326-13334

Mój wkład w powstanie tej publikacji obejmował opracowanie koncepcji pracy oraz metodyki badań, autorstwo konstrukcji systemu LARAPPI/CI, kierowanie badaniami związanymi z optymalizacją i walidacją tego układu, nadzór nad pomiarami wykonywanymi z jego wykorzystaniem, przygotowanie pierwszej wersji manuskryptu, pełnienie funkcji autora korespondencyjnego, w tym opracowanie odpowiedzi na recenzje, a także nadzór naukowy nad realizacją pracy. Mój udział w powstaniu publikacji oceniam na 33,3%.

[P6] S. Krupa, W. Szuberla, J. Nizioł, A. Ossolińska, K. Ossoliński, **T. Ruman**, Broadband collision-induced dissociation mass spectrometry imaging, *Journal of the American Society for Mass Spectrometry,* 2025, 36, 1443-1455

Mój wkład w powstanie tej publikacji obejmował opracowanie koncepcji pracy oraz metodyki badań, kierowanie badaniami nad optymalizacją i walidacją metody, nadzór nad pomiarami wykonywanymi z wykorzystaniem systemu LARAPPI/CI, sprawowanie nadzoru naukowego nad realizacją pracy, przygotowanie pierwszej wersji manuskryptu oraz udział w opracowaniu jego wersji ostatecznej. Mój udział w powstaniu publikacji oceniam na 35%

[P7] J. Szulc, T. Grzyb, J. Nizioł, S. Krupa, W. Szuberla, **T. Ruman**, Direct 3D Mass Spectrometry Imaging Analysis of Environmental Microorganisms, *Molecules*, 2025, 30, 1317

Mój wkład w powstanie tej publikacji obejmował współudział w opracowaniu koncepcji pracy i metodyki badań, nadzór nad pomiarami wykonywanymi z wykorzystaniem techniki LARAPPI/CI-2D/3D-MSI, prowadzenie części badań z wykorzystaniem UHPLC-HRMS obejmujące opracowanie metody pomiarowej oraz wstępne przygotowanie danych do analizy statystycznej, udział w interpretacji uzyskanych wyników, sprawowanie nadzoru naukowego nad realizacją badań, udział w redakcji manuskryptu, w tym w przygotowaniu odpowiedzi na recenzje i opracowaniu jego ostatecznej wersji. Mój udział w powstaniu publikacji oceniam na 15%.

[P8] S. Krupa, **T. Ruman,** J. Nizioł, Metabolic Impact of Pesticides on Radish: 2D and 3D Mass Spectrometry Imaging of Metabolites in *Raphanus sativus, Journal of Agricultural and Food Chemistry,* 2025, 73, 29229-29244

Mój wkład w powstanie tej publikacji obejmował współudział w opracowaniu metodyki badań, sprawowanie nadzoru nad pomiarami wykonywanymi z wykorzystaniem techniki LARAPPI/CI-2D/3D-MSI, prowadzenie części badań z wykorzystaniem UHPLC-HRMS, w tym opracowanie metody pomiarowej oraz wstępne przygotowanie danych do analizy statystycznej, a także udział w redakcji ostatecznej wersji manuskryptu. Mój udział w powstaniu publikacji oceniam na 20%

POLITECHNIKA
RZESZOWSKA
im. IGNACEGO ŁUKASIEWICZA

al. Powstańców Warszawy 12, 35-029 Rzeszów
tel.: +48 17 865 1100, e-mail: kancelaria@prz.edu.pl
prz.edu.pl

[P9] S. Krupa, **T. Ruman**, W. Szuberla, J. Nizioł Analysis of the spatial distribution of metabolites in *Aloe vera* leaves by mass spectrometry imaging and UHPLC-HRMS, *Scientific Reports*, 2025, 15, 3502

Mój wkład w powstanie tej publikacji obejmował współudział w opracowaniu metodyki badań, nadzór nad pomiarami wykonywanymi z wykorzystaniem techniki LARAPPI/CI-MSI, prowadzenie części badań z wykorzystaniem UHPLC-HRMS, w tym opracowanie metody pomiarowej oraz wstępne przygotowanie danych do analizy statystycznej, udział w redakcji ostatecznej wersji manuskryptu oraz pozyskanie finansowania części badań związanych z analizą UHPLC-HRMS ze środków programu Regionalna Inicjatywa Doskonałości finansowanego przez Ministerstwo Nauki i Szkolnictwa Wyższego na podstawie umowy nr RID/SP/0032/2024/01. Mój udział w powstaniu publikacji oceniam na 10%.

T. Ruman
....

Politechnika Łódzka
Katedra Biotechnologii Środowiskowej

dr hab. inż. Justyna Szulc, prof. PŁ

Politechnika Łódzka
Wydział Biotechnologii i Nauk o Żywności
ul. Wólczańska 171/173, 90-924 Łódź

Łódź, 27.04.2026 r.

OŚWIADCZENIE

Jako współautorka następującej publikacji:

[P7] **J. Szulc**, T. Grzyb, J. Nizioł, **S.** Krupa, W. Szuberla, T. Ruman, Direct 3D Mass Spectrometry Imaging Analysis of Environmental Microorganisms, *Molecules*, 2025, 30, 1317

wchodzącej w skład rozprawy doktorskiej mgr inż. Sumi Krupy, oświadczam, że mój wkład obejmował opracowanie koncepcji i metodologii badań mikrobiologicznych, pozyskanie materiału biologicznego, nadzór nad hodowlą drobnoustrojów oraz przygotowaniem próbek do analiz, a także udział w przygotowaniu pierwotnej wersji manuskryptu, jego redakcji oraz nadzorze merytorycznym. Część badań związana z hodowlą mikrobiologiczną stanowiła rezultat prac realizowanych w ramach grantu nr 00077.DDD.6509.000167.2022.05, pozyskanego przeze mnie i finansowanego przez Agencję Restrukturyzacji i Modernizacji Rolnictwa. Mój udział w powstaniu publikacji oceniam na 30%.

Justyna Szulc
....

Politechnika Łódzka
Katedra Biotechnologii Środowiskowej

mgr Tomasz Grzyb

Politechnika Łódzka
Wydział Biotechnologii i Nauk o Żywności
ul. Wólczańska 171/173, 90-924 Łódź

Łódź, 27.04.2026 r.

OŚWIADCZENIE

Jako współautor następującej publikacji:

[P7] J. Szulc, **T. Grzyb**, J. Nizioł, S. Krupa, W. Szuberla, T. Ruman, Direct 3D Mass Spectrometry Imaging Analysis of Environmental Microorganisms, *Molecules*, 2025, 30, 1317

wchodzącej w skład rozprawy doktorskiej mgr inż. Sumi Krupy, oświadczam, że mój wkład obejmował przygotowanie pierwotnej wersji manuskryptu, udział w redakcji publikacji oraz wizualizacji wyników. Pełniłem również funkcję autora korespondencyjnego publikacji. Mój udział w powstaniu publikacji oceniam na 20%.

Tomasz Grzyb
....

Kolbuszowa, 31.03.2026 r.

lek. Anna Ossolińska

Samodzielny Publiczny Zakład Opieki Zdrowotnej w Kolbuszowej
Oddział Urologii Ogólnej i Onkologicznej
ul. Grunwaldzka 4, 36-100 Kolbuszowa

OŚWIADCZENIE

Jako współautorka następującej publikacji:

[P6] S. Krupa, W. Szuberla, J. Nizioł, **A. Ossolińska**, K. Ossoliński, T. Ruman, Broadband collision-induced dissociation mass spectrometry imaging, *Journal of the American Society for Mass Spectrometry,* 2025, 36, 1443-1455

wchodzącej w skład rozprawy doktorskiej mgr inż. Sumi Krupy, oświadczam, że mój wkład polegał na pozyskaniu materiału biologicznego od pacjentów oraz udziale w opracowaniu danych klinicznych i histopatologicznych dotyczących badanych przypadków. Mój udział w powstaniu publikacji oceniam na 5%.

Anna Ossolińska
specjalista urolog FEBU
2960223

....

Kolbuszowa, 31.03.2026 r.

dr n. med. Krzysztof Ossoliński

Samodzielny Publiczny Zakład Opieki Zdrowotnej w Kolbuszowej
Oddział Urologii Ogólnej i Onkologicznej
ul. Grunwaldzka 4, 36-100 Kolbuszowa

OŚWIADCZENIE

Jako współautor następującej publikacji:

[P6] S. Krupa, W. Szuberla, J. Nizioł, A. Ossolińska, **K. Ossoliński**, T. Ruman, Broadband collision-induced dissociation mass spectrometry imaging, *Journal of the American Society for Mass Spectrometry,* 2025, 36, 1443-1455

wchodzącej w skład rozprawy doktorskiej mgr inż. Sumi Krupy, oświadczam, że mój wkład polegał na pozyskaniu materiału biologicznego od pacjentów oraz udziale w opracowaniu danych klinicznych i histopatologicznych dotyczących badanych przypadków. Mój udział w powstaniu publikacji oceniam na 5%.

Krzysztof Ossoliński
....

POLITECHNIKA RZESZOWSKA
im. IGNACEGO ŁUKASIEWICZA

al. Powstańców Warszawy 12, 35-029 Rzeszów
tel.: +48 17 865 1100, e-mail: kancelaria@prz.edu.pl
prz.edu.pl

Rzeszów, 01.04.2026 r.

mgr inż. Wiktoria Szuberla

OŚWIADCZENIE

Jako współautorka publikacji wchodzących w skład rozprawy doktorskiej Pani mgr inż. Sumi Krupy, oświadczam, że mój wkład w powstanie poszczególnych publikacji przedstawia się następująco:

[P1] J. Nizioł, S. Krupa, **W. Szuberla**, T. Ruman, Advances in metallic nanostructures-assisted laser desorption/ionization mass spectrometry imaging of biological samples: A review, *Analytica Chimica Acta*, 2025, 1366, 344256

Mój wkład w powstanie tej publikacji obejmował udział w przeglądzie źródeł literaturowych oraz opracowaniu części materiału wykorzystanego w publikacji. Mój udział w powstaniu publikacji oceniam na 5%.

[P6] S. Krupa, **W. Szuberla**, J. Nizioł, A. Ossolińska, K. Ossoliński, T. Ruman, Broadband collision-induced dissociation mass spectrometry imaging, *Journal of the American Society for Mass Spectrometry,* 2025, 36, 1443-1455

Mój wkład w powstanie tej publikacji obejmował analizę części danych uzyskanych w analizach LARAPPI/CI-MSI oraz udział w pracowaniu części teoretycznej manuskryptu. Mój udział w powstaniu publikacji oceniam na 5%.

[P7] J. Szulc, T. Grzyb, J. Nizioł, S. Krupa, **W. Szuberla**, T. Ruman, Direct 3D Mass Spectrometry Imaging Analysis of Environmental Microorganisms, *Molecules*, 2025, 30, 1317

Mój wkład w powstanie tej publikacji obejmował udział w pracach eksperymentalnych oraz udział w opracowaniu części teoretycznej manuskryptu. Mój udział w powstaniu publikacji oceniam na 5%.

[P9] S. Krupa, T. Ruman, **W. Szuberla**, J. Nizioł Analysis of the spatial distribution of metabolites in *Aloe vera* leaves by mass spectrometry imaging and UHPLC-HRMS, *Scientific Reports*, 2025, 15, 3502

Mój wkład w powstanie tej publikacji obejmował analizę części danych uzyskanych w analizach LARAPPI/CI-MSI oraz udział w opracowaniu części teoretycznej manuskryptu. Mój udział w powstaniu publikacji oceniam na 5%.

Szuberla Wiktoria
....

POLITECHNIKA
RZESZOWSKA
im. IGNACEGO ŁUKASIEWICZA

al. Powstańców Warszawy 12, 35-029 Rzeszów
tel.: +48 17 865 1100, e-mail: kancelaria@prz.edu.pl
prz.edu.pl

Rzeszów, 31.03.2026 r.

dr inż. Artur Kołodziej

OŚWIADCZENIE

Jako współautor następującej publikacji:

[P2] A. Płaza-Altamer, **A. Kołodziej**, S. Krupa, J. Nizioł, T. Ruman, Infrared pulsed fiber laser-produced gold and silver-109 nanoparticles for laser desorption/ionization mass spectrometry of steroid hormones, *Rapid Communications in Mass Spectrometry*, 2023, 37, e9621

wchodzącej w skład rozprawy doktorskiej mgr inż. Sumi Krupy, oświadczam, że mój wkład w powstanie tej publikacji obejmował przeprowadzenie syntezy nanocząstek srebra-109 oraz złota metodą LASiS oraz udział w opracowaniu danych wykorzystanych w publikacji. Mój udział w powstaniu publikacji oceniam na 20%.

Kołodziej Artur
....

WYDZIAŁ
CHEMICZNY
POLITECHNIKI RZESZOWSKIEJ

al. Powstańców Warszawy 6, 35-029 Rzeszów
tel.: +48 17 865 1652, e-mail: chemia@prz.edu.pl
wch.prz.edu.pl

POLITECHNIKA
RZESZOWSKA
im. IGNACEGO ŁUKASIEWICZA

al. Powstańców Warszawy 12, 35-029 Rzeszów
tel.: +48 17 865 1100, e-mail: kancelaria@prz.edu.pl
prz.edu.pl

Rzeszów, 31.03.2026 r.

dr inż. Aneta Płaza-Altamer

OŚWIADCZENIE

Jako współautorka następującej publikacji:

[P2] **A. Płaza-Altamer**, A. Kołodziej, S. Krupa, J. Nizioł, T. Ruman, Infrared pulsed fiber laser-produced gold and silver-109 nanoparticles for laser desorption/ionization mass spectrometry of steroid hormones, *Rapid Communications in Mass Spectrometry*, 2023, 37, e9621

wchodzącej w skład rozprawy doktorskiej mgr inż. Sumi Krupy, oświadczam, że mój wkład w powstanie tej publikacji obejmował współudział w opracowaniu metodyki badań, przygotowaniu próbek do analiz, wykonanie pomiarów z wykorzystaniem ^{109}AgNPs-LDI-MS przy użyciu spektrometru MALDI-ToF/ToF, opracowanie i interpretację uzyskanych widm masowych, przeprowadzenie formalnej analizy danych, opracowanie graficzne wyników, przygotowanie pierwotnej wersji manuskryptu, pełnienie funkcji autora korespondencyjnego oraz udział w opracowaniu odpowiedzi na recenzje i redakcji ostatecznej wersji manuskryptu. Mój udział w powstaniu publikacji oceniam na 20%.

Aneta Płaza-Altamer
....

POLITECHNIKA
RZESZOWSKA
im. IGNACEGO ŁUKASIEWICZA

al. Powstańców Warszawy 12, 35-029 Rzeszów
tel.: +48 17 865 1100, e-mail: kancelaria@prz.edu.pl
prz.edu.pl

Rzeszów, 31.03.2026 r.

dr Maria Misiorek

OŚWIADCZENIE

Jako współautorka następującej publikacji:

[P4] J. Nizioł, **M. Misiorek**, S. Krupa, T. Ruman, Infrared Laser-Based Selected Reaction Monitoring Mass Spectrometry Imaging of Banana (*Musa spp.*) Tissue—New Method for Detection and Spatial Localization of Metabolites in Food, Food Analytical Methods, 2023, 17, 236-250

wchodzącej w skład rozprawy doktorskiej mgr inż. Sumi Krupy, oświadczam, że mój wkład obejmował współudział w opracowaniu koncepcji badań, pozyskanie materiału roślinnego do badań, przygotowanie ekstraktów do analizy UHPLC-HRMS. Mój udział w powstaniu publikacji oceniam na 25%.

Maria Misiorek